ASME
SETTING THE STANDARD

Editor, **YOGESH JALURIA** (2010)
Assistant to the Editor, **S. PATEL**

Associate Editors
Gautam Biswas, Indian Inst. of Tech., Kanpur (2009)
Louis C. Burmeister, Univ. of Kansas (2008)
Minking Chyu, Univ. of Pittsburgh (2009)
Suresh V. Garimella, Purdue Univ. (2007)
A. Haji-Sheikh, Univ. of Texas at Arlington (2008)
Anthony M. Jacobi, Univ. of Illinois (2008)
Yogendra Joshi, Georgia Inst. of Tech. (2008)
Satish G. Kandlikar, Rochester Inst. of Tech. (2007)
Jay M. Khodadadi, Auburn Univ. (2007)
Sai C. Lau, Texas A&M Univ. (2009)
Ben Q. Li, Univ. of Michigan, Dearborn (2009)
Raj M. Manglik, Univ. of Cincinnati (2009)
Chang H. Oh, Idaho National Lab. (2007)
Ranga Pitchumani, Univ. of Connecticut (2007)
Ramendra P. Roy, Arizona State Univ. (2007)
Jamal Seyed-Yagoobi, Illinois Inst. of Tech. (2009)
Bengt Sunden, Lund Inst. of Tech., Sweden (2008)
Walter W. Yuen, Univ. of California–Santa Barbara (2008)

Past Editors
V. DHIR
J. R. HOWELL
R. VISKANTA
G. M. FAETH
K. T. YANG
E. M. SPARROW

HEAT TRANSFER DIVISION
Chair, **RODNEY DOUGLASS**
Vice Chair, **TIM TONG**
Past Chair, **MICHAEL JENSEN**

PUBLICATIONS COMMITTEE
Chair, **BAHRAM RAVANI**

OFFICERS OF THE ASME
President, **SAM Y. ZAMRIK**
Executive Director,
VIRGIL R. CARTER
Treasurer,
THOMAS D. PESTORIUS

PUBLISHING STAFF
Managing Director, Publishing
PHILIP DI VIETRO
Manager, Journals
COLIN McATEER
Production Coordinator
JUDITH SIERANT
Production Assistant
MARISOL ANDINO

Transactions of the ASME, Journal of Heat Transfer (ISSN 0022-1481) is published monthly by The American Society of Mechanical Engineers, Three Park Avenue, New York, NY 10016. Periodicals postage paid at New York, NY and additional mailing offices. POSTMASTER: Send address changes to Transactions of the ASME, Journal of Heat Transfer, c/o THE AMERICAN SOCIETY OF MECHANICAL ENGINEERS, 22 Law Drive, Box 2300, Fairfield, NJ 07007-2300. **CHANGES OF ADDRESS** must be received at Society headquarters seven weeks before they are to be effective. Please send old label and new address.
STATEMENT from By-Laws. The Society shall not be responsible for statements or opinions advanced in papers or ... printed in its publications (B7.1, Para. 3). **COPYRIGHT © 2007** by The American Society of Mechanical Engineers. For authorization to photocopy material for internal or personal use under those circumstances not falling within the fair use provisions of the Copyright Act, contact the Copyright Clearance Center (CCC), 222 Rosewood Drive, Danvers, MA 01923, tel: 978-750-8400, www.copyright.com. Request for special permission or bulk copying should be addressed to Reprints/Permission Department. Canadian Goods & Services Tax Registration #126148048

Journal of Heat Transfer

Published Monthly by ASME

VOLUME 129 • NUMBER 7 • JULY 2007

TECHNICAL PAPERS

(Contents continued on inside back cover)

This journal is printed on acid-free paper, which exceeds the ANSI Z39.48-1992 specification for permanence of paper and library materials. ♾™
♻ 85% recycled content, including 10% post-consumer fibers.

Journal of Heat Transfer Volume 129, Number 7 JULY 2007

Heat Exchangers

TECHNICAL BRIEFS

DISCUSSION

The ASME Journal of Heat Transfer is abstracted and indexed in the following:

Applied Science and Technology Index, Chemical Abstracts, Chemical Engineering and Biotechnology Abstracts (Electronic equivalent of Process and Chemical Engineering), Civil Engineering Abstracts, Compendex (The electronic equivalent of Engineering Index), Corrosion Abstracts, Current Contents, E & P Health, Safety, and Environment, Ei EncompassLit, Engineered Materials Abstracts, Engineering Index, Enviroline (The electronic equivalent of Environment Abstracts), Environment Abstracts, Environmental Engineering Abstracts, Environmental Science and Pollution Management, Fluidex, Fuel and Energy Abstracts, Index to Scientific Reviews, INSPEC, International Building Services Abstracts, Mechanical & Transportation Engineering Abstracts, Mechanical Engineering Abstracts, METADEX (The electronic equivalent of Metals Abstracts and Alloys Index), Petroleum Abstracts, Process and Chemical Engineering, Referativnyi Zhurnal, Science Citation Index, SciSearch (The electronic equivalent of Science Citation Index), Theoretical Chemical Engineering

Direct Numerical Simulation of Heat Transfer in Converging–Diverging Wavy Channels

E. Stalio[1]
Dipartimento di Ingegneria Meccanica e Civile,
Università degli Studi di Modena
e Reggio Emilia,
via Vignolese 905/b,
41100 Modena, Italy
e-mail: enrico.stalio@unimore.it

M. Piller
Dipartimento di Ingegneria Civile e Ambientale,
Università degli Studi di Trieste,
Sezione Georisorse e Ambiente,
via A. Valerio 10,
34127 Trieste, Italy
e-mail: piller@units.it

Corrugated walls are widely used as passive devices for heat and mass transfer enhancement; they are most effective when operated at transitional and turbulent Reynolds numbers. In the present study, direct numerical simulation is used to investigate the unsteady forced convection in sinusoidal, symmetric wavy channels. A novel numerical method is employed for the simulations; it is meant for fully developed flows in periodic ducts of prescribed wall temperature. The algorithm is free of iterative procedures; it accounts for the effects of streamwise diffusion and can be used for unsteady problems. Results of two simulations in the transitional regime for Reynolds numbers based on average duct height and average velocity of Re=481 *and* Re=872 *are reported. Time averaged and instantaneous velocity and temperature fields together with second-order statistics are interpreted in order to describe the mechanism associated with heat transfer augmentation. Heat flux distributions locate the most active areas in heat transfer and reveal the effects of convective mixing. Slanted traveling waves of high temperature are identified; peak values of Nusselt number are attained when the high-temperature fluid of the waves reaches the converging walls.* [DOI: 10.1115/1.2717235]

Keywords: forced convection, streamwise periodic ducts, uniform wall temperature, axial diffusion, heat transfer enhancement, wavy walls

1 Introduction

The use of corrugated channels is one of the passive techniques that can enhance heat and mass transfer by increasing turbulent mixing; wavy walls are commonly used for application in medical devices and in compact heat exchangers [1,2]. Since in gas–liquid heat exchangers, the heat transfer resistance at the liquid side is usually small in comparison with that at the gas side, the latter is the main target of this study.

A significant body of research on flow and heat transfer in wavy channels of different configurations is available in the literature; the following literature review is restricted to the investigations in sinusoidal, symmetric wavy channels. The experimental investigation by Nishimura et al. [3] elucidates the main features of fluid flow in wavy ducts; they point out the presence of a circulation region at $Re > 15$ and the onset of unsteady vortex motion and turbulent flow features about a Reynolds number, Re=350. The location of separation and reattachment points, the friction factor, and the wall shear stress distribution, are provided for a wide range of Reynolds numbers, in the laminar and fully turbulent regime.

Guzmán and Amon [4,5] study the transition from laminar to chaotic flow in wavy ducts of the same geometry through the use of a spectral element method. The transition to chaos in converging–diverging channels occurs through a sequence of intermediate states of self-sustained periodic, quasi-periodic, and finally aperiodic or chaotic regimes.

While the studies cited so far are limited to the analysis of the fluid flow, mass transfer rates between two sinusoidal wavy plates placed symmetrically about the flow axis are measured by Nishimura and co-workers [6]; the restart of the concentration boundary layer gives place to a mass transfer enhancement which is larger in the turbulent regime. Developing flow and heat transfer is described in an experimental work by Rush et al. [7]; they examine the effect of changes in phase angle, amplitude of the passage, and wavelength of the wavy surfaces on the local Nusselt number.

To the authors' knowledge, all the previous numerical investigations of convective heat transfer in converging–diverging wavy channels adopt a two-dimensional approach. Results of two-dimensional numerical studies that do not use turbulence models are limited to the laminar regime. Wang et al. [8] and Ničeno et al. [9] report on fully developed convective heat transfer in an unsteady, laminar regime in wavy channels of the same geometry as the experiments by Nishimura et al. [3]. Stone et al. [10] and Bahaidarah et al. [11] focus on developing flow and heat transfer. The effects of variations in geometrical parameters on heat transfer in an unsteady, laminar regime is addressed by Hossain et al. [12].

Corrugated channels are an effective heat transfer device only at transitional and turbulent Reynolds numbers [13,14]. In the currently available numerical studies that examine turbulent convection in similar geometries [15], turbulence is modeled. The use of turbulence models does not allow for a detailed description of the three-dimensional, time-dependent phenomena of forced convection in corrugated ducts while, as Jacobi and Shah stated [2], new enhanced surfaces for compact heat exchangers can only be conceived starting from a clear understanding of the flow and the mechanism associated with heat transfer augmentation.

In order to extend the current understanding of the heat transfer enhancing mechanism in conditions close to applications, a three-dimensional, time-dependent numerical study of heat transfer in symmetric wavy-walled channels is presented in this paper. The investigation focuses upon a constant property fluid with Prandtl number Pr=0.7, which is representative of air. The two cases con-

[1]Corresponding author.

Contributed by the Heat Transfer Division of ASME for publication in JOURNAL OF HEAT TRANSFER. Manuscript received March 25, 2006; final manuscript received August 5, 2006. Review conducted by Gautam Biswas.

 Copyright © 2007 by ASME

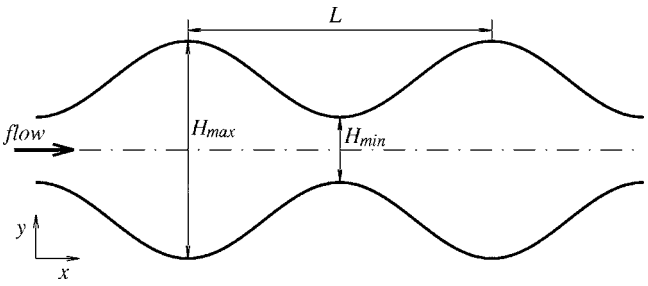

Fig. 1 Geometry of the problem, longitudinal view

sidered have Reynolds numbers of Re=481 and Re=872; they fall, respectively, in the range of the quasiperiodic and chaotic regime described by Guzmán and Amon [4].

Heat transfer statistics are reported to locate the areas of stronger mixing and to determine the main features of convection in different regimes. The heat transfer mechanism is investigated through the observation of temperature patterns in instants of relative maximum and minimum Nusselt number.

Larger mechanical pumping power compared to the channel flow at a given flow rate is required to induce heat transfer enhancement by turbulent[2] mixing in wavy channels. Accurate calculations of both friction factor and Nusselt number are reported to provide information on the performance of the symmetric sinusoidal passages.

A major contribution of the present study is in the new numerical algorithm for the simulation of fully developed turbulent convection in ducts of uniform wall temperature. The proposed technique descends from the analysis of Patankar et al. [16]. It uses the same form of the equations as in the work by Greiner et al. [17] but it is not limited to the use for steady or time-periodic flows. Moreover, in contrast with the methods usually adopted in the unsteady cases, like the one described by Wang et al. [8], and also in contrast with the algorithms cited above [16,17], the proposed technique is free of iterative strategy, ensuring a considerable economy of computational effort.

2 Computational Domain

A longitudinal view of the domain geometry is shown in Fig. 1, together with the coordinate system. The ratio between maximum and minimum channel height is $H_{\max}/H_{\min}=10/3$, while the periodic length is $L/H_{\min}=14/3$ in all computations; the domain is homogeneous in the spanwise direction z. This three-dimensional configuration corresponds to the one considered in the experimental work by Nishimura et al. [3] and the two-dimensional numerical studies of Wang et al. [8] and Ničeno and Nobile [9].

The size of the domain and the number of grid points for the two cases reported are given in Table 1, where the reference length scale δ corresponds to half of the maximum duct height. The adequacy of the computational domain size in spanwise direction is confirmed by the autocorrelation function of the velocity fluctuations, that substantially vanishes within the half-domain length. Along the x direction, simulations are performed over one periodicity L after which the flow and temperature patterns repeat themselves; the periodic assumption is deemed to provide a reasonable model for understanding the fundamental processes that govern heat transfer in symmetric wavy channels. A detail of the 129×129 computational mesh in the x-y plane over the sinusoidal waves is illustrated in Fig. 2.

[2]In order to avoid clumsy turns of phrases, expressions like "turbulent mixing," "turbulent fluxes," "turbulent stress" will be used in the present discussion, even though the cases considered belong to the transitional regime and the use of the term "turbulent" in this context may not be appropriate.

Table 1 Parameters for the simulations

Re	L/δ	L_z/δ	$N_x\times N_y\times N_z$
872	2.8	2.0	$129\times129\times65$
481	2.8	1.0	$65\times129\times33$

3 Formulation and Numerical Methods

3.1 Momentum Equations. The momentum equations are set in dimensionless form using δ as a reference quantity for spatial coordinates, the friction velocity $u_\tau=(\beta\delta/\rho)^{1/2}$ for velocities, and $t_{\text{ref}}=\delta/u_\tau$ for time. In the definition of the friction velocity, β is the constant pressure drop imposed in the x direction along one periodicity, divided by L

$$\frac{\bar{P}(x,y,z)-\bar{P}(x+L,y,z)}{L}=\beta \tag{1}$$

where the bar denotes time averaging. The pressure field P is subdivided into a linear and an unsteady, periodic contributions

$$P(x,y,z,t)=-\beta x+p(x,y,z,t) \tag{2}$$

where periodic boundary conditions are assigned to the pressure fluctuation p in the streamwise direction. The conservation equations for mass and momentum in dimensionless form result in

$$\nabla\cdot\mathbf{u}=0 \tag{3}$$

$$\frac{\partial\mathbf{u}}{\partial t}+\nabla\cdot(\mathbf{uu})=-\nabla p+\frac{1}{\mathrm{Re}_\tau}\nabla^2\mathbf{u}+\mathbf{b} \tag{4}$$

where $\mathbf{b}$ is the unit vector in the x direction since in the nondimensional form, $\beta=1$; Re_τ is the friction Reynolds number; and $\mathrm{Re}_\tau=u_\tau\delta/\nu$. No-slip boundary conditions are enforced at the sinusoidal walls, and periodicity is set in the homogeneous spanwise direction and in the streamwise direction.

3.2 Energy Equation. In this Subsection we present a novel technique for the numerical simulation of time-dependent, fully developed temperature fields with uniform temperature boundary conditions. For clarity, the numerical method is described at first for ducts having uniform cross section; the extension to ducts with periodic variations of cross-sectional area is provided in Sec. 3.2.2.

3.2.1 Uniform Temperature Boundary Conditions in a Flat Channel. The proposed technique descends from the analysis of Patankar et al. [16]. It uses the same form of the energy equation as used by Greiner et al. [17] but it has the characteristic of avoid-

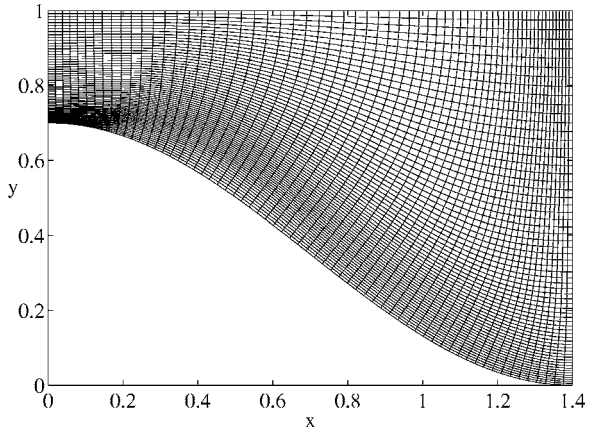

Fig. 2 Detail of the orthogonal grid

ing any iterative procedure to compute the temperature field together with the temperature decay rate λ, the latter being determined through an energy balance.

The definition of thermally developed flow expresses the fact that the shapes of the time-averaged temperature profiles at successive streamwise locations are self-similar

$$\frac{\partial}{\partial x}\left[\frac{\bar{T}(x,y)-\bar{T}_w(x)}{\bar{T}_b(x)-\bar{T}_w(x)}\right]=0 \tag{5}$$

where the bulk temperature is defined as $T_b(x)=u_m^{-1}\int_A uTdA$, and the dash indicates time averaged quantities. For channel flow in fully developed conditions and prescribed wall temperature, the temperature difference, $\bar{T}-T_w$, decays exponentially with the streamwise coordinate; this is usually demonstrated using an energy balance equation where the axial diffusion contribution is neglected. Such hypothesis is unnecessary and the effects of axial diffusion, which might play a role in the low Péclet cases, can also be included in the simulations.

The energy balance equation in the unit spanwise length of a fully developed turbulent flat channel is given by

$$Hu_m\frac{d\bar{T}_b}{dx}=2\alpha\frac{\partial\bar{T}}{\partial\eta}+H\alpha\frac{d^2\bar{T}_m}{dx^2} \tag{6}$$

where η is the coordinate normal to the wall pointing outward; α is the thermal diffusivity of the fluid ($\alpha=k/\rho c$); and the last term on the right side accounts for the streamwise diffusion. For the case of uniform wall temperature, the energy balance can be cast in terms of the temperature difference $\varphi=T-T_w$ using condition (5)

$$H\frac{\bar{\varphi}_m}{\bar{\varphi}_b}\alpha\frac{d^2\bar{\varphi}_b}{dx^2}-Hu_m\frac{d\bar{\varphi}_b}{dx}+2\alpha\frac{d}{d\eta}\left(\frac{\bar{\varphi}}{\bar{\varphi}_b}\right)\bar{\varphi}_b=0 \tag{7}$$

Both $\bar{\varphi}/\bar{\varphi}_b$ and $\bar{\varphi}_m/\bar{\varphi}_b$ are independent of x; the energy balance Eq. (7) is a linear, homogeneous, second-order differential equation in $\bar{\varphi}_b$, with coefficients

$$a_2=H\frac{\bar{\varphi}_m}{\bar{\varphi}_b}\alpha;\quad a_1=-Hu_m;\quad a_0=2\alpha\frac{d}{d\eta}\left(\frac{\bar{\varphi}}{\bar{\varphi}_b}\right) \tag{8}$$

Since a_0 is negative and zero only in the case of uniform temperature fluid, the characteristic equation has two real roots, $\kappa_1<0$ and $\kappa_2>0$; it follows from physical considerations that the solution to Eq. (7) is in the form: $\bar{\varphi}_b(x_0)e^{\kappa_1(x-x_0)}$. In fully developed conditions with prescribed wall temperature, the time-averaged temperature field also decays exponentially in the streamwise direction when axial diffusion is included. A positive constant λ representing the temperature decay rate is defined as

$$\lambda=-\frac{\frac{d}{dx}[\bar{T}_b(x)-T_w]}{[\bar{T}_b(x)-T_w]} \tag{9}$$

it is straightforward to recognize that $\lambda=-\kappa_1$. The streamwise variation of the mean temperature profiles is

$$\bar{T}(x,y)=\bar{T}(x_0,y)e^{-\lambda(x-x_0)} \tag{10}$$

where T_w is set to zero for simplicity. It is then possible to define a normalized temperature θ whose averaged value $\bar{\theta}$ does not depend on x

$$\theta(x,y,z,t)=\frac{T(x,y,z,t)}{e^{-\lambda x}} \tag{11}$$

Unlike the temperature T, periodic boundary conditions can be imposed on the normalized temperature θ in the streamwise direction, and this new variable is better suited for being computed in direct numerical simulations of turbulent convection in ducts. The energy equation with no heat sources nor sinks, neglecting viscous dissipation and assuming constant thermophysical properties, is given by

$$\frac{\partial T}{\partial t}+\nabla\cdot(\mathbf{u}T)=\alpha\nabla^2T \tag{12}$$

substitution of Eq. (11) into the energy Eq. (12) yields

$$\frac{\partial\theta}{\partial t}+\nabla\cdot(\mathbf{u}\theta)=\alpha\nabla^2\theta+(\alpha\lambda^2+u\lambda)\theta-2\alpha\lambda\frac{\partial\theta}{\partial x} \tag{13}$$

The time-dependent simulation of fully developed flow and heat transfer in a conventional duct with uniform temperature walls is therefore reduced to the calculation of the temperature decay rate λ and the solution of the transport Eq. (13) for the streamwise periodic variable θ. In the solution algorithm, λ is computed at every time step from Eq. (14) with the coefficients a_i being determined from their expressions (8) through the use of moving averages

$$\lambda=\frac{a_1+\sqrt{a_1^2-4a_2a_0}}{2a_2} \tag{14}$$

Only few generalizations have to be accomplished for the application of this method to ducts having streamwise periodic variations of the cross section.

3.2.2 Extension to Periodic Ducts. In this section, the technique for dealing with uniform temperature walls is extended in order to account for periodic, streamwise variations of the cross-flow area; the proposed technique is valid for time-dependent, fully developed thermal fields. The discussion is limited to domains that are symmetric with respect to a $x-z$ plane, but the adaptation to a more general, periodic geometry is possible.

Following the definition given in Ref. [16], a thermally developed regime in streamwise periodic ducts is characterized by self-similar profiles of temperature at x locations separated by the period length L; in the uniform wall temperature case, this is expressed as

$$\frac{\bar{T}(x,y)-T_w}{\bar{T}_b(x)-T_w}=\frac{\bar{T}(x+L,y)-T_w}{\bar{T}_b(x+L)-T_w} \tag{15}$$

When considering ducts of varying cross section, the temperature decay rate is still defined by Eq. (9) but λ is no longer uniform along x, $\lambda=\lambda(x)$. It can be proved [16] that when the variations in section are periodic along the direction of the flow and for the fully developed regime, λ is periodic; therefore the integral over one periodicity

$$\lambda_L=\frac{1}{L}\int_{x_0}^{x_0+L}\lambda(x)dx \tag{16}$$

is independent of the starting point and λ_L is uniform. It descends from the integration of Eq. (9) in the x direction where T_w is set to zero

$$\bar{T}_b(x+L)=\bar{T}_b(x)e^{-\lambda_L L} \tag{17}$$

that the energy equation can be solved in terms of a new temperature-like variable

$$\theta(x,y,z,t)=\frac{T(x,y,z,t)}{e^{-\lambda_L x}} \tag{18}$$

having the favorable property that its time-averaged value is periodic in the streamwise direction

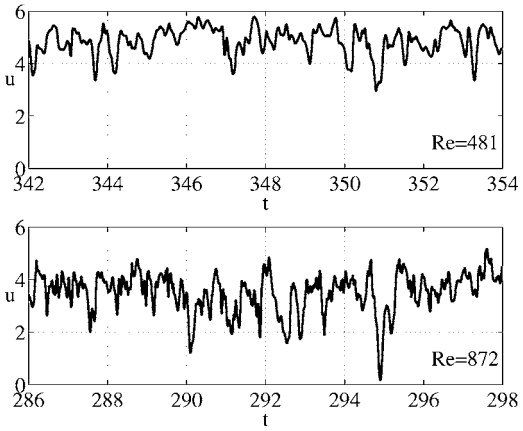

Fig. 3 Time traces of the streamwise component of the velocity vector in the center of the computational domain ($x=L/2, y=H_{max}/2$) for Re=481 and Re=872

$$\bar{\theta}(x,y,t) = \frac{\bar{T}(x,y,t)}{e^{-\lambda_L x}} = \frac{\bar{T}(x+L,y,t)}{e^{-\lambda_L (x+L)}} = \bar{\theta}(x+L,y,t) \tag{19}$$

This property is not restricted to $\bar{T}_b(x,t)/e^{-\lambda_L x}$ since the shapes of temperature profiles at successive streamwise locations at a distance L, are self-similar. The temperature decay rate λ_L can be evaluated from the integration over a periodic module of the time-averaged energy equation. Starting from the energy equation in terms of the periodic temperature

$$\frac{\partial \theta}{\partial t} + \nabla \cdot (\mathbf{u}\theta) = \alpha \nabla^2 \theta + (\alpha \lambda_L^2 + u\lambda_L)\theta - 2\alpha\lambda_L \frac{\partial \theta}{\partial x} \tag{20}$$

the integral energy conservation equation is obtained using the periodicity of θ and $\mathbf{u}$ and the fact that at the walls both $\mathbf{u}$ and θ equal zero

$$0 = \alpha \int_{S_w} \frac{\partial \bar{\theta}}{\partial \eta} dS + \alpha \lambda_L^2 \int_V \bar{\theta}\, dV + \lambda_L L_z \int_0^L H u_m \bar{\theta}_b\, dx \tag{21}$$

Equation (21) is a quadratic equation in λ_L of coefficients

$$b_2 = \alpha \int_V \bar{\theta} dV; \quad b_1 = L_z \int_0^L H u_m \bar{\theta}_b\, dx; \quad b_0 = \alpha \int_{S_w} \frac{\partial \bar{\theta}}{\partial \eta} dS \tag{22}$$

Since b_2 and b_1 are positive, while b_0 is negative, λ_L is evaluated from

$$\lambda_L = \frac{-b_1 + \sqrt{b_1^2 - 4b_2 b_0}}{2b_2} \tag{23}$$

The nondimensional form of the energy equation and the expression for λ are obtained through the same reference quantities as for the momentum equations, together with a reference temperature T_{ref} that can be assumed as the bulk temperature at the inlet of an arbitrary periodic element of the duct.

The second-order finite-volume code used for the simulations does not differ from the one used in a former study of the flow and heat transfer over riblets [18]. The transport equation for θ is solved using standard numerical techniques; periodic boundary conditions are enforced on θ in the streamwise and spanwise directions; and $\theta=0$ is set on the solid walls. The temperature decay rate is evaluated through Eq. (23) at every timestep before advancing in time the temperature Eq. (20). Time averages for the calculation of coefficients Eq. (22) are performed backward for a Δt_a time extent through a moving average.

Table 2 Nondimensional time intervals

Re	Δt_s	Δt_a	Δt
481	100.1	27.0	$1.8\cdot10^{-4}$
872	105.4	42.0	$1.4\cdot10^{-4}$

In the following discussion, the Reynolds number, the Nusselt number, and the friction factor are defined as

$$\mathrm{Re} = \frac{Q_s}{\nu}; \quad \mathrm{Nu} = \frac{2H_{av}h}{k}; \quad f = -\frac{\Delta P}{L}\frac{H_{av}}{2\rho u_{av}^2} \tag{24}$$

where $H_{av}=(H_{max}+H_{min})/2$ and $u_{av}=Q_s/H_{av}$. In the numerical code and in terms of nondimensional quantities, they are evaluated by

$$\mathrm{Re} = \mathrm{Re}_\tau Q_s; \quad \mathrm{Nu} = -\frac{2H_{av}}{(\langle T_b\rangle - T_w)}\frac{\partial \langle T\rangle}{\partial \eta}; \quad f = \frac{H_{av}}{2u_{av}^2} \tag{25}$$

where angular brackets denote a spatial average; while the temperature field is averaged over the three-dimensional domain for obtaining $\langle T\rangle$, the average is performed only in x for $\langle T_b\rangle$. The instantaneous Re, Nu, and f are further integrated in time for obtaining their time-averaged values.

4 Results and discussion

In order to first check the accuracy of the proposed computational procedure, a set of simulations have been performed in the laminar regime at different Reynolds numbers ranging from Re=20 to Re=180. Results are in general agreement with other authors' work for the friction factor [3,9], the reattachment point position [3] and the Nusselt number [8,9]. Since the laminar flow and heat transfer in wavy channels is already well known from the cited literature, results in the laminar regime are reported in the present discussion only for the description of turbulent mixing effects on heat transfer.

As the Reynolds number increases, the laminar flow in wavy channels passes through a transition process becoming periodic, quasiperiodic, and chaotic. Results of two simulations in unsteady regime are presented in the paper: one for a Reynolds number in quasiperiodic range Re=481, and the other in the chaotic range Re=872. The power spectrum of a quasiperiodic dynamical system is characterized by two or three fundamental frequencies and their linear combinations; in the Re=481 simulation, a broadband continuous spectrum appears in the background of the typical quasiperiodic pattern, as commented by Guzmán and Amon [4] with reference to their Re=500 simulation. Accordingly, the quasiperiodic features of the Re=481 time trace displayed in Fig. 3, is superimposed on the broadband noise characteristic of chaos and does not differ substantially from the aperiodic behavior of the Re=872 signal.

In the unsteady regimes, when a statistical steady state is reached, the integration continues in order to achieve statistically stable local and global quantities. In Table 2, the dimensionless time interval for the evaluation of statistics Δt_s, the amplitude of moving averages Δt_a, and timesteps are reported. During the sampling time period Δt_s, a velocity and a temperature fields are stored every $0.2\delta/u_\tau$. The symmetry features of the second-order moments calculated reveal the adequacy of the sampling interval; a longer sampling would not modify the results of the present analysis.

A plot of the instantaneous velocity and temperature fields in the computational volume is shown in Fig. 4 for Re=872. Trajectories of virtual particles and contours of the velocity module on three spanwise planes are displayed in Fig. 4(*a*), while Fig. 4(*b*) shows isosurfaces of temperature fluctuations at level $1/2T'_{max}$

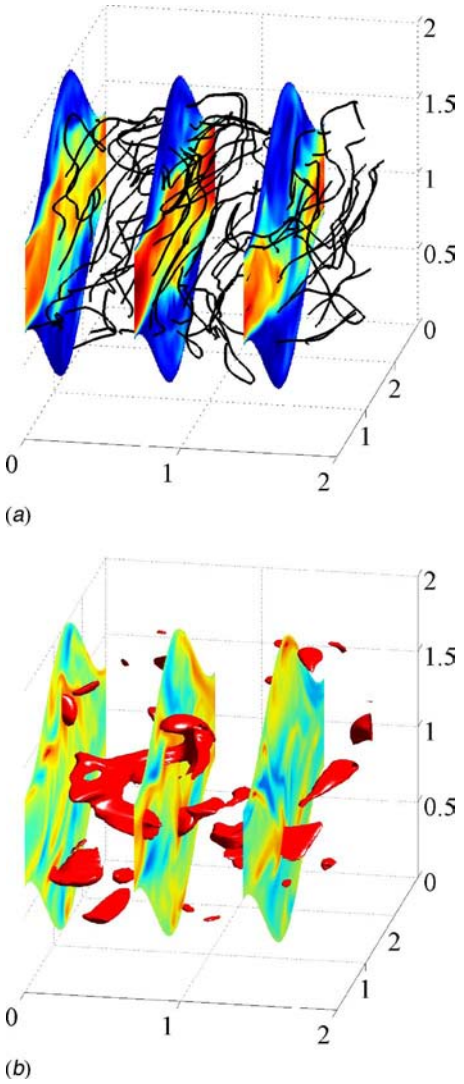

Fig. 4 Instantaneous plots of the velocity and temperature fields for Re=872: (*a*) trajectories of virtual particles and contours of the velocity module on three spanwise planes; and (*b*) isosurfaces of temperature fluctuations at level $T' = \frac{1}{2} T'_{max}$ and T' contours

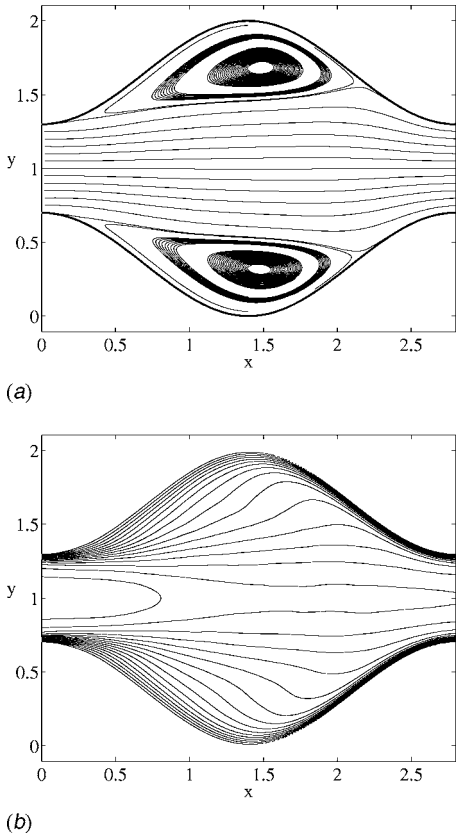

Fig. 5 Time averaged velocity and temperature fields of the Re=872 case: (*a*) streamlines; and (*b*) temperature contours

together with contours of instantaneous temperature fluctuations. The T' isosurfaces can be interpreted as traveling waves of high temperature and will be discussed in more detail in Sec. 4.1.

Streamlines of the time-averaged velocity field are displayed in Fig. 5(*a*); they show large circulation regions in the channel valleys. The size of the mean spanwise vortices varies depending on the Reynolds number. In agreement with previous experimental results [3], the time-averaged reattachment point for Re=481 is calculated in $x/L=0.82$, while for Re=872 it is located in $x/L=0.78$.

Figure 5(*b*) shows contours of the mean temperature field; larger temperature gradients are found next the converging walls. Temperature profiles for the two cases are compared in Fig. 6(*a*); the Re=872 profiles show a more uniform distribution of high-temperature values. This is consistent with the higher Nusselt number calculated.

Nusselt numbers and friction factors for the two unsteady cases considered are reported in Table 3; values calculated for the laminar, Re=71 case are produced for comparison purposes. A common practice to evaluate the performances of enhanced surfaces is to relate the friction factor and Nusselt number of the corrugated channel to the values for a flat channel at the same flow rate. In Table 3, the reference values f_f and Nu_f for the cases considered are calculated for Reynolds numbers of the hydraulic diameter $\mathrm{Re}_D=2\mathrm{Re}$. Since in this Reynolds number range only the laminar regime is sustained in a parallel channel, the reference values are calculated analytically as $f_f=24/\mathrm{Re}_D$ and $\mathrm{Nu}_f=7.5407$ [19]. In the laminar regime there is no major increase in Nu with respect to the value for a laminar flow between parallel plates. The heat transfer coefficient in the transitional regime is considerably increased with respect to the laminar value in wavy channels and the value calculated for the aperiodic Re=872 case is almost twice the value for Re=481. Also the normalized friction factor f/f_f experiences a considerable increase with Re.

Profiles of the intensity of temperature fluctuations $\overline{T'T'}$ are shown in Fig. 6(*b*), the peak values are placed in the same area as $\overline{v'T'}$, and also $\overline{u'u'}$, $\overline{v'v'}$ and $\overline{u'v'}$, not shown here for brevity. Stronger fluctuations and turbulent stress are calculated in the zone where the fast fluid coming from the minimum cross section meets the slower fluid of the expansions giving place to a shear layer. In the Re=872 case, a narrow layer of large temperature fluctuations can be observed parallel to the converging walls, at a distance of $\eta \approx -0.04$ from the walls. The presence of those peaks will be explained in Sec. 4.1 from the observation of instantaneous T' fields.

A comparison between contours of the mean advective term in the y direction $\bar{v}\bar{T}$ in the laminar and transitional regime of Fig. 7 reveals that the poor heat transfer performances in steady regime can be ascribed to the lack of convective mixing between the mainstream and the circulation regions. Unlike the laminar regime, in the Re=872 case of Fig. 7(*b*), positive and negative peaks are found near the walls, especially in the downstream half of the passage, where the cold fluid of the conductive substrate is efficiently mixed with the warm fluid of the core region. The

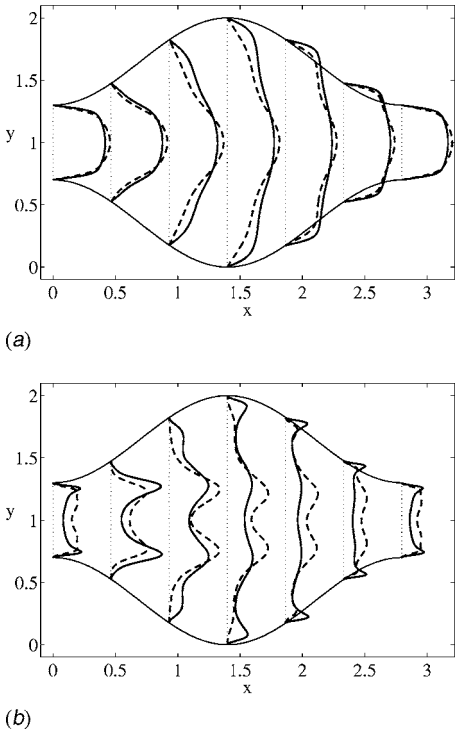

Fig. 6 Mean temperature profiles and intensity of temperature fluctuations $\overline{T'T'}$: (*a*) mean temperature profiles in seven *x* positions; dashed lines identify profiles for Re=481, solid lines for Re=872; and (*b*) $\overline{T'T'}$ profiles; dashed lines for the Re =481 case, solid lines for Re=872

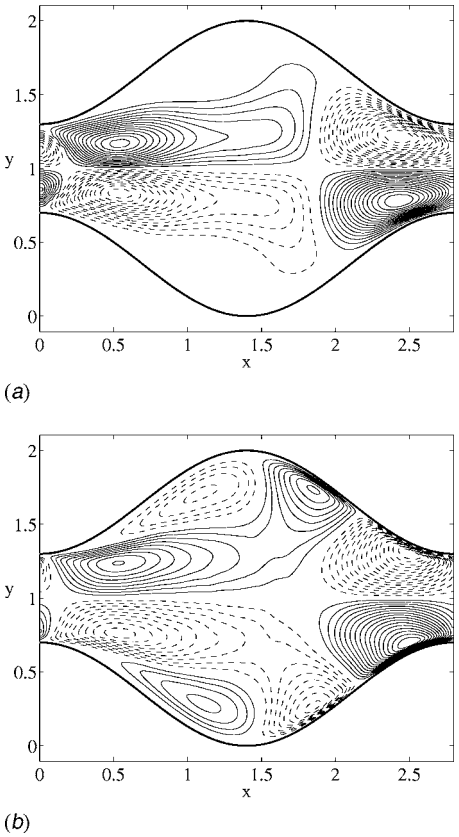

Fig. 7 Mean advective term $\bar{v}\bar{T}$ in the *y* direction: (*a*) laminar, Re=71 case; and (*b*) transitional, Re=872 case. Dashed lines show negative contours and solid lines show positive contours.

relative magnitude of advective fluxes is displayed in Fig. 8(*a*); larger advective fluxes are calculated for higher Reynolds numbers. The nondimensional $\bar{v}\bar{T}$ maxima for Re=71, Re=481, and Re=872 are 0.14, 0.49 and, 0.68 respectively.

Profiles of the $v'T'$ advective fluxes are shown in Fig. 8(*b*); the maximum is higher in the Re=872 case, the nondimensional maxima being 0.097 and 0.13. Moreover peaks are placed closer to the diverging walls, where the unsteady mixing can be more effective in contributing to the heat transfer.

4.1 Observation of Instantaneous Temperature Patterns. In this section, several snapshots representing the instantaneous temperature fluctuations $T'=T-\bar{T}$ are shown for the Re=872 case. They are taken in instants of relative maximum and minimum Nusselt number on the spanwise plane $z=1/2L_z$ of the computational domain in order to describe the physical events that are associated with peak heat transfer rate.

The instantaneous T' distributions are shown in Figs. 9 and 10. All T' plots show slanted traveling waves of high-temperature gradient which move with higher velocity than the average. The high Nusselt number plots of Fig. 9 are characterized by the presence of one or two high-temperature layers near the converging walls and parallel to them. As confirmed by the observation of conditionally averaged plots, peaks of Nusselt are attained when a traveling wave of high temperature reaches the wall on the downstream half of the channel. The occasional presence of such waves near the converging walls also explains the presence of larger temperature fluctuations in the same area, clearly visible in the $\overline{T'T'}$ plot of Fig. 6(*b*), for Re=872.

A marked similarity is observed between the T' fields of Figs. 9 and 10 and the corresponding u' fields, not reported here for brevity. This observation is consistent with the Pr=0.7 fluid of the present study. When a high Nusselt is calculated on the bottom wall, the velocity boundary layer is also thin and drag forces increase; the opposite is true in instants of low Nusselt number.

Table 3 Main flow and heat transfer results

Re	f	f/f_f	Nu	$\mathrm{Nu}/\mathrm{Nu}_f$
71.1	0.348	2.06	7.90	1.05
481	0.121	4.85	16.5	2.19
872	0.148	10.8	29.7	3.94

5 Concluding Remarks

Forced convection in sinusoidal wavy channels is investigated for a Pr=0.7 fluid, in the transitional Reynolds number range that is particularly important to applications. The study is conducted by means of direct numerical simulation of the three-dimensional, time-dependent flow and energy equations.

The heat transfer enhancement effect of the wavy walls with respect to a corresponding flat walled channel is primarily due to an anticipated transition to unsteady conditions. Heat transfer rates calculated for wavy channels in the transitional regime show a sensible increase with respect to the steady flow values. The reason for the remarkable heat transfer augmentation is found in the analysis of heat fluxes; unlike the laminar regime, in the aperiodic case the $\bar{v}\bar{T}$ heat fluxes show strong interaction with the cold fluid near the wall region, especially in the downstream half of the channel. Mean and turbulent heat fluxes in the *y* direction are larger in the Re=872 case than for Re=481; peaks of $\bar{v}\bar{T}$ and $\overline{v'T'}$ are placed closer to the walls where they are more efficient

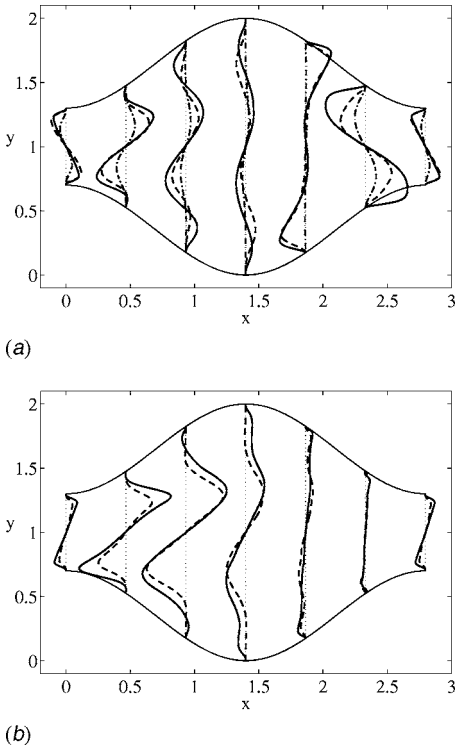

Fig. 8 Advective fluxes in the *y* direction, dashdot lines show profiles for the laminar Re=71 case, dashed lines for the Re =481 case, and solid lines for Re=872: (*a*) mean heat fluxes $\bar{v}\bar{T}$; and (*b*) turbulent heat fluxes $\overline{v'T'}$

in the mixing of the cold fluid from the walls with the warm fluid of the core. Accordingly, the Nusselt number nearly doubles between Re=481 and Re=872.

The algorithm used for the simulations improves the feasibility of performing direct numerical simulations of heat transfer in the periodic passages of compact heat exchangers. Accurate three-dimensional, time-dependent numerical simulations can complement experiments in revealing the mechanisms associated with heat transfer augmentation over different corrugated geometries; this would assist designers in conceiving new enhanced surfaces by exploiting clearly identified physical mechanisms.

Acknowledgment

The authors wish to thank Professor Claudio Giberti for his advice on the interpretation of the velocity time traces and the anonymous reviewers for the valuable comments and suggestions.

Nomenclature

A = cross-sectional area
$\mathbf{b}$ = unit vector in the streamwise direction
c = specific heat
f = friction factor, Eq. (24)
H_{max} = maximum channel height
H_{min} = minimum channel height
H_{av} = average channel height $H_{av}=(H_{max}+H_{min})/2$
h = heat transfer coefficient
k = thermal diffusion coefficient
L = periodic length in the x direction
L_z = length of the domain in the z direction
Nu = Nusselt number, Eq. (24)
N_x,N_y,N_z = number of grid points in x,y,z direction
p = periodic part of the pressure field
P = pressure field

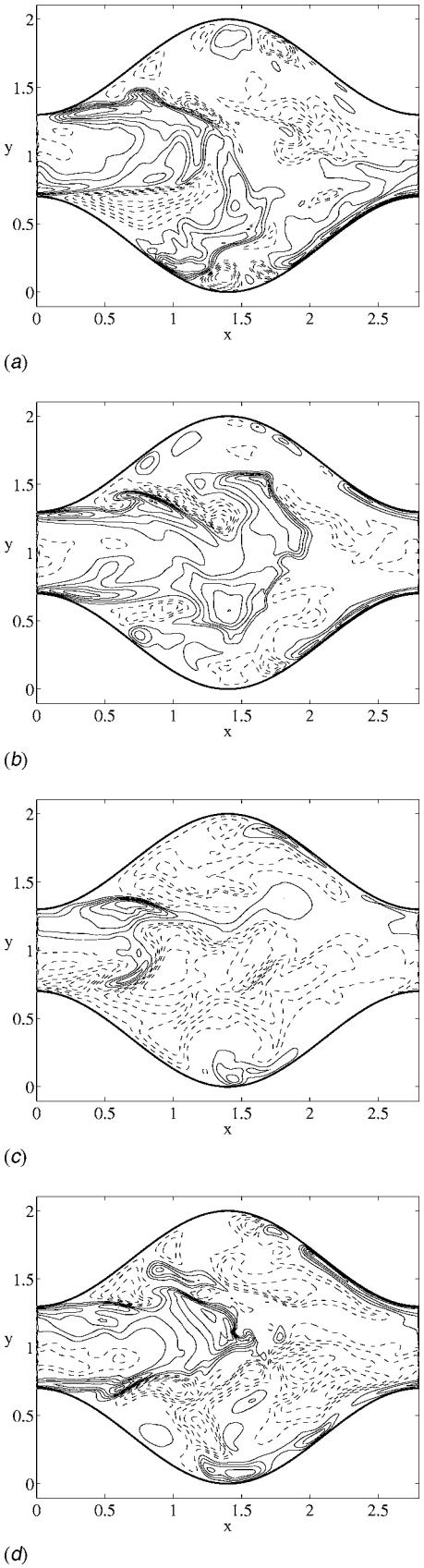

Fig. 9 Temperature fluctuations T' in instants of relative maximum Nusselt for Re=872: (*a*) t=147.9 and Nu=39.9; (*b*) t =151.3 and Nu=41.1; (*c*) t=160.9 and Nu=34.8; and (*d*) t =163.7 and Nu=40.8. Dashed lines are negative contours and solid lines are zero and positive contours.

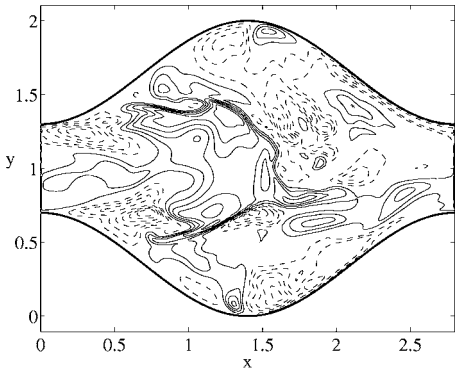

(*a*)

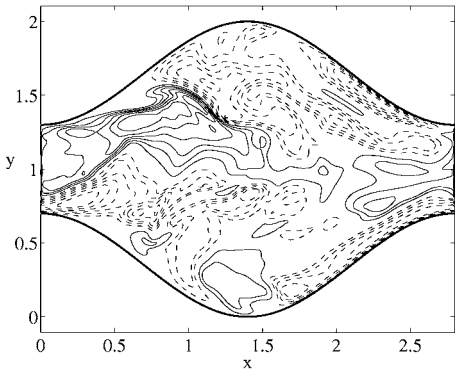

(*b*)

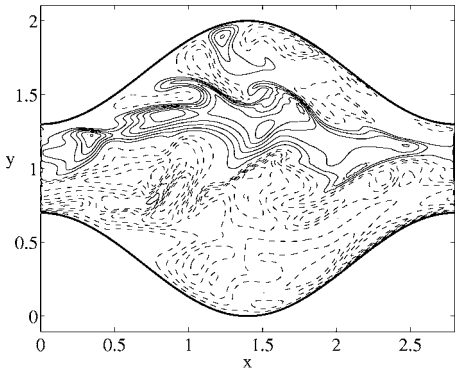

(*c*)

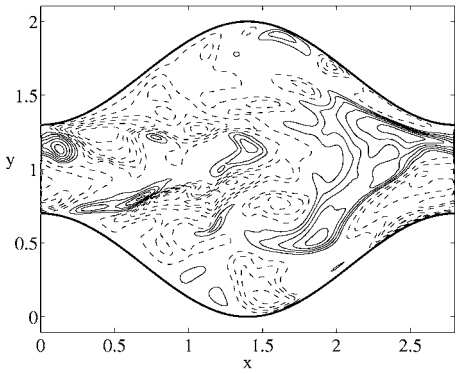

(*d*)

Fig. 10 Temperature fluctuations T' in instants of relative minimum Nusselt number for Re=872: (*a*) t=149.1 and Nu =24.3; (*b*) t=153.1 and Nu=19.4; (*c*) t=159.9 and Nu=20.7; and (*d*) t=163.3 and Nu=22.6. Dashed lines are negative contours and solid lines are zero and positive contours.

Pr	=	molecular Prandtl number, $\mathrm{Pr}=\nu/\kappa$
Q	=	volumetric flow rate
Q_s	=	volumetric flow rate per unit spanwise length, $Q_s=Q/L_z$
Re	=	bulk Reynolds number, $\mathrm{Re}=Q_s/\nu$
Re_D	=	Reynolds number based on the hydraulic diameter
Re_τ	=	Reynolds number based on the friction velocity, $\mathrm{Re}_\tau=u_\tau\delta/\nu$
T	=	temperature field
t	=	time
t_{ref}	=	reference time, $t_{\mathrm{ref}}=\delta/u_\tau$
$\mathbf{u}$	=	velocity vector, $\mathbf{u}=(u,v,w)$
u_τ	=	friction velocity, $u_\tau=(\beta\delta/\rho)^{1/2}$
u_{av}	=	average velocity, $u_{\mathrm{av}}=Q_s/H_{\mathrm{av}}$
u_m	=	mean velocity, $u_m(x)=Q_s/H(x)$
x,y,z	=	Cartesian coordinates

Greek Letters

α	=	thermal diffusivity $\alpha=k/\rho c$
β	=	imposed pressure drop per unit length
Δt	=	timestep
Δt_s	=	statistical sampling time interval
Δt_a	=	time extension for moving averages
δ	=	reference length
η	=	coordinate normal to the wall, pointing outward
θ	=	periodic temperature
λ	=	temperature decay rate, Eq. (9)
ν	=	kinematic viscosity
ρ	=	density
φ	=	temperature difference with the wall $T-T_w$

Subscripts and Symbols

av	=	average
b	=	bulk
f	=	flat channel
m	=	mean
ref	=	reference
w	=	wall
$\bullet'$	=	fluctuating value
$\bar{\bullet}$	=	time averaged value
$\langle\bullet\rangle$	=	space averaged value

References

[1] Kays, W. M., and London, A. L., 1958, *Compact Heat Exchangers*, Mc Graw–Hill, New York.

[2] Jacobi, A. M., and Shah, R. K., 1998, "Air-Side Flow and Heat Transfer in Compact Heat Exchangers: A Discussion of Enhancement Mechanisms," Heat Transfer Eng., **19**(4), pp. 29–41.

[3] Nishimura, T., Ohori, Y., and Kawamura, Y., 1984, "Flow Characteristics in a Channel With Symmetric Wavy Wall for Steady Flow," J. Chem. Eng. Jpn., **17**(5), pp. 466–471.

[4] Guzmán, A. M., and Amon, C. H., 1994, "Transition to Chaos in Converging-Diverging Channel Flows: Ruelle-Takens-Newhouse Scenario," Phys. Fluids, **6**(6), pp. 1994–2002.

[5] Guzmán, A. M., and Amon, C. H., 1996, "Dynamical Flow Characterization of Transitional and Chaotic Regimes in Converging-Diverging Channels," J. Fluid Mech., **321**, pp. 25–57.

[6] Nishimura, T., Murakami, S., Arakawa, S., and Kawamura, Y., 1990, "Flow Observations and Mass Transfer Characteristics in Symmetrical Wavy-Walled Channels at Moderate Reynolds Numbers for Steady Flows," Int. J. Heat Mass Transfer, **33**(5), PP. 835–845.

[7] Rush, T. A., Newell, T. A., and Jacobi, A. M., 1999, "An Experimental Study of Flow and Heat Transfer in Sinusoidal Wavy Passages," Int. J. Heat Mass Transfer, **42**, pp. 1541–1553.

[8] Wang, G., and Vanka, S. P., 1995, "Convective Heat Transfer in Periodic Wavy Passages," Int. J. Heat Mass Transfer, **38**, pp. 3219–3230.

[9] Ničeno, B., and Nobile, E., 2001, "Numerical Analysis of Fluid Flow and Heat Transfer in Periodic Wavy Channel," Int. J. Heat Fluid Flow, **22**, pp. 156–167.

[10] Stone, K., and Vanka, S. P., 1999, "Numerical Study of Developing Flow and Heat Transfer in a Wavy Passage," ASME J. Fluids Eng., **121**(4), pp. 713–719.

[11] Bahaidarah, H. M. S., Anand, N. K., and Chen, H. C., 2005, "Numerical Study

of Heat and Momentum Transfer in Channels With Wavy Walls," Numer. Heat Transfer, Part A, **47**, pp. 417–439.
[12] Hossain, M. Z., and Sadrul Islam, A. K. M., 2004, "Fully Developed Flow Structures and Heat Transfer in Sine-Shaped Wavy Channels," Int. Commun. Heat Mass Transfer, **31**(6), pp. 887–896.
[13] Goldstein, L., and Sparrow, E. M., 1977, "Heat and Mass Transfer Characteristics for Flow in a Corrugated Wall Channel," ASME J. Heat Transfer, **99**, pp. 187–195.
[14] Stasiek, J. A., 1998, "Experimental Studies of Heat Transfer and Fluid Flow Across Corrugated-Undulated Heat Exchanger Surfaces," Int. J. Heat Mass Transfer, **41**, pp. 889–914.
[15] Habib, M. A., Ul-Haq, I., Badr, H. M., and Said, S. A. M., 1998, "Calculation of Turbulent Flow and Heat Transfer in Periodically Converging-Diverging Channels," Comput. Fluids, **27**(1), pp. 95–120.
[16] Patankar, S. V., Liu, C. H., and Sparrow, E. M., 1977, "Fully Developed Flow and Heat Transfer in Ducts Having Streamwise-Periodic Variations of Cross-Sectional Area," ASME J. Heat Transfer, **99**, pp. 180–186.
[17] Greiner, M., Faulkner, R. J., Van, V. T., Tufo, H. M., and Fisher, P. F., 2000, "Simulation of Three Dimensional Flow and Augmented Heat Transfer in a Symmetrically Grooved Channel," ASME J. Heat Transfer, **122**, pp. 653–660.
[18] Stalio, E., and Nobile, E., 2003, "Direct Numerical Simulation of Heat Transfer Over Riblets," Int. J. Heat Fluid Flow, **24**, pp. 356–371.
[19] Shah, R. K., and London, A. L., 1978, "Laminar Flow Forced Convection in Ducts—A Source Book for Compact Heat Exchanger Analytical Data," *Advances in Heat Transfer*, T. F. Irvine, Jr. and J. P. Hartnett, eds., Academic, New York, Supplement 1.

Investigation of Detached Eddy Simulations in Capturing the Effects of Coriolis Forces and Centrifugal Buoyancy in Ribbed Ducts

Aroon K. Viswanathan

Danesh K. Tafti
e-mail: dtafti@vt.edu

High Performance Computational Fluids-Thermal Sciences and Engineering Group, Mechanical Engineering Department, Virginia Polytechnic Institute and State University, Blacksburg, VA 24061

The predictive capability of Detached Eddy Simulations (DES) is investigated in stationary as well as rotating ribbed ducts with relevance to the internal cooling of turbine blades. A number of calculations are presented at Re = 20,000 and rotation numbers ranging from 0.18 to 0.67 with buoyancy parameters up to 0.29 in a ribbed duct with ribs normal to the main flow direction. The results show that DES by admitting a LES solution in critical regions transcends some of the limitations of the base RANS model on which it is based. This feature of DES is exemplified by its sensitivity to turbulence driven secondary flows at the rib side-wall junction, to the effect of Coriolis forces, and centrifugal buoyancy effects. It is shown that DES responds consistently to these noncanonical effects when RANS and URANS with the same model cannot, at a cost which is about a tenth of that of LES for the geometry and Reynolds number considered in this study. [DOI: 10.1115/1.2717944]

Keywords: detached eddy simulations (DES), Coriolis forces, centrifugal buoyancy, ribbed ducts, turbine blade internal cooling

Introduction

Despite the continual development of computational schemes to predict turbulent flows over the last few decades, the computation of highly unsteady, separated flows at high Reynolds number is still a major challenge. Reynolds averaged Navier Stokes (RANS) approaches have been traditionally applied to a variety of flows. This approach is cost effective, but, in spite of several improvements in RANS models, they are not able to predict flows far from their calibration regime. Large eddy simulation (LES) is a viable alternative for accurate computations. However, the near wall resolution required for LES makes it prohibitively expensive at high Reynolds numbers. This is the rationale behind the continual development and application of hybrid RANS-LES methods, which combine the advantages of both the schemes.

Out of this family of hybrid techniques, detached eddy simulation (DES) is a technique that has gained popularity since it was proposed by Spalart [1] in 1997. DES involves sensitization of a RANS model to grid length scales, thereby allowing it to function as a subgrid scale model in regions of interest. This allows the natural instabilities of the flow in this region to develop. A finer grid (in the region of interest) allows the energy cascade to grow and improves the quality of the solution.

This technique, initially proposed based on the Spalart-Allmaras turbulence model, treats the inner wall layer in a RANS mode and, by modifying the length scale in the destruction term, the model switches to a subgrid type formulation in regions away from the wall. This eliminates the fine grid resolution needed in wall parallel directions to resolve the small scale turbulent eddies responsible for production of turbulence, which results in considerable cost savings.

Later this technique was generalized by Strelets [2], who defined an analogous DES formulation for the Menter's shear stress transport model. By this modified definition, DES is made more sensitive to the local flow features by defaulting to a RANS solution in regions (even away from the wall) where the turbulent length scale is less than the grid length scale.

DES has been used in the prediction of a wide range of flow regimes, especially for high Reynolds number flows undergoing separation. The first application of DES after it was proposed was in 1999 when Shur et al. [3] applied DES to the study of flow around a NACA0012 airfoil at high angles of attack. DES was subsequently used by Travin et al. [4] to predict the flow past a circular cylinder and Constantinescu et al. [5,6] to predict the flow around a sphere. These geometries belonged to a class of separated flows where the separation is not fixed by the geometry and so the prediction of the three-dimensional separation is a challenge for the prediction scheme. The three-dimensional time dependent flow in the wake of these geometries was predicted well by DES in both these cases, which proved to be a motivating factor for the further application of DES.

DES was further extended to flow around other complex geometries. Viswanathan et al. [7] applied DES to the flow around an aircraft forebody to consider the stability and control of the aircraft at high angles of attack. This study performed for a high Reynolds number was significant as it was representative of realistic flight conditions. The effect of mesh refinement was highlighted in this study and it was observed that as the mesh was refined in the detached regions of the flow, a wider range of scales were resolved. Kotapati-Apparao et al. [8] used DES to accurately predict the complex physics aft of a prolate spheroid undergoing a pitchup maneuver. The primary and the secondary separations observed in experiments, which URANS failed to capture, were captured accurately by DES.

Forsythe et al. [9] carried out a study of the flow around an F-15 aircraft at a high angle of attack. In this study, DES and URANS were compared and the superiority of DES in predicting the turbulent structures around the aircraft was highlighted. The

Contributed by the Heat Transfer Division of ASME for publication in the JOURNAL OF HEAT TRANSFER. Manuscript received September 4, 2006; final manuscript received January 5, 2007. Review conducted by Minking Chyu.

 Copyright © 2007 by ASME

effects of DES on mesh and time step refinement were also studied. Similar DES studies were carried out on other aircrafts [9–11] to study wing stall and vortex bursts. Kapadia et al. [12] used DES to model the flow behind an Ahmed car model. This study applied DES to a mildly separated case, which was prone to reattachment, and thus broadened the application base of DES.

Though diverse in application, one common feature of the above flows is that they pertain to external flow regimes undergoing separation, for which DES was originally proposed. The first study that applied DES to internal flows was reported by Nikitin et al. [13] in a turbulent channel flow with the Spalart-Allmaras model. The wall parallel grid was sufficiently coarse that DES behaved as a subgrid scale model with a built-in wall function. The modeled and the resolved turbulent shear stresses in the channel were studied and the effect of the grid spacing on turbulent shear stress evaluated.

A ribbed duct flow is a further extension of DES to internal flows. The homogeneous channel flow considered by Nikitin et al. maintained a constant grid in the streamwise and spanwise directions. Additional complexity is added to the grid design in ribbed ducts due to the presence of no slip boundaries at the side walls and the ribs, which calls for finer grids in their vicinity. This paper describes developments in the application of DES to noncanonical flow and heat transfer predictions in ribbed ducts, which has direct applications to the internal cooling of turbine blades.

Detached Eddy Simulations—Menter's SST Model. A majority of the DES computations reported in the open literature use the one equation Spalart-Allmaras model as the base model. The Spalart-Allmaras based DES model is hardwired to use RANS in the near wall region and LES away from the wall solely based on the grid distribution and so is insensitive to the local flow features. In order to facilitate the computation to be cognizant of the eddy length scales and hence behave as RANS or LES depending on the instantaneous local conditions, a two equation SST model [14,15] has been used to model the effects of turbulence. The formulation of the SST based DES is discussed by Strelets [2].

The turbulent kinetic energy (k) and the dissipation rate (ω) from the SST equation [14,15] are used to define the eddy viscosity as $\nu_t = k/\omega$. The RANS length scale, $l_{k\text{-}\omega} (= \sqrt{k}/0.09\omega)$, is replaced by a DES length scale δ, where $\delta = \min(l_{k\text{-}\omega}, C_{\mathrm{DES}}\Delta)$. C_{DES} is defined as 0.61 when the k-ε model is active and as 0.78 when the k-ω model is active, based on studies on decaying homogeneous isotropic turbulence [2]. The resulting subgrid model reduces to a Smagorinsky-type model. Based on this, the dissipation term in the k-transport equation is reduced to $D^k = \rho k^{3/2}/\delta$.

Hence if the grid length scale is larger than the eddy length scale, DES uses a RANS derived eddy viscosity model to treat the eddy. Thus the relaxation of the grid in the wall-parallel direction ensures that the inner boundary layer is treated in a RANS mode, where RANS is calibrated to perform well. In addition, the model evaluates the grid density with reference to the local turbulent length scale and accordingly switches between LES and URANS. When the grid is finer than the local instantaneous turbulent length scale, the model behaves as a subgrid model and eddies are directly resolved on the grid. This allows the energy cascade to extend to length scales close to the grid spacing. In contrast, if the local instantaneous length scale is larger, the RANS turbulence model gains full control of the solution. One prominent feature of the DES version of the SST model is that although an instantaneous discontinuity may exist between the RANS region and the LES region, in the mean, however, a smooth transition takes place from RANS to LES and vice versa. The smooth and continuous velocity and the eddy viscosity fields make DES a nonzonal technique.

Internal Cooling Ducts

Flows in ribbed ducts are of interest in the study of internal cooling of turbine blades. Ribs (or turbulators) act as roughness elements and continuously trip the boundary layer, enhancing the heat transfer coefficient and cooling capacity. Although geometrically simple, the flow downstream of a rib has several complex flow features such as separation of the boundary layer, a curved shear layer, primary and secondary recirculation, reattachment of the boundary layer, recovery, etc. Hence the flow inside the ribbed duct is a function of the flow Reynolds number, geometrical parameters of the duct and the ribs such as the rib height to hydraulic diameter ratio, the rib pitch, the aspect ratio of the duct, the angle of the rib with respect to the flow, and the shape of the rib as shown by previous studies. Additionally, Coriolis forces (due to rotation) and centrifugal buoyancy (due to thermal gradients) introduce extra strains that significantly alter the flow and heat transfer in the duct.

Over the last two decades, several researchers have carried out computational studies on internal cooling channels. Several three-dimensional studies using RANS have been carried out for stationary internal cooling ducts by Saidi and Sunden [16], Jia et al. [17–19], Iacovides et al. [20], Ooi et al. [21,22], and several other groups (Prakash and Zerkle [23]). Computations on rotating ducts using RANS have been reported by Jang et al. [24], Chen et al. [25], Su et al. [26], and Iacovides et al. [27,28]. In spite of the widespread application of RANS, the models lack consistency and universality, especially in capturing the nonlinear effects of rotation.

Application of LES to these flows is also not uncommon. Several studies by Murata and Mochizuki [29], Watanabe and Takahashi [30], and Tafti [31] have successfully applied LES to predict the turbulent as well as the time averaged features of flow in stationary ducts. LES was also observed to successfully capture the effects of Coriolis forces and centrifugal buoyancy as reported in studies by Abdel-Wahab and Tafti [32,33], Sewall and Tafti [34,35], and Saha et al. [36]. Though LES is accurate, the computational cost makes it expensive, especially as the Reynolds number of the flow increases.

Thus hybrid LES-RANS schemes, like DES, are potential candidates for application in internal cooling ducts. The objectives of this study are threefold—to extend and verify DES to noncanonical internal flow configurations; to investigate the performance of DES in predicting the effects of rotation induced Coriolis forces; and further to assess the capability of DES in predicting the effects of centrifugal buoyancy. This is the first study to undertake a detailed investigation of DES in internal ribbed duct flows.

Computational Details

An in-house computer program GenIDLEST (Generalized Incompressible Direct and Large-Eddy Simulations of Turbulence) has been used to study heat transfer and flow characteristics. GenIDLEST has been used extensively to study air-side heat transfer augmentation in compact heat exchangers and internal cooling in gas turbines (Abdel-Wahab and Tafti [32,33], Cui and Tafti [37], Sewall and Tafti [34,35,38–40], Tafti [31]). Details about the algorithm, functionality, and capabilities can be found in Tafti [41].

In all the cases fully developed flow and thermal conditions are assumed. The walls (ribbed and side walls) and the ribs are heated by a constant heat flux (q''). The governing flow and energy equations are nondimensionalized by a characteristic length scale, which is chosen to be the hydraulic diameter of the channel (D_h), a characteristic velocity scale given by the friction velocity (u_τ), and a characteristic temperature scale given by $q''D_h/k$. The augmentation of heat transfer and friction factor is presented with reference to a smooth duct under the same set of conditions.

The flow is periodic in the streamwise direction while a no-slip wall boundary condition is applied at the ribs, side walls, and the top and bottom walls. The computational domain consists of a ribbed square channel, with two ribs placed at the center of the channel, at the top and the bottom. The rib-pitch to rib height is 10 and the rib height to hydraulic diameter is 0.1. The flow and heat

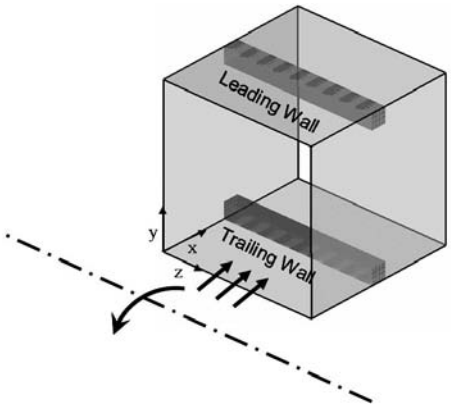

Fig. 1 Computational domain considered for the fully developed ribbed channel with normal ribs. Flow is in the positive *x* direction and is periodic in this direction.

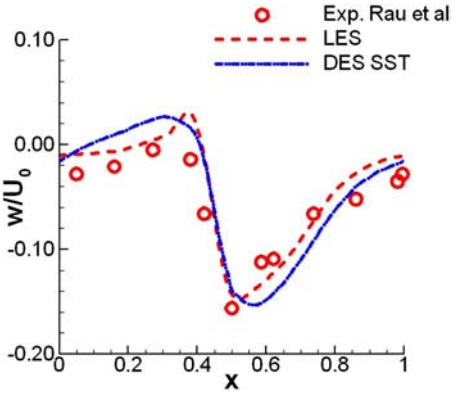

Fig. 3 Comparison of the secondary velocities predicted at $y/D_h=0.15$, $z/D_h=0.5$

transfer are presented at a nominal Reynolds number of 20,000. The computation domain and the coordinate system used are shown in Fig. 1.

Stationary Duct. The flow in normal ribbed ducts is characterized by massive separation downstream of the rib, which must be resolved with LES. Hence, any grid distribution should be cognizant of this region. The performance of DES on different grid densities for a stationary ribbed duct was reported by Viswanathan and Tafti [42]. Based on these computations it was concluded that a 64^3 grid was optimal for DES. The a posteriori evaluation of the grid showed that the y^+ values range from 0.2 to a maximum of 2.89. The streamwise and the spanwise grid resolutions were observed to be dense near the ribs and the walls. A coarser grid density of about $x^+=90$ and $z^+=120$ was maintained in the interrib region. A nondimensional time step of 5×10^{-5} was used in all cases.

The mean flow pattern observed in the symmetry plane of the span is shown in Fig. 2. Flow patterns produced by the LES cases [31], the RANS models [22], and the experiments [43] show a similar pattern. The flow is characterized by a recirculating eddy in front of the rib, followed by shear layer separation on the rib, and the presence of a recirculation region on top of the rib and behind it. Between the main recirculation region and the rib there is an additional counter-rotating eddy. The reattachment length is calculated as $4.1e$ from the rib, as compared to the LES predictions of $4.1e$ and the experimentally observed value of $4.0e-4.25e$.

Strong localized secondary flows exist in the vicinity of the rib junction with the smooth side walls. These secondary flow structures are generated by the unsteady vortices upstream of the ribs, drawing the flow towards the side walls. Figure 3 shows the comparison of the spanwise velocities as predicted by DES as compared to experimental observations by Rau et al. [43] and LES [31]. While DES is able to resolve the secondary flow, earlier studies [22,42] have shown that (U)RANS does not predict the secondary velocities accurately. Hence, DES, by resolving the large scale fluctuations on the grid in critical regions, overcomes the limitations of the base RANS model.

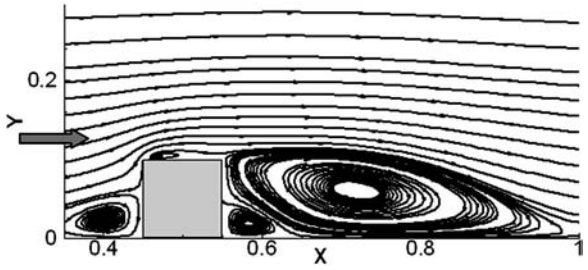

Fig. 2 Separation and reattachment of the shear layer due to the presence of the rib. The arrow shows the direction of the flow.

The heat transfer at the ribbed walls is affected by the shear layer separation and reattachment while the impinging secondary flows play a major role on the side wall heat transfer. The heat transfer distributions at the ribbed walls show the maximum heat transfer in front of the rib as a result of the unsteady secondary junction vortices in this region (Fig. 4)[1]. These secondary vortices stir up the fluid in this region, entraining fluid from the main stream, thereby transferring heat from the hot walls to the core of the channel. Further downstream the primary recirculation region enhances the heat transfer from the walls, and the heat transfer reaches a maximum value at about $3.5e$ downstream of the rib. The location of maximum heat transfer is slightly upstream of the reattachment and coincides with the region of maximum shear.

The distribution of the heat transfer augmentation ratios on the ribbed wall is plotted in Fig. 5(a) along the centerline and compared to experiments and LES computations. DES slightly underpredicts the heat transfer in the interrib spacing. But, overall, the heat transfer augmentation predicted by DES is consistent with experiments and LES.

While the heat transfer on the ribbed wall is enhanced due to the primary streamwise flow, secondary flow impingement plays a major role in the heat transfer on the side walls. At the side walls the heat transfer is observed to be highest in line with the rib. The heat transfer gradually decreases on moving towards the center of the duct. This trend was reproduced accurately by DES. Computations using two-equation RANS models reported by Viswanathan and Tafti [42] showed the incapability of RANS models to predict the heat transfer distribution accurately both at the side walls and the ribbed walls.

Thus it is observed that DES, by switching to a LES mode in regions of interest, captures the primary and secondary flow features, and ensuing heat transfer in the ribbed duct, with accuracy.

Rotating Duct—Effects of Coriolis Forces. Early studies in turbulent channel flow [44,45] have established two important effects of rotation. When the rotational axis is perpendicular to the plane of mean shear, Coriolis forces have a considerable effect on the mean flow as well as on turbulent fluctuations. These effects are manifested as stabilization/destabilization of turbulence at leading/trailing walls and the generation of spanwise roll cells or

[1]Although the whole domain is considered in the computations, because of the two-way symmetry in the y and z directions, only a quadrant of the domain is presented in the results.

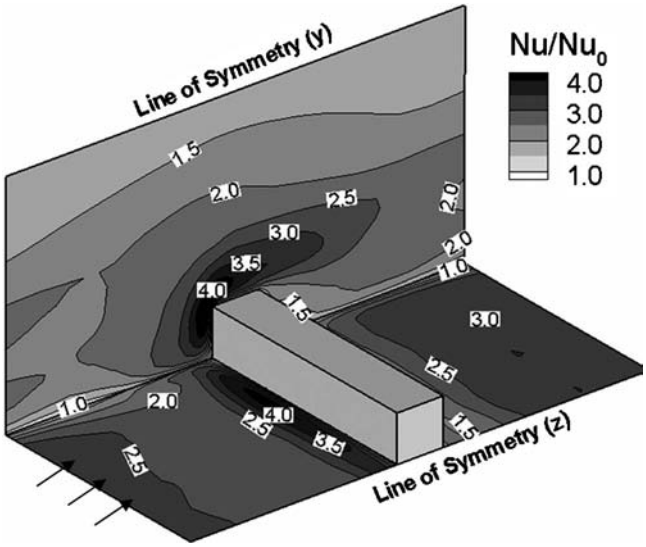

Fig. 4 Heat transfer distribution in one quadrant of the duct with normal ribs. Direction of the flow is indicated by the arrows.

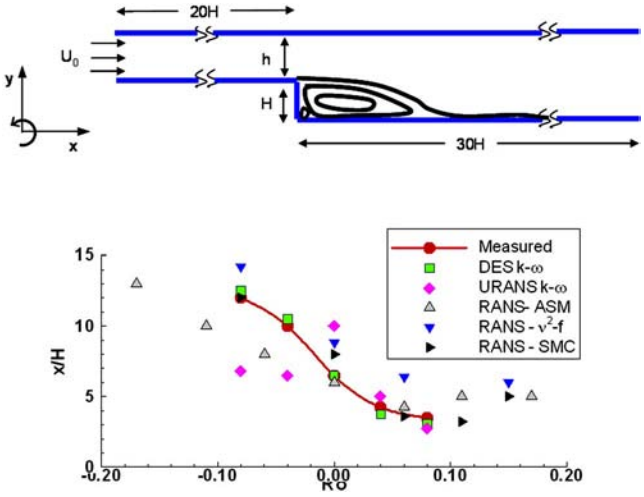

Fig. 6 Geometry of a rotating sudden expansion duct used to study the effect of Coriolis forces (top). Variation of the reattachment length with rotation as predicted by DES and RANS studies (bottom).

secondary flow patterns. The secondary flow patterns are a direct result of the action of Coriolis forces on mean shear and are also observed in laminar flows subjected to system rotation.

It is well established that the production of turbulence in the near wall region and in shear layers is caused by the exchange of momentum through intense interactions between the fluctuating streamwise and cross-stream velocities. The interaction in the shear region is similar to the exchange of momentum through the action of bursts $[-u', +v']$ and sweeps $[+u', -v']$ in the near wall region. When Coriolis forces act in tandem with these events, turbulence is augmented, whereas it is attenuated when the two act in opposition.

In order to validate the capability of DES in capturing the effects of Coriolis forces an expansion duct with an expansion ratio of 2 is considered and the effect of rotation on the reattachment length downstream of the step in the duct is compared with measurement by Rothe and Johnston at $Re=10,000$ [46]. Rotation is varied from negative ($Ro=-0.08$) to positive ($Ro=0.08$), which suppresses and augments turbulence, respectively. A comparison of the predicted reattachment lengths show that DES results are in good agreement with experiments as shown in Fig. 6 [47]. On the other hand, RANS computations from the literature [20,48] and our current computations show that RANS models do not predict the effects of Coriolis forces accurately.

Rotational Coriolis forces have a similar effect in ribbed ducts. For radially outward flow (Fig. 1) turbulence is augmented on the trailing side of the duct, whereas it is attenuated at the leading side. Modern propulsion turbines used in aircrafts typically have $Ro=0.1-0.2$, whereas power generation turbines have higher rotation numbers. In the study, three rotation numbers, $Ro=0.18$, 0.35, and 0.67, are examined, which cover a wide range of turbine applications. The results obtained using DES are evaluated against the results obtained from LES [32] on a 128^3 grid.

Rotational Coriolis forces affect the size of the recirculation zones and so the flow is asymmetric about the center y plane of the duct. Figure 7 shows the comparison of the flowfield as predicted by LES and DES for $Ro=0.35$. The reattachment length increases to $5.5e$ at the leading wall and decreases at the trailing wall to $3.5e$. The DES computations are consistent with the LES predictions [32].

As the rotation number is increased, an increase in the heat transfer is observed at the trailing wall, especially in regions immediately upstream of the rib and near the reattachment point. This is countered by a decrease at the leading wall in the corresponding regions.

Figure 8 shows the heat transfer at the leading (upper half) and the trailing walls (lower half) comparing results predicted by DES

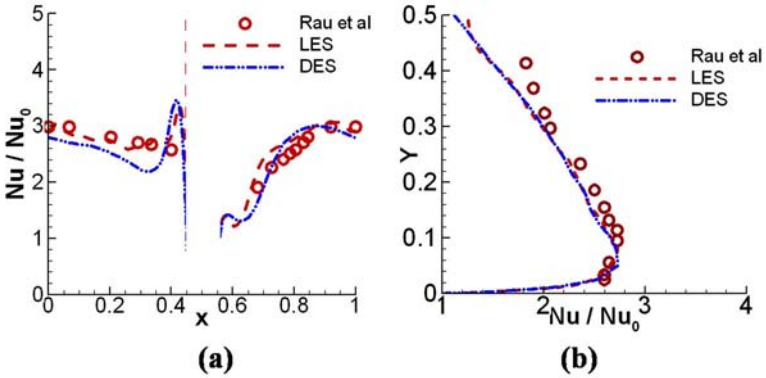

Fig. 5 Comparison of the augmentation ratios (*a*) at the center of the ribbed floor and (*b*) side walls upstream of the rib

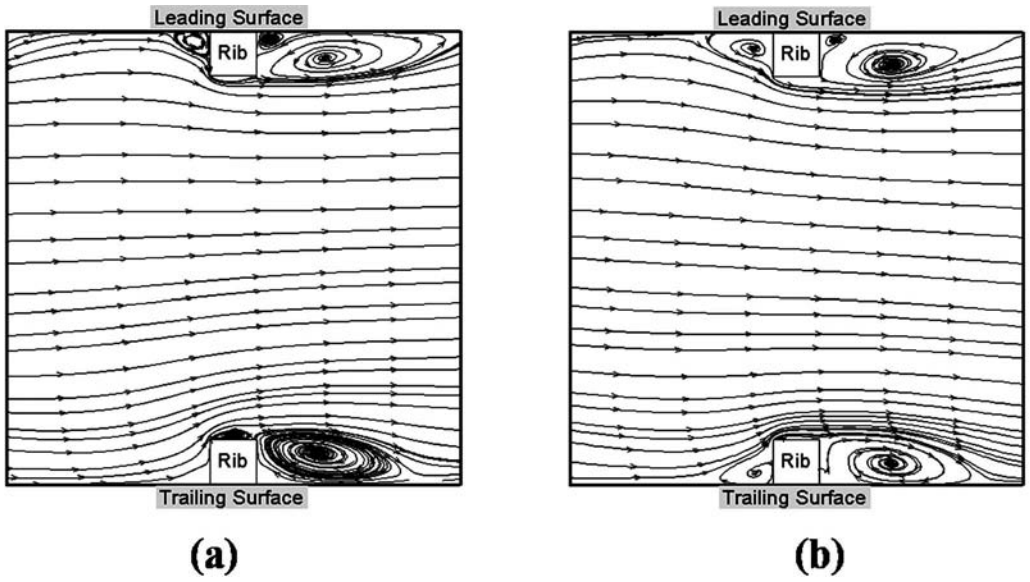

Fig. 7 Streamlines showing the flow in a fully developed duct rotating at Ro=0.35 at *Z*=0.5 as predicted by (*a*) LES and (*b*) DES. *Y*=0 represents the trailing wall, while *Y*=1 represents the leading wall. Flow direction is from left to right.

with LES results at Ro=0.35. The heat transfer augmentation predicted by DES agrees quite well with the LES computations. The shift of peak heat transfer on the trailing wall in the region of shear layer reattachment away from the center due to the effect of secondary flows is captured reasonably well by DES. Heat transfer augmentations at the trailing wall reach values close to 5.0 immediately upstream of the rib where the unsteady junction vortices enhance the heat transfer. DES overpredicts the spatial extent of this region. Earlier computations using RANS models [49] show the incapability of two-equation URANS models in predicting the heat transfer distribution accurately.

The flow at the leading wall is stabilized so the overall heat transfer at the leading wall is almost half the heat transfer at the trailing wall. Upstream of the rib, heat transfer levels are almost 2.5 times that observed in a smooth duct case. Once again, DES overpredicts the extent and augmentation in this region. The heat transfer levels drop to values close to the smooth duct heat transfer values immediately behind the rib, but the augmentation increases to values close to 1.5 downstream of the reattachment point. The trends predicted by DES are consistent with the LES results [32], with the exception of the region immediately upstream of the rib where higher levels of heat transfer are predicted.

As in stationary ducts, the secondary flows in the rotation cases also play an important role in the heat transfer at the side walls. Along the smooth (side) walls the heat transfer increases on moving from the trailing wall and reaches a maximum at the top front corner of the rib as a result of the secondary flow impingement on the wall. The heat transfer decreases on the side walls towards the center of the duct. Though the heat transfer patterns are the same for the stationary and the rotation cases, the magnitudes of heat transfer are different when rotation is introduced. However, an increase in rotation does not show much effect on the side wall

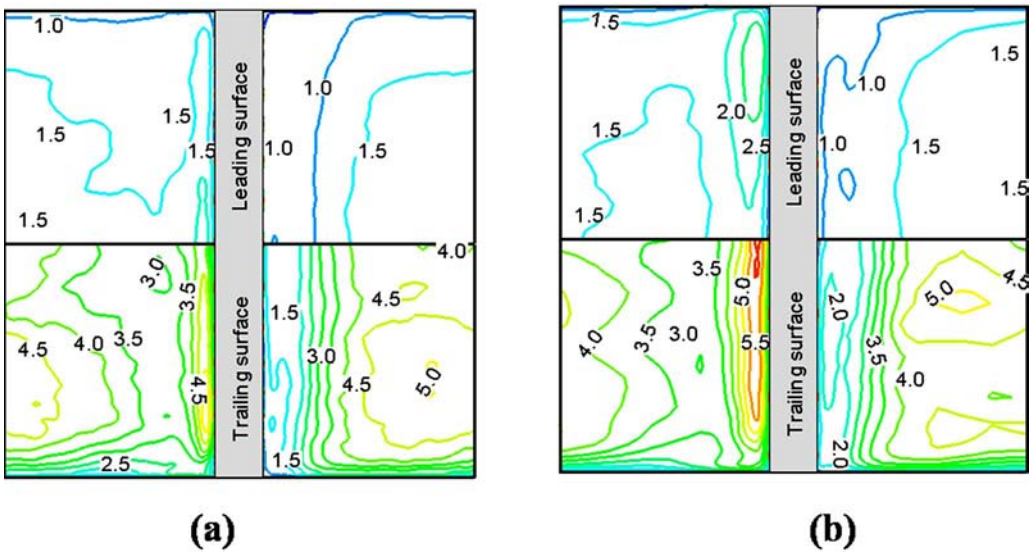

Fig. 8 Heat transfer augmentation (Nu/Nu_0) predicted at the leading (upper half of the plot) and the trailing walls (lower half of the plot) for the Ro=0.35 case by (*a*) LES and (*b*) DES. Flow direction is from left to right.

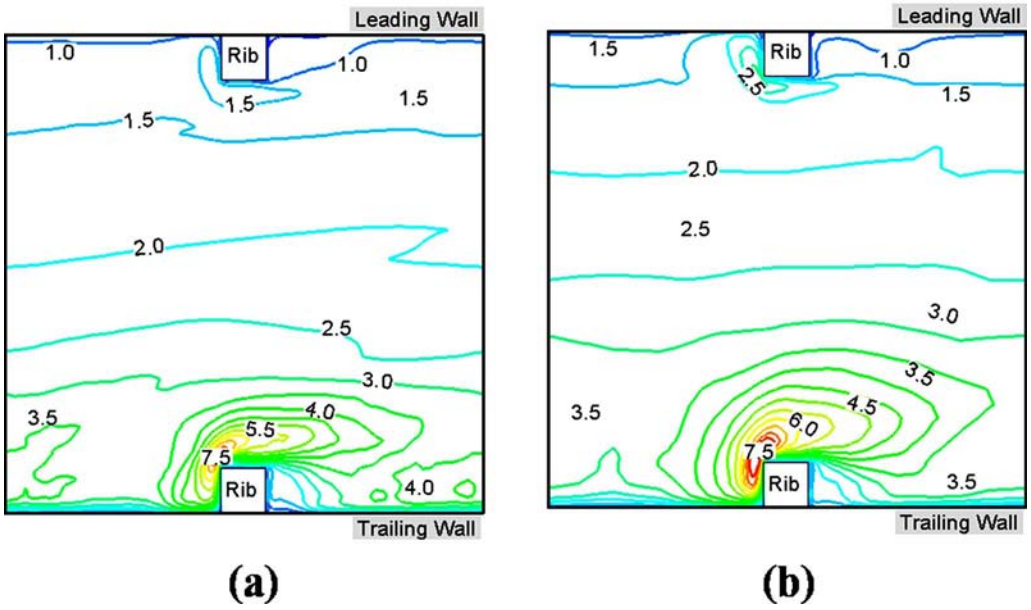

Fig. 9 Heat transfer augmentation (Nu/Nu_0) predicted at the side wall for the Ro=0.35 case by (*a*) LES and (*b*) DES. Flow direction is from left to right.

heat transfer. This behavior is consistent with the observations of Wagner et al. [50], who observed little or no change in the heat transfer at the side walls as rotation rate increased. Figure 9 compares the side wall heat transfer predicted by DES with LES for Ro=0.35. The DES predictions compare well with LES.

A comparison of the pitch averaged side wall heat transfer (Fig. 10) shows a gradual, but small, increase in the average heat transfer augmentation as the rotation number increases from 0.18 to 0.67. DES predicts these trends accurately but slightly underpredicts the augmentation compared to LES at higher rotation rates.

The effect of rotation is more prominent at the leading and the trailing walls. Results for averaged Nusselt numbers on the leading and trailing faces for the three rotation numbers are compared with the experiments of Liou et al. [51], Parsons et al. [52], and Wagner et al. [50]. The experimental data of Liou et al. [51] are at Re=10,000 for $e/D_h=0.136$ and $P/e=10$ and Parsons et al. [52] data are obtained at Re=5000 for $e/D_h=0.125$ and $P/e=10$. The data of Wagner et al. [50] includes the effects of buoyancy with a buoyancy parameter of 0.04 for a staggered rib arrangement with $e/D_h=0.1$ and $P/e=10$ at Re=25,000. In all cases, fully developed data are extracted for comparison. It is observed that the DES predictions agree well with experiments and LES (Fig. 11). A maximum deviation (from LES) of 11% is observed at the trailing surface for Ro=0.18.

Rotating Ducts—Effects of Coriolis Forces and Centrifugal Buoyancy. The capability of DES in predicting the effects of buoyancy in flows with thermal gradients is validated by evaluating the flow and thermal fields in a cavity driven by the shear provided by a channel flow and buoyancy due to the heated top wall [47]. The flow geometry and measurement locations are shown in Fig. 12. As buoyancy effects increase, the tendency of warmer fluid to remain near the top heated wall increases. Two different Archimedes numbers (ratio of buoyancy forces due to thermal gradients to viscous forces, $Ar=g\beta\Delta TL/U_0^2$) were considered and the effects of heating the top wall (Ar=0.37) studied. The temperature variation at the vertical and the horizontal center were compared with measurements by Grand at Ro=10,000 [53]. The DES computations were carried out on a 32^3 grid, which was eight times coarser than the 64^3 grid used for an analogous LES computation [47]. It is observed that DES captures the effects of shear and buoyancy and the predictions show good agreement with the experiments [54].

DES is next tested in ribbed ducts under the influence of centrifugal buoyancy. The difference in heat transfer at the trailing and leading surfaces due to the action of Coriolis forces in a rotating duct results in warmer fluid near the leading surface and relatively cooler fluid near the trailing wall. Hence centrifugal

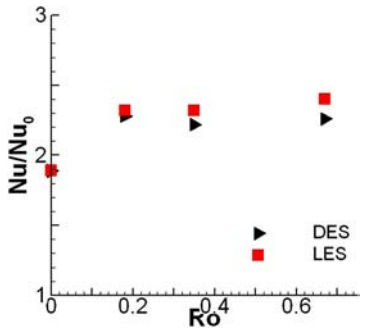

Fig. 10 Side wall heat transfer predicted by LES and DES for the various rotation cases

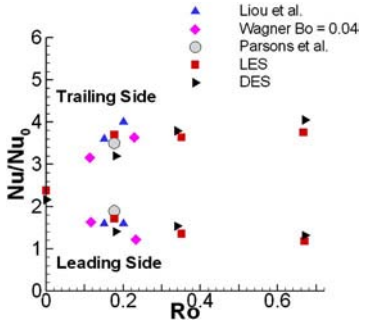

Fig. 11 Comparison of pitch averaged Nusselt number augmentation ratios at the leading and trailing sides with experiments

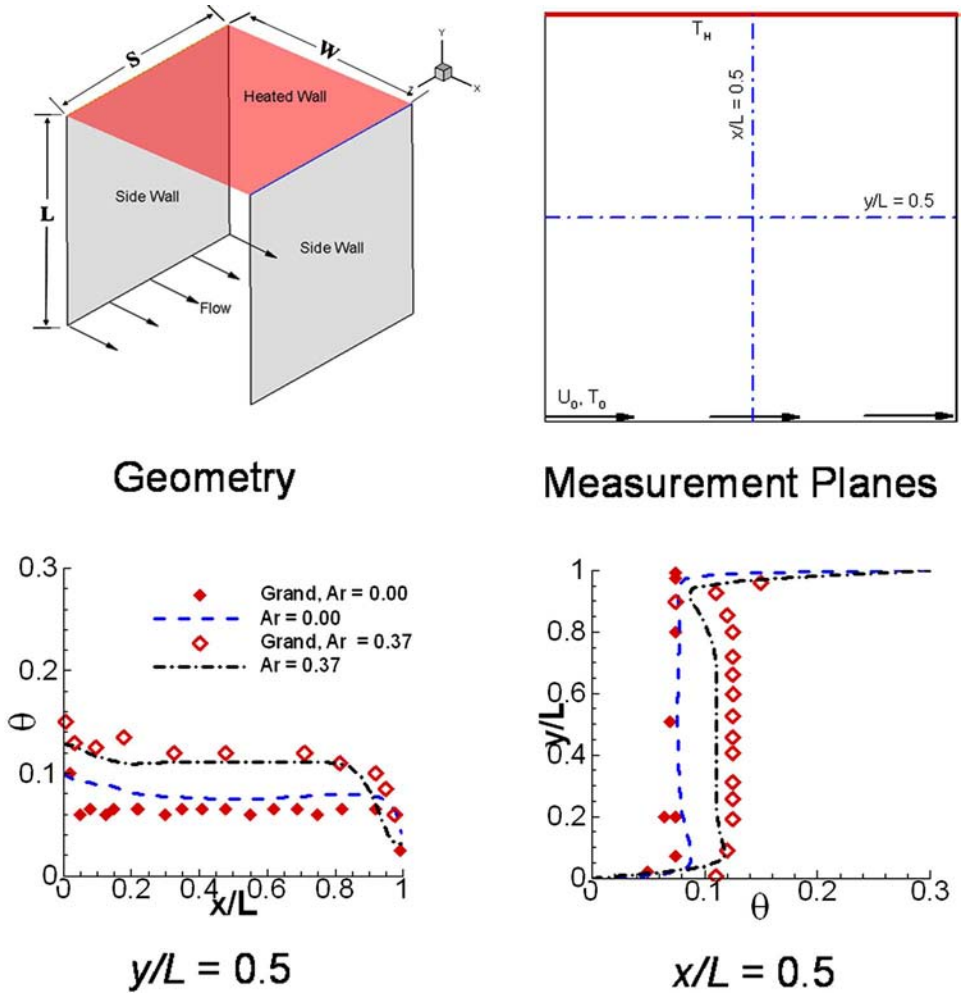

Fig. 12 Comparison of the temperature variation in the cavity predicted by DES in comparison with experimental measurements by Grand [53]

forces acting on the fluid give rise to a differential force on the leading and trailing sides of the duct, which is referred to as the centrifugal buoyancy force. For radially outward flow, centrifugal buoyancy reinforces the Coriolis forces, further destabilizing the flow at the trailing wall and stabilizing it on the leading wall.

Three different rotation cases are considered—Ro=0.18, 0.35, and 0.67. Three different density ratios are studied to evaluate the capability of DES in predicting the effects of buoyancy. The effective buoyancy parameters (Bo) for the three cases are evaluated to be 0.00, 0.12, and 0.29, respectively. In the present context the density difference and the buoyancy parameter are related as $\text{Bo} = (\Delta\rho/\rho_0)(r/D_h)\text{Ro}^2$. In all the cases the centrifugal buoyancy complements the effects of Coriolis forces. In typical gas turbine applications the buoyancy parameters can reach values of up to 1.0. However, since detailed LES results [32] are available for the buoyancy parameters in the range of 0.00–0.30, the current studies are carried out in this range.

The detailed flow and heat transfer physics is compared with LES prediction [32] on a 128^3 grid. Considering the grid sizes and the time scales used for the LES and DES calculations, the cost of the DES computation is almost an order of magnitude less than the LES computation.

Centrifugal buoyancy, like Coriolis forces, affects the recirculation region at the leading wall. Figure 13 shows the recirculation regions at the leading wall for a constant rotation rate of Ro =0.35 and different buoyancy parameters. It is observed that as the buoyancy parameter is increased from a value of Bo=0.00 to Bo=0.29, the recirculation region grows until one large recirculation zone is observed at the leading wall for Bo=0.29. A comparison with LES shows concurrence. The structures of the recirculation regions for Bo=0.00 and 0.12 are reproduced by DES. For Bo=0.29, while one large recirculation region is observed in between the ribs, the structure of the recirculation regions is different as predicted by LES and DES.

The effect of buoyancy for a constant rotation of Ro=0.35 is shown in Fig. 14. It is observed that as the buoyancy increases from Bo=0.00 to Bo=0.29, the heat transfer augmentation in the vicinity of the reattachment region increases from a value of 4.5 to around 6.0. The reattachment point at the trailing surface does not vary much as the buoyancy is increased and so the region of high heat transfer is observed to be at a distance of around $3.0D_h$ from the ribs at the trailing surface. The variation in the heat transfer is directly correlated to the variation in the TKE values. Higher TKE (more destabilization) at the trailing surface results in high heat transfer and so as buoyancy increases the heat transfer also increases.

Minimal differences are observed in the heat transfer at the leading surface. The effect of buoyancy is in the direction opposite to the main stream velocity. So, as the buoyancy is increased, the stabilizing effect at the leading surface increases, resulting in lower and relatively constant heat transfer augmentation.

While the heat transfer at the ribbed walls is observed to be affected by both rotation and buoyancy, the heat transfer distribution at the side wall is less sensitive to rotation and buoyancy. This

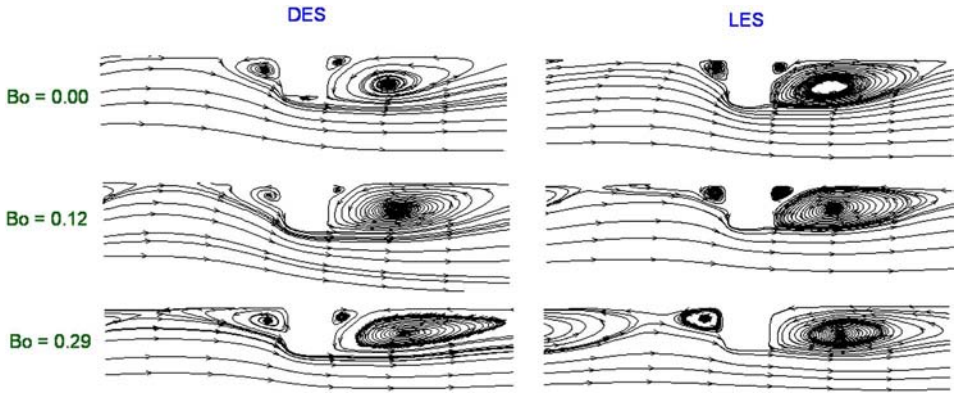

Fig. 13 Comparison of the recirculation regions at the leading edge for the three different buoyancy cases with Ro=0.35

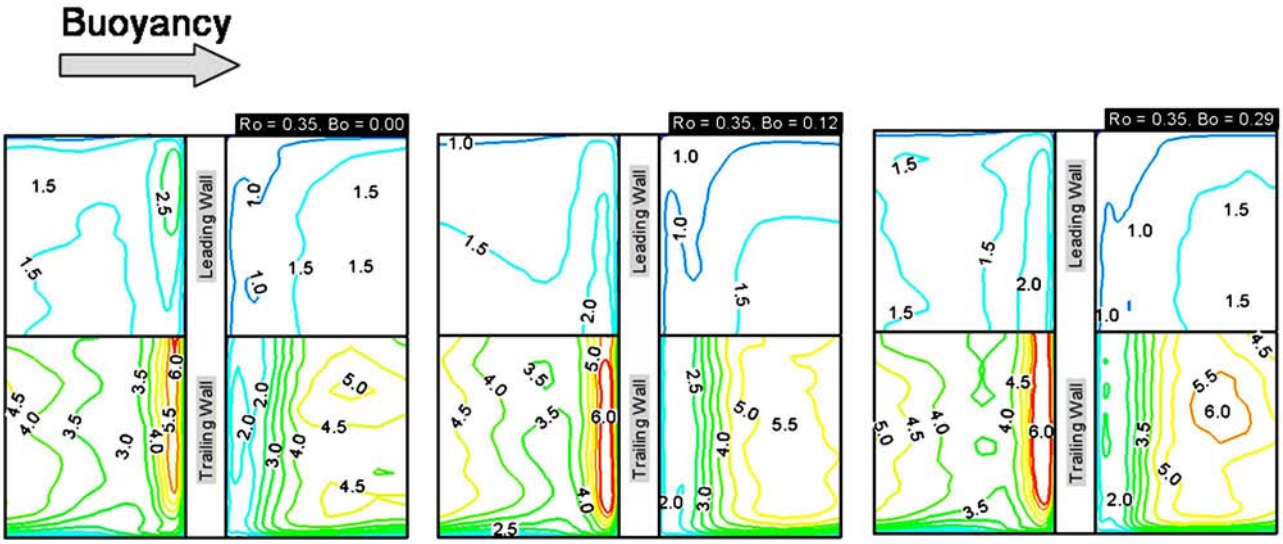

Fig. 14 Heat transfer distribution at the ribbed walls for varying buoyancy parameters for a constant Ro=0.35

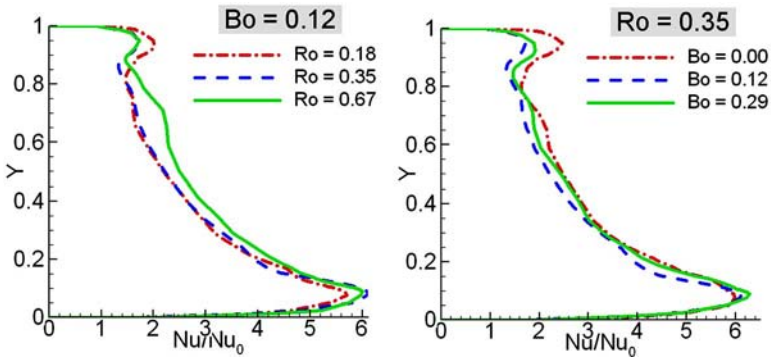

Fig. 15 Effect of the variation of rotation and buoyancy on the heat transfer at the side walls, plotted at a distance of 0.5*e* upstream of the ribs

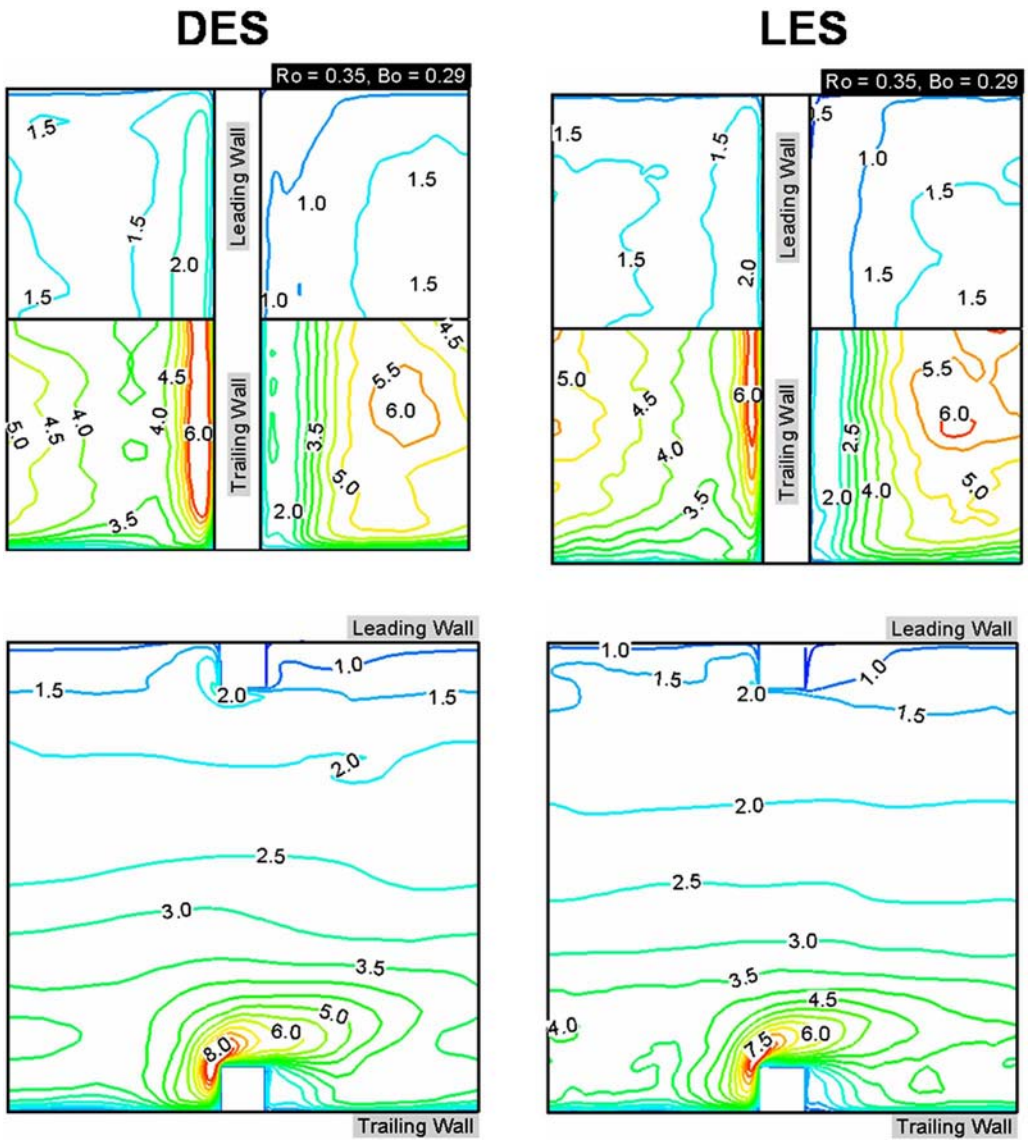

Fig. 16 Comparison of the ribbed (top) and side wall (bottom) heat transfer predicted by DES and LES for Ro=0.35 and Bo=0.29

feature predicted by DES is in agreement with the observations of Wagner et al. [50], who observed small changes in the heat transfer at the outer and inner walls of the first pass of their internal cooling duct. Similar trends were also observed by LES [32].

Figure 15 shows the comparison of the heat transfer profiles at the side wall, slightly upstream of the rib. For a constant Buoyancy parameter of 0.12 it is observed that as the rotation rate increases, the peak heat transfer augmentation at the trailing side increases from a value of around 5.5 for Ro=0.18 in the vicinity of the ribs to a value of around 6.0 for Ro=0.67. At the leading side the peak heat transfer decreases from a value of around 2.3 (Ro=0.18) to a value of around 1.8 (Ro=0.67) in the vicinity of the ribs.

For a constant rotation number of 0.35, as the buoyancy is increased it is observed that the peak heat transfer augmentation at the trailing wall almost remains constant at a value of around 6.0. In the vicinity of the leading wall the peak heat transfer decreases from a value of around 2.5 for Bo=0.00 to a value of around 2.0 for Bo=0.29. The heat transfer at the center of the side wall is not very different for the three cases studied. Very small differences are observed in the secondary flow features, especially the lateral velocities, as buoyancy is varied and hence there is little difference in the side wall heat transfer at the center of the duct.

Figure 16 shows the comparison of the heat transfer predicted by DES at the ribbed walls and the side walls for Ro=0.35 and Bo=0.29 with LES. Heat transfer profiles at both the leading and trailing walls show good agreement with the LES predictions. The region of high heat transfer upstream of the ribs predicted by DES is observed to be larger at both the ribbed surfaces. The heat transfer at the ribbed walls is influenced by the primary flow features and the turbulence in the vicinity of the ribbed walls. Since DES captures the primary flow features and the turbulence in this region accurately, the heat transfer augmentation predicted by DES is consistent with LES.

At the side walls the heat transfer augmentation is observed to decrease from a value of around 8.0 in the vicinity of the rib at the trailing surface to a value of around 1.5–2.0 at the rib at the leading surface. The heat transfer contours, which are dictated by the secondary flow, are also predicted accurately by DES.

Figure 17 shows the surface averaged heat transfer at the trailing and leading side walls. The heat transfer augmentation obtained using DES is compared with predictions by LES [32] and experimental results by Wagner et al. [50] for the different buoyancy cases. For the lower buoyancy case (Bo=0.12) it is observed

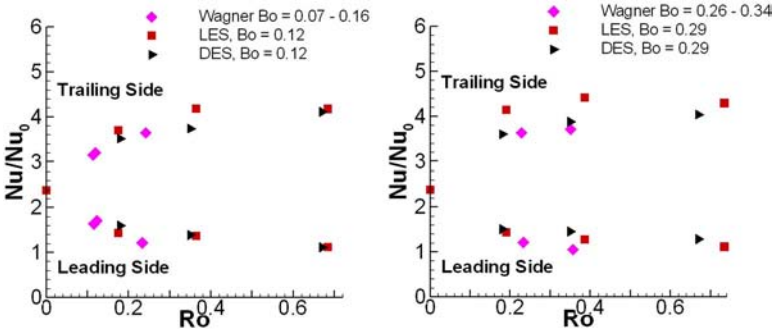

Fig. 17 Comparison of the surface averaged ribbed wall heat transfer augmentation

that the heat transfer augmentation predicted at the trailing and leading side wall compares well with the experimental measurements as well as the LES computations. The heat transfer augmentation at the trailing wall is observed to increase from a value of around 3.5 to a value of around 4.1 as the rotation is increased from Ro=0.18 to Ro=0.67. At the leading wall the heat transfer augmentation decreases from a value of around 1.6 to a value of 1.1. For the highest buoyancy case (Bo=0.29) the heat transfer augmentation at the leading and trailing surfaces differ from the values predicted by LES by a factor of 15%. However, a comparison with the experimental measurements of Wagner et al. [32] shows good agreement.

Figure 18 shows the comparison of the side wall heat transfer as predicted by DES in comparison with the heat transfer reported by LES studies [32]. The side wall heat transfer augmentation predicted by DES compares well with LES. It is observed that the surface averaged heat transfer augmentation increases as the rotation is increased from 0.18 to 0.35, but remains constant as rotation is further increased to Ro=0.67. A slight difference is observed in the side wall heat transfer for the Ro=0.67 and Bo =0.29 between DES and LES. However, the value predicted by DES is within 7.5% of the value predicted by LES.

Summary and Conclusions

This study investigates the performance of detached eddy simulation (DES) in predicting the flow and heat transfer in ribbed ducts with applications to the internal cooling of turbine blades. Though initially proposed as a wall model using the Spalart-Allmaras model, DES can also be used as a general purpose RANS-LES model, which adjusts to the local flow conditions via the turbulent length scale and the grid specification. Since its inception, DES has been applied to a wide variety of flow fields, but has been mostly limited to unbounded external flows. Only a handful of studies have applied DES to internal flows. This is the first study to apply and validate DES to predict the internal flow and heat transfer in noncanonical flows of relevance in internal cooling of gas turbine blades.

DES is observed to be a viable turbulence modeling scheme for predicting the dynamics of separation and reattachment and in resolving secondary flows that affect the heat transfer, with a LES-like accuracy at a lower computational cost. In a series of calculations it is shown that DES successfully predicts the physics of rotation induced Coriolis forces and centrifugal buoyancy. DES by using LES-like resolution of the large scales allows itself to be receptive to secondary strains that the base RANS model fails to capture. The main contribution of this work is showing that DES can be successfully applied to internal flows that are dominated by rotation induced Coriolis forces and centrifugal buoyancy.

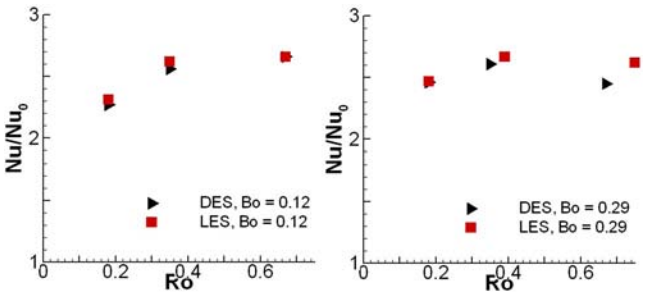

Fig. 18 Comparison of the side wall heat transfer augmentations

Acknowledgment

This research was supported by the U.S. DOE, Office of Fossil Energy, and National Energy Technology Laboratory. Any opinions, findings, conclusions, or recommendations expressed herein are those of the authors and do not necessarily reflect the views of the DOE.

Nomenclature

- Ar = Archimedes number ($=g\beta\Delta TL/U_0^2$) for the cavity case used for validating the effects of buoyancy
- Bo = buoyancy parameter ($=(\Delta\rho/\rho)(r/D_h)\mathrm{Ro}^2$)
- C_{DES} = DES constant
- D_k = destruction term in the k equation
- D_h = hydraulic diameter; reference length for the ribbed duct cases (=dimensions of the square duct)
- e = rib height ($e/D_h=0.1$)
- H = step height, for the validation case used for studying the effects of Coriolis forces; reference length for the backward facing step case
- h = height of the duct upstream of the backward facing step
- k = thermal conductivity or turbulent kinetic energy
- L = width of the cavity; reference length for the cavity case
- $l_{k\text{-}\omega}$ = turbulent (RANS) length scale
- Nu = local Nusselt number
- P = rib pitch ($P/e=10$)
- q'' = constant heat flux on duct walls and rib
- r = radius from rotation axis
- Re = Reynolds number based on the reference length (L_r) and reference velocity ($=U_0L_r/\nu$)

Ro = rotation number based on the reference length (L_r) and the rotation rate ($=\Omega L_r/U_0$)
S = spanwise width of the cavity
T_0 = temperature of the fluid at the bottom wall of the cavity
T_H = temperature of the top wall of the cavity
U_0 = mean bulk velocity; reference velocity for computing the Reynolds number
u, v, w = Cartesian velocities
W = width of the cavity
$\begin{Bmatrix} X, & Y, & Z \\ x, & y, & z \end{Bmatrix}$ = physical coordinates in nondimensional form
Δ = grid (LES) length scale
δ = modified (DES) length scale
ν = viscosity
Ω = rotation rate
ω = specific dissipation rate

Subscripts

0 = smooth duct
t = turbulent parameters
τ = values based on friction velocity

References

[1] Spalart, P. R., Jou, W. H., Streletes., M., and Allmaras., S. R., 1997, "Comments on the Feasibility of LES for Wings and a Hybrid RANS/LES Approach," First AFSOR Int. Conf. on DNS/LES, Aug. 4–8, in *Advances in DNS/LES*, C. Liu and Z. Liu, Eds., Greyden Press, Columbus, OH.

[2] Strelets, M., 2001, "Detached Eddy Simulation of Massively Separated Flows," AIAA Paper No. 2001-0879.

[3] Shur, M., Spalart, P. R., Strelets, P. R., and Travin, A., 1999, "Detached-Eddy Simulation of an Airfoil at High Angle of Attack," 4th Int. Symposium on Eng. Turb. Modelling and Experiments, May 24–26, Corsica, W. Rodi and D. Laurence, eds., Elsevier, Amsterdam.

[4] Travin, A., Shur, M. L., Strelets, M., and Spalart, P. R., 2000, "Detached Eddy Simulation Past a Circular Cylinder," Flow, Turbul. Combust., **63**, pp. 193–313.

[5] Constantinescu, G., and Squires, K. D., 2000, "LES and DES Investigations of Turbulent Flow Over a Sphere," AIAA Paper No. AIAA-2000-0540.

[6] Constantinescu, G. S., Pacheco, R., and Squires, K. D., 2002, "Detached-Eddy Simulation of Flow Over a Sphere," AIAA Paper No. 2002-0425.

[7] Viswanathan, A. K., Squires, K. D., Klismith, K., and Forsythe, J. R., 2003, "Detached-Eddy Simulation Around a Forebody at High Angle of Attack," AIAA Paper No. 2003-0263.

[8] Kotapati-Apparao, R. B., Squires, K. D., and Forsythe, J. R., 2003, "Prediction of a Prolate Spheroid Undergoing a Pitchup Maneuver," AIAA Paper No. 2003-0269.

[9] Forsythe, J. R., Squires, K. D., Wurtzler, K. E., and Spalart, P. R., 2002, "Detached-Eddy Simulation of Fighter Aircraft at High Alpha," AIAA Paper No. 2002-0591.

[10] Morton, S. A., Steenman, M. B., Cummings, R. M., and Forsythe, J. R., 2003, "DES Grid Resolution Issues for Vertical Flows on a Delta Wing and an F-18C," AIAA Paper No. 2003-1103.

[11] Squires, K. D., Forsythe, J. R., Morton, S. A., Blake, D. C., Serrano, M., Wurtzler, K. E., Strang, W. E., Tomaro, R. F., and Spalart, P. R., 2002, "Analysis of Full Aircraft With Massive Separation Using Detached-Eddy Simulation," Proceedings of the High Performance Computing Modernization Program 2002 Users Group Conference, Austin, TX, June 9–14.

[12] Kapadia, S., Roy, S., Vallero, M., Wurtzler, K. E., and Forsythe, J. R., 2003, "Detached Eddy Simulation Over a Reference Ahmed Car Model," AIAA Paper No. 2003-0857.

[13] Nikitin, N. V., Nicoud, F., Wasistho, B., Squires, K. D., and Spalart, P. R., 2000, "An Approach to Wall Modeling in Large-Eddy Simulation," Phys. Fluids, **12**(7), pp. 1629–1632.

[14] Menter, F. R., 1992, "Improved Two-Equation k-ω Turbulence Models for Aerodynamic Flows," NASA Technical Memorandum 103975.

[15] Menter, F. R., 1993, "Zonal Two Equation k-ω Turbulence Models for Aerodynamic Flows," AIAA Paper No. 93-2906.

[16] Saidi, A., and Sunden, B., 2001, "On Prediction of Thermal-Hydraulic Characteristics of Square-Sectioned Ribbed Cooling Ducts," ASME J. Turbomach., **123**, pp. 614–621.

[17] Jia, R., Saidi, A., and Sunden, B., 2002, "Heat Transfer Enhancement in Square Duct With V-Shaped Ribs of Various Angles," ASME Paper No. GT 2002-3029, ASME Turbo Expo 2002, June 3–6, Amsterdam, The Netherlands.

[18] Jia, R., Saidi, A., and Sunden, B., 2003, "Heat Transfer Enhancement in Square Duct With V-shaped Ribs," ASME J. Turbomach., **125**, pp. 788–791.

[19] Jia, R., Sunden, B., and Faghri, M., 2005, "Computational Analysis of Heat Transfer Enhancement in Square Ducts With V-shaped Ribs: Turbine Blade Cooling," ASME J. Heat Transfer, **127**, pp. 425–433.

[20] Iacovides, H., and Raisee, M., 1999, "Recent Progress in the Computation of Flow and Heat Transfer in Internal Cooling Passages of Turbine Blades," Int. J. Heat Fluid Flow, **20**, pp. 320–328.

[21] Iaccarino, G., Ooi, A., Pettersson Rief, B. A., and Durbin, P., 1999, "RANS Simulations of Rotating Flows," Center of Turbulence Research, Annual Research Briefs, pp. 257–266.

[22] Ooi, A., Iaccarino, G., Durbin, P. A., and Behnia, M., 2002, "Reynolds Averaged Simulation of Flow and Heat Transfer in Ribbed Ducts," Int. J. Heat Fluid Flow, **23**, pp. 750–757.

[23] Prakash, C., and Zerkle, R., 1992, "Prediction of Turbulent Flow and Heat Transfer in a Radially Rotating Square Duct," ASME J. Turbomach. **114**, pp. 835–846.

[24] Jang, Y. J., Chen, H. C., and Han, J. C., 2001, "Flow and Heat Transfer in a Rotating Square Channel With 45 deg Angled Ribs by Reynolds Stress Turbulence Model," ASME J. Turbomach., **123**(1), pp. 124–132.

[25] Chen, H. C., Jang, Y. J., and Han, J. C., 1999, "Computation of Flow and Heat Transfer in a Rotating Two-Pass Square Channel by a Reynolds Stress Model," ASME Paper No. 99-GT-174.

[26] Su, G., Teng, S., Chen, H. C., and Han, J. C., 2003, "Computation of Flow and Heat Transfer in Rotating Rectangular Channels (AR=4) With V-shaped Ribs by a Reynolds Stress Turbulence Model," ASME Paper No. GT 2003-38348, ASME Turbo Expo 2003, June 16–19, Atlanta, GA.

[27] Iacovides, H., 1998, "Computation of Flow and Heat Transfer Through Rotating Ribbed Passage," Int. J. Heat Fluid Flow, **19**, pp. 393–400.

[28] Iacovides, H., Launder, B. E., and Li, H. Y., 1996, "The Computation of Flow Development Through Stationary and Rotating U-Ducts of Strong Curvature," Int. J. Heat Fluid Flow, **17**, pp. 22–33.

[29] Murata, A., and Mochizuki, S., 2001, "Comparison Between Laminar and Turbulent Heat Transfer in Stationary Square Ducts With Transverse or Angled Rib Turbulators," Int. J. Heat Mass Transfer, **44**, pp. 1127–1141.

[30] Watanabe, K., and Takahashi, T., 2002, "LES Simulation and Experimental Measurement of Fully Developed Ribbed Channel Flow and Heat Transfer," Proceedings of the ASME Turbo Expo, Amsterdam, The Netherlands, June.

[31] Tafti, D. K., 2005, "Large Eddy Simulations of Heat Transfer in A Ribbed Channel for Internal Cooling of Turbine Blades," Int. J. Heat Fluid Flow, **26**(1), pp. 92–104.

[32] Abdel-Wahab, S., and Tafti, D. K., 2004, "Large Eddy Simulations of Flow and Heat Transfer in a 90° Ribbed Duct With Rotation—Effect of Coriolis and Centrifugal Buoyancy Forces," ASME J. Turbomach., **126**, pp. 627–636.

[33] Abdel-Wahab, S., and Tafti, D. K., 2004, "Large Eddy Simulation of Flow and Heat Transfer in a Staggered 45 degrees Ribbed Duct," Proc. ASME Turbo Expo, Paper No. 2004-GT-53800.

[34] Sewall, E. A., and Tafti, D. K., 2004, "Large Eddy Simulation of the Developing Region of a Rotating Ribbed Internal Turbine Blade Cooling Channel," ASME Turbo Expo: 2004, Vienna, Austria, ASME Paper No. GT2004-53833.

[35] Sewall, E. A., and Tafti, D. K., 2007, "Large Eddy Simulation of Flow and Heat Transfer in the Developing Flow Region of a Rotating Gas Turbine Blade Internal Cooling Duct With Coriolis and Buoyancy Forces," ASME J. Turbomach., accepted for publication.

[36] Saha, A. K., and Acharya, S., 2005, "Flow and Heat Transfer in an Internally Ribbed Duct With Rotation: An Assessment of Large Eddy Simulations and Unsteady Reynolds-Averaged Navier-Stokes Simulations," ASME J. Turbomach., **127**(2), pp. 306–320.

[37] Cui, J., and Tafti, D. K., 2002, "Computations of Flow and Heat Transfer in a Three-Dimensional Multilouvered Fin Geometry," Int. J. Heat Mass Transfer, **45**, pp. 5007–5023.

[38] Sewall, E. A., and Tafti, D. K., 2004, "Large Eddy Simulation of Developing Region of a Stationary Ribbed Internal Turbine Blade Cooling Channel," ASME Turbo Expo: 2004, Vienna, Austria, ASME Paper No. GT2004-53832.

[39] Sewall, E. A., Tafti, D. K., Graham, A., and Thole, K. A., 2006, "Experimental Validation of Large Eddy Simulation of Flow and Heat Transfer in a Stationary Ribbed Duct," Int. J. Heat Fluid Flow, **27**(2), pp. 243–258.

[40] Sewall, E. A., and Tafti, D. K., 2006, "Large Eddy Simulation of Flow and Heat Transfer in the 180 Degree Bend Region of a Stationary Gas Turbine Blade Ribbed Internal Cooling Duct," ASME J. Turbomach., **128**(4), pp. 763–771.

[41] Tafti, D. K., 2001, "GenIDLEST—A Scalable Parallel Computational Tool for Simulating Complex Turbulent Flows, Proc. ASME Fluids Engineering Division," FED Vol. 256, ASME-IMECE, New York.

[42] Viswanathan, A. K., and Tafti, D. K., 2005, "Detached Eddy Simulation of Turbulent Flow and Heat Transfer in a Duct," ASME J. Fluids Eng., **127**(5), pp. 888–896.

[43] Rau, G., Cakan, M., Moeller, D., and Arts, T., 1998, "The Effect of Periodic Ribs on Local Aerodynamic and Heat Transfer Performance of a Straight Cooling Channel," ASME J. Turbomach., **120**, pp. 368–375.

[44] Halleen, R. M., and Johnston, J. P., 1967, "The Influence of Rotation of Flow in a Long Rectangular Channel—An Experimental Study," Report MD-18, Thermosciences Division, Dept. of Mech. Eng., Stanford University.

[45] Lezius, D. K., and Johnston, J. P., 1976, "Roll-Cell Instabilities in Rotating Laminar and Turbulent Channel Flows," J. Fluid Mech., **77**(1), pp. 153–175.

[46] Rothe, P. H., and Johnston, J. P., 1979, "Free Shear Layer Behavior in Rotating Systems," ASME J. Fluids Eng., **101**, pp. 117–120.

[47] Viswanathan, A. K., 2006, "Detached Eddy Simulation of Turbulent Flow and Heat Transfer in Turbine Blade Internal Cooling Ducts," Ph.D. dissertation, Virginia Polytechnic Institute and State University, Blacksburg, VA.

[48] Nilsen, P. J., and Andersson, H. I., 1990, "Rotational Effects on Sudden-Expansion Flows," Proc. of Int. Sym, Dubrovnik, Yogoslavia, in *Engineering*

Turbulence Modelling and Experiments, Elsevier Science, Rodi and Ganić, pp. 65–72, September 24–28.
[49] Viswanathan, A. K., and Tafti, D. K., 2006, "Detached Eddy Simulation of Turbulent Flow and Heat Transfer in a Fully-Developed Duct Subjected to Rotation," Int. J. Heat Fluid Flow, **27**(3), pp. 351–370.
[50] Wagner, J. H., Johnson, B. V., Graziani, R. A., and Yeh, F. C., 1992, "Heat Transfer in Rotating Serpentine Passages With Trips Normal to the Flow," ASME J. Turbomach. **114**, pp. 847–857.
[51] Liou, T. M., Chen, M. Y., and Tsai, M. H., 2001, "Fluid Flow and Heat Transfer in a Rotating Two-Pass Square Duct With In-Line 90° Ribs," ASME Turbo Expo, ASME Paper No. 2001-GT-0185.
[52] Parsons, J. A., Han, J. C., and Zang, Y. M., 1994, "Wall Heating Effect on Local Heat Transfer in a Rotating Two-Pass Square Channel With 90° Rib Turbulators," Int. J. Heat Mass Transfer, **37**, pp. 1411–1420.
[53] Grand, D., 1975, "Contribution a l'etude des courant de recirculation," PhD thesis, L'Universite Scientifique et Medicale et Institut Nationale, Polytechnique, Grenoble, France.
[54] Ideriah, F. J. K., 1980, "Prediction of Turbulent Cavity Flow Driven By Buoyancy and Shear," J. Mech. Eng. Sci., **22**(6), pp. 287–295.

Influence of Phonon Dispersion on Transient Thermal Response of Silicon-on-Insulator Transistors Under Self-Heating Conditions

Rodrigo A. Escobar
Departamento de Ingeniería Mecánica y Metalúrgica,
Pontificia Universidad Católica de Chile,
Vicuña Mackenna 4860, Macul,
Santiago, Chile
e-mail: rescobar@ing.puc.cl

Cristina H. Amon[1]
Fellow ASME
Raymond Lane Distinguished Professor
Mechanical Engineering Department,
Carnegie Mellon University,
Pittsburgh, PA 15213;
Faculty of Applied Science and Engineering,
University of Toronto,
Toronto, Ontario M5S 1A4, Canada
e-mail: cristina.amon@utoronto.ca

Lattice Boltzmann method (LBM) simulations of phonon transport are performed in one-dimensional (1D) and 2D computational models of a silicon-on-insulator transistor, in order to investigate its transient thermal response under Joule heating conditions, which cause a nonequilibrium region of high temperature known as a hotspot. Predictions from Fourier diffusion are compared to those from a gray LBM based on the Debye assumption, and from a dispersion LBM which incorporates nonlinear dispersion for all phonon branches, including explicit treatment of optical phonons without simplifying assumptions. The simulations cover the effects of hotspot size and heat pulse duration, considering a frequency-dependent heat source term. Results indicate that, for both models, a transition from a Fourier diffusion regime to a ballistic phonon transport regime occurs as the hotspot size is decreased to tens of nanometers. The transition is characterized by the appearance of boundary effects, as well as by the propagation of thermal energy in the form of multiple, superimposed phonon waves. Additionally, hotspot peak temperature levels predicted by the dispersion LBM are found to be higher than those from Fourier diffusion predictions, displaying a nonlinear relation to hotspot size, for a given, fixed, domain size. [DOI: 10.1115/1.2717243]

Keywords: conduction, electronics, phonon transport, LBM, BTE, nanoscale

Introduction

Thermal effects are becoming increasingly important for the proper behavior and operation of microelectronic components. This is particularly relevant for the silicon-on-insulator (SOI) transistor, in which a thin silicon layer is deposited on top of a silicon dioxide layer, thus allowing faster device switching speeds due to the reduced capacitive coupling with the substrate. SOI technology reduces electronic leaking and enhances the electrostatic characteristics of the device, while at the same time reducing short-channel effects. However, thermal boundary resistance at the interface between layers greatly reduces the heat flux from the channel area, and small-scale heat sources can increase the local peak power generation rate to an order of magnitude. These effects, when combined, can result in a temperature increase that might surpass the safe operation point of the device. In addition, the silicon dioxide layer has poor thermal conduction and, as a result, most of the heat generated within the SOI device is confined to the thin silicon film, making it susceptible to thermal failure under electrostatic discharge events (ESD) or even normal switching activity while in operation conditions.

With the current gate length in the 90 nm technology node (International Technology Roadmap for Semiconductors, ITRS 2004 update, [1]), transistors produce about 0.1 mW of Joule heating per unit length, which results in power dissipation on the order of 10 $W/\mu m^3$ within a hotspot zone with dimensions on the order of 10–30 nm [2,3], which is smaller than the nominal value of phonon mean free path. This value, when applying a gray model based on the Debye assumption, is computed to be 41 nm [4]. As a result of the small-scale dimensions of SOI devices, the continuum assumption is no longer valid, and these transistors exhibit subcontinuum heat transfer effects, which make the thermal management of the devices an important concern, in addition to the challenges of microfabrication. In subcontinuum energy transport regimes, the Fourier heat conduction equation is not valid, and the methodology of choice must consider the contribution of the different energy carriers. Thus, in crystalline semiconductors such as silicon, the use of the more fundamental Boltzmann transport equation (BTE) for phonon transport is required.

Since subcontinuum heat conduction is very difficult to observe and measure, numerical simulations begin to play a critical role in thermal design of semiconductor devices with micro- and nano-sized features. Subcontinuum heat transfer effects impede the appropriate cooling of field-effect transistors, thus degrading their performance and reliability. Miniaturization of the devices increases the effect of boundary resistances and the heat generation per unit volume, which when coupled with the subcontinuum effects, result in larger temperature increases than what is predicted by continuum thermal models. Overall, a coupled electro-thermal design methodology is needed in order to take into account both electronic and thermal issues and optimize device performance.

According to the ITRS [1], characteristic dimensions of the complementary metal–oxide–semiconductor (CMOS) transistors have significantly decreased in past years, and currently produced commercial transistors have gate lengths of approximately 50 nm, projected to reach 20 nm shortly after 2010. This continuous aim for improving the performance and density of microprocessors has provided the driving force for system scaling following Moore's law, in which the resulting increases in transistor counts and higher clock frequencies lead to higher chip power density generation. Thus, more power-efficient processor designs are needed to increase the power dissipation and maintain the device at reliable temperature levels. Recently, Intel has developed the 65 nm technology node, in which transistors are designed and built with

[1]Corresponding author.

Contributed by the Heat Transfer Division of ASME for publication in the JOURNAL OF HEAT TRANSFER. Manuscript received December 22, 2005; final manuscript received September 19, 2006. Review conducted by Suresh V. Garimella. Paper presented at the 2005 ASME International Mechanical Engineering Congress (IMECE2005), Orlando, FL, USA, November 5–11, 2005.

 Copyright © 2007 by ASME

gate lengths as small as 35 nm [5]. This transistor is expected to work in the Terahertz range, which translates the switching activity well into the picosecond time scale. During transistor operation, electrons from the source are accelerated and travel through the silicon layer until they reach the drain. In this process, they often collide with phonons, which are excited by receiving part of the electron system energy.

The electron-phonon scattering process proposed by Pop et al. [6] can be summarized as follows: low-energy electrons interact with acoustic phonons in a time scale of approximately 0.1 ps, while high energy electrons interact with optical phonons in a similar time scale. The highly energetic but slow-propagating optical phonons then decay into low-energy, fast propagating acoustic phonons in a time scale of approximately 5 ps. Heat conduction typically occurs by acoustic phonon propagation in time scales longer than milliseconds. Past modeling efforts have considered several techniques to predict magnitude, duration, and spatial localization of the region subject to Joule heating, which can be caused by electron–phonon scattering during normal operation of the device, or by an accidental electrostatic discharge event (ESD).

Sverdrup et al. [7] presented electro-thermal modeling and simulation techniques for sub-micron devices, for which simulations of a phonon BTE under the energy density formulation were conducted in an attempt to predict maximum temperature rise in a device subject to an ESD event. Heat conduction in SOI transistors has been studied by Sverdrup et al. [8], where a phonon BTE was solved in a silicon film, coupled with the heat conduction in the silicon dioxide beneath the transistor. Predicted temperature peaks in the silicon film using the phonon BTE were found to be 160% higher than predictions from the heat conduction equation, suggesting intense electron-phonon energy transfer. Experimental evidence of Fourier regime failure in microstructures was provided by Sverdrup et al. [9], where a severe departure from equilibrium was found at a hotspot in a suspended silicon membrane. Temperature rise exceeded Fourier predictions by 60% when the computed phonon mean free path was 30 times larger than the resistor thickness, which was found to be consistent with a numerical conduction model that considered a two-fluid, steady state approach to phonon transport. Localized heating effects and scaling of CMOS devices were studied by Pop et al. [6]. A two-fluid, steady-state phonon BTE in the energy density formulation was used to numerically predict phonon distributions for devices with channel lengths as low as 90 nm. Localized drain hotspots were found to alter drain characteristics, which can affect the resistance and electron injection characteristics at the source. Additionally, higher temperature rises were reported when using the BTE formulation than those predicted by traditional diffusion theory.

Pop et al. [10] developed a Monte Carlo simulation method for calculating the Joule heating in electronic nanostructures, considering electron-phonon scattering effects. The model incorporated energy dissipation rates from electrons to each frequency dependent phonon mode, thus accounting for non-equilibrium energy transfer from the electron to the phonon systems. Predicted phonon emission rates can be applied to a variety of devices accounting for Joule heating. This phonon emission spectrum was further refined by Pop et al. [11], thus providing an important tool for electro-thermal analysis of nanodevices. Sinha and Goodson [12] presented a two-fluid phonon BTE model to analyze the energy bottleneck between faster propagating modes and slower reservoir modes in the context of nanometer-size hotspots. The model predicts an extra resistance that scales with the square of the ratio of mean free path and hotspot dimension. Thermal analysis of ultrathin devices was studied by Pop et al. [13] in the context of device scaling analysis. It was found that device temperatures are very sensitive to the choice of device geometry, especially on the drain and channel dimensions. It concludes that ITRS power guidelines for devices below 25 nm should be revised if isothermal scaling of thin-body devices is desired. Narumanchi et al. [14] presented a finite volume solution to a set of equations based on the BTE, considering dispersion in the acoustic modes and a single frequency band optical mode to simulate sub-micron SOI devices under Joule heating and ESD events. A comparison of the application of a heat source term to different phonon modes rendered significantly different results when the source term was applied to either acoustic or optical modes. BTE-based solutions predicted a temperature rise larger than that obtained with the Fourier heat conduction equation.

Escobar et al. [15] and Escobar and Amon [16] showed that phonon propagation in subcontinuum regimes is in the form of superimposed traveling waves, in which the slowest optical modes have a longer residence time within the hotspot area and, therefore, cause increased temperature rises compared to Fourier predictions. A molecular dynamics study on the three-phonon scattering process at hotspots in silicon was conducted by Sinha et al. [3,17], where a comparison between the decay modes of phonons in hotspots revealed that decay mechanisms are the same for longitudinal optical (LO), longitudinal acoustic (LA), and transverse acoustic (TA) modes, only differing in their scattering rates. Dominance of low group velocity transverse modes after the decay indicates a possible reduction in thermal conductance in the transistor, which could increase injection at the source and junction resistance at the drain. While a variety of modeling approaches and techniques has been applied to the prediction of thermal response of sub-micron transistors with different success levels, it is clear that subcontinuum effects in submicron and nanoscale transistors have a great influence on the overall temperature rise, especially when hotspot regions are present.

Recent efforts have focused on considering the effect of the previously neglected optical modes, by giving them an increased role in electro-thermal models. It is, therefore, one of the goals of this work to apply a dispersion lattice Boltzman method (LBM) model to the prediction of the transient thermal response of SOI transistors, which incorporates more accurate physics than those currently in existence, and at a more fundamental level. Assumptions of the relative importance of different phonon modes are not required, instead relying only on the underlying physics of the BTE to handle the contributions of each mode. We first characterize the transition from a Fourier diffusion regime to a ballistic phonon transport regime, and then compare predictions for SOI thermal response to Joule heating obtained by the Fourier heat conduction equation and the LBM.

Thermal Modeling of SOI Devices

The heat transfer process between the silicon layer and the silicon dioxide layer is composed by two phenomena: the reduced thermal conductivity of the oxide layer and the boundary resistance existing between layers. Narumanchi et al. [18] have demonstrated that this thermal boundary resistance at the silicon/oxide interface, in addition to the reduced thermal conductivity of the oxide layer, effectively acts as a strong heat barrier that prevents most of the heat from leaving the silicon layer. Therefore, in this simplified model we choose to consider only the thin silicon layer following the reported results from Sverdrup et al. [8] and Narumanchi et al. [18], which indicate that an adiabatic boundary condition at the silicon/oxide interface is a good assumption. The silicon layer is modeled to have a length L and a thickness h. The top and bottom boundaries are considered to be adiabatic, a condition resulting from phonon reflection conditions. Right and left boundaries are kept at a constant temperature level of 300 K, effectively acting as heat sinks. The hotspot is modeled as a circular region of diameter d, as shown in Fig. 1. A special case of a one-dimensional model is also used to capture the main features that characterize the transition from Fourier diffusion to ballistic phonon transport. In that case, the computational domain has a length L, and the hotspot width is d, located at the domain center.

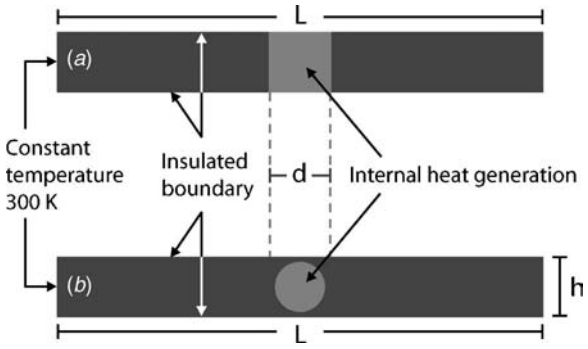

Fig. 1 SOI simplified silicon layer modeling: (*a*) one-dimensional model; and (*b*) two-dimensional model

Source Term Modeling

The source term due to electron-phonon scattering in a transistor has been the subject of several studies. Basically, these studies can be grouped into three categories: source term shape, duration and form of application. The most basic model of this source term corresponds to Sverdrup et al. [8], where a constant term was applied to a steady state BTE simulation of a silicon layer, resulting in a moderate temperature increase, which nevertheless was higher than what was predicted by Fourier diffusion. Narumanchi et al. [19] used a single heat pulse of varying duration in semi-gray BTE simulations of a symmetric section of a SOI transistor. Following that work, we consider here a single heat pulse characterized by a magnitude Q that lasts for a period of time t_q. After this time, the pulse magnitude becomes zero. Pulse duration and magnitude effects are studied for both the gray and dispersion LBM models.

An accurate model of the heat source term necessarily has to include the contribution of electron-phonon interactions, which would require the simultaneous simulation of both the electron and phonon systems. Very little information exists in the literature about this topic. Promising preliminary research has been performed by Ghai et al. [20] using a coupled electron–phonon LBM, and by Sinha et al. [17,21], where an Monte Carlo (MC) method is applied. The peak heat generation rate in an SOI device can vary, as stated by different authors [17,19], and in general can also be model dependent. Recently, LBM simulations by Escobar and Amon [16] revealed that the hotspot peak temperature is linear with an increase on the heat source term magnitude, information that allows numerical simulations to focus on phonon physics rather than on temperature levels. Another important point to address refers to how the energy from the source term is distributed to the different phonon branches, and how the energy received by a phonon branch is distributed among its frequency spectrum. For the gray LBM model, all energy from the source term is applied to the single phonon mode defined by the Debye assumption [4,15,22]. When considering a dispersion model, Narumanchi et al. [23] observed significant differences in the results in cases when the heat pulse was applied to only one branch in the phonon spectrum, which leads us to think that a proper treatment of the source term is necessary to obtain accurate, physically meaningful results. However, the approach followed by Narumanchi et al. [23] only assigns the full value of the source term to a single phonon branch, without distinction being made as to how it was distributed among the phonon frequency spectrum. The only results available in the literature that report frequency-dependent source terms are those of Sinha et al. [24], where MC simulations of the electron–phonon scattering process were presented. Following this approach, the total amount of energy that the source term contributes to a phonon branch can be found by performing an integration of the frequency-dependent source term over the phonon frequency spectrum for a given phonon branch. A constant factor is then used to multiply the integration result, in order to obtain the desired source term magnitude. Narumanchi et al. [23] and Escobar and Amon [16] demonstrated that the frequency dependence of the heat source term is critical to the final temperature rise of the device. As a result of the previous discussion, the model presented here includes the source term as afrequency-dependent quantity based on the data from Sinha and Goodson [24].

The Lattice Boltzmann Method

The LBM is a discrete development of the BTE, which can be used to simulate energy transport problems within the applicability range of the BTE; that is, within time scales larger than the collision time, and length scales larger than the phonon wavelength, with no upper boundary on either length or time scale. However, the computational expense of the LBM grows exponentially with the length scale, thus making it unsuitable for large-scale computations in the diffusive transport regime, which can be described accurately and at a much lower computational expense by the Fourier heat diffusion equation. Therefore, a computationally efficient strategy implements the LBM at continuum scales only to verify the model's accuracy using Fourier heat diffusion as a baseline. Here, we present only the more general aspects of the method. Additional details can be obtained from Succi [25], Zhang and Fisher [26], Escobar et al. [15], and Escobar and Amon [16,27]. The LBM discretizes the space domain by defining lattice sites where the phonon distributions are computed. Phonons generated at a particular lattice site will propagate to a neighboring lattice site by traveling at the phonon propagation speed, and collide with phonons generated at that lattice site. The time domain is also discretized by restricting the phonons to travel from one lattice site to the neighboring lattice site in a definite time step, which corresponds to the site-to-site transport restriction. The LBM makes it possible to incorporate additional details of phonon physics into the system and, at the same time, handle different length and time scales. The earliest research on the LBM for phonon transport only considered the gray model of LA phonons under the Debye assumption. Even though it has been argued that optical phonons do not contribute a greatly to the energy transport process, mainly because of their reduced group velocity when compared to acoustic phonons, they are indeed important when electron–phonon scattering events are present, and contribute a significant portion of a crystalline material heat capacity. The dispersion LBM aims at improving phonon modeling by incorporating the contributions of all phonon branches. The dispersion LBM starts with the phonon BTE in the phonon distribution function formulation, as in Eq. (1), where the equilibrium phonon distribution function is given by the Bose–Einstein distribution, as in Eq. (2)

$$\frac{\partial f}{\partial t} + \mathbf{v} \cdot \nabla f = \frac{f^0 - f}{\tau} + Q_{e-p} \tag{1}$$

$$f^0(\omega) = \frac{1}{e^{\hbar\omega/k_b T} - 1} \tag{2}$$

In Eq. (1), the term f corresponds to the phonon distribution function; f^0 is the equilibrium phonon distribution function; $\mathbf{v}$ is the frequency-dependent phonon propagation speed; τ is the frequency-dependent phonon relaxation time; t is time; and $Q_{e\text{-}p}$ is a source term which accounts for energy exchange between the electron and phonon systems. In Eq. (2), ω is the phonon frequency; $\hbar$ is Planck's constant divided by 2π, k_b is the Boltzmann constant; and T is the temperature. Details of this formulation can be found in Escobar and Amon [16,27], and in Escobar [28]. The dispersion LBM first considers nonlinear dispersion relations for all phonon branches, which are obtained from Dolling [29]. It then discretizes the frequency spectrum by defining frequency bands of given bandwidth that give origin to a discrete set of phonon group

velocities, and then solves frequency-dependent, simultaneous lattice Boltzmann kinetic equations (LBKEs) for each discrete frequency band. The behavior of each frequency band is coupled to others by a temperature constraint in the phonon equilibrium distribution function and by the frequency-dependent phonon relaxation time. The LBKE in a phonon distribution formulation is

$$f_i(x+\Delta x, t+\Delta t) = (1-W_i) f_i(x,t) + W_i f_i^0(x,t) + \Delta t Q_{e-p} \quad (3)$$

where the term f_i corresponds to the discrete phonon distribution function which is defined as the population of phonons propagating along the specific direction i in the lattice; f_i^0 is the equilibrium phonon distribution function of phonons propagating along the specific direction i in the lattice; Δx is the distance between two consecutive lattice points; Δt is the time step magnitude; and W_i is a weight factor equal to $\Delta t/\tau$. The total phonon distribution function is the sum of discrete phonon energy density distributions over all the two-dimensional lattice directions

$$f(x,t) = \sum_{i=1}^{d_1} f_i(x,t) \quad (4)$$

In the dispersion LBM, in order to successfully simulate the thermal behavior of a crystalline structure, adequate expressions for the dispersion relations (from which the phonon propagation speed is derived) and phonon relaxation times are needed. As noted above, adequate dispersion relations can be obtained from the literature. However, finding frequency-dependent relaxation time expressions for all phonon branches is more challenging. Here, we have resorted to implementing three-phonon interactions following what is described by Han and Klemens [30]. This approach has been demonstrated to be able to recover the bulk value of thermal conductivity for silicon [18]. However, as this analysis is based on perturbation theory, it relies on the assumption of low temperatures [30] and, thus, is expected to fail at higher temperatures. The Han and Klemens model considers three-phonon processes based on energy (frequency) and momentum (wave vector) conservation. In this model, inverse relaxation times for a specific process have the general form given by

$$\frac{1}{\tau_{ij}} = \frac{a\gamma^2\hbar}{3\pi\rho \cdot v_{ph}^b \cdot v_g^c} \cdot \omega_i \omega_j \omega_k \cdot R_c^2 \left(\frac{1}{e^{\hbar\omega_j/k_B T} - 1} - \frac{1}{e^{\hbar\omega_k/k_B T} - 1} \right) \quad (5)$$

where τ_{ij} is the relaxation time that accounts for energy exchange between the bands i and j of frequency ω_i and ω_j; ω_k is the intermediate phonon frequency that completes the three-phonon interaction; v_g is the phonon group velocity at ω_j; and ν_{ph} is the phase velocity of the i mode. The effective relaxation time for a discrete frequency band centered on ω_i is found as the combination of all phonon scattering processes in a Matthiessen sense. Additional details on the model can be found in Han and Klemens [30], Narumanchi [14], and Narumanchi et al. [18]. After solving Eq. (3) for all frequency bands, the frequency-dependent phonon energy density is computed by the product of the phonon distribution function, phonon frequency, Planck's constant divided by 2π, and the frequency-dependent phonon density of states $D(\omega)$

$$e_p'' = \hbar \cdot \omega \cdot f \cdot D(\omega) \quad (6)$$

The phonon energy density is given by the integration of the frequency-dependent phonon energy density over a frequency interval $\Delta\omega_p$ characteristic of each branch and polarization

$$e_p' = \int_{\Delta\omega_p} \hbar \cdot \omega \cdot f \cdot D(\omega) \cdot d\omega \quad (7)$$

Finally, the total phonon energy, which is a function of temperature, is given by the contributions of each branch and polarization, which includes longitudinal and traverse acoustic (LA and TA) and optical (LO and TO) phonons

$$e_L = \sum e_p = e_{\mathrm{LA}} + 2 \cdot e_{\mathrm{TA}} + e_{\mathrm{LO}} + 2 \cdot e_{\mathrm{TO}} \quad (8)$$

Once the total phonon energy has been found, the lattice temperature is computed from an analytical $e(T)$ expression obtained from Eqs. (7) and (8), where T is common for all phonon modes. Then, the new equilibrium phonon distribution function for each phonon mode is found from the Bose–Einstein distribution, Eq. (2).

The dispersion LBM can accurately model the phonon physics, at the cost of increased computational expense, which is derived from the need to solve simultaneous LBKEs corresponding to each frequency band for every mode. This makes it impracticable for problems within the diffusive (Fourier) regime, other than for validation purposes.

Results

In what follows, results are first presented for the transition from Fourier diffusion to ballistic transport in a one-dimensional (1D) model, as both the hotspot and domain sizes are decreased, considering a single heat pulse. Then, we present an analysis of the peak temperature as a function of both the hotspot size and pulse duration for a 2D model of fixed domain dimensions. A comparison with Fourier diffusion results allows for the observation of the differences between diffusive and ballistic transport.

In all cases, mesh refinement studies were conducted until the numerical solution was independent of both the spatial and temporal discretizations. A useful rule of thumb indicates that, for the gray model, lattice spacing should be at least one-third of the phonon mean free path value. For the dispersion model, this rule is also applied to all frequency bands, taking into account each band's frequency dependent phonon mean free path.

Transition From Fourier Diffusion to Ballistic Transport. This section characterizes the transition from Fourier diffusion to ballistic transport in a 1D computational model of an SOI device. Unlike the gray model, which had clear definitions for the Knudsen number and dimensionless time [4,15,26], the dispersion model does not lend itself to an easily understandable dimensionless nomenclature to describe its control parameters. Each frequency band is characterized by a frequency-dependent relaxation time and propagation speed, and therefore, a frequency-dependent Knudsen number can be defined for each one of them. In our understanding, a dimensional approach presents itself as easier to comprehend, and at the same time, gives a straight, clear account of how close the models are to actual devices.

For this 1D model, both the domain length L and the hotspot width d are progressively reduced, maintaining a d/L ratio of 1/10. The justification for keeping a constant d/L ratio is related to the computational expense inherent to the LBM. As has been mentioned elsewhere [15,31], the LBM can reach the diffusive regime only at a very high computational expense. The simulation of a small-scale SOI device implies the use of spatial discretizations on the order of nanometers, a resolution that simply cannot be maintained for a diffusive regime simulation. Thus, it is unfeasible to keep the domain length L at a diffusive regime value, while reducing only the hotspot size d. While reducing L can be argued to have an influence on the boundary effect that is observed, it can also be argued that it does not influence another important size effect that is presented in what follows.

Figure 2 shows the time evolution of the temperature distributions in a domain of $L=1000$ nm, with a hotspot region of width of $d=100$ nm. The heat pulse is applied during the first 100 ps of a 1000 ps simulation. The domain length defines this case to be close to, or within, the diffusive regime. It is observed that the dimensionless temperature profiles correspond very closely to the general trend expected for a Fourier diffusion solution, comparison that can be better seen in the time history of temperature displayed by Fig. 5. The Fourier and gray LBM results for a similar case are presented in Escobar et al. [15]. A marked difference with the gray LBM results can be observed, as the gray

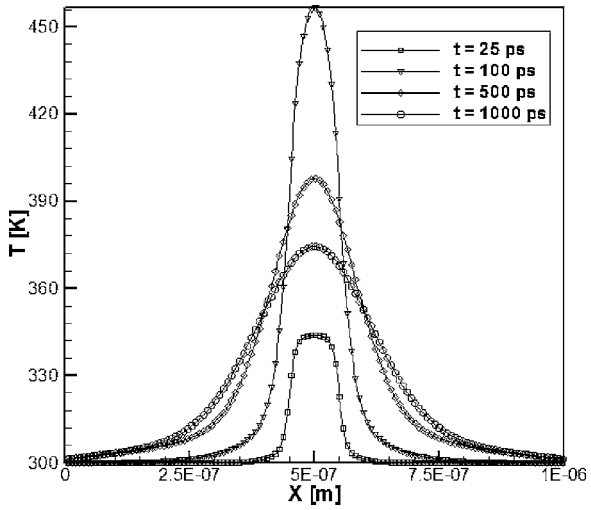

Fig. 2 Instantaneous temperature distributions in a model of an SOI device of length $L=1000$ nm (within the diffusive regime)

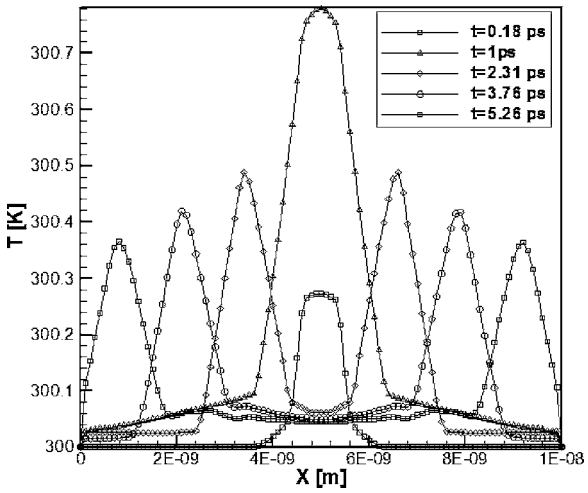

Fig. 4 Instantaneous temperature distributions in a model of an SOI device of length $L=10$ nm (within the ballistic regime)

model displays a constant temperature level within the hotspot previous to the heat pulse end, while the dispersion model displays a rounded temperature distribution in the hotspot region (at times $t=25$ ps and $t=100$ ps).

Decreasing the domain length by one order of magnitude to $L=100$ nm and the hotspot width to $d=10$ nm places the solution within the transitional regime. In this case, the heat pulse is applied for 10 ps and the total simulation time is 100 ps. As can be seen in Fig. 3, the region outside the hotspot region displays a temperature distribution comparable to that of Fourier diffusion, with a clearly defined steeper temperature increase inside the hotspot (for $t=1.8$ ps and $t=10$ ps). This change of slope in the temperature distribution corresponds to phonon confinement effects, of which the faster acoustic modes propagate quickly and leave the hotspot region, where the slower, highly capacitive optical modes remain confined and unable to leave the region. After the heat pulse is turned off (at $t=10$ ps), the temperature distribution clearly shows the existence of phonon waves traveling away from the hotspot region, with symmetric, propagating wave fronts displaying temperature values higher than those inside the hotspot area (as seen at $t=23.1$ ps). These wave fronts get attenuated and eventually disappear into a smooth temperature profile ($t=37.6$ ps and $t=75.1$ ps). Significant temperature slip conditions exist at the boundaries, with a magnitude of approximately 0.6 K.

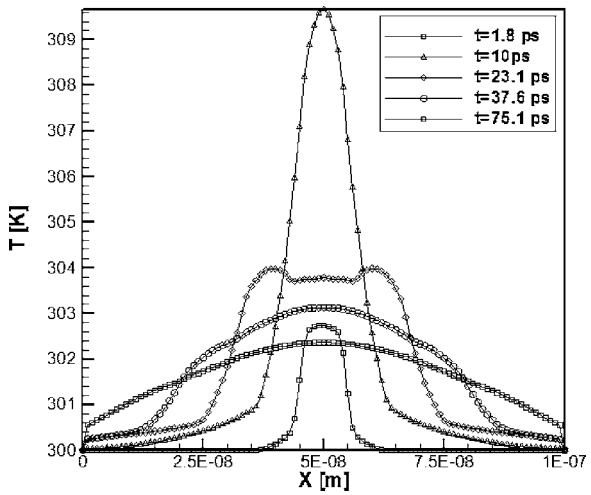

Fig. 3 Instantaneous temperature distributions in a model of an SOI device of length $L=100$ nm (within the transitional regime)

The ballistic transport regime is reached by further decreasing the domain length and hotspot size to $L=10$ nm and $d=1$ nm. The heat pulse in this case is applied for 1 ps, with a total simulation time of 10 ps. While the heat pulse is turned on ($t=0.18$ ps and $t=1$ ps), three regions with distinct characteristics are observed in Fig. 4: a linear temperature distribution outside the hotspot region, a region of steep temperature rise, and a rounded distribution inside the hotspot. Phonon confinement effects are strong, with the peak hotspot temperature being more than 700% higher than the highest temperature outside the hotspot.

After the heat pulse is turned off at $t=1$ ps, symmetric phonon traveling waves are clearly seen. These waves propagate toward the boundaries, and develop temperature slip conditions upon reaching them. Unlike what was observed in the gray LBM [4,15], these phonon waves dissipate energy and, as a result, do not maintain a constant peak temperature as they travel away from the hotspot ($t=2.31-5.26$ ps). Here it seems appropriate to reiterate that each phonon discrete frequency band has a characteristic relaxation time and propagation speed, and, as a consequence, a frequency-dependent Knudsen number. It is likely that some of the bands have a Knudsen number that defines them within the diffusive regime, while others are located within the transitional regime and even the ballistic regime. Overall, the presence of bands belonging to different regimes causes the solution to share characteristics from each regime, and thus, purely ballistic behavior is unlikely to be found for meaningful device dimensions where the BTE-based description is valid.

To clarify the departure from Fourier diffusion as the domain length, hotspot width, and pulse duration are decreased, Figure 5 presents the time history of the hotspot peak temperature for a range of simulations, and compare them to results obtained with a Fourier solver. Here, we have converted the data to a dimensionless form by defining the dimensionless time t^* as $t^*=t/t_{\max}$, where $t_{\max}$ is the total simulation time, and a dimensionless temperature as $T^*=(T-T_0)/(T_{\max}-T_0)$, where $T_{\max}$ is the hotspot peak temperature (which is different for each case) and T_0 is the initial domain temperature, always set to a level of $T_0=300$ K. This allows us to directly compare solutions of the thermal response of an SOI with lengths from $L=1000$ nm down to $L=10$ nm, with the hotspot width defined as $d=0.1\,L$. The heat pulse duration is defined as $0.1t_f$, with t_f being the total simulation time. By doing this, all dimensionless temperature data ranges

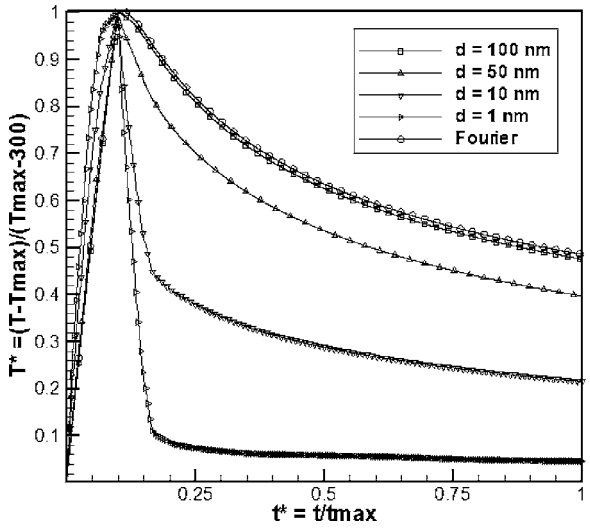

Fig. 5 Dimensionless comparison of hotspot peak temperature time history for decreasing hotspot width

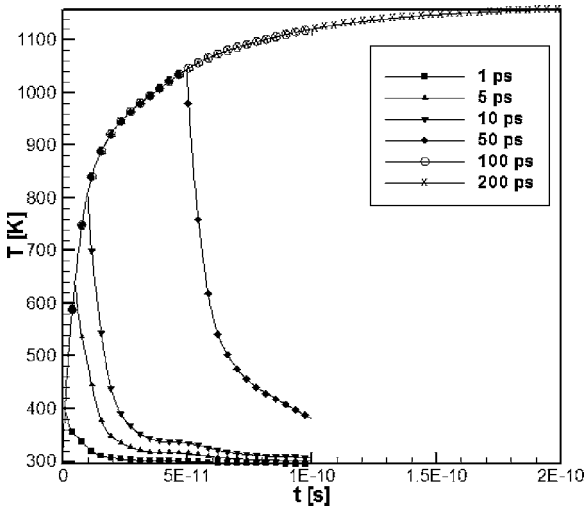

Fig. 6 Pulse duration effect on the hotspot peak temperature, for a 30 nm hotspot, dispersion LBM

from 0 (initial temperature level) to 1 (hotspot peak temperature), while dimensionless time ranges from 0 (initial time) to 1 (total simulation time).

It is observed that Fourier diffusion presents a linear temperature increase through the duration of the heat pulse. The case with $L=1000$ nm and $d=100$ nm agrees very well with the Fourier diffusion solution, although the temperature decay displays temperature levels marginally lower than Fourier, which was a trend also present in the gray LBM solution for diffusive regime. This is due to the small, but nonzero, Knudsen number resulting from the simulation constraint of a finite domain, which prevents the method from reaching a purely diffusive regime. The transition to ballistic transport is easily observed as the domain and hotspot size are decreased, and two main effects characterize it. First, the temperature increase while the heat pulse is turned on ceases to be linear, and it becomes steeper at the beginning of the heat pulse. Second, the effect of phonon traveling waves appears as a rapidly decreasing temperature followed by a slow cooling once the phonon waves have left the hotspot area. This effect becomes more pronounced as the hotspot width is decreased.

In summary, decreasing the hotspot size causes the solution to depart from Fourier diffusion, a process that is manifested by the appearance of phonon propagating waves. This effect, which to the best of our knowledge has not been previously reported in the literature in the context of SOI simulations, is negligible for solutions close to Fourier diffusion (as in Fig. 2), but can be observed for film thickness defined to be within the transitional and ballistic regimes, as in Figs. 3 and 4. More importantly, this ballistic effect can be seen as independent of any boundary effect, as it takes place before any thermal energy wave from the hotspot reaches the boundary. As can be seen in Figs. 3 and 4, the phonon wave propagation is not influenced by the boundary, although a boundary effect does in fact appear as the phonon waves reach the boundary.

It is also worth noting once again that, by considering phonon dispersion, there is no clear definition of a unique mean free path. Every frequency band has a mean free path value and, therefore, the phonon system can behave both diffusively and ballistically at the same time for different frequency bands.

This ends the analysis performed with the 1D model. The results presented from here on correspond to the 2D model. The 2D model allows the investigation of the effects of thermal energy confinement in a small-scale SOI device, a model considered more realistic than the 1D simplification presented above.

Heat Pulse Duration Effect. In this section, the time history of hotspot temperature with increasing heat pulse duration is presented, for both the gray and dispersion LBM. Both models are then compared in dimensionless form, in order to analyze their differences.

Figure 6 depicts the time history of temperature at the hotspot center, as predicted by the dispersion LBM. Simulations were performed for a 80×40 nm domain, with a hotspot diameter of $d=30$ nm and a heat pulse magnitude of $Q=1e20$ W/m^3. As can be seen, it displays a nonlinear increase on temperature, up to a pulse duration of approximately 200 ps, where a steady maximum temperature level is reached. The hotspot temperature decays rapidly after the heat pulse is turned off, but unlike the behavior displayed by the gray model, this decay is continuous in time.

A comparison of the time history of hotspot temperature for the gray and dispersion models is shown next (Fig. 7) for a pulse duration of 50 ps, which in both cases is shorter than the heat pulse duration necessary for steady maximum temperature. To make both signals comparable, a dimensionless time is defined as $t^*=t/50e-12$ s. This allows the peak temperature to be reached at $t^*=1$. A dimensionless value of temperature is obtained by defin-

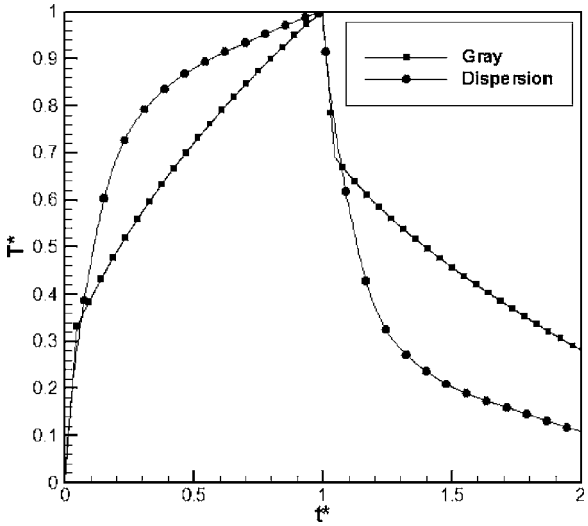

Fig. 7 Time history of temperature for a 30 nm hotspot subject to a 50 ps heat pulse, comparison between gray and dispersion LBM

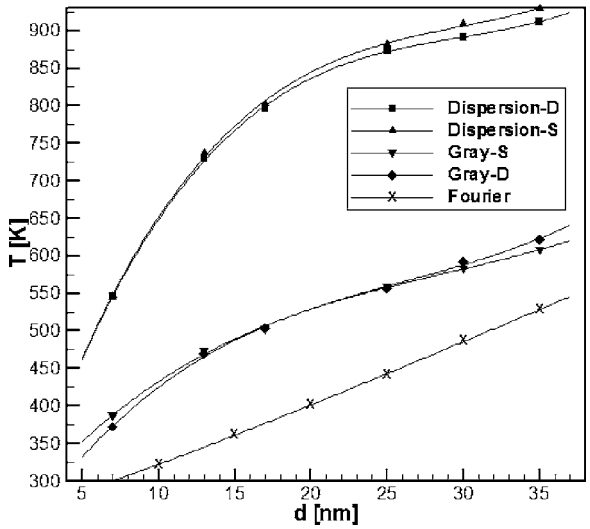

Fig. 8 Hotspot peak temperature as function of size, comparison between gray, dispersion, and Fourier diffusion results

ing $T^*=(T-T_0)/(T_{max}-T_0)$, where T_{max} is the hotspot peak temperature (which is different for each case) and T_0 is the initial domain temperature, always set to a level of $T_0=300$ K. As the figure clearly shows, significant differences exist between both cases. The temperature rise in the dispersion model is steeper than in the gray model and follows a gentle curve, while the gray model begins with a discontinuous increase and stabilizes later with a smaller slope. After the heat pulse is turned off, the dispersion model displays a faster temperature decay when compared to the gray model, which displays first a sudden discontinuous temperature decrease followed by an exponential decay. Attempting to explain this behavior, it is possible recall the fact that propagating phonons in the dispersion model are faster than those in the gray model. The faster propagating LA modes in the dispersion model travel at a speed of approximately 8000 m/s, considerably faster than the gray phonons, which travel only at 6400 m/s. This causes an efficient cooling effect once capacitive optical modes start decaying into propagating acoustic modes at a time scale close to 5 ps. In contrast, gray phonons leave the hotspot region constantly, and can therefore transport thermal energy only at a constant rate.

Hotspot Size Effect. We consider here a silicon layer of length $L=80$ nm and height $h=40$ nm, dimensions which are similar to the previous case. Computational requirements for the dispersion model limit the simulation of larger geometries, and thus, we find this to be the upper limit of what is feasible to simulate with the dispersion LBM, without resorting to supercomputers or parallel processing. Additionally, the selected dimensions are consistent with the actual size of an SOI device. The hotspot diameter is progressively decreased while keeping the domain dimensions fixed, in order to study the effect of hostpot size. The total simulation time is 30 ps, with a heat pulse duration of 10 ps. Results are presented considering specular and diffuse phonon boundary scattering, for both the gray and dispersion models. Fourier diffusion results are also included in order to better understand the effects of subcontinuum thermal energy transport.

As can be seen in Fig. 8, Fourier diffusion solutions present a linear increase of hotspot maximum temperature with increasing hotspot size, which is essentially a result independent of the length scale involved. In contrast, gray LBM simulations allow observing phonon confinement effects and nonequilibrium conditions that translate into an increased hotspot maximum temperature when compared to Fourier diffusion. These effects are manifested in the nonlinearity of the hotspot peak temperature versus hotspot diameter, which is evident at hotspot diameters much smaller than the phonon mean free path value.

A hotspot Knudsen number can be defined as $Kn=\Lambda/d$, where Λ is the nominal value of the phonon mean free path for the gray model (41 nm), and d is the hotspot diameter. It can be seen that for $Kn>2$ ($d=20.5$ nm), the hotspot peak temperature versus hotspot diameter is highly nonlinear, with a tendency to intersect the Fourier diffusion curve at a hotspot of vanishing size. For $Kn<2$, the hotspot peak temperature versus hotspot diameter for the gray model resembles an asymptotic trend, bound to merge with the Fourier diffusion curve at a vanishing value of the Knudsen number. This is consistent with our previous findings that the gray LBM accurately matches Fourier diffusion solutions in both thin film heating and hotspot warming for small Knudsen numbers that locate the solution within the diffusive regime. It is worth noting that the gray LBM matches Fourier diffusion results at two extreme points: vanishing hotspot size, where both methodologies give the trivial result of null temperature increase with respect to the initial condition, and at a hotspot size large enough that the phonon mean free path is of negligible length compared to it.

The dispersion model displays a similar trend. Starting with a null temperature increase for a vanishing hotspot size, the hotspot peak temperature rapidly increases as the hotspot diameter is also increased. This steep increase then gradually morphs into an asymptotic trend bound to merge with the Fourier diffusion curve at very large hotspot diameters. Again, this result is consistent with our previous findings that the dispersion LBM matches Fourier diffusion solutions in thin film heating and hotspot warming for sufficiently large length scales that locate the solution within the diffusive regime. Phonon confinement effects and nonequilibrium transport are more evident in the dispersion LBM, which result in much larger hotspot peak temperature increases than the gray LBM when compared to Fourier diffusion. The difference between the dispersion LBM and Fourier diffusion predictions can be as large as ~700% for a 20 nm hotspot, which clearly indicates the critical nature of subcontinuum heat transport and the importance of developing an adequate energy transport methodology that takes into account these effects.

Finally, a brief discussion about computational expense is presented next. In general, 1D simulations for cases within the ballistic regime require processing times on the order of tens of minutes in a Pentium 4 processor, depending on the simulation final time. The 1D diffusive simulations require processing times on the order of hours, due to the extremely high number of lattice points involved. For 2D models, the processing time can be as high as 8 days for a 30 ps simulation of the 80×40 nm domain, in a single Pentium 4 processor PC running under Linux. These processing times are higher than those required by the finite volume methodologies presented in Refs. [18,19] for a similar problem in a domain of comparable dimensions, although it must be remembered that the finite volume methodologies still employ a simplified model for optical phonons. This issue is of fundamental importance since in the course of this work, we determined that including optical phonons increases computational expenses the most, due to the spatial and temporal discretizations requirements imposed by the slow propagation speed of the phonon modes.

Conclusions

The dispersion LBM is developed and presented as a discrete formulation of the BTE. The dispersion LBM explicitly includes the contributions of phonon dispersion and polarization effects, thus not requiring the use of simplifying assumptions such as Debye modeling of phonons. The dispersion LBM is used to predict the transient thermal response in 1D and 2D computational models of a SOI transistor, subject to Joule heating conditions due to electron–phonon scattering processes that create a hotspot region of nonequilibrium phonons. The SOI device is modeled as a thin film of silicon, with an imposed heat generation source term

to simulate the hotspot region. It is found that subcontinuum effects in SOI Joule heating are important when the heat pulse is shorter than the phonon relaxation time, when the hotspot region is smaller than the phonon mean free path, and with combinations of those. These subcontinuum effects become apparent in three ways: first, a wave-like energy propagation of energetic phonons is observed as time scales and hotspot sizes are decreased. Second, LBM simulations show nonequilibrium phonon confinement that results in higher peak temperatures than what is predicted by Fourier diffusion. Finally, boundary effects are also observed when a propagating phonon wave reaches a constant temperature boundary, thus giving origin to temperature slip conditions. This analysis has sought to demonstrate the fundamental differences existing between both LBM models and Fourier diffusion predictions. The more accurate physical formulation of the dispersion LBM makes it a useful tool for predicting high hotspot temperatures. Dispersion LBM results offer increased accuracy at a higher computational cost; however, the advantage of accurate modeling compensates for the increase of computational resources needed. In view of these results, it can be concluded that the dispersion LBM is an adequate method for predicting heat conduction in semiconductors at the submicron length scale. However, the method also has several shortcomings that need to be corrected. Improved expressions for frequency-dependent phonon relaxation time are needed, and electron–phonon interactions need to be better modeled in order to obtain realistic heat source terms.

Acknowledgment

The authors gratefully acknowledge support from the National Science Foundation Grant No. CTS-0103082, the ICES Pennsylvania Infrastructure Technology Alliance (PITA) program, sponsored by the Commonwealth of Pennsylvania's Department of Community, and Economic Development, and the Pontificia Universidad Católica de Chile.

References

[1] International Technology Roadmap for Semiconductors, ITRS, 2004, update, http://public.itrs.net/

[2] Cahill, D., Ford, W., Goodson, K., Mahan, G., Majumdar, A., Maris, H., Merlin, R., and Phillpot, S., 2003, "Nanoscale Thermal Transport," J. Appl. Phys., **93**(2), p. 793–818.

[3] Sinha, S., Shelling, P. K., Phillpot, S. R., and Goodson, K. E., 2005, "Scattering of g-Process Longitudinal Phonons at Hotspots in Silicon," J. Appl. Phys., **97**(2), pp. 023702-1–023702-9.

[4] Escobar, R., Ghai, S., Jhon, M., and Amon, C., 2006, "Multi-Length and Time Scale Thermal Transport Using the Lattice Boltzmann Method with Application to Electronics Cooling," Int. J. Heat Mass Transfer, **49**, pp. 97–107.

[5] Bai, P. C., et al., 2004, "A 65 nm Logic Technology Featuring 35 nm Gate Length, Enhanced Channel Strain, 8 Cu Interconnect Layers, Low-k ILD and 0.57 μm^2 SRAM Cell," *Proceedings 2004 IEEE International Electron Devices Meeting*, IEDM04, San Francisco, December 13-15.

[6] Pop, E., Banerjee, G., Sverdrup, P., Dutton, R., and Goodson, K. E., 2001, "Localized Heating Effects and Scaling of Sub-0.18 Micron CMOS Devices," *Proceedings IEEE International Electron Devices Meeting*, IEDM01, pp. 677–80, Washington, DC, December 3-5.

[7] Sverdrup, P., Banerjee, K., Dai, C., Shih, W., Dutton, R., and Goodson, K., 2000, "Sub-continuum Thermal Simulations of Deep Sub-Micron Devices Under ESD Conditions," *Proceedings IEEE International Conference on Simulation of Semiconductor Processes and Devices* (SISPAD), Seattle, September 6-8, pp. 54–57.

[8] Sverdrup, P., Ju, Y., and Goodson, K., 2006, "Sub-continuum Simulations of Heat Conduction in Silicon-on-Insulator Transistors," J. Heat Transfer, **123**, pp. 130–137.

[9] Sverdrup, P., Sinha, S., Asheghi, M., Uma, S., and Goodson, K., 2001, "Measurement of Ballistic Phonon Conduction Near Hotspots in Silicon," Appl. Phys. Lett., **78**, pp. 3331–3333.

[10] Pop, E., Sinha, S., and Goodson, K., 2002, "Monte Carlo Modeling of Heat Generation in Electronic Nanostructures," *Proceedings ASME International Mechanical Engineering Congress and Exposition, IMECE02*, New Orleans, November 17-22.

[11] Pop, E., Dutton, R., and Goodson, K., 2003, "Thermal Analysis of Ultra-thin Body Device Scaling," *Proceedings IEEE International Conference on Simulation of Semiconductor Processes and Devices* (SISPAD), Cambridge, MA, September 3-5.

[12] Sinha, S., Pop, E., Dutton, R., and Goodson, K., 2006, "Non-Equilibrium Phonon Distributions in Sub-100 nm Silicon Transistors," J. Heat Transfer, **128**, pp. 638-647.

[13] Pop, E., Dutton, R., and Goodson, K., 2003, "Detailed Heat Generation Simulations via the Monte Carlo Method," *Proceedings IEEE International Conference on Simulation of Semiconductor Processes and Devices* (SISPAD), Cambridge, MA, September 3-5.

[14] Narumanchi, S., Murthy, J., and Amon, C., 2006, "Boltzmann Transport Equation-based Thermal Modeling Approaches for Hotspots in Microelectronics," Heat Mass Transfer, **42**(6), pp. 478–491.

[15] Escobar, R., Ghai, S., Jhon, M., and Amon, C., 2003, "Time-Dependent Simulations of Sub-continuum Heat Generation Effects in Electronic Devices Using The Lattice Boltzmann Method," ASME Paper No. IMECE2003-41522.

[16] Escobar, R., and Amon, C., 2005, "Lattice Boltzmann Modeling of the Thermal Response of SOI Transistors Under Joule Heating Conditions Including Phonon Dispersión," ASME Paper No. IMECE2005-80025.

[17] Sinha, S., Schelling, P., Phillpot, S., and Goodson, K., 2003, "Atomistic Simulations of Non-Equilibrium Phonons in Nanotransistors," *Proceedings SRC-TECHCON*, Dallas, TX, August 25-27.

[18] Narumanchi, S., Murthy, J., and Amon, C., 2004, "Submicron Heat Transport Model in Silicon Accounting for Phonon Dispersion and Polarization," J. Heat Transfer, **126**, pp. 946–955.

[19] Narumanchi, S., Murthy, J., and Amon, C., 2003, "Simulation of Unsteady Small Heat Source Effects in Sub-micron Heat Conduction," J. Heat Transfer, **125**, pp. 896–903.

[20] Ghai, S., Kim, W., Escobar, R., Amon, C., and Jhon, M., 2005, "A Novel Heat Transfer Model and its Application to Information Storage Systems," J. Appl. Phys., **97**, p. 10P703.

[21] Sinha, S. Pop, E., and Goodson, K., 2004, "A Split-flux Model for Phonon Transport Near Hotspots," *Proceedings ASME International Mechanical Engineering Congress and Exposition* IMECE2004, Anaheim, CA, November 14-19.

[22] Ashcroft, N., and Mermin, N., 1976, *Solid State Physics*, Harcourt, Fort Worth, TX.

[23] Narumanchi, S., Murthy, J., and Amon, C., 2005, "Comparison of Different Phonon Transport Models for Predicting Heat Conduction in Silicon-on-Insulator Transistors," J. Heat Transfer, **127**, pp. 713–723.

[24] Sinha, S., and Goodson, K. E., 2004, "Thermal Conduction in sub-100 nm Transistors," *Proceedings Thermal Investigations of ICs and Systems (THERMINIC)*, Sophia Antipolis, France, September 29–October 10.

[25] Succi, S., 2001, *The Lattice Boltzmann Equation for Fluid Dynamics and Beyond*, Clarendon, Oxford, UK.

[26] Zhang, W., and Fisher, T., 2002, "Application of the Lattice Boltzmann Method to Sub-continuum Heat Conduction," ASME Paper No. IMECE2002-32122.

[27] Escobar, R., and Amon, C., 2004, "Lattice Boltzmann Modeling of Subcontinuum Energy Transport in Silicon-on-Insulator Microelectronics Including Phonon Dispersion Effects," *Proceedings ITHERM-2004*, Las Vegas, NV, June 1-4.

[28] Escobar, R., 2005, "Lattice Boltzmann Modeling of Phonon Transport in Silicon Films," Ph.D. thesis, Carnegie Mellon University, Pittsburgh, PA.

[29] Dolling, G., 1963, "Lattice Vibrations in Crystals with the Diamond Structure," *Proceedings Symposium on Inelastic Scattering of Neutrons in Solids and Liquids*, Chalk River, Canada, pp. 37–48.

[30] Han, Y.-J., and Klemens, P., 1993, "Anharmonic Thermal Resistivity of Dielectric Crystals at Low Temperatures," Phys. Rev. B, **48**, pp. 6033–6048.

[31] Escobar, R., Smith, B., and Amon, C., 2006, "Lattice Boltzmann Modeling of Sub-continuum Energy Transport in Crystalline and Amorphous Microelectronic Devices," J. Electron. Packag., **128**, pp. 115–124.

M. Adjim
Département d'Hydraulique,
Faculté des Sciences de l'Ingénieur,
Université Abou-Bekr Belkaid de Tlemcen,
Zemcen 13000, Algeria

R. Pillai

A. Bensaoula[1]
e-mail: bens@uh.edu

Physics and Electrical and
Computer Engineering Departments,
Texas Center for Advanced Materials,
University of Houston,
724 S&R Building 1,
Houston, TX 77004

D. Starikov

C. Boney

Integrated Micro Sensors, Inc.,
10814 Atwell Drive,
Houston, TX 77096

A. Saidane
Département de Génie Electrique,
ENSET d'Oran,
B.P. 1523,
M'Naouer-Oran 1523, Algeria

Thermal Analysis of Micro-Column Arrays for Tailored Temperature Control in Space

Lightweight yet precise, temperature control protocols are critical in a variety of applications. This is especially true in space where weight and volume are at a premium and reliability is paramount. In space, complex processes to manage the heat fluxes generated from within and absorbed from space by the spacecraft are usually implemented. Surfaces having different heat fluxes might need to be controlled separately and maintained at different temperatures. The work presented in this paper evaluates a novel laser surface modification process to form micro-column arrays (MCA) on any material for use as highly adaptive radiators. The MCA-structured surfaces have experimentally been shown to have excellent emissive properties. Finite element methods have been used to simulate the temperature profiles for surfaces with and without MCA compared to pin fin structures as a function of input heat flux density. In the case of Ti, our models show that pin fin arrays are better heat radiating surfaces than equivalent MCA structures with cone-like profiles. Such structures, however, are difficult to modify and usually require complicated and expensive fabrication processes. Overall, MCA structures are shown to allow good control over base surface temperature for varying heat fluxes and different MCA aspect ratios. For Ti, under steady state conditions, an aspect ratio of 12 has been shown to be optimal for surface heat reduction. Preliminary experimental results show that the temperature drop is inline with that theoretically predicted. [DOI: 10.1115/1.2717246]

Keywords: micro-column arrays, emissivity, blackbody, spectrum, space

1 Introduction

Universal and efficient heat transfer methods are important in many applications where devices and instruments need to function under strict optimal operating conditions. The trend toward further miniaturization has also increased systems heat power density manyfold, making heat management a critical design component. As a result, significant efforts are directed toward improving heat removal efficiency. Heat transfer mechanisms, used for cooling of various devices and systems, are based on either direct or indirect heat removal. Examples of commonly used heat removal systems include: heat spreading and forced convection, passive cooling, heat pipes, jet and spray impingement, and solid–liquid phase change. Recent research has also focused on microchannels and integrated micropumps, solid-state cooling devices based on the Peltier effect for nanostructures, and microscale ion driven cooling devices for micro electromechanical systems (MEMS) [1–8].

In the case of larger structures, such as in space structures and instrumentation (e.g., satellites, space vehicles, and platforms), heat loss control requires very complex thermal management protocols. For example, parts of an orbiting vehicle can change surface temperature from 116 K to 400 K, as a result of the diurnal cycle. This problem becomes crucial in maintaining the optimal temperature for crew members, on-board equipment, and liquid coolants such as ammonia (freezing temperature 196 K). Apart from external heating, other parts of the vehicle, such as the rocket motor casing or the rocket nozzle, generate large amounts of heat. The heat generated on such parts has to be removed with a much higher efficiency than from other areas. Under normal operation, convectional heat transfer is negligible in space, therefore radiative cooling remains the main mechanism for heat removal.

There are many intriguing variations of heat transfer methods, promoting the idea of optimization and improvement of device/machinery/system performance and life in space. One such simple method has been the use of high emissivity coatings to achieve better heat loss through thermal radiation [9–11]. Thermal control performed in this manner usually faces problems associated with: (1) bonding of the coatings to the surfaces to be cooled; (2) changes in the material properties when exposed to mildly different environments, such as ozone in space applications; and (3) normal degradation of the coating and electrostatic charging of the coatings, which may damage very sensitive on board equipment.

In 1981, Tuckerman and Pease [12] predicted that single-phase heat transfer methods in micro-channels could be used for circuits with power densities as high as 1000 W/cm^2. Single-phase liquid heat transfer methods, however, require very high fluid flow rates [13,14]. One solution to overcoming the problems associated with the high fluid flow is the use of two-phase forced convection in microchannels, as explained by Ziang et al. [15]. The results may seem to be very promising but their actual fabrication is complicated and expensive. In addition, it is usually very difficult and sometimes inefficient to have materials for two phase cooling of external parts on a spacecraft such as in the vicinity of the thrust-

[1]Corresponding author.

Contributed by the Heat Transfer Division of ASME for publication in the JOURNAL OF HEAT TRANSFER. Manuscript received February 2, 2006; final manuscript received August 14, 2006. Review conducted by Yogendra Joshi.

 Copyright © 2007 by ASME

ers. Employment of materials that feature a combination of high emissivity that provides for efficient radiative heat loss, as well as large surface area that results in high convective heat loss, may avoid the need to use such drastic measures.

The work described in this paper is focused on heat removal properties of micro-column-array (MCA) structures fabricated in our laboratory on various materials by pulsed laser ablation. In order to compare the efficiency of the MCA structures with other radiative surfaces and perform preliminary optimization of their geometry, thermal simulation was carried out using finite element analysis methods. The simulated results were then compared to experimental results using a simple experimental setup described below. The production rate of the MCA structure is directly proportional to the average laser power. Thus, the power required for a production rate of 0.6 cm^2/s is 600 W and for 0.8 cm^2/s is 800 W. This means that production scaleup is simply a matter of increasing the laser power. Since it is possible to fabricate MCA on virtually any material, managing the thermal characteristics of a system or a component would simply require proper microstructuring of its surface. In this fashion, space equipment would particularly benefit from the reduction of volume and weight, compared to those encountered using conventional radiators. Furthermore, many compatibility issues resulting from using materials with different coefficients of thermal expansion, chemical inertness, and resistance to space radiations, will be eliminated since no adhesives or additional materials are used. We also suppress the critical issue of electrostatic discharge by avoiding employment of adhesives and paints for thermal management.

2 Fabrication and Properties

The MCA were fabricated by pulsed laser ablation using a Cu vapor laser (510.6 nm) with a pulse duration of 20 ns and a repetition rate of 8 kHz. The diameter of the laser spot was between 30 μm and 70 μm. The samples were placed on a computer-driven *X-Y* stage allowing displacement under the laser beam. The materials used were foils of refractory metals such as W, Mo, Ta, and Ti, and high-temperature stainless steels such as alloy 321 and Hastelloy C276. Irradiation of the foils was carried out in open air. The cone-shaped micro-columns produced had a height of 20 μm, base of 20 μm in diameter, and were situated approximately 20 μm apart. We carried out in-depth spectral and surface analyses of the structured micro-column arrays and have shown their enhanced emissive properties. Further details of these processes and results are described elsewhere [16].

The reflectance and absorptance measurements (Fig. 1(*a*)) were performed for the MCA treated area (front side) and the backside of the sample (untreated area), in order to compare the effect of the MCA treatment on the emission properties of each material. The samples were measured with an AZTek LPSR300 spectroreflectrometer which scans the reflectance in the range from 250 nm to 2.8 μm and also calculates an integrated absorbance over that range. The range is covered using a combination of a deuterium and tungsten lamps on the optical irradiation side, with an ultraviolet (UV) enhanced silicon photodiode and a cooled PbS detector for detection [16]. It is clearly seen that the treated area has a significantly higher absorptance and much lower reflectance. It should be noted that changes in the intrinsic emissivity of the material are negligible in comparison with the effective emissivity changes resulting from the modification of the surface geometry and morphology. The material's chemical composition is unchanged but for a thin oxide layer that may form during laser treatment, which can be removed post-processing.

The behavior of the MCA structured material as a near-blackbody is unfolded in Fig. 1(*b*). In this experiment, the MCA was placed in a small vacuum chamber and resistively heated to high temperatures while the optical emission was measured as a function of wavelength. As a calibration, the optical emission of a blackbody cavity source at the same temperatures was also measured. The calibration was only relative since it was not possible

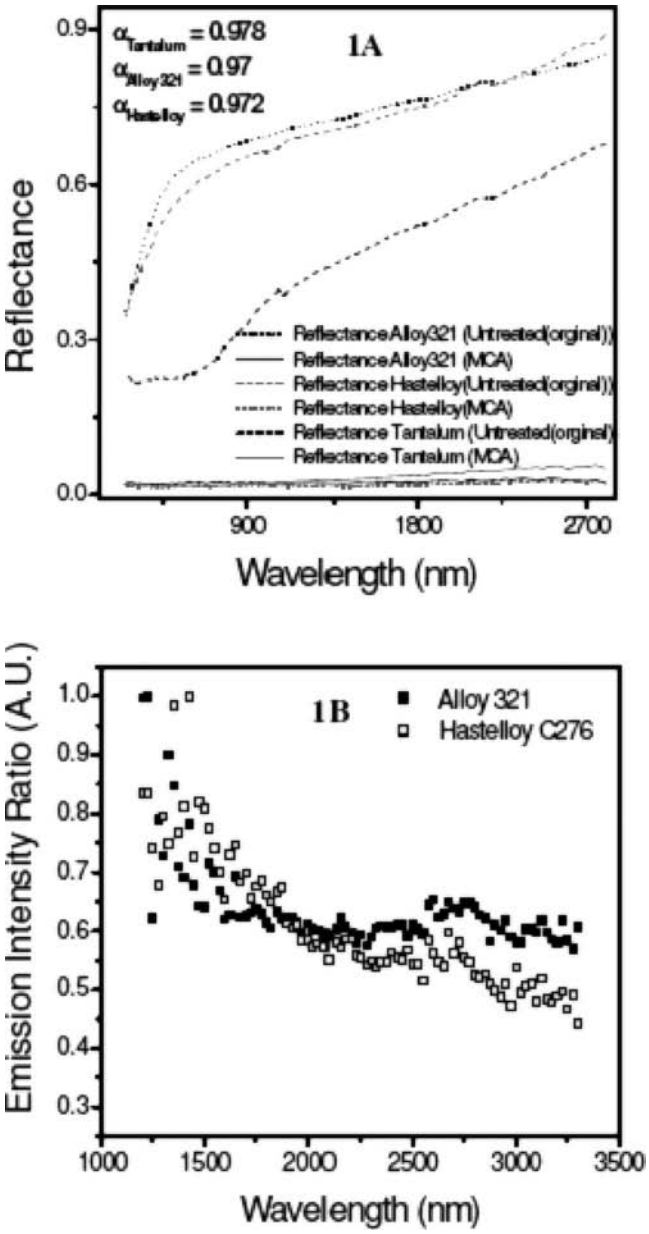

Fig. 1 (*a*) Plots of reflectance measurements for MCA processed and unprocessed Alloy 321, Hastelloy C276, and tantalum. The values of α provided correspond to the absorptivity integrated over the entire measurement range for the three MCA structured samples. (*b*) Ratios of the relative normalized spectral emission from Alloy321 to a blackbody spectrum and Hastelloy C276 to a blackbody spectrum at 1073 K, the linear portion indicating the optical emission curves are similar.

to equilibrate the optical power density coming from the two sources as a result of the necessary measurement geometry differences of the sources. Thus Fig. 1(*b*) depicts the relative emission intensity ratio between MCA from Alloy 321 and Hastelloy C276 foils and the blackbody source. Since a blackbody has unity emissivity at all wavelengths, a constant or near-constant ratio like those shown in Fig. 1(*b*) indicate that the emissivity of the MCA is also maintaining a steady value over the wavelength range. Since the spectral emission at a fixed temperature is directly proportional to the emissivity, the plot indirectly indicates that the effective emissivities of the laser treated Alloy 321 and Hastelloy C726 are similar to that of a blackbody source. Optical emission spectra measured in the temperature range from 973 K to 1473 K

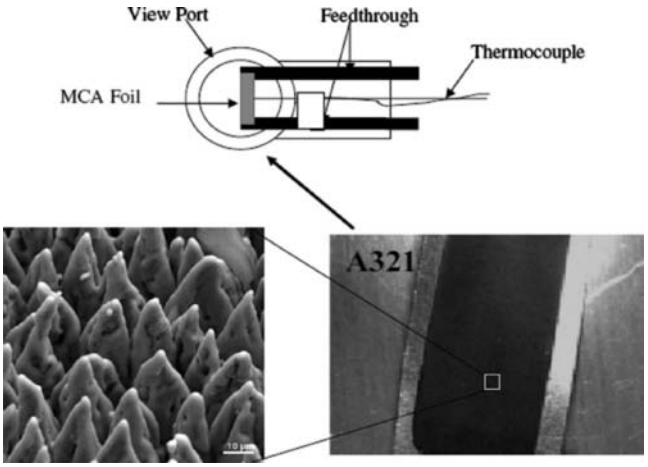

Fig. 2 Experimental setup for measuring temperature characteristics of MCA sample

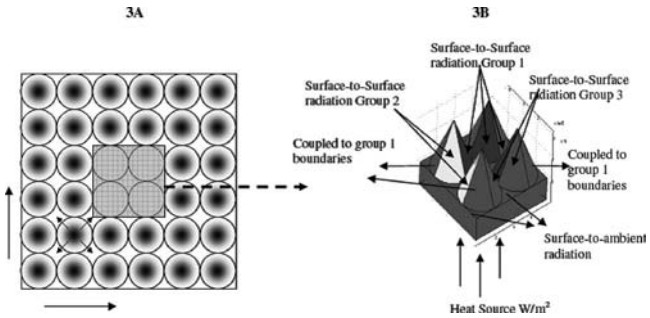

Fig. 3 (*a*) Top view schematic of an array of micro-cones representing an actual surface with MCA. (*b*) 3D schematic describing the boundary conditions for the model, indicating the surface-to-surface radiation and surface-to-ambient radiation boundaries. Groups 4 and 5 are the surfaces equivalent to groups 2 and 3 on the upper right and upper left of the figure, respectively.

(data not shown) indicate no noticeable change up to a temperature of 1633 K with only a slight change at higher temperatures, possibly due to modification in the material properties resulting from surface sublimation and/or oxidation.

3 Temperature Control Capability of MCA Structures

As shown above, the MCA treated surfaces have a higher effective emissivity, which would indicate that, under constant input power, a surface temperature reduction should be observed. To that end we have carried out simulations to optimize the MCAs and demonstrate their temperature reduction capabilities for different aspect ratios. Preliminary experiments to prove the validity of our simulations were also performed.

3.1 Experiment. To test the validity of our simulations we fabricated MCA structures on thin (~0.06 mm) Alloy 321 foils. Laser processed and nontreated foils were heated by direct current injection using two high current feedthroughs installed on an ultrahigh vacuum chamber. A type C thermocouple was spot welded to the sample surface to monitor its temperature during heating. A simplified setup schematic is shown in Fig. 2. The injected power was measured using a current clamp across one feedthrough while simultaneously monitoring the voltage across them. The net power was then divided by the sample area to yield the heat flux in W/cm^2. The initial experiments were limited to Alloy 321 foils since the available processed foils for the remaining simulated materials (Molybdenum, Ti, etc.) were too thick and would have required currents near or above the feedthroughs maximum specifications.

3.2 Simulation

3.2.1 Model. The software FEMLAB®COMSOL AB is an environment for modeling engineering problems based on solving partial differential equations (PDEs). The inbuilt physics models allow definition of physical parameters such as material properties, loads, constraints, sources, and fluxes, without the need to define the underlying equations. The software has several different modules, one of them being the heat transfer module, which is what has been used throughout this simulation. This module supports fundamental heat transfer mechanisms such as conductive, convective, and radiative heat transfer. For radiative heat transfer the software includes models for both surface-to-surface radiation and surface-to-ambient radiation.

The boundary condition for the heat flux with surface-to-surface radiation condition is defined by Eq. (1). The first two terms on the right side of this equation are interpreted in the same way as for the heat flux condition without radiation. The third term on the right side defines the radiative heat flux

$$-n(-k\nabla T) = q_o + h(T_{\text{inf}} - T) + \varepsilon(G - \sigma T^4) \tag{1}$$

$$\rho G = J_o - \varepsilon\sigma T^4 \tag{2}$$

$$J = (1-\varepsilon)\left[\int_{S'} \frac{(-\bar{n}'\cdot\bar{r})(\bar{n}\cdot\bar{r})}{\pi|\bar{r}|^4} J' dS + F_{\text{amb}}\sigma T_{\text{amb}}^4\right] + \varepsilon\sigma T^4 \tag{3}$$

Equations (2) and (3) are best understood if we consider a point x on which we are computing the effect of surface-to-surface radiation and a point x' which is on surface S' that is irradiating the point x. The net radiation J_o at point x due to irradiation G from x' and surface-to-ambient radiation from surface x, is given by Eq. (2). The sum of the complete integral of the irradiation of all points on surface S' and the surface-to-ambient radiation gives the total radiosity of the point x, as shown in Eq. (3).

To design the model, we first assume an infinite series of microcones as shown in Fig. 3(*a*), with every microcone being surrounded by eight neighboring cones. In a vacuum environment, each cone radiates heat to the ambient, but a certain portion of the radiated heat will be reradiated onto adjacent cones. In this model, the cone contributes to cooling the base surface but also heating the adjacent surfaces. The combined effect of the surface-to-ambient radiation and the surface-to-surface radiation determines the efficiency of the MCA in heat removal. A crucial simulation parameter is the structures' aspect ratio, which for a constant MCA density, can be defined as the ratio of the total extended surface area to the base area. A model was built consisting of four microcones interacting with each other. A two-dimensional (2D) visualization of the infinite array is shown in Fig. 3(*a*) with a more detailed diagram of the actual model in Fig. 3(*b*).

The critical aspect of these simulations is the surface-to-surface radiation, which determines the upper limit on the aspect ratio. In order for the simple four cone model to approximate an infinite array, appropriate boundary conditions were chosen. For surface-to-surface radiation the cone's inner surfaces were defined to be in the view angle of each other, thus they were made members of group one. Similarly, adjacent surfaces of the cones were classified in four separate groups, which are groups 2–5 (groups 4 and 5 are not shown in Fig. 3(*b*) for clarity but are functionally equivalent to groups 2 and 3). The bottom surface is set with boundary conditions of an input heat flux where the heat source is defined in W/m^2 and the side surfaces with insulated boundary conditions. The facets of the cone facing away from the center of the unit cell, situated on the corners of the unit cell, are coupled to

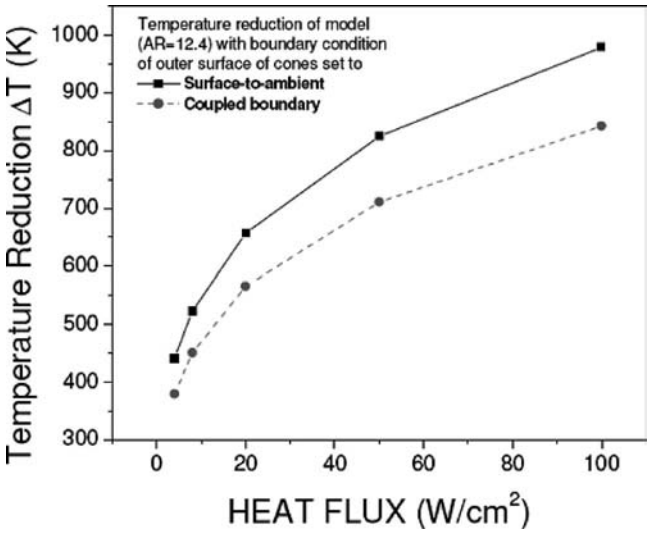

Fig. 4 Simulations carried out on the MCA model of aspect ratios 12.4, with outer boundary conditions set as surface-to-ambient as in previous models, compared to MCA model with coupled boundary conditions

the internal boundaries. In this manner, we simulate surface-to-surface radiation on the outer boundaries, which in this model have no surfaces in their radiation view angle. This is achieved by integrating the total surface radiosity of the inner boundary and inputting the value as the radiosity of the outer boundary. In this fashion, we compute the steady state temperature by inputting the integrated heat flux of the inner boundary (group 1) onto the outer boundaries simultaneously. The solution is computed iteratively until the error determined as the difference between the current and previous solutions, is below a set relative tolerance factor. For our simulation this is set to 1×10^{-6}, since this number corresponded to a delta temperature below 0.001 K and had a relatively fast convergence time (six times faster than for 1×10^{-7} without significant improvement in temperature accuracy).

The above described method, while more accurate, is computationally intensive and causes the simulation to break down as the aspect ratio increases. Therefore a more simplified model was implemented in which the outer surfaces radiate only to the ambient and not to one another, while the inner surfaces still interact with one another. Results from the initial and simplified models, shown in Fig. 4, suggest that errors in temperature reduction arising from the simplified model are not higher than 16.2%. Though the trend shows the plots separating further at higher heat fluxes, it should be noted that the temperatures are higher, too, and a quick calculation shows that the error is still around 16%. For example, when a heat flux of 4 W/cm^2 is applied to the base, the model with coupled boundary has a final base temperature of 773.93 K and the model with surface-to-ambient radiation on the outer boundaries has a final temperature of 712.92 K, while the nonstructured base would have a temperature of 1153.77 K. Similarly when a heat flux of 20 W/cm^2 is applied to the base, the model with coupled boundary has a final base temperature of 1158.18 K and the model with surface-to-ambient radiation on the outer boundaries has a final temperature of 1066.93 K, while the nonstructured base would have a temperature of 1723.91 K.

While the computationally intensive model approximates an infinite array, the simplified model is closer to an isolated array. The macroscopic MCA samples fabricated in this work lie somewhere in between since, near the center, the cones behave as an infinite array, while near the periphery, the cones are subjected more to the ambient as in the simplified model. Thus the 16.2% represents a maximum possible error, with the real error being less. The simplified model was deemed an acceptable approximation to the MCA samples and was used to evaluate the heat loss of MCA with various aspect ratios without having to fabricate and test each sample type.

The ambient temperature for the simulations was set to 0 K and the heat transfer coefficient h, which determines the heat loss to the ambient, was set to zero, corresponding to space vacuum and to the boundary condition of insulating sides of the base structure, respectively. The base in the simulations has a 10 μm thickness, but the simulations are essentially independent of this parameter due to the boundary conditions of the slab and the fact that it is the final steady-state temperature which is being calculated.

In one set of simulations, a rectangular cross-section pin fin array was analyzed in order to compare in a simple form the heat rejection of a conical pin fin to a rectangular cross-section pin fin. The models for the pin fin arrays and cones are similar, with the constraint that the extended structures have the same volume and height. The pin fin has four boundaries on the sides and one boundary on the top. The top boundary and the two outer boundaries that do not radiate onto other structures are defined to have surface-to-ambient radiation. The inner adjacent boundaries that face each other are grouped together and defined to have surface-to-surface radiation.

A different simulation was performed in order to directly compare the experimental and theoretical temperature reduction from an MCA structure on Alloy 321 based on the setup in Fig. 2. Due to the physical dimensions of the MCA sample, a simple model of the macroscopic surface emissivity was employed. In the model, the front surface of the Alloy 321 was assigned emissivities of 0.97–0.85 based on the absorptance measurements in Fig. 1(*a*). The unprocessed back side of the Alloy 321 was assigned an emissivity of 0.3. The ambient temperature was assumed to be 300 K. Other factors taken into account were conductive heat loss to the stainless-steel electrical feedthroughs, radiative emission from the rods, and the resistive heating of the rods. The only mechanism not accounted for in the simulations was reflective reradiation from the vacuum chamber.

4 Results and Discussion

4.1 Simulation Results. As previously outlined, the described approach is applicable to a variety of applications. It is particularly attractive in space applications where payload volume and weight are important design parameters. From that perspective Ti has the lowest density (4.5 g/cm^3) when compared to tantalum (16.4 g/cm^3), Hastelloy C276 (8.94 g/cm^3), and Alloy321 (7.92 g/cm^3). Moreover, Ti is more stable than other lightweight metals such as aluminum to space radiation and other extreme environments. As a result, we have used Ti as the base material for our optimization simulations. The peak emission wavelength of a blackbody material between 2500 K and 1500 K varies from 1.1 μm to 1.9 μm. The corresponding emissivity for Ti at those wavelength ranges from 0.5 to 0.3 [17]. Since the MCA treatment only negligibly affects the intrinsic emissivity of the material, but rather greatly enhances the effective emissivity due to changes in the surface geometry and morphology, the value of 0.4 was chosen for the emissivity of Ti.

Figure 5 shows that for a titanium structure of 40 μm $\times$40 μm$\times$10 μm, with an aspect ratio of 5.4, subjected to a heat flux of 4 W/cm^2, the steady-state temperature is found to be 1153.8 K. Under similar conditions, structures with extended pin fins and MCAs yield final temperatures of 888.3 K and 977.8 K respectively, giving a temperature reduction of 265 K for the pin fin model and 176 K for the MCA model. Although the pin fin array is a more effective radiator, it is also more difficult to produce on the micron size scale due to the use of lithography-based fabrication. By comparison, the MCA are easily produced and can be fabricated with different aspect ratios by simply varying the laser parameters during processing.

The dependence of the temperature reduction on the aspect ra-

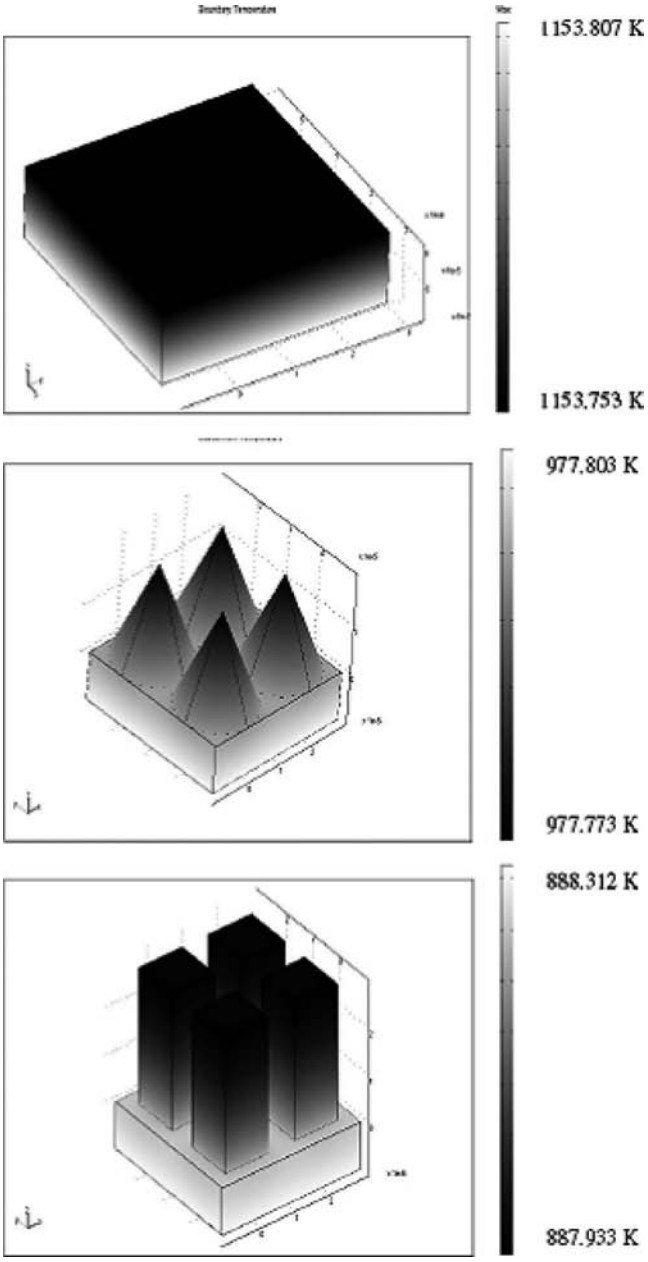

Fig. 5 Simulations of different extended surface structures on a 40 μm×40 μm surface of titanium subjected to a heat flux of 4 W/cm^2 showing the individual steady-state temperatures. A temperature decrease of 176 K based on MCAs and 265 K based on the rectangular cross-section pin fin arrays is observed.

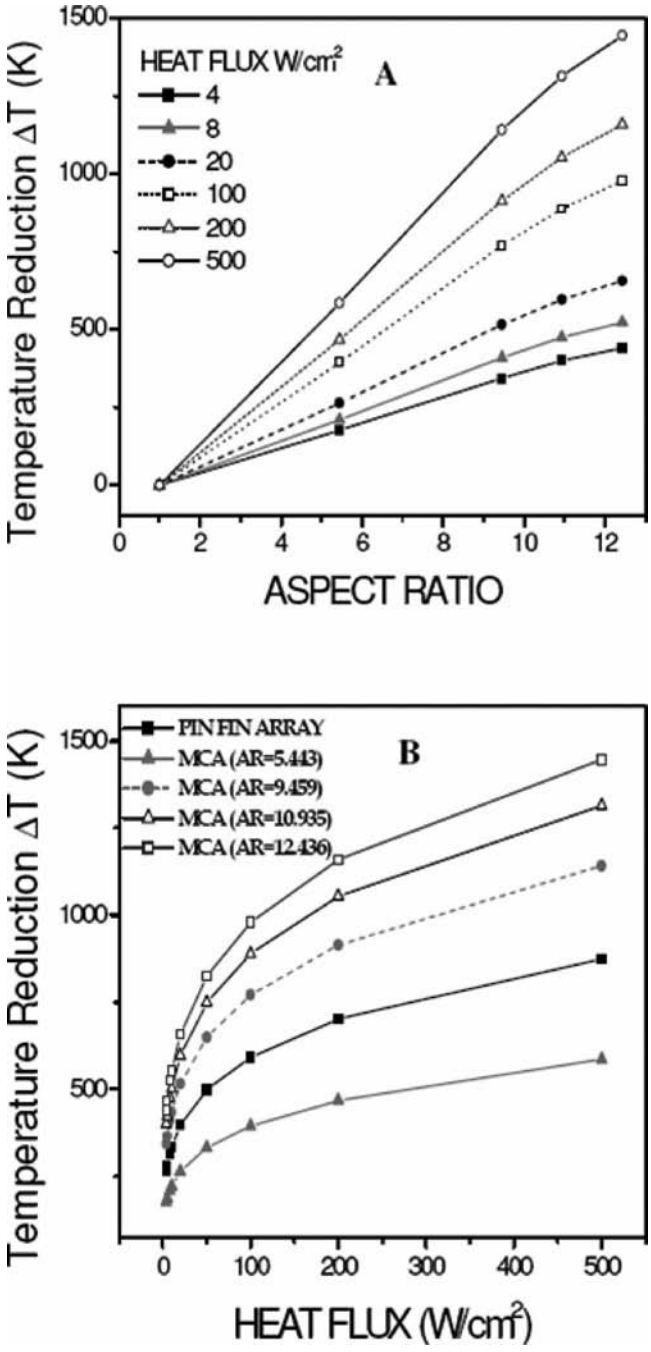

Fig. 6 (*a*) Simulations carried out on the MCA model of different aspect ratios fabricated on Ti, showing temperature reduction (ΔT) of the base for a wide range of heat fluxes at different aspect ratios. Saturation is shown to occur for an AR ~12. (*b*) Plot of the same data in Fig. 8(*a*) to indicate the temperature reduction (ΔT) of the base surface with applied heat flux.

tio of the MCA is illustrated in Fig. 6. In Fig. 6(*a*), the steady-state temperature reduction for arrays of microcones of different aspect ratios (ARs) fabricated on titanium is shown as a function of input heat fluxes. It is clear that higher aspect ratios result in better temperature reduction of the base surface in this model. A saturation regime is however seen for ratios greater than ~12. This is most likely due to the dominant effect of the surface-to-surface heating component. Figure 6(*b*) is a plot of the same data in Fig. 6(*a*), showing the drop in base temperature versus heat flux for MCA with higher aspect ratios. This demonstrates that for the same material, engineering the surface microstructure can be an important design parameter in controlling the allowed temperature range (max and min).

The results in Fig. 6 suggest that, depending on the particular application, one could modify the MCA aspect ratios to optimize the heat removal process. Thus, if the base is part of the outer surface of a spacecraft cabin compartment, with a heat flux density of 0.9 W/cm^2 (due to cabin crew, electronics, or fuel combustion) the steady-state temperature of the base without the MCA is 467 K (194 °C). If the goal is to lower its temperature to below 291 K (18 °C) then MCA with aspect ratio 9.4 are sufficient. By contrast if our goal is to lower the temperature to 276 K (3 °C),

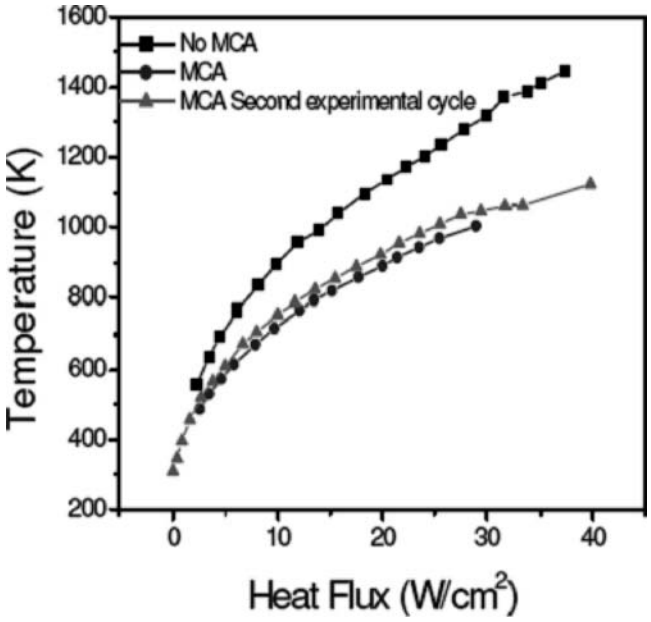

Fig. 7 Plot of temperature versus heat flux for Alloy 321 MCA (aspect ratio of ~5.4) structured and flat foils. For the MCA structured surface we have plotted the temperature versus heat flux for a second thermal cycle.

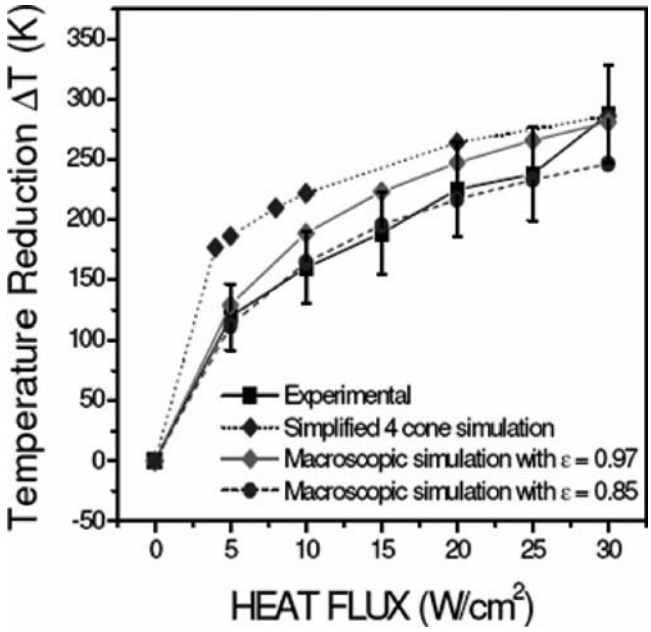

Fig. 8 Comparison of experimentally observed decrease in temperature versus simulated results on Alloy321 using different models. The macroscopic model includes conduction heat loss due to the feedthrough rods but does not account for heating due to radiation reflected from the vacuum chamber, while the simplified four cone MCA model only includes heat loss due to radiation.

say for example to cool pipes that carry cooling water around the cabin, then employing MCA with an aspect ratio of 12.4 will be required.

4.2 Experimental Results and Comparison With Simulations. The temperature characteristics versus input heat flux for both MCA structured and flat foils of Alloy 321 were measured and are shown in Fig. 7. The MCA structures were approximately 20 μm in height and 20 μm in base diameter, which corresponds to an aspect ratio of ~5.4. This aspect ratio value was then used in a four cone simplified simulation of Alloy 321 MCA over a similar heat flux input range. This simulation overestimated by 20–50% the heat loss from the MCA, although the overall trend in temperature reduction was reproduced. The overestimation stems from the differences between the microscopic four cone MCA model and the actual macroscopic experimental setup. In the heating experiments, heat loss due to conduction out of the ends of the foil into the clamps used to hold the foil sample was present and could not be accounted for in the microscopic simulations. In addition, the MCA are not uniformly shaped and spaced as estimated in the microscopic simulation. To better model the experiment, a macroscopic simulation based on the physical experimental setup was performed in which the MCA surface was approximated by a material with a high emissivity. A comparison of the experimental results with the four cone MCA model and the macroscopic experimental model is shown in Fig. 8. The macroscopic model exhibits an improved fit to the experimental data over the four cone model. For an average emissivity value of 0.97, the model still overestimates the temperature reduction by 10–15%. A lower value of the emissivity, 0.85, better reproduces the experimental results with differences typically lower than 4%. In actuality, the effective average emissivity of the MCA foils lies between these two values. This is due to the heating from radiation reflection from the vacuum chamber walls back onto the foil which was not accounted for in the experimental simulation, the effect of which would be to further reduce the heat loss values at a given flux.

4.3 Application to Thermal Control in Space. In space, temperature control protocols are critical to proper functionality of electronics and maintaining habitability of crew modules. The thermal solutions implemented in space have the additional constraints of weight, volume, and reliability. This generally means complex processes are required. As an alternative, MCA offers high levels of cooling through radiative emission, coupled with the advantages of: (1) being a simple, passive solution; and (2) lightweight construction when fabricated from titanium. The one minor drawback of the MCA structures is that their high emissivity occurs throughout the spectral range, which means that intense visible radiation sources, such as the sun, would be heat sources when exposed to MCA structures. This deficiency could easily be compensated for through the use of MCA in nonsolar facing orientations or through the use of relatively simple active control measures.

5 Conclusion

Micro-column arrays have been fabricated by pulsed laser ablation on different metals. Spectral analysis of the fabricated MCA indicates that the samples have low reflectance, high emissivity, and blackbody-like characteristics. Finite element methods were undertaken to simulate the radiative heat loss properties of the MCA. The simulations revealed that MCA structures show a larger base temperature reduction with higher aspect ratios. However, beyond an aspect ratio of 12, there is a saturation effect, which is likely due to an increase of the surface-to-surface radiation component. When compared to a pin fin array of similar mass and volume, MCA exhibited less heat loss by radiation. However, MCA fabrication by laser ablation is simpler and more easily tailored when compared to the lithography and etching processes necessary for pin fins. The overall simulation model was validated experimentally by comparing the final temperatures of MCA and untreated Alloy 321 metal foils heated in vacuum. The difference of 20–50% between the theoretical four cone model and experimental heat loss values can be explained by chamber- and sample-holding effects which the microscopic model cannot account for. However, the model is still useful in predicting trends of MCA

behavior for different cone geometries. An improved fit to the experimental data, with differences as low as 4%, was obtained using a macroscopic model based on the physical experimental setup. Overall, we have shown that MCA under different heat fluxes and aspect ratios are an effective method for temperature reduction, supporting the idea of MCA for thermal management in both space and terrestrial applications.

Acknowledgment

We would like to acknowledge support from an Air Force SBIR Program Contract No. F40600-02-C-0011 to IMS, Inc., monitored by Captain Lance Baxter of AEDC, and a Mini Grant and a Post Doctoral Fellowship Grant from the Institute of Space Systems and Operations (Houston, TX) to the University of Houston team. We would also like to thank Dr. Rodrigo Devivar and Dr. David Moore at NASA JSC for use of their spectroreflectrometer, and Dr. G.A. Shafeev and Dr. A.V. Simakin of the Wave Research Center, General Physics Institute of the Russian Academy of Science for supplying some of the samples.

Nomenclature

G = surface irradiation (W/m^2)
h = heat transfer coefficient (W/m^2 K)
$J_o=J$ = surface radiosity expression at x (W/m^2)
J' = surface radiosity from x' (W/m^2)
k = thermal conductivity (W/m K)
n = normal vector at the point x
n' = normal vector at the point x'
r = vector connecting x and x' (m)
T = temperature of point x (K)
T_{amb} = ambient temperature (K)
T_{inf} = external bulk temperature (K)
ε = surface emissivity
ρ = reflectance
σ = Stefan–Boltzmann constant, 5.669×10^{-08} W/m2 K^4
F_{amb} = view factor for ambient surroundings radiating onto the body

References

[1] Kobus, C. J., and Oshio, T., 2005, "Predicting the Thermal Performance Characteristics of Staggered Vertical Pin Fin Array Heat Sinks under Combined Mode Radiation and Mixed Convection With Impinging Flow," Int. J. Heat Mass Transfer, **48**(13), pp. 2684–2696.
[2] Minakarni, K., Ishizuka, M., and Mochizuki, S., 1995, "Performance Evaluation of Pin-Fin Heat Sinks Utilizing a Local Heating Method," J. Enhanced Heat Transfer, **2**(1–2), pp. 17–22.
[3] Chang, S. W., Liou, T.-M., and Juan, W.-C., 2005, "Influence of Channel Height on Heat Transfer Augmentation in Rectangular Channels With Two Opposite Rib-Roughened Walls," Int. J. Heat Mass Transfer, **48**(13), pp. 2806–2813.
[4] Zuckerman, N., and Lior, N., 2005, "Impingement Heat Transfer Correlations and Numerical Modeling," J. Heat Transfer, **127**, pp. 544–552.
[5] Kercher, D. S., Lee, J. B., Brand, O., Allen, M. G., and Glezer, A., 2003, "Microjet Cooling Devices for Thermal Management of Electronics," IEEE Trans. Compon. Packag. Technol., **26**(2), pp. 359–366.
[6] Dewan, A., Mahanta, P., Raju, S. K., and Suresh Kumar, P., 2004, "Review of Passive Heat Transfer Augmentation Techniques," Proc. Inst. Mech. Eng., Part A, **218**, pp. 509–527.
[7] Webb, R. L., 2005, "Next Generation Devices for Electronic Cooling With Heat Rejection to Air," J. Heat Transfer, **127**, pp. 2–10.
[8] Li, D., Huxtable, S. T., Abramson, A. R., and Majumdar, A., 2005, "Thermal Transport in Nanostructured Solid-State Cooling Devices," J. Heat Transfer, **127**, pp. 108–114.
[9] Grob, L. M., and Swanson, T. D., 2000, "Parametric Study of Variable Emissivity Radiators," AIP Conf. Proc., **504**, pp. 809–814.
[10] Darrin, A. G., Osiander, R., Champion, J., Swanson, T., and Douglas, D., 2000, "Variable Emissivity Through MEMS Technology," AIP Conf. Proc., **504**, pp. 803–808.
[11] Razelos, P., 2003, "A Critical Review of Extended Surface Heat Transfer," Heat Transfer Eng., **24**(6), pp. 11–28.
[12] Tuckerman, D. B., and Pease, R. F. W., 1981, "High-Performance Heat Sinking for VLSI," IEEE Electron Device Lett., **2**, pp. 126–129.
[13] Sobhan, C. B., and Garimella, S. V., 2001, "A Comparitive Analysis of Studies on Heat Transfer and Fluid Flow in Microchannels," Microscale Thermophys. Eng., **5**, pp. 293–311.
[14] Kim, S. J., 2004, "Methods for Thermal Optimization of Microchannel Heat Sinks," Heat Transfer Eng., **25**(1), pp. 37–49.
[15] Zhang, L., Koo, J. M., Jiang, L., Asheghi, M., Goodson, K. E., Santiago, J. G., and Kenny, T. W., 2002, "Measurements and Modeling of Two-Phase Flow in Microchannels With Nearly Constant Heat Flux Boundary Conditions," J. Microelectromech. Syst., **11**(1), pp. 12–19.
[16] Starikov, D., Boney, C., Pillai, R., Bensaoula, A., Shafeev, G. A., and Simakin, A. V., 2004, "Spectral and Surface Analysis of Heated Micro-Column Arrays Fabricated by Laser-Assisted Surface Modification," Infrared Phys. Technol., **45**, pp. 159–167.
[17] Touloukian, Y. S., and DeWitt, D. P., 1970, "Thermal Radiative Properties of Metallic Elements and Alloys," *Thermophysical Properties of Matter, The TPRC Data Series*, Vol. 7, IFI/Plenum, New York, pp. 732–733.

The Compatibility of Thin Films and Nanostructures in Thermoelectric Cooling Systems

Andrew Miner
Romny Scientific,
San Francisco, CA 94121
e-mail: miner@romny-scientific.com

The compatibility of low-dimensional thermoelectric materials in forms such as thin films and nanowires for use in thermoelectric coolers is examined. First-order thermoelectric theory predicts that the cold and hot junction temperatures of a thermoelectric circuit are governed solely by the nondimensional figure of merit, ZT. Performance predictions based on this traditional theory have been more broadly applied to the performance of thermoelectric cooler systems, thereby implying that these coolers may be miniaturized without loss of performance and that system performance is dictated principally by ZT. A nondimensional thermoelectric system model for a cooler is developed and typical performance metrics for thermoelectric coolers are presented along with predictions from traditional theory. Performance is examined as a function of thermoelectric element length for representative system conditions. This system study shows that cooler performance may drop significantly when miniaturized, particularly if the cooling elements are realized at the scale of many recently proposed thermoelectric thin films and nanostructured materials. The system theory illustrates that performance is governed by three nondimensional parameters: an effective thermoelectric figure of merit, Z_eT_a, the relative ability for heat to be drawn into the cooler, and the relative ability for heat to be rejected from the cooler to the ambient environment. As cooler performance depends both on material properties (Z_eT_a) as well as the relative scale of the materials with respect to system thermal conductances, the applicability of some low-dimensional forms of materials such as thermoelectric elements may require reevaluation. The realization of high performance coolers based on thermoelectric effects must rely on developing high quality materials realized at an appropriate, application-dependent scale.
[DOI: 10.1115/1.2717941]

Keywords: energy conversion, thermoelectric cooling, refrigeration, Peltier effect, microelectronic cooling, nanostructures, thin films, nanowires, nanomaterials

Introduction

The thermoelectric effect has been applied to provide useful cooling, generate electrical power, and provide measurement of temperature for many decades. Thermoelectric phenomenon was discovered in 1821 by Thomas Johann Seebeck and the theory was more completely refined by Jean Charles Peltier in 1834. The application of these thermoelectric effects to cooling in the 1950s created great expectation of this technology to provide an environmentally benign, energy efficient alternative to vapor compression refrigeration. A revolution in cooling did not materialize, but thermoelectrics have been utilized widely in certain applications where features such as their compactness, gravity independence, or solid state nature outweigh their relatively poor efficiency. The efficiency and performance of these applications may be improved by the enhancement of three thermophysical properties of the materials used in these systems: increase of Seebeck coefficient, S, suppression of electrical resistivity, ρ, and suppression of thermal conductivity, λ. These three properties are often grouped into the composite thermoelectric property known as the nondimensional thermoelectric figure of merit, $ZT=S^2T/\rho\lambda$. Materials developed beginning in the 1940s up to the early 1990s have exhibited thermoelectric figures of merit, ZT, near room temperature approaching unity [1–3].

Figure 1 shows a schematic diagram of thermoelectric elements interconnected to provide cooling by the application of electrical current. A single pair of elements is shown, though in practice an array of alternating n- and p-type thermoelectric elements is commonly implemented. The elements are arranged with electrical interconnections such that electrical current may flow through all elements in series, but heat flows in parallel from the right side of the schematic to the left. The maximum temperature difference between the cold thermoelectric junction, T_c, and the hot thermoelectric junction, T_h, is obtained when there is no power generation in the object to be cooled. Under the assumptions that the thermophysical properties of the materials are temperature independent, heat and charge flow is one dimensional in the thermoelements, and no electrical resistances exist due to interfaces or interconnections, the maximum temperature difference between junctions under steady state operation may be shown to be only a function of the composite material property Z [1],

$$\Delta T_{\max} = (T_h - T_c)_{\max} = ZT_c^2/2 \tag{1}$$

This relation requires that Z be defined as the effective Z of both thermoelectric elements and that the aspect ratios of n and p elements be scaled for optimal temperature drop as follows [1]:

$$Z = \frac{(S_p - S_n)^2}{(\sqrt{\lambda_n\rho_n} + \sqrt{\lambda_p\rho_p})^2} \tag{2}$$

$$\frac{L_nA_p}{L_pA_n} = \sqrt{\frac{\rho_p\lambda_n}{\rho_n\lambda_p}} \tag{3}$$

A second operating condition of interest is the condition where the cold and hot thermoelectric junctions are of equal temperature due to power dissipation by an object to be cooled. This maximum

Contributed by the Heat Transfer Division of ASME for publication in the JOURNAL OF HEAT TRANSFER. Manuscript received March 21, 2006; final manuscript received September 11, 2006. Review conducted by Suresh V. Garimella.

 Copyright © 2007 by ASME

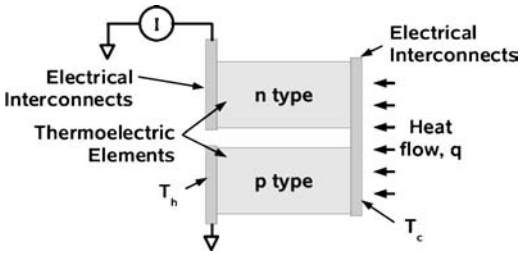

Fig. 1 A schematic diagram of a single-element pair of thermoelectric coolers. Thermoelectric materials, typically *n*- and *p*-type semiconductors, are electrically connected in series. The geometry is such that the elements are thermally in parallel, drawing heat from the left of the figure and dissipating heat to the right. A thermoelectric element-based model (or traditional model) for cooler performance is developed from the elements shown, including the material properties of the elements and the temperatures of the hot and cold junctions, T_h and T_c, respectively.

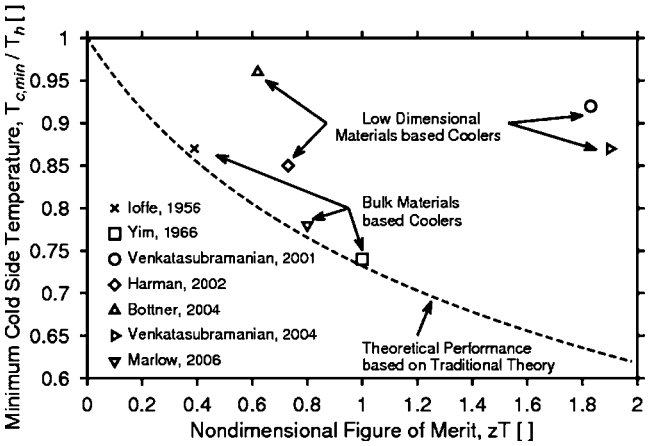

Fig. 2 The minimum cold-side temperature achievable by a thermoelectric cooler (nondimensionalized as $T_{c,\min}/T_h$) is shown as a function of the nondimensional figure of merit, ZT_h. The dashed line illustrates ideal cooler performance as predicted by traditional thermoelectric theory. Various experimental results from literature are overlaid, based on the published experimental cooling performance, T_c/T_h and experimentally measured figure of merit, ZT_h. [1,4,5,20–23]. The degree of departure from the theoretically predicted performance is distinctly more significant for coolers based on low-dimensional materials.

cooling power condition may be shown to be only a function of S^2/ρ and the length of the thermoelectric element, L. Under the same assumptions stated for the development of Eq. (2), the maximum heat flux may be presented as [2,3]:

$$q_{\max} = \frac{A}{2L}\frac{S^2}{\rho}T_h^2 \tag{4}$$

The object to be cooled is assumed to be thermally isolated from surroundings and without parasitic paths of energy transport between the cold and hot thermoelectric junctions other than within the thermoelectric elements.

These relations hold true when describing the performance of thermoelectric element pairs or arrays of thermoelectric element pairs, and are referred to herein as the thermoelectric element based theory or traditional thermoelectric theory. In Eqs. (1) and (4) and as shown in Fig. 1, temperatures are defined as the local temperatures at the hot and cold thermoelectric junctions (at T_h and T_c, respectively). By applying this traditional theory of thermoelectric element arrays to the performance of thermoelectric coolers in operation, several observations are often made in literature and have become widely held impressions of thermoelectric technology in general: The performance of thermoelectric coolers in terms of maximum temperature difference or efficiency is simply a function of Z (or ZT) [4–6]; the performance of thermoelectric coolers is independent of the geometric scale of the cooler [7]; and the realization of a material exhibiting a ZT of approximately 3 will allow thermoelectric coolers to perform competitively in terms of efficiency with vapor compression thermodynamic cooling cycles [6,8–10].

The application of traditional thermoelectric theory to cooler performance has led to intense pursuit of new materials exhibiting attractive thermoelectric properties (high Z and/or high S^2/ρ). The traditional theory also predicts that the cooling power density of coolers increases as the inverse of the thermoelectric element's length, L. This has also fueled interest in thin films and nanostructured materials as thermoelectric elements. These nanomaterials, or nanostructured materials, include those termed in literature as nanowires, nanotubes, multilayered structures, superlattices, nanostructured thin films, quantum dot materials, etc. [4–6,11–19].

It has been theorized that nanowires and nanotube materials in certain material systems with small diameters may exhibit an enhancement of the Seebeck coefficient, due to the transition of the electronic density of states from a three-dimensional system to a dominantly one-dimensional system. Experimental work has also shown that the scale of structures can enhance thermoelectric properties. The reduction of the diameter of these nanowire structures can lead to a reduction in thermal conductivity due to the increase in boundary scattering of the phonons at small dimensions [6,11–16].

The demonstrated reduction in thermal conductivity demonstrated in multilayered structures and superlattice thermoelectric materials has been attributed to influences including the additional phonon scattering caused by the added periodicity of the structure (mini-band formation), acoustic mismatch scattering of phonons at the boundaries, or simply the reduction in thermal transport with a less pronounced decrease in electrical conductivity due to the increased interface density [12,18,19]. Periodic structures have also been theorized to confine electron transport to two dimensions, resulting in gains in the Seebeck coefficient [17].

Enhancement of S, ρ, or λ has been demonstrated by several researchers. Notable experimental work has shown that p-type semiconducting superlattice thin films composed of Bi_2Te_3 and Sb_2Te_3 have ZT of 2.4 at room temperature [4], while structures of localized nodes, or quantum dots embedded in superlattice structures composed of PbSeTe/PbTe exhibit ZT of 1.3 to 1.8 at room temperature [5].

Traditional thermoelectric theory, based on an element model depicted in Fig. 1, is often used as a predictor of performance. The theoretical minimum cold side temperature as predicted from this theory may be found through manipulation of Eq. (1) as

$$T_c/T_h = \frac{2}{\left(1+\sqrt{1+2ZT_h}\right)} \tag{5}$$

Limited published data exist in which both ZT and minimum cooler cold-side temperature are measured independently for a working cooler, but several available examples are shown in Fig. 2. The figure shows experimentally measured minimum cold-side temperature (no applied heat flux) as the ratio of cold to hot temperature T_c/T_h as a function of the measured figure of merit, ZT_h. Results for several coolers composed of bulk, thin film, and nanostructured materials are shown [1,4,5,20–23]. The level of performance predicted by traditional theory in Eq. (5) is also shown in Fig. 2 as a dashed line.

The degree of departure from the theoretically predicted performance is distinctly more pronounced for coolers based on thin

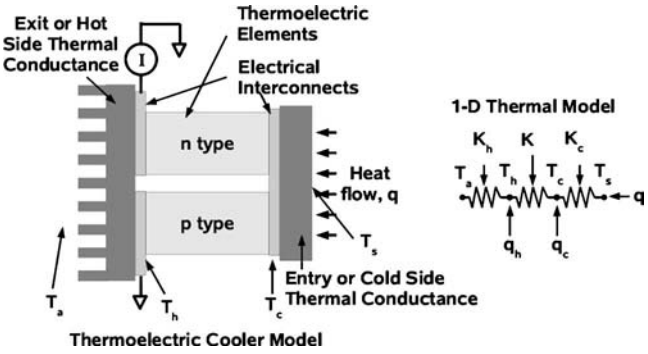

Fig. 3 A thermoelectric cooler is shown schematically at the left. The electrically active elements are shown interconnected as in Fig. 1. Additional elements that determine cooler performance are shown including the finite thermal conductance between the source of heat to be cooled and the finite conductance between the hot junctions and the ambient environment. To the right, a one-dimensional thermal model is shown with each isothermal region labeled (T_a, T_h, T_c, and T_s) and one-dimensional approximations of the thermal conductances shown (exit conductance, K_h, element array conductance, K, entry conductance, K_c).

films and nanostructured materials than those composed with bulk thermoelectric materials (characteristic dimension typically greater than 100 μm). Potential reasons for the departure of cooler performance from theoretical predictions can be traced to parasitic paths of heat flow from the hot side of the cooler to the cold, interface electrical resistances [24], restriction of heat flow from the hot side of the cooler to the ambient environment [25–27], and the nonideal matching of n- and p-type geometries (Eq. (3)).

This work develops a thermoelectric system model that incorporates several nonideal influences on cooler performance that are not captured in the traditional thermoelectric theory. The model is generalized in nondimensional form and the predicted performance for minimum cold-side temperature, cooling power density, and coefficient of performance are presented. To illustrate impact on cooler performance when element size is reduced to scales of common thin films and nanostructures, the minimum cold side temperature and maximum cooling power density are examined in representative operating conditions.

The Departure of a Thermoelectric System from Traditional Element Theory

Figure 3 shows a thermoelectric cooling system, incorporating some of the nonideal elements that cause the performance of the system to deviate from that predicted by traditional thermoelectric theory. As shown in Fig. 3, the inefficiencies of the cooler as well as the heat drawn from the source being cooled must flow from the cooler to an ambient environment through a finite thermal conductance. This causes the temperature of the thermoelectric junctions where the Peltier heating is liberated (at T_h) to vary, rather than being a constant. There has been a general tendency in literature to use traditional thermoelectric theory to predict cooler performance and assume that T_h is constant. Coolers draw heat from a source with a characteristic temperature, denoted as T_s in Fig. 3, through a finite thermal conductance to the location of the Peltier cooling effects (at T_c). In addition to the Peltier heating and cooling effects at the interfaces of thermoelectric materials, heating in electrical interconnects and at electrical interfaces play a role in cooler performance. Additionally, the backflow of heat through parasitic paths external to the thermoelectric materials, as well as radiative parasitics can play a role under certain conditions.

The system issues related to thermoelectric cooling design, such as the ability to optimize the performance considering the effectiveness of heat removal, has been studied [25–27], yet has not been effectively posed in generalized terms with broad applicability to thermoelectric systems. Literature addressing the impact of system constraints on thermoelectric cooling devices utilizing thin films and nanostructures is limited. The influences of interfaces and interconnects have been studied as issues relating to cooler design, including the impact on performance of electrical and thermal contact resistances of miniaturization [3,24,28,29]. This work seeks to bring together the impact of the paths of heat flow to thermoelectric device, paths from the device to the ambient environment, and interfaces using nondimensionalization to reveal key performance parameters.

A Generalized Thermoelectric System Theory

The finite paths of heat flow, as well as electrical parasitics and thermal parasitic paths of heat flow, are modeled and generalized here to provide a framework for examining the applicability of low-dimensional thermoelectric materials and the scalability of thermoelectric coolers. The relations derived from this broader thermal model are referred to herein as the thermoelectric system theory.

A schematic of the thermoelectric cooler model is shown at the right of Fig. 3. The ambient environment is assumed to be at a constant temperature, T_a, and the maximum temperature of the source of heat is T_s. The electrical interconnect region, including the thermoelectric-interconnect interfaces, is assumed to be isothermal at T_h and T_c for the hot and cold sides, respectively. The analysis presented here is simplified by assuming that the n- and p-type materials are thermoelectrically symmetric, that is having equal electrical resistivity, $\rho_n=\rho_p=\rho$ and thermal conductivity, $\lambda_n=\lambda_p=\lambda$. Under this assumption the Seebeck coefficients are of equal magnitude, $-S_n=S_p=S$, and the cross-sectional areas of n and p elements are equal as required by Eq. (3). The following analysis may be performed without the assumption of thermoelectric symmetry with some added complexity. Heat flow from the source to the cold thermoelectric junctions, between the hot and cold junctions, and from the hot junctions to the ambient environment, are modeled as one-dimensional thermal conductances, K_c, K, and K_h, respectively. Thermophysical properties are assumed to be temperature independent, and as such, Thompson effects are neglected. The system is assumed to be operating in steady state conditions.

Under the stated assumptions an energy balance at the hot and cold regions yield

$$(T_a - T_h)K_h + IST_h + (T_c - T_h)K + I^2(R/2 + R_i) = 0 \tag{6}$$

$$(T_h - T_c)K + I^2(R/2 + R_i) - IST_c + (T_s - T_c)K_c = 0 \tag{7}$$

In Eqs. (6) and (7), I represents the sum of the magnitudes of electrical currents (i_n in the n type, i_p in the p type) in the m elements composing a given cooler

$$I = \sum_{j=1}^{m/2} (|i_n| + |i_p|) \tag{8}$$

The total electrical resistance of the thermoelectric elements operating electrically in parallel is R, and the thermal conductance of all thermoelectric elements as well as parasitic paths for heat flow from the hot to the cold junction in parallel is defined by the thermal conductance K. Electrical interface resistances as well as the finite electrical resistance of the interconnects are captured in the term R_i.

The competing effects in this thermal system may be better understood by nondimensionalizing the governing Eqs. (6) and (7). Each temperature is scaled by the ambient temperature, yielding nondimensional temperatures $\theta_h=T_h/T_a$, $\theta_c=T_c/T_a$, and $\theta_s=T_s/T_a$. Electrical current is nondimensionalized with respect to the Seebeck coefficient and total element conductance as $\gamma=IS/K$. The exit and entry thermal conductances are scaled with

respect to the total element thermal conductance as $\kappa_h = K_h/K$ and $\kappa_c = K_c/K$. The nondimensionalized governing equations yield a nondimensional effective thermoelectric figure of merit, defined as

$$Z_e T_a = \frac{S^2 T_a}{K(R + 2R_i)} \tag{9}$$

Thus, the system can be solved for the cold and hot thermoelectric junction temperatures as

$$\theta_c = \frac{(\kappa_h + 1 - \gamma)(\gamma^2/2Z_e T_a + \kappa_c \theta_s) + \gamma^2/2Z_e T_a + \kappa_h}{(\kappa_h + 1 - \gamma)(\kappa_c + 1 + \gamma) - 1} \tag{10}$$

and

$$\theta_h = \frac{(\kappa_c + 1 + \gamma)(\gamma^2/2Z_e T_a + \kappa_h) + \gamma^2/2Z_e T_a + \kappa_c \theta_s}{(\kappa_h + 1 - \gamma)(\kappa_c + 1 + \gamma) - 1} \tag{11}$$

Equation (10) defines the temperature of the cold Peltier junction as a function of the effective nondimensional figure of merit, $Z_e T_a$, relative exit and entry thermal conductances, κ_h and κ_c, current, γ, and the temperature of the heat source. An optimum current level may be found analytically for certain cooler operating conditions such as the maximum temperature difference, maximum cooling power, or maximum efficiency.

Thermoelectric Cooler Performance Metrics

Minimum Cold-Side Temperature. The minimum cold-side temperature achievable by a cooler is a performance metric often quoted and compared in literature. This is the condition where there is no power generated in the object to be cooled and this object is assumed to be in thermal isolation from the environment. Traditional thermoelectric theory predicts the minimum relative temperature of the cold-side as the following relation, derived from Eq. (1),

$$\theta_{c,\min,\text{trad}} = \frac{\sqrt{1 + 2ZT_a} - 1}{ZT_a} \tag{12}$$

Equation (10) may be used to describe the minimum cold side temperature for the cooler shown in Fig. 3 by assuming that there is no heat drawn from the source. This implies that $\theta_s = \theta_c$, simplifying Eq. (10),

$$\theta_{c,\min} = \frac{(\kappa_h + 2 - \gamma_0)\gamma_0^2/2Z_e T_a + \kappa_h}{(\kappa_h + 1 - \gamma_0)(\gamma_0 + 1) - 1} \tag{13}$$

A minimum cold-side temperature occurs at a certain optimum current, γ_0. The full expression for this optimum current is not included here for brevity, but may be found by minimizing Eq. (10) with respect to γ for the conditions of minimum temperature ($\theta_s = \theta_c$).

The dependence of the minimum cold-side temperature on the ability for the cooler to reject heat to the ambient environment is shown in Fig. 4. The minimum cold side temperature, $\theta_{c,\min} = T_c/T_a$ is shown as a function of the relative exit conductance, κ_h. Cold-side temperature is shown for three values of the nondimensional figure of merit, ($Z_e T_a$ and ZT_h). The performance predicted by the thermoelectric system theory (the minimization of Eq. (13)) shows that cooler performance may be significantly degraded as the conductance of heat to the ambient environment diminishes with respect to the thermal conductance of the thermoelectric elements ($\kappa_h = K_h/K$). In contrast, the traditional thermoelectric theory applied to the performance of a thermoelectric cooler neglects the effects of the exit thermal conductance.

Minimum cold-side temperature for a thermoelectric cooler is a strong function of the relative exit conductance, κ_h. This dependence degrades cooler performance as the hot-side heat removal is reduced (poor heat sinking) and/or the thermal conductance of the thermoelectric element array increases (as through the reduction of the element's length, L).

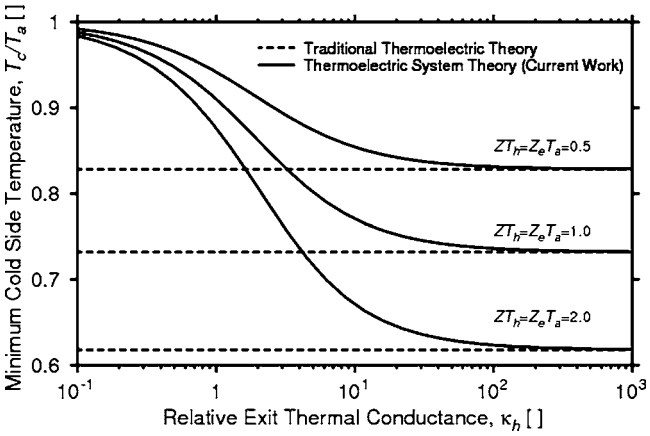

Fig. 4 The nondimensional minimum cold-side temperature is shown as a function of the cooler's relative exit thermal conductance. The performance predicted by thermoelectric system theory (current work) as well as traditional thermoelectric theory is shown for values of thermoelectric figure of merit, $ZT_h = Z_eT_a = 0.5$, 1.0, and 2.0. As the exit thermal conductance decreases (due to poor heat sinking and/or miniaturization of the thermoelectric element array), the minimum temperature approaches 1.0 (no cooling below the ambient temperature). The performance predicted by traditional theory is also shown as dashed lines.

Maximum Cooling Power. The maximum amount of heat a thermoelectric cooler can draw from a heat source which is maintained at ambient temperature provides another useful metric in the field of thermoelectricity [2,3]. The amount of heat drawn from a source, q, may be nondimensionalized with respect to the thermal conductance of the thermoelectric element array, K, and the ambient temperature. Traditional thermoelectric theory predicts that the maximum nondimensional heat flux is a constant and solely dependent on the nondimensional figure of merit [1].

$$\psi_{\text{trad}} = \frac{q}{KT_h} = \frac{ZT_h}{2} \tag{14}$$

The maximum nondimensional heat flux developed in this work may be defined in terms of the amount of heat drawn across the finite thermal conductance between the source of heat and the cold thermoelectric junctions,

$$\psi = \frac{q}{KT_a} = (\theta_s - \theta_{c,\psi_{\max}})\kappa_c \tag{15}$$

This condition is typically evaluated in the condition where the source of heat is held at the ambient temperature, and as such, $\theta_s = 1$ in Eq. (15). $\theta_{c,\psi_{\max}}$ is the cold junction temperature defined in Eq. (10), optimized with respect to γ under the conditions $\theta_s = 1$ to maximize the cooling power, ψ. An analytic expression for this optimum current γ_0 has been omitted here for brevity.

The dependence of the cooling power on the ability of the cooler to reject heat to the ambient environment is shown in Fig. 5. The nondimensional cooling power, $q/(KT_a)$, predicted by thermoelectric system theory (Eq. (15)), is shown as a function of the relative exit conductance, κ_h. The cooling power is also a function of the relative cold side thermal conductance, κ_c, and results are shown for $\kappa_c = 10$ and 1000. These results are shown for three values of the nondimensional figure of merit ($Z_e T_a$ or ZT_h). The performance predicted by thermoelectric system theory shows that cooler performance may be significantly degraded as conductance of heat to the ambient environment diminishes with respect to the thermal conductance of the thermoelectric elements (low κ_h), as well as constraints on the heat flow from the source of heat to the thermoelectric cooling junction (low κ_c). In contrast, the tradi-

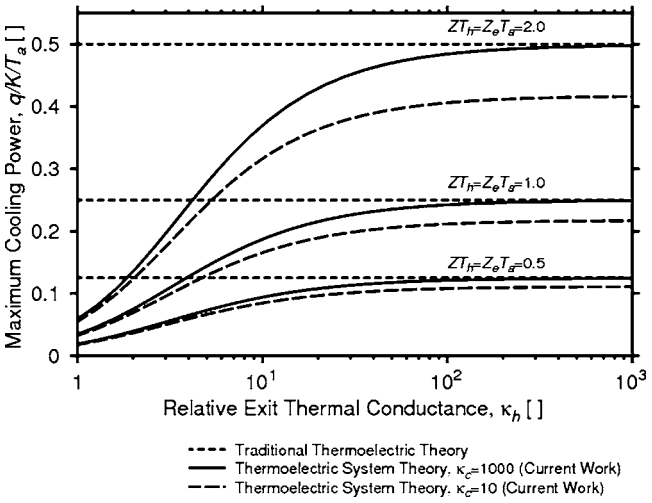

Fig. 5 The nondimensional maximum cooling power is shown as a function of the cooler's relative exit thermal conductance. The performance predicted by thermoelectric system theory (current work) is shown for values of thermoelectric figure of merit, $ZT_h=Z_eT_a$=0.5, 1.0, and 2.0, each for two values of the relative entry thermal conductance. As the exit or entry thermal conductance is decreased (due to poor heat sinking, highly localized or poorly attached heat source, and/or miniaturization of the thermoelectric element array), cooling power is degraded. The performance predicted by traditional thermoelectric theory is also shown for each value of the figure of merit.

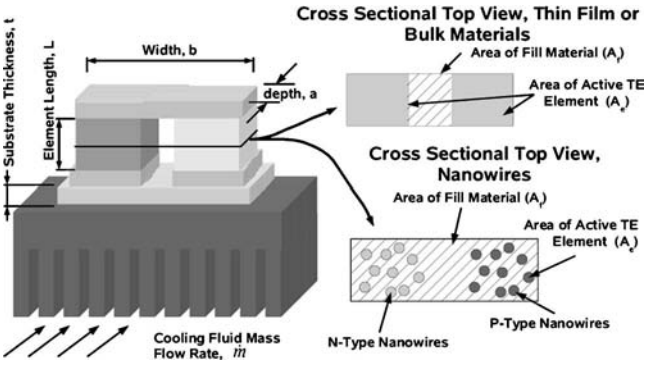

Fig. 6 A schematic diagram of a thermoelectric cooler is shown with elements fabricated on a substrate, which in turn is mounted on a heat sink as a means of heat removal. A single thermoelectric element pair is shown for simplicity, however multiple elements may be arrayed and utilized. To the left, two schematics of a typical cross section are shown. The upper section shows active thermoelectric elements of a certain area, A_e, as well as an electrically inactive "fill" area, A_f. The lower schematic depicts a representative section from a cooler that may be fabricated from vertically aligned wire. The area between each wire as well as between the *n*- and *p*-wire arrays constitutes the electrically inactive region, A_f.

tional thermoelectric theory (Eq. (14)), if applied to the performance of a thermoelectric cooler, predicts a constant nondimensional cooling power since it neglects influence of the thermal paths into and out of the cooler.

Cooling power of a thermoelectric cooler is a strong function of the relative exit conductance, κ_h, and a weaker function of the entry conductance, κ_c. This dependence degrades cooler performance as the hot-side heat removal is reduced (poor heat sinking), the ability for the cooler to draw heat from the source is reduced, and/or the thermal conductance of the thermoelectric element array is increased (by, for example, the reduction of the element's physical scale).

Coefficient of Performance. Traditional thermoelectric theory predicts that the coefficient of performance of a thermoelectric cooling system is only a function of the figure of merit, Z, and the system temperatures (T_m, T_s, and T_a) [2,3],

$$\phi_{\text{trad}} = \frac{T_s}{T_a - T_s}\frac{\sqrt{1+ZT_m} - T_a/T_s}{\sqrt{1+ZT_m}+1} = \frac{\theta_s}{1-\theta_s}\frac{\sqrt{1+ZT_m}-1/\theta_s}{\sqrt{1+ZT_m}+1} \tag{16}$$

By considering the restrictions on heat flowing into and out of the system (κ_c and κ_h), as well as parasitic degradation of the nondimensional figure of merit (captured in Z_e), the coefficient of performance for thermoelectric system theory is as follows:

$$\phi = \frac{\kappa_c(\theta_s - \theta_c(\gamma))}{\gamma(\theta_h(\gamma) - \theta_c(\gamma)) + \gamma^2/Z_eT_a} \tag{17}$$

The optimum coefficient of performance is found by optimizing Eq. (17) with respect to electrical current, γ. The cold and hot-side temperatures, $\theta_c(\gamma)$ and $\theta_h(\gamma)$, are expressed by Eqs. (10) and (11).

As with the minimum cold side temperature and cooling power density, the coefficient of performance is not only a function of figure of merit, but also depends on the entry and exit thermal conductances of the system, κ_c and κ_h.

Parasitic Degradation of the Nondimensional Figure of Merit

The thermoelectric system theory presented herein illustrates that cooler performance is not dependent on the material properties S, ρ, and λ alone, but rather on an effective figure of merit that also captures the influence of thermal and electrical parasitic effects (Eq. (9)). Figure 6 shows a schematic of a thermoelectric cooler and representative cross sections for two types of cooler element construction: film or bulk materials (upper right), and nanowire composite arrays (lower right). In both cases there is an electrically active cross-sectional area composed of a thermoelectric material, A_e, and an electrically inactive cross section composed of a gas or solid fill material of area A_f. Considering the heat and current flow through the thermoelectric elements and heat flow through the fill material to be one dimensional along the length of the element, the thermal conductance of the element array, K, may be expressed as $\lambda_eA_e/L+\lambda_fA_f/L$. The electrical resistance, R, of the element may be expressed as $\rho L/A_e$. Neglecting the electrical resistance of the metal interconnects and only considering a characteristic electrical interface resistance to be present as r_i, the effective nondimensional figure of merit may be expressed as

$$Z_eT_a = T_a\frac{S^2}{(\lambda_e + \lambda_fA_f/A_e)\left(\rho + \dfrac{2r_i}{L}\right)} \tag{18}$$

Introducing a fill factor as $\beta=A_e/A_f$, the degradation of the figure of merit due to parasitics may be expressed as

$$\frac{Z_eT_a}{ZT_a} = \frac{1}{\left(1+\dfrac{\lambda_f}{\lambda_e\beta}\right)\left(1+\dfrac{2r_i}{\rho L}\right)} \tag{19}$$

Equation (19) illustrates two effects that can be highly detrimental to a thermoelectric system: the degradation of performance due to the relative conductance of the fill materials, and the degradation due to potentially nonnegligible interface resistances. These effects can be significant in nanowire and thin-film thermoelectrics where solid fill materials, low fill factors, and short elements are generally prevalent. For example, the thermoelectric nanowires in a proposed cooler may exhibit an inherent thermal

conductivity of $\lambda_e=0.5$ W m^{-1} K^{-1}, yet it is not unusual for fabrication techniques of nanowire arrays to exhibit low fill factors, such as $\beta=1/50$. Should the nanowire array require a solid fill material for structural support, such as low thermal conductivity polymers ($\lambda_f=0.2$ W m^{-1} K^{-1}), by Eq. (19) such a cooler would present an effective figure of merit of only 4.8% of the material's inherent ZT_a. The inclusion of the electrical interface resistance (r_i) in Eq. (2) can further degrade such a material's ability to perform as a thermoelectric element.

Miniaturization of Thermoelectric Cooling Systems

Miniaturization of thermoelectric coolers can have a pronounced effect on performance. This may be illustrated by examining the behavior of a cooler as depicted in Fig. 6 with approximations for the entry and exit thermal conductances. The cooler depicted in Fig. 6 is shown on a substrate that is attached to an air cooled heat sink. Thermal interface resistances between substrate and heat sink are neglected for simplicity, making this analysis more ideal and the predicted results more optimistic than in practical application. The performance of heat sinks is a well-developed technical field [30–33], and two limits of heat sink performance may be readily examined: solid conduction limited heat removal, and air flow limited heat removal [33].

Solid Conduction Limited Systems: Minimum Cold-Side Temperature. In order to show the influence of miniaturization on a representative cooler, the heat is assumed to flow one dimensionally through the substrate on which the cooler is fabricated (Fig. 6), thereby exhibiting thermal conductance of $ab\lambda_{\text{sub}}/t$. The system dissipates heat through a heat sink. As the lateral dimensions of substrate are reduced below the thickness of the solid heat sink material, the thermal conductance into the heat sink becomes limited by the three-dimensional flow of heat through this relatively large solid material. Under these conditions the thermal conductance may be modeled by considering a constant heat flux into a semi-infinite body. The exit thermal conductance may be expressed as the combination of the one-dimensional flow through the substrate and the spreading into the heat sink as [34]

$$K_{h,\text{spreading}} = \frac{ab\lambda_{\text{sink}}\pi/2}{a\ \text{Sinh}^{-1}(b/a) + b\ \text{Sinh}^{-1}(a/b)} \tag{20}$$

Using the definition of fill factor, the area of the cooler may be expressed as $ab=A_e(1+1/\beta)$, and the relative exit conductance may be expressed in terms of the system geometric and material parameters,

$$\kappa_h^{-1} = \left(1 + \frac{\lambda_f}{\lambda_e\beta}\right)\left(\frac{\lambda_e}{\lambda_{\text{sink}}}\frac{2(a\ \text{Sinh}^{-1}(b/a) + b\ \text{Sinh}^{-1}(a/b))}{\pi L(1+1/\beta)} + \frac{\lambda_e t}{\lambda_{\text{sub}}L}\right) \tag{21}$$

Equation (21) provides the relative exit thermal conductance κ_h required for the minimization of Eq. (13). The influence on minimum temperature with element length is shown in Fig. 7. The minimum temperature predicted by the traditional thermoelectric model (Eq. (12)) is independent of element length, L, as shown in Fig. 7. The thermoelectric cooler modeled is assumed to have an area of $ab=1$ mm^2 and is fabricated on a silicon substrate ($\lambda_{\text{sub}}=150$ W m^{-1} K^{-1}) 300 μm thick. The substrate is in intimate thermal contact on a high conductivity heat sink material ($\lambda_{\text{sink}}=300$ W m^{-1} K^{-1}). Predicted performance for element fill factors of 1/5 and 1/50 are shown. These span the range from typical fill factors of commercially available bulk coolers to those in sparsely filled thermoelectric nanowire arrays. As the performance of devices is also dependent on the ratio of the thermal conductivity of the thermoelectric element to that of the fill material (λ_e/λ_f), performance is shown for two such ratios, 38.5 and 1. Assuming that the active thermoelectric material has a thermal conductivity of 1.0 W m^{-1} K^{-1}, these thermal conductivity ratios represent two extremes: filling the gap between the elements with air at ambient pressure and with silicon dioxide, respectively.

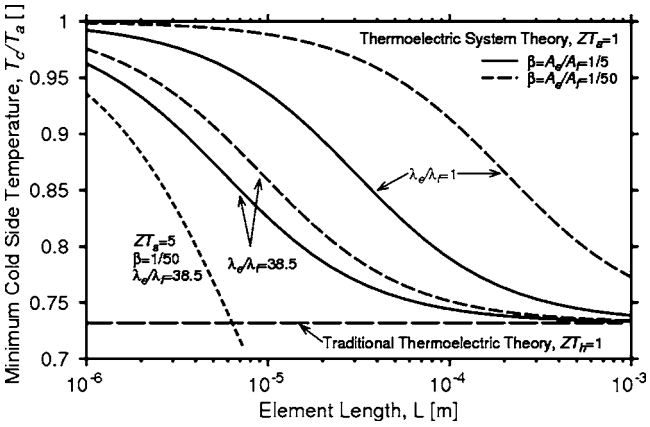

Fig. 7 The nondimensional cold side temperature of a cooler is shown as a function of cooler element length, *L*. The cooler is modeled as dissipating heat through a substrate ($\lambda_{\text{sub}}=150$ W m^{-1} K^{-1}, t=300 μm) on a semi-infinite heat sink ($\lambda_{\text{sink}}=300$ W m^{-1} K^{-1}). The predicted performance for several geometries and material properties reflecting a ZT_a of 1.0 and a single representative result at $ZT_a=5$ are shown. The degradation of performance as the element length decreases, the degree of degradation being a function of the element fill factor, β, and the relative thermal conductivity of the fill material λ_e/λ_f. Thermal conductivity ratios are shown representing what would be found using a fill material of ambient air and silicon dioxide. The model illustrates the influence of scale and cooler structure, showing conditions where a microscale element with a ZT_a of 5 may be outperformed by a cooler of larger scale and a ZT_a of 1.0.

As shown in the Fig. 7, the minimum cold-side temperature is dependent on several factors besides a figure of merit (ZT_h or Z_eT_a), and as the length of the element decreases to lengths that are on the order of thin films and typical nanowires, performance can be severely degraded. For perspective, the predicted performance for a system integrating a material with a $ZT_a=5$ is also shown in Fig. 7. If this high ZT_a material was a thin film, nanowire, or nanostructured material with element lengths less than approximately 7 μm, the device would be outperformed by a bulk cooler ($L\geq 1$ mm) with a figure of merit of 1.

Airflow Limited Systems: Maximum Cooling Power. Another condition that provides an illustrative example of thermoelectric device miniaturization effects is the cooling system where the amount of airflow from the ambient environment is the limiting factor in heat removal [33]. Such systems have relatively large area sources but with relatively limited amounts of airflow from the ambient environment. The theoretical minimum conductance based on airflow is $K_h=\dot{m}C$ [33].

The amount of heat removed from a heat source at ambient temperature ($\theta_s=1$) by a cooler such as shown in Fig. 6 may be found from Eq. (15). The airflow limited expression for the relative exit thermal conductance is

$$\kappa_h = \frac{\dot{m}CL(1+1/\beta)}{ab\lambda_e(1+\lambda_f/\lambda_e/\beta)} \tag{22}$$

The maximum cooling power density as a function of element length is shown in Fig. 8 for two sets of performance conditions: where the source being cooled is held at ambient temperature ($\theta_s=T_s/T_a=1$), and when the source is below ambient conditions at $\theta_s=0.85$. The air side limited model for the hot-side thermal conductance (Eq. (22)) is used in an optimization of Eq. (15) (using Eq. (10)), with three levels of airflow: 25, 2.5, and

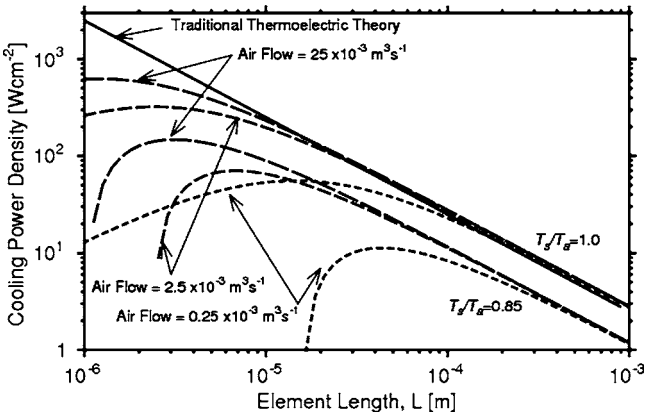

Fig. 8 Cooling power density of a cooler is shown as a function of cooler element length, *L*. The thermal conductance between the hot-side of the cooler and the ambient temperature is modeled as the airflow limit, $K_h = \dot{m}C_p$. The predicted performance for three values of cooling fluid mass flow rate are shown with all coolers having materials exhibiting a ZT_a of 1.0. Performance for a heat source held at the ambient temperature ($T_s/T_a = 1$) and a source operating below ambient temperatures ($T_s/T_a = 0.85$) are shown. The loci of maximum shifts to longer element lengths as the available hot side heat dissipation decreases, contrary to the $1/L$ behavior predicted by traditional thermoelectric element theory.

0.25 $m^3 s^{-1}$. These conditions span a typical range of the available cooling air in microelectronic and optoelectronic equipment cooling applications (ranging from servers to light notebook computers). The entry conductance is calculated assuming one-dimensional heat flow through a source of heat through a silicon substrate ($\lambda = 150$ W m^{-1} K^{-1}) that is 300 μm thick. The cooling power density predicted from traditional thermoelectric theory (Eq. (14)) is also included in Fig. 8. This figure illustrates the departure of actual cooling system performance from that predicted by traditional theory, showing the fact that there is an optimum cooling element length. This optimum length is highly sensitive to level of heat removal to the ambient environment as well as the desired operating temperature of the source to be cooled. As the model for the heat removal (κ_h) is refined beyond the simple air side limit used here to include all significant impedances to heat flow to the ambient environment, the optimum element lengths shift toward elements of larger length.

Conclusion

The performance of thermoelectric coolers is not simply a function of the nondimensional figure of merit, ZT. The minimum cold-side temperature achievable is better predicted by two-nondimensional terms, the effective figure of merit, Z_eT_a, and the relative exit conductance, κ_h. In operating conditions where the cooler is drawing a finite amount of heat from a source, the performance is defined by three-nondimensional terms, Z_eT_a, κ_h, and κ_c. The efficiency of thermoelectric coolers, and their ability to potentially compete with other thermodynamic cooling cycles, must be framed in terms of material properties as well as relative scale. As these broader figure of merits show, the performance of thermoelectric coolers is dependent on the physical scale of the device. Should materials be developed exhibiting high ZT_a, yet only be manufacturable at small scales (such as thin films, nanowires, etc.), they may be outperformed by materials of moderate ZT_a that can be produced at a geometric scale more compatible with application's entry and exit thermal conductances. The thermoelectric model based on the new thermoelectric figures of merit introduced here, Z_eT_a, κ_h, and κ_c, puts a new perspective on what materials have the potential to provide high performance cooling. The best materials for thermoelectric cooling must exhibit appropriate thermophysical properties at the scale appropriate for the application.

Nomenclature

$\dot{m}$ = mass flow rate (kg s^{-1})
A = area (m^2)
a = depth (m)
b = width (m)
C = heat capacity (J kg^{-1} K^{-1})
I = electrical current (A)
i = electrical current, single element (A)
K = thermal conductance (W K^{-1})
L = length of the thermoelectric element (m)
m = number of elements composing a thermoelectric cooler array
q = cooling power (W)
q'' = cooling power density (W m^{-2})
R = electrical resistance (Ω)
r = interface electrical resistivity (Ω m^2)
S = Seebeck coefficient (V K^{-1})
T = temperature (K)
t = thickness (m)
Z = thermoelectric figure of merit (K^{-1})
ZT = nondimensional thermoelectric figure of merit

Greek Symbols

β = fill factor, area ratio
γ = nondimensional electrical current
κ = nondimensional thermal conductance
λ = thermal conductivity (W m^{-1} K^{-1})
ϕ = coefficient of performance
ψ = nondimensional cooling power
ρ = electrical resistivity (Ω m)
θ = nondimensional temperature

Subscripts

0 = optimized quantity
ψ_{max} = optimized under maximum cooling power conditions
a = ambient environment
c = element-interconnect interface region where Peltier cooling occurs
e = effective
e = element
f = fill material
h = element-interconnect interface region where Peltier heating occurs
i = interface
m = mean
max = maximum
min = minimum
n = n-type thermoelectric element
p = p-type thermoelectric element
s = source of heat, or object to be cooled
sink = heat sink
sub = substrate
trad = based on a traditional model for thermoelectric performance

References

[1] Ioffe, A. F., 1956, *Semiconductor Thermoelements and Thermoelectric Cooling*, Infosearch Limited, London, Part II, Chaps. 1 and 2.
[2] Rowe, D. M., ed., 1995, *CRC Handbook of Thermoelectrics*, CRC Press, Boca Raton, FL, Chap. 1.
[3] Nolas, G. S., Sharp, J., and Goldsmid, H. J., 2001, *Thermoelectrics-Basic Principles and New Materials Developments*, Springer, Berlin, Chap. 1.
[4] Venkatasubramanian, R., Siivola, E., Colpitts, T., and O'Quinn, B., 2001, "Thin-Film Thermoelectric Devices With High Room-Temperature Figures of

Merit," Nature (London) **413**, pp. 597–602.
[5] Harman, T. C., Taylor, P. J., Walsh, M. P., and LaForge, B. E., 2002, "Quantum Dot Superlattice Thermoelectric Materials and Devices," Science, **297**, pp. 2229–2232.
[6] Li, D., Huxtable, S., Abrahamson, A., and Majumdar, A., 2005, "Thermal Transport in Nanostructured Solid-State Cooling Devices," ASME J. Heat Transfer, **127**(1), pp. 108–114.
[7] Chung, D. Y., Hogan, T., Brazis, P., Rocci-Lane, M., Kannewurf, C., Bastea, M., Uher, C., and Kanatzidis, M. G., 2000, "$CsBi_4Te_6$: A High-Performance Thermoelectric Material for Low-Temperature Applications," Science, **287**, pp. 1024–1027.
[8] Mahan, G., Sales, B., and Sharp, J., 1997, "Thermoelectric Materials: New Approaches to an Old Problem," Phys. Today, **50**(3), pp. 42–47.
[9] DiSalvo, F., 1999, "Thermoelectric Cooling and Power Generation," Science, **285**, pp. 703–706.
[10] Abramson, A. R., Kim, W. C., Huxtable, S. T., Yan, H., Wu, Y., Majumdar, A., Tien, C.-L., and Yang, P., 2004, "Fabrication and Characterization of a Nanowire/Polymer-Based Nanocomposite for a Prototype Thermoelectric Device," J. Microelectromech. Syst., **13**(3), pp. 505–513.
[11] Hicks, L. D., and Dresselhaus, M. S., 1993, "Thermoelectric Figure of Merit of a One-Dimensional Conductor," Phys. Rev. B, **47**(24), pp. 16631–16634.
[12] Chen, G., 2000, "Phonon Heat Conduction in Nanostructures," Int. J. Therm. Sci., **39**(4), pp. 471–480.
[13] Zou, J., and Balandin, A., 2001, "Phonon Heat Conduction in a Semiconductor Nanowire," J. Appl. Phys., **89**(5), pp. 2932–2938.
[14] Huxtable, S. T., Abramson, A., Majumdar, A., Tien, C.-L., Zeng, G., LaBounty, C., Shakouri, A., Bowers, J. E., and Croke, E., 2002, "Thermal Conductivity of Si/SiGe and SiGe/SiGe Superlattices," Appl. Phys. Lett., **80**(10), pp. 1737–1739.
[15] Dresselhaus, M. S., Lin, Y.-M., Rabin, O., and Dresselhaus, G., 2003, "Bismuth Nanowires for Thermoelectric Applications," Microscale Thermophys. Eng., **7**(3), pp. 207–219.
[16] Zhou, J., Jin, C., Seol, J. H., Li, X., and Shi, L., 2005, "Thermoelectric Properties of Individual Electrodeposited Bismuth Telluride Nanowires," Appl. Phys. Lett., **87**, p. 133109.
[17] Hicks, L. D., and Dresselhaus, M. S., 1993, "Effect of Quantum-Well Structures on Thermoelectric Figure of Merit," Phys. Rev. B, **47**(19), pp. 12727–12731.
[18] Chen, G., Zeng, T., Borac-Tasciuc, T. and Song, D., 2000, "Phonon Engineering in Nanostructures for Solid-State Energy Conversion," Mater. Sci. Eng., A, **292**(2), pp. 155–161.
[19] Venkatasubramanian, R., 2000, "Lattice Thermal Conductivity Reduction and Phonon Localization Like Behavior in Superlattice Structures," Phys. Rev. B, **61**(4), pp. 3091–3097.
[20] Yim, W. M., Fitzke, E. V., and Rosi, F. D., 1966, "Thermoelectric Properties of Bi_2Te_3-Sb_2Te_3-Sb_2Se_3 Pseudo-Ternary Alloys in the Temperature Range 77 to 300 K," J. Mater. Sci., **1**, pp. 52–65.
[21] Bottner, H., Nurnus, J., Gavrikov, A., Kuhner, G., Jagle, M., Kunzel, C., Eberhard, D., Plescher, G., Shubert, A., and Schlereh, K. H., 2004, "New Thermoelectric Components Using Microsystem Technologies," J. Microelectromech. Syst., **13**(3), pp. 414–420.
[22] Venkatasubramanian, R., 2004, "Superlattice Thermoelectric Technology," DOE/EPRI High Efficiency Thermoelectrics Workshop. San Diego, CA.
[23] Marlow, 2006, Marlow Industries, product specifications. Web site: www.marlow.com
[24] da Silva, L., and Kaviany, M., 2004, "Micro-Thermoelectric Cooler: Interfacial Effects on Thermal and Electrical Transport," Int. J. Heat Mass Transfer, **47**(10-11), pp. 2417–2435.
[25] Huang, B. J., Chin, C. J., and Duang, C. L., 2000, "A Design Method of Thermoelectric Cooler," Int. J. Refrig., **23**, pp. 208–218.
[26] Astrain, D., Vian, J. G., and Domnguez, M., 2003, "Increase of COP in the Thermoelectric Refrigeration by the Optimization of Heat Dissipation," Appl. Therm. Eng., **23**(17), pp. 2183–2200.
[27] Zheng, W., and Xu, G., 1996, "Influence of Air Heat Sink Geometry in the Performance of Thermoelectric Cooling Modules," in 15th International Conference on Thermoelectrics, Pasadena, CA, pp. 311–314.
[28] Min, G., and Rowe, D. M., 1999, "Cooling Performance of Integrated Thermoelectric Microcooler," Solid-State Electron., **43**(5), pp. 923–929.
[29] Min, G., and Rowe, D. M., 2000, "Improved Model for Calculating the Coeficient of Performance of a Peltier Module," Energy Convers. Manage., **41**(2), pp. 163–171.
[30] Ellison, G. N., 2003, "Maximum Thermal Spreading Resistance for Rectangular Sources and Plates With Nonunity Aspect Ratios," IEEE Trans. Compon., Hybrids, Manuf. Technol., **26**(2), pp. 439–454.
[31] Saini, M., and Webb, R. L., 2003, "Heat Rejection Limits of Air Cooled Plane Fin Heat Sinks for Computer Cooling," IEEE Trans. Compon. Packag. Technol., **26**(1), pp. 71–79.
[32] Jacobs, M. E., 1989, "The Practical Limits of Forced-Air Cooling of Electronics Equipment," in 11th International Telecommunication Energy Conference, INTELEC 1989, Florence, Italy, pp. 4–8.
[33] Miner, A., and Ghoshal, U., 2006, "Limits of Heat Removal in Microelectronic Systems," IEEE Transactions on Components and Packaging Technology, in press.
[34] Carslaw, H. S., and Jaeger, J. C., 1959, *Heat Conduction in Solids*, Oxford University Press, Oxford, Great Britain, 265 pp.

Analysis of Thermally Expandable Flexible Fluidic Thin-Film Channels

A.-R. A. Khaled
Thermal Engineering and Desalination Technology Department,
King AbdulAziz University,
Jeddah, 21589, Saudi Arabia

K. Vafai[1]
Department of Mechanical Engineering,
University of California, Riverside,
Riverside, CA 92521

Heat transfer inside thermally expandable and flexible fluidic thin-film channels is analyzed in this work. Two categories are analyzed: the first category is when the upper plate of the thin film is mobile and flexible, and the second is when the side plates of the thin film are flexible and mobile. The expansion in the thin-film heights (category I) or widths (category II) are linearly related to the local fluid pressure and the local temperature of the heated plate based on the principles of linear elasticity and constant volumetric thermal expansion coefficient. The governing Reynolds, momentum, and energy equations are properly nondimensionalized and solved numerically using an implicit method. The Peclet number, stiffness parameter, thermal expansion parameter, and aspect ratio are found to be the main controlling parameters. It is found that thermally expandable flexible thin films that belong to category I can produce significant increase in cooling as the heating load increases, especially when operated at lower Peclet numbers, whereas the cooling effect for those that belong to category II is almost unaffected by the expansion. This work paves the way to practically utilize thermally expandable flexible thin films, especially in MEMS and electronic cooling applications. [DOI: 10.1115/1.2712853]

Keywords: thin films, heat transfer, flexible plate, seals, thermal expansion, electronic cooling, MEMS

1 Introduction

Various engineering applications utilize fluidic thin films as cooling devices, such as heat pipes [1–3] and microchannel heat sinks [4–11]. These devices are widely used in electronic cooling applications where rapid development in electronics industry necessitates seeking methods for increasing the cooling capacity. Several solutions are proposed to increase the cooling capacity of fluidic thin films. For example, Bowers and Mudawar [12] have shown that two-phase flow in a minichannel is capable of removing maximum heat fluxes generated by electronic packages; however, the system may become unstable near certain operating conditions. Furthermore, the use of a porous medium in cooling of electronic devices can enhance heat transfer [13–15]. However, the porous medium can create a substantial increase in the pressure drop inside the thin film.

Recently, flexible fluidic thin films were introduced in the works of Khaled and Vafai [16–19], in which they describe a new method for enhancing the cooling capability of fluidic thin films. In summary, flexible thin films utilize soft seals to separate between their plates instead of having rigid thin-film construction. Khaled and Vafai [16,18] have demonstrated that more cooling is achievable when flexible fluidic thin films are utilized. The expansion of the flexible thin film, including a flexible microchannel heat sink, is directly related to the average internal pressure inside the microchannel [16–19]. Additional increase in the pressure drop across the flexible microchannel not only increases the average velocity but also expands the microchannel, causing an apparent increase in the coolant flow rate, which, in turn, increases the cooling capacity of the thin film.

Khaled and Vafai [19] have demonstrated that the cooling effect of flexible thin films can be further enhanced if the supporting soft seals contain closed cavities filled with a gas that is in contact with the heated plate boundary of the thin film. They referred to this kind of sealing assembly as "flexible complex seals." The resulting fluidic thin-film device is expandable according to an increase in the working internal pressure or an increase in the heated plate temperature. It should be noted that flexible thin films analyzed in the works of Khaled and Vafai [16–19] considered special designs that result in a uniform displacement of the thin-film mobile plate. In contrast, the displacement of the mobile plate in other flexible thin-film designs can be nonuniform, especially if the mobile plate itself is flexible.

In this work, heat transfer inside thermally expandable fluidic and flexible thin films is analyzed. The mobile parts (upper plate or side plates) of the thin film are considered to be flexible such that the fluidic region inside the thin film is allowed to expand as functions of both the pressure inside the thin film and the local heated plate temperature via utilizing flexible complex seals or bimaterial plates (made from two different materials, having different volumetric thermal expansion coefficient, on top of each other). The expansion of the thin film is considered to be in the transverse direction of the fluid flow direction when the upper plate is flexible (category I), whereas it is along the thin-film width when the side plates are flexible (category II). The expansion in the thin-film heights or widths is related to both the local internal pressure and local heated plate temperature. The governing equations for flow and heat transfer are properly nondimensionalized and reduced into simpler forms. The resulting equations are then solved numerically and various pertinent results are obtained. The controlling parameters are obtained, and their role on the thermal behavior of thermally expandable fluidic flexible thin films is established.

2 Problem Formulation

Consider a two-dimensional thin film that has a small height h compared to its length B. The x-axis is taken in the direction of the length of the thin film while y-axis is taken along the height of the thin film as shown in Fig. 1. The z-axis is taken along the half thin-film width D, where it is large enough such that two-

[1]Corresponding author.

Contributed by the Heat Transfer Division of ASME for publication in the JOURNAL OF HEAT TRANSFER. Manuscript received March 15, 2006; final manuscript received October 2, 2006. Review conducted by Satish G. Kandlikar.

 Copyright © 2007 by ASME

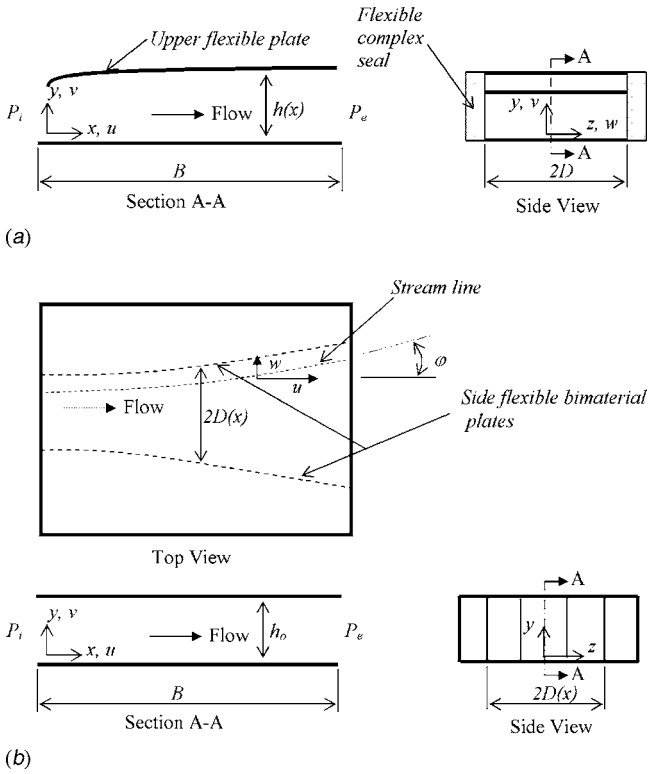

Fig. 1 (*a*) Thermally expandable flexible thin film with mobile flexible upper plate (category I) and (*b*) Thermally expandable flexible thin film with mobile flexible side plates (category II)

dimensional flow inside the thin film can be assumed. Both the thin-film height and width are allowed to vary with the axial distance. The flow is assumed to be laminar, and the convective terms are neglected compared to diffusion terms in the momentum equation (hydrodynamically fully developed flow is assumed). Under these conditions, the velocity field, Reynolds equation, and energy equation are obtained as

$$u(x,y,z) = \frac{[h(x)]^2}{2\mu}\frac{\partial P}{\partial x}\left(\left[\frac{y}{h(x)}\right]^2 - \left[\frac{y}{h(x)}\right]\right) \tag{1}$$

$$v(x,y,z) = \frac{[h(x)]^3}{2\mu}\left(\frac{\partial^2 P}{\partial x^2} + \frac{\partial^2 P}{\partial z^2}\right)\left(\frac{1}{2}\left[\frac{y}{h(x)}\right]^2 - \frac{1}{3}\left[\frac{y}{h(x)}\right]^3\right) + \frac{[h(x)]^2}{2\mu}\frac{\partial P}{\partial x}\left(\frac{1}{2}\left[\frac{y}{h(x)}\right]^2\frac{dh}{dx}\right) \tag{2}$$

$$w(x,y,z) = \frac{[h(x)]^2}{2\mu}\frac{\partial P}{\partial z}\left(\left[\frac{y}{h(x)}\right]^2 - \left[\frac{y}{h(x)}\right]\right) \tag{3}$$

$$\frac{\partial}{\partial x}\left([h(x)]^3\frac{\partial P}{\partial x}\right) + \frac{\partial}{\partial z}\left([h(x)]^3\frac{\partial P}{\partial z}\right) = 0 \tag{4}$$

$$\rho c_p\left(u\frac{\partial T}{\partial x} + v\frac{\partial T}{\partial y} + w\frac{\partial T}{\partial z}\right) = k\frac{\partial^2 T}{\partial y^2} \tag{5}$$

where T, u, v, w, ρ, P, μ, c_p, and k are the fluid temperature, axial velocity, normal velocity, velocity component in the z direction, fluid density, pressure, fluid dynamic viscosity, fluid specific heat, and fluid thermal conductivity, respectively.

The following dimensionless variables are used in this work:

$$X = \frac{x}{B} \tag{6a}$$

$$Y = \frac{y}{h_o} \tag{6b}$$

$$Z = \frac{z}{D_o} \tag{6c}$$

$$U = \frac{u}{u_o} \tag{6d}$$

$$V = \frac{v}{u_o(h_o/B)} \tag{6e}$$

$$W = \frac{w}{u_o(D_o/B)} \tag{6f}$$

$$\theta = \frac{T - T_1}{qh_o/k} \tag{6g}$$

$$\bar{P} = \frac{P - P_e}{P_i - P_e} \tag{6h}$$

$$H = \frac{h}{h_o} \tag{6i}$$

$$\bar{D} = \frac{D}{D_o} \tag{6j}$$

where q, u_o, T_1, h_o, and D_o are the heat flux at the lower plate, reference velocity, inlet temperature, a reference thin-film height, and a reference half thin-film width, respectively. The reference thin-film height h_o and width D_o are taken to be the thin-film height and width at the inlet when both the flow and the heat flux in the thin film are zero. The Reynolds and energy equations can be written as

$$\left(\frac{D_o}{B}\right)^2\frac{\partial}{\partial X}\left([H(X)]^3\frac{\partial \bar{P}}{\partial X}\right) + \frac{\partial}{\partial Z}\left([H(X)]^3\frac{\partial \bar{P}}{\partial Z}\right) = 0 \tag{7}$$

$$U\frac{\partial \theta}{\partial X} + V\frac{\partial \theta}{\partial Y} + W\frac{\partial \theta}{\partial Z} = \frac{1}{\mathrm{Pe}\,\varepsilon}\frac{\partial^2 \theta}{\partial Y^2} \tag{8}$$

where the Peclet number (Pe) and the aspect ratio ε are defined as

$$\mathrm{Pe} = \frac{\rho c_p u_o h_o}{k} \tag{9a}$$

$$\varepsilon = \frac{h_o}{B} \tag{9b}$$

2.1 Flexible Thin Films With Mobile Flexible Upper Plate (Category I). In this category, the lower plate of the thin film is considered to be fixed, whereas the upper plate is flexible and separated from the lower plate by soft complex seals that allow a local expansion in the thin-film heights due to both changes in internal pressure and the lower (heated) plate temperature (Fig. 1(*a*)). Similar effects are expected when the upper plate is a bimaterial plate separated from the lower plate via soft seals. The thin-film height varies linearly with local pressure and local lower plate temperature according to the following relations [17,19]:

$$H(X) = \frac{h(x)}{h_o} = 1 + \frac{\bar{P}(X)}{S_1} + F_{T1}\theta_B(X) \tag{10}$$

where F_{T1} is the thermal expansion parameter, which is equal to

$$F_{T1} = \beta \frac{q h_o}{k} \tag{11}$$

The coefficient β is thermal expansion coefficient of the flexible complex seals. The parameter F_{T1} increases as the heating load q, the thermal expansion coefficient β and the reference thin-film height increase, while F_{T1} decreases as the fluid thermal conductivity k decreases. The stiffness parameter S_1 is related to the elastic properties [20] of the flexible complex seals. When the thin-film width is uniform ($D=D_o$), the velocity field (Eqs. (1)–(3)) reduces to the following:

$$U(X,\eta,Z) = \frac{u(X,\eta,Z)}{u_o} = -6\frac{d\bar{P}}{dX}H^2(\eta-\eta^2); \quad u_o = \frac{(P_i-P_e)h_o^2}{12\mu B} \tag{12}$$

$$V(X,\eta,Z) = [H(X)]^2\left(\frac{d\bar{P}}{dX}\right)\left(\frac{dH}{dX}\right)(\eta^3-\eta^2) \tag{13}$$

$$W(X,\eta,Z) = 0 \tag{14}$$

where $\xi=X$, $\eta=Yh_o/h(x)$. As such, Eq. (8) can be written as

$$-6\frac{d\bar{P}}{dX}H^4(\eta-\eta^2)\frac{\partial\theta}{\partial\xi} = \frac{1}{\mathrm{Pe}\,\varepsilon}\frac{\partial^2\theta}{\partial\eta^2} \tag{15}$$

where $d\bar{P}/dX$ is evaluated from the following reduced form of the Reynolds equation:

$$\frac{\partial}{\partial X}\left([H(X)]^3\frac{\partial\bar{P}}{\partial X}\right) = 0 \tag{16}$$

2.1.1 Thermal Boundary Conditions. Uniform wall heat flux is assumed at the lower plate while the upper plate is considered to be insulated. This models a case where the fluidic thin film with a thin conductive lower plate is placed on the top of a heated surface while its upper plate is made from a less conductive flexible material (e.g., plastics). The boundary conditions are

$$\theta(X,0) = 0, \quad \left.\frac{\partial\theta}{\partial\eta}\right|_{X,\eta=0} = -H(X),$$

$$\left.\frac{\partial\theta}{\partial\eta}\right|_{X,\eta=1} = -\varepsilon^2 H(X)(H(X)-1) \quad \left.\frac{\partial\theta}{\partial\eta}\right|_{X,\eta=1} \cong 0 \tag{17}$$

The Nusselt number is defined as

$$\mathrm{Nu}(X) \equiv \frac{h_c h_o}{k} = \frac{1}{\theta_B(X)-\theta_m(X)} = \frac{1}{\theta(X,0)-\theta_m(X)} \tag{18}$$

where h_c, θ_m, and θ_B are the local convection coefficient, dimensionless mean bulk temperature, and dimensionless lower plate temperature, respectively, and are defined as follows:

$$\theta_m(X) = \frac{1}{U_m(X)H}\int_0^H U(X,Y)\,\theta(X,Y)dY$$

$$U_m(X) = \frac{1}{H}\int_0^H U(X,Y)dY \tag{19}$$

where $U_m(X)$ is the average velocity inside the thin film at the dimensionless axial distance X.

2.2 Flexible Thin Films With Mobile Flexible Side Plates (Category II). In this category, both the thin-film lower and upper plates are considered to be fixed and horizontal, resulting in a uniform thin-film height ($h=h_o$). However, the thin-film width is considered to be nonuniform because it can vary with the local pressure and local lower (heated) plate temperature (Fig. 1(*b*)). As such, the thin-film half width $D(x)$ has the following functional form:

$$\bar{D}(X) = \frac{D(x)}{D_o} = 1 + \frac{\bar{P}(X)}{S_2} + F_{T2}\theta_B(X) \tag{20}$$

This category can be attained when the side mobile plates are bimaterial plates such that they deflect, increasing the thin film width, as the heated plate temperature increases. The dimensionless velocity field for this category can be written as

$$U(X,\eta,Z) = \frac{u(X,\eta,Z)}{u_o} = -6\frac{\partial\bar{P}}{\partial X}(Y-Y^2); \quad u_o = \frac{(P_i-P_e)h_o^2}{12\mu B} \tag{21}$$

$$V(X,\eta,Z) = 0 \tag{22}$$

$$W(X,\eta,Z) = \frac{w(X,\eta,Z)}{u_o(D_o/B)} = -6\left(\frac{B}{D_o}\right)^2\frac{\partial\bar{P}}{\partial Z}(Y-Y^2) \tag{23}$$

With $\xi=X$, $\eta=Y$ and $\xi=Z/\bar{D}$, the energy equation, Eq. (8), reduces to

$$6\frac{\partial\bar{P}}{\partial X}(\eta^2-\eta)\frac{\partial\theta}{\partial\xi} + \frac{6}{\bar{D}}\left[\left(\frac{B}{D_o}\right)^2\frac{\partial\bar{P}}{\partial Z} - \varsigma\frac{\partial\bar{D}}{\partial X}\frac{\partial\bar{P}}{\partial X}\right](\eta^2-\eta)\frac{\partial\theta}{\partial\xi} = \frac{1}{\mathrm{Pe}\,\varepsilon}\frac{\partial^2\theta}{\partial\eta^2} \tag{24}$$

For this category, Eq. (7) reduces to

$$\left(\frac{D_o}{B}\right)^2\frac{\partial^2\bar{P}}{\partial X^2} + \frac{\partial^2\bar{P}}{\partial Z^2} = 0 \tag{25}$$

2.2.1 Boundary Conditions. The thermal boundary conditions for this category are

$$\theta(\xi,0) = 0, \quad \left.\frac{\partial\theta}{\partial\eta}\right|_{\xi,\eta=0,\varsigma} = -1.0, \quad \left.\frac{\partial\theta}{\partial\eta}\right|_{\xi,\eta=1,\varsigma} = 0$$

$$\left.\frac{\partial\theta}{\partial\xi}\right|_{\xi,\eta,\varsigma=0} = 0, \quad \left.\frac{\partial\theta}{\partial\xi}\right|_{\xi,\eta,\varsigma=0.5} = -\left(\frac{D_o}{B}\right)^2\bar{D}\frac{d\bar{D}}{dX}\left.\frac{\partial\theta}{\partial\xi}\right|_{\xi,\eta,\varsigma=0.5} \cong 0 \tag{26}$$

2.2.2 Approximate Model. The velocity normal to the stream line shown in Fig. 1(*b*) is equal to $u\sin(\varphi)-w\cos(\varphi)$, which is equal to zero where φ is the angle that the stream line makes with the axial direction (x-axis). Knowing that $\tan(\varphi)$ can be by $\tan(\varphi)\cong\varsigma\left(\frac{D_o}{B}\right)\frac{d\bar{D}}{dX}$. As such, the second term on the left-hand side of Eq. (24) represents the velocity normal to the stream line, which is equal to zero. Moreover, $\partial^2\bar{P}/\partial Z^2 \le 0.04\partial^2\bar{P}/\partial X^2 \cong 0$ when $D_o/B < 0.2$ (refer to Eq. (25)). As such, Eq. (24) can be approximated by the following:

$$6\frac{d\bar{P}_{\mathrm{avg}}}{dX}(\eta^2-\eta)\frac{\partial\theta}{\partial\xi} = \frac{1}{\mathrm{Pe}\,\varepsilon}\frac{\partial^2\theta}{\partial\eta^2} \tag{27}$$

As the coolant flow rate is constant through the thin film, the following condition has to be satisfied:

$$\frac{d}{dX}\left(\bar{D}\frac{d\bar{P}_{\mathrm{avg}}}{dX}\right) = 0 \tag{28}$$

3 Numerical Methodology

Equations (15), (16), (28), and (27) were descritized using three-point central differencing in the transverse direction (η di-

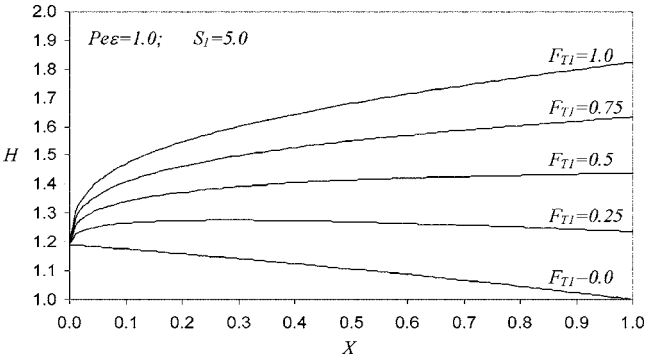

Fig. 2 Variation of the dimensionless thin film height H with the thermal expansion parameter F_{T1} (category I)

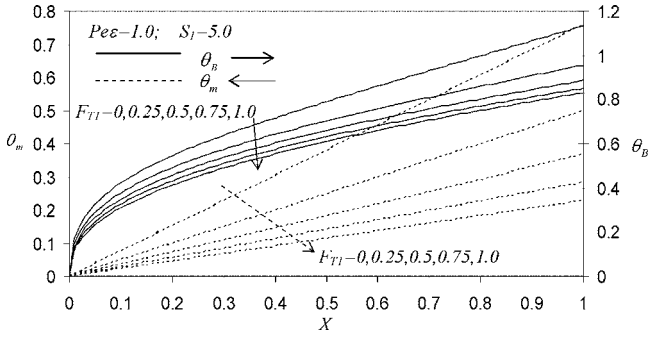

Fig. 3 Variation of the dimensionless mean bulk temperature θ_m and dimensionless lower plate temperature θ_B with the thermal expansion parameter F_{T1} (category I)

rection) while two-point differencing was utilized in the axial direction (X-direction). The finite difference equations for Eqs. (16), (15), (28), and (27) are the following, respectively:

$$\bar{P}_{i-1} - \left[1 + \left(\frac{H_{i+1/2}}{H_{i-1/2}}\right)^3\right]\bar{P}_i + \left(\frac{H_{i+1/2}}{H_{i-1/2}}\right)^3 \bar{P}_{i+1} = 0 \tag{29}$$

$$-6\left(\frac{\bar{P}_i - \bar{P}_{i-1}}{\Delta\xi}\right)H_i^4(\eta_j - \eta_j^2)\left(\frac{\theta_{i,j} - \theta_{i-1,j}}{\Delta\xi}\right) = \frac{1}{\mathrm{Pe}\,\varepsilon}\left(\frac{\theta_{i,j+1} - 2\theta_{i,j} + \theta_{i,j-1}}{\Delta\eta^2}\right) \tag{30}$$

$$(\bar{P}_{\mathrm{avg}})_{i-1} - \left[1 + \left(\frac{\bar{D}_{i+1/2}}{\bar{D}_{i-1/2}}\right)\right](\bar{P}_{\mathrm{avg}})_i + \left(\frac{\bar{D}_{i+1/2}}{\bar{D}_{i-1/2}}\right)(\bar{P}_{\mathrm{avg}})_{i+1} = 0 \tag{31}$$

$$-6\left(\frac{(\bar{P}_{\mathrm{AVG}})_i - (\bar{P}_{\mathrm{AVG}})_{i+1}}{\Delta\xi}\right)(\eta_j - \eta_j^2)\left(\frac{\theta_{i,j} - \theta_{i,j-1}}{\Delta\xi}\right) = \frac{1}{\mathrm{Pe}\,\varepsilon}\left(\frac{\theta_{i,j+1} - 2\theta_{i,j} + \theta_{i,j-1}}{\Delta\eta^2}\right) \tag{32}$$

where i and j are the location of the descretized point in the X and η directions, respectively. The resulting tridiagonal systems of algebraic equations, Eqs. (29)–(32), were then solved using the well-established Thomas algorithm [21]. The same procedure was repeated for the consecutive i values of $\bar{P}_i$ and $\theta_{i,j}$ until j reached the value M ($M=101$) at which $X=1.0$.

A thin film with $h_o=200$ μm and $B=3$ mm results in $\mathrm{Pe}\,\varepsilon=1.0$ when $u_o=0.075$ m/s (water as coolant) and it results in $\mathrm{Pe}\,\varepsilon=50$ when $u_o=0.04$ m/s (oil as coolant). It should be noted that a 100% increase in the heated plate temperature relative to the inlet fluid temperature, $(T_W-T_1)/T_1=1.0$, results in an expansion of the thin-film height: of the orders of $1.0<H(X=1.0)<2.0$. The value of $H(X=1.0)=2.0$ occurs when both lateral expansions and elastic forces in the flexible complex seal are negligible as well as when an ideal gas is contained in the closed cavities of these seals.

4 Discussion of Results

Figure 2 shows the variation of the dimensionless thin-film height H with dimensionless axial distance X and the thermal expansion parameter F_{T1} for category I. It is noted that the thin-film height increases as F_{T1} increases and that the maximum gradient of H occurs near the thin-film inlet. This increases normal stresses due to bending in this region. The increase in F_{T1} (when $\mathrm{Pe}\,\varepsilon=1.0$ and $S_1=5.0$) enhances cooling inside the thin film as shown in Fig. 3, where the mean bulk temperature θ_m at the exit is reduced by 70% by increasing F_{T1} from $F_{T1}=0.0$ to $F_{T1}=1.0$. The lower plate temperature θ_B at the exit is reduced by 25% when F_{T1} is changed from $F_{T1}=0.0$ to $F_{T1}=1.0$. The reduction in θ_B is apparent when $F_{T1}<1.0$ for the parameters shown in Fig. 3.

The expansion in the local thin-film height and the lower plate temperatures decrease as the Peclet number Pe or the aspect ratio ε increase as shown in Figs. 4 and 5, respectively. The decrease in H, θ_m, and $\mathrm{Pe}\,\varepsilon$ as $\mathrm{Pe}\,\varepsilon$ increases is apparent when $\mathrm{Pe}\,\varepsilon<10$. Figure 6 shows that the proposed cooling device can provide maximum enhancement in the cooling effect of 45% and above (compared to the performance ordinary flexible fluidic thin films) as the heating load increases when $\mathrm{Pe}\,\varepsilon$ is decreased below $\mathrm{Pe}\,\varepsilon=0.5$. This indicates that thermally expandable flexible fluidic thin films are recommended to be used in MEMS and electronic cooling applications. It is worth noting that increasing the thermal expansion parameter beyond certain values will decrease the coolant velocity near the heated plate, which can result in a reduction in the cooling enhancement (as can be seen from Fig. 6). This fact

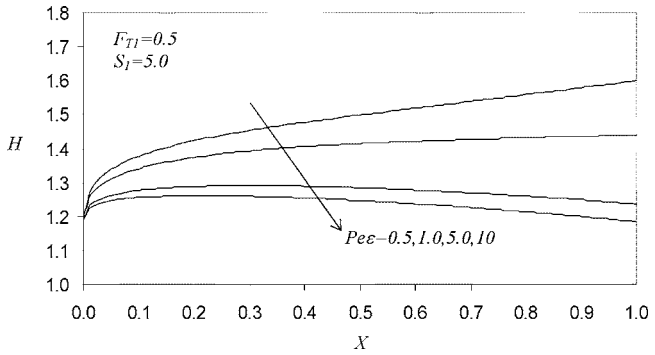

Fig. 4 Variation of the dimensionless thin film height H with $\mathrm{Pe}\,\varepsilon$ (category I)

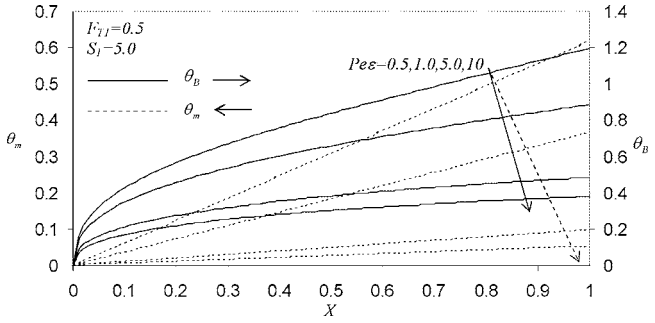

Fig. 5 Variation of the dimensionless mean bulk temperature θ_m and dimensionless lower plate temperature θ_B with $\mathrm{Pe}\,\varepsilon$ (category I)

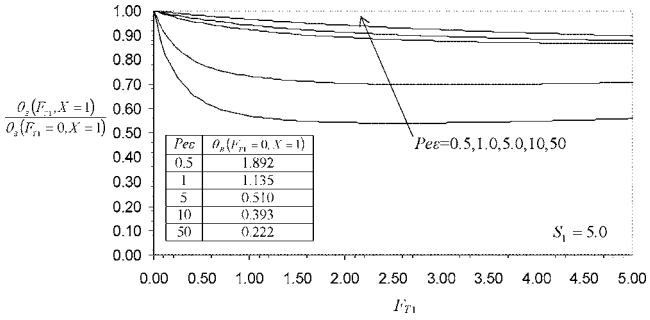

Pe ε	$\theta_B(F_{T1}=0, X=1)$
0.5	1.892
1	1.135
5	0.510
10	0.393
50	0.222

Fig. 6 Variation of the lower plate temperature at the exit $\theta_B(F_{T1}, X=1)$ relative to that when $F_{T1}=0$ with Pe ε and F_{T1} (category I)

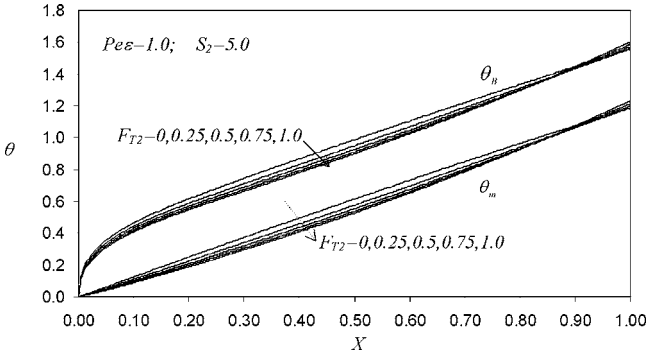

Fig. 9 Variation of the dimensionless mean bulk temperature θ_m and dimensionless lower plate temperature θ_W with the thermal expansion parameter F_{T2} (category II)

can also be seen from Fig. 7, where the average Nusselt number decreases to a minimum and then increases as F_{T1} increases. For full and stable utilization of thermally expandable flexible fluidic thin films, the thermal expansion parameter is recommended to be lower than the following critical value:

$$F_{T1} < (F_{T1})_{\text{crit}} = 0.642\ \text{Pe}\ \varepsilon + 2.363 \tag{33}$$

Figure 8 shows the variation of the dimensionless width D of the thin film with dimensionless axial distance X and the thermal expansion parameter F_{T2} for category II. It is noted that the thin-film width increases as F_{T2} increases and that the maximum gradient of D occurs near the thin-film inlet. This increases normal stresses due to bending in this region. However, the increase in F_{T2} produces no insignificant cooling inside the thin film, as shown in Fig. 9, when compared to that for category I (Fig. 3).

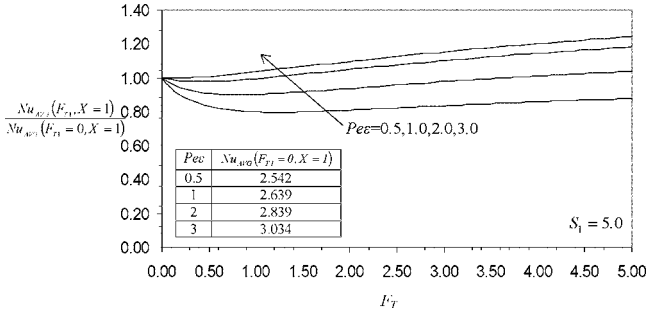

Pe ε	$Nu_{avg}(F_{T1}=0, X=1)$
0.5	2.542
1	2.639
2	2.839
3	3.034

Fig. 7 Variation of the average Nusselt number $Nu_{avg}(F_{T1}, X=1)$ relative to that when $F_{T1}=0$ with Pe ε and F_{T1} (category I)

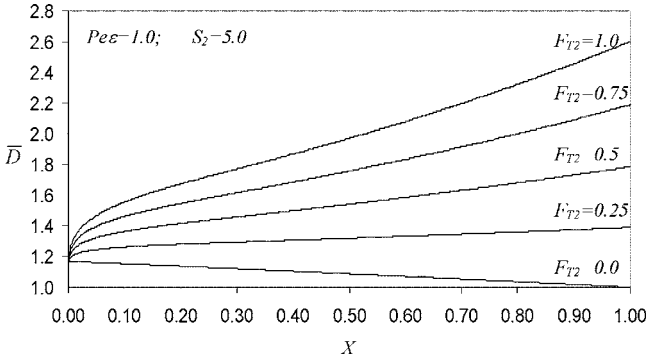

Fig. 8 Variation of the dimensionless thin film width $\bar{D}$ with the thermal expansion parameter F_{T2} (category II)

5 Pertinent Correlations

The following correlations are for $(\text{Nu})_{\text{avg}}$ and $(\theta_m)_{\text{avg}}$ for thin films supported by flexible complex seals with flexible upper plates (category I) for the specified range of parameters, $1.0 < S_1 < 10$, $1.0 < \text{Pe}\ \varepsilon < 50$, and $0 < F_{T1} < 1.0$:

$$\text{Nu}_{\text{avg}} = \frac{0.0455(\text{Pe}\ \varepsilon)^{0.6793} F_{T1}^{0.8345} + 1.5285(\text{Pe}\ \varepsilon)^{0.2877} S_1^{0.3225}}{(0.5169 S_1^{0.620} + 1.255 \times 10^{-3} F_{T1}^{1.8691})^{0.5503}};$$

$$R^2 = 0.996 \tag{34}$$

$$(\theta_m)_{\text{avg}} = \frac{1.3709(\text{Pe}\ \varepsilon)^{-0.7717} F_{T1}^{1.6939} + 1.1520(\text{Pe}\ \varepsilon)^{-0.9898} S_1^{-0.4380}}{(2.1144 S_1^{-0.3449} + 1.8401 F_{T1}^{1.3294})^{2.4686}};$$

$$R^2 = 0.992 \tag{35}$$

6 Conclusions

Heat transfer inside flexible fluidic thin films that are expandable due to pressure and heat was analyzed in this work. The upper plate of the thin film was assumed to be flexible and mobile for one of the investigated categories (category I), whereas the side plates were taken to be flexible and mobile for the second category (category II). The expansion in the thin-film heights and widths for categories I and II, respectively, was linearly related to the local fluid pressure and local lower plate (heated). The governing Reynolds, momentum, and energy equations were properly nondimensionalized and cast in proper forms. These equations were solved numerically using an implicit method.

The following parameters, stiffness parameter, Peclet number, thermal expansion parameter, aspect ratio, and the ratio of the width to the thin-film length were found to be the main controlling parameters. It was found that thin films characterized under the first category produce significant increase in cooling capacity as the heating load increases especially those operated with lower Peclet numbers. The expansion in thin films characterized under the second category was found be produce negligible effects on the cooling capacity as the heating load increases. Finally, thermally expandable flexible fluidic thin films are recommended to be utilized in small-sized thin films as for MEMS and electronic cooling applications.

Nomenclature

B = thin-film length (m)
D = half thin-film width (m)
D_o = reference half thin-film width (m)
c_p = specific heat of the fluid (J/kg K)
F_{T1} = thermal expansion parameter for flexible complex seal (category I)

F_{T2} = thermal expansion parameter for side biomaterial side supports
H = dimensionless thin-film height
H_1 = dimensionless inlet thin-film height
h = thin-film height (m)
h_o = reference thin-film height (m)
h_c = convective heat transfer coefficient ($W/m^2 K$)
k = thermal conductivity of the fluid ($W/m K$)
Nu = Nusselt number
P = pressure (Pa)
P_i = inlet pressure (Pa)
P_e = exit pressure (Pa)
Pe = Peclet number
P = fluid pressure (Pa)
q = heat flux at the lower plate (W/m^2)
$S_{1,2}$ = stiffness parameter for flexible complex seal or bimaterial plate
T, T_i = temperature in fluid and the inlet temperature (K)
U, u = dimensionless and dimensional axial velocities
u_o = reference axial velocity (m/s)
V, v = dimensionless and dimensional normal velocities
W, w = dimensionless and dimensional spanwise velocities
X, x = dimensionless and dimensional axial coordinates
Y, y = dimensionless and dimensional normal coordinates
Z, z = dimensionless and dimensional spanwise coordinates

Greek Symbols

ε = aspect ratio
μ = dynamic viscosity of the fluid
θ, θ_m = dimensionless temperature and dimensionless mean bulk temperature
θ_B = dimensionless temperature at the lower plate
ρ = density of the fluid (kg/m^3)
η = variable transformation for the dimensionless Y coordinate

References

[1] Moon, S. H., Yun, H. G., Hwang, G., and Choy, T. G., 2000, "Investigation of Packaged Miniature Heat Pipe for Notebook PC Cooling," Int. J. Microcircuits Electron. Packag., **23**, pp. 488–493.
[2] Sugumar, D., and Tio, K. K., 2006, "Thermal Analysis of Inclined Micro Heat Pipes," ASME J. Heat Transfer, **128**, pp. 198–202.
[3] Lefevre, F., and Lallemand, M., 2006, "Coupled Thermal and Hydrodynamic Models of Flat Micro Heat Pipes for the Cooling of Multiple Electronic Components," ASME J. Heat Transfer, **49**, pp. 1375–1383.
[4] Tuckerman, D. B., and Pease, D. B., 1981, "High-Performance Heat Sinking for VLSI," IEEE Electron Device Lett., **EDL-2**, pp. 126–129.
[5] Missaggia, L. J., Walpole, J. N., Liau, Z. L., and Philips, R. J., 1989, "Microchannel Heat Sinks for Two Dimensional High-Power-Density Diode Laser Arrays," IEEE J. Quantum Electron., **25**, 1988–1992.
[6] Kleiner, M. B., Kuhn, S. A., and Haberger, K., 1995, "High Performance Forced Air Cooling Scheme Employing Micro-Channel Heat Exchangers," IEEE Trans. Compon., Packag. Manuf. Technol., Part A, **18**, pp. 795–804.
[7] Samalam, V. K., 1989, "Convective Heat Transfer in Micro-Channels," J. Electron. Mater., **18**, pp. 611–617.
[8] Lee, D. Y., and Vafai, K., 1999, "Comparative Analysis of Jet Impingement and Microchannel Cooling for High Heat Flux Applications," Int. J. Heat Mass Transfer, **42**, pp. 1555–1568.
[9] Fedorov, A. G., and Viskanta, R., 2000, "Three-Dimensional Conjugate Heat Transfer in the Microchannel Heat Sink for Electronic Packaging," Int. J. Heat Mass Transfer, **43**, pp. 399–415.
[10] Vafai, K., and Zhu, L., 1999, "Analysis of a Two-Layered Micro Channel Heat Sink Concept in Electronic Cooling," Int. J. Heat Mass Transfer, **42**, pp. 2287–2297.
[11] Harms, T. M., Kazmierczak, M. J., and Gerner, F. M., 1999, "Developing Convective Heat Transfer in Deep Rectangular Microchannels," Int. J. Heat Fluid Flow, **20**, pp. 149–157.
[12] Bowers, M. B., and Mudawar, I., 1994, "Two-Phase Electronic Cooling Using Mini-Channel and Micro-Channel Heat Sink," ASME J. Electron. Packag., **116**, pp. 290–305.
[13] Hadim, A., 1994, "Forced Convection in a Porous Channel With Localized Heat Sources," ASME J. Heat Transfer, **116**, pp. 465–472.
[14] Huang, P. C., and Vafai, K., 1994, "Analysis of Forced Convection Enhancement in a Channel Using Porous Blocks," J. Thermophys. Heat Transfer, **8**, pp. 562–573.
[15] Huang, P. C., and Vafai, K., 1994, "Internal Heat Transfer Augmentation in a Parallel Plate Channel Using an Alternate Set of Porous Cavity-Block Obstacles," Numer. Heat Transfer, Part A, **25**, pp. 519–540.
[16] Khaled, A.-R. A., and Vafai, K., 2002, "Flow and Heat Transfer Inside Thin Films Supported by Soft Seals in The Presence of Internal and External Pressure Pulsations," Int. J. Heat Mass Transfer, **45**, pp. 5107–5115.
[17] Khaled, A.-R. A., and Vafai, K., 2004, "Control of Exit Flow and Thermal Conditions Using Two-Layered Thin Films Supported by Flexible Complex Seals," Int. J. Heat Mass Transfer, **47**, pp. 1599–1611.
[18] Khaled, A.-R. A., and Vafai, K., 2005, "Analysis of Flexible Microchannel Heat Sinks," Int. J. Heat Mass Transfer, **48**, pp. 1739–1746.
[19] Khaled, A.-R. A., and Vafai, K., 2003, "Cooling Enhancements in Thin Films Supported by Flexible Complex Seals in The Presence of Ultrafine Suspensions," ASME J. Heat Transfer, **125**, pp. 916–925.
[20] Norton, R. L., 1998, *Machine Design An Integrated Approach*, 2nd ed., Prentice-Hall, Englewood Cliffs, NJ.
[21] Blottner, F. G., 1970, "Finite-Difference Methods of Solution of the Boundary-Layer Equations," AIAA J., **8**, pp. 193–205.

Three-Dimensional Mixed Convection in Plane Symmetric-Sudden Expansion: Bifurcated Flow Regime

M. Thiruvengadam

B. F. Armaly

J. A. Drallmeier

Department of Mechanical and Aerospace Engineering,
University of Missouri—Rolla,
Rolla, MO 65401

Simulations of three-dimensional laminar mixed convection in a vertical duct with plane symmetric sudden expansion are presented to illustrate the effects of the buoyancy-assisting force and the duct's aspect ratio on flow bifurcation and heat transfer. The stable laminar bifurcated flow regime that develops in this geometry at low buoyancy levels leads to nonsymmetric temperature and heat transfer distributions in the transverse direction, but symmetric distributions with respect to the center width of the duct in the spanwise direction. As the buoyancy force increases, due to increases in wall heat flux, flow bifurcation diminishes and both the flow and the thermal fields become symmetric at a critical wall heat flux. The size of the primary recirculation flow region adjacent to the sudden expansion increases on one of the stepped walls and decreases on the other stepped wall as the wall heat flux increases. The maximum Nusselt number that develops on one of the stepped walls in the bifurcated flow regime is significantly larger than the one that develops on the other stepped wall. The critical wall heat flux increases as the duct's aspect ratio increases for fixed Reynolds number. The maximum Nusselt number that develops in the bifurcated flow regime increases as the duct's aspect ratio increases for fixed wall heat flux and Reynolds number. [DOI: 10.1115/1.2712850]

Introduction

Flow separation and reattachment due to sudden changes in geometry occur in many engineering applications where heating or cooling is required. These applications appear in electronic cooling equipment, cooling of turbine blades, combustion chambers, and many other heat exchanging devices. The flow and the heat transfer in most of these applications exhibit three-dimensional (3D) flow behavior, but most of the published heat transfer results deal only with the two-dimensional (2D) flow. Experimental [1–4] and numerical [3–6] studies have shown that laminar isothermal flow in plane symmetric sudden expansion exhibits symmetric steady laminar flow behavior for Reynolds number lower than the critical value, and asymmetric steady laminar bifurcated flow behavior for Reynolds number higher than the critical value. As the Reynolds number continues to increase, the stable laminar bifurcated flow regime transforms into unsteady bifurcated flow regime and moves toward turbulent transition at higher Reynolds number. Tsui and Shu [7] and Alimi et al. [8] reported results from simulating laminar mixed convection in a 2D plane symmetric sudden expansion. Three-dimensional simulations of laminar mixed convection adjacent to backward-facing step are presented by Li and Armaly [9], in which the governing equations are cited. Nie and Armaly [10] simulated three-dimensional forced convection in plane symmetric sudden expansion in symmetric flow regime. They reported the presence of swirling jetlike flow near the side wall in the separating shear layer and its influence on the Nusselt number distribution and friction coefficient on the stepped walls. Bifurcated forced convection results in 3D plane symmetric sudden expansion were published by Thiruvengadam et al. [11], and to the authors' knowledge none have been published on the effects of buoyancy force on bifurcated 3D flow and heat transfer in this geometry. This fact, along with the realization that such geometry appears regularly in many industrial heat transfer devices, motivated the present study.

Problem Statement and Solution Procedure

The problem that is treated in this study is an extension to the one reported by Thiruvengadam et al. [11] on bifurcated forced convection in similar geometry. Their study illustrated the development of several jetlike flows that develop at the corners of the sudden expansion near the side walls, which impinges on the stepped wall to form several recirculation flow regions. The jetlike flow impingement location is a critical point on the stepped walls from which streamlines originate and where the streamwise and the spanwise components of the wall shear stress (i.e., $\mu(\partial u/\partial y)$ and $\mu(\partial w/\partial y)$) are zero. The jetlike flow impingement on the stepped walls is responsible for the peak that develops in the Nusselt number distribution in that area near the side wall. They illustrated the development of several focal and saddle points in the flow region downstream from the sudden expansion. They presented the effects of the Reynolds number on the x_u-line (where $\partial u/\partial y_{\text{at wall}}=0$) distributions and pointed out that the region that is bounded by the x_u line represents approximately the size of the primary recirculation flow region that develops adjacent to the two stepped walls downstream from the sudden expansion. In the present study, the effects of buoyancy assisting force and the duct's aspect ratio on the flow and heat transfer are examined, and a schematic of the computational domain is presented in Fig. 1. The duct's heights (H) and (h) downstream and upstream of the sudden expansion, respectively, are fixed at 0.04 m and 0.02 m, resulting in an expansion ratio (ER=H/h) of 2. The step height S is fixed at 0.01 m and different duct widths W are considered to examine the effects of duct's aspect ratio (upstream aspect ratio (AR=W/h)) on the results. The origin of the coordinate system is located at the bottom corner of the sudden expansion as shown in Fig. 1. The directions of the streamwise (x), transverse (y), and spanwise (z) coordinates are also shown in Fig.

Contributed by the Heat Transfer Division of ASME for publication in the JOURNAL OF HEAT TRANSFER. Manuscript received January 27, 2006; final manuscript received July 25, 2006. Review conducted by Louis C. Burmeister.

 Copyright © 2007 by ASME

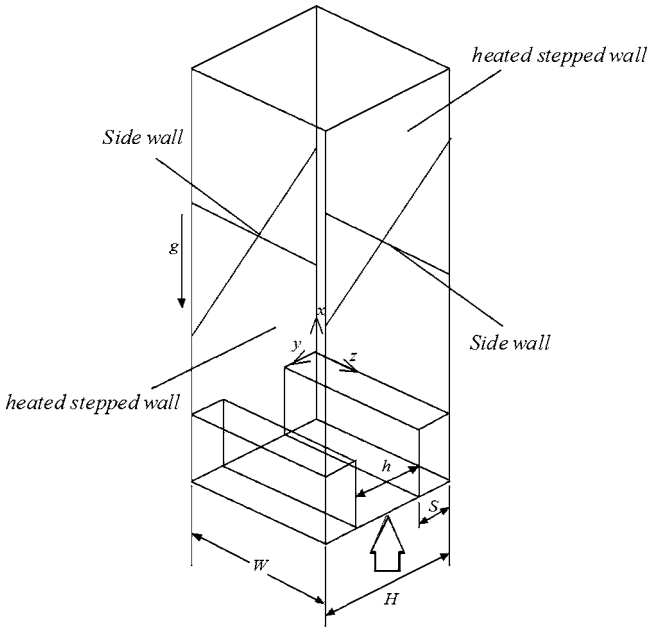

Fig. 1 Schematic of the computational domain

1. The length of the computational domain is 1 m downstream and 0.02 m upstream of the sudden expansion, respectively, i.e., $-2 \le x/S \le 100$. This choice is made to insure that the flow at the inlet section of the duct ($x/S=-2$) is not affected by the sudden expansion in geometry, and the flow at the exit section of the duct ($x/S=100$) can be treated as fully developed. The use of a longer computational domain did not change the flow or the thermal behavior in the important region downstream from the sudden expansion ($x/S<50$). The governing equations for laminar, incompressible, three-dimensional, buoyancy-assisting mixed convection (with gravity g in the streamwise direction) with constant properties under both steady and unsteady conditions are formulated for continuity, momentum, and energy conservation. Thermal buoyancy effects are modeled using the Boussinesq approximation. The full elliptic 3D coupled governing equations are solved numerically using a finite volume method to simulate the flow and the temperature fields in this computation domain. The results from the solution of the steady form of the governing equations compared very well to the results from the solution of the unsteady form of the governing equations. Details of the formulation and solution can be found in Li and Armaly [9] as applied to the backward-facing step geometry and will not be restated here due to space limitations.

The physical properties are treated as constants and evaluated for air at the inlet temperature of $T_0=20°C$ (i.e., density (ρ) is 1.205 kg/m^3, specific heat (C_p) is 1005 J/Kg °C, dynamic viscosity (μ) is 1.81×10^{-5} kg/m s, thermal conductivity (k) is 0.0259 W/m °C, and volumetric coefficient of thermal expansion (β) is 0.00341 1/K). Inlet flow (at $x/S=-2$, $1 \le y/S \le 3$, for all z) is considered to be isothermal ($T_0=20°C$), hydrodynamically steady and fully developed with a distribution for the streamwise velocity component (u) equal to the one described by Shah and London [12]. The other velocity components (transverse (v) and spanwise (w)) are set to be equal to zero at that inlet section. The no-slip boundary condition (zero velocities) is applied to all of the wall surfaces. Uniform wall heat flux ($q_w = -k\,\partial T/\partial y|_{y=0 \text{ and } y=0.04}$) is specified, and it is the same for the two stepped walls (at $y/S=0$ and 4, $0 \le x/S \le 100$, for all z), while the other walls are treated as adiabatic surfaces. The magnitude of the uniform wall heat flux is varied while keeping the Reynolds number ($\mathrm{Re}=2\rho u_0 h/\mu$, where u_0 is the average inlet velocity) fixed at 800 to investigate the effects of the buoyancy assisting force on the flow and heat transfer. Similarly, the magnitude of the wall heat flux is fixed at 3 W/m^2, and the Reynolds number is fixed at 800 while the aspect ratio is varied to investigate its effect on the flow and heat transfer. Because of the symmetry in the spanwise direction in this geometry, the width of the computation domain is chosen as half of the actual width of the duct, $L=W/2$, and symmetry boundary conditions are applied at the center plane of the duct, i.e., at $z=L$, $w=0$, and the gradient of all the other quantities with respect to z are set equal to zero. Fully developed flow and thermal conditions are imposed at the exit section (at $x/S=100$, for all y and z) of the calculation domain.

Numerical solution of the governing equations and boundary conditions are performed by utilizing the commercial computational fluid dynamics (CFD) code FLUENT 6.2. The mesh is generated using FLUENT's preprocessor GAMBIT. Hexahedron volume elements are used in the simulation. At the end of each iteration, the residuals for each of the conserved variables is computed and stored, thus recording the convergence history. The convergence criterion required that the scaled residuals be smaller than 10^{-10} for the mass and the momentum equations and smaller than 10^{-11} for the energy equation. Calculations are performed on DELL workstation, and the CPU time for converged solution for Re =800 is ~24 h. Significantly longer time is needed for cases where the wall heat flux is very close to the critical value and where the stable bifurcated flow regime changes to a stable symmetric flow regime. The SIMPLEC algorithm is used for the pressure velocity coupling, and the momentum and energy equations are discretized with the second-order upwind scheme in order to improve the accuracy of the simulations. Detailed description of the CFD code and the solution procedure may be found in the FLUENT manual.

The computational grid distribution is selected to ensure high density near the bounding walls and in the regions of the sudden expansion where high gradients exist, in order to ensure the accuracy of the simulation. Grid independence tests were performed using different grid densities for Re=800 for all aspect ratios. The velocities in x, y, and z directions, and temperature at the location $x/S=5$, $y/S=0.5$, and $z/L=0.25$, and the reattachment length at $z/L=1$ and $y/S=0.01$ in the computational domain are presented in Table 1 for different grid densities for the aspect ratio AR=8.

Table 1 Velocities and temperatures at $x/S=5$, $y/S=0.5$, and $z/L=0.25$ for different computational grids (Re=800 and AR=8 for $q_w=3$ W/m^2)

Grid	$x\times y\times z$ Grid size (downstream)	u (m/s)	v (m/s)	w (m/s)	T (K)	x_u/S at $z/L=1$ and $y/S=0.01$
1	$100\times32\times20$	0.0376303	−0.00248227	0.0226579	293.226	9.62730
2	$150\times40\times30$	0.0328437	−0.00194104	0.0232115	293.219	9.50386
3	$180\times52\times40$	0.0334497	−0.00201063	0.0236612	293.219	9.50456
4	$220\times64\times50$	0.0319877	−0.00176851	0.0239029	293.219	9.51968
5	$240\times72\times60$	0.0320299	−0.0018307	0.0241013	293.218	9.51878

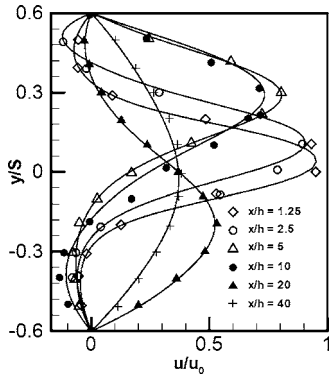

Fig. 2 Comparison to measured results of Fearn et al. [4] (solid lines represent simulated values)

Comparison of these results from grids 4 and 5 show a difference of $<1\%$. For that reason, grid 4 ($220\times64\times50$) is used downstream of the sudden expansion ($0\le x/S\le100$) and a grid of $20\times32\times50$ is used upstream of the sudden expansion ($-2\le x/S\le0$) for half of the duct's width ($0\le z/L\le1$). This grid size is used for duct's aspect ratio smaller or equal to 8 ($AR\le8$). Similarly, grid independent studies for AR=16 show that a grid of $220\times64\times60$ provides grid-independent results for that aspect ratio, and this grid size is used downstream of sudden expansion for $8<AR\le16$. The very favorable comparison that is shown in Fig. 2 between measured results by Fearn et al. [4] and the simulated results validate the simulation code. Additional results on code validation could be found in Thiruvengadam et al. [11].

Results and Discussion

Effects of Buoyancy. The results presented in this study focus on the laminar steady bifurcated flow regime that develops in this geometry. Because of space limitations and the fact that the results exhibit similar behavior for different Reynolds numbers, all of the presented results are for Re=800. The uniform wall heat flux on the two stepped walls is varied to examine the influence of the buoyancy-assisting force, and the duct's aspect ratio is varied to examine its effect on the results. The effects of the buoyancy-assisting force is examined by fixing the Reynolds number at 800 and the duct's aspect ratio at 4 (AR=4) while varying the wall heat flux (q_w) from 0–5 W/m^2, thus covering the bifurcated and the nonbifurcated flow regimes for this aspect ratio and Reynolds number. The general flow features in the bifurcated mixed convection flow regime are similar to the ones presented by Thiruvengadam et al. [11] for bifurcated forced convection flow regime. The general flow features are presented in Fig. 3(a) for $q_w=1$ W/m^2 and in Fig. 3(b) for $q_w=5$ W/m^2. For this aspect ratio and Reynolds number, the bifurcated flow regime exists only for $q_w<3.52$ W/m^2. When the wall heat flux exceeds that critical value, the flow bifurcation disappears and a symmetric nonbifurcated flow develops as illustrated in Fig. 3(b). Increasing the buoyancy force by increasing the wall heat flux increases the streamwise velocity component adjacent to the two stepped walls and that reduces the length of the primary recirculation flow region. Changes in the length of the recirculation flow region influence the pressure distribution in that streamwise location. The resulting change in the pressure distribution causes the length of the recirculation region to decrease on one stepped wall and increase on the other stepped wall with increasing buoyancy force until symmetric flow is reached. The buoyancy-assisting force in the neighborhood of the bifurcation flow region (at $x/S=6$) at the critical wall heat flux as defined by Gr_x/Re^2 (where Gr_x is the local Grashof number$=\rho^2 g\beta q_w x^4/\mu^2 k$) is equal to 0.41.

The effects of the wall heat flux on the distributions of the x_u lines (where $\partial u/\partial y_{\text{at wall}}=0$) are presented in Fig. 4. The region that is bounded by this line represents approximately the size of the primary recirculation flow region that develops adjacent to the two stepped walls downstream from the sudden expansion. The size of that region at the duct's center decreases on one of the stepped walls and increases on the other stepped wall as the wall heat flux increases until the bifurcated flow regime is transformed into a symmetric flow regime when $q_w\ge3.52$ W/m^2. Near the side wall, however, the size of that region decreases on both of the stepped walls as the wall heat flux increases. The jetlike flow that develops near the side wall impinges on the stepped walls, and its impingement locations are identified in Fig. 4. The jetlike flow impingement location is a critical point on the stepped walls from which streamlines originate and where the streamwise and the spanwise components of the wall shear stress (i.e., $\mu(\partial u/\partial y)$ and $\mu(\partial w/\partial y)$) are zero. The jetlike flow impingement on the stepped walls is responsible for the peak that develops in the Nusselt number distribution in that area near the side wall. Two jetlike flow

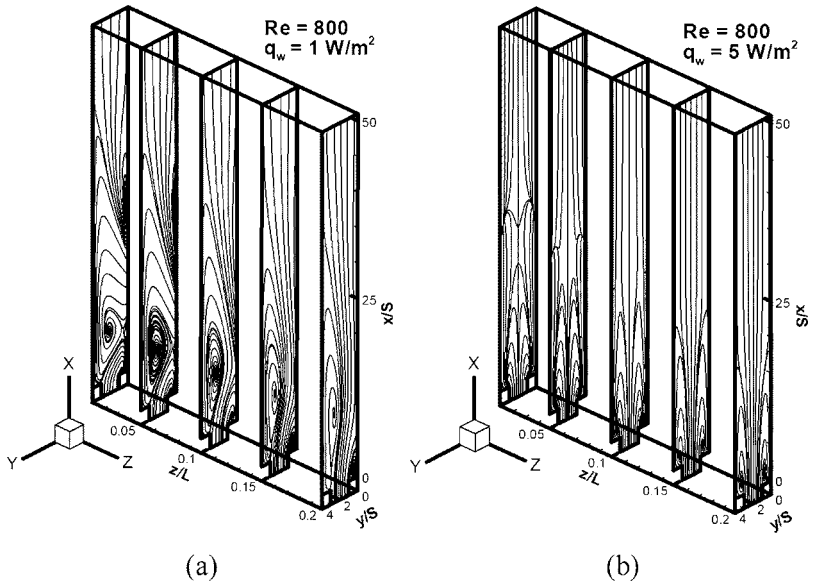

Fig. 3 Streamlines in the bifurcated and nonbifurcated flow regimes (AR=4)

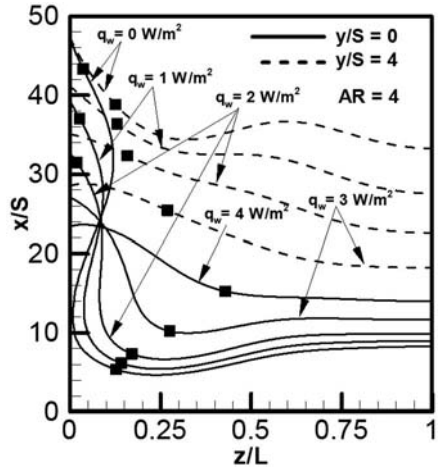

Fig. 4 Effects of wall heat flux on the x_u lines (■ locations of the jetlike flow impingement)

impingement locations develop on one of the stepped walls (at $y/S=0$) when $q_w \leq 2$ W/m^2, but only one impingement location develops when $q_w > 2$ W/m^2 as shown in Fig. 4. The first jetlike flow impingement location is close to the sudden expansion and the second location develops farther downstream. The first jetlike flow impingement location on the two stepped walls moves away from the side wall, while the second impingement location that develops on one of the stepped walls at $y/S=0$ moves toward the side wall when the wall heat flux increases.

The effects of the wall heat flux on the streamwise distributions of the Nusselt number ($\mathrm{Nu}=q_w S/k(T_w-T_0)$, where T_w is the local wall temperature) on the two stepped walls are presented at the center of the duct (at $z/L=1$) and near the side wall (at $z/L=0.1$) in Fig. 5. The Nusselt number increases rapidly after the sudden expansion, reaches a peak value and then decreases asymptotically to its fully developed value as x/S continues to increase. The peak in that distribution is higher near the side wall and on the stepped wall with the smaller primary recirculation flow region (i.e., at $y/S=0$). On this stepped wall, the peak in the Nusselt

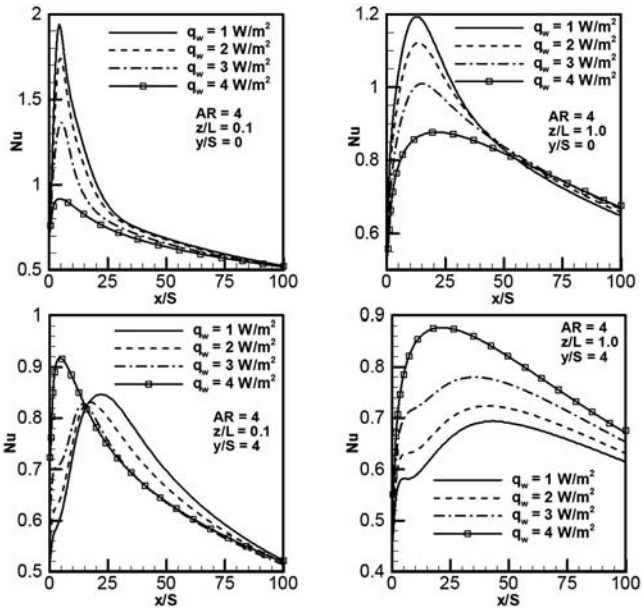

Fig. 5 Effects of wall heat flux on the streamwise distributions of the Nusselt number

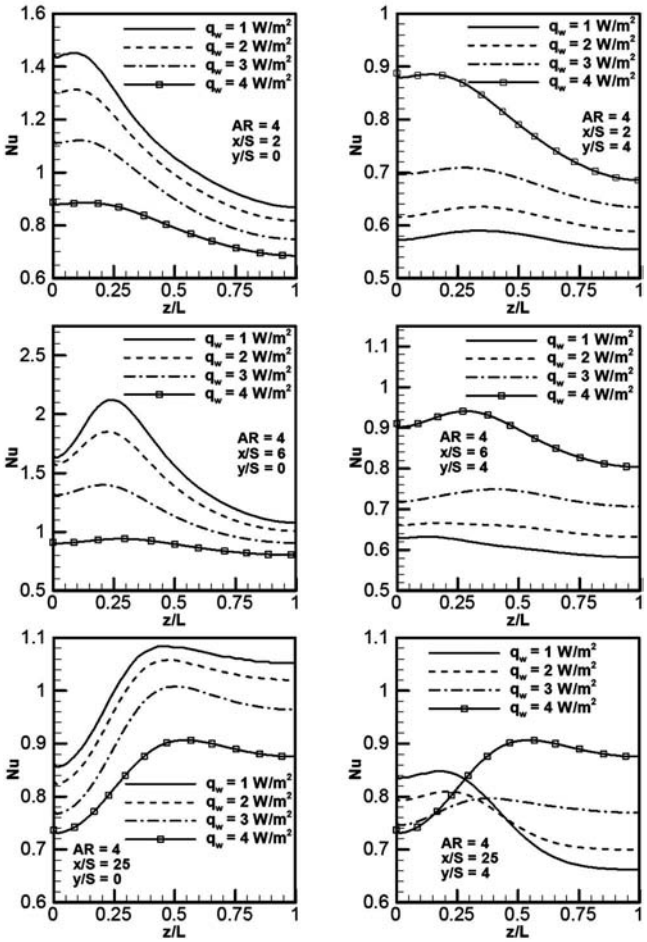

Fig. 6 Effects of wall heat flux on the spanwise distributions of the Nusselt number

number distribution increases as the wall heat flux decreases in the bifurcated flow regime, and it is higher than the one that develops in the symmetric nonbifurcated flow regime (i.e., at $q_w = 4$ W/m^2). The peak in the Nusselt number is due to the jetlike flow impingement in that region (higher transverse velocity impinges on the stepped wall in that region) causing the wall temperature to decrease. This decrease in wall temperature causes the Nusselt number to increase locally in that region (the Nusselt number is inversely proportional to the wall temperature). The transverse velocity component that impinges on the stepped wall with smaller recirculation flow region ($y/S=0$) is one magnitude higher than the one that impinges on the other stepped wall ($y/S=4$) with the larger recirculation flow region, and that is why a lower Nusselt number develops on that stepped wall ($y/S=4$) in the bifurcated flow regime. Smaller recirculation flow region produces higher jet impingement velocity and that results in a higher Nusselt number. The Nusselt number that develops on that stepped wall ($y/S=0$) in the bifurcated flow regime is higher than the one that develops in the symmetric nonbifurcated flow regime. The differences in the Nusselt number for the two stepped walls disappear when bifurcation ceases to exist and symmetric flow develops for higher wall heat flux. In the symmetric nonbifurcated mixed convection flow regime, the maximum Nusselt number increases as the wall heat flux increases.

The effects of the wall heat flux on the spanwise distributions of the local Nusselt number on the two stepped walls are presented at three streamwise locations of $x/S=2$, 6, and 25 in Fig. 6. These streamwise locations are selected to represent one location inside

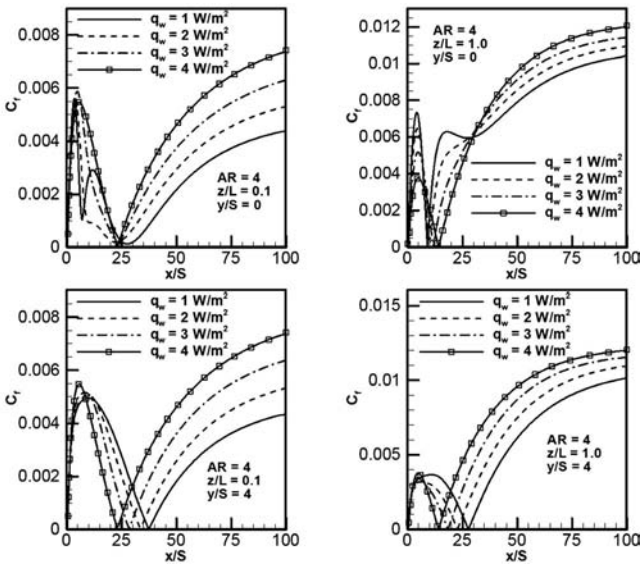

Fig. 7 Effects of wall heat flux on the streamwise distributions of the friction coefficient

the primary recirculation flow region, a second location in the region of flow reattachment on one of the stepped walls ($y/S=0$), and a third location in the region of flow reattachment on the other stepped wall (at $y/S=4$). Inside the recirculation flow region and upstream of the jetlike flow impingement region, i.e., at $x/S=2$, a maximum in the spanwise Nusselt number distribution develops near the side wall and decreases gradually to its value at the center of the duct. On the other hand, a peak in the spanwise Nusselt number distribution develops near the side wall in the jetlike flow impingement region, i.e., at $x/S=6$ for $y/S=0$ and $x/S=25$ for $y/S=4$, and that peak moves toward the center of the duct as the streamwise location increases beyond the jetlike flow impingement region, i.e., at $x/S=25$ for $y/S=0$. The influence of the buoyancy force, or wall heat flux, on the magnitude of the Nusselt number is the same as discussed previously for Fig. 5, which is decreasing as the wall heat flux increasing for the wall at $y/S=0$ and the reverse is true for the wall at $y/S=4$.

The effects of the wall heat flux on the streamwise distributions of the friction coefficient ($C_f=2\tau_w/\rho u_0^2$, where τ_w is the local wall shear stress $=\mu\sqrt{(\partial u/\partial y)^2+(\partial w/\partial y)^2}$) on the two stepped walls are presented at the center of the duct (at $z/L=1$) and near the side wall (at $z/L=0.1$) in Fig. 7. The friction coefficient increases rapidly after the sudden expansion, and a local maximum develops inside the primary recirculation flow region. Its magnitude decreases rapidly after that peak as x/S continues to increase until it reaches its minimum value at the x_u-line (the approximate edge of the recirculation flow region). The gradient of the streamwise velocity component ($\partial u/\partial y|_{y=0 \text{ and } y=0.04}=0$) is zero on this line, causing the friction coefficient to reach its minimum value in that region. The distribution of the friction coefficient at a given location is dependent on its closeness to the x_u line. Its magnitude then increases rapidly as x/S continues to increase and develops a maximum at the center of the duct in the fully developed flow region. In that region (at large x/S), its magnitude increases as the wall heat flux increases, and the maximum that develops adjacent to the side wall is smaller than the maximum that develops at the center of the duct. The increase in friction coefficient in the fully developed region with increasing wall heat flux is due to the increased streamwise velocity and its gradient at higher buoyancy force. Inside the primary recirculation flow region at the center of the duct, the maximum friction coefficient decreases as the wall heat flux increases. This is expected because increased buoyancy force reduces the reversed streamwise velocity component in the recirculation region. The presence of the second recirculation flow region on the stepped wall ($y/S=0$) near the sidewall for lower values of wall heat flux significantly influences the distribution of the friction coefficient, as can be seen in Fig. 7, but does not influence the Nusselt number distribution. Velocity and temperature distributions in the bifurcated flow regime are generally similar to the ones presented by Thiruvengadam et al. [11], and they illustrate the bifurcated nature on the velocity and thermal fields. They are not presented here due to space limitations.

Effects of Duct's Aspect Ratio. Flow bifurcation that develops for a given Reynolds number in this geometry ceases to exist when the wall heat flux exceeds a critical value. The critical wall heat flux for each aspect ratio is determined by using the bifurcation diagram that was described by Drikakis [5]. A sample of a bifurcation diagram is shown in Fig. 8 for the case of AR=8. The difference in the reattachment length on the two stepped walls (Δx_u) is plotted against the wall heat flux. It can be seen that the critical wall heat flux for this aspect ratio is 5.61 W/m^2. Similar diagrams can be plotted for other aspect ratios and the results show that this critical wall heat flux increases with increasing aspect ratio reaching its maximum when AR=∞ (i.e., 2D flow) as tabulated in Table 2 for this geometry at Reynolds number of 800.

The effects of the aspect ratio are examined by fixing the Rey-

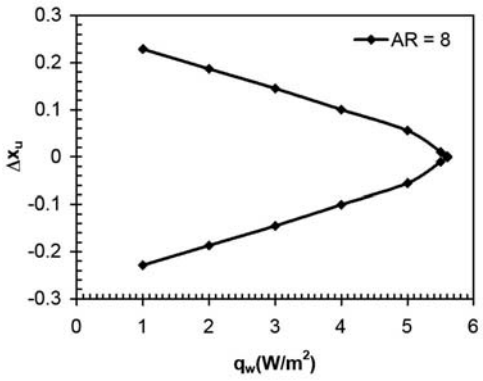

Fig. 8 Bifurcation diagram for AR=8

Table 2 Critical wall heat flux (Re=800)

Duct's aspect ratio	4	6	8	12	16	2-D
Critical wall heat flux (W/m^2)	3.52	4.83	5.61	6.14	6.18	6.21

nolds number at 800 and the wall heat flux at 3 W/m^2 while varying only its magnitude between 4 and ∞. Its effects on the x_u lines are presented in Fig. 9, in which the jetlike flow impingement locations on the two stepped walls are also identified. The level of bifurcation increases as the aspect ratio increases for a fixed wall heat flux. It should be noted that the level of bifurcation is relatively smaller for the case of AR=4 at the selected wall heat flux of $q_w=3$ W/m^2 because this heat flux is relatively close to the critical wall heat flux for this aspect ratio, which is 3.52 W/m^2. The primary jetlike flow impingement locations move toward the center of the duct as the aspect ratio decreases or with decreasing level of bifurcation. These jetlike flow impingements influence significantly the magnitude and the distribution of the Nusselt number. The secondary jetlike flow impingement locations that appear on one of the stepped walls (at $y/S=0$) downstream from the primary ones (for some of the aspect ratios) are relatively weak and do not have significant influence on the Nusselt number. They appear to move closer to the side wall as the aspect ratio decreases and disappear as the bifurcation level decreases.

The effects of the aspect ratio on the streamwise distributions of the local Nusselt number on the two stepped walls are presented at the center of the duct (at $z/L=1$) and near the side wall (at $z/L=0.1$) in Fig. 10. The general streamwise behavior is similar to the one presented in Fig. 5. The peak value of the Nusselt number that develops near the side wall increases with increasing aspect ratio. This is due to the increased level of bifurcation for higher aspect

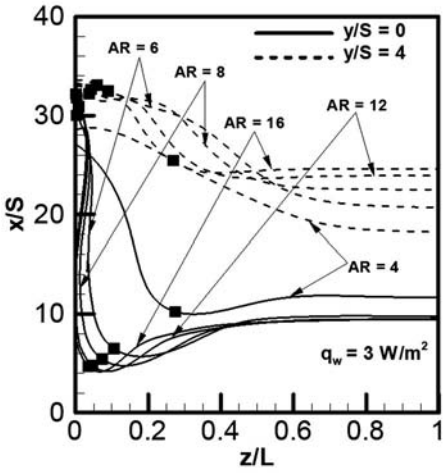

Fig. 9 Effects of duct's aspect ratio on x_u lines (■ locations of the jetlike flow impingement)

ratio. Significant three-dimensional effects (influence of the side walls) continue to exist for the largest duct's aspect ratio of 16, as can be seen when comparing its results to those for the two-dimensional flow. The Nusselt number increases as the duct's aspect ratio decreases at the center of the duct (at $z/L=1$), but a reverse trend develops in the region near the side wall (at $z/L=0.1$) in the fully developed flow region. The magnitude of the Nusselt number on one of the stepped walls (at $y/S=0$) is significantly greater than what develops on the other stepped wall (at $y/S=4$) for all duct's aspect ratios due to the higher jetlike flow impingement velocity when the recirculation flow region is

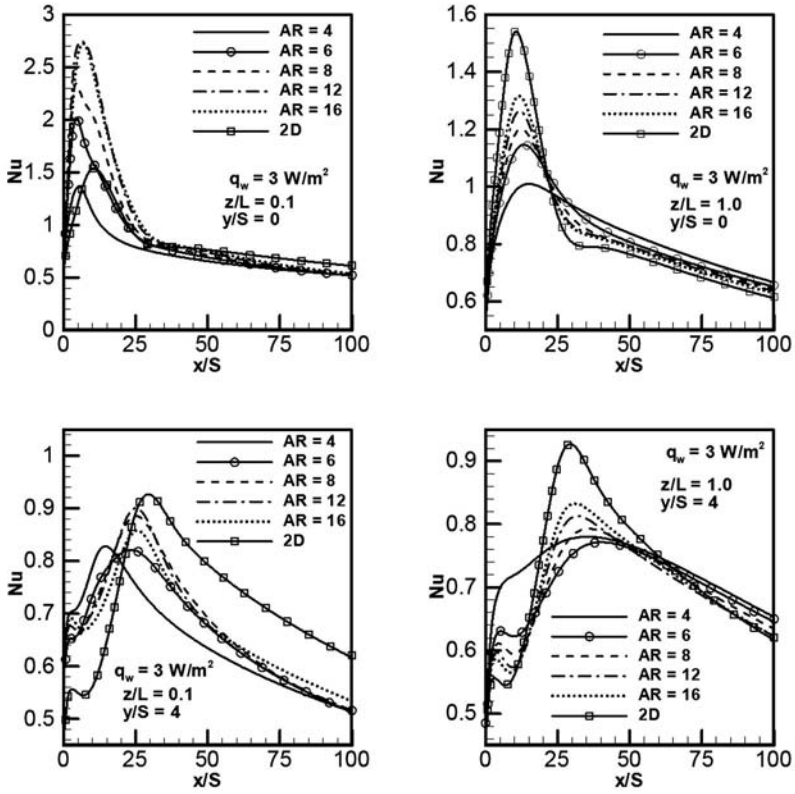

Fig. 10 Effects of duct's aspect ratio on the streamwise distributions of the Nusselt number

Table 3 Locations of Nu_{max} on $y/S=0$ for $q_w=3$ W/m^2

x/S	y/S	z/L	Nu_{max}	AR
6.17	0	0.205	1.4	4
6.38	0	0.185	2.16	6
5.77	0	0.149	2.47	8
6.03	0	0.117	2.76	12
6.47	0	0.092	2.82	16
10.42	0	–	1.54	2D

smaller (as discussed previously). The magnitudes of the maximum Nusselt number and the locations where it occurs are listed in Tables 3 and 4 for Reynolds number of 800 and wall heat flux of 3 W/m^2 for different duct's aspect ratios.

The effects of the duct's aspect ratio on the spanwise distributions of the local Nusselt number on the two stepped walls are presented at three streamwise locations of $x/S=2$, 6, and 25 in Fig. 11. These streamwise locations are selected at the same locations as in Fig. 6. The spanwise distributions of Nusselt number develop a peak near the side wall in the jetlike flow impingement region, i.e., $x/S=6$ for $y/S=0$ and $x/S=25$ for $y/S=4$, but that peak decreases as the aspect ratio decreases due to decreasing level of the bifurcation. At the center of the duct in these regions, the Nusselt number increases as the aspect ratio increases with noted exception for aspect ratios between 4 and 6 at $y/S=4$ and $x/S=25$. The level of bifurcations for this range of aspect ratios is low due to the proximity of the wall heat flux to the critical value, and that is the reason for such a deviation. Upstream of the jetlike flow impingement region (inside the primary recirculation flow region, i.e., $x/S=2$ for $y/S=0$ and $x/S=2$ and 6 for $y/S=4$) and at the center of the duct, the Nusselt number increases with aspect ratio on one of the stepped walls ($y/S=0$), but the reverse trend develops on the other stepped wall ($y/S=4$). The changing trends in the size of the recirculation flow regions with aspect ratio are responsible for that behavior. Downstream from the jetlike flow impingement region for $y/S=0$, i.e., $x/S=25$ at the center of the duct, the Nusselt number decreases with increasing aspect ratio.

The effects of the duct's aspect ratio on the streamwise distributions of the friction coefficient on the two stepped walls are presented at the center of the duct (at $z/L=1$) and near the side wall (at $z/L=0.1$) in Fig. 12. The streamwise behavior is similar to the one presented in Fig. 7. In the fully developed flow region its magnitude increases as the aspect ratio increases near the side wall (at $z/L=0.1$), but at the center of the duct (at $z/L=1$) that trend is reversed. The level of bifurcation and the location where the jetlike flow impinges on the stepped walls influence significantly the magnitude and the distributions of the friction coefficient.

Conclusions

The effects of buoyancy assisting force and duct's aspect ratio on flow bifurcation and on heat transfer for three-dimensional laminar mixed convection in a vertical plane symmetric sudden expansion is simulated, and results are presented for a duct with expansion ratio of two at a Reynolds number of 800. Flow bifurcation that develops for a given Reynolds number in this geometry decreases as the wall heat flux (buoyancy force) increases, and bifurcation ceases to exist when the wall heat flux exceeds a critical value. This critical wall heat flux increases with increasing duct's aspect ratio, reaching its maximum value of 6.21 W/m^2 for the two-dimensional flow (AR$=\infty$) in the geometry that is considered in this study. In the bifurcated flow regime, the flow and the thermal fields are not symmetric in the transverse direction but are symmetric relative to the center of the duct in the spanwise direction. The maximum Nusselt number, that increases as the duct's aspect ratio increases, decreases as the wall heat flux increases. For a given aspect ratio at the center of the duct, the Nusselt number increases on one of the stepped walls (the wall with larger primary recirculation flow region) and decreases on the other stepped wall as the wall heat flux increases. For a given wall heat flux at the center of the duct and inside the recirculation flow region, the Nusselt number decreases on one of the stepped walls (the wall with larger primary recirculation flow region) and increases on the other stepped wall as the aspect ratio increases. The presented results illustrate the effects of buoyancy assisting force and duct's aspect ratio on the distributions of the Nusselt number and the friction coefficient on the two stepped walls in the bifurcated flow regime.

Table 4 Locations of Nu_{max} on $y/S=4$ for $q_w=3$ W/m^2

x/S	y/S	z/L	Nu_{max}	AR
15.16	4	0.186	0.830	4
23.56	4	0.116	0.822	6
25.27	4	0.085	0.888	8
24.12	4	0.0613	0.938	12
24.69	4	0.0512	0.973	16
29.02	4	–	0.927	2D

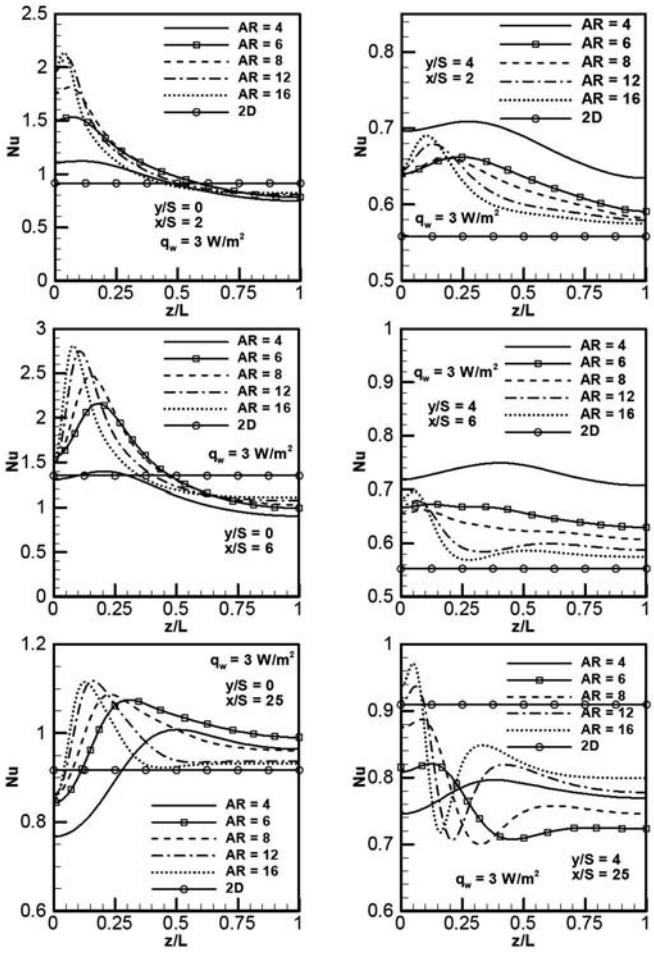

Fig. 11 Effects of duct's aspect ratio on the spanwise distributions of the Nusselt number

Acknowledgment

This work was supported in part by a DOE Basic Energy Sciences Grant No. DE-FG02-03ER46067, and by NSF Grant No. CTS-0352135.

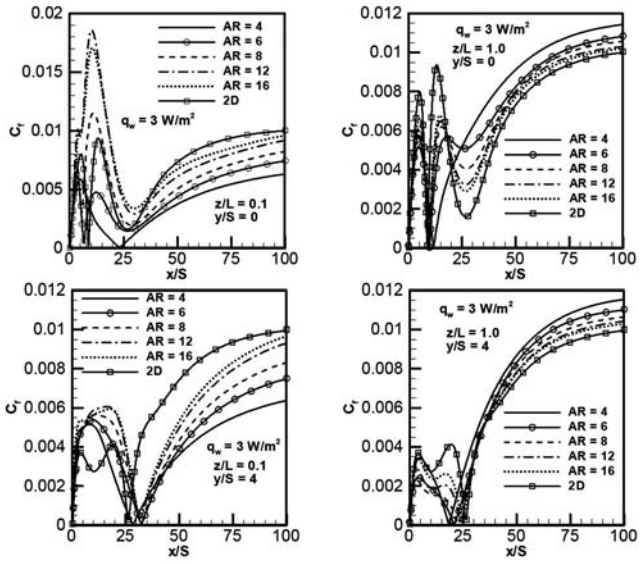

Fig. 12 Effects of duct's aspect ratio on the streamwise distributions of the friction coefficient

Nomenclature

- AR = upstream aspect ratio $=W/h$
- C_f = skin friction coefficient $=2\tau_w/\rho u_0^2$
- C_p = specific heat
- ER = expansion ratio $=H/h$
- H = duct height downstream from the step
- h = duct height upstream from the step
- k = thermal conductivity
- L = half width of the duct
- Nu = Nusselt number $=q_w S/k(T_w-T_0)$
- q_w = wall heat flux $=-k\,\partial T/\partial y|_{y=0 \text{ and } y=0.04}$
- Gr_x = local Grashof number $=\rho^2 g\beta q_w x^4/\mu^2 k$
- Re = Reynolds number $=2\rho u_0 h/\mu$
- S = step height
- T_w = local wall temperature
- T_0 = inlet fluid temperature
- u = velocity component in the x-coordinate direction
- u_0 = average inlet velocity
- v = velocity component in the y-coordinate direction
- W = width of the duct
- w = velocity component in the z-coordinate direction
- x = streamwise coordinate
- y = transverse coordinate
- z = spanwise coordinate
- x_u = locations where the streamwise velocity gradient is zero ($\partial u/\partial y_{\text{at wall}}=0$)
- Δx_u = difference in the reattachment length for the two stepped walls

Greek Letters

- β = volumetric coefficient of thermal expansion
- μ = dynamic viscosity
- ρ = density
- τ_w = wall shear stress $=\mu\sqrt{(\partial u/\partial y)^2+(\partial w/\partial y)^2}$ on the stepped walls

References

[1] Durst, F., Melling, A., and Whitelaw, J. H., 1974, "Low Reynolds Number Flow Over a Plane Symmetric Sudden Expansion," J. Fluid Mech., **64**, pp. 111–128.

[2] Cherdron, W., Durst, F., and Whitelaw, J. H., 1978, "Asymmetric Flows and Instabilities in Symmetric Ducts With Sudden Expansions," J. Fluid Mech., **84**, pp. 13–31.

[3] Durst, F., Pereira, J. C. F., and Tropea, C., 1993, "The Plane Symmetric Sudden-Expansion Flow at Low Reynolds Numbers," J. Fluid Mech., **248**, pp. 567–581.

[4] Fearn, R. M., Mullin, T., and Cliffe, K. A., 1990, "Nonlinear Flow Phenomena in a Symmetric Sudden Expansion," J. Fluid Mech., **211**, pp. 595–608.

[5] Drikakis, D., 1997, "Bifurcation Phenomena in Incompressible Sudden Expansion Flows," Phys. Fluids, **9**(1), pp. 76–87.

[6] Hawa, T., and Rusak, Z., 2001, "The Dynamics of a Laminar Flow in a Symmetric Channel With a Sudden Expansion," J. Fluid Mech., **436**, pp. 283–320.

[7] Tsui, Y. Y., and Shu, S. J., 1998, "Effects of Buoyancy and Orientation on the Flow in a Duct Preceded with a Double-Step Expansion," Int. J. Heat Mass Transfer, **41**, pp. 2687–2695.

[8] Alimi, S. E., Orfi, J., and Nasrallah, S. B., 2005, "Buoyancy Effects on Mixed Convection Heat and Mass Transfer in a Duct With Sudden Expansions," Heat Mass Transfer, **41**, pp. 559–567.

[9] Li, A., and Armaly, B. F., 2000, "Mixed Convection Adjacent to 3–D Backward-Facing Step," *Proc., of ASME-IMECE Conference*, ASME, New York, ASME HTD, 366–2, pp. 51–58.

[10] Nie, J. H., and Armaly, B. F., 2004, "Three-Dimensional Forced Convection in Plane Symmetric Sudden Expansion," ASME J. Heat Transfer, **126**, pp. 836–839.

[11] Thiruvengadam, M., Nie, J. H., and Armaly, B. F., 2005, "Bifurcated Three-Dimensional Forced Convection in Plane Symmetric Sudden Expansion," Int. J. Heat Mass Transfer, **48**, pp. 3128–3139.

[12] Shah, R. K., and London, A. L., 1978, *Laminar Forced Convection in Ducts*, Academic Press, New York, pp. 196–198.

Compounded Heat Transfer Enhancement in Enclosure Natural Convection by Changing the Cold Wall Shape and the Gas Composition

El Hassan Ridouane[1]
e-mail: eridouan@cems.uvm.edu

Antonio Campo

Department of Mechanical Engineering,
The University of Vermont,
201 Votey Bldg.,
33 Colchester Ave.,
Burlington, VT 05405

This article addresses compound heat transfer enhancement for gaseous natural convection in closed enclosures; that is, the simultaneous use of two passive techniques to obtain heat transfer enhancement, which is greater than that produced by only one technique itself. The compounded heat transfer enhancement comes from two sources: (1) reshaping the bounded space and (2) the adequacy of the gas. The sizing of enclosures is of great interest in the miniaturization of electronic packaging that is severely constrained by space and/or weight. The gases consist in a subset of binary gas mixtures formed with helium (He) as the primary gas. The secondary gases are nitrogen (N_2)*, oxygen* (O_2)*, carbon dioxide* (CO_2)*, methane* (CH_4)*, and xenon (Xe). The steady-state flow is governed by a system of 2-D coupled mass, momentum, and energy conservation equations, in conjunction with the ideal gas equation of state. The set of partial differential equations is solved using the finite volume method, for a square and a right-angled isosceles triangular enclosure, accounting for the second-order accurate QUICK and SIMPLE schemes. The grid layouts rendered reliable velocities and temperatures for air and the five gas mixtures at high* $Ra=10^6$*, producing errors within 1% were 18,500 and 47,300 elements for the square and triangle enclosures, respectively. In terms of heat transfer enhancement, helium is better than air for the square and the isosceles triangle. It was found that the maximum heat transfer conditions are obtained filling the isosceles triangular enclosure with a He–Xe gas mixture. This gives a good trade-off between maximizing the heat transfer rate while reducing the enclosure space in half; the maximum enhancement of triangle/square went up from 19% when filled with air into 46% when filled with He–Xe gas mixture at high* $Ra=10^6$*.* [DOI: 10.1115/1.2712857]

Keywords: square and triangular enclosures, finite volume method, gas mixture, optimal gas composition, compounded heat transfer enhancement

1 Introduction

From fluid physics, when a gas or a single-phase liquid is placed inside a stationary closed space, circulatory convective flow is sustained when a temperature difference is applied at two or more active walls. The state-of-the art chapters written by Yang [1], Raithby and Hollands [2], and Jaluria [3] disclosed an important subclass of enclosure problems in several branches of engineering, geophysics, environmental sciences, etc.

The literature is rich on natural convection in square and rectangular enclosures as evidenced by the articles cited in [1–3]. However, the literature is scarce in the area of natural convection in right-angled isosceles triangular enclosures and two articles by Elicer-Cortés et al. [4,5] have been identified on this topic. As expected, a prominent application of this kind of enclosure arises in the miniaturization of electronic packaging, subject to strict space and/or weight constraints (Simons et al. [6], Bar-Cohen et al. [7]).

In general the heat transfer enhancement by natural convection is a difficult task because of the low fluid velocities that can be imparted by the gravitational flow. Owing to this adverse effect, it is of fundamental and practical interest to explore passive methods that invigorate the natural convection flows in square enclosures to be installed in engineering devices. With the exception of the works by Misumi and Kitamura [8], Bhavnani and Bergles [9], and Hitt and Campo [10] that basically dealt with roughening and finning the wall surface, potential avenues for augmenting natural convection are limited. Another viable option for heat transfer enhancement that is gaining popularity lately regards the shape optimization of enclosures (Campo and Landon [11], Ridouane and Campo [12]). In these two papers, the idea is to reshape the wall(s) in order to streamline the buoyant gas flows.

Among the nine passive techniques described by Bergles [13] in his classification, one is called additive of gases. The examples of additive of gases that he cites include liquid droplets or solid particles, in either dilute phase or dense phase, which are introduced in convective gases.

Any two passive and/or active techniques may be employed simultaneously to obtain heat transfer enhancement that is greater than that produced by only one technique itself. This concurrent utilization is termed compound enhancement in Manglik [14]. This is precisely the topic of this article, in which the compounded heat transfer enhancement comes from two sources: (1) reshaping the bounded space and (2) addition of gases. With respect to the latter, the gases consist in a subset of gas mixtures formed with helium (He) as the primary gas. The secondary gases are nitrogen

[1]Corresponding author.

Contributed by the Heat Transfer Division of ASME for publication in the JOURNAL OF HEAT TRANSFER. Manuscript received May 2, 2006; final manuscript received July 12, 2006. Review conducted by Gautam Biswas.

 Copyright © 2007 by ASME

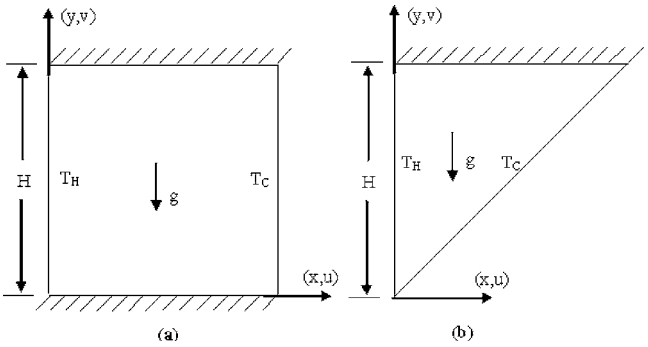

Fig. 1 Sketch of the square and triangular enclosures

(N_2), oxygen (O_2), carbon dioxide (CO_2), methane (CH_4), and xenon (Xe). From fluid physics, it is known that four thermo-physical properties influence convection heat transfer: density ρ, viscosity μ, thermal conductivity λ, and heat capacity at constant pressure C_p. For single gases, these thermo-physical properties depend on the operating temperature and pressure. In the case of gas mixtures, in addition to temperature and pressure, the thermo-physical properties are affected by the molar gas composition.

Numerical predictions of the velocity and temperature fields induced by buoyant air and buoyant gas mixtures in square and right-angled isosceles triangular enclosures (half of the square) under the influence of different Rayleigh numbers are carried out in this paper. A finite volume based computer code was employed to perform the numerical computations.

The body of the paper is divided into four sections. The first section describes the physical systems and the mathematical formulation. The computational procedure with the finite volume method and its validation are explained in the second section. The third section contains the estimation of the thermo-physical properties of the gas mixtures. The numerical velocity and temperature fields as well as the total heat transfer rates through the hot vertical wall common to both enclosures, are presented in the fourth section.

2 Mathematical Model

A schematic diagram of the geometry under study appears in Fig. 1. It consists of a square enclosure heated at the left vertical wall and cooled at the right vertical wall, while the connecting horizontal walls are insulated (Fig. 1(*a*)). When the basic enclosure is cut diagonally in half, it results in an isosceles triangular enclosure as shown in Fig. 1(*b*). In the latter figure, the isosceles triangular enclosure is heated from the left vertical wall, the inclined wall is cooled and the top wall is insulated. First, the heat transfer is quantified for the two enclosures filled with air. Second, the same two enclosures are filled with five gas mixtures. The temperature levels within the two enclosures are assumed to be small-to-moderate, as to consider the effects of surface radiation upon heat transfer negligible (Siegel and Howell [15]). In addition, Soret diffusion effects due to solutal buoyancy are not taken into account (Weaver and Viskanta [16]). For the sake of generality, the air and the gas mixtures are assumed to be compressible fluids. Accordingly, the mathematical formulation when written in Cartesian tensor notation ($j=1,2$) is synthesized by

$$\text{Mass:} \quad \frac{\partial(\rho u_j)}{\partial x_j} = 0 \tag{1}$$

$$\text{Momentum:} \quad \rho u_j \frac{\partial u_i}{\partial x_j} = \frac{\partial \sigma_{ij}}{\partial x_j} + X_i \tag{2}$$

where the fluid stress tensor σ_{ij} is

$$\sigma_{ji} = \mu\left(\frac{\partial u_i}{\partial x_j} + \frac{\partial u_j}{\partial x_i}\right) - \frac{2}{3}\mu\frac{\partial u_k}{\partial x_k}\delta_{ij} \tag{3}$$

and X_i stands for the body force, which equates to $X_1=0$ in the horizontal direction and $X_2=g(\rho-\rho_0)$ in the vertical direction.

$$\text{Energy:} \quad C_p u_j \frac{\partial T}{\partial x_j} = \lambda \frac{\partial^2 T}{\partial x_j^2} \tag{4}$$

$$\text{Ideal gas equation of state:} \quad p = \rho R T \tag{5}$$

The reference density ρ_0 in X_2 is evaluated at a reference temperature T_{ref}. Given the specified geometry and temperature differential T_H-T_C, along with the thermo-physical properties of the gas mixture, the Rayleigh number for the different gases is adjusted by tuning the gravitational constant g.

The velocity boundary conditions are based on the two standard assumptions: first, the walls are rigid and impermeable and second, the fluid does not slip at the solid walls; this translates into $u=v=0$. The temperature boundary conditions pertain to a hot temperature T_H applied at the left vertical wall and a cold temperature T_C at the right wall in the square or inclined wall in the triangle, whereas the horizontal wall(s) are thermally insulated.

3 Solution Method

A non-uniform mesh is laid out with elements packed close to the solid boundaries to resolve the near-wall viscous effects. Owing to the simplicity of the physical domains, the computational mesh has been constructed completely with quadrilateral elements. The velocity and temperature results were tested for grid independence using grid sizes varying from 10,000 to 30,000 elements for the square enclosure and from 30,000 to 60,000 elements for the isosceles triangular enclosure. For the two enclosures, the grid layouts that provided a good compromise between the computational efforts and the accuracy in the velocity and temperature fields for air and all the gas mixtures at high Ra $=10^6$ is within 1%. This results in modest mesh sizes of 18,500 and 47,300 elements for the square and triangle enclosures, respectively.

The steady-state flow is governed by a system of 2-D coupled mass, momentum, and energy conservation equations (1)–(4), in conjunction with the ideal gas equation of state. We assumed the air and the gas mixture behave as perfect gases. The governing equations are solved using the finite volume method of Patankar [17]. In all numerical cases performed, a constant temperature differential $(T_H-T_C)=26$ K has been imposed between the hot and cold walls. Given the small operating temperature differential between the active walls, all thermo-physical properties of the gas mixture (except density) are taken as constants and are evaluated at the reference temperature T_{ref}. An implicit segregated solver was used and all discretization schemes employed are second-order accuracy or higher. The QUICK scheme was implemented for discretizing the momentum, energy, and density equations. A second-order body-force-weighted scheme was utilized in the pressure discretization and the SIMPLE scheme was employed in the pressure-velocity coupling. Convergence of a simulation was assessed through the monitoring of computed residuals of the velocity, energy, and mass conservation equations and also through the convergence of point and/or surface monitors for velocity, temperature, and heat flux at selected locations in the domain.

Once the reliable solution have been obtained, the local heat transfer coefficient h_y was computed along the hot wall with

$$h_y(y,w) = -\lambda(w)\left[\frac{\partial T(0,y)}{\partial x}\right]\frac{1}{T_H - T_C} \tag{6}$$

Next, the mean convection coefficient $h(w)$ on the hot wall is defined as

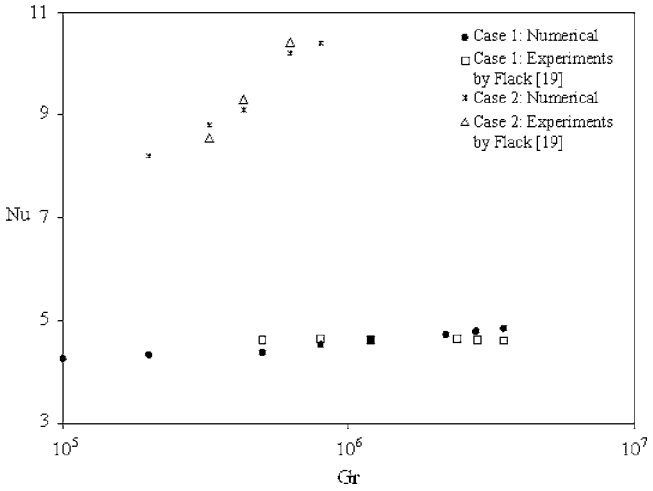

Fig. 2 Comparison between the numerical and experimental mean Nusselt numbers within an isosceles triangular cavity filled with air for Case 1 (hot upper walls and cold base) and Case 2 (cold upper walls and hot base)

$$h(w) = \frac{1}{H}\int_0^H h_y(y,w)dy \tag{7}$$

where the numerical integration of Eq. (7) is carried out with the 1/3 Simpson rule for improved accuracy.

Two validations of the numerical code have been done with air as the working fluid. First, a reference square enclosure with hot and cold vertical sidewalls and two insulated horizontal walls was chosen. At the local level, the magnitude of the dimensionless vertical velocity $V_{\max}=221.80$ at a relatively high value $\mathrm{Ra}=10^6$ is within 2% of the benchmark results of 217.36 by De Vahl Davis [18]. Also at the global level for $\mathrm{Ra}=10^6$, agreements to less than 1% of the mean Nusselt number based on $\mathrm{Nu}=8.75$ from this work versus 8.799 in [18]. Second, the experimental heat flow measurements in an isosceles triangle conducted by Flack [19] were singled out. We chose an isosceles triangle holding an intermediate apex angle of 45 deg between the horizontal base and the upper inclined walls as representative. Figure 2 illustrates the excellent parity between the experimental and the numerical Nusselt numbers Nu for both heating/cooling scenarios. For case 1 (hot upper walls and cold base), the invariance of Nu with the Grashof number Gr, staying around 4.63, indicates that the heat is transported by conduction. For case 2 (cold upper walls and hot base), Nu exhibited a generalized parabolic dependence with respect to Gr. The maximum deviation between the numerical and experimental Nusselt number is within a 3.5% band for both cases.

4 Accurate Evaluation of the Thermophysical Properties of a Gas Mixture

The inducement of natural convection in Newtonian fluids when caused by an external temperature differential depends upon four thermo-physical properties; namely, the viscosity μ, thermal conductivity λ, density ρ, and heat capacity at constant pressure C_p. The four thermo-physical properties μ, λ, ρ, and C_p of the participating single gases at atmospheric conditions, temperature of 25°C (~300 K) and pressure of 1 atm are taken from the NIST Reference Databases [20].

In the case of a given gas mixture at a fixed temperature T and pressure P, each thermo-physical property μ_m, λ_m, ρ_m, and $C_{p,m}$ varies with the molar gas composition w exclusively. The subscript "m" represents a gas mixture.

The molar gas composition w_q of a gas mixture is defined as the mass fraction of the molecular gas component q (Poling et al. [21])

$$w_q = x_q\left(\frac{M_q}{M_m}\right) \quad \text{for } q = 1,2 \tag{8}$$

Based on the kinetic theory of gases (Hirschfelder et al. [22]), the viscosity of a gas mixture μ_m is calculated from the matrix formula:

$$\mu_m = -\frac{\begin{vmatrix} H_{AA} & H_{AB} & x_A \\ H_{BA} & H_{BB} & x_B \\ x_A & x_B & 0 \end{vmatrix}}{\begin{vmatrix} H_{AA} & H_{AB} \\ H_{AB} & H_{BB} \end{vmatrix}} \tag{9}$$

First, the elements along the main diagonal H_{AA} and H_{BB} are

$$H_{AA} = \frac{x_A^2}{\mu_A} + \frac{2x_Ax_B}{\mu_{AB}}\frac{m_Am_B}{(m_A+m_B)^2}\left(\frac{5}{3A_{AB}^*} + \frac{m_B}{m_A}\right) \tag{10a}$$

Second, the elements of the main diagonal H_{AB} and H_{BA} are

$$H_{AB}(A \neq B) = -\frac{2x_Ax_B}{\mu_{AB}}\frac{m_Am_B}{(m_A+m_B)^2}\left(\frac{5}{3A_{AB}^*} - 1\right) \tag{10b}$$

The interaction viscosity μ_{AB} is given by

$$\mu_{AB} = \frac{5}{16}\left[\left(\frac{2m_Am_B}{m_A+m_B}\right)\frac{kT}{\pi}\right]^{1/2}\frac{1}{\sigma_{AB}^2\Omega_{AB}^{*(2,2)}(T_{AB}^*)} \tag{11}$$

in which the subscripts "A" and "B" identify the heavier and lighter gas components (Bzowski et al. [23]).

For the thermal conductivity of a gas mixture λ_m, Schreiber et al. [24] developed the matrix formula

$$\lambda_m = -\frac{\begin{vmatrix} L_{AA} & L_{AB} & x_A \\ L_{AB} & L_{BB} & x_B \\ x_A & x_B & 0 \end{vmatrix}}{\begin{vmatrix} L_{AA} & L_{AB} \\ L_{AB} & L_{BB} \end{vmatrix}} \tag{12}$$

The elements L_{AA}, L_{BB}, and L_{AB} of the upper and lower matrices are taken from the relations

$$L_{AA} = \frac{x_A^2}{\lambda_A} + \frac{25x_Ax_B}{8A_{AB}^*\lambda_{AB}}\left(\frac{R}{C_{pA}^0}\right)^2\left[\frac{25}{4}y_B^4 + \frac{15}{2}y_A^4 - 3y_B^4B_{AB}^* + 4y_A^2y_B^2A_{AB}^* + \left(\frac{C_{pA}^0}{R} - 2.5\right)\right] \tag{13a}$$

$$L_{BB} = \frac{x_B^2}{\lambda_B} + \frac{x_Ax_B}{2A_{AB}^*\lambda_{AB}}\left(\frac{25}{4}y_A^4 + \frac{15}{2}y_B^4 - 3y_A^4B_{AB}^* + 4y_A^2y_B^2A_{AB}^*\right) \tag{13b}$$

$$L_{AB} = -\frac{5x_Ax_By_A^2y_B^2}{4A_{AB}^*\lambda_{AB}}\left(\frac{R}{C_{pA}^0}\right)\left(\frac{55}{4} - 3B_{AB}^* - 4A_{AB}^*\right) \tag{13c}$$

where λ_A and λ_B are the thermal conductivity of gases A and B, respectively, and λ_{AB} is the interaction thermal conductivity. Moreover, in Eqs. (13*a*) and (13*c*), A^* and B^* are collision integral ratios, and x_q is the mole fraction of the species q. The symbol y_q represents the mass ratio of species q, which is obtained from

$$y_q^2 = \frac{M_q}{M_A + M_B} \tag{14}$$

where M_q is the molar mass of species q. Besides, the interaction thermal conductivity λ_{AB} is evaluated with the equation

$$\lambda_{AB} = \frac{15}{8} R \left(\frac{M_A + M_B}{M_A M_B} \right) \mu_{AB} \tag{15}$$

At low pressures, the molar density of a gas mixture ρ_m is usually determined through the truncated virial equation of state [21]

$$Z = \frac{P}{\rho_m RT} = 1 + B_2 \rho_m \tag{16}$$

where Z is the compressibility factor. Herein, the second virial coefficient B_2 in the right term of Eq. (16) is estimated from the correlation equation due to Dymond and Smith [25]

$$\frac{B_2 P_c}{RT_c} = B^{(0)} + \omega B^{(1)} \tag{17}$$

The values of $B^{(0)}$ and $B^{(1)}$ are obtained from the expressions

$$B^{(0)} = 0.1445 - \frac{0.33}{T_r} - \frac{0.1385}{T_r^2} - \frac{0.0121}{T_r^3} - \frac{0.000607}{T_r^8} \tag{18a}$$

$$B^{(1)} = 0.0637 + \frac{0.331}{T_r^2} - \frac{0.423}{T_r^3} - \frac{0.008}{T_r^8} \tag{18b}$$

so that T_c, P_c, and ω for the pure components are taken from [21].

The isobaric heat capacity of a gas mixture $C_{p,m}$ at low densities obeys the mixing rule [21]

$$C_{p,m} = \sum_q x_q C_{p,q}^0 \tag{19}$$

The isobaric molar heat capacity of species q identified by $C_{p,q}^0$ satisfies the equality

$$C_p^0 - C_v^0 = R \tag{20}$$

5 Discussion of Results

For the realistic design of gas-filled enclosures, three elements have to be weighted: (1) the enclosure shape, (2) the specification of the temperature differential $T_H - T_C$ at the two active walls, and (3) the adequacy of the working gas. To comply with the goals of the present study, we fixed item (2) while varying items (1) and (3).

The heat transfer enhancement will be analyzed in two parts: first by changing the shape of the enclosure while keeping the air as the working fluid (this will be referred as the "first enhancement,") and second, by modifying the thermofluidic properties of the working fluid (this will be named the "second enhancement.")

5.1 First Heat Transfer Enhancement. In this section, the square and the derived isosceles triangular enclosure sharing the hot wall contain air. Several values of the height-based Rayleigh number were selected starting with a low $\mathrm{Ra}=10^3$ and ending with a high $\mathrm{Ra}=10^6$. In order to point out the dual influence of Ra and the shape upon the heat transfer throughout the pair of enclosures, a sample of results is reported in terms of the mean Nusselt number.

The response of Nu to increments in Ra is described by two almost parallel Nu curves of exponential shape as illustrated in Fig. 3. It is observable that the separation ΔNu between the upper and lower Nu curves diminishes as Ra expands from a low 10^3 to a high 10^6. The lower Nu curve representative of the square enclosure (the baseline case) begins with a conduction-dominant value of $\mathrm{Nu}=1$ at $\mathrm{Ra}=10^3$. This Nu curve climbs up gradually until reaching a convection-dominant value of $\mathrm{Nu}=8.75$ at $\mathrm{Ra}=10^6$. Meanwhile, the upper Nu curve representative of the isosceles triangular enclosure begins with a conduction-dominant $\mathrm{Nu}=4.34$ for $\mathrm{Ra}=10^3$. The Nu curve climbs up at a lower rate until reaching a convection-dominant value of $\mathrm{Nu}=10.5$ for $\mathrm{Ra}=10^6$.

To assess the thermo-fluid performance of the square enclosure and the isosceles triangular enclosure concurrently, we need to take into consideration three geometric quantities: (1) the heated wall length, (2) the cooled wall length, and (3) the shape of the enclosure. These geometric quantities have to be grouped with the mean heat transfer coefficient at the common hot wall. For a fixed heated wall length H in the square and isosceles triangle (Figs. 1(*a*) and 1(*b*)), the cold wall length gets increased from H to $1.41H$, this is equivalent to a wall enlargement of 41%. It is self-evident that the cross-sectional area A_c of the derived isosceles triangle is 50% smaller than the cross-sectional area of the original square enclosure. Under a dominant conduction condition for a low $\mathrm{Ra}=10^3$, the heat transfer across the hot wall of the derived isosceles triangle is an enormous 334% higher than that of the original square. In contrast, for a dominant convection condition for a high $\mathrm{Ra}=10^6$ this margin diminishes to 19%, still a significant improvement.

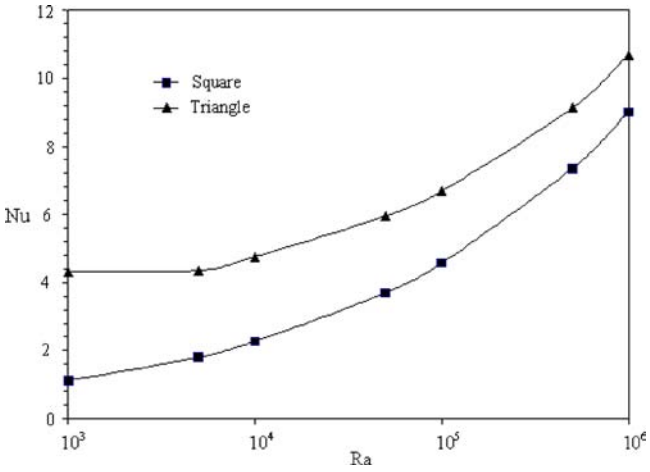

Fig. 3 Influence of Rayleigh number Ra on the mean Nusselt number Nu for the square cavity and the isosceles triangular cavity when both are filled with air

5.2 Second Heat Transfer Enhancement. In this section we are interested in examining how the boundary layer behaves near the hot wall and how each gas mixture is capable of carrying heat away from this wall to the cold wall. The numerical calculation procedure is implemented for the analysis of laminar natural convection at $\mathrm{Ra}=10^6$, which consists of three sequential steps. First, a molar gas composition w of a gas mixture is chosen in the w-interval [0, 1]. Second, at the reference temperature T_{ref}, the thermo-physical properties: viscosity μ_m, thermal conductivity λ_m, density ρ_m, heat capacity at constant pressure $C_{p,m}$ are evaluated with the accurate formulas given by Eqs. (9), (13), (17), and (19). Third, the system of partial differential equations (1)–(6) is solved using a code based on the finite volume method.

Table 1 lists the molar mass M of the six single gases He, N_2, O_2, CO_2, CH_4, and Xe, accompanied by the molar mass difference ΔM between each secondary gas N_2, O_2, CO_2, CH_4 and Xe,

Table 1 Molar mass M and molar mass difference ΔM of the pure gases

Single gas	M (g/mol)	ΔM (g/mol) with respect to He
He	4.003	···
CH_4	16.043	12.04
N_2	28.014	24.01
O_2	31.999	28.00
CO_2	44.010	40.00
Xe	131.29	127.87

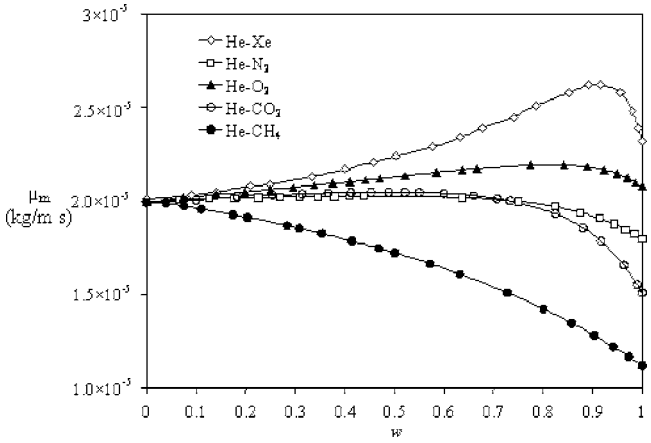

Fig. 4 Evolution of the molecular viscosity with the molar gas composition of binary gas mixtures at T_{ref} =300 K

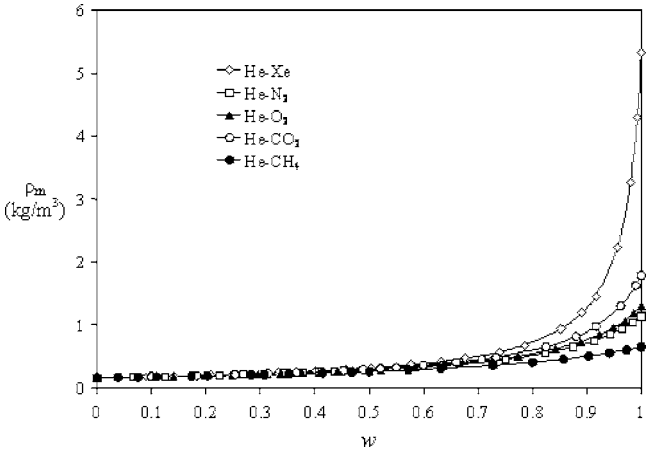

Fig. 6 Evolution of the density with the molar gas composition of a binary gas mixtures at T_{ref} =300 K

and the primary gas He. The items in the table indicate that the largest ΔM=127.87 g/mol correspond to the He–Xe gas mixture. In contrast, the smallest ΔM=12.04 g/mol corresponds to the He-CH_4 gas mixture. The other three gas mixtures lie between these two bounds. For the five gas mixtures, the variations of the thermo-physical properties: λ_m, μ_m, ρ_m, and $C_{p,m}$, with the molar composition w at 300 K are illustrated in Figures 4–7. The family of curves for $\mu_m(w)$, $\lambda_m(w)$, and $\rho_m(w)$ exhibit a common pattern in Figs. 4–6. That is, in each figure the uppermost curves are associated with the He–Xe gas mixture having the largest ΔM, as opposed to the lowermost curves which are connected to the He–CH_4 gas mixture having the smallest ΔM. This order is then reversed for the family of curves for $C_{p,m}(w)$; namely, the uppermost curve is linked to the He–CH_4 gas mixture, whereas the lowermost curve is linked to the He–Xe gas mixture. Moreover, a striking peculiarity of the trio of thermo-physical properties λ_m, ρ_m, and $C_{p,m}$ is their monotonic decreasing paths with increments in w. However, the $\mu_m(w)$ curve deviates from this pattern in the sense that the uppermost curve for the He–Xe gas mixture passes through a maximum located near w=0.9. Moving down through the other curves, it is observable that the maxima get debilitated. In fact, the lowermost curve for the He–CH_4 gas mixture resembles a negatively sloped straight line.

The convective heat transfer coefficient at the hot wall is determined using the calculated temperatures inside the thermal boundary layer by means of Eqs. (6) and (7). This is done for various molar gas compositions in the interval [0, 1] and the outcome is plotted in Figs. 8 and 9 for the square and the triangle, respectively. In these figures, the format of the abscissa indicates that the left extreme w=0 belongs to the primary gas component He, whereas the right extreme w=1 corresponds to the secondary gas component. In addition, the figures contain a horizontal line re-

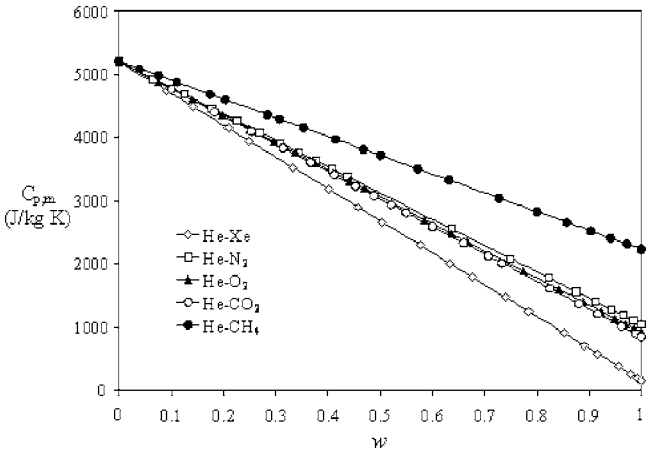

Fig. 7 Evolution of the heat capacity at constant pressure with the molar gas composition of binary gas mixtures at T_{ref} =300 K

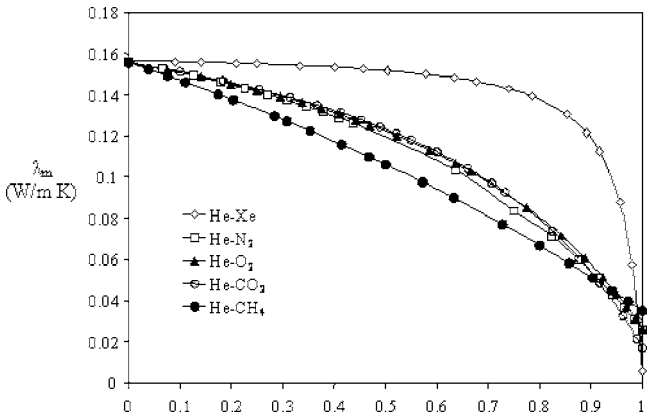

Fig. 5 Evolution of the thermal conductivity with the molar gas composition of binary gas mixtures at T_{ref} =300 K

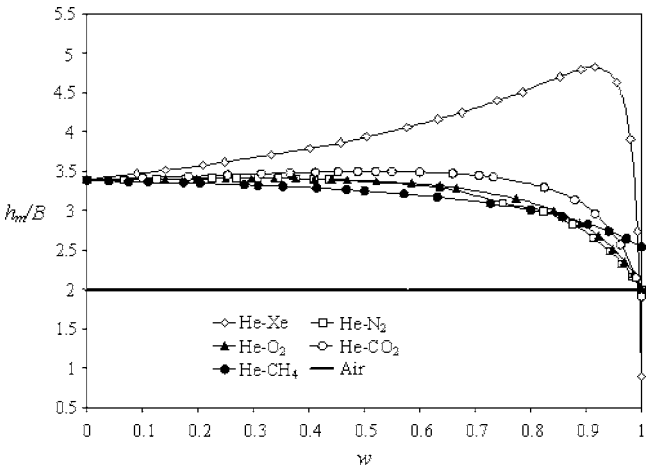

Fig. 8 Variation of the relative heat transfer coefficient h_m/B, across the square cavity, with molar gas composition of binary gas mixtures at T_{ref} =300K and Ra=10^6

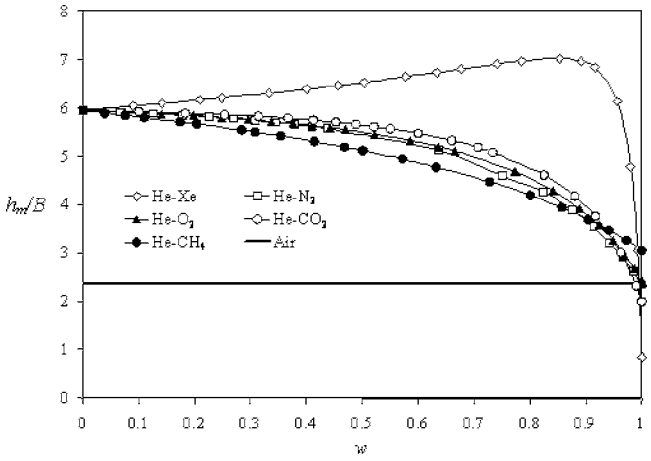

Fig. 9 Variation of the relative heat transfer coefficient h_m/B across the triangular cavity with molar gas composition of binary gas mixtures at $T_{ref}=300$ K and Ra=10^6

lated to the allied convection coefficient for air h_a/B, the so-called baseline case. The constant B was introduced to absorb the gravitational acceleration and the ratio between the temperature difference and the reference temperature contained in Eq. (4). Essentially, h_m/B can be conceived as an allied convection coefficient of the gas mixture. For the case of a standard gravity with $g=9.8\ \mathrm{m/s^2}$, B simplifies to a standardized power law expression

$$B = 0.1\left(\frac{T_H - T_C}{T_{\mathrm{ref}}}\right)^{1/3} \tag{21}$$

Fixing the reference temperature at $T_{ref}=300$ K, the two points of reference for comparison purposes are the allied mean convection coefficients for pure He and for air. Correspondingly, the heat transfer augmentation $(h_{He}-h_a)/h_a$ rendered by He with respect to air for the square enclosure amounts to a significant 71%. Interestingly, the heat transfer enhancement doubles for the isosceles triangle and $(h_{He}-h_a)/h_a$ increases from 71% (square) to 152% (triangle). When the two enclosure systems filled with He are compared, the triangle is found to be favorable to heat transfer. In quantitative form, $[h_{He}(T)-h_{He}(S)]/h_{He}(S)$ gives rise to heat transfer enhancement of 76%. This value was found to be only 19% with respect to the enclosures filled with air.

It is observable in Figs. 8 and 9 that the allied mean heat transfer coefficient h_m/B curve passes through a maximum for the He–Xe gas mixture characterized by a peak in the upper right part of the plane. This illustrates that an enormous maximum for the allied mean convection coefficient $h_{m,max}/B$ is furnished in the w-domain [0, 1]. This particular ordinate occurs at an optimal molar gas composition $w_{opt}=0.92$ (8% He and 92% Xe) in the case of the square. This optimal value w_{opt} is reduced to 0.85 (15% He and 85% Xe) in the case of the triangle. Relative to He, the heat transfer enhancement $(h_{m,max}-h_{He})/h_{He}$ delivered by the He–Xe gas mixture ascends to a remarkable 42% for the square and only to 18% for the triangle. However, when the two systems filled with He–Xe gas mixture are compared by way of $[h_{m,max}(T)-h_{m,max}(S)]/h_{m,max}(S)$, the heat transferred within the triangle is 46% more than for the square.

The He–CO_2 gas mixture in the square exhibits a maximum of allied mean convection coefficient $h_{m,max}/B=3.5$ that takes place at an optimal molar gas composition $w_{opt}=0.52$ (48% He and 52% CO_2). Except for this case, all the h_m/B curves related to other gas mixtures decrease monotonically with w. In other word, the heat transfer enhancement is higher using pure helium than the mixture.

The trends observed in Figs. 8 and 9 and Table 1 suggest that the allied convection coefficients $h_{m,max}/B$ strongly respond to the molar mass difference ΔM between the primary gas He and the secondary gas Xe. As noted in Table 1, the He–Xe gas mixture possesses the largest molar mass difference $\Delta M=127.87$ g/mol. This translates into the highest global maximum allied mean convection coefficient h_m/B. The He–CO_2 gas mixture with the second largest molar mass difference $\Delta M=40$ g/mol, comes at a distant second. The smallest $\Delta M=12.04$ g/mol for the He–CH_4 gas mixture reveals no maximum allied mean convection coefficient h_m/B.

The structure of the solution channeled through streamlines and isotherms for air and the five gas mixtures, at a molar gas composition $w=w_{opt}=0.85$ for the triangular enclosure, is given in Fig. 10. From Fig. 10(*a*), we observed a contour plot of the stream function where two counter-rotating vortices coexist; the main vortex of high strength and large size is rotating clockwise and a secondary vortex of small size located in the right upper corners of the enclosure. As evidenced from the stream function gradient, the velocity is highest near the active walls and thin boundary layers are formed in these regions. In contrast, the enclosure nucleus contains slow moving fluid as shown by the low gradient area in the center. The isotherms indicate a large isothermal core with sharp gradients near the walls. When the He–CH_4 mixture is inserted into the enclosure (Fig. 10(*b*)), the fluid velocity is reduced significantly compared to the air velocity in Fig. 10(*a*); He–CH_4 is found to display lower velocities also when compared to the other gas mixtures. The size of the upper secondary vortex decreased resulting in a large isothermal subregion under the upper insulated wall as reflected in the corresponding isothermal plots. The He–N_2, He–O_2, and He–CO_2 gas mixtures in Figs. 10(*c*)–10(*e*) exhibit flow characteristics that are similar to ones for He–CH_4. The fluid velocity and the size of the upper vortex increase when the enclosure is filled with He–N_2, He–O_2, and He–CO_2 mixtures, respectively. The He–Xe mixture in Fig. 10(*f*) attests the thinnest boundary layer along the active walls resulting in higher fluid velocities. The upper secondary vortex intensifies and pushes the main vortex down toward the core of the enclosure.

6 Conclusions

The compounded heat transfer enhancement was analyzed in two parts. First by comparing the thermofluid behavior of the square enclosure with that of an isosceles triangular enclosure, both filled with air. This enhancement was referred as the "first enhancement." Second, the air is replaced by five gas mixtures formed with helium (He) as the primary gas component, and carbon dioxide (CO_2), methane (CH_4), nitrogen (N_2), oxygen (O_2), and xenon (Xe) as the secondary gas components. When the square and the isosceles triangular enclosures are filled with the five gas mixtures, then the thermo-fluid behavior of the two enclosures was named the "second enhancement." For a fixed heated wall length H in the square and isosceles triangle, the cold wall length was increased from H in the square to $1.41H$ in the triangle, corresponding to a cold wall enlargement of 41%. In addition, the cross-sectional area A_c of the derived isosceles triangle is half of the cross-sectional area of the original square enclosure. Under a dominant conduction condition for a low Ra=10^3, the heat transfer enhancement across the hot wall of the isosceles triangle is an enormous 334% higher than that of the original square. The enhancement levels tend to diminish with increments in Ra. In fact, for a dominant convection condition for a high Ra=10^6 the heat transfer enhancement margin delivers a modest 19%.

Switching to the gas mixtures, for the He–Xe gas mixture, the allied mean heat transfer coefficient h_m/B curve passes through a maximum in the w-domain [0, 1]. This particular ordinate $h_{m,max}/B$ occurs at an optimal molar gas composition $w_{opt}=0.92$ (8% He and 92% Xe) in the case of the square and $w_{opt}=0.85$ (15% He and 85% Xe) in the case of the triangle. Relative to pure

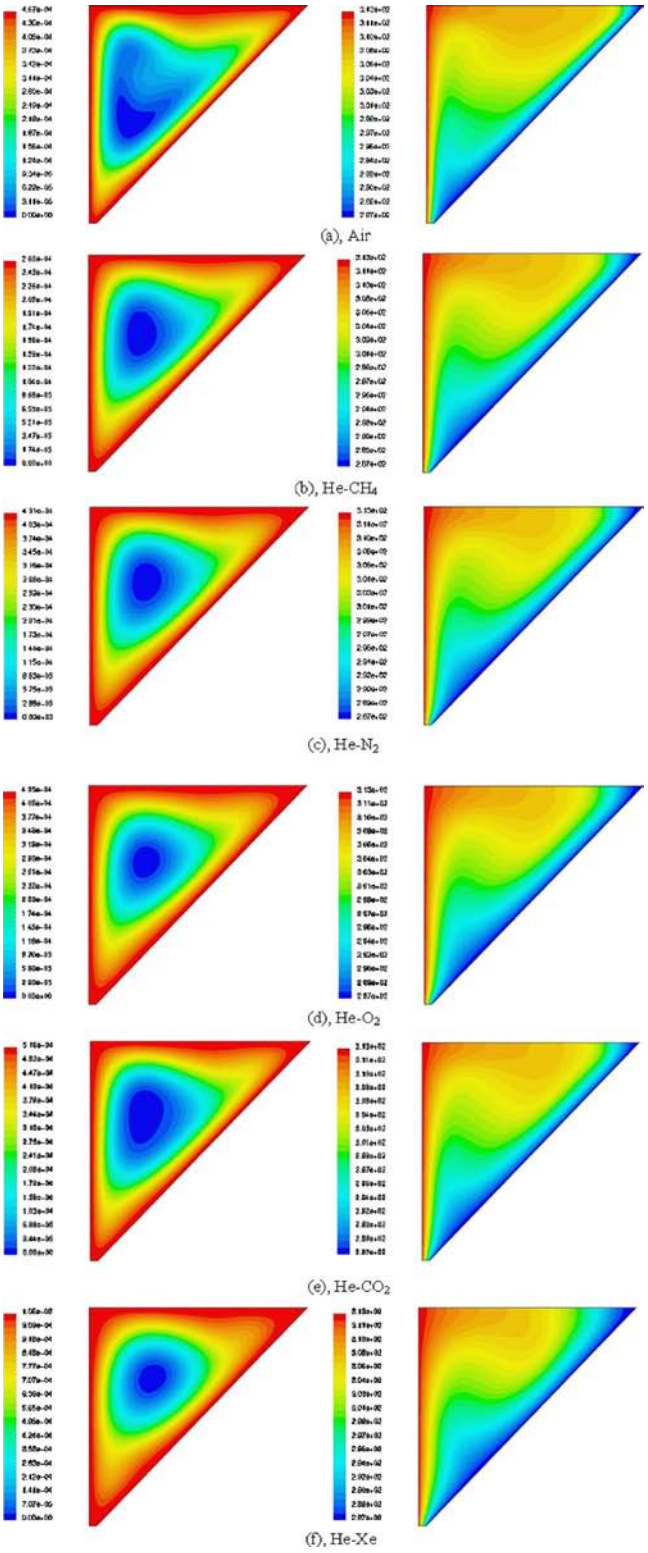

Fig. 10 Structure of the solution at Ra=10^6 and w=0.85 for air and the five binary gas mixtures trapped inside the triangular cavity: streamlines on the left and isotherms on the right

He, the heat transfer enhancement of the He–Xe gas mixture represented by $(h_{m,\max}-h_{\mathrm{He}})/h_{\mathrm{He}}$ ascends to a remarkable 42% for the square and 18% for the triangle. However, when the two enclosures filled with a He–Xe gas mixture are compared by way of $[h_{m,\max}(T)-h_{m,\max}(S)]/h_{m,\max}(S)$, the triangle outperforms the square by a margin of 46%. The global heat transfer enhancement is between the square filled with air and the triangle filled with He–Xe, which can be determined by way of $[h_{m,\max}(T)-h_a(S)]/h_a(S)$; the global heat transfer enhancement of 255% is obtained at $w_{\mathrm{opt}}=0.85$.

Nomenclature

B = constant related to the mean heat transfer coefficient
B_2 = second virial coefficient (m^3 mol^{-1})
C_p = mass heat capacity at constant pressure (J kg^{-1} K^{-1})
C_p^0 = molar heat capacity at constant pressure of an ideal gas (J mol^{-1} K^{-1})
C_v = mass heat capacity at constant volume (J kg^{-1} K^{-1})
C_v^0 = molar heat capacity at constant volume of an ideal gas (J mol^{-1} K^{-1})
g = acceleration of gravity, (m s^{-2})
H = vertical side of enclosure (m)
h = mean heat transfer coefficient (W m^{-2} K^{-1})
h_y = local heat transfer coefficient (W m^{-2} K^{-1})
m = molecular mass (kg)
M = molar mass (kg mol^{-1})
p = pressure (Pa)
Pr = Prandtl number, $\mu c_p/\lambda$
q_w = local wall heat flux (W m^{-2} K)
R = gas constant (J mol^{-1} K^{-1})
Ra = Rayleigh number, $g\beta(T_H-T_C)H^3\,\mathrm{Pr}/\nu^2$
T_c = critical temperature (K)
T_C = cold wall temperature (K)
T_H = hot wall temperature (K)
T_{ref} = reference temperature $(T_H+T_C)/2$ (K)
T_r = reduced temperature T/T_c
u,v = velocities in the x- and y-directions (m s^{-1})
x,y = axial and transversal coordinates (m)
Y = dimensionless vertical coordinate, y/H
x_q = mole fraction of pure gas q
w = molar gas composition of a gas mixture
w_{opt} = optimal molar gas composition of a gas mixture

Greek Symbols

α = thermal diffusivity λ/C_p (m^2 s^{-1})
β = volumetric coefficient of thermal expansion (K^{-1})
λ = thermal conductivity (W m^{-1} K^{-1})
μ = molecular dynamic viscosity (kg m^{-1} s^{-1})
υ = molecular kinematic viscosity (m^2 s^{-1})
ρ = density (kg m^{-3})
ω = acentric factor

Subscripts

a = air
q = pure gas q
i,j = refer to x and y directions in Eqs. (1)–(4)
m = gas mixture
max = maximum

References

[1] Yang, K. T., 1987, "Natural Convection in Enclosures," *Handbook of Single-Phase Heat Transfer*, S. Kakac et al., eds., John Wiley, New York, Chap. 13.
[2] Raithby, G. D., and Hollands, K. G. T., 1998, "Natural Convection," *Handbook of Heat Transfer*, 3rd ed., W. M. Rohesnow et al., eds., McGraw-Hill, New York, Chap. 4.
[3] Jaluria, Y., 2003, "Natural Convection," *Heat Transfer Handbook*, A. Bejan and A. D. Kraus, eds., John Wiley, New York, Chap. 7.

[4] Elicer-Cortés, J. C., Kim-Son, D., and Coutanceau, J., 1990, "Transfert de Chaleur Dans un Dèdre a Géométrie Variable," Int. Commun. Heat Mass Transfer, **17**, pp. 759–769.
[5] Elicer-Cortés, J. C., and Kim-Son, D., 1993, "Natural Convection in a Dihedral Enclosure," Exp. Heat Transfer, **6**, pp. 205–213.
[6] Simons, R. E., Antonnetti, V. W., Nakayawa, W., and Oktay, S., 1997, "Heat Transfer in Electronic Packages," *Microelectronics Packaging Handbook*, 2nd ed., R. Tummala et al., eds., Chapman and Hall, New York, pp. 315–403.
[7] Bar-Cohen, A., Watwe, A. A., and Prasher, R. S., 2003, "Heat Transfer in Electronic Equipment," *Heat Transfer Handbook*, A. Bejan and A. D. Kraus, eds., John Wiley, New York, Chap. 13.
[8] Misumi, T., and Kitamura, K., 1993, "Heat Transfer Enhancement of Natural Convection and Development of a High-Performance Heat Transfer Plate," JSME Int. J., **36**, pp. 143–152.
[9] Bhavnani, S. H., and Bergles, A. E., 1990, "Effect of Surface Geometry and Orientation on Laminar Natural Convection Heat Transfer From a Vertical Flat Plate With Transverse Roughness Elements," Int. J. Heat Mass Transfer, **33**, pp. 965–981.
[10] Hitt, D. L., and Campo, A., 2004, "Influence of Transverse Fins Attached to the Heated Wall of a Rayleigh-Benard Cavity," *Proc. ASME IMECE Conference*, Vol. 1, Anaheim CA.
[11] Campo, A., and Landon, M. D., 2004, "Design Optimization of an Air-Filled Cavity: Control of the Constrained Maximum Temperature at the Directly Heated Vertical Wall," Int. J. Numer. Methods Heat Fluid Flow, **14**, pp. 718–733.
[12] Campo, A., and Ridouane, E. H., 2005, "Enhancement of Natural Convection Transport in Slender Right-Angled Triangular Cavities by Way of Molding the Upper Insulated Wall," J. Enhanced Heat Transfer, **12**, pp. 327–341.
[13] Bergles, A. E., 1999, "Techniques to Enhance Heat Transfer," *Handbook of Heat Transfer*, W. M. Rosehnow et al., eds., McGraw-Hill, New York, Chap. 11.
[14] Manglik, R. M., 2003, "Heat Transfer Enhancement," *Heat Transfer Handbook*, A. Bejan and A. D. Kraus, eds., John Wiley, New York, Chap. 14.
[15] Siegel, R., and Howell, J. R., 1992, *Thermal Radiation Heat Transfer*, 3rd ed., Hemisphere, Washington, DC.
[16] Weaver, J. A., and Viskanta, R., 1991, "Natural Convection Due to Horizontal Temperature and Concentration Gradients—2. Species Interdiffusion, Soret and Dufour Effects," Int. J. Heat Mass Transfer, **34**, pp. 3121–3133.
[17] Patankar, S. V., 1980, *Numerical Heat Transfer and Fluid Flow*, Hemisphere, Taylor & Francis Group, New York.
[18] De Vahl Davis, G., 1983, "Natural Convection of Air in a Square Cavity: A Benchmark Numerical Solution," Int. J. Numer. Methods Fluids, **11**, pp. 249–264.
[19] Flack, R. D., 1980, "The Experimental Measurement of Natural Convection Heat Transfer in Triangular Enclosures Heated or Cooled From Below," ASME J. Heat Transfer, **102**, pp. 770–772.
[20] *NIST Chemistry Workbook*, NIST, Washington, DC, available at http://webbook.nist.gov/chemistry
[21] Poling, B. E., Prausnitz, J. M., and O'Connell, J. P., 2001, *The Properties of Gases and Liquids*, 5th ed., McGraw-Hill, New York, pp. A.5–A.19.
[22] Hirschfelder, J. O., Curtis, C. F., and Bird, B. R., 1964, *Molecular Theory of Gases and Liquids*, John Wiley, New York.
[23] Bzowski, J., Kestin, J., Mason, E. A., and Uribe, F. J., 1990, "Equilibrium and Transport Properties of Gas Mixtures at Low Density: Eleven Polyatomic Gases and Five Noble Gases," J. Phys. Chem. Ref. Data, **19**, pp. 1179–1185.
[24] Schreiber, M., Vesovic, V., and Wakeham, W. A., 1997, "Thermal Conductivity of Atom-Molecule Dilute Gas Mixtures," High Temp. - High Press., **29**, pp. 653–660.
[25] Dymond, J. H., and Smith, E. B., 1980, *The Virial Coefficients of Pure Gases and Mixtures: A Critical Compilation*, Oxford University Press, London.

Magnetofluidconvection in a Rotating Porous Layer Under Modulated Temperature on the Boundaries

B. S. Bhadauria
Department of Mathematics and Statistics,
Jai Narain Vyas University,
Jodhpur-342005, India

Thermal instability in an electrically conducting fluid saturated porous medium, confined between two horizontal walls, has been investigated in the presence of an applied vertical magnetic field and rotation, using the Brinkman model. The temperature gradient between the walls of the fluid layer consists of a steady part and a time-dependent oscillatory part. Only infinitesimal disturbances are considered. The combined effect of permeability, rotation, vertical magnetic field, and temperature modulation has been investigated using Galerkin's method and Floquet theory. The value of the critical Rayleigh number is calculated as function of amplitude and frequency of modulation, Chandrasekhar number, Taylor number, porous parameter, Prandtl number, and magnetic Prandtl number. It is found that rotation, magnetic field, and porous medium all have a stabilizing influence on the onset of thermal instability. Further, it is also found that it is possible to advance or delay the onset of convection by proper tuning of the frequency of modulation of the walls' temperature. In addition the results corresponding to the Brinkman model and Darcy model have been compared for neutral instability.
[DOI: 10.1115/1.2712851]

Keywords: thermal instability, temperature modulation, Rayleigh number, Chandrasekhar number, porous medium, Taylor number

1 Introduction

The study of convective flow in a porous medium under the influence of an imposed magnetic field and rotation is of great interest in geophysics, particularly in the study of the earth's core, where the molten fluid is conducting, and can become convectively unstable as a result of differential diffusion. A detailed review of most of the related findings has been given by Nield and Bejan [1]. Although the research topic is quite old, only limited literature is available on this subject. The problem of thermal instability in a rotating porous medium or under a vertical magnetic field subject to uniform temperature gradient has been investigated by several authors for both Darcy and Brinkman models; e.g., Patil and Rudraiah [2], Rudraiah and Vortmeyer [3], Patil and Vaidyanathan [4], Rudraiah [5], Vadasz [6–8], Alchaar et al. [9], Qin and Kaloni [10] and Bian et al. [11] for different mathematical models, considering both free-free and rigid-rigid boundary conditions. Recently, Desaive et al. [12] have investigated the convective instability in a rotating porous medium, for rigid-rigid boundaries, using the Brinkman model.

However, there are many situations of practical importance in which temperature gradient is a function of both space and time. This non-uniform temperature gradient (temperature modulation), which is a function of both space and time, can be used as an effective mechanism to control the convective flow by proper tuning of its parameters, namely, amplitude and frequency of modulation. There can be an appreciable enhancement of heat, mass, or momentum if an imposed modulation can destabilize an otherwise stable system. Similarly, if it can stabilize an otherwise unstable system, higher efficiency can be achieved in many processing techniques, particularly in solidification processes.

Contributed by the Heat Transfer Division of ASME for publication in the JOURNAL OF HEAT TRANSFER. Manuscript received February 13, 2006; final manuscript received July 12, 2006. Review conducted by Jose L. Lage.

Venezian [13] was first to consider the effect of temperature modulation on thermal instability in a horizontal fluid layer. Later on, Rosenblat and Herbert [14], Rosenblat and Tanaka [15], Yih and Li [16], Roppo et al. [17], and Bhadauria and Bhatia [18] also studied the effect of temperature modulation on thermal stability in a fluid layer, considering different physical models. Recently Bhadauria [19,20] investigated the effect of temperature modulation on thermal instability in a horizontal fluid layer, and studied the effects of rotation and vertical magnetic field. However, the study of thermal convection in a porous medium with time-dependent thermal boundary conditions has received only limited attention. The effect of thermal modulation on the onset of convection in a porous medium has been studied by Catlagirone [21], Chhuon and Caltagirone [22], Rudraiah and Malashetty [23,24], Malashetty and Wadi [25], Malashetty and Basavaraja [26,27], and Bhadauria [28], for both Darcy and Brinkman models, using both free-free and rigid-rigid boundaries. However, literature on convection in a porous medium with temperature modulation, subjected to rotation or magnetic field, is scarce. Recently, only Bhadauria [29] has investigated the effect of temperature modulation on thermal instability in a rotating porous layer, considering Brinkman's model, and using rigid-rigid boundaries. To the best of author's knowledge, no study is available in which combined effect of rotation, vertical magnetic field, and temperature modulation has been considered on convective flow in a porous medium.

Although most of the studies on convection in a porous medium have been described using the Darcy model, it is now being realized that this model is applicable only under special circumstances; therefore, a generalized model for the accurate prediction of convection in a porous medium must include Forchheimer's inertia term and Brinkman's viscous term. For example, when the porous medium has a sparse distribution of pores, at which the fluid experiences the Darcy resistance, we must take into account the usual viscous dissipation along with the Darcy resistance; i.e.,

 Copyright © 2007 by ASME

we must include the viscous term $[\mu\nabla^2\mathbf{V}]$ along with the Darcy resistance $[(\mu/k)\mathbf{V}]$ (since in the case of sparse distribution of the particles, the porous medium will have large void spaces that give rise to viscous shear in addition to the usual Darcy resistance). Walker and Hosmy [30], while studying the convective instability in a porous medium, have demonstrated theoretically the need to consider both usual viscous resistance and Darcy resistance for large values of permeability.

Further, the horizontal boundaries bounding a porous medium can be either free or rigid. In real situations such as geothermal regions, the layer under consideration cannot be isolated to avoid the penetrations of the fluid from the surrounding regions, and therefore one has to consider the free boundaries. However, it is also known that the free boundaries are less accessible to experiment; therefore, under laboratory conditions, one comes across only rigid boundaries where no slip condition can be applied.

The motivation of the present study is to see the combined effect of temperature modulation, permeability, rotation, and vertical magnetic field on the stability of flow through a porous medium with rigid boundaries. Since the porous medium considered is sparsely packed, Brinkman's model, which accounts for friction caused by microscopic shear, has been used. To modulate the walls' temperature, a sinusoidal function has been taken. The results have been obtained for the following three cases: (a) when the plate temperatures are modulated in phase, (b) when the modulation is out of phase, and (c) when only the lower plate temperature is modulated, with the upper plate held at fixed constant temperature. The findings of the present study are believed to bridge the gap between the results valid for the Darcy model (low permeability) and those valid for classical viscous fluids. Further, the present results may have a bearing on the onset of convection in geothermal areas where the ground water flows through a porous medium and is subjected to the earth's rotation and magnetic field.

2 Formulation

We consider a porous medium, which is composed of sparse distribution of particles completely saturated with Boussinesq fluid, and confined between two parallel horizontal walls, at $z=-d/2$ and $z=d/2$, a distance d apart. The fluid is electrically conducting, and the walls are infinitely extended in x and y directions, and are rigid. Let a vertical magnetic field is applied across the porous layer and the system be rotating uniformly about the z axis with a constant angular velocity $\mathbf{\Omega}$. For distances not too far from the axis of rotation, one can assume the gravity buoyancy to be dominant and can neglect the centrifugal effects, hence limiting the effect of rotation to the Coriolis force. The porous medium is regarded as an assemblage of small, identical, spherical particles fixed in the space of porosity close to unity. Under the Boussinesq approximation, the governing equations for the study of rotating magnetoconvection in a fluid-saturated sparsely packed porous medium, are

$$\frac{\partial \mathbf{V}}{\partial t} + \mathbf{V}\cdot\nabla\mathbf{V} - \frac{\mu_m}{\rho_R}\mathbf{H}\cdot\nabla\mathbf{H} + 2\mathbf{\Omega}\times\mathbf{V} = -\frac{1}{\rho_R}\nabla p + \frac{\rho_f}{\rho_R}\mathbf{g} - \frac{\nu}{k}\mathbf{V} + \nu\nabla^2\mathbf{V} \tag{1}$$

$$(\rho C_p)_m\frac{\partial T}{\partial t} + (\rho C_p)_f\mathbf{V}\cdot\nabla T = \kappa_m\nabla^2 T \tag{2}$$

$$\frac{\partial \mathbf{H}}{\partial t} + \mathbf{V}\cdot\nabla\mathbf{H} - \mathbf{H}\cdot\nabla\mathbf{V} = \eta\nabla^2\mathbf{H} \tag{3}$$

$$\nabla\cdot\mathbf{V} = 0 \tag{4}$$

$$\nabla\cdot\mathbf{H} = 0 \tag{5}$$

$$\rho_f = \rho_R[1-\alpha(T-T_R)] \tag{6}$$

where ρ is the fluid density, ρ_R and T_R are (constant), reference density and temperature, respectively, $\mathbf{g}=(0,0,-g)$ is the acceleration due to gravity, $\mathbf{\Omega}=(0,0,\Omega)$, is the angular velocity, $\mathbf{H}=(H_1,H_2,H_3)$ is the intensity of the magnetic field. ν is the kinematic viscosity, κ_m is the thermal diffusivity, α is the coefficient of volume expansion, μ_m is magnetic permeability, k is the permeability of the porous medium, $\eta=1/\mu_m\sigma$ is the magnetic viscosity, while σ is electrical conductivity. $\mathbf{V}=(u,v,w)$, p, and T are respectively, the fluid velocity, pressure, and temperature, fields, while t is the time. For temperature modulation, we write the following conditions

(i) When the temperature of the lower boundary as well as of the upper boundary is modulated, we have

$$T(t) = T_R + \beta d(1+\varepsilon\cos\omega\mathbf{t}) \quad \text{at } z=-d/2 \tag{7a}$$

$$= T_R + \beta d\varepsilon\cos(\omega\mathbf{t}+\phi) \quad \text{at } z=d/2 \tag{7b}$$

(ii) When the upper boundary is held at a fixed constant temperature and only lower boundary temperature is modulated, then

$$T(t) = T_R + \beta d(1+\varepsilon\cos\omega\mathbf{t}) \quad \text{at } z=-d/2 \tag{8a}$$

$$= T_R \quad \text{at } z=d/2 \tag{8b}$$

Here, T_R represents the non-modulated temperature of the upper boundary, ϵ is the amplitude of modulation, β is thermal gradient, and ϕ is phase angle.

2.1 Basic State. Equations (1)–(5), (7), and (8) admit an equilibrium solution in which the basic state is

$$\mathbf{V}=(\mathrm{u},\mathrm{v},\mathrm{w})=0,\quad T=T_b(z,t),\quad p=p_b(z,t),\quad \rho=\rho_b(z,t) \tag{9}$$

The basic temperature $T_b(z,t)$, basic pressure p_b, and basic density ρ_b are given by the equations

$$\gamma\frac{\partial T_b}{\partial t} = \kappa\frac{\partial^2 T_b}{\partial z^2} \tag{10}$$

$$\frac{\partial p_b}{\partial z} = \rho_b g \tag{11}$$

and

$$\rho_b = \rho_R[1-\alpha(T_b-T_R)] \tag{12}$$

where $\gamma=(\rho C_p)_m/(\rho C_p)_f$ and $\kappa=\kappa_m/(\rho C_p)_f$. For both the above cases (i) and (ii), the solution of the differential equation (10) under the boundary conditions (7) and (8) can be written as

$$T_H(z,t) = T_R + T_S(z) + \epsilon\,\mathrm{Re}\{T_1(z,t)\} \tag{13}$$

where $T_S(z)$ is the steady temperature field, T_1 is the oscillating part and Re stands for real part. We then have

$$T_S(z) = \Delta T\left(\frac{1}{2}-\frac{z}{d}\right), \tag{14}$$

and

$$T_1(z,t) = \frac{\Delta T}{\sinh\lambda}\left\{e^{i\phi}\sinh\lambda\left(\frac{1}{2}+\frac{z}{d}\right)+\sinh\lambda\left(\frac{1}{2}-\frac{z}{d}\right)\right\}e^{i\omega\mathbf{t}} \tag{15}$$

where

$$\lambda^2 = i\omega\gamma d^2/\kappa \tag{16}$$

2.2 Linear Stability Analysis. Let the basic state (9) of the system be slightly perturbed, and then we have

$$\mathbf{V}=\mathbf{V}'=(u',v',w'),\quad T=T_b(z,t)+\theta'\quad p=p_b(z,t)+p'$$

$$\mathbf{H} = \mathbf{H}_b + h' \quad \rho = \rho_b + \rho' \tag{17}$$

A constant magnetic field $H=|H_b|$ is maintained externally, in the vertical direction; h' is the perturbation in the magnetic field caused by the motions and the induced currents in the field. Here, $\mathbf{V}'$, θ', p', and ρ' represent the perturbed quantities, which are assumed to be small. We substitute (17) into Eqs. (1)–(6) and linearize with respect to the quantities $\mathbf{V}'$, θ' and $\mathbf{h}'$. Then taking curl, twice of the reduced Eq. (1), and once of the reduced Eq. (3), the system of equations becomes

$$\frac{\partial}{\partial \mathrm{t}}\nabla^2 w' = \nu\nabla^4 w' - \frac{\nu}{k}\nabla^2 w' + \alpha g \nabla_1^2 \theta' + \frac{\mu_m H_b}{\rho_R}\nabla^2\left(\frac{\partial h_z}{\partial z}\right) - 2\Omega\frac{\partial \zeta'}{\partial z} \tag{18}$$

$$\frac{\partial \theta'}{\partial \mathrm{t}} = -w'\frac{\partial T_b}{\partial z} + \kappa\nabla^2\theta' \tag{19}$$

$$\frac{\partial h_z'}{\partial \mathrm{t}} = H_\tau \frac{\partial w'}{\partial z} + \eta\nabla^2 h_z' \tag{20}$$

$$\frac{\partial \zeta'}{\partial \mathrm{t}} = 2\Omega\frac{\partial w'}{\partial z} + \nu\nabla^2\zeta' - \frac{\nu}{k}\zeta' + \frac{\mu_m H_b}{\rho_R}\frac{\partial \xi'}{\partial z} \tag{21}$$

$$\frac{\partial \xi'}{\partial \mathrm{t}} = H_b\frac{\partial \xi'}{\partial z} + \eta\nabla^2\xi' \tag{22}$$

where w', h_z', ζ', ξ' are the vertical components of the perturbed velocity field $\mathbf{V}'$, magnetic field $\mathbf{h}'$, the vorticity, and the current density, respectively. In the above equations the value of γ is set equal to 1. Now using normal mode technique, we seek solutions for the five unknown fields in the form

$$w'(x,y,z,t) = w'(z,t)\exp[i(a_x'x + a_y'y)] \tag{23}$$

$$\theta'(x,y,z,t) = \theta'(z,t)\exp[i(a_x'x + a_y'y)] \tag{24}$$

$$h_z'(x,y,z,t) = h_z'(z,t)\exp[i(a_x'x + a_y'y)] \tag{25}$$

$$\zeta'(x,y,z,t) = \zeta'(z,t)\exp[i(a_x'x + a_y'y)] \tag{26}$$

$$\xi'(x,y,z,t) = \xi'(z,t)\exp[i(a_x'x + a_y'y)] \tag{27}$$

Here, $a' = (a_x'^2 + a_y'^2)^{1/2}$ is the horizontal wave number. If we scale length, time, temperature, wave number, velocity, magnetic field, vorticity, current density, and the frequency according to

$$\mathbf{r}' = d\mathbf{r}^* \quad t' = t^*/\omega \quad T_b = \beta d T_b^* \quad \theta' = \beta d\theta^*$$
$$a'^2 = d^2 a^{*2} \quad \mathbf{V}' = (\alpha g\beta d a'^2/\nu)\mathbf{V}^* \tag{28}$$

$$\mathbf{h}' = H_b\mathbf{h}^* \quad \zeta' = (\alpha g\beta a'^2/\nu)\zeta^* \quad \xi' = \left(\frac{H_b}{d}\right)\xi^* \quad \omega = \omega^*\kappa/d^2$$

then the non-dimensionalized governing equations in linear form are

$$\omega^*(D^2 - a^{*2})\frac{\partial w^*}{\partial t^*} = P_r(D^2 - a^{*2})[(D^2 - a^{*2}) - P_l^{-1}]w^* - P_r\theta^* + \frac{P_r P_m Q}{a^{*2}R}(D^2 - a^{*2})\frac{\partial h_z^*}{\partial z^*} - \sqrt{T_a}P_r\frac{\partial \zeta^*}{\partial z^*} \tag{29}$$

$$\omega^*\frac{\partial \theta^*}{\partial t^*} = -a^2 R\left(\frac{\partial T_b^*}{\partial z^*}\right)w^* + (D^2 - a^{*2})\theta^* \tag{30}$$

$$\omega^*\frac{\partial h_z^*}{\partial t^*} = a^{*2}R\frac{\partial w^*}{\partial z^*} + P_m(D^2 - a^{*2})h_z^* \tag{31}$$

$$\omega^*\frac{\partial \zeta^*}{\partial t^*} = \sqrt{T_a}P_r Dw^* + P_r\{(D^2 - a^{*2}) - P_l^{-1}\}\zeta^* + \frac{P_r P_m Q}{a^{*2}R}\frac{\partial \xi^*}{\partial z^*} \tag{32}$$

$$\omega^*\frac{\partial \xi^*}{\partial t^*} = a^{*2}R\frac{\partial \zeta^*}{\partial z^*} + P_m(D^2 - a^{*2})\xi^* \tag{33}$$

where $D \equiv \partial/\partial z^*$, $P_r = \nu/\kappa$ is the Prandtl number, $P_m = \nu/\eta$ is the magnetic Prandtl number, $P_l = k/d^2$ is the porous parameter, $R = \alpha g\Delta T d^3/\nu\kappa$ is the Rayleigh number, $Q = \mu_m H_b^2 d^2/\rho_R \nu\eta$ is the Chandrasekhar number, and $T_a = 4\Omega^2 d^4/\nu^2$ is the Taylor number. Henceforth, the asterisk will be dropped in the above equations. The temperature gradient $\partial T_b/\partial z$, obtained from the dimensionless form of Eq. (13), is

$$\frac{\partial T_b}{\partial z} = -1 + \epsilon\,\mathrm{Re}[f(z)e^{it}] \tag{34}$$

where

$$f(z) = \frac{\lambda}{\sinh\lambda}\left\{e^{i\phi}\cosh\lambda\left(\frac{1}{2} + z\right) - \cosh\lambda\left(\frac{1}{2} - z\right)\right\} \tag{35}$$

and

$$\lambda^2 = i\omega \tag{36}$$

The boundary conditions for rigid and conducting walls are given by

$$w = Dw = \theta = 0 \quad \text{on } z = \pm\frac{1}{2} \tag{37}$$

$$h_z = \zeta = D\xi = 0 \quad \text{on } z = \pm\frac{1}{2} \tag{38}$$

Darcy Model. Neglecting the viscous resistance term $\mu\nabla^2\mathbf{V}$ in comparison to the Darcy resistance term $(\mu/k)\mathbf{V}$ in Eq. (1), we obtain the governing equations (1)–(6) for the Darcy model.

Walker and Hosmy [30] have studied the effect of the presence of a porous medium of different permeabilities on convective instability and proposed suitable ranges of permeability for which the Brinkman and Darcy models can be used ($P_l \geq 10^{-3}$ for the Brinkman model and $P_l \leq 10^{-3}$ for the Darcy model).

3 Method

Here we transform the above partial differential equations (29)–(33) into a system of ordinary differential equations, using the Galerkin technique. These equations are then solved numerically. We set

$$w(z,t) = \sum_{m=1}^{N} A_m(t)\psi_m(z) \tag{39}$$

$$\theta(z,t) = \sum_{m=1}^{N} B_m(t)\varphi_m(z) \tag{40}$$

$$h_z(z,t) = \sum_{m=1}^{N} C_m(t)\phi_m(z) \tag{41}$$

$$\zeta(z,t) = \sum_{m=1}^{N} D_m(t)\zeta_m(z) \tag{42}$$

$$\xi(z,t) = \sum_{m=1}^{N} E_m(t)\xi_m(z) \tag{43}$$

where

$$\psi_m(z) = \xi_m(z) = \begin{cases} \dfrac{\cosh \mu_m z}{\cosh \dfrac{\mu_m}{2}} - \dfrac{\cos \mu_m z}{\cos \dfrac{\mu_m}{2}} & \text{if } m \text{ is odd} \\ \dfrac{\sinh \mu_m z}{\sinh \dfrac{\mu_m}{2}} - \dfrac{\sin \mu_m z}{\sin \dfrac{\mu_m}{2}} & \text{if } m \text{ is even} \end{cases} \tag{44}$$

$$\varphi_m(z) = \sqrt{2} \sin m\pi\left(z + \frac{1}{2}\right) \tag{45}$$

$$\phi_m(z) = \zeta_m(z) = \sqrt{2} \sin\left[(m+1)\pi z + (m-1)\frac{\pi}{2}\right]$$
$$(m = 1,2,3, \ldots, N) \tag{46}$$

The above functions $\psi_m(z)$, $\varphi_m(z)$, $\phi_m(z)$, and $\zeta_m(z)$ are defined in such a manner that they vanish at $z = \pm\frac{1}{2}$. For the derivatives of $\psi_m(z)$ and $\xi_m(z)$ to vanish at $z = \pm\frac{1}{2}$, it is required that μ_m are to be the roots of the characteristic equation ([31], p. 636)

$$\tanh \frac{1}{2}\mu_m - (-1)^m \tan \frac{1}{2}\mu_m = 0 \tag{47}$$

It is clear that the functions $\psi_m(z)$, $\varphi_m(z)$, $\phi_m(z)$, $\zeta_m(z)$, and $\xi_m(z)$, each form an orthonormal set in the interval $\left(-\frac{1}{2}, \frac{1}{2}\right)$. We substitute (39)–(43) into Eqs. (29)–(33) and then multiply these equations by $\psi_n(z)$, $\varphi_n(z)$, $\phi_n(z)$, $\zeta_n(z)$, and $\xi_n(z)$, respectively, $n = 1,2,3, \ldots, N$. The resulting equations are then integrated with respect to z in the interval $\left(-\frac{1}{2}, \frac{1}{2}\right)$. The outcome is a system of $L = 5N$, ordinary differential equations for the unknown coefficients $A_n(t)$, $B_n(t)$,$C_n(t)$, $D_n(t)$, and $E_n(t)$

$$\omega \sum_{m=1}^{N} [K_{nm} - a^2\delta_{nm}]\frac{dA_m}{dt} = P_r \sum_{m=1}^{N} [\{(\mu_m^4 + a^4)\delta_{nm} - 2a^2 K_{nm}\} - P_l^{-1}(K_{nm} - a^2\delta_{nm})]A_m - P_r \sum_{m=1}^{N} P_{nm}B_m - \frac{P_r P_m Q}{a^2 R}\sum_{m=1}^{N} [(m+1)^2\pi^2 + a^2]L_{nm}C_m - \sqrt{T_a}P_r \sum_{m=1}^{N} L_{nm}D_m \tag{48}$$

$$\omega \frac{dB_n}{dt} = a^2 R \sum_{m=1}^{N} [P_{mn} - \epsilon \,\mathrm{Re}\{F_{mn}e^{it}\}]A_m - (n^2\pi^2 + a^2)B_n \tag{49}$$

$$\omega \frac{dC_n}{dt} = a^2 R \sum_{m=1}^{N} R_{nm}A_m - P_m[(n+1)^2\pi^2 + a^2]C_n \tag{50}$$

$$\omega \frac{dD_n}{dt} = \sqrt{T_a}P_r \sum_{m=1}^{N} R_{nm}A_m - P_r[(n+1)^2\pi^2 + a^2 + P_l^{-1}]D_n + \frac{P_r P_m Q}{a^2 R}\sum_{m=1}^{N} R_{nm}E_m \tag{51}$$

$$\omega \frac{dE_n}{dt} = a^2 R \sum_{m=1}^{N} L_{nm}D_m + P_m \sum_{m=1}^{N} (K_{nm} - a^2\delta_{nm})E_m$$
$$(n = 1,2, \ldots, N) \tag{52}$$

where δ_{nm} is the Kronecker delta. The other coefficients, which occur in Eqs. (48)–(52) are

$$K_{nm} = \int_{-1/2}^{1/2} D^2\psi_m(z) \cdot \psi_n(z)dz \tag{53}$$

$$P_{nm} = \int_{-1/2}^{1/2} \varphi_m(z) \cdot \psi_n(z)dz \tag{54}$$

$$L_{nm} = \int_{-1/2}^{1/2} D\phi_m(z) \cdot \psi_n(z)dz \tag{55}$$

$$R_{nm} = \int_{-1/2}^{1/2} D\psi_m(z) \cdot \phi_n(z)dz \tag{56}$$

$$F_{nm} = \int_{-1/2}^{1/2} f(z) \cdot \psi_m(z) \cdot \varphi_n(z)dz \tag{57}$$

The above coefficients have been evaluated numerically using Simpson's 1/3 rule ([32], p. 125). For computational convenience, we introduce the notations

$$x_1 = A_1,\ x_2 = B_1,\ x_3 = C_1,\ x_4 = D_1,\ x_5 = E_1,\ x_6 = A_2,\ x_7 = B_2, \ldots \text{etc.} \tag{58}$$

and write the system of Eqs. (48)–(52) in the form

$$\frac{dx_i}{dt} = G_{ij}(t) \cdot x_j, \quad (i,j = 1,2,3, \ldots, 5N). \tag{59}$$

where $[G_{ij}(t)]$ is the matrix of the coefficients in the Eqs. (48)–(52). Since the coefficients $G_{ij}(t)$ are periodic in t with period 2π, the stability of solution of the system (59) can be discussed on the basis of the classical Floquet theory ([33], p. 55). Runge-Kutta-Gill procedure ([32], pp. 217 and 227) has been used to integrate the system (59) and the fundamental matrix $C = [x_{in}(2\pi)]$ of the solution is obtained. To discuss the stability of the solution, eigenvalues of the matrix C are obtained with the help of the Rutishauser method ([34], p. 116).

4 Results and Discussion

The critical values of the Rayleigh number (R_c) and the corresponding wave number (a_c) for the Brinkman model, in the absence of modulation, i.e., for steady temperature gradient ($\epsilon = 0$), are found as given below

$$T_a = 0.0 \quad Q = 0.0 \quad P_1^{-1} = 0.0 \quad a_c = 3.114 \quad R_c = 1709.1 \tag{60}$$

These values of the critical Rayleigh number and critical wave number given in (60) for non-rotating, non-magneto, non-porous convection with $N = 4$ in (59) are very close to those given by Chandrsekhar ([31], p. 43). Therefore, we feel that it is sufficient to take $N = 4$ for calculating the present results, so the results have been calculated by solving the Eqs. (59) for $x_1, x_2, x_3, \ldots, x_{20}$ (total 20 equations).

The values of the critical Rayleigh number and critical wave number at marginal stability for different parameters are given in Tables 1 and 2 for the Brinkman model and in Tables 3 and 4 for the Darcy model. The inhibiting effects of the rotation and magnetic fields on the onset of convection is apparent as the values of R_c and a_c increase on increasing T_a and Q. In addition, on de-

Table 1 Brinkman model; $Q=100.0$, $\epsilon=0$

No.	P_l	T_a	a_c	R_c
1.1	∞	0.0	4.009	3783.3
		100.0	4.013	3801.4
		500.0	4.030	3873.6
		1000.0	4.053	3963.4
1.2	1.0	0.0	4.002	3828.3
		100.0	4.006	3846.2
		500.0	4.023	3917.7
		1000.0	4.045	4006.7
1.3	0.1	0.0	3.946	4231.2
		100.0	3.95	4247.8
		500.0	3.965	4314.1
		1000.0	3.983	4396.5
1.4	0.01	0.0	3.646	8176.4
		100.0	3.649	8186.0
		500.0	3.654	8224.4
		1000.0	3.661	8272.3
1.5	0.0001	0.0	3.254	428200.2
		100.0	3.254	428200.5
		500.0	3.254	428201.3
		1000.0	3.254	428202.4

creasing P_l, the value of R_c increases, which shows the stabilizing effect of lower permeability. Further, for a porous medium of larger permeability (Brinkman model), the effect of rotation is clearly observed, which is indicated by large increase in the values of R_c and a_c (Table 1). However, when the porous medium is of smaller permeability (Darcy model, Table 3) the stabilizing effect of rotation is not much. It can be seen even in the case of the Brinkman model for $P_l=10^{-2}$, where the variation in the values of R_c and a_c is not much affected by rotation. Thus, we observe that for a medium of large permeability the stabilizing effect of rotation predominates, but for a medium of small permeability the effect of rotation is small and the stabilizing effect of permeability predominates. This can be explained as follows: when the porous medium is of large permeability (Brinkman model, $P_l \geq 10^{-3}$) the distortions of the flow path of the fluid particles would be greater due to rotation, so that the cell shape is distorted more by rotation and hence the stability of the system is enhanced considerably. On the other hand, when the fluid percolates through the medium of very small permeability, it has to seep through the pores with very small velocity, hence rotation cannot affect the flow path altogether so that the effect of rotation is small.

Table 2 Brinkman model; $T_a=500.0$, $\epsilon=0$

No.	P_l	Q	a_c	R_c
2.1	∞	0.0	3.317	1942.9
		100.0	4.030	3873.6
		200.0	4.450	5622.2
		500.0	5.174	10426.0
2.2	1.0	0.0	3.313	1982.7
		100.0	4.023	3917.7
		200.0	4.442	5668.8
		500.0	5.164	10478.3
2.3	0.1	0.0	3.285	2346.2
		100.0	3.965	4314.1
		200.0	4.370	6086.3
		500.0	5.082	10944.6
2.4	0.01	0.0	3.251	6147.4
		100.0	3.654	8224.4
		200.0	3.943	10129.1
		500.0	4.527	15358.0
2.5	0.0001	0.0	3.246	426029.5
		100.0	3.258	428202.1
		200.0	3.262	430368.0
		500.0	3.286	436838.2

Table 3 Darcy model; $Q=100.0$, $\epsilon=0$

No.	P_l	T_a	a_c	R_c
3.1	10^{-4}	0.0	3.253	426183.3
		100.0	3.253	426183.5
		500.0	3.253	426184.4
		1000.0	3.253	426185.4
3.2	$5.\times10^{-5}$	0.0	3.249	850195.7
		100.0	3.249	850195.8
		500.0	3.249	850196.3
		1000.0	3.249	850196.8

However, for the case of a magnetic field, the results are slightly different from those of rotation. In this case, the effect of magnetic field predominates at low permeability, while at large permeability the stabilizing effect of magnetic field is small and the permeability effect predominates, which is clear from the Tables 2 and 4.

Now we compare the results of 1.5 from Table 1 and 2.5 of Table 2 (Brinkman model) with the corresponding results of 3.1 and 4.1 from Tables 3 and 4 (Darcy model). We find that the values of the critical Rayleigh number in the presence of the viscous term $\mu\nabla^2\mathbf{V}$ (Brinkman model) are markedly greater than that of the Darcy model. This clearly shows the inhibiting effect of the viscous dissipation ($\mu\nabla^2\mathbf{V}\neq 0$) on the onset of thermal instability. The physical reason is that in addition to the dissipation of energy by Joule heating, rotation, and Darcy resistance, there will be viscous dissipation also in the Brinkman model, whereas in the case of the Darcy model the instability sets in earlier in the absence of viscous dissipation.

Now for temperature modulation we consider $\epsilon\neq 0$ and investigate the combined effects of rotation, vertical magnetic field, porous medium, and the temperature modulation on the onset of convection. The values of R_c with variation in ω have been shown in Figs. 1–9 at different values of other parameters.

The variation of R_c with ω, for cases (a), (b), and (c), have been depicted in Figs. 1–3, respectively, at different values of the Taylor number T_a, the other parameters are $P_l=1.0$, $\epsilon=0.4$, $P_r=1.0$, $P_m=1.0$, $Q=100.0$. From Fig. 1 we observe that for a particular value of T_a, initially the effect of modulation is destabilizing as convection occurs at an earlier point than in the steady temperature gradient case (see Table 1). This effect of modulation is small when ω is small and falls off to zero as $\omega\rightarrow\infty$. For intermediate values of ω, the effect of modulation is maximum near $\omega=19$, and then reduces as ω increases. Modulation stabilizes the system at around $\omega=90$, and then its effect reduces to zero as ω becomes very large. However in Figs. 2 and 3, which correspond to out-of-phase modulation and only lower plate temperature modulation, respectively, we find that effect of modulation is greatest near $\omega=0$, and disappears altogether when the

Table 4 Darcy model; $T_a=500.0$, $\epsilon=0$

No.	P_l	Q	a_c	R_c
4.1	10^{-4}	0.0	3.245	424012.3
		100.0	3.253	426184.4
		200.0	3.261	428351.3
		500.0	3.285	434821.8
4.2	$5.\times10^{-5}$	0.0	3.245	848022.9
		100.0	3.250	850196.3
		500.0	3.253	852367.0
		1000.0	3.265	858864.0

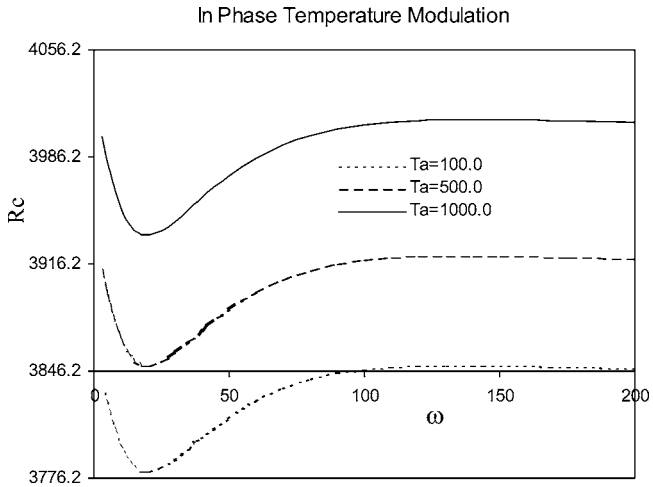

Fig. 1 Variation of R_c with ω. ε=0.4, P_r=1.0, P_m=1.0, Q=100.0, P_l=1.0.

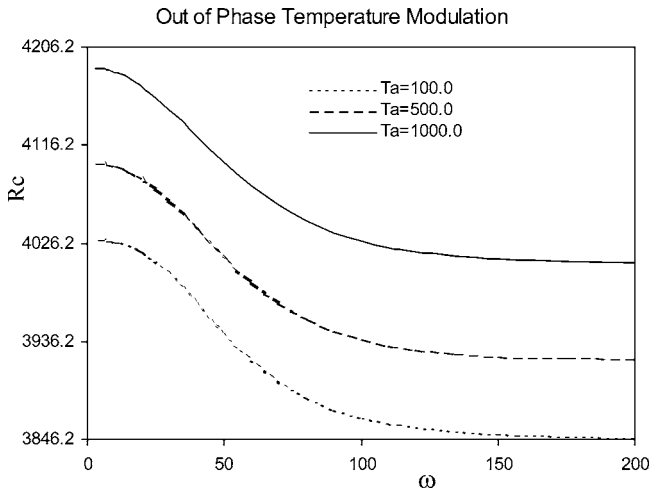

Fig. 2 Variation of R_c with ω. ε=0.4, P_r=1.0, P_m=1.0, Q=100.0, P_l=1.0.

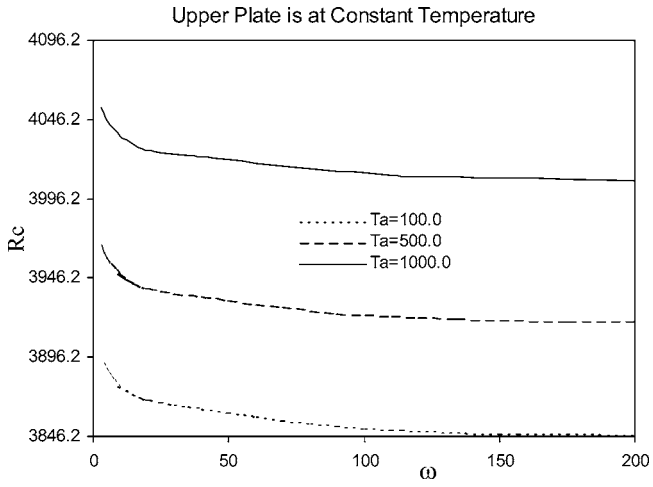

Fig. 3 Variation of R_c with ω. ε=0.4, P_r=1.0, P_m=1.0, Q=100.0, P_l=1.0.

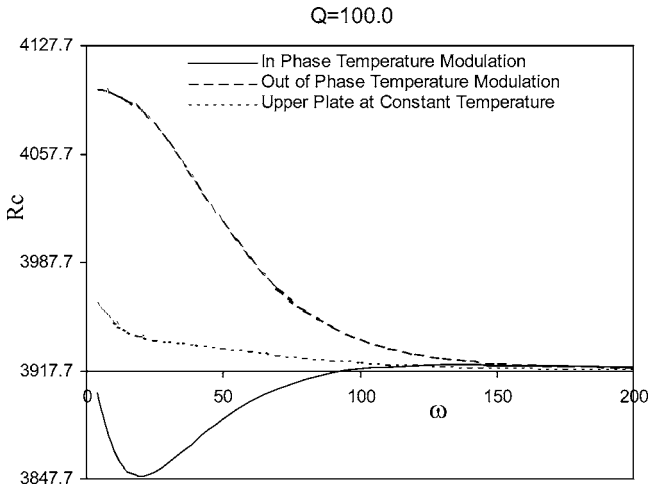

Fig. 4 Variation of R_c with ω. ε=0.4, P_r=1.0, P_m=1.0, T_a=500.0, P_l=1.0.

frequency ω becomes sufficiently large. To find the effect of Taylor number on the stability of the system, we compare the different graphs in Figs. 1 and 2 or 3. We find from Figs. 1–3 that an increase in the value of the Taylor number T_a increases the value of R_c; thus the effect of large values of the Taylor number T_a is to stabilize the system.

Figures 4–6 show the variation of R_c with ω at Q=100, 200, and 500 respectively, the values of other parameters are ϵ=0.4, P_r=1.0, P_m=1.0, P_l=1.0, T_a=500.0. If we compare the values of R_c, from these figures, in respective cases, we find that R_c increases as Q increases, thus showing the stabilizing effect of the magnetic field. From Fig. 4, for case (a), we find that initially the effect of modulation is destabilizing as convection occurs at an earlier point than in the steady temperature gradient case (see Table 2). The modulation effect is small when ω is small, becomes maximum near ω=20 and then falls off to zero as $\omega \to \infty$. But for case (b), where the temperature modulation is out of phase or for case (c), where the upper plate is at constant temperature, we find stabilizing effect. The stabilizing effect of modulation is found to be greatest near ω=0 and disappears altogether when the frequency ω becomes sufficiently large. In Fig. 5 also, which corresponds to Q=200, we find the similar results. However in Fig. 6, which corresponds to Q=500, the results are slightly different.

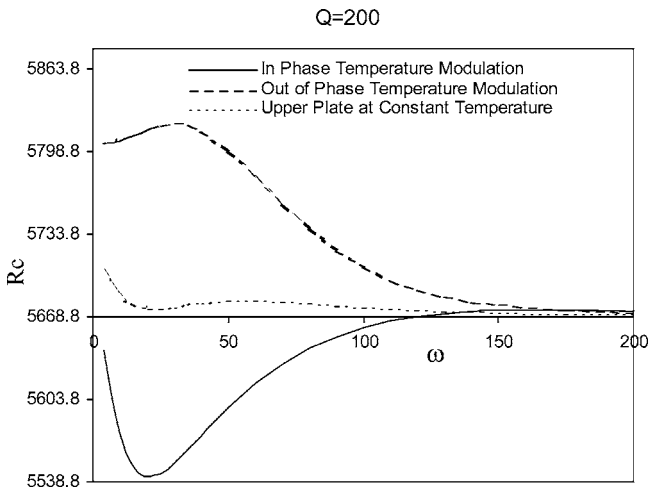

Fig. 5 Variation of R_c with ω. ε=0.4, P_r=1.0, P_m=1.0, T_a=500.0, P_l=1.0.

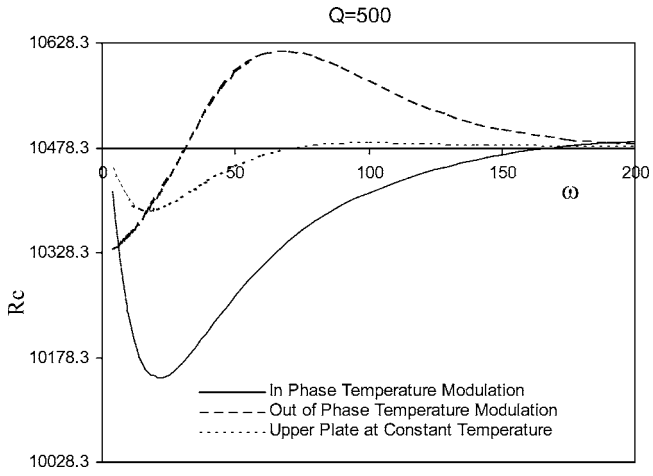

Fig. 6 Variation of R_c with ω. ε=0.4, P_r=1.0, P_m=1.0, T_a =500.0, P_l=1.0.

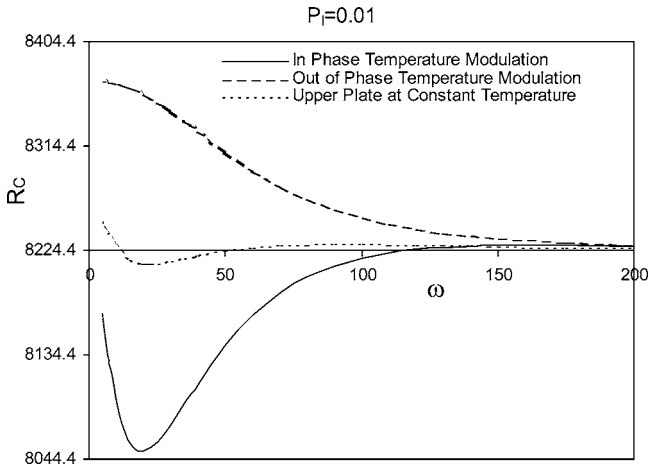

Fig. 8 Variation of R_c with ω. ε=0.4, P_r=1.0, P_m=1.0, T_a =500.0, Q=100.0.

Here, initially the effect of modulation is destabilizing for all the three cases, and then it becomes stabilizing as ω becomes sufficiently large. This difference may be because at higher Chandrasekhar number Q, the temperature modulation plays a more dominating role.

The variation of R_c with ω, for all the three cases, have been shown in Figs. 1, 7, and 8, at P_l=1.0, 0.1 and 0.01, respectively, the values of other parameters are ϵ=0.4, P_r=1.0, P_m=1.0, Q =100.0, T_a=500.0. From the figures, we observe that an increase in the value of P_l decreases the value of R_c, thus, the effect of large values of the porous parameter P_l is to advance the onset of convection. However as the value of P_l becomes smaller, R_c increases, thus showing the stabilizing effect on the system. In Figs. 1, 7, and 8 for case (a) we find that for small values of ω the effect of modulation is destabilizing; this destabilizing effect is maximum near ω=20, and falls off to zero as ω becomes very large. For cases (b) and (c), Figs. 7 and 8 show that for small and intermediate values of ω, the effect of modulation is stabilizing and falls of to zero as ω goes to infinity. However, the maximum stabilizing effect was found near ω=0.

When the frequency of modulation is small, the effect of modulation is felt throughout the porous layer. If the modulation is in phase, the time-dependent part of temperature profile becomes more and more significant as the amplitude of modulation increases. Therefore, due to finite amplitude effect of this part, onset of convection takes place at lower Rayleigh number than that predicted by the linear theory with steady temperature gradient (Figs. 1 and 4–8). However, when the temperature modulation is out of phase or the upper plate is at constant temperature, the effect is one of stabilization, decreasing with increasing frequency ω (Figs. 2–8). The stabilization is greatest near ω=0 and disappears altogether when the frequency ω is sufficiently large. Here, at low frequency, the convective wave propagates across the porous layer, thereby inhibiting the instability, so that the convection occurs at higher Rayleigh number than that predicted by the theory with a steady temperature gradient. Further, at high frequency, since the modulation becomes very fast, temperature in the porous layer is unaffected by the modulation except for a thin layer, so that we find almost the same value of R_c as for zero modulation (ε=0), in all the three cases.

To check the validity of the present model, we have obtained some known results as the particular cases of this model. These results are shown in Fig. 9. The first graph in the figure corresponds to Fig. 1 of Rosenblat and Tanaka [15] for ϵ=0.4, T_a =0.0, Q=0.0, P_l^{-1}=0.0, P_m=1.0, and P_r=1.0, the second graph corresponds to Fig. 4 of Bhadauria [19] for T_a=20.0, Q=1.0, ϵ =0.4, P_l^{-1}=0.0, P_m=1.0, and P_r=1.0. We find very good qualitative agreement between the present results and those of Rosenblat and Tanaka [15] and Bhadauria [19]. However, the values of R_c in

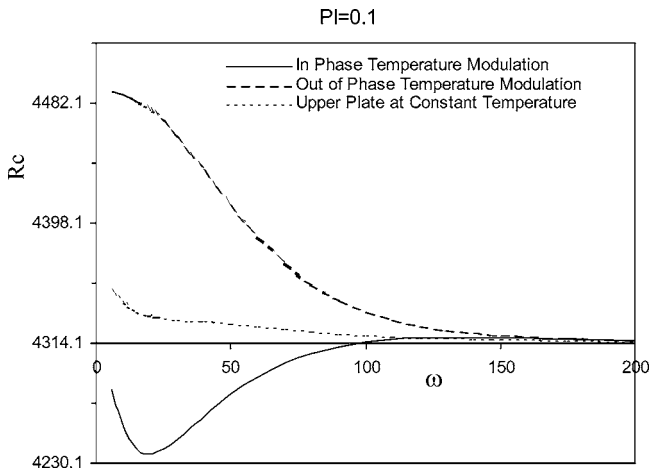

Fig. 7 Variation of R_c with ω. ε=0.4, P_r=1.0, P_m=1.0, T_a =500.0, Q=100.0.

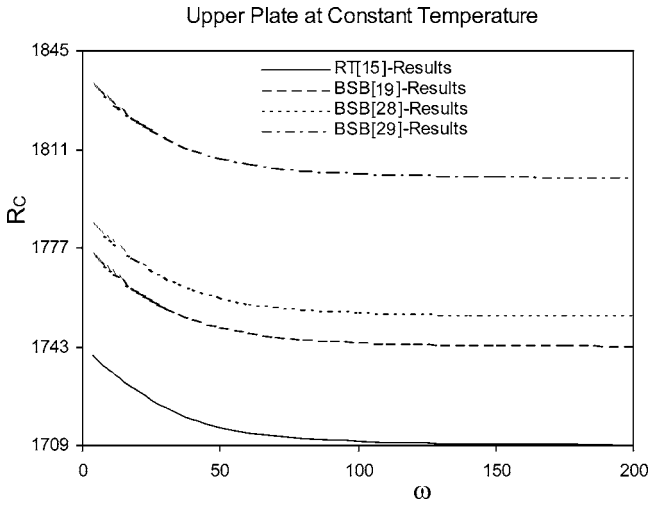

Fig. 9 Variation of R_c with ω. ε=0.4, P_r=1.0, P_m=1.0. RT-Rosenblat and Tanaka, BSB-Bhadauria.

the present model are slightly less than those of Rosenblat and Tanaka [15] and Bhadauria [19]. This is because, in the present study, the results have been calculated using $N=4$, while Rosenblat and Tanaka [15] and Bhadauria [19] obtained the results by taking $N=2$ only. Another reason is that in Bhadauria [19], results were obtained for $\epsilon=0.5$, whereas here we have taken $\epsilon=0.4$. The next two graphs of Fig. 9 correspond to Figs. 3 of Bhadauria [28,29], respectively, at $Q=0.0$, $T_a=0.0$, $P_l=1.0$, $P_r=1.0$, $P_m=1.0$, $\epsilon=0.4$, and $Q=0.0$, $T_a=100.0$, $P_l=1.0$, $P_r=1.0$, $P_m=1.0$, $\epsilon=0.4$. For these two graphs we find very good agreement between the present results and that of Bhadauria [28,29].

5 Conclusion

The linear stability problem of convective flow in a fluid-saturated rotating porous medium subject to a vertical magnetic field has been investigated under time periodic heating of the rigid boundaries. Three types of modulation effects, i.e., in-phase modulation, out-of-phase modulation, and only lower wall temperature modulation, have been considered. The solution is obtained under the assumptions that disturbances are infinitesimal, and the amplitude of the applied temperature field is small. The following conclusions are drawn:

1. For in-phase modulation, initially when ω is small the effect of modulation is destabilizing, then at around $\omega=17$ it becomes most destabilizing. The effect decreases for intermediate values of ω, becomes stabilizing on further increasing the value of ω, and finally disappears when ω becomes very large.
2. For out-of-phase modulation or when only the lower wall temperature is modulated, the effect of modulation is found to be most stabilizing near $\omega=0$. It becomes less stabilizing for intermediate values of ω, and finally disappears altogether when ω goes to infinity.
3. The value of the critical Rayleigh number R_c decreases on increasing the value of porous parameter P_l. This shows that the effect of large permeability is to advance the onset of convection in the presence of thermal modulation.
4. The results of Brinkman's model may be used to bridge the gap between the viscous fluid limit and the Darcy limit in the sense that when $P_l^{-1}\to 0$ (high permeability) we get the results of viscous fluid layer, and when $P_l\to 0$ (low permeability) we find the Darcy limit results.
5. The values of R_c in the Darcy model are found to be less than that of Brinkman's model, which clearly shows the effect of the absence of the viscous dissipation term in the Darcy model.
6. It is apparent from the results that the effect of rotation and magnetic field is to stabilize the system as, on increasing the values of Taylor number and Chandrasekhar number, the values of R_c also increase.
7. For a porous medium of small permeability the effect of rotation on convection is not much, however, at large permeability it predominates the convection. The reverse effect is found in the case of magnetic field. Here the effect of the magnetic field is large in a porous medium of small permeability; however, it is small in large permeability porous medium.

In a work now in progress, the author will study the effect of temperature modulation on rotating magnetoconvection in a porous medium for both Brinkman and Darcy models considering more realistic boundary conditions; i.e., free boundaries.

Acknowledgment

This work was carried out as part of a major research project (No. F.8-10/2003(SR)) awarded by University Grants Commission (UGC), India to the author. The financial assistance from UGC is gratefully acknowledged.

Nomenclature

a = horizontal wave number, $(a_x^2+a_y^2)^{1/2}$
a_c = critical wave number
d = depth of the porous layer
g = gravitational acceleration
k = permeability of the porous medium
κ_f = thermal conductivity of the fluid
κ_S = thermal conductivity of the solid
κ_m = effective thermal conductivity of porous media, $\delta\kappa_f+(1-\delta)\kappa_s$
p = pressure
P_l = porous parameter, k/d^2
P_r = Prandtl number, ν/κ
R = thermal Rayleigh number, $\alpha g\Delta T d^3/\nu\kappa$
Q = Chandrasekhar number, $\mu_m H_r^2 d^2/\rho_R\nu\eta$
T_a = Taylor number, $4\Omega^2 d^4/\nu^2$
R_c = critical Rayleigh number
T = temperature
θ = perturbed temperature
ΔT = temperature difference between the walls
$\mathbf{V}$ = mean filter velocity (u,v,w)
x,y,z = space coordinates
$(\rho c_p)_f$ = heat capacity of the fluid
$(\rho c_p)_s$ = heat capacity of the solid
$(\rho c_p)_m$ = relative heat capacity of the porous medium, $\delta(\rho c_p)_f+(1-\delta)(\rho c_p)_s$

Greek Symbols

α = coefficient of thermal expansion
β = thermal gradient
ϵ = amplitude of modulation
δ = porosity
γ = heat capacity ratio, $(\rho c_p)_m/(\rho c_p)_f$
κ = effective thermal diffusivity, $\kappa_m/(\rho c_p)_f$
μ_e = effective viscosity of the medium
μ = fluid viscosity
ν = kinematic viscosity, μ/ρ_R
ρ = density
ω = modulation frequency
ϕ = phase angle

Subscripts

b = basic state
c = critical
f = fluid
s = solid
R = reference value

Superscripts

$*$ =
$/$ =

Other Symbols

∇_1^2 = $\partial^2/\partial x^2+\partial^2/\partial y^2$
∇^2 = $\nabla_1^2+\partial^2/\partial z^2$
D = $\partial/\partial z$

References

[1] Nield, D. A., and Bejan, A., 1999, *Convection in Porous Media*, Springer-Verlag, New York.
[2] Patil, R. Prabhamani, and Rudraiah, N., 1973, "Stability of Hydromagnetic Thermoconvective Flow Through Porous Medium," ASME J. Appl. Mech., **E40**, pp. 879–884.
[3] Rudrauah, N., and Vortmeyer, D., 1978, "Stability of Finite-Amplitude and Overstable Convection of a Conducting Fluid Through Fixed Porous Bed," Waerme- Stoffuebertrag., **11**, pp. 241–254.
[4] Patil, P. R., and Vaidyanathan, G., 1983, "On Setting Up of Convective Currents in a Rotating Porous Medium Under the Influence of Variable Viscosity," Int. J. Eng. Sci., **21**, pp. 123–130.
[5] Rudraiah, N., 1984, "Linear and Non-linear Magnetoconvection in a Porous

Medium," Proc. Indian Acad. Sci., Math. Sci., **93**, pp. 117–135.
[6] Vadasz, P., 1992, "Natural Convection in a Porous Media Induced by the Centrifugal Body Force: The Solution for Small Aspect Ratio," ASME J. Energy Resour. Technol., **114**, pp. 250–254.
[7] Vadasz, P., 1994, "Centrifugally Generated Free Convection in a Rotating Porous Box," Int. J. Heat Mass Transfer, **37**, pp. 2399–2404.
[8] Vadasz, P., 1998, "Coriolis Effect on Gravity-Driven Convection in a Rotating Porous Layer Heated From Below," J. Fluid Mech., **376**, pp. 351–375.
[9] Alchaar, S., Vasseur, P., and Bilgen, E., 1995, "Effect of a Magnetic Field on the Onset of Convection in a Porous Medium," Heat Mass Transfer, **30**, pp. 259–267.
[10] Qin, Y., and Kaloni, P. N., 1995, "Nonlinear Stability Problem of a Rotating Porous Layer," Q. Appl. Math., **53**, pp. 129–142.
[11] Bian, W., Vasseur, P., and Bilgen, E., 1996, "Effect of an External Magnetic Field on Buoyancy Driven Flow in a Shallow Porous Cavity," Numer. Heat Transfer, Part A, **29**, pp. 625–638.
[12] Desaive, Th., Hennenberg, M., and Lebon, G., 2002, "Thermal Instability of a Rotating Saturated Porous Medium Heated From Below and Submitted to Rotation," Eur. Phys. J. B, **29**, pp. 641–647.
[13] Venezian, G., 1969, "Effect of Modulation on the Onset of Thermal Convection," J. Fluid Mech., **35**(2), pp. 243–254.
[14] Rosenblat, S., and Herbert, D. M., 1970, "Low Frequency Modulation of Thermal Instability," J. Fluid Mech., **43**, pp. 385–398.
[15] Rosenblat, S., and Tanaka, G. A., 1971, "Modulation of Thermal Convection Instability," Phys. Fluids, **14**(7), pp. 1319–1322.
[16] Yih, C. S., and Li, C. H., 1972, "Instability of Unsteady Flows or Configurations. Part 2. Convective Instability," J. Fluid Mech., **54**(1), pp. 143–152.
[17] Roppo, M. N., Davis, S. H., and Rosenblat, S., 1984, "Benard Convection With Time-Periodic Heating," Phys. Fluids, **27**(4), pp. 796–803.
[18] Bhadauria, B. S., and Bhatia, P. K., 2002, "Time-Periodic Heating of Rayleigh-Benard Convection," Phys. Scr., **66**(1), pp. 59–65.
[19] Bhadauria, B. S., 2005, "Time-Periodic Heating of a Rotating Horizontal Fluid Layer in a Vertical Magnetic Field," Z. Naturforsch., A: Phys. Sci., **60**, pp. 583–592.
[20] Bhadauria, B. S., 2006, "Time-Periodic Heating of Rayleigh-Benard Convection in a Vertical Magnetic Field," Phys. Scr., **73**(3), pp. 296–302.
[21] Catlagirone, J. P., 1976, "Stabilite D'une Couche Poreuse Horizontale Soumise a Des Conditions Aux Limites Periodiques," Int. J. Heat Mass Transfer, **18**, pp. 815–820.
[22] Chhuon, B., and Caltagirone, J. P., 1979, "Stability of a Horizontal Porous Layer With Timewise Periodic Boundary Conditions," ASME J. Heat Transfer, **101**, pp. 244–248.
[23] Rudraiah, N., and Malashetty, M. S., 1988, "Effect of Modulation on the Onset of Convection in a Porous Media," Vignana Bharathi, **11**(1), pp. 19–44.
[24] Rudraiah, N., and Malashetty, M. S., 1990, "Effect of Modulation on the Onset of Convection in a Sparsely Packed Porous Layer," ASME J. Heat Transfer, **112**, pp. 685–689.
[25] Malashetty, M. S., and Wadi, V. S., 1999, "Rayleigh-Benard Convection Subject to Time Dependent Wall Temperature in a Fluid Saturated Porous Layer," Fluid Dyn. Res., **24**, pp. 293–308.
[26] Malashetty, M. S., and Basavaraja, D., 2002, "Rayleigh-Benard Convection Subject to Time Dependent Wall Temperature/Gravity in a Fluid Saturated Anisotropic Porous Medium," Heat Mass Transfer, **38**, pp. 551–563.
[27] Malashetty, M. S., and Basavaraja, D., 2003, "The Effect of Thermal/Gravity Modulation on the Onset of Convection in a Horizontal Anisotropic Porous Layer," Appl. Mech. Eng., **8**(3), pp. 425–439.
[28] Bhadauria, B. S., 2007, "Thermal Modulation of Raleigh-Benard Convection in a Sparsely Packed Porous Medium," J. Porous Media, **10**(2), in press.
[29] Bhadauria, B. S., 2007, "Fluid Convection in a Rotating Porous Layer Under Modulated Temperature on the Boundaries," J. Porous Media, **67**(2), 297–215.
[30] Walker, K., and Hosmy, G. H., 1977, "A Note on Convective Instability of Boussinesq Fluids in a Porous Media," ASME J. Heat Transfer, **99**(2), pp. 338–339.
[31] Chandrasekhar, S., 1961, *Hydrodynamic and Hydromagnetic Stability*, Oxford University Press, London.
[32] Sastry, S. S., 1993, *Introductory Methods of Numerical Analysis*, Prentice-Hall of India Private Limited, New Delhi.
[33] Cesari, L., 1963, *Asymptotic Behavior and Stability Problems*, Springer Verlag, Berlin.
[34] Jain, M. K., Iyengar, S. R. K., and Jain, R. K., 1991, *Numerical Methods for Scientific and Engineering Computation*, Wiley Eastern Limited, New Delhi.

Critical Heat Flux of R-123 in Silicon-Based Microchannels

Ali Koşar

Yoav Peles[1]
e-mail: pelesy@rpi.edu

Department of Mechanical, Aerospace and Nuclear Engineering,
Rensselaer Polytechnic Institute,
Troy, NY 12180

Critical heat flux (CHF) of R-123 in a silicon-based microchannel heat sink was investigated at exit pressures ranging from 227 kPa to 520 kPa. *Critical heat flux data were obtained over effective heat fluxes ranging from* 53 W/cm^2 to 196 W/cm^2 *and mass fluxes from* 291 kg/m^2 s to 1118 kg/m^2 s. *Flow images and high exit qualities suggest that dryout is the leading CHF mechanism. The effect of mass velocity, exit quality, and system pressure were also examined, and a new correlation is presented to represent the effect of these parameters.* [DOI: 10.1115/1.2712852]

Keywords: critical heat flux, boiling, microchannels, flow pattern, MEMS

1 Introduction

Forced convection boiling in microchannels is recognized as an enabling heat transfer mode that can be effectively exploited to dissipate heat for future ultra-high-power density electronic components, such as integrated circuits (ICs) and laser diodes. Perhaps one of the most important limiting conditions in flow boiling systems is the critical heat flux (CHF) condition, which marks the transition from a very effective boiling heat transfer process to a very ineffective one. The sharp reduction in the local heat transfer coefficient following CHF conditions results from the replacement of liquid by vapor adjacent to the heat transfer surface. For this, the CHF sets an upper limit for the maximum heat flux that can be dissipated from a heated surface, for many practical engineering applications.

Numerous studies on forced flow boiling [1–13] and pool boiling [14–19] in conventional macrochannels and minichannels have been dedicated to collect data and elucidate the fundamental thermal and hydraulic processes leading to CHF conditions. Despite their importance in boiling, relatively limited studies have been dedicated to unveil the critical heat flux conditions in microchannels.

Conventional scale knowledge suggests that the critical heat flux is closely linked to the heat transfer mechanism (which is also connected to the flow morphology) at impending CHF conditions [20]. When the critical heat flux precedes convective boiling heat transfer mechanism, the CHF condition is a result of liquid dryout on the heated wall and the "liquid deficient region" is initiated. On the other hand, when CHF is instigated during subcooled or saturated nucleate boiling, the triggering mechanism is one where insufficient liquid is able to reach the heated surface due to the nucleation rate. Under these conditions, the heat transfer mechanism following CHF conditions is film boiling (either subcooled or saturated).

In recent years, flow boiling in microchannels has received increasing interest; nevertheless, a literature survey of recent archival papers [8,21–24] reveals the lack of general agreement regarding the dominating heat transfer mechanism pertaining to microdomains. Nucleate boiling, convective boiling, and three-zone boiling mechanisms were suggested as the controlling mechanisms. In the absence of clear understanding of the physical processes governing flow boiling in microdomains, it is imprudent to predict the CHF characteristics in microchannels without in-depth experimental studies. To ameliorate the aforementioned lack of knowledge, this paper reports an experimental study of the critical heat flux conditions of refrigerant R-123 in silicon-based microchannels. The effect of mass velocity, exit quality, and system pressure are examined and discussed. Collected data of the CHF values are compared to the results obtained in large-scale systems and also used to evaluate the mechanisms triggering the critical heat flux conditions.

2 Experimental Device

Figure 1 schematically displays the microchannel device consisting of five 1 cm long, 200 μm wide, and 264 μm deep parallel microchannels on a thin silicon substrate ($\sim$150 μm), spaced 200 μm apart. In order to minimize ambient heat losses, an air gap is formed on the two ends of the side walls, and an inlet and exit plenum are etched on the thin silicon substrate. A heater is deposited on the backside under the microchannels to deliver the heating power over the heated surface area of all microchannels (A_s) and also to serve as a thermistor for temperature measurements. Moreover, it is designed to completely overlap the planform area ($A_p = 2.1 \times 10\ mm^2 \approx 0.55 \times A_s$) of the device. A Pyrex® substrate seals the device from the top and allows flow visualization. Five orifices, each 20 μm wide 400 μm long, orifices are installed at the entrance to each channel to suppress flow instabilities. Flow distributive pillars are employed to provide homogeneous distribution of flow in the inlet. They are arranged in two columns of 12 circular pillars having a diameter of 100 μm. The transverse pitch between the pillars is 150 μm and equal to the longitudinal pitch.

3 Device Fabrication, Experimental Setup, and Experimental Procedure

3.1 Microchannel Fabrication Method. The MEMS (microelectromechanical systems) device is micromachined on a polished double-sided *n*-type ⟨100⟩ single-crystal silicon wafer employing techniques adapted from IC manufacturing. A 1 μm thick high-quality oxide film is deposited on both sides of the silicon wafer to protect the bare wafer surface during processing and serves as an electrical insulator. The heater and the vias are formed on the backside of the wafer (on top of the thermistors) by CVC sputtering. A 70 Å thick layer of titanium is initially deposited to improve adhesion characteristics, which is followed by sputtering a 1 μm thick layer of aluminum containing 1% silicon and 4% copper. Subsequent photolithography and concomitant wet bench processing create the heater on the backside of the wafer. A 1 μm thick plasma enhanced chemical vapor deposition (PECVD) oxide is deposited to protect the heater during further processing.

Next, the microchannels are formed on the top side of the wafer. The wafer undergoes a photolithography step and an oxide

[1]Corresponding author.

Contributed by the Heat Transfer Division of ASME for publication in the JOURNAL OF HEAT TRANSFER. Manuscript received March 1, 2006; final manuscript received July 10, 2006. Review conducted by Satish G. Kandlikar.

 Copyright © 2007 by ASME

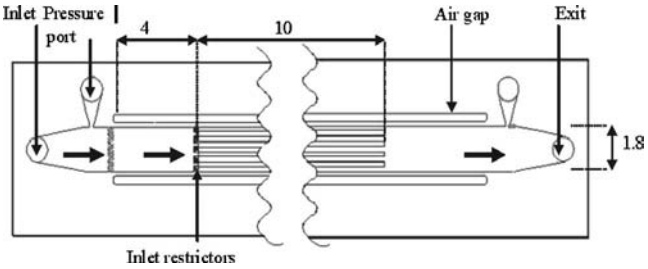

Fig. 1 CAD model of the microchannel device (units in millimeters)

removal process by reactive ion etching (RIE) to mask certain areas on the wafer that are not to be etched during the deep reactive ion etching (DRIE) process. The wafer is subsequently etched in a DRIE process, and silicon is removed from places not protected by the photoresist/oxide mask. The DRIE process forms deep vertical trenches on the silicon wafer with a characteristic scalloped side-wall possessing a peak-to-peak roughness of $\sim 0.3\ \mu$m. A profilometer and scanning electron microscope (SEM) are employed to measure and record various dimensions of the device.

The wafer is flipped, and the backside is then processed to create an inlet, outlet, side air gap, and pressure port taps for the transducers. Photolithography followed by a buffer oxide etching (BOE) (6:1) oxide removal process is carried out to create a pattern mask. The wafer is then etched through in a DRIE process to create the fluidic ports. Thereafter, electrical contacts/pads are opened on the backside of the wafer by performing another round of photolithography and RIE processing. Finally, the processed wafer is stripped of any remaining resist or oxide layers and anodically bonded to a 1 mm thick polished Pyrex (glass) wafer to form a sealed device. After the successful completion of the bonding process, the processed stack is die sawed to separate the devices from the parent wafer.

The MEMS device is packaged by sandwiching it between two plates. The fluidic seals are forged using miniature o-rings, while the external electrical connections to the heater are achieved from beneath through spring-loaded pins, which connect the heater and thermistors to electrical pads residing away from the main microchannel body.

3.2 Experimental Test Setup and Procedure. The setup, shown in Fig. 2, consists of the flow loop section, instrumentation, and a data acquisition system. The test section includes the MEMS-based microchannel device and its fluidic and thermal packaging module. The microchannel device is installed on the fluidic packaging module through o-rings to ensure a leak-proof system. The fluidic packaging delivers the working fluid to the microchannels and allows access to the pressure transducers.

The main flow loop contains the microchannel device, a pulseless gear pump, a reservoir, and a flow meter. The microheater is connected to a power supply with an adjustable DC current to provide power to the device. While the inlet pressure and test section pressure drop are collected, the boiling process in the microchannels is recorded by a Phantom V4.2 high-speed camera (maximum frame rate of 90,000 frames/s (fps), and 2 μs exposure time) mounted over a Leica DMLM microscope. Images were captured at a frame speed of 4000 fps.

Prior to the experiments, the calibration of the average heater temperature is done by placing the device in an oven. As the temperature of the oven is increased, the resistance across the device is recorded so that the heater electrical resistance-temperature calibration curve is generated. The temperature resistance curve of the aluminum heater is linear, and therefore, the electrical resistance is an accurate measure of the average temperature.

The R-123 flow rate was fixed at the desired value, and experiments were conducted after steady flow conditions were reached at the five different exit pressures. Inlet liquid temperatures were set to room temperature in all the experiments. First, the electrical resistance of the device was measured at room temperature. Thereafter, voltage was applied in 0.5 V increments to the heater, and the current/voltage data were recorded once steady state was reached. At impeding critical heat flux condition, a meager increase in the applied power causes a severe temperature rise (more than 10°C). Once this condition is attained, the power was

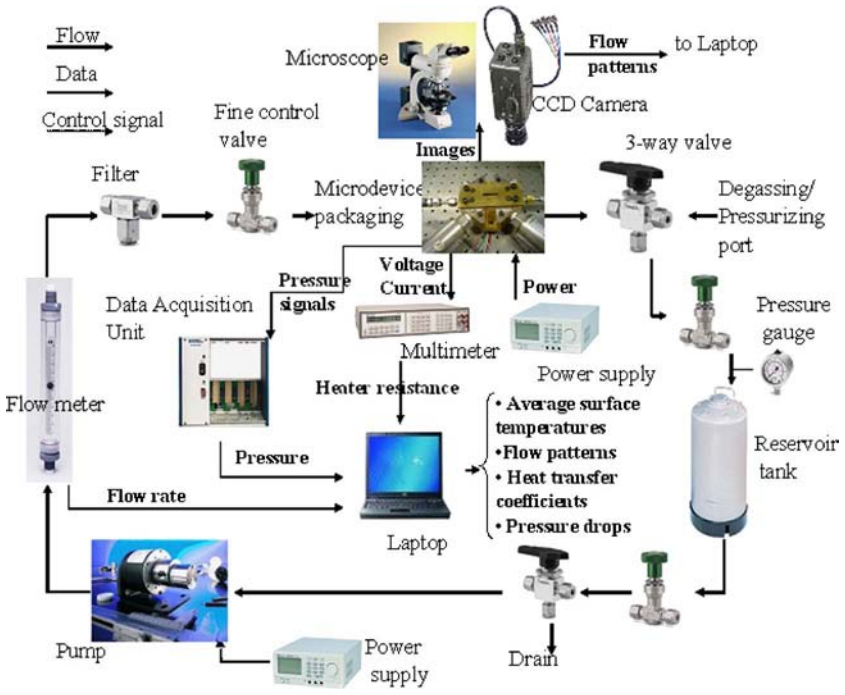

Fig. 2 Experimental setup

switched off to prevent potential burnout. Flow visualization through the high-speed camera and microscope complements the measured data. The procedure is repeated for different flow rates for each device.

To estimate heat losses, electrical power was applied to the test section after evacuating the working fluid from the test loop. Once the temperature of the test section became steady, the temperature difference between the ambient and test section was recorded with the corresponding power so that the plot of power versus temperature difference was generated to calculate the heat loss ($\dot{Q}_{\text{loss}}$) associated with each experimental data point. The heat losses were found in the light of this plot. The heat losses at the CHF condition and a system pressure of 450 kPa for $G=291$, 456, 622, 787, 953, and 1118 kg/m^2 s are estimated to be 17.7%, 11.8%, 10.4%, 8.3%, 7.4%, and 4.9%, respectively. Similar heat loss values have been obtained for the other system pressures.

4 Data Reduction and Uncertainties

Data obtained from the voltage, current, and pressure measurements were used to calculate the average surface temperature across the microchannels. The electrical input power and heater resistance, respectively, were determined with

$$P = V \times I \tag{1}$$

and

$$R = V/I \tag{2}$$

The heater electrical resistance-temperature calibration curve is used to determine the heater temperature. The surface temperature at the base of the microchannels is then calculated as

$$\bar{T} = \bar{T}_{\text{heater}} - \frac{q''_{\text{eff}} t}{k_s} \tag{3}$$

where

$$q''_{\text{eff}} = \frac{(P - \dot{Q}_{\text{loss}})}{A_p} \tag{4}$$

The critical heat flux is the heat flux based on the microchannel surface area corresponding to the critical heat flux condition and expressed as

$$q''_{\text{CHF}} = q''_{\text{eff,CHF}} \frac{A_p}{A_s} \tag{5}$$

Finally, the exit quality can be calculated with the known mass flow rate and net power supplied to the device as

$$x_e = \frac{(P - \dot{Q}_{\text{loss}}) - \dot{m} c_p (T_{\text{sat}} - T_i)}{\dot{m} h_{FG}} \tag{6}$$

Mean absolute error is used to compare the experimental results to various correlations according to the following expression

$$\text{MAE} = \frac{1}{M} \sum_{j=1}^{M} \frac{|U_{\text{exp}} - U_{\text{theoretical}}|}{U_{\text{exp}}} \times 100\% \tag{7}$$

The uncertainties of the measured values are obtained from the manufacturer's specification sheets, while the uncertainties of the derived parameters are calculated using the method developed by Kline and McClintock [25]. Uncertainties in the flow rate, pressure, average surface temperature, and critical heat flux are estimated to be 1%, 0.25%, 1 °C, and 2%, respectively.

5 Results and Discussion

5.1 Boiling Curves. Figure 3 shows the average surface temperature as a function of the heat flux at six different mass velocities for each exit pressure. During single-phase flow, the curves are linear for all mass velocities, and with the onset of nucleate boiling, the heat flux-temperature slope becomes much steeper. With increasing pressure, the saturation temperature increases and the boiling curve shifts downward as a result of increase in the inlet subcooled liquid temperature. As the heat flux is further increased, a certain value is reached where the surface temperature abruptly surges with a meager rise of heat flux, indicating the emergence of CHF conditions, which is also verified visually as dry spots near the channel exit region.

5.2 Flow Morphology. Several flow patterns were identified in this study depending on the thermal and hydraulic conditions and longitudinal position along the microchannel, which generally concur with previous studies on microchannels [21,24,26]. These are bubbly, slug, intermittent, and annular/spray-annular flow patterns. Following the single-phase flow, a region of small bubbles departing from the microchannel surface was detected and is referred to as bubbly flow region. Further downstream, the bubbles coalesce to form a slug occupying the entire microchannel cross section. At some position along the microchannel, the vapor slug becomes unstable with rapid vapor-liquid mixing. This flow pattern is denoted as intermittent flow. Further downstream, intermittent flow pattern becomes annular flow.

Two different annular flow patterns were detected depending on the mass velocity. At low mass velocity, a typical annular flow pattern consisting of a liquid sublayer around the microchannel wall (darker color) and a vapor core (lighter color) were visible (Fig. 4), whereas at high mass velocities small liquid droplets (typical size of ~3–5 μm) entrained in the vapor core were observed, and this flow is referred to as spray-annular flow.

5.3 Parametric Trends in Critical Heat Flux (CHF). In conventional macroscale systems, several independent variables are known to strongly affect CHF, namely, the inlet flow rate, the inlet temperature, the system pressure, the hydraulic diameter, the tube length, and the type of fluid such that

$$\text{CHF} = f(G, \Delta T_{\text{sub,i}}, p, d_h, L] \tag{8}$$

The inlet subcooled condition is occasionally replaced by the exit mass quality [20]

$$\text{CHF} = f(G, x_e, p, d_h, L) \tag{9}$$

Effects such as the surface finish and wall thickness might also be important but are much less understood. In the current study, three variables were parametrically studied: the mass velocity, the system pressure, and the exit quality.

5.3.1 Effects of Mass Velocity and Exit Quality. Referring to Eq. (8), CHF values were obtained as a function of mass velocity while maintaining the other four independent variables fixed. As shown in Fig. 5, the CHF increases fairly linearly with mass velocity. The increase of CHF with mass velocity is in general agreement with correlations that are based on both conventional and microscale experimental studies [6,9,20,27] and is primarily a result of the reduction in exit quality with increasing flow rate (for a given heat flux). A fairly general trend of saturated flow boiling in conventional scale studies suggests that the exit mass quality at the critical heat flux condition decreases with increasing mass velocity at fixed pressure, which concurs with the current results as shown in Fig. 6. CHF is triggered at relatively high qualities during annular flow. It is widely believed that when the flow is in the churn or annular regime an increase in flow velocity is generally accompanied by an increase in droplet entrainment in the vapor core [28]. This is also in accordance with the flow visualization study given in previous section. Since a greater portion of the liquid inventory flows as entrained droplets on the core, less liquid flows in the liquid film, making it more difficult to maintain the walls fully wetted.

Interestingly, the slopes of the curves vary with the pressure (Fig. 5). When the system pressure was maintained at 315 kPa, a maximum was obtained and CHF values were greater than for the

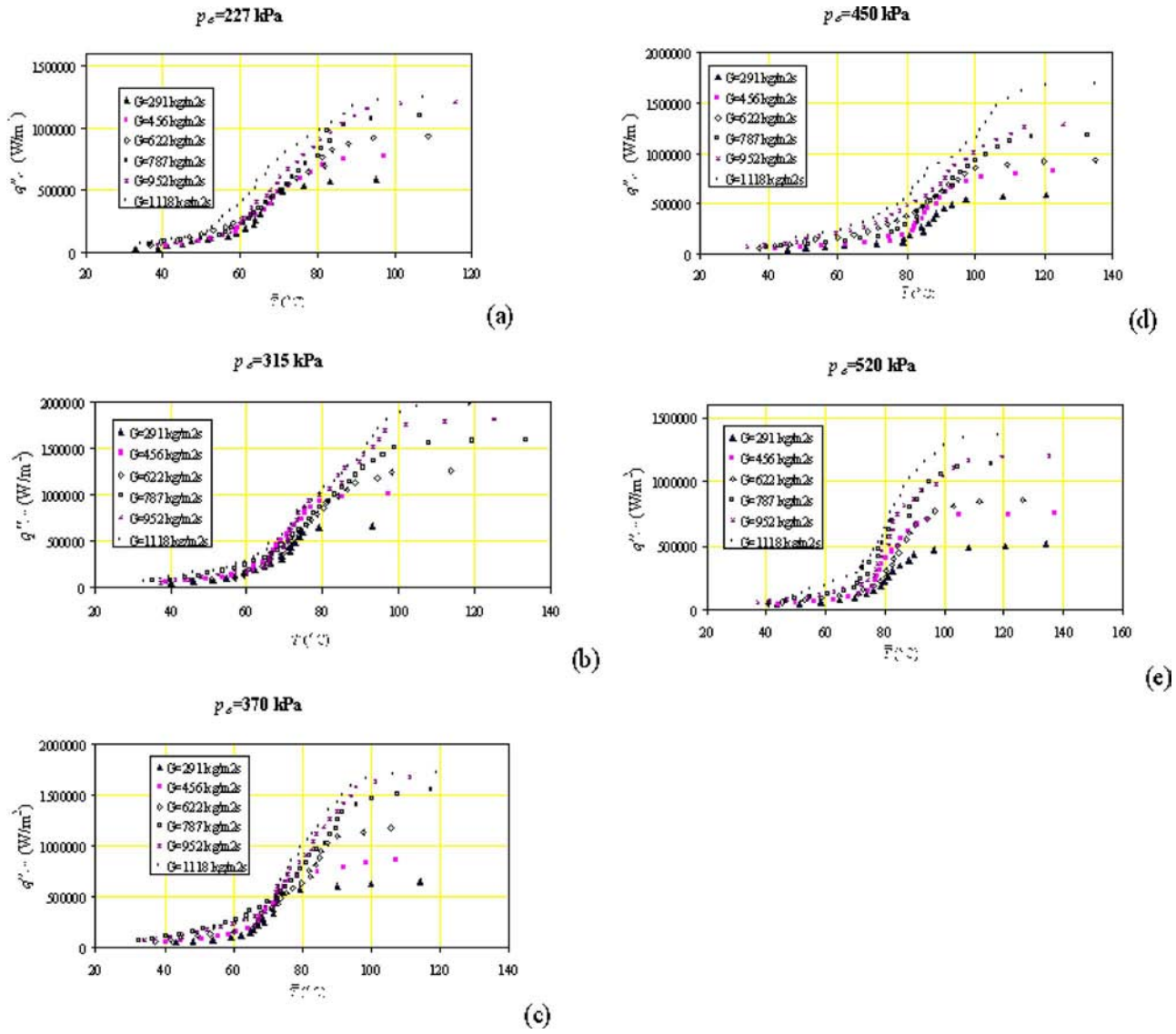

Fig. 3 q''_{eff} **versus** $\bar{T}$ **curve**

four other pressures. This suggests that an optimum pressure exists that maximizes CHF over the range of the tested pressures.

5.3.2 Effect of Pressure. Studies on the CHF advocate that the effect of pressure on CHF is very complex [27,28], and no comprehensive understanding is provided in the literature. As indicated in Sec. 5.3.1, a maximum CHF over the pressure range exists, which can be clearly seen in Fig. 7. With increasing pressure, the CHF increases until a maximum is reached at 315 kPa. The effect of pressure could not be independently isolated because several key parameters are altered when the system pressure is changed: the latent heat of vaporization, the liquid to vapor density ratio (ρ_L/ρ_G), the surface tension, and the inlet subcooled conditions. With increasing saturation pressure, the surface tension, latent heat of vaporization, and liquid-to-vapor density ratio decrease, whereas the subcooled inlet condition increases (for the same inlet temperature). As can be inferred from various correlations [6,7,9,11–13,29,30], decreasing ρ_L/ρ_G and increasing subcooled inlet temperature tend to increase CHF with increasing system pressure, whereas the decreasing surface tension and latent heat of vaporization tend to reduce CHF. The two adverse effects manifest themselves as a local maximum in the CHF value when plotted as a function of system pressure.

5.4 CHF Mechanism. Two different mechanisms leading to the CHF condition are reported in the literature [20,27,28]: departure from nucleate boiling (DNB) and dryout. Under subcooled or low-quality flow boiling conditions, where nucleate boiling is the predominant heat transfer mechanism, CHF is referred to as DNB [20,24,25], and for annular flow configuration the transition to CHF corresponds to dryout of the liquid film on the channel wall.

The annular flow patterns revealed during the visualization study suggest that CHF is a result of dryout of the liquid film on the channel wall. Figure 8 depicts the microchannel before and after the occurrence of the CHF condition. At low heat fluxes, the liquid film is relatively thick (Fig. 8(*a*)). With increasing heat flux, the film thickness diminishes (Fig. 8(*b*)), until dry spots appear on the surface near the exit region (Fig. 8(*c*)). As the heat flux is further increased, more dry spots form, and an abrupt increase in the surface temperature confirms the arrival of the CHF conditions. These visualization studies, coupled with the relatively high exit quality at CHF conditions, suggest that CHF is a result of dryout at least under the conditions tested in the present study.

5.5 Comparison to the Existing Correlations. Figure 9 displays the predictions of existing correlations recommended for the dryout mechanism, which are also listed in Table 1. Three of the

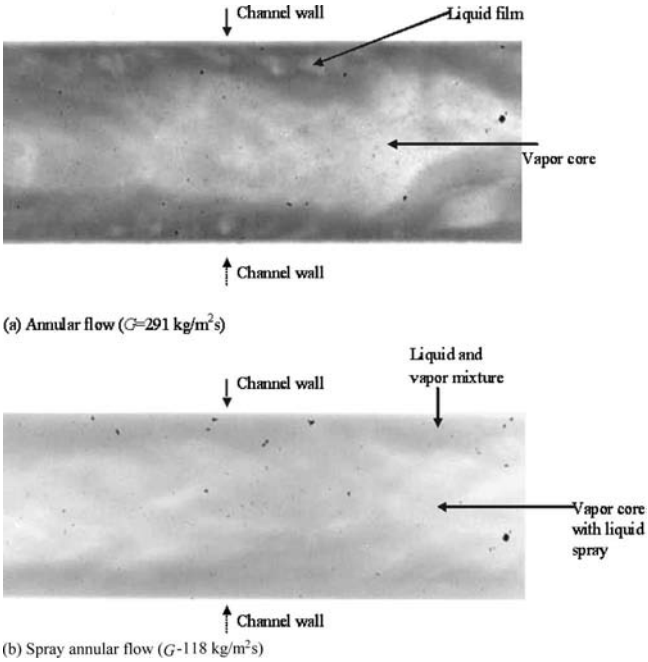

Fig. 4 Annular flow patterns

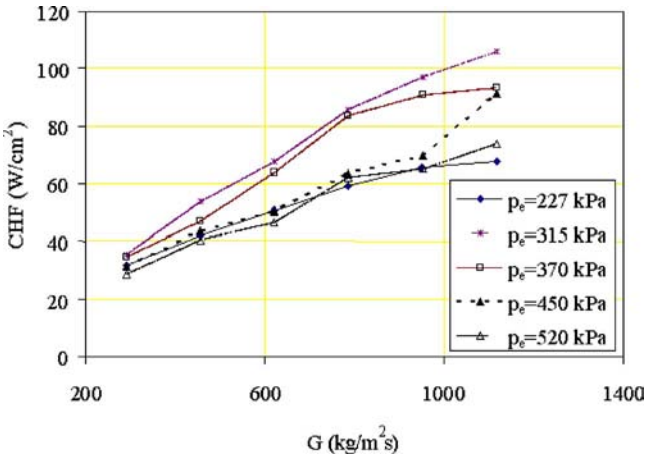

Fig. 5 q''_{CHF} dependence on G

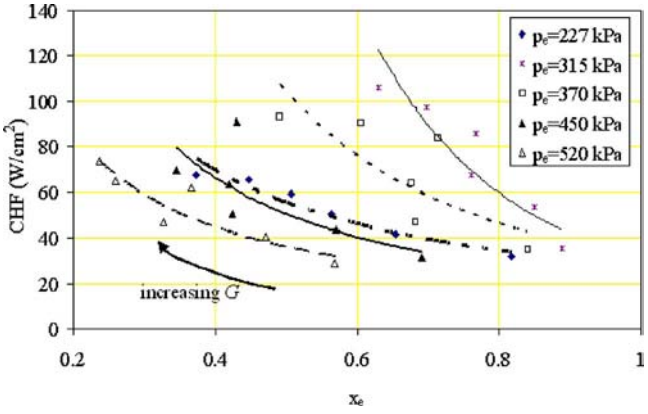

Fig. 6 CHF dependence on x_e

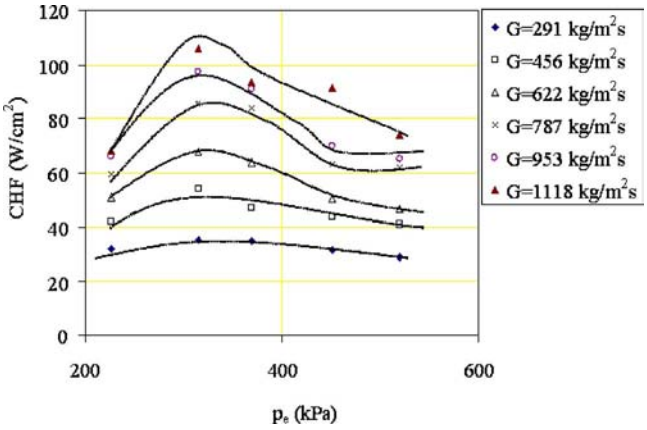

Fig. 7 CHF dependence on p_e

correlations were recommended for minichannels and microchannels, whereas the other two were developed for conventional channels. The Katto and Ohne [29] and Shah [30] correlations developed for conventional channels provided significantly better predictions with a mean absolute error of 24.7% and 26.4%, respectively. This is perhaps because these correlations account for a large range of working fluids and are based on large data set. The correlations of Koşar et al. [11] (MAE=51%), Bowers and Mudawar [6] (MAE=153.5%), and Qu and Mudawar [9] (MAE

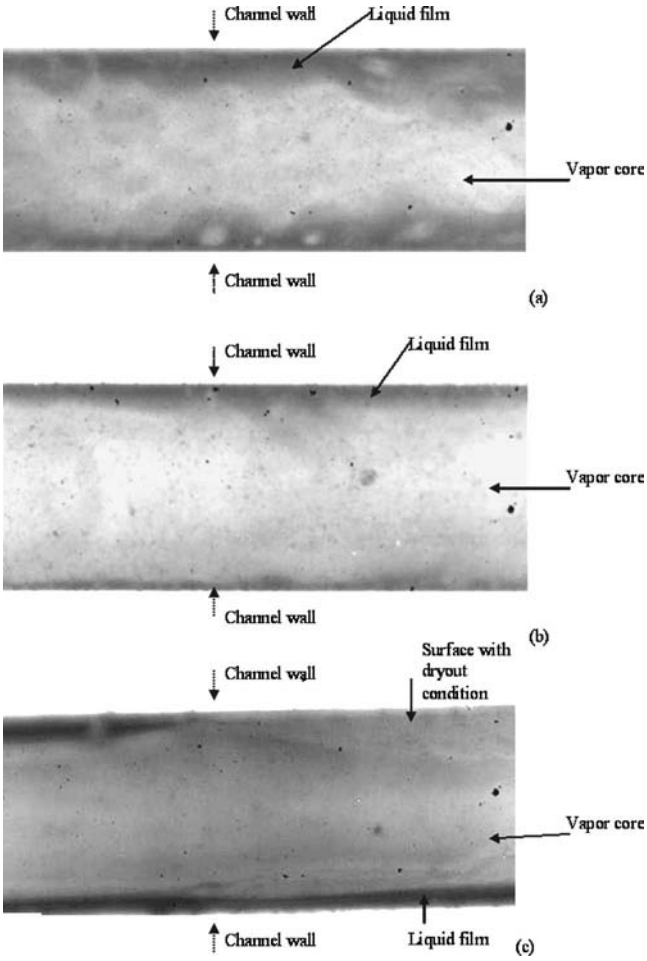

Fig. 8 Change in the annular flow pattern with heat flux (G =622 kg/m² s, p_e=315 kPa): (a) q''_{eff}=99 W/cm² (b) q''_{eff}

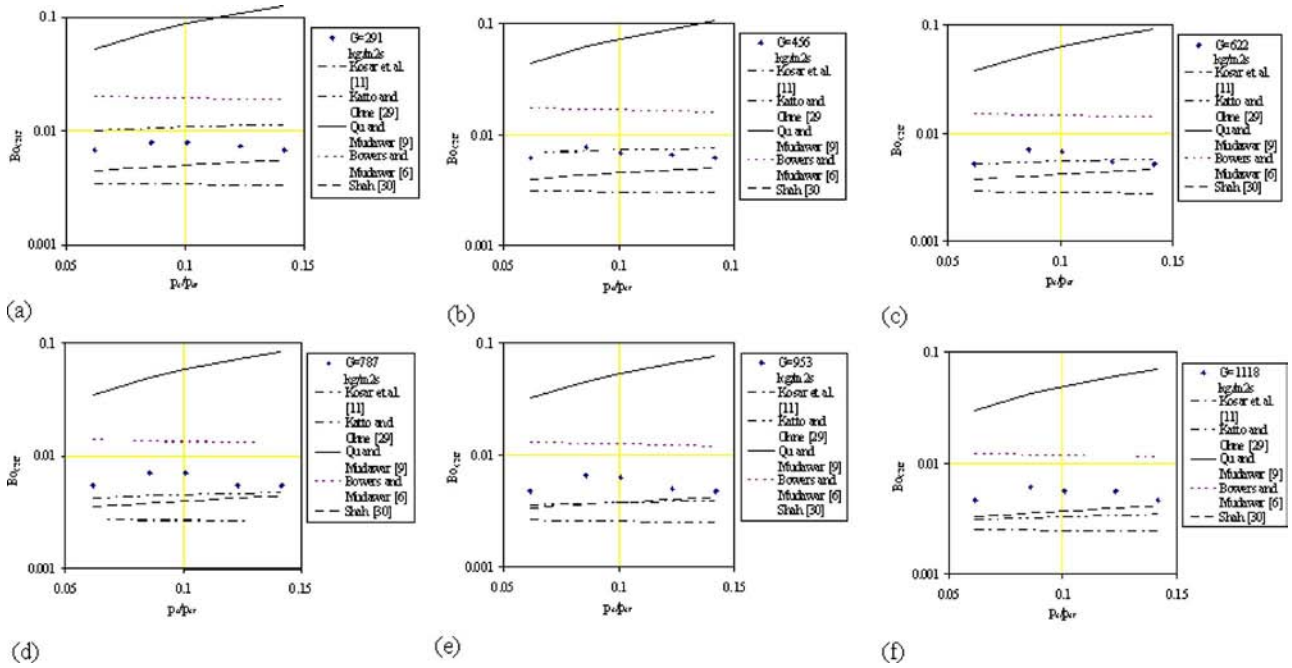

Fig. 9 Predictions of the existing correlations

=1071%) were based on results of different working fluids (water, R-113) and were generated based on limited data. Thus, the agreements of these correlations with the experimental data are not as good as those of Katto and Ohne correlation [29] and Shah [30]. It should also be noted that all existing correlations fail to follow the CHF trend with pressure. In order to account for pressure effects on CHF, the following correlation has been developed as a function of the exit pressure:

$$Bo_{\mathrm{CHF}} = \frac{q''_{\mathrm{CHF}}}{Gh_{FG}} = \left\{ \left[9.34 \times 10^{-2} \frac{p_e}{p_{cr}} - 0.34 \left(\frac{p_e}{p_{cr}} \right)^2 - 1.3 \times 10^{-4} \right] x_e^{0.59} \right\}^{1/1.08} \tag{10}$$

The above correlation successfully captures the CHF trend observed in the present study with an MAE of 3.8%. This formula-

Table 1 CHF correlations

Correlation number	Reference	Recommended channel size and fluid	Correlation	MAE (%)
1	Katto and Ohne [27]	Circular, conventional channels	$q''_{\mathrm{CHF}} = XG[h_{FG} + K(\Delta h_{\mathrm{sub}})_i]$ where $X = \dfrac{0.098(\rho_G/\rho_F)^{0.133}\left(\dfrac{\sigma\rho_F}{G^2L}\right)^{0.433}(L/d_h)^{0.27}}{1.0+0.003(L/d_h)}$ $K = \dfrac{0.261}{0.25\left(\dfrac{\sigma\rho_F}{G^2L}\right)^{0.0433}}$	24.7
2	Shah [28]	Circular, conventional channels	$q''_{\mathrm{CHF}} = 0.124Gh_{FG}\left(\dfrac{d_h}{L}\right)^{0.89}\left(\dfrac{10^4}{Y}\right)^n(1-x_i)$ where $n = \left(\dfrac{d_h}{L}\right)^{0.54}$ $Y = \left(\dfrac{Gd_hC_{P,F}}{k_F}\right)\left(\dfrac{G^2}{\rho_F^2 g d_h}\right)^{0.4}\left(\dfrac{\mu_F}{\mu_G}\right)^{0.6}$	26.4
3	Bowers and Mudawar [6]	Circular d_h=0.51-2.54 mm R-113	$q''_{\mathrm{CHF}} = 0.16Gh_{FG}\mathrm{We}^{-0.19}\left(\dfrac{L}{d_h}\right)^{-0.54}$	153.5
4	Qu and Mudawar [9]	Rectangular, d_h=0.38–2.54 mm R-113, water	$q''_{\mathrm{CHF}} = 33.43Gh_{FG}\mathrm{We}^{-0.21}\left(\dfrac{\rho_G}{\rho_L}\right)^{1.1}\left(\dfrac{L}{d_h}\right)^{-0.36}$	1071
5	Koşar et al. [11]	5 parallel rectangular channels d_h=0.223 mm Convective boiling, Water	$q''_{\mathrm{CHF}} = 0.0035Gh_{FG}\mathrm{We}^{-0.12}$	51

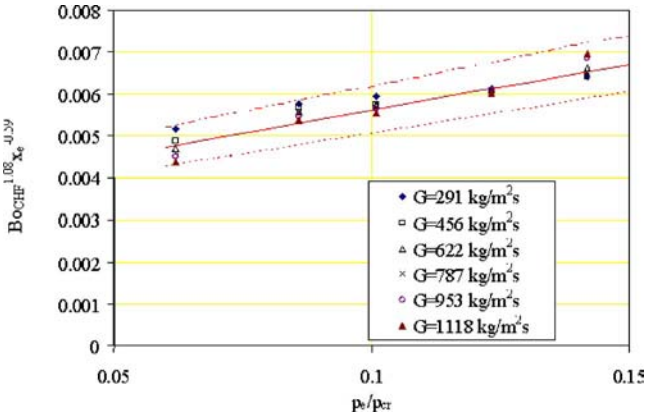

Fig. 10 Presentation of the experimental data with dimensionless parameters

tion also suggests that the data can be represented well using the Boiling number, the dimensionless pressure ratio (p_e/p_{cr}), and the exit mass quality x_e, as shown in Fig. 10.

6 Conclusions

In this study, experiments on CHF of R-123 have been conducted in a microchannel heat sink. Flow visualization aided the identification of the CHF mechanism at five different system pressures. The effects of mass velocity, exit quality, and system pressure have been also discussed. The main conclusions drawn from this study are:

- dryout is the leading CHF mechanism for boiling of R-123, at least for the experimental conditions in the present work.
- similar to previous studies, saturated flow boiling CHF increases with mass velocity and decreases with exit quality.
- increasing the pressure leads to an increase in CHF values up to a certain pressure, beyond which CHF declines.
- although some of the existing correlations provide reasonable agreement with the experimental results, none of them is able to capture the effect of system pressure on CHF. Thus, a new correlation is developed to fully represent this effect based on the trends in the experimental data.
- the experimental data can be successfully represented by three dimensionless parameters: the Boiling number, the dimensionless pressure ratio, and the exit mass quality.
- bubbly, slug, intermittent annular, and annular/spray-annular flow patterns are identified depending on the heat flux, location, and mass velocity, which is consistent with the literature.

Acknowledgment

This work was supported by the Office of Naval Research through the Young Investigator Program, under contract No. N00014-05-1-0582 (Program Officer: Dr. Mark Spector). The Facility (a member of the National Nanotechnology Infrastructure Network) which is supported by the National Science Foundation under Grant ECS-0335765, its users, Cornell University, and industrial affiliates.

Nomenclature

A_p = planform area, m^2
A_s = total heated microchannel surface area, m^2
Bo = boiling number, $Bo=q''/Gh_{FG}$
CHF = critical heat flux, W cm^{-2}
c_p = specific heat at constant pressure, kJ kg^{-1} $°C^{-1}$
d_h = channel hydraulic diameter, m
G = mass velocity, kg m^{-2} s^{-1}
h = enthalpy, kJ kg^{-1}
h_{FG} = latent heat of vaporization, kJ kg^{-1}
I = current, A
K = parameter in the CHF correlation in Table 1
k_s = thermal conductivity of the surface (silicon), W m $°C^{-1}$
L = channel length, m
M = number of data points
$\dot{m}$ = mass flow rate, kg s^{-1}
MAE = mean absolute error
n = parameter in the CHF correlation in Table 1
p = pressure, kPa
p_{cr} = critical pressure of R-123 (≈3668 kPa), kPa
P = electrical power, W
q'' = heat flux based on the heated surface area, W cm^{-2}
q''_{eff} = effective heat flux, W cm^{-2}
$\dot{Q}_{\text{loss}}$ = heat loss, W
R = electrical resistance, Ω
t = thickness of the silicon block, m
T = temperature, °C
$\bar{T}$ = average temperature, °C
$\bar{T}_{\text{heater}}$ = average temperature at the heater, °C
U = parameter being evaluated
V = voltage, V
We = Weber number, $We=G^2\ d/(\sigma\rho)$
X = parameter in the CHF correlation in Table 1
x_e = exit quality
Y = parameter in the CHF correlation in Table 1

Greek

ρ = density, kg m^{-3}
σ = surface tension, N m^{-1}

Subscripts

CHF = critical heat flux
cr = critical
e = exit
exp = experimental
F = fluid
fin = fin
G = gas
i = inlet
j = index in Eq. (7)
sat = saturation
sub = subcooled

References

[1] Lee, C. H., and Mudawar, I., 1988, "A Mechanistic Critical Heat Flux Model for Subcooled Flow Boiling Based on Local Bulk Flow Conditions," Int. J. Multiphase Flow, **14**, pp. 711–728.
[2] Weisman, J., 1992, "The Current Status of Theoretically Based Approaches to the Prediction of the Critical Heat Flux in Flow Boiling," Nucl. Technol., **99**, pp. 1–21.
[3] Katto, Y., 1994, "Critical Heat Flux," Int. J. Multiphase Flow, **20**, pp. 563–590.
[4] Vandervort, C. L., Bergles, A. E., and Jensen, M. K., 1994, "An Experimental Study of Critical Heat Flux in Very High Heat Flux Subcooled Boiling," Int. J. Heat Mass Transfer, **37**(Supp), pp. 161–173.
[5] Celata, G. P., Cumo, M., and Mariani, A., 1994, "Assessment of Correlations and Models for the Prediction of CHF in Subcooled Flow Boiling," Int. J. Heat Mass Transfer, **37**(2), pp. 237–255.
[6] Bowers, M. B., and Mudawar, I., 1994, "High Flux Boiling in Low Flow Rate, Low Pressure Drop Mini-Channel and Micro-Channel Heat Sinks," Int. J. Heat Mass Transfer, **37**(2), pp. 321–334.
[7] Ammerman, C. N., and You, W. M., 2001, "Enhancing Small-Channel Convective Boiling Performance Using a Microporous Surface Coating," ASME J. Heat Transfer, **123**(5), pp. 976–983.
[8] Kandlikar, S. G., 2004, "Heat Transfer Mechanisms During Flow Boiling in Microchannels," ASME J. Heat Transfer, **126**(1), pp. 8–16.
[9] Qu, W., and Mudawar, I., 2004, "Measurement and Correlation of Critical

Heat Flux in Two-Phase Micro-Channel Heat Sinks," Int. J. Heat Mass Transfer, **47**, pp. 5749–5763.
[10] Bergles, A. E., and Kandlikar, S. G., 2005, "On the Nature of Critical Heat Flux in Microchannels," ASME J. Heat Transfer, **127**, pp. 101–107.
[11] Koşar, A., Kuo, C. J., and Peles, Y., 2005, "Boiling Heat Transfer in Rectangular Microchannels With Reentrant Cavities," Int. J. Heat Mass Transfer, **48**, pp. 4867–4886.
[12] Koşar, A., Kuo, C. J., and Peles, Y., 2005, "Reduced Pressure Boiling Heat Transfer in Rectangular Microchannels With Interconnected Reentrant Cavities," ASME J. Heat Transfer, **127**, pp. 1106–1114.
[13] Koşar, A., Kuo, C. J., and Peles, Y., 2006, "Suppression of Boiling Flow Oscillations in Parallel Microchannels by Inlet Restrictors," ASME J. Heat Transfer, **128**, pp. 251–260.
[14] Harurama, Y., and Katto, Y., 1983, "New Hydrodynamic Model of Critical Heat Flux Applicable Widely to Both Pool and Forced Convection Boiling on Submerged Bodies in Saturated Liquids," Int. J. Heat Mass Transfer, **26**, pp. 379–399.
[15] Dhir, V. K., and Liaw, S. P., 1989, "Framework for a Unified Model for Nucleate and Transition Pool Boiling," ASME J. Heat Transfer, **111**, pp. 739–746.
[16] Sadasivan, P., Unal, C., and Nelson, R., 1995, "Perspective: Issues in CHF Modeling—The Need for New Experiments," ASME J. Heat Transfer, **117**, pp. 558–567.
[17] Golobič, I., and Bergles, A. E., 1997, "Effects of Heater-Side Factors on the Saturated Pool Boiling Critical Heat Flux," *Experimental Thermal and Fluid Science 1997*, Elsevier, New York, pp. 43–51.
[18] Howard, A. H., and Mudawar, I., 1999, "Orientation Effects on Pool Boiling Critical Heat Flux (CHF) and Modeling of CHF for Near-Vertical Surfaces," Int. J. Heat Mass Transfer, **42**, pp. 1665–1688.
[19] Kandlikar, S. G., 2001, "A Theoretical Model to Predict Pool Boiling CHF Incorporating Effects of Contact Angle and Orientation," ASME J. Heat Transfer, **123**, pp. 1071–1079.
[20] Collier, J. G., and Thome, J. R., 1994, Convective Boiling and Condensation, 3rd ed., Oxford Science Publications, Oxford.
[21] Kandlikar, S. G., 2002, "Fundamental Issues Related to Flow Boiling in Minichannels and Microchannels," Exp. Therm. Fluid Sci., **26**, pp. 389–407.
[22] Qu, W., and Mudawar, I., 2003, "Flow Boiling Heat Transfer in Two-Phase Micro-Channel Heat Sink—I. Experimental Investigation and Assessment of Correlation Methods," Int. J. Heat Mass Transfer, **46**(15), pp. 2755–2771.
[23] Bergles, A. E., Lienhard, J. H., Kendall, G. E., and Griffith, P., 2003, "Boiling and Evaporation in Small Diameter Channels," Heat Transfer Eng., **24**(1), pp. 18–40.
[24] Thome, J. R., 2004, "Boiling in Microchannels: A Review of Experiment and Theory," Int. J. Heat Fluid Flow, **25**, pp. 128–139.
[25] Kline, S., and McClintock, F. A., 1953, "Describing Uncertainties in Single-Sample Experiments," Mech. Eng. (Am. Soc. Mech. Eng.), **75**(1), pp. 3–8.
[26] Cornwell, K., and Kew, P. A., 1992, "Boiling in Small Parallel Channels," Energy Efficiency Process Technol., **37**(2), pp. 624–638.
[27] Celata, G. P., and Mariani, A., 1999, *CHF and Post-CHF (Post-Dryout) Heat Transfer-Handbook of Phase Change: Boiling and Condensation*, Taylor&Francis, New York, pp. 443–493.
[28] Carey, V. P., 1992, *Liquid-Vapor Phase Change Phenomena*, Hemisphere, New York, pp. 483–564.
[29] Katto, Y., and Ohne, H., 1984, "An Improved Version of the Generalized Correlation of Critical Heat Flux for Convection Boiling in Uniformly Heated Vertical Tubes," Int. J. Heat Mass Transfer, **27**(9), pp. 1641–1648.
[30] Shah, M. M., 1987, "Improved General Correlation for Critical Heat Flux During Upflow in Uniformly Heated Vertical Tubes," Int. J. Heat Fluid Flow, **8**(4), pp. 326–335.

Solidification Microstructure Evolution Model for Laser Cladding Process

Y. Cao

J. Choi
e-mail: jchoi@umr.edu

Department of Mechanical and Aerospace Engineering,
University of Missouri-Rolla,
Rolla, MO 65409-1060

The laser cladding process inherently includes multiscale, highly nonlinear, and nonequilibrium transport phenomena due to nonuniform and rapid heat flow caused by the laser and the material interaction. In this work, a process model of solidification microstructure evolution for the laser cladding process has been studied by utilizing a phase-field method. The phase-field method has become a widely used computational tool for the modeling of solidification micro-structure evolution with the advantage of avoiding tracking the interface explicitly and satisfying interfacial boundary conditions. In the present work, the numerical solutions of a phase-field model have been analyzed. The linking of the macroscale process and solidification microstructure evolution was examined by considering the relationship of macro- and micro-parameters. The effects of melt undercooling and anisotropy on the solidification micro-structure have also been studied. The predicted results with different undercoolings were compared with the microsolvability theory and a good agreement was found. Different solidification morphologies of different locations in the melt-pool are also investigated. To quantitatively study the effect of heat flux on the dendritic growth, the dendrite tip analysis was carried out. It was observed that the dendrite tip that grows in the same direction with the heat flux shows a much higher velocity than a tip that grows in the opposite direction of the heat flux. [DOI: 10.1115/1.2712856]

Keywords: laser cladding, solidification microstructure, phase-field model, multi-scale model

1 Introduction

Laser cladding is an additive manufacturing process in which a laser generates a melt-pool on the substrate material while a second material in a powder or wire form is injected into that melt-pool. The cladding alloy can form a strong bond to the substrate, with a minimum melting of the substrate. Among all laser processes, laser cladding offers the most extensive variety of possibilities to alter a component at its surface. For example, laser cladding can be used for the protection of materials against wear, corrosion, and oxidation, and for refurbishing a high cost industrial product by using a coating with improved properties.

The laser cladding process inherently includes multiscale, highly nonlinear, and nonequilibrium transport phenomena due to nonuniform and rapid heat flow caused by the laser and the material interaction. In these complex phenomena, thermal transport, fluid flow, and mass transport in the melt pool can be modeled on a macroscopic scale, while the solute diffusion in the mushy zone and the solidification process should be studied on a meso/microscale. Heat and fluid flow have been studied numerically and experimentally by other researchers [1,2]. There are many researchers who observed the microstructure evolution of the laser cladding process by using optical, scanning and transmission electron microscope techniques [3–6]; however, the modeling of micro-structure evolution of the solidification process during the laser cladding has not been fully developed and studied. Therefore, there is a growing demand to develop systematic modeling and simulation approaches for the multiscale problem.

There are two different sets of ideas to model the multi-scale problem. The first set of ideas [7] is to pre-define a set of coarse-grained variables. By expressing the microscopic model in terms of the coarse-grained variables, one can derive a relationship that expresses the macroscopic data in terms of microscopic quantities. This relationship is a starting point of micro/macrocoupling. The other set of ideas [8] is to divide the computation domain into macro- and micro-regions. Separate models are used in different regions and an explicit matching condition is used to bridge the two regions. The latter method is employed in current study to coupling the macroscopic laser cladding process and microscopic solidification process.

Phase-field method has recently become a widely used technique to model the formation of complex interfacial patterns in the solidification process. It has been the main topic of recent literature reviews [9–11]. The most valuable property of the phase-field model is the fact that there is no need to explicitly track the interface or even provide interfacial boundary conditions [12]. Wheeler, Boettinger, and McFadden developed the so-called WBM phase-field model to deal with alloy solidification [13,14]. This model was derived in a thermodynamically consistent way and used to study the solute trapping of the isothermal binary alloy in rapid solidification [15]. It was shown that the solute trapping occurs when the solute diffusion length is comparable to the diffuse interface thickness. This model has been widely used in many applications, including dendrite growth, solute trapping, eutectic solidification, sidearm branching, etc. [9]. Kim et al. [16] proposed another phase-field model by using a different definition of the free energy density for the interfacial region. This model was used to study the binary alloy solidification and dendrite growth. Their results are in good agreement with the experimental observations. Wheeler et al. [13] have shown that the interface thickness must be smaller than the capillary length for the solution to converge to the sharp-interface limit. Karma and Rappel [17] reconsidered this issue and proposed a thin interface analysis. They found that the interface thickness only needs to be small compared to the "mesoscale" of the heat and/or solute diffusion field. Their asymptotic analysis greatly enhanced the computa-

Contributed by the Heat Transfer Division of ASME for publication in the JOURNAL OF HEAT TRANSFER. Manuscript received May 1, 2006; final manuscript received August 10, 2006. Review conducted by Suresh V. Garimella.

 Copyright © 2007 by ASME

tional efficiency of the phase-field simulation and they made the first fully resolved computations for three-dimensional dendritic growth [18,19]. Beckermann et al. [12,20,21] further conducted much effective work in this area. They presented a simpler derivation of the phase-field equation starting from the classical velocity-dependent Gibbs-Thomson interface condition. They also studied the pure metal dendritic growth, binary alloy solidification coupled with heat and solute diffusion, and the solidification phenomena with fluid flow [21].

Very few models for microstructure evolution of laser cladding process have been reported [3,22], and almost all the above models [12–21] were used to deal with the ideal process (pure metal, isothermal binary alloy, etc.). Zhang et al. [23] developed a numerical diffusion model to simulate the kinetics of the austenite to ferrite transformation in 2205 duplex stainless steel during welding. They confirmed their results by experiments using an X-ray diffraction technique. However, their model is limited in one-dimensional. In this paper, a two-dimensional phase-field model based on Karma and Ramirez's analysis [19,20] was developed to explore the microstructure evolution in a real physical process, laser cladding. The anisotropy effect was included in this model, while the interface kinetics was neglected by properly choosing the calculation parameters. This phase-field model was coupled with the macroprocess model and served as microscale model to simulate the laser cladding process.

This paper is structured as follows: The macroscale model of laser cladding process is presented first. This model is used to get the macrotemperature field and other related physical parameters, and followed by the phase-field model. The linking between the macroscale model and phase-field model is carried out, considering the relationship of the macro- and microscale process parameters. The phase-field model is validated, comparing the interface shape and dendrite tip velocity with other researchers' results for pure metal dendrite growth. Next, a typical two-dimensional binary alloy dendrite growth is presented for the case of coupled heat and solute diffusion. The effects of melt undercooling and anisotropy on the final micro-structure have also been studied. Different solidification morphologies of different locations in the melt-pool are also investigated.

2 Macroscale Model

The macro-scale model was used in this study to get the macroscale temperature field, which will be used in the phase-field calculation. The transport phenomena in the melt-pool were studied, including the melt-pool shape and size. Most work in this section is based on the previous study of the author's research group [24].

The basic assumptions of this model are as follows:

1. A laser beam having a defined power distribution strikes the surface of an opaque material of finite depth and length.
2. Only part of the energy is absorbed by the workpiece and powder. Studies show that the amount of laser energy absorbed by the different materials is 37–60% [25,26]. However, in this study, the absorptivity of laser power was chosen as 0.3 with the consideration of the substrate material property and the surface condition of the substrate. It should be noted that further experiment work needs to be done to verify this assumption.
3. The absorbed energy induces surface tension driven flow due to the high-temperature gradient.
4. The liquid metal is Newtonian, so the Navier-Stokes equation is applicable. Given the small velocity of fluid flow (about 0.1 m/s) in the melt-pool and characteristic distance (about 0.5–1.5 mm), the Reynolds number can be approximated as about 57.5–172 by using the material properties shown in Table 1, which is fairly below the 500 usually used as the limit for laminar flow in open channels. Thus, the fluid flow in the melt-pool can be assumed to be laminar.
5. All properties of the liquid and solid metal are constant, independent of temperature. (This allows simplifications of the model; however, variable properties can be treated with slight modifications.)

Table 1 Material properties and process parameters

Property	Symbol	Value
Powder absorptivity	β_1	0.35
Power absorptivity	β_2	0.3
Specific heat of liquid	c_{pl}	800 J/(kgK)
Specific heat of solid	c_{ps}	700 J/(kgK)
Diameter of powder	D	120 μm
Conductivity of liquid	k_l	21 W/(mK)
Conductivity of solid	k_s	21 W/(mK)
Latent heat of melt	L_m	2.7×10^5 J/kg
Latent heat of evaporation	L_v	6.34×10^6 J/kg
Powder mass rate	m_p	5 g/min
Power of laser beam	P_{laser}	1000 W
Density of liquid	ρ_l	6900 kg/m^3
Density of solid	ρ_s	7800 kg/m^3
Radius of laser beam	R	0.7 mm
Liquidus temperature	T_l	1700 K
Solidus temperature	T_s	1630 K
Melting temperature	T_m	1665 K
Dynamic viscosity	μ_l	6×10^{-3} kg/(ms)
Velocity of laser beam	V_{laser}	12.7 mm/s
Powder velocity	V_{powder}	0.15 m/s

2.1 Governing Equations. The continuity equation, momentum equation, and energy equations based on the continuum formulation are modified and used in the present study.

The continuity equation is shown in Eq. (1)

$$\frac{\partial}{\partial t}(\rho)+\nabla\cdot(\rho\mathbf{V})=0 \tag{1}$$

The momentum equations are shown in Eqs. (2) and (3)

$$\frac{\partial}{\partial t}(\rho u)+\nabla\cdot(\rho\mathbf{V}u)=\nabla\cdot\left(\mu_l\frac{\rho}{\rho_l}\nabla u\right)-\frac{\partial p}{\partial x}-\frac{\mu_l}{K}\frac{\rho}{\rho_l}(u-u_s) \tag{2}$$

$$\frac{\partial}{\partial t}(\rho v)+\nabla\cdot(\rho\mathbf{V}v)=\nabla\cdot\left(\mu_l\frac{\rho}{\rho_l}\nabla v\right)-\frac{\partial p}{\partial y}-\frac{\mu_l}{K}\frac{\rho}{\rho_l}(v-v_s)+\rho\cdot g \tag{3}$$

The energy equation is shown in Eq. (4)

$$\frac{\partial(\rho h)}{\partial t}+\nabla\cdot[(\rho\mathbf{V}h)=\nabla\cdot(k_t\nabla T)-\nabla\cdot(\rho(h_l-h)(\mathbf{V}-\mathbf{V}_s))] \tag{4}$$

The evolution of free surface is expressed in Eq. (5)

$$\frac{\partial F}{\partial t}+(\mathbf{V}\cdot\nabla)F=0 \tag{5}$$

Note that the momentum and energy equations contain the phase interaction terms. In Eqs. (1)–(4), the subscripts "l" and "s" denote liquid and solid, respectively. The density ρ and thermal conductivity k_t are defined as the average value of liquid and solid state based on the solid volume fraction g_s and liquid volume fraction g_l. The specific heat c_p, velocity $\mathbf{V}$, and the enthalpy h are defined as the average value of the liquid and solid states based on the solid mass fraction f_s and liquid mass fraction f_l. u and u are the X and Y components of velocity, respectively. u_s and v_s are the tangential and normal velocity components at the free surface, respectively. K is the permeability of the two-phase mushy region, which is modeled as a porous media. μ_l is the dynamic viscosity.

In Eq. (5), F expresses the fractional volume occupied by fluid in that computational cell. F takes a value of unity at a cell in a

space occupied by fluid and a value of zero if fluid does not occupy that cell, and cells with F value between zero and unity are partially filled with fluid and identified as surface cells. The liquid-vapor interface is located at the $F=0.5$ contour.

2.2 Boundary Conditions. With the liquid-vapor free surface, the shear stress and normal stress balance is considered to get the boundary condition of the velocity at the free surface. The energy balance included the effect of laser heating, as well as heat loss from convection, radiation, and evaporation. With other boundary surfaces, the velocity is considered to be zero and the energy balance takes into account the heat loss from convection and radiation. Details of the formulations for the boundary conditions can be found in Ref. [24].

3 Phase-Field Model

One macrocell adjacent to the solid-liquid interface will be chosen to carry out the microstructure evolution calculation. Thus, the whole calculation domain will be this macrocell. The behavior of the phase-field variable in this domain is governed by the phase-field equation, which is coupled with equations for heat and solute diffusion. The interface between liquid and solid is represented by a smooth but rapid change of the phase-field variable. The following assumptions were made for the phase-field model:

1. Influence of fluid flow is not considered in the phase-field model. A forced fluid flow can significantly affect the pattern of solidification, which is shown by other researchers in this area [12,21]. However, in this study, a laminar flow is assumed and only a very tiny macrocell is picked up to carry out the micro-phase-field calculation. Thus, the effect of fluid flow is neglected for the simplicity of the calculation.
2. The thermophysical properties such as thermal conductivity, specific heat, density, and so on are assumed to be constant and equal in the liquid and solid states.
3. Considering the solute diffusivity in the solid state is very small compared with that in the liquid state, the solute diffusion in the solid state is neglected.
4. The interface kinetics effect is neglected.
5. For the sake of simplicity, the partition coefficient of the solidification process is assumed to be the same as the one in the equilibrium state.

3.1 Governing Equations. To compare the result with other researchers, the dimensionless temperature and composition are employed as in Eqs. (6) and (7):

$$\theta = \frac{T - T_m - mc_\infty}{L/c_p} \tag{6}$$

$$\chi = \frac{c - c_\infty}{(1-k)c_\infty} \tag{7}$$

where T_m is the melting temperature of pure solvent; m is the liquidus line slope of the alloy phase diagram; c_∞ is the value of composition c far from the interface, which equals the initial composition of the alloy; L is latent heat of melting; and k is the equilibrium partition coefficient. It should be noted here the dimensionless undercooling has the same value as the dimensionless temperature with opposite sign. Additionally, the following dimensionless variables are defined in Eqs. (8) and (9)

$$z = \ln\left[\frac{2c/c_\infty}{1+k-(1-k)\phi}\right] \tag{8}$$

and

$$U = \frac{e^z - 1}{1-k} \tag{9}$$

where z is a dimensionless measure of the deviation of the chemical potential from its equilibrium value at a reference temperature, and U is used to change the variable of the composition equation and is considered to be the dimensionless composition.

The phase-field equation, composition equation, and energy equation are obtained in terms of the dimensionless temperature and composition as follows [20]

$$\tau\frac{\partial\phi}{\partial t} = W^2\nabla^2\phi + \phi - \phi^3 - (1-\phi^2)^2\lambda(\theta + Mc_\infty U) \tag{10}$$

$$\frac{1+k}{2}\frac{\partial U}{\partial t} = \frac{1}{2}\frac{\partial}{\partial t}\{\phi[1+(1-k)U]\} + \nabla\cdot\left\{D\frac{1-\phi}{2}\nabla U + \frac{W}{2\sqrt{2}}[1+(1-k)U]\frac{\partial\phi}{\partial t}\frac{\nabla\phi}{|\nabla\phi|}\right\} \tag{11}$$

$$\frac{\partial\theta}{\partial t} = \alpha\nabla^2\theta + \frac{1}{2}\frac{\partial\phi}{\partial t} \tag{12}$$

where τ is the relaxation time in the phase-field model, W is the interface thickness, λ is a dimensionless parameter that controls the strength of the coupling between the phase and thermal/solutal diffusion fields, and D is the solutal diffusivity in the liquid. M is the scaled liquidus slope, which is defined as

$$M = \frac{-m(1-k)}{L/c_p} \tag{13}$$

To eliminate the interface kinetics, τ is chosen to be a function of U in the phase-field model, which is defined in Eq. (14)

$$\tau = \tau_0\left\{\frac{D}{\alpha} + Mc_\infty[1+(1-k)U]\right\} \tag{14}$$

where τ_0 is the measure scale of time in this study.

It should be noted the governing equations used in this study are exactly the same as those in Ref. [20]. This microscopic phase-field model was coupled with the macrothermal model to investigate the solidification process during laser cladding. With the parameters involved in this model, for example, τ, W, λ, D, and ε_4, the same values were taken as those in [20] to compare the results of current model with the available results in literature.

3.2 Anisotropy Effect. To include the anisotropy effect, a standard fourfold anisotropy was chosen as in Eqs. (15) and (16)

$$W(n) = W_0 a_s(n) \quad \tau(n) = \tau_0 a_s^2(n) \tag{15}$$

$$a_s(n) = 1 - 3\varepsilon_4 + 4\varepsilon_4\frac{(\partial\phi/\partial x)^4 + (\partial\phi/\partial y)^4}{|\nabla\phi|^4} \tag{16}$$

Combining Eqs. (14)–(16), Eq. (17) is obtained

$$\tau = \tau_0 a_s^2(n)\left\{\frac{D}{\alpha} + Mc_\infty[1+(1-k)U]\right\} \tag{17}$$

In this manner, the anisotropy effect can be incorporated and the interface kinetics can be eliminated at the same time.

3.3 Boundary Conditions. The temperature boundary condition can be obtained from the macroneighbor cells of the selected cell. The outermost microcells were set to time-dependent temperatures, which were calculated by interpolating the nearest neighbor macrocell temperature to the boundary. Because it is assumed there is no fluid flow in the previously selected cell, there is also no convective mass flow between the whole calculation domain and the neighbor cells. Considering the quite small rate of solute diffusion process, the Dirichlet boundary condition is also applied for the composition field. To the phase-field variable, a zero-flux Newmann condition is employed to describe the boundary of the calculation domain with the coupling scheme, while in the pure metal and binary alloy case, the constant value is chosen as the phase-field boundary condition.

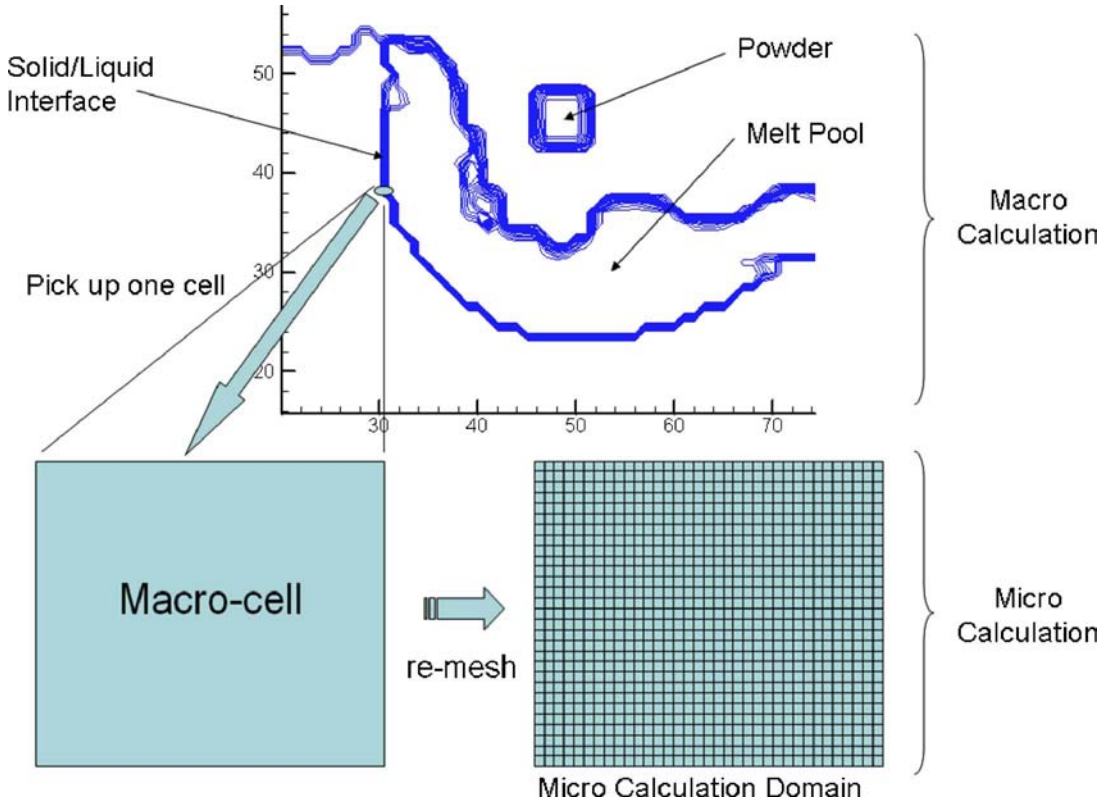

Fig. 1 Scheme of macro/micro-scale coupling method

4 Numerical Method

In the present study, the macro-model was employed to calculate the temperature, fluid pressure, and velocity fields of the whole calculation domain. Each macrocell had four state variables: temperature, pressure, velocity, and fractional volume (F). One macrocell near the solid-liquid interface was chosen to carry out the microscale calculation in order to simulate the evolution of the solidification microstructure. This macrocell was re-meshed, making much finer microcells. Each microcell had three state variables: temperature, phase-field, and concentration. In the temporal domain, there were two time steps: Δt for macro-calculation and much smaller δt for phase-field calculation. Each Δt was again divided into five small microtime steps in current calculation. Figure 1 shows this macro- and microscale coupling scheme.

To couple the two different scale calculations, the temperature of the neighbor cells of the micro-calculation domain was applied as the temperature boundary condition. In each macro-time step, this boundary temperature was considered to be constant. At the next macrotime step, this boundary temperature was changed to another value, which was determined by the macroscale model.

A semi-implicit solution algorithm–volume of fluid (SOLA-VOF) [27] based algorithm was used for the solutions of the continuity and momentum equations (1)–(3) in the macroscale model. The thermal energy transport equation (4) was solved using an explicit finite volume approximation. A fixed-grid system of 200 $\times$ 100 uniform grid points was utilized for the cladding domain of 4 mm $\times$ 2 mm. Each grid had a cell size of 20 μm $\times$ 20 μm. An explicit finite difference scheme was used to solve the phase-field equation, composition equation, and energy equation as described in Eqs. (10)–(12) in the microscale model. The grid numbers used in this study were either 1000 $\times$ 1000 or 1500 $\times$ 1500 in different cases.

It was assumed that the nucleation began under a certain undercooling. Initially, the micro-calculation domain was filled with an amount of supercooled melt. Once the undercooling reached the given value, the nucleation took place instantly and a solid seed was present in the center of the calculation domain. After this, the growth process of the solid seed was controlled by the phase-field model and appropriate boundary conditions.

4.1 Iteration Procedures. The steps of the iteration procedure for the macroscale calculation were as follows:

(1) Initialize the velocities, pressure, temperature, and VOF function.
(2) Solve the momentum equations utilizing a two-step projection method. Surface tensions are solved and included into the momentum equations as body forces. In this step, new velocities and pressure are solved.
(3) Advance the VOF function in the time domain to update the new free surface.
(4) Solve the energy equation using new velocities obtained in Step 2.
(5) Check the undercooling. If it reaches the given value, then the phase-field calculation will begin. If not, go to Step 6.
(6) Update old velocities, pressure, temperature, and the VOF function using new values, then go back to Step 2 for the next iteration until the time to finish the calculation is reached.

The iteration procedures for the micro-calculation are as follows:

(1) Initialize the temperature, composition, and phase-field variable.
(2) Solve the phase-field equation utilizing an explicit finite difference method.
(3) Solve the composition equation using new phase-field variables obtained in Step 2.
(4) Solve the energy equation using the new phase-field variable obtained in Step 2.
(5) Update the old temperature, concentration, and phase-field

variable using the new values, then go back to Step 2 for the next iteration until the phase-field or composition field reach the boundary of the calculation domain (i.e., the values of phase-field variable or composition changes more than 5%).

4.2 Numerical Stability. With the macroscale calculation, the numerical difference equations are subjected to linear numerical stability conditions that are detailed in [28].

For the phase-field model, the time step is determined by Eq. (18)

$$\delta t = \frac{1}{4}\min(\delta t_1, \delta t_2) \tag{18}$$

where

$$\delta t_1 = \frac{1}{2\alpha}(\Delta x^2 + \Delta y^2) \quad \delta t_2 = \frac{\tau_0 \Delta x^2}{W_0^2} \tag{19}$$

δt_1 is derived from the thermal energy equation and δt_2 is derived from phase-field equation. It is difficult to determine the stable time step for the composition equation. However, from the numerical test, it was found that the time step determined by Eq. (18) can keep the composition calculation stable.

5 Simulation Results and Discussion

The results of different cases are presented in this section. First, the macroscale process was simulated using the macroscale model developed above. To validate the current microscale model, a pure metal solidification case was calculated and compared with the micro-solvability theory [19]. A binary alloy dendrite growth was also simulated. Finally, three coupling cases were calculated with different locations in the melt pool. Simulations of all the cases were based on the material properties of H13 tool steel, and the process parameters are shown in Table 1. To make the calculation simple, the material used in this study was assumed to be a binary alloy.

5.1 Results by Macro-Scale Model. To carry out the phase-field calculation, the macroscale model was used first to calculate the whole domain temperature field. Several snapshots of the calculation results are shown in Fig. 2. Figure 2(*a*) shows the temperature field at the simulation time 40 ms, and every 5 ms until 55 ms, as shown in Figs. 2(*b*)–2(*d*). Figure 2 also shows the powder injection process. From Figs. 2(*b*) and 2(*c*), it can be clearly seen that the first two powders appeared in Fig. 2(*b*), and then fell into the melt pool as shown in Fig. 2(*c*).

5.2 Pure Metal Dendrite Growth. To validate the current phase-field model, a pure metal solidification case was calculated. In a pure metal case, only the phase-field equation and thermal equation need to be solved. And the Mc_∞ term in the phase-field equation should be zero in this pure metal solidification case. The dimensionless undercooling threshold value was 0.55 in the present study. According to Karma [19], the length of the solidification microstructure was scaled by W_0 and the time by τ_0. Setting $W_0=1$ and $\tau_0=1$, other parameters used in this pure metal calculations were adopted from [19] as follows: $\lambda=6.3829$, $\alpha=4$, $\Delta x=\Delta y=0.4$, $\delta t=0.008$, and $\varepsilon_4=0.05$. The grid number was 1000×1000. Only the first quarter of the calculation domain was calculated considering the symmetry. For the comparison with Karma's results, the interface shape was calculated as shown in Fig. 3(*a*), and the interface position was chosen at the $\phi=0$ contour, which was calculated every 5000 iterations. It is evident that this interface shape is almost identical to that of Karma's [19], which confirmed that this model is qualitatively correct.

The dendrite tip velocity was also calculated in this pure metal case according to Eq. (20)

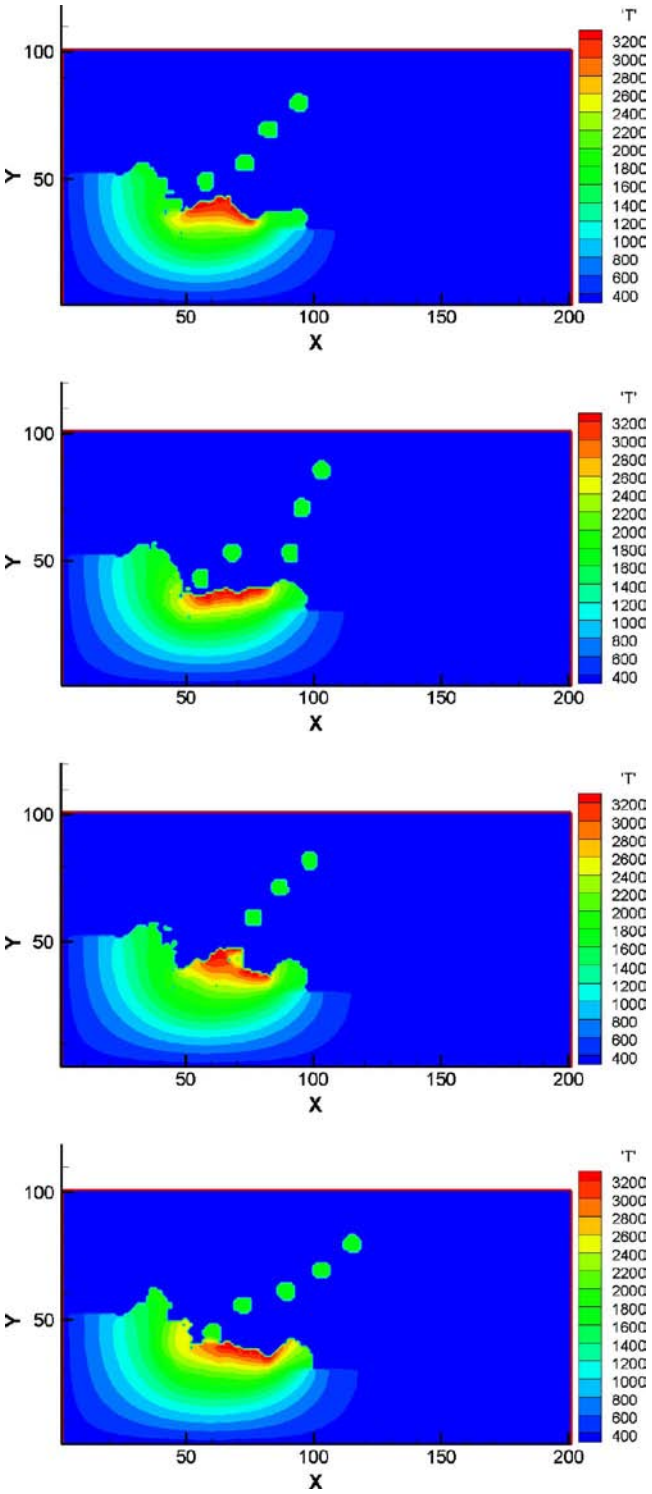

Fig. 2 Calculation results of macro-model (powder velocity 0.15 m/s, powder diameter 120 μm, laser beam power 1000 W, radius of laser beam 0.7 mm, powder interval 0.2 ms, and laser absorptivity, 0.3)

$$V_{\text{tip}} = \frac{\partial \phi / \partial t}{|\nabla \phi|} \tag{20}$$

The dimensionless dendrite tip velocity is calculated based on Eq. (21)

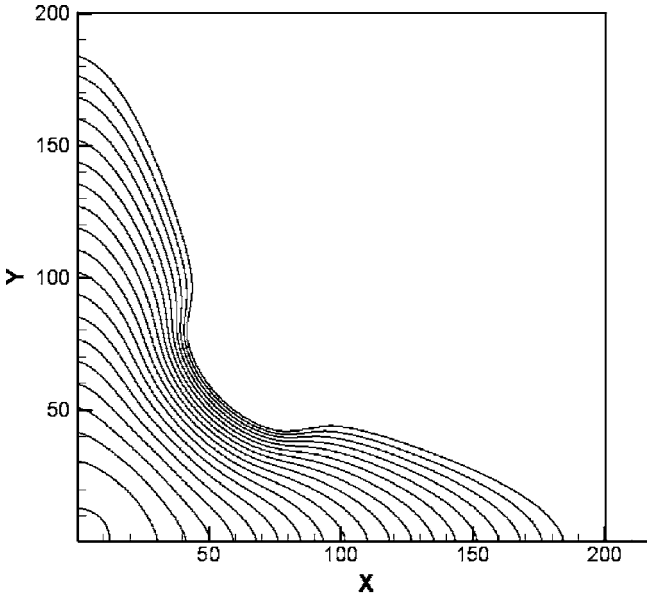

(*a*)

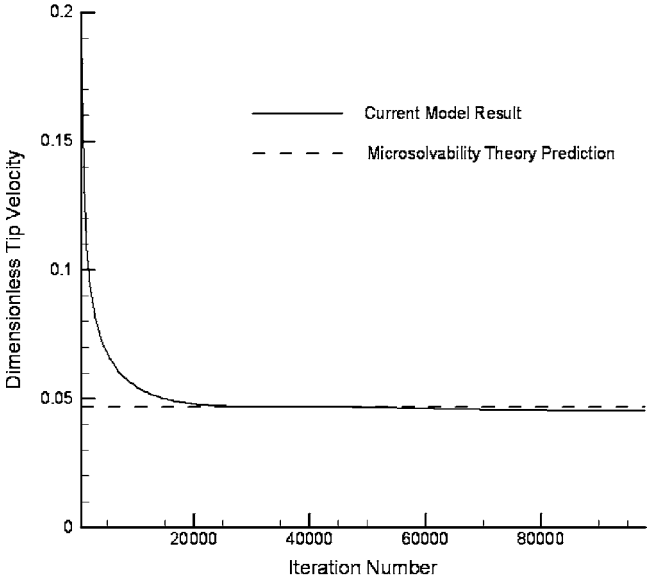

(*b*)

Fig. 3 Pure metal dendrite growth: (*a*) interface shape (contour $\phi=0$) shown every 5000 iterations; (*b*) convergence of dimensionless dendrite tip velocity as increasing iteration number (simulation parameters $\lambda=1.5957$, $\Delta=0.65$, $\alpha=1$, $\Delta x=\Delta y=0.4$, $\delta t=0.02$, $\varepsilon_4=0.05$)

$$\bar{V}_{\text{tip}} = \frac{V_{\text{tip}} d_0}{\alpha} \tag{21}$$

where d_0 is the capillary length. According to the micro-solvability theory [19], the steady state dimensionless dendrite tip velocity is 0.0469. In the current model, the converged dendrite tip velocity, as shown in Fig. 3(*b*), is 0.0451, which is fairly close to the micro-solvability theory prediction. It appears that this model is quantitatively correct, and the difference is about 3.8%.

5.3 Binary Alloy Solidification. In order to compare our calculation with the comparable results available in the literature [20], it is suitable to define similar parameters. Thus, the Lewis number (Le), which is defined as the ratio of thermal diffusivity α to solute diffusivity D, is chosen and used for this comparison. Based on the validation of pure metal solidification, dendrite growth for binary alloy was simulated with different Lewis numbers, which are 10, 20, and 40. Correspondingly, the dimensionless time steps δt for these three cases are 0.0008, 0.0004, and 0.0002, respectively. Other simulation parameters are chosen as follows: $MC_\infty=0.1$, $k=0.15$, $D=4.0$, $\lambda=6.3829$. The remaining parameters were kept the same as in the pure metal dendrite growth case.

Figure 4 shows the calculation results of the phase-field (ϕ), dimensionless composition field (U), and dimensionless temperature field (θ) with different Lewis numbers in the current model. The first column of Fig. 4 is the results obtained from Le=10 case. And the results of the second and third columns come from Le=20 and Le=40 cases, respectively. The final solid/liquid composition can be calculated with Eqs. (8) and (9). Comparing the second row with the third row of Fig. 4, it appears that the thermal boundary layer thickness is much larger than that of the solutal boundary layer. This arises from the fact that the thermal diffusivity is 10 to 40 times larger than the solutal diffusivity. It also can be seen from Figs. 4(*a*)–4(*c*) that the second arm appears along with the primary dendrite arm, and that the second arms begin to interact and grow competitively with the increase of Lewis number.

The results of the current model were compared with Ramirez's model [20]. Excellent agreement was found except for the range of the composition field. It was explained that a different value of Lewis number and different values of λ were used in the calculation, which were $\lambda=6.3829$, Le=10, 20, and 40 in the current model, but $\lambda=1.5957$, Le=50 in Ramirez's calculation. It should be noted that a higher value Lewis number (in the magnitude of 10^3) is more realistic in a binary alloy. To keep the analysis stable, however, a much smaller time step needs to be adopted and the computation time will be increased significantly. Thus, no calculation efforts were made for a higher Lewis number case in the current work.

5.4 Results for Coupling Cases. Three different coupling cases based on the location in the melt-pool were investigated in this study. The cell location is shown in Fig. 5. All other simulation parameters were kept the same in these three cases. To facilitate the understanding of the solidification process in these three cell locations, the temperature history of these cells is plotted in Fig. 6, which was obtained from the macroscopic model calculation.

5.4.1 Case 1. The macrocell was chosen from cell location 1 in Fig. 5, which is located on the solid/liquid interface and on the left of the melt pool. Considering the workpiece move direction (to the left), one can figure out that there will be certain incoming heat transfer from the right to the left during the following time step. Figure 7(*a*) shows the microstructure interface evolution of cell location 1 from dimensionless time: 0 to 120. The number on each curve shows the time at which the interface shape was obtained.

An interesting observation is that the left dendrite tip shows a greater growth velocity than the right one with the incoming heat flux from the right to the left side. To analyze the effect of heat flux on the tip velocity quantitatively, a new code was developed to count this effect. Figure 7(*b*) shows the dendrite tip velocity analysis of a cell located on the left side of the melt-pool.

From Fig. 7(*b*), it is evident that the left tip velocity tends to stabilize before iteration 140,000, which corresponds to the region that the thermal boundary layer of the dendrite tip is far away from the calculation domain boundary. The left tip velocity increases significantly after iteration 150,000 due to the interaction between the tip boundary layer and calculation domain boundary. The right tip velocity keeps decreasing before iteration 140,000, and the tip even begins to re-melt at iteration 140,000. The bottom and top tips show growth patterns similar to that of the left tip; the

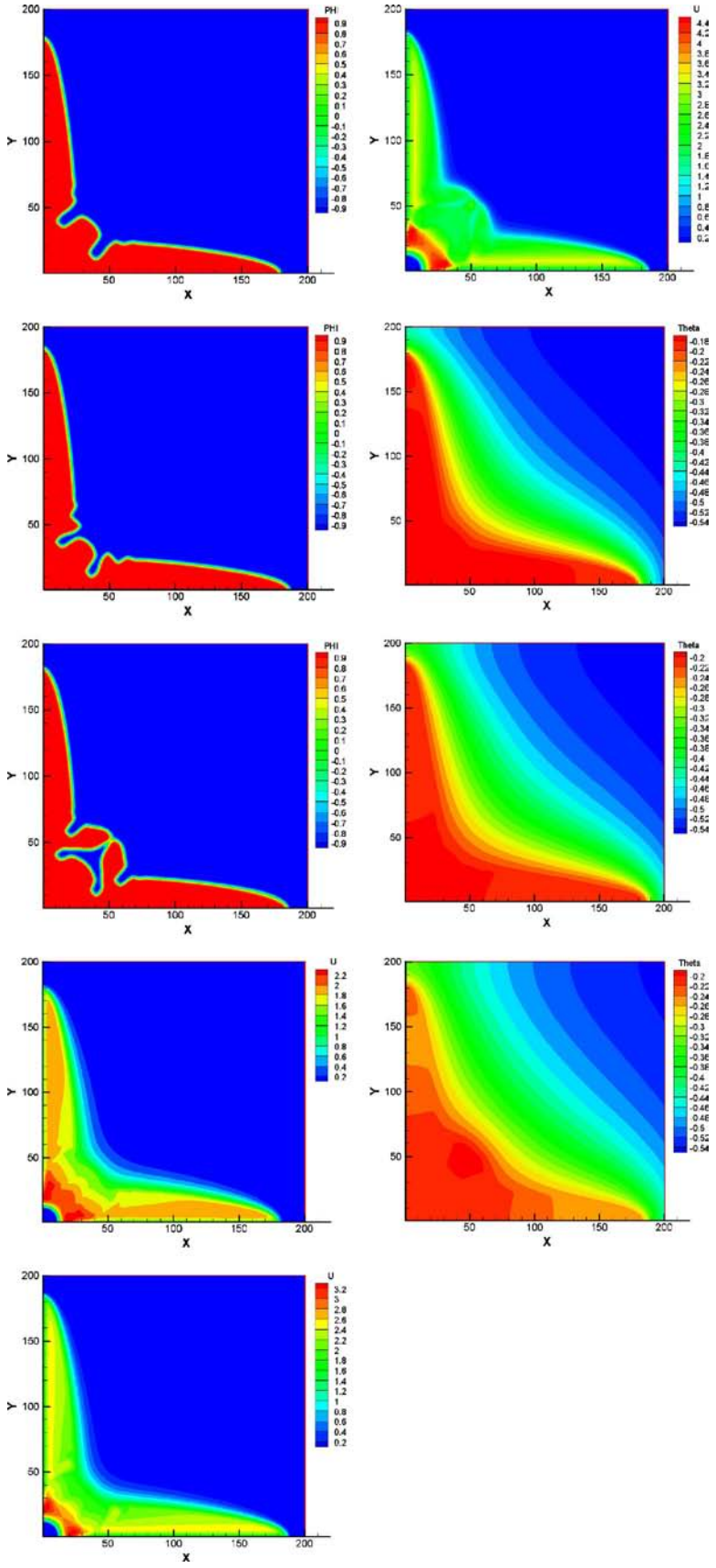

Fig. 4 Calculation Results for alloy solidification with different Lewis numbers (MC_∞=0.1, k=0.15, λ=6.3829, D=4.0, Δx=Δy=0.4, ε_4=0.05)

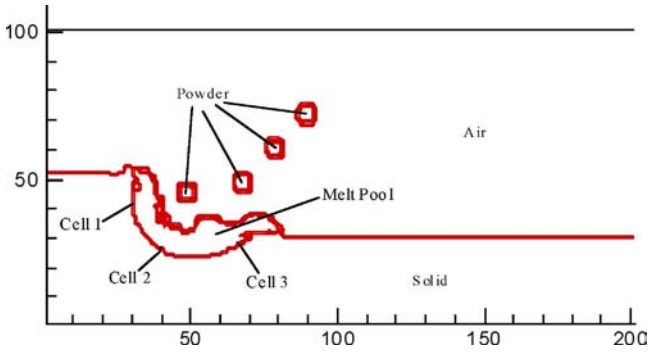

Fig. 5 Scheme of cell location

only difference is that the dimensionless tip velocity of these two tips lies between the velocity of the left tip and right tip.

5.4.2 Case 2. The macrocell was picked up from the left bottom corner of the melt-pool, which is cell location 2 in Fig. 5. The interface evolution and dendrite tip velocity analysis were shown in Fig. 8. The number on each curve has the same meaning as in Fig. 7(*a*). It can be found that the heat flux direction in this case is along the diagonal of the calculation domain, from the right top corner to the left bottom corner, and that the left and bottom dendrite tips grow faster than the right and top ones.

It is also observed that the size of the dendrite arms at the left and bottom branches are larger than that at the right and top due to the heat flux direction. From Fig. 8(*b*), it can be clearly seen that the left and bottom tips shared almost the same tip velocity, and the right and top tips shared nearly an identical tip velocity. This is just because the thermal gradient direction is nearly 45 deg to the *x*-axis, and it exerts the same effects on the growth pattern of the left and bottom tips. Certainly, the same thermal effects are applied to the right and top tips.

5.4.3 Case 3. The macrocell was selected from the cell location 3 shown in Fig. 5. This cell locates itself in the right front of the melt-pool, which will soon be heated by the external energy source (laser in this study). Figure 9(*a*) shows the evolution of the microstructure interface. The initial seed in the calculation domain undergoes a growth before dimensionless time 40 and subsequently melts in the remaining time. The interesting point is that

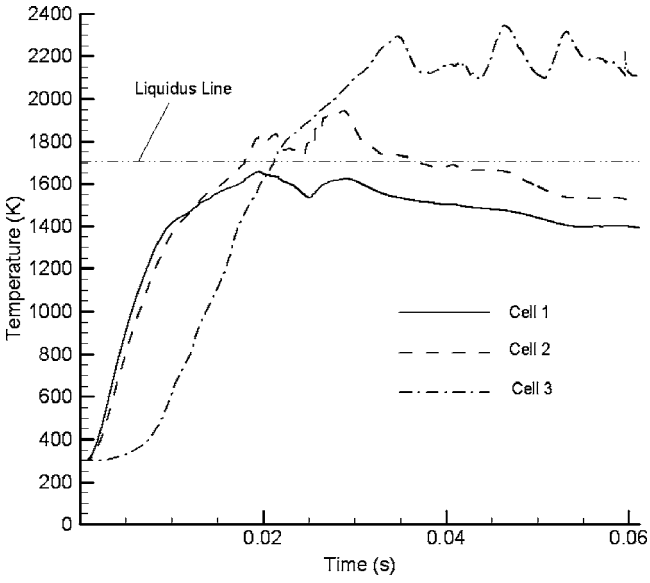

Fig. 6 Temperature history of cell 1, cell 2, and cell 3

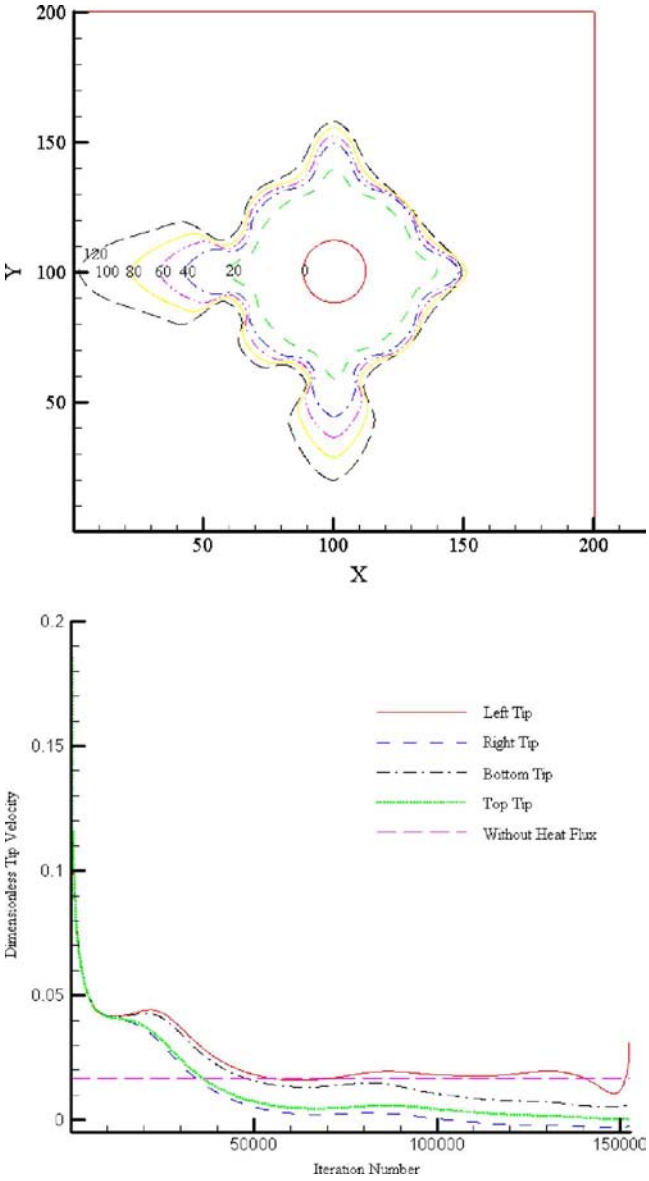

Fig. 7 Dendritic growth with heat flux case 1 (cell 1) (MC_∞ =0.1, k=0.15, D=4.0, λ=6.3829, Le=10, δt=0.0008, Δx=Δy=0.4, ε_4=0.05)

the faster growth direction before dimensionless time 40 is identical to the heat flux direction, which is from the left top corner to the right bottom corner.

Figure 9(*b*) shows the corresponding dendrite tip analysis for case 3. It can be observed that the steady state growth is not reached because the cell locates before the laser beam and soon it will become the melt-pool. The continuous incoming of heat flux makes the seed finally re-melt.

Based on the observation of the above three cases, which share the same calculation parameters except for the location in the melt-pool, one may conclude that it was the heat transfer that dominates the dendrite growth pattern in the binary alloy solidification during the laser cladding process. With the fluid flow effect neglected and no macroscale mass transfer included in this model, however, the thermal-solutal coupling effect on the dendrite growth pattern may need to be considered in the future work.

5.5 Effect of Undercooling. The effect of undercooling on the dendrite growth pattern of the solidification microstructure was also investigated. In this study, all other parameters were kept

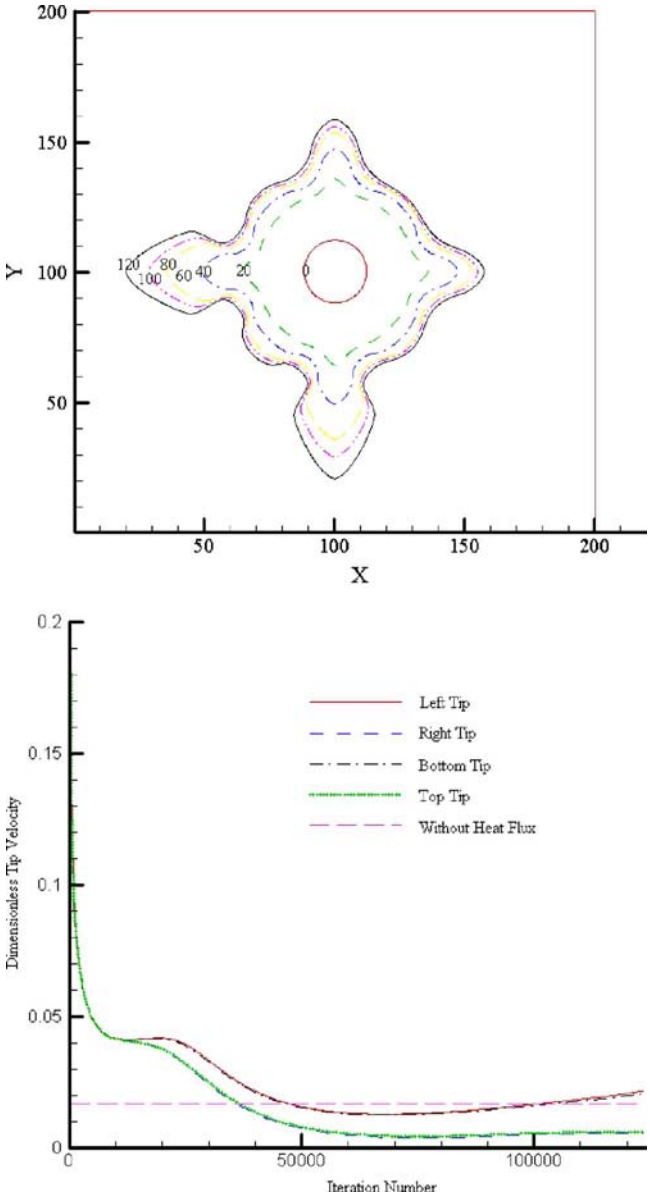

Fig. 8 Dendritic growth with heat flux case 2 (cell 2) (MC_∞ =0.1, k=0.15, D=4.0, λ=6.3829, Le=10, δt=0.0008, Δx=Δy=0.4, ε_4=0.05)

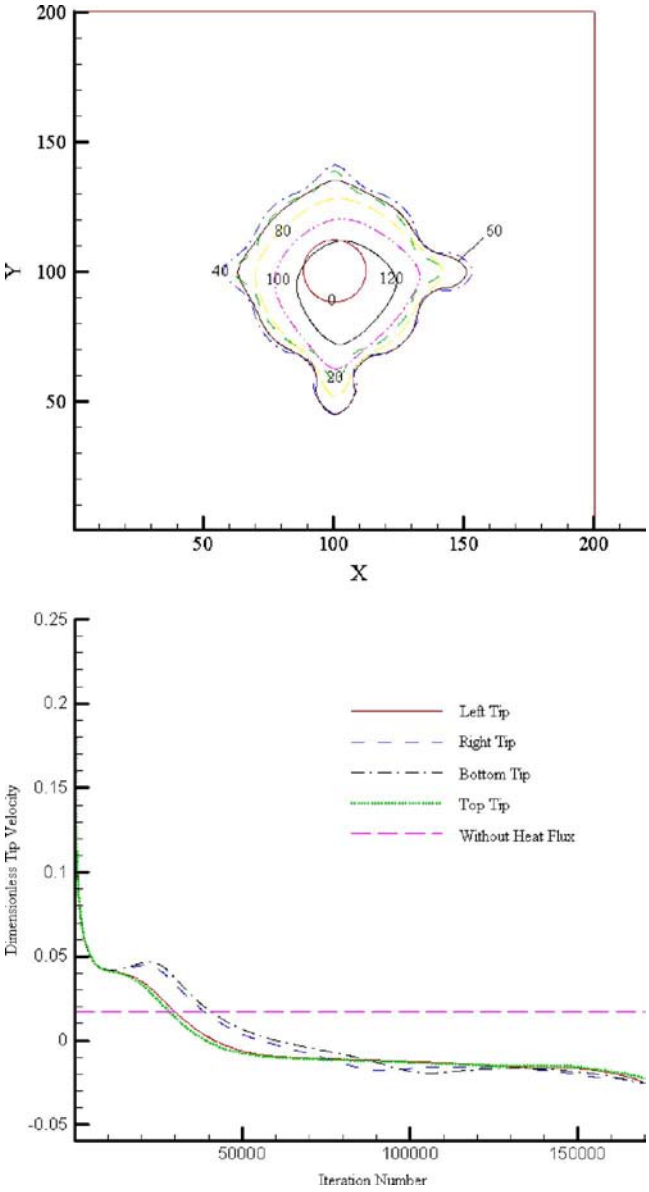

Fig. 9 Dendritic growth with heat flux case 3 (cell 3) (MC_∞ =0.1, k=0.15, D=4.0, λ=6.3829, Le=10, δt=0.0008, Δx=Δy=0.4, ε_4=0.05)

the same with the pure metal case, and only the threshold undercooling was varied from 0.45 to 0.75. Given the symmetry of the calculation domain, only a quarter of the domain was calculated in this case for simplicity.

Figure 10 shows the calculated phase-field with different undercooling. It is clear that one can get a sharp and smooth dendrite shape if Δ=0.45 was chosen, as shown in Fig. 10(*a*). With an increase in the undercooling, the necking phenomenon was observed at the root of the dendrite arm, as shown in Figs. 10(*b*)–10(*d*). In addition, the extent of the necking increased with an increase in the undercooling. The solidification pattern of Δ =0.75 is more like the binary alloy case as presented in Fig. 4(*b*). The secondary arm is also observed in the growth process of the dendrite with a higher undercooling.

It was also observed that the CPU time for the simulation decreased dramatically with an increase in the undercooling. Considering the same domain size, it is evident that the dendrite tip velocity increases dramatically with an increase in the undercooling. Figure 11 shows the dendrite tip velocity with the elapse of time (i.e., iteration number). The simulation result of case Δ =0.45 was compared with the prediction from the microsolvability theory [19], and an excellent agreement was found. Figure 11 clearly shows a higher dendrite tip velocity with a higher undercooling.

This phenomenon was also reported by Zhao et al. [29], and according to their analysis, the dendrite tip velocity is proportional to Δ^2 in the 2-D case with a small Péclet number. Figure 12 shows the relationship between the steady state dendrite tip velocity and the square of the undercooling. A nearly linear trend was observed in Fig. 12, which confirms the accuracy of the current model.

6 Concluding Remarks

A multiscale model for the microstructure evolution during laser cladding process has been developed by coupling the macroscale model based on the VOF formulation with the microscale model based on the phase-field model. In the phase-field model, the effect of anisotropy was included in predicting the dendrite growth pattern, but the interface kinetics was neglected to sim-

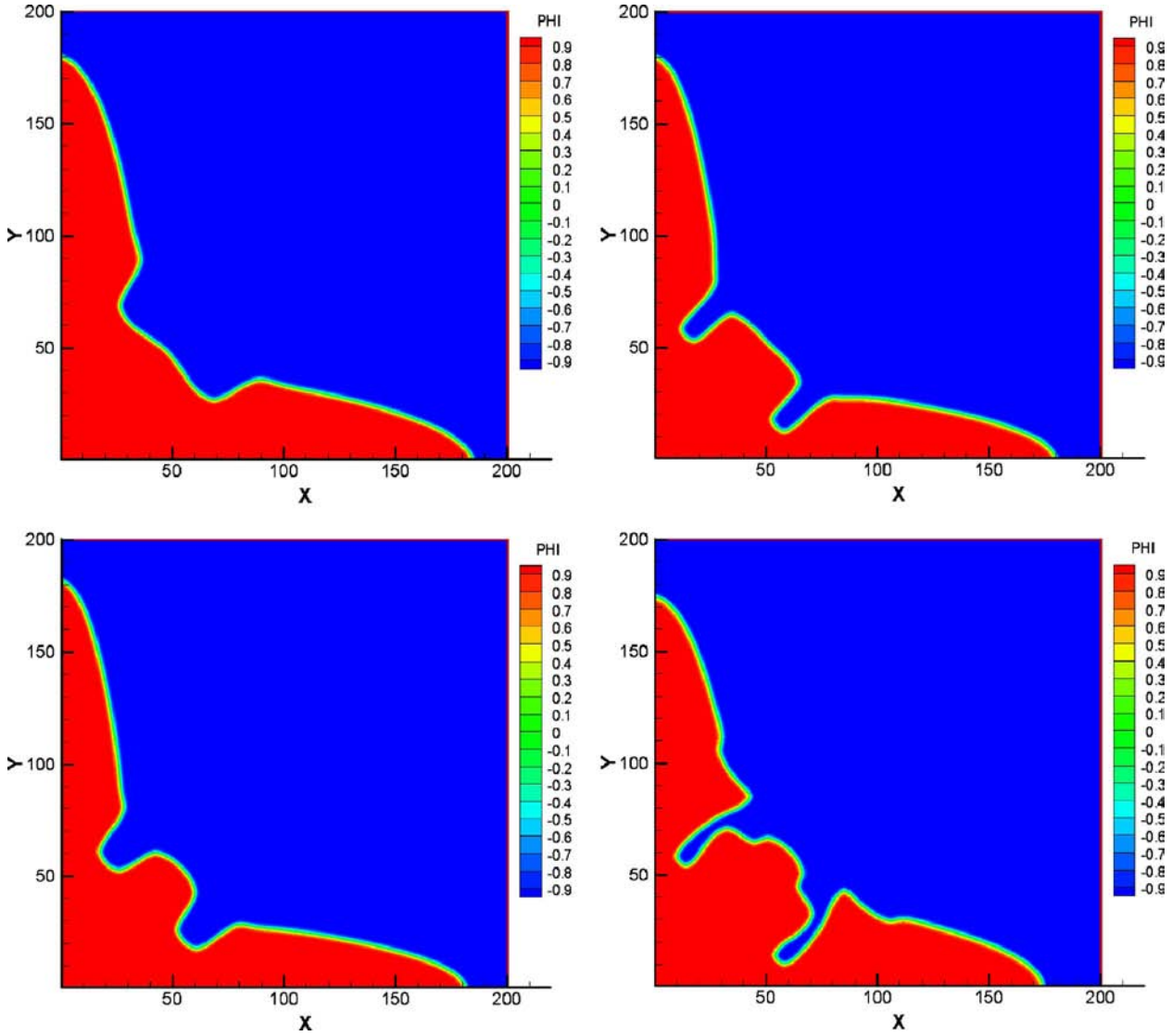

Fig. 10 Effect of undercooling (Δ) on dendrite growth pattern (λ=6.3829, α=4.0, Δx=Δy=0.4, δt=0.08, ε_4=0.05)

plify the modeling work. This multiscale model has excellent potential to simulate the microstructure evolution during the laser cladding process.

To verify the microscale model based on the phase-field approach, pure metal dendrite growth was investigated. A good agreement was found with the results reported in the literature. Dendritic growth for the binary alloy was also simulated, and the temperature and composition distribution in the dendritic growth showed similar patterns observed by other researchers.

This study also investigated the phase-field, dimensionless temperature, and composition evolution at different cell locations in the melt-pool during the laser cladding process linking the macroscale model with the microscale model. To quantitatively study the effect of heat flux on the dendritic growth, the dendrite tip analysis was carried out. It was observed that the dendrite tip that grows in the same direction with the heat flux shows a much higher velocity than a tip that grows in the direction opposite the heat flux.

The effects of undercooling on the growth pattern of solidification microstructure were also studied. It was found that if the undercooling was chosen appropriately, a smooth dendrite pattern with a suitable dendrite tip velocity could be obtained. A higher dendrite tip velocity can be achieved with a greater undercooling.

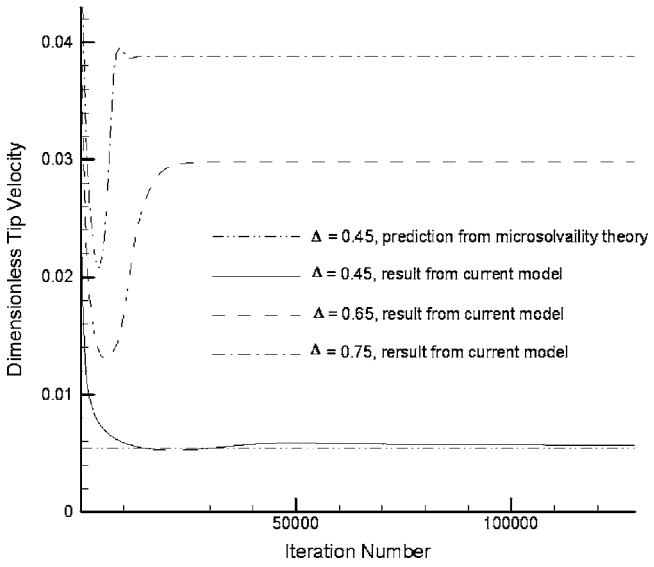

Fig. 11 Dimensionless tip velocity evolution with different undercooling

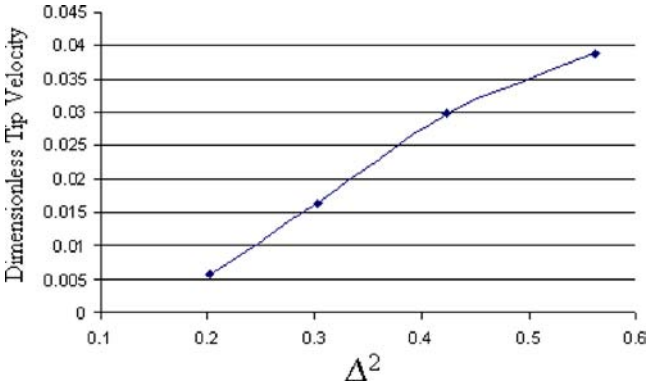

Fig. 12 Relationship between dimensionless tip velocity and square of undercooling

A nearly linear relationship between the steady state dendrite tip velocity and the square of the undercooling was also observed.

It should be noted that all the results and conclusions obtained in this study are based on the assumptions listed in Secs. 2 and 3. Without these assumptions, the conclusions may not hold for all the cases. For example, the temperature distribution in the melt pool may be significantly different if the thermophysical parameters of the substrate and powder materials are dependent of temperature. In fact this situation is very likely to take place with the high temperature gradient in the melt-pool. If the fluid flow is included, the governing equations of the micromodel need to be re-written and thus the evolution of the phase-field, temperature, and composition will be totally different with the results shown in this work. Both of these two situations will be taken into account in the future work of current project.

Acknowledgment

The authors gratefully acknowledge partial supports for this work from the Science & Engineering Service (Grant #: DAH001-02-S-0003/TYPE) and Air Force Research Laboratory (Contract No.: FA8650-04-C-5704). The authors would like to express special thanks to Dr. J. C. Ramirez from the Los Alamos National Laboratory for providing the relevant valuable codes, and Y. Sun from the University of Iowa for effective discussion with the phase-field model.

Nomenclature

$a_s(n)$ = anisotropy
c = composition of material
C_{pl} = specific heat of liquid
C_{ps} = specific heat of solid
c_∞ = composition far from the interface
d_0 = capillary length
D = solutal diffusivity
F = volume of fluid function
f_l = liquid mass fraction
f_s = solid mass fraction
g_l = liquid volume fraction
g_s = solid volume fraction
h = enthalpy
h_l = liquid enthalpy
h_s = solid enthalpy
I = grid number in x-direction
J = grid number in y-direction
k = equilibrium partition coefficient
k_t = thermal conductivity
K = permeability of the two-phase mushy region
L = latent heat of melting
L_e = Lewis number
L_m = latent heat of fusion of material
L_v = latent heat for liquid-vapor phase change
m = slope of liquidus line
M = scaled liquidus slope
p = pressure
S = thermal noise strength
T = temperature
T_l = liquidus temperature
T_m = melting temperature of pure solvent
T_s = solidus temperature
t = time
Δt = macro-time step
δt = micro-time step
U = dimensionless measure of composition
u = velocity in X-direction
v = velocity in Y-direction
u_s = tangential velocity at free surface
v_s = normal velocity at free surface
$\mathbf{V}$ = velocity vector
V_{tip} = dendrite tip velocity
$\bar{V}_{\text{tip}}$ = dimensionless dendrite tip velocity
W = interface thickness
W_0 = length scale in current study
Δ = undercooling
Δx = mesh spacing along X axis
Δy = mesh spacing along Y axis

Subscripts

l = liquid phase
s = solid phase

Greek Symbols

α = thermal diffusivity
χ = dimensionless composition
ε_4 = anisotropy coefficient
ϕ = phase-field
μ_l = dynamic viscosity of liquid metal
λ = strength of coupling between phase and diffusion fields
θ = dimensionless temperature
ρ = density
ρ_l = density of liquid
ρ_s = density of solid
τ = relaxation time in phase-field model
τ_0 = time scale in current study
ξ = random number between −1 and 1

References

[1] Hoadley, A. F. A., and Rappaz, M., 1992, "A Thermal Model of Laser Cladding by Powder Injection," Metall. Trans. B, **23B**, pp. 631–643.
[2] Picasso, M., Marsden, C., Wagnieres, J.-D., Frenk, A., and Rappaz, M., 1994, "A Simple but Realistic Model for the Laser Cladding process," Metall. Mater. Trans. B, **25B**, pp. 281–291.
[3] Kar, A., and Mazumder, J., 1989, "Extended Solid Solution and Nonequilibrium Phase Diagram for Ni-Al Alloy Formed During Laser Cladding," Metall. Trans. A, **20A**, pp. 363–371.
[4] Zhong, M. L., Yao, K. F., Liu, W. J., Goussain, J. C., Mayer, C., and Becker, A., 2001, "High-Power Laser Cladding Stellite 6+WC With Various Volume Rates," J. Laser Appl., **13**(6), pp. 247–251.
[5] Choi, J., Choudhuri, S. K., and Mazumder, J., 2000, "Role of Preheating and Specific Energy Input on the Evolution of Microstructure and Wear Properties of Laser Clad Fe-Cr-C-W Alloys," J. Mater. Sci., **35**(13), pp. 3213–3219.
[6] Sircar, S., Chattopadhyay, K., and Mazumder, J., 1992, "Nonequilibrium Synthesis of $NbAl_3$ and Nb-Al-V Alloys by Laser Cladding. 1. Microstructure Evolution," Metall. Trans. A, **23**(9), pp. 2419–2429.
[7] Weinan, E., Engquist, B., and Huang, Z., 2003, "Heterogeneous Multi-Scale Method—A general Methodology for Multi-Scale Modeling," Phys. Rev. B, **67**(9), pp. 092101.
[8] Weinan, E., and Huang, Z., 2001, "Matching Conditions in Atomistic-Continuum Modeling of Materials," Phys. Rev. Lett., **87**(13), pp. 135501.
[9] Boettinger, W. J., Warren, J. A., Beckermann, C., and Karma, A., 2002, "Phase-Field Simulation of Solidification," Annu. Rev. Mater. Res., **32**, pp. 163–194.

[10] Chen, L.-Q., 2002, "Phase-Field Models for Microstructure Evolution," Annu. Rev. Mater. Res., **32**, pp. 113–140.
[11] Sekerka, R. F., 2004, "Morphology: From Sharp Interface to Phase Field Models," J. Cryst. Growth, **264**, pp. 530–540.
[12] Beckermann, C., Diepers, H.-J., Steinbach, I., Karma, A., and Tong, X., 1999, "Modeling Melt Convection in Phase-Field Simulation of Solidification," J. Comput. Phys., **154**, pp. 468–496.
[13] Wheeler, A. A., Boettinger, W. J., and McFadden, G. B., 1992, "Phase-Field Model for Isothermal Phase Transitions in Binary Alloys," Phys. Rev. A, **45**, pp. 7424–7440.
[14] Wheeler, A. A., Boettinger, W. J., and McFadden, G. B., 1993, "Phase-Field Model of Solute Trapping During Solidification," Phys. Rev. E, **47**, pp. 1893–1909.
[15] Ahmad, N. A., Wheeler, A. A., Boettinger, W. J., and McFadden, G. B., 1998, "Solute Trapping and Solute Drag in a Phase-Field Model of Rapid Solidification," Phys. Rev. E, **58**, pp. 3436–3450.
[16] Kim, S. G., Kim, W. T., and Suzuki, T., 1999, "Phase-Field Model for Binary Alloys," Phys. Rev. E, **60**, pp. 7186–7197.
[17] Karma, A., and Rappel, W.-J., 1996, "Phase-Field Method for Computationally Efficient Modelling of Solidification With Arbitrary Interface Kinetics," Phys. Rev. E, **53**, pp. 3017–3020.
[18] Karma, A., and Rappel, W.-J., 1996, "Numerical Simulation of Three-Dimensional Dendritic Growth," Phys. Rev. Lett., **77**, pp. 4050–4053.
[19] Karma, A., and Rappel, W.-J., 1998, "Quantitative Phase-Field Modelling of Dendritic Growth in Two and Three Dimensions," Phys. Rev. E, **57**, pp. 4323–4349.
[20] Ramirez, J. C., Beckermann, C., Karma, A., and Diepers, H.-J., 2004, "Phase-Field Modeling of Binary Alloy Solidification With Coupled Heat and Solute Diffusion," Phys. Rev. E, **69**, p. 051607.
[21] Tong, X., Beckermann, C., Karma, A., and Li, Q., 2001, "Phase-Field Simulations of Dendritic Crystal Growth in a Forced Flow," Phys. Rev. E, **63**, pp. 061601.
[22] Hung, C.-F., and Lin, J., 2004, "Solidification Model of Laser Cladding With Wire Feeding Technique," J. Laser Appl., **16**(3), pp. 140–146.
[23] Zhang, W., DebRoy, T., Palmer, T. A., and Elmer, J. W., 2005, "Modeling of Ferrite Formation in a Duplex Stainless Steel Weld Considering Non-uniform Starting Microstructure," Acta Mater., **53**, pp. 4441–4453.
[24] Choi, J., Han, L., and Hua, Y., 2005, "Modeling and Experiments of Laser Cladding With Droplet Injection," ASME J. Heat Transfer, **127**, pp. 978–986.
[25] Li, L. J., and Mazumder, J., 1985, in Proceedings of Laser Processing of Materials, Metallurgical Society of American Institute of Metallurgical Engineers, Warrendale, PA, pp. 35–50.
[26] Gedda, E., Powel, J., Wahlstöm, G., Li, W.-B., Engström, H., and Magnusson, C., 2002, "Energy Redistribution During CO_2 Laser Cladding," J. Laser Appl., **14**(2), pp. 78–82.
[27] Nichols, B. D., Hirt, C. W., and Hotchkiss, R. S., 1980, "SOLA-VOF: A Solution Algorithm for Transient Fluid Flow With Multiple Free Boundaries," LA-8355, Los Alamos National Laboratory.
[28] Hirt, C. W., and Nichols, B. D., 1981, "Volume of fluid (VOF) Method for the Dynamics of Free Boundaries," J. Comput. Phys., **39**, pp. 201–225.
[29] Zhao, D., Tao, J., and Liu, B., 2003, "Influence of Phase-Field Parameters on the Dendrite Morphology," Acta Metall. Sin., **39**(8), pp. 813–816 (in Chinese).

Numerical Study of Single Bubble Dynamics During Flow Boiling

Ding Li

Vijay K. Dhir[1]
e-mail: vdhir@seas.ucla.edu

Mechanical and Aerospace
Engineering Department,
Henry Samueli School of Engineering
and Applied Science,
University of California, Los Angeles,
420 Westwood Plaza,
Los Angeles, CA 90095-1597

Three-dimensional numerical simulation of single bubble dynamics during nucleate flow boiling is performed in this work. The range of bulk liquid velocities investigated is from 0.076 to 0.23 m/s. The surface orientations at earth normal gravity are varied from an upward facing horizontal surface to vertical through 30, 45, and 60 deg. The gravity levels on an upward facing horizontal surface are varied from $1.0g_e$ to $0.0001g_e$. Continuity, momentum, and energy equations are solved by finite difference method and the level set method is used to capture the liquid-vapor interface. Heat transfer within the liquid micro layer is included in this model. The numerical results have been compared with data from experiments. The results show that the bulk flow velocity, heater surface orientation, and gravity levels influence the bubble dynamics. [DOI: 10.1115/1.2717942]

Keywords: numerical simulation, single bubble, flow boiling

Introduction

Nucleate boiling is a very efficient mode of heat transfer. A large number of nucleate boiling studies have been published in the literature, ever since Nukiyama [1] obtained the first boiling curve in 1934. Although nucleate boiling under forced flow condition has also been studied extensively, some important aspects of the problems, such as the effect of bulk velocity, surface orientation, and the magnitude of gravity levels on bubble dynamics, have not been resolved. In order to develop a better understanding of the process, three-dimensional numerical simulations of flow boiling are carried out in this study.

Experimental Studies

Bubble Dynamics. Gunther [2] was one of the earliest to study nucleate boiling under forced convection conditions. High-speed, high-resolution photographic study was used to investigate the effect of forced convection on the mechanisms of heat transfer. It was found that the bubble size and the bubble lifetime decreased as bulk fluid velocity was increased.

Van Helden et al. [3] carried out an experimental study of bubble detachment in vertical flow. They studied nitrogen bubbles and steam bubbles in saturated water. The variation of bubble departure radii, and the advancing and receding contact angles with liquid bulk velocity were investigated. They confirmed the inverse relationship between detachment radius and liquid velocity.

Thorncroft et al. [4] investigated vapor bubble growth and departure in vertical up-flow and down-flow conditions in a 12.7 mm square duct, 30 cm long with a nichrome heater strip attached to one side of the test section. They used FC87, a perfluorocarbon fluid, at velocities ranging from 0.11 to 0.38 m/s, liquid subcoolings from 1°C to 5°C, and wall superheats up to 7°C. In upflow, bubbles were observed to remain attached to the heating surface assuming caplike shape while sliding along the surface. However, in downflow they observed three regimes of bubble detachment. At velocities around 0.11 m/s, the bubbles departed in upward direction against the bulk fluid velocity. At slightly higher velocities of about 0.18 m/s, bubbles lifted off directly above the nucleation sites without sliding. At still higher velocities of about 0.38 m/s, bubbles slid downwards. Liftoff was very regular and heat transfer coeffcient was calculated to be lower than that in upflow. Since vapor bubbles continue to slide along the heating surface during upflow, they attributed the increase in heat transfer in upflow conditions to the vapor bubble sliding.

Maity [5] experimentally investigated the effect of bulk velocity, liquid subcooling, and angle of inclination of the boiling surface with the direction of gravity on bubble dynamics in flow boiling. He conducted experiments on micro-machined silicon wafers, with velocities varying from 0.076 to 0.23 m/s, surface orientations from horizontal to vertical through 30, 45, and 60 deg, and for an inclined downward facing surface. The test fluid was de-ionized water. Liquid subcooling was studied from 0.2°C to 5.5°C and wall superheats from 4.6°C to 6.9°C. It was found that the upstream and downstream contact angles were different. The bubble departure diameter and liftoff diameter decreased with increasing velocity at all orientations. Liftoff diameter was found to increase when the component of gravity normal to the heater was decreased.

Dynamic Contact Angle in Flow Boiling. Contact angle is the angle formed at a point on the line of contact of three phases, liquid, vapor or gas, and solid. Static contact angle depends primarily on the interfacial tensions between solid and liquid, vapor and liquid, and solid and vapor. However, the mechanism of dynamic contact angle is complex and has not been resolved yet. Only a few studies have been conducted concerning the contact angle variation during boiling process.

Al-Hayes and Winterton [6] calculated surface tension force using different contact angles at the upstream and downstream fronts of the bubble. The existence of contact angle hysteresis under dynamic conditions has also been reported by Marsh et al. [7], Chibowski and Gonzalez [8], Shoji and Zhang [9], and Lin et al. [10]. Ramanujapu and Dhir [11] studied contact angle dynamics on a vapor bubble growing and detaching under pool boiling conditions at a single nucleation site on a silicon wafer surface. They found that the contact angle variation depends on the sign of interface velocity.

Klausner et al. [12] studied the vapor bubble departure in a 25×25 mm^2 horizontal test section with a nichrome heater surface 457 mm long. They conducted experiments with R-113, for flow velocities up to 1 m/s and wall superheats varying from 10°C to 21°C. They found upstream and downstream contact angles to be around 45 and 36 deg, respectively, for a typical bubble. They developed expressions for surface tension force

[1]Address all correspondence to this author.

Contributed by the Heat Transfer Division of ASME for publication in the JOURNAL OF HEAT TRANSFER. Manuscript received May 17, 2006; final manuscript received January 16, 2007. Review conducted by Raj M. Manglik. Paper presented at the 2004 ASME International Mechanical Engineering Congress (IMECE2004), November 13–19, 2004, Anaheim, CA.

 Copyright © 2007 by ASME

based on some assumed variation of contact angle along the periphery of the bubble base and concluded that surface tension alone was not able to prevent vapor bubble from departure. The liquid drag on the bubble due to asymmetrical bubble growth acting in the direction opposite to liquid flow was important in holding the bubble to its nucleation site prior to departure. Klausner et al. [13] developed an expression for drag force on an asymmetrical bubble due to flow.

Bibeau and Salcudean [14] investigated bubble ebullition in vertical upflow in a cylindrical annular test section. In the experiments water was used as the test liquid at velocities ranging from 0.08 to 1.2 m/s, inlet pressure of 2 to 3 bars, subcooling of 10°C to 60°C, and a heat flux on the stainless steel cylindrical heater between 100 and 1200 kw/m^2. At typical bulk velocity of 0.084 m/s, subcooling of 10°C, and wall heat flux of 200 kw/m^2 they observed an upstream contact angle of 43 to 53 deg. The downstream contact angle increased from 40 to 44 deg and then decreased slightly as the bubble elongated in normal direction.

Qiu and Van der Geld [15] reported an apparent downstream contact angle for an injected nitrogen bubble, which touched the heater surface at the side. They concluded that the upstream contact angle was higher than the downstream contact angle.

Kandlikar and Stumm [16] conducted an experimental study of upstream and downstream contact angles. They used water as the test liquid in a rectangular aluminum channel, 3×50 mm^2 cross section and 300 mm long. The upstream and downstream contact angles were measured from the top and the side views of bubbles. A model based on a control volume approach was developed for the front and rear regions of the bubble. They concluded that the upstream and downstream contact angles were dependent on the flow velocity. It was stated that as the surface velocities increase, the receding contact angle drops to a low value and then remains almost constant for higher velocities. However, the advancing contact angle did not change appreciably with the interface velocity.

Effect of Gravity. Flow boiling offers attractive means for increasing heat transfer in micro-gravity environments. Most of the studies reported in literature have been conducted at earth normal gravity either in vertical up- or downflow directions or horizontal with the heater facing upwards.

Kirk et al. [17] studied flow boiling at various orientations of the heater surface. They used R-113 at velocities of 0.041 to 0.324 m/s, subcooling from 2°C to 11°C, and wall heat fluxes less than 130 kw/m^2. The test surface had a thin gold film deposited on a copper heater. They observed that a decrease in the normal component of buoyancy force increases heat transfer. For a negative normal component of buoyancy, heat transfer is enhanced only at low levels of heat flux as long as flow velocity is enough to sweep away the bubbles. Increasing flow velocity, however, reduces the effect of buoyancy. In downward facing conditions, bubbles tend to coalesce and depart as vapor slugs. Their conclusion was that the effect of flow velocity on nucleate boiling heat transfer depends strongly on surface orientation at low velocities.

Lee and Merte [18] measured vapor bubble growth in microgravity using R-113 with transient heating of a flat surface. Measurements of vapor bubble growth were compared to a hemispherical bubble model for a combination of an initially uniform and a nonuniform superheated liquid layers. They found that the bubble growth rate depended upon the initial temperature distribution around the bubble, which is directly related to the heat flux and heating time leading up to nucleation.

Qiu and Dhir [19] presented an experimental study of growth and detachment processes of single and multiple bubbles formed on a heated surface in pool conditions. This study was conducted in the low gravity environment during the parabola flights of KC-135 aircraft. Water was used as the test fluid. They found that for single bubbles, the bubble departure diameter can be approximately related to the gravity level through the relation $D_d \propto 1/\sqrt{g}$. The growth periods were found to be very sensitive to liquid subcooling at a given wall superheat. Horizontal mergers of two to three bubbles were also observed. The base areas of vapor stems underneath the bubbles on the heater surface rapidly decreased after the merger. During and after bubble merger the liquid still filled the space between the vapor mass and the heater surface so as to form mushroom type bubbles. They also found that the merger caused liftoff of the vapor mass from the surface with a smaller equivalent diameter than that of a single bubble departure diameter at the same gravity level. As such the variation of bubble diameter at departure as inverse square root of gravity did not hold good for bubbles that departed after merger. Straub [20] has reported from low-gravity boiling experiments that the bubble diameter at departure varies approximately as $1/\sqrt[3]{g}$. These data were not obtained for single bubbles but were obtained when boiling occurred on the entire surface. Thus it is quite possible that vapor bubble merger occurred on the heater surface prior to bubble departure.

Ma and Chung [21] reported results of a single vapor bubble that nucleated and grew in a flow field of FC-72 on a flat surface in terrestrial gravity and in micro-gravity. Bubble nucleation, growth, and departure in micro-gravity with different flow rates were observed with a CCD camera. They found that the forced convection would affect the downstream side of a bubble significantly in micro-gravity while the upstream edge of a bubble seemed to be unaffected by the flow. They observed that the high flow rate would offset the buoyancy effects. As a result, the bubble shape and bubble generation frequency tended to be similar to that in normal gravity.

Numerical Studies. It is a challenging task to develop a numerical technique for two-phase flow with moving interfaces from a computational point of view. The shape and movement of the interface and the geometric configuration of each phase need to be computed as part of the solution. The large property jumps, associated with phase change, also add to the complexity of the solution method.

Sussman et al. [22] presented a level-set approach for computing incompressible two-phase flow without phase change. By keeping the level set as a distance function, the interface was easily captured by the zero level-set. The calculations were made for air bubbles in water and falling water drops in air with satisfactory results. Though the level-set method is easy to use, the numerical discretization of the level-set formulation does not satisfy mass conservation in general. Chang et al. [23] introduced a volume correction step to the level-set formulation in 1996. By solving an additional Hamilton-Jacobi equation, the mass was forced to be conserved.

Son et al. [24] developed a model for growth of a single bubble on a heated surface using complete numerical simulations. The model, based on Sussman's level-set approach, captures the evolving bubble interface and offers many improvements over previously published semi-empirical and analytical models. The improvements include simultaneous treatment of micro and macro regions and calculation of evolving shape of the bubble (see for example, Stephan and Hammer [25]). The model of Son et al. yields the spatial and temporal distribution of the wall heat flux, the microlayer contribution, and the interfacial heat transfer. In the model a static contact angle was used both for the advancing and receding phases of the interface. The numerical results were found to agree well with data from experiments. One possible reason for the good agreement is that the constant contact angle used in the numerical model nearly represents the average value of the advancing and receding contact angles (static contact angle) and the bubble is symmetrical in pool boiling. Also, the time over which the receding contact angles prevails is much shorter than that for the advancing contact angle. In 2001, Son [26] modified Chang et al.'s [23] formulation and included the volume correction into the

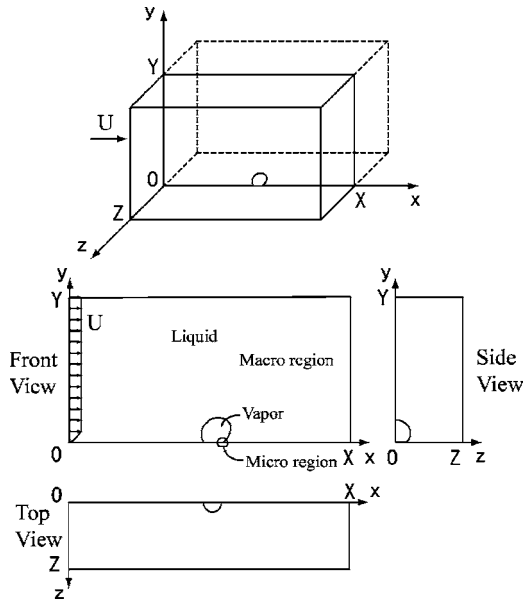

Fig. 1 Computational domain used in the numerical simulation

boiling heat transfer model. Abarajith and Dhir [27] used the model to study the effect of contact angle on the growth and departure of a single bubble on a horizontal heated surface during pool boiling under normal gravity conditions. They showed that for contact angles between 90 and 20 deg the bubble departure diameter decreased nearly linearly with decrease in contact angle. The growth period, however, decreased nonlinearly with reduction in contact angle. Abarajith et al. [28] also studied the effects of gravity and bubble merger on bubble departure diameter and departure time for water and PF5060. For a given gravity level both were found to depend on the spacing between adjacent nucleation sites. Mukherjee and Dhir [29] presented bubble dynamics and heat transfer associated with lateral bubble merger during transition from partial to fully developed nucleate boiling. The results show that merger of multiple bubbles significantly increases the overall wall heat transfer. This enhanced wall heat transfer is caused by trapping of the liquid layer between the bubble bases during merger and by drawing of cooler liquid towards the wall during contraction of the bubble base after merger.

Takahira and Banerjee [30] presented a numerical simulation of bubble growth and detachment in flow boiling. In their work, gas was injected into liquid through a small opening. Dirichlet boundary conditions for the level-set function were used to keep the level-set function zero at the edge of the opening. The numerical results were compared with experimental data and were found to be qualitatively in agreement with data from experiments.

Numerical Model

This section presents the computational model used in this study. The model is based on the level-set formulation, which is used to track the interface. In this model, the computational domain is divided into the micro and macro regions. The micro region contains the thin film that forms underneath the bubble whereas the macro region consists of the bubble and the liquid surrounding the bubble. Equations governing each of these regions are discussed in the following sections.

Figure 1 shows the three-dimensional computational domain used in the numerical simulation under an imposed flow field. The domain is rectangular in shape, with the calculations performed using Cartesian coordinates. The bottom of the domain is defined as the wall. A nucleating bubble is placed on the wall. The simulations are carried out with a uniform grid. All simulations consider only one-half of the bubble, exploiting the planar symmetry of the geometry.

Micro Region. The microlayer contribution to heat flux is determined through solving the conservation equations under the assumption of applicability of lubrication theory. Lay and Dhir [31] and Son et al. [24] have modeled and numerically solved for the shape of the microlayer underneath the bubble using the lubrication theory. The radial variation in thickness of the microlayer is governed by capillary pressure, disjoining pressure, recoil pressure, and viscous stresses. The evaporative heat flux across the liquid-vapor interface is calculated using the modified Clausis-Clayperon equation. A fourth-order ordinary differential equation for microlayer thickness is obtained by combining mass, momentum, and energy equations as:

$$\delta''' = f(\delta, \delta', \delta', \delta'') \tag{1}$$

where the δ' denoted $\partial/\partial r$.

The boundary conditions for the above equation are as follows:

(i) at $r=R_0$ (radius of inner edge of microlayer)

$$\delta = \delta_0, \quad \delta' = \delta'' = 0 \tag{2}$$

where δ_0 is of the order of molecular size.

(ii) at $r=R_1$ (radius of outer edge of microlayer)

$$\delta = \frac{h}{2}, \quad \delta' = 0 \tag{3}$$

where $h/2$ is the vertical distance to the first computational node for the level-set function, from the wall. In implementing the above boundary conditions the radius R_1 is determined from the solution of the macro region. For a given dispersion constant, the micro layer formulation (Eq. (1)) and R_0 are solved with the five boundary conditions (Eqs. (2) and (3)). In this work an apparent contact angle is defined as,

$$\tan\varphi = \frac{h/2}{(R_1 - R_0)} \tag{4}$$

An iterative procedure is used to satisfy Eq. (4).

For sliding bubbles, the apparent contact angle is different in the upstream and downstream directions as described later. The contact angles between the upstream and downstream sides are interpolated using,

$$\varphi = \varphi_{dn} + \frac{(\varphi_{up} - \varphi_{dn})}{2}[1 + \tanh(\pi - 2\beta)] \tag{5}$$

where angle β varies from 0 (upstream side) to π (downstream side) and φ_{up} and φ_{dn} are the upstream and downstream contact angles, respectively. An expression for the rate at which vapor is produced from the microlayer is written as,

$$\dot{V}_{micro} = \int_{R_0}^{R_1} \frac{k_l(T_w - T_{int})}{\rho_v h_{fg} \delta \Delta V_{micro}} \tag{6}$$

where ΔV_{micro} is a vapor side control volume near the micro region, which has been arbitrarily chosen to be $R_1 - 3h \leq r \leq R_1$, and $0 \leq y \leq h$. $\dot{V}_{micro}$ is included in the mass conservation equation used in the solution of the macro region. It should be noted that both the micro and macro regions are coupled through the matching of the contact angle at the outer edge of the microlayer and through the inclusion of $\dot{V}_{micro}$ as a source term in the solution of the macro region. The two-dimensional solution of the microlayer is used even in the three-dimensional cases under the assumption that no cross flow exists. As such the microlayer solution is obtained for discrete points along the periphery of the bubble base.

Macro Region

Governing Equations. The governing equations for the macro region are discussed in this section. Note that on account of the presence of vapor-liquid interface and evaporation, additional terms are included in the momentum and continuity equations. The momentum equation, which includes surface tension force and buoyancy force, can be written as,

$$\rho(\mathbf{u}_t + \mathbf{u}\cdot\nabla\mathbf{u}) = -\nabla p + \rho\mathbf{g} - \rho\beta_T(T - T_{sat})\mathbf{g} - \sigma\kappa\nabla H + \nabla\cdot\mu\nabla\mathbf{u} + \nabla\cdot\mu\nabla\mathbf{u}^T \quad (7)$$

where σ is the surface tension, H is the Heaviside function, and κ is the curvature of the interface. The Boussinesq approximation is used to model the buoyancy term. By assuming vapor temperature as saturation temperature, the energy equations for liquid and vapor phases are written as,

$$\rho c_{pl}(T_t + \mathbf{u}\cdot\nabla T) = \nabla\cdot k\nabla T \quad \text{for } H > 0 \quad (8)$$

$$T = T_{sat} \quad \text{for } H = 0 \quad (9)$$

The continuity equation is derived by including the effect of volume expansion due to liquid-vapor phase change at the interface and contribution from microlayer,

$$\nabla\cdot\mathbf{u} = \frac{\mathbf{m}}{\rho^2}\cdot\nabla\rho + \dot{V}_{micro} \quad (10)$$

where $\dot{V}_{micro}$ is obtained from the microlayer solution. The curvature of the interface is defined as,

$$\kappa(\phi) = \nabla\cdot\left(\frac{\nabla\phi}{|\nabla\phi|}\right) \quad (11)$$

The mass flux of liquid evaporating at the interface is given by,

$$\mathbf{m} = \rho_l(\mathbf{u}_{int} - \mathbf{u}_l) = \rho_v(\mathbf{u}_{int} - \mathbf{u}_v) = \frac{k\nabla T}{h_{fg}} \quad (12)$$

To prevent numerical instability arising from discontinuous material properties across the interface, the Heaviside function, H, defined over three grid spacings, is utilized for smoothing out the property variations:

$$H = \begin{cases} 1, & \phi \geqslant +1.5h \\ 0, & \phi \leqslant -1.5h \\ 0.5 + \dfrac{\phi}{3h} + \sin\left(\dfrac{2\pi\phi}{3h}\right)\Big/(2\pi), & \phi \leqslant +1.5h \end{cases}$$

where h is equal to one grid spacing. H remains 1 in the liquid phase and 0 in the vapor phase. The density, viscosity, and apparent conductivity are defined using Heaviside function as,

$$\rho = \rho_v + (\rho_l - \rho_v)H \quad (13)$$

$$\mu^{-1} = \mu_v^{-1} + (\mu_l^{-1} - \mu_v^{-1})H \quad (14)$$

$$k^{-1} = k_l^{-1}H \quad (15)$$

It may be noted that Eq. (15) is consistent with the assumption that the vapor temperature remains constant at T_{sat}.

The level-set function, ϕ, is defined as the signed distance function from the interface. It is positive in the liquid phase and negative in the vapor phase. The interface separating the two phases is set as zero. The level-set function, ϕ, is advanced at the rate of interfacial velocity, u_{int}.

$$\phi_t + \mathbf{u}_{int}\cdot\nabla\phi = 0 \quad (16)$$

This ensures that the zero level-set is always maintained at the liquid-vapor interface. Generally, this equation does not satisfy the condition that the level set function should be maintained as a distance function, $|\nabla\phi|$. Therefore, the level-set function, ϕ, is reinitialized as a distance function from the interface at each time step by obtaining a steady-state solution of the equation,

$$\phi_\tau = \frac{\phi_0}{\sqrt{\phi_0 + h^2}}(1 - |\nabla\phi|) \quad (17)$$

where ϕ_0 is a solution of Eq. (16) and τ is an artificial time. While the level-set function is computed numerically from Eqs. (16) and (17), it is found that the total mass of vapor region is not conserved accurately. To preserve the mass conservation during the calculation process, the following volume correction step is added to the level set formulation,

$$\phi_\tau = (V - V_0)|\nabla\phi| \quad (18)$$

where V is the bubble volume computed from ϕ and V_0 is the bubble volume when mass conservation is satisfied. The rate of evaporation or condensation at the interface is determined by the rate of heat transfer from the liquid side, the accuracy of which depends on the grid size. Thus the magnitude of error that is propagated with time is dependent on the grid size that is employed.

In carrying out numerical simulation, the characteristic length, l_0, and the characteristic velocity, u_0, are defined as,

$$l_0 = \sqrt{\sigma/g(\rho_l - \rho_v)} \quad (19)$$

$$u_0 = \sqrt{gl_0} = \left(\frac{\sigma g}{\rho_l - \rho_v}\right)^{1/4} \quad (20)$$

The characteristic time is obtained by dividing the characteristic length with characteristic velocity. When analyzing reduced gravity cases, l_0 and u_0 for earth normal gravity are used.

Assumptions. The following assumptions are made during the analysis;

- Flow is incompressible.
- The thermodynamic properties of the individual phases are assumed constant since the investigation is performed for low superheats.
- The vapor inside the bubble is at saturation temperature.
- The wall temperature remains constant. Under constant heat flux conditions the wall temperature will vary spatially and temporally. The effect of this variation on bubble dynamics is not considered to be of first order.
- The flow is symmetric about the mid plane, thus only half of the domain needs to be calculated.
- The flow is laminar.

Solution Method. The projection method is used to solve the complete incompressible Navier-Stokes equations. In the first step, a preliminary velocity field is computed utilizing the momentum equations. This velocity does not satisfy the continuity equation. In the second step, a Poisson type equation derived using the continuity equation is solved to obtain the pressure. In the last step, the preliminary velocity field is projected onto a divergence-free velocity field using the computed pressure. In this study, the projection method is formulated in a staggered grid system in which the locations for velocity components are displaced from those for pressure and temperature. The semi-discrete equations are given as,

$$\rho\left(\frac{\mathbf{u}^* - \mathbf{u}^n}{\Delta t} + \mathbf{u}^n\cdot\nabla\mathbf{u}^n\right) = -\nabla p^n + \rho\mathbf{g} - \rho\beta_T(T - T_{sat})\mathbf{g} - \sigma\kappa\nabla H + \nabla\cdot\mu\nabla\mathbf{u}^* + \nabla\cdot\mu(\nabla\mathbf{u}^n)^T \quad (21)$$

$$\mathbf{u}^{**} = \mathbf{u}^* + \Delta t\frac{\nabla p^n}{\rho} \quad (22)$$

Equation (21) is solved using the pressure evaluated at the previous time step. Thereafter, the resulting velocity, $\mathbf{u}^*$, which does not satisfy the continuity equation, is corrected, as given by Eq.

(22). Substituting Eq. (22) into the continuity equation (Eq. (10)), the governing equation for pressure is obtained as,

$$\nabla \cdot \frac{\nabla p^{n+1}}{\rho} = \frac{1}{\Delta t}\left(\nabla \cdot \mathbf{u}^{**} - \frac{\mathbf{m}}{\rho^2} \cdot \nabla \rho - \dot{V}_{micro}\right) \tag{23}$$

Thus, the velocity at time step $n+1$ can be obtained as,

$$\mathbf{u}^{n+1} = \mathbf{u}^{**} - \Delta t \frac{\nabla p^{n+1}}{\rho} \tag{24}$$

To accelerate computations, multigrid and block correction methods are used. The discretized equations are solved by a line-by-line TDMA (tridiagonal matrix algorithm). During the computations, time steps are small enough to satisfy the CFL condition.

Initial Condition. Initially, at $t=0$, it is assumed that a fully developed thermal and hydrodynamic boundary layer is present on the surface. The initial thermal boundary layer thickness, δ_T, is evaluated from the turbulent boundary layer heat transfer correlation for an isothermal flat plate [32] as $\mathrm{Nu}_x = 0.0287\mathrm{Re}_x^{0.8}\mathrm{Pr}^{0.6}$. In this study, x, which is the distance from the inlet to the cavity, is taken to be 0.15 m to facilitate comparisons with the experiments of Maity [5]. It should be noted that because no precaution was taken in the experiments to laminarize the flow, the measured temperature profile in the thermal layer was more representative of turbulent boundary layer even at Reynolds numbers smaller than those at transition from laminar to turbulent flow. After δ_T is obtained, the hydrodynamic boundary layer thickness, δ, is calculated from the expression $\delta/\delta_T = 1.026\mathrm{Pr}^{1/3}$.

The initial temperature and velocity profiles are written as,

$$\frac{u_{in}}{U} = \left(\frac{y}{\delta}\right)^{1/7} \tag{25}$$

$$\frac{T_{in} - T_{sat}}{T_w - T_{sat}} = 1 - \left(\frac{y}{\delta_T}\right)^{1/7} \tag{26}$$

The computational model assumes the flow to be laminar. However, the initial thickness of the hydrodynamic and thermal boundary layers is for the turbulent boundary layer. This seemingly contradictory approach was taken to better simulate the conditions that existed in the experiments at bubble inception and where no effort was made to laminarize the flow. The limitation of the present work is that it does not simultaneously model turbulent hydrodynamics and thermal boundary layers. It should also be noted that after growth and departure of a bubble, the temperature and velocity profiles in the vicinity of the nucleation site will be distorted. However, in time these profiles will recover to their initial condition. In the absence of quantitative information regarding the waiting time, in the present work, it is assumed that the profiles fully recover (i.e., the waiting time is infinite). Any deviation, in the experiments, from this assumption will lead to some differences in the predicted and observed bubble growth rate and bubble departure and liftoff times. The assumed initial temperature profile does influence the bubble growth rate and departure and liftoff times. However, the resulting deviation diminishes as the bubble begins to slide because of the disturbance created by the bubble plays a more pronounced role.

Boundary Conditions. The boundary conditions for the governing equations are as follows,

$$\begin{gathered}
u = u_{in}(y), \quad v = 0, \quad w = 0, \quad T = T_{in}(y), \quad \phi_x = 0 \quad \text{at } x = 0 \\
u = 0, \quad v = 0, \quad w = 0, \quad T = T_w, \quad \phi_y = -\cos\varphi \quad \text{at } y = 0 \\
u = 0, \quad v = 0, \quad w = 0, \quad T_z = 0, \quad \phi_z = 0 \quad \text{at } z = 0 \\
u_x = 0, \quad v_x = 0, \quad w_x = 0, \quad T_x = 0, \quad \phi_x = 0 \quad \text{at } x = X \\
u = 0, \quad v = 0, \quad w = 0, \quad T_y = 0, \quad \phi_y = 0 \quad \text{at } y = Y
\end{gathered} \tag{27}$$

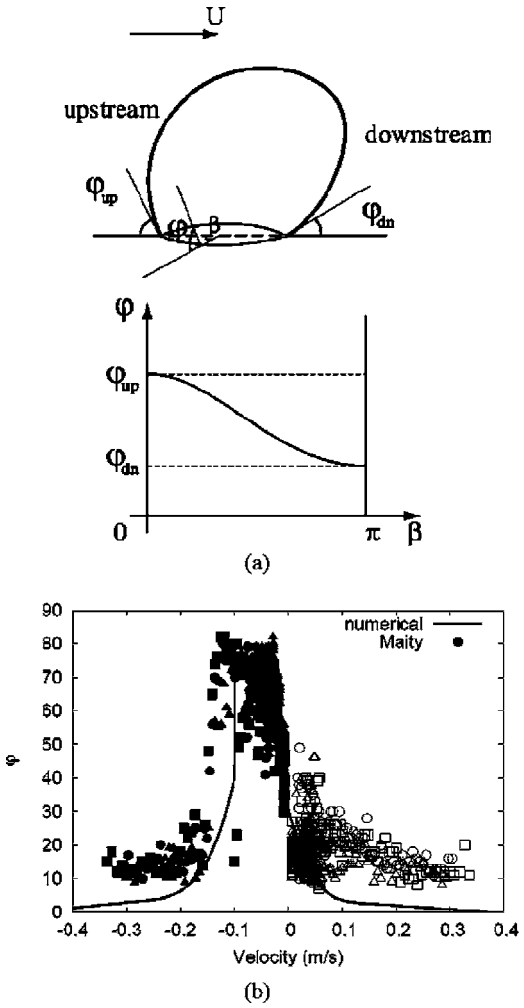

Fig. 2 (*a*) The definition of sliding velocity. (*b*) Dynamic contact angle as a function of sliding velocity.

$$u = 0, \quad v = 0, \quad w = 0, \quad T_z = 0, \quad \phi_z = 0 \quad \text{at } z = Z$$

In flow boiling, the contact angle that forms at the downstream side is defined as the downstream contact angle and the corresponding interface velocity is taken as positive. The contact angle that forms at the upstream side is defined as the upstream contact angle and the corresponding interface velocity is taken as negative. Figure 2 shows the dynamic contact angle that was reduced from the video pictures of Maity [5]. Note that Maity used water as the working fluid and the heating surface was made of a silicon wafer in his experiments. When the velocity is zero, the static contact angle is about 30–50 deg. As the interface velocity increases, the downstream contact angle decreases, which behaves like a receding contact angle since the interface moves over wet surface. The upstream contact angle increases, which acts like an advancing contact angle since the interface moves over dry region. However, at high velocities, both downstream and upstream contact angles decrease. This is probably because the interface may drag some liquid underneath the bubble when the interface velocity is high. Hence there may be a thin liquid layer present between the bubble and the heating surface. This causes the dynamic contact angle on the upstream side to be small as well. At present we do not have a theoretical basis for the a priori prediction of the upstream and downstream contact angles. The solid line representing a fit to the data is used as input to the numerical model. Because, at low contact angles, the measurement uncertainty is large and the measured contact angles are generally larger than the actual contact angles, the best fit is purposely made to

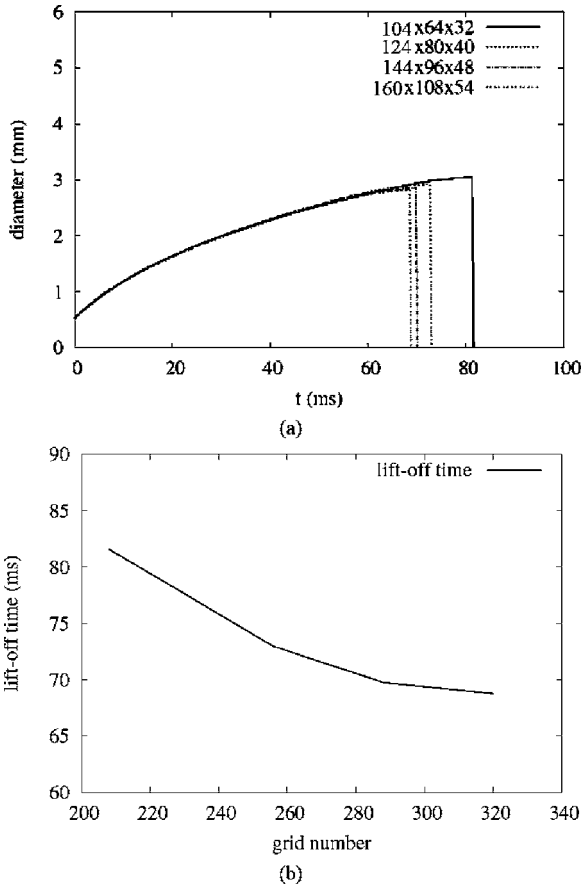

Fig. 3 (*a*) Grid sensitivity check. (*b*) Bubble liftoff time as a function of grid number.

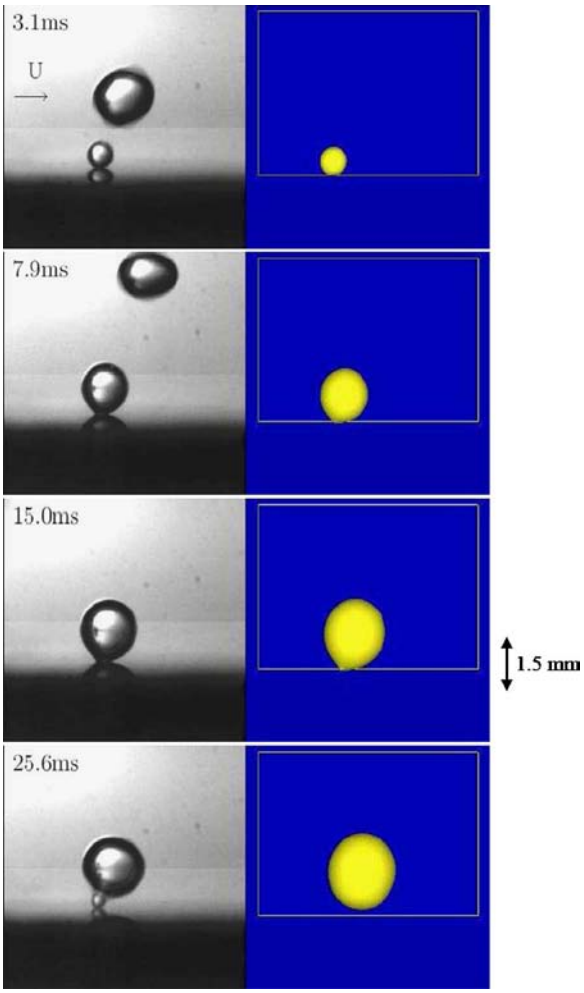

Fig. 4 The comparison of bubble shape for single bubble on horizontal surface, U=0.076 m/s, ΔT_w=5.3°C

underpredict the low contact angle data. Uncertainty in the contact angle affects the shape of the bubble, departure and liftoff diameters, the sliding distance and the growth period. Because of the variation of the upstream and downstream contact angles during bubble growth, no meaningful systematic study to quantify the effect of variation in the best fit to the contact angle data has been performed. Nevertheless, it was found that larger contact angles lead to larger bubbles at departure, longer sliding distance, and longer growth periods. The departure diameter is defined as the bubble diameter when the bubble begins to slide from the nucleation site, whereas the liftoff diameter is the diameter at which the bubble leaves the heater surface.

Convergence Check. To choose an appropriate mesh size, grid sensitivity was tested with 104, 128, 144, and 160 mesh points in the flow direction of dimensionless length 15. The results are plotted in Fig. 3. As the number of grids increases, the relative difference in the bubble growth rates becomes small. For 144 and 160 grid points, the difference in the bubble growth periods is less than 5%. The corresponding difference in the bubble liftoff time is less than 2%. To save computing time without losing too much accuracy, all computations in this study were carried out with 144 grid points.

Results

In this section, results from numerical simulations carried out on a horizontal surface are described and compared with data from experiments. The test fluid is water. First, the effect of bulk flow velocity is described. The effects of surface orientation and gravity levels are discussed in the subsequent sections.

Effect of Bulk Velocity. Bulk flow velocity is one of the main parameters considered in this study on nucleate flow boiling. Simulations are performed for three different bulk velocities of 0.076, 0.135, and 0.23 m/s.

Figure 4 shows a comparison of bubble shapes obtained from numerical calculations and those observed in experiments on a horizontal surface for U=0.076 m/s and ΔT_w=5.3°C. The shapes seen in both cases are similar. The bubble is nearly spherical and symmetrical in the initial stages. As the bubble grows in size, it starts to slide and becomes tilted in the direction of flow and the bubble grows asymmetrically thereafter. The upstream contact angle increases while the downstream contact angle decreases. In Fig. 5, the bubble shapes obtained from numerical prediction are superimposed on the experimental images at four different time steps. Except for small differences near the base and in the downstream direction, good agreement between the bubble shapes can be seen for all times. Bubbles are assumed to detach from the surface when the bubble base becomes smaller than the grid size.

Figures 6 and 7 show the velocity and temperature fields, respectively, at the mid-plane of the bubble. The isotherms are plotted between 0 (saturated liquid) and 1 (wall). The ΔT between isotherms is about 1°C. During the sliding motion and liftoff, the thermal boundary layer at the downstream side thickens and, as a result, isotherms are pushed outward. The opposite is true on the upstream side.

A quantitative comparison between numerical simulation and experimental data for bubble growth rate is shown in Fig. 8. It is

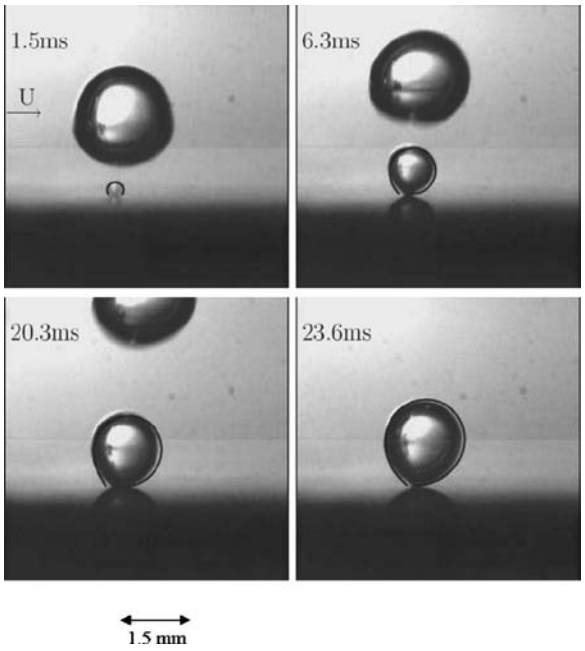

Fig. 5 Quantitative comparison of bubble shapes, U =0.076 m/s, ΔT_w=5.3°C

seen that results of the numerical simulation agree reasonably well with experimental data. However, the liftoff diameter is somewhat overpredicted. In the experiment the bubble liftoff diameter was about 1.5 mm whereas from the numerical calculations the bubble liftoff diameter is 1.7 mm.

Figure 9 shows the comparison of bubble growth rate on the horizontal surface for U=0.23 m/s and ΔT_w=5.3°C. During the early phase the bubble growth predicted from numerical simulations is in good agreement with data. But bubble departure diameter and growth period are overpredicted by the numerical simulation.

A comparison of bubble liftoff diameter as a function of bulk flow velocity between numerical simulation results and the experimental data of Maity [5] is presented in Fig. 10 for the horizontal surface for ΔT_w=5.3°C. The numerical simulations somewhat overpredict the bubble liftoff diameter. However, the same trend is found both in numerical simulation and experimental data, i.e., as the bulk velocity increases, the bubble liftoff diameter decreases. Figure 11 shows a similar comparison for bubble growth period. The growth period from numerical simulation is overpredicted at higher bulk velocities. The reason for the overprediction in higher bulk velocity could be the inaccuracy in specification of upstream and downstream contact angles.

Effect of Surface Orientation. The effect of heater surface orientation is studied in this section. By changing the surface orientation from horizontal to vertical through 30, 45, and 60 deg, the magnitude of gravity, both normal and parallel to the heater surface, could be varied. The variation affects the bubble dynamics.

Figure 12 shows a comparison of bubble shapes predicted from numerical calculations and those observed in experiments on vertical surface, U=0.076 m/s and ΔT_w=5.0°C. Generally, a resonable agreement is observed between bubble location and shape during the entire process of growth at the nucleation site, sliding motion, and liftoff. In Fig. 13 the bubble shapes predicted from numerical simulation are overlayed on those observed in the experiments. Overall the numerical simulations capture the bubble shape.

Figures 14 and 15 show the velocity and temperature fields, respectively, around the mid-plane of the bubble. The thermal

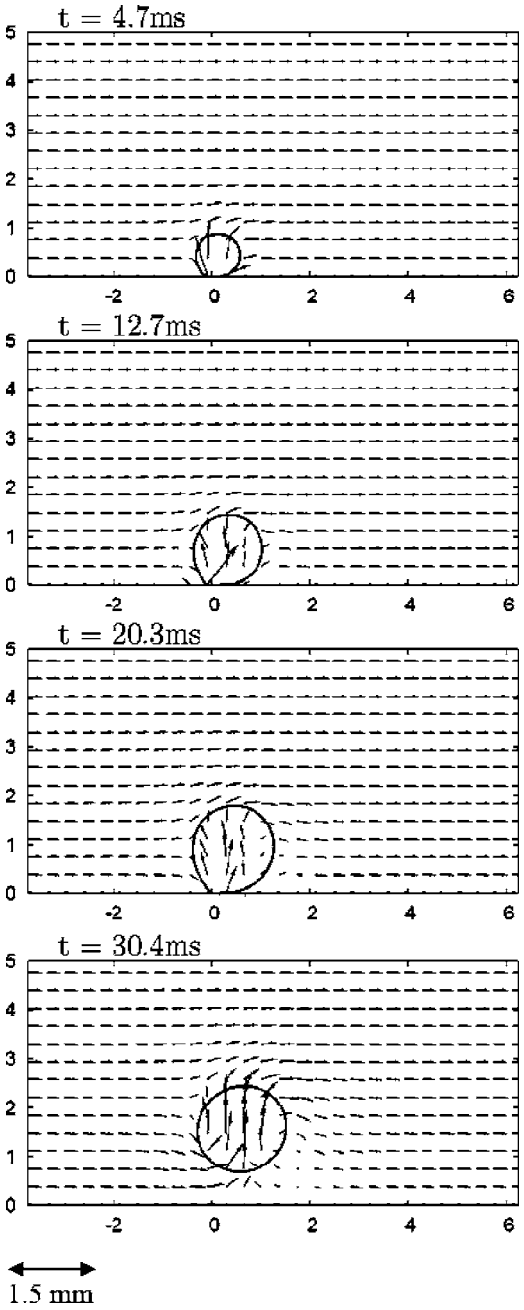

Fig. 6 Velocity field at the center plane around single bubble on a horizontal surface, U=0.076 m/s, ΔT_w=5.3°C

layer underneath the bubble is thin, indicating a high rate of heat transfer there. As the bubble slides, it accelerates and, prior to liftoff, its velocity exceeds the flow velocity. During the sliding motion of the bubble, a wake with low heat transfer region develops upstream of the bubble.

Figure 16 shows the comparison of the bubble growth rate obtained from numerical calculations and that observed in experiments on a vertical surface for U=0.076 m/s and ΔT_w=5.0°C. From experiments the bubble growth period is found to be about 60 ms and the bubble liftoff diameter is 2.5 mm; in contrast with numerical simulation, the bubble grows to around 3 mm in diameter in 70 ms before liftoff.

Figure 17 shows the pressure contours when the bubble is about to liftoff from the vertical surface. The pressure on the top of the bubble is less than that around the lower portion of the bubble. As

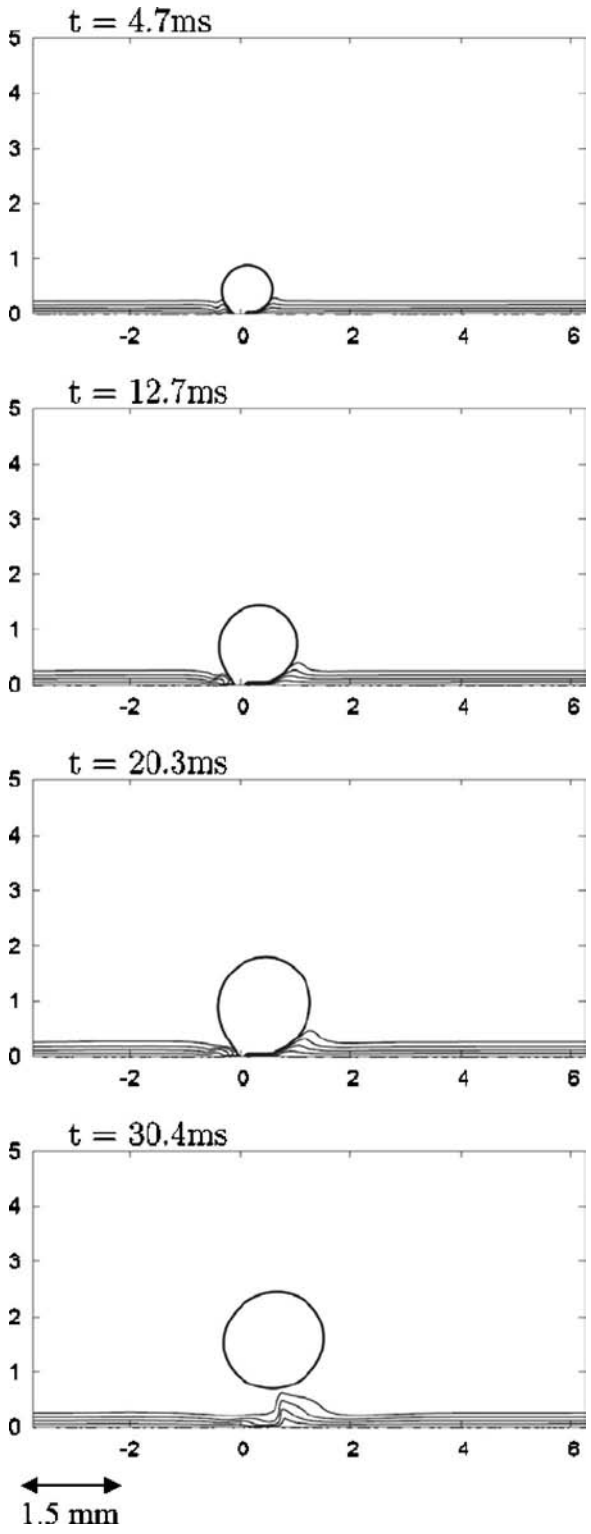

Fig. 7 Temperature field at the center plane around single bubble on a horizontal surface, U=0.076 m/s, ΔT_w=5.3°C

a result of this pressure difference between bottom and top, the bubble lifts off normal to the vertical heater surface while gravity acts parallel to the surface.

A comparison of bubble shapes observed in experiments on a 45 deg inclined surface for U=0.076 m/s and ΔT_w=5.3°C and predicted from numerical simulations is shown in Fig. 18. Good agreement is observed during the entire process of growth and

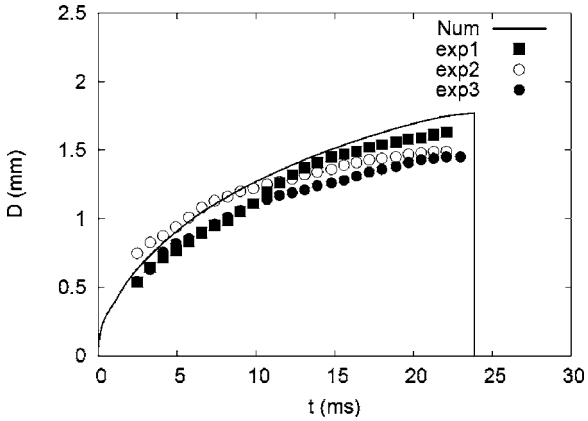

Fig. 8 The comparison of bubble diameter predicted from numerical simulation with experimental data obtained by Maity [5] on a horizontal surface, U=0.076 m/s, ΔT_w=5.3°C

sliding until liftoff. Figure 19 shows a quantitative comparison of the bubble growth rate predicted from numerical simulations with that observed in the experiments. In the experiments, the bubble lifts off between 30 and 45 ms and the bubble liftoff diameter is 2.0 mm, whereas from numerical calculation the bubble growth period is nearly 51 ms and the bubble diameter at liftoff is 2.4 mm. Figure 20 shows the relation between liftoff diameter and surface orientation for U=0.076 m/s and ΔT_w=5.3°C. The mag-

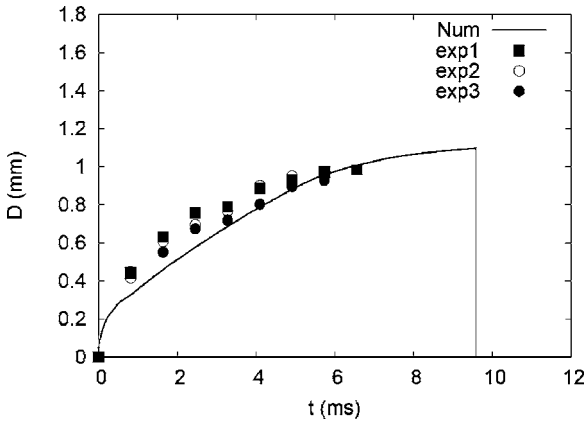

Fig. 9 The comparison of bubble diameter predicted from numerical simulation with experimental data obtained by Maity [5] on a horizontal surface, U=0.076 m/s, ΔT_w=5.3°C

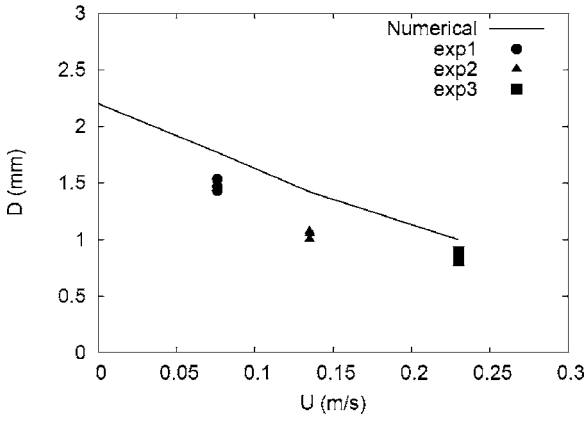

Fig. 10 Effect of bulk velocity on lift off diameter, experimental data obtained by Maity [5]

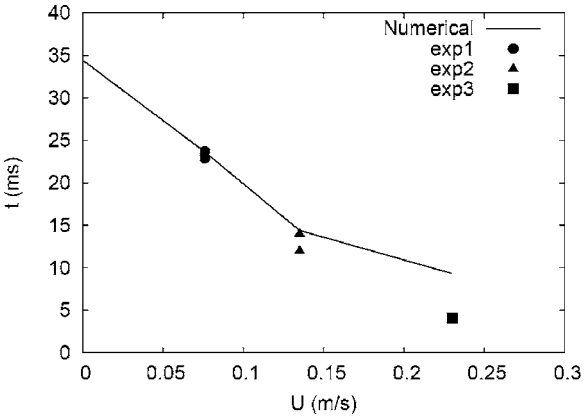

Fig. 11 Effect of bulk velocity on growth period, experimental data obtained by Maity [5]

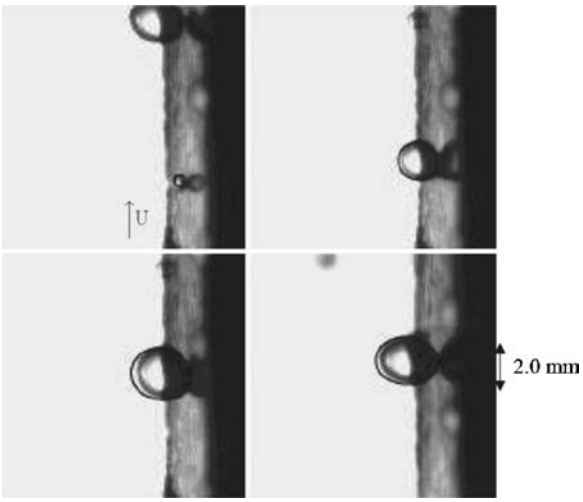

Fig. 13 Comparison of bubble shapes, U=0.076 m/s, ΔT_w =5.3°C

nitude of gravity, both normal and parallel to the heater surface, changes with the heater surface orientation varying from 0 deg (horizontal) to 30 deg and then 45, 60, and 90 deg (vertical up). This affects the bubble liftoff diameter. The normal component of gravity decreases with an increase in the angle of inclination. Thus, the contribution of buoyancy towards liftoff becomes smaller when the angle of inclination is increased. Therefore, the bubble needs to grow to a larger size to have enough lift to overcome the forces that keep the bubble on the heated surface. For a vertical surface, the gravity component normal to the surface is zero, but the bubble still lifts off. The liftoff, as pointed out earlier, occurs due to the pressure difference that develops between the lower and upper portions of the bubble during the sliding motion. The results from numerical simulation show the same trend as that observed from experimental data for bulk flow velocity U =0.076 m/s. As the bulk flow velocity increases, the deviation between prediction from numerical simulation and data from ex-

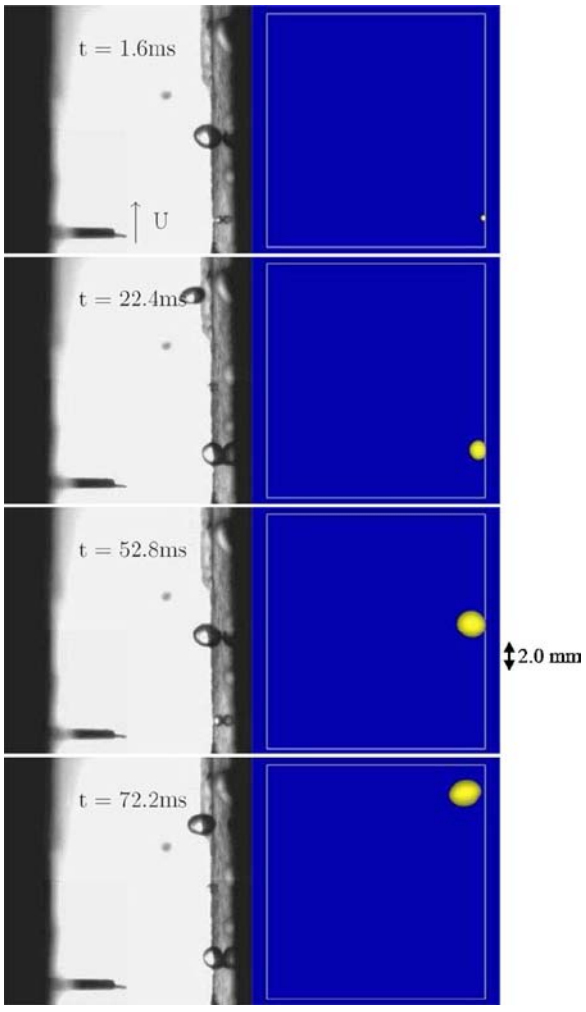

Fig. 12 The comparison of bubble shape for single bubble on vertical surface, U=0.076 m/s, ΔT_w=5.3°C

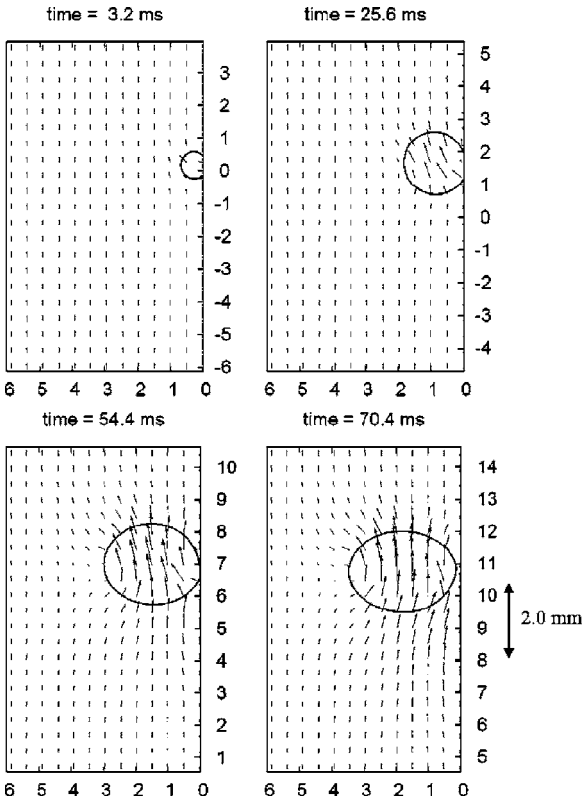

Fig. 14 Velocity field during bubble growth, sliding and liftoff on a vertical surface, U=0.076 m/s, ΔT_w=5.3°C

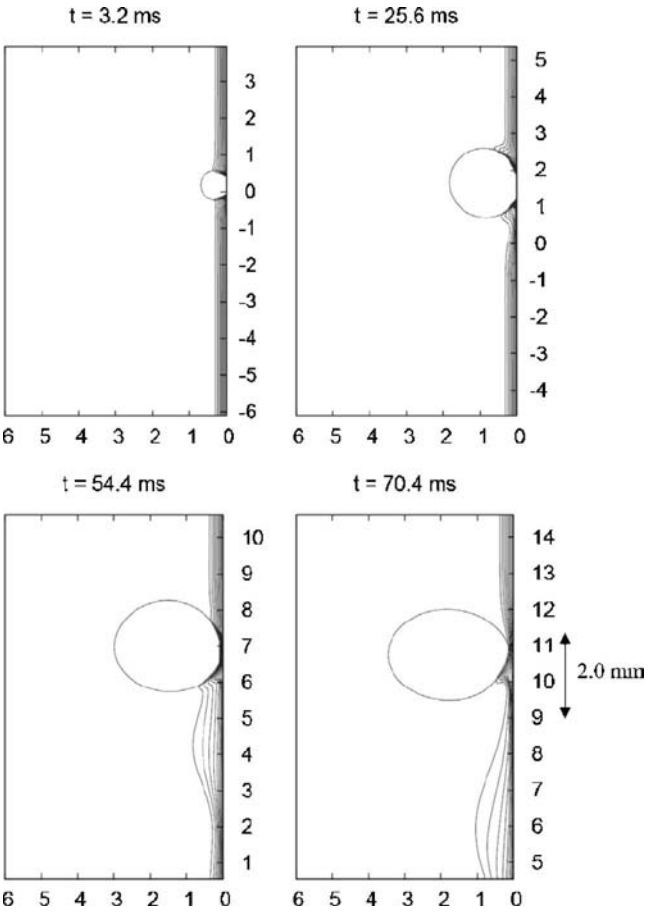

Fig. 15 Temperature field with temperature interval of 0.5°C on vertical surface, U=0.076 m/s, ΔT_w=5.3°C

periments increases. One reason could be the extent of dry region under the sliding bubble being larger in numerical simulations than that existed in the experiments.

Effect of Reduced Magnitude of Gravity. In pool boiling, the gravity level affects signifcantly the bubble growth period and the size of the bubbles at liftoff. Although the level of gravity continues to infuence bubble dynamics, its effect under flow conditions is reduced. Figure 21 shows the bubble diameter at liftoff as a function of dimensionless gravity level for an upward facing hori-

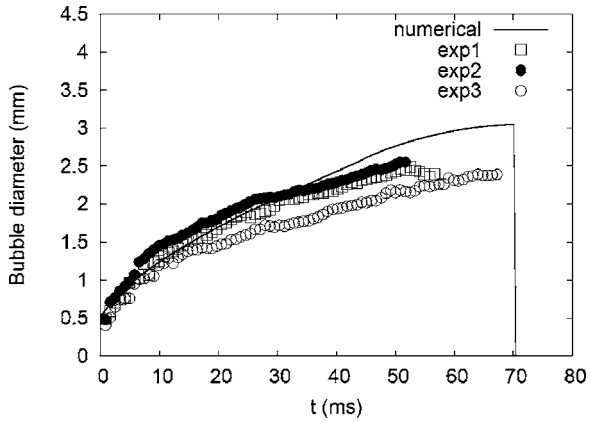

Fig. 16 The comparison of bubble diameter predicted from numerical simulation with experimental data obtained by Maity [5] on a vertical surface, U=0.076 m/s, ΔT_w=5.3°C

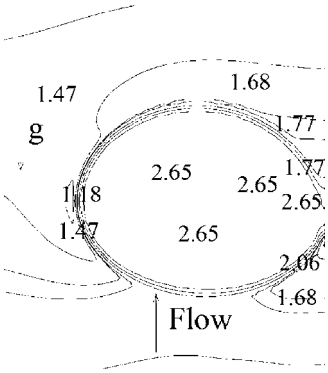

Fig. 17 The dimensionless pressure contours near the bubble when the bubble is about to lift off from the vertical surface, U=0.076 m/s, ΔT_w=5.3°C

zontal surface. The bubble diameter has been normalized with that (2.2 mm) calculated for earth normal gravity for pool boiling conditions with a static contact angle of 38 deg. The dependence of bubble diameter on gravity for pool boiling is also included. It can

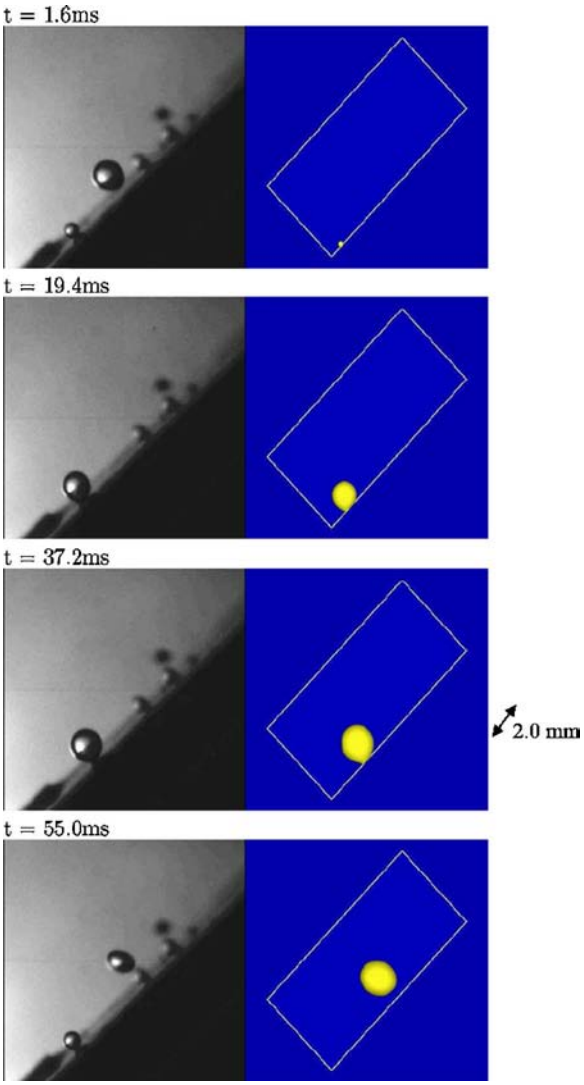

Fig. 18 Comparison of bubble shape predicted from numerical simulation and observed in experiment for a single bubble on 45 deg inclined surface, U=0.076 m/s, ΔT_w=5.3°C

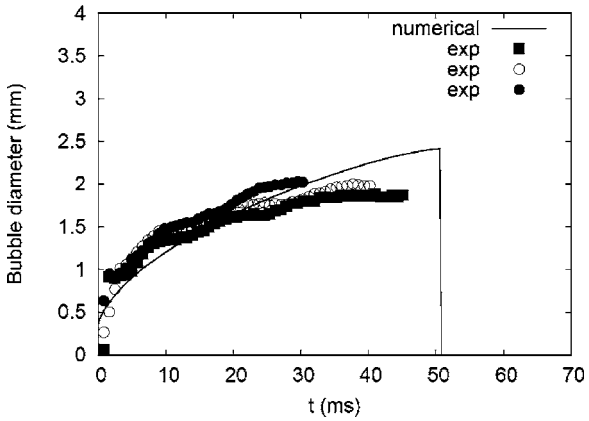

Fig. 19 The comparison of bubble diameter as a function of time predicted from numerical simulation with experimental data obtained by Maity [5] on 45 deg inclined surface, U =0.076 m/s, ΔT_w=5.3°C

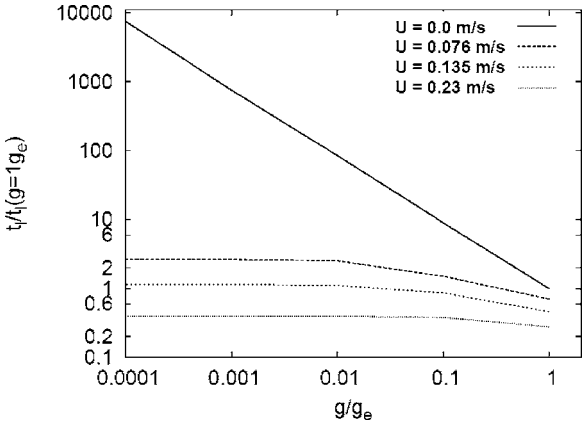

Fig. 22 Bubble growth period on an upward facing horizontal surface as a function of the gravity level, ΔT_w=5.3°C

be seen that the effect of the magnitude of gravity on bubble liftoff diameter diminishes as flow velocity is increased. Figure 22 shows the ratio of the bubble growth period normalized with that at earth normal gravity, 34.0 ms, as a function of gravity level. The effect of the magnitude of gravity on bubble growth period is reduced also as bulk velocity is increased.

Figures 23 and 24 respectively show the dimensionless bubble diameter and growth period for different gravity levels as a function of bulk flow velocity. It can be seen that the magnitude of gravity shows little effect on the liftoff diameter and growth period when flow velocity is 0.23 m/s.

One set of low gravity data from the experiments conducted aboard NASA's KC-135 aircraft is available. During the parabolic trajectory of the aircraft, a gravity level of a few percent of earth normal gravity is sustained for about 20 s. Figure 25 shows a comparison between the prediction of bubble growth from numerical simulations with data from experiments when the gravity

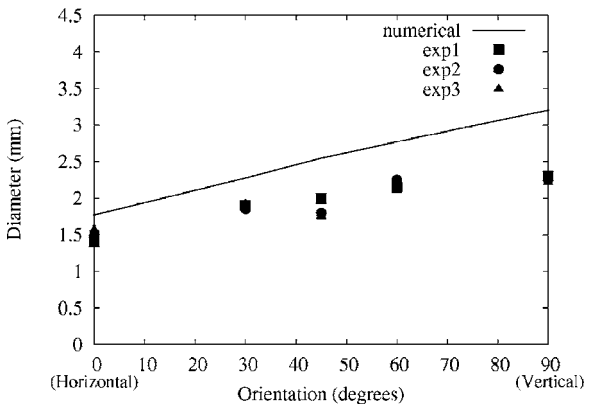

Fig. 20 Effect of orientation on bubble liftoff diameter, experimental data obtained by Maity [5], U=0.076 m/s, ΔT_w=5.3°C

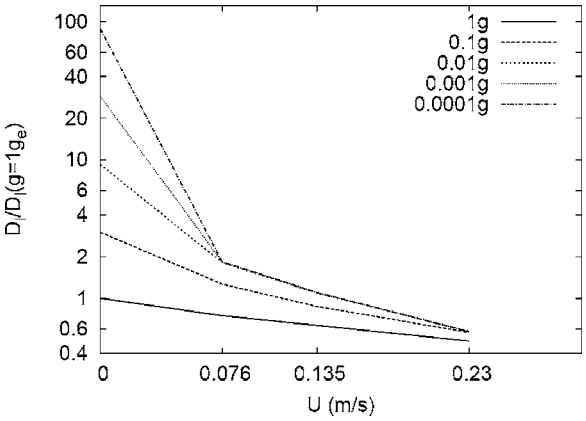

Fig. 23 Bubble diameter at liftoff as a function of the bulk flow velocity for different gravity levels, ΔT_w=5.3°C

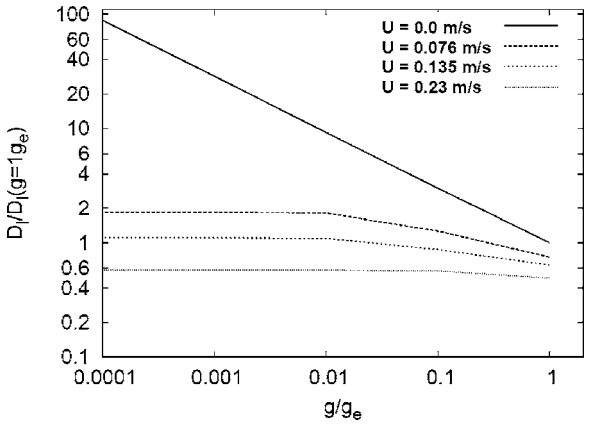

Fig. 21 Bubble diameter at liftoff on an upward facing horizontal surface as a function of gravity level, ΔT_w=5.3°C

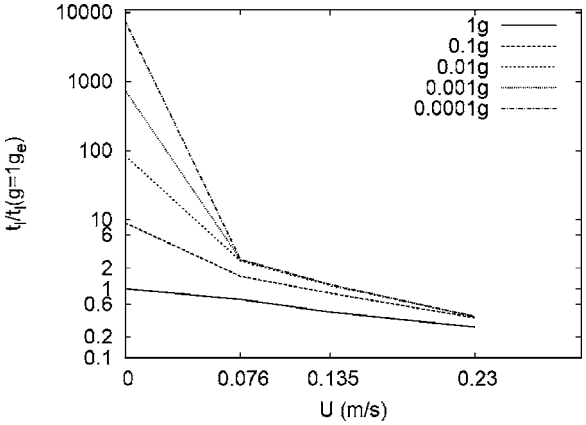

Fig. 24 Bubble growth period as a function of the bulk flow velocity for different gravity levels

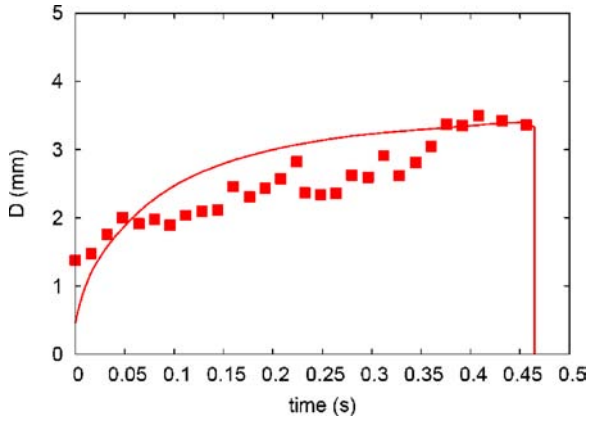

Fig. 25 Comparison of measured bubble diameter and numerical predictions for reduced gravity conditions, $g=0.05g_e$, $\Delta T_w=3.8°C$, $\Delta T_{sub}=1.5°C$, $U=0.076$ m/s

level in the KC-135 aircraft was about 1/20 of earth normal gravity. The bubble liftoff diameter predicted from numerical simulations is reasonably in agreement with that observed in experiments when the liquid had a subcooling of about 1.75°C. The experimental data show some oscillations. The reason for this is attributed to the turbulence experienced by the airplane. The sloshing of the liquid appears to influence the bubble growth pattern. Because of limited experimental data it is difficult to identify the exact mechanism of the observed oscillations in the bubble growth pattern. Nonetheless, the liftoff diameter and growth period are reasonably well predicted from the numerical simulations.

CONCLUSIONS

1. Numerical simulations of single bubble dynamics during nucleate flow boiling are carried out without making any approximation to the bubble shape. The effect of micro-layer evaporation is included in the study. However, the model does include empirical input from experiments with respect to the dependence of upstream and downstream contact angles on the interface velocity.
2. Bubble sliding motion prior to liftoff as observed in experiments is fairly well predicted from numerical simulations.
3. The bubble liftoff diameter is found to decrease with bulk flow velocity but increases when the component of gravity normal to the heater surface is decreased.
4. The pressure difference that develops between lower and upper parts of the bubble during the sliding motion helps the bubble liftoff from the surface for the vertical up-flow boiling case and reduced gravity conditions.
5. The effect of the magnitude of gravity on bubble liftoff diameter weakens as flow velocity is increased. For flow velocity of 0.23 m/s, the magnitude of gravity appears to have little effect on bubble liftoff diameter and growth period.

Acknowledgment

This work received support from NASA under Microgravity Fluid Physics Program.

Nomenclature

c_p = specific heat
$\mathbf{g}$ = gravity vector
g_e = earth normal gravity
h = grid spacing
h_{fg} = latent heat of vaporization
H = step function
k = thermal conductivity
l_0 = characteristic length scale
$\mathbf{m}$ = mass flux vector
p = pressure
Pr = Prandtl number
r = radius
Re = Reynolds number
$\mathbf{u}$ = velocity vector
U = bulk velocity parallel to the heater surface
u_0 = characteristic velocity
V = bubble volume
$\dot{V}_{micro}$ = rate of vapor volume production from the microlayer
X = length of computational domain in x direction
Y = height of computational domain in y direction
Z = depth of computational domain in z direction

Greek

β_T = coefficient of thermal expansion
δ = hydrodynamic layer thickness
δ_T = thermal layer thickness
ϕ = level set function
η = dimensionless similarity variable
φ = contact angle
κ = interfacial curvature
μ = dynamic viscosity
θ = inclination angle
ρ = density
σ = surface tension
τ = artificial time

Subscripts

dn = downstream
in = inlet
int = interface
l = liquid
sat = saturation
t = ∂/∂t
up = upstream
v = vapor
w = wall
x = ∂/∂x
y = ∂/∂y
z = ∂/∂z
t = ∂/∂t

Superscripts

T = matrix transpose
$*$ = temporary variable

References

[1] Nukiyama, S., 1934, "Maximum and Minimum Values of Heat Transmitted From a Metal to Boiling Water under Atmospheric Pressure," J. Soc. Mech. Eng. (Japan), **37**, pp. 367–374.
[2] Gunther, F. C., 1951, "Photographic Study of Surface-Boiling Heat Transfer to Water With Forced Convection," Trans. ASME, **73**, pp. 115–123.
[3] Van Helden, W. G. J., Van der Geld, C. W. M., and Boot, P. G. M., 1995, "Forces on Bubble Growing and Detaching in Flow Along a Vertical Wall," Int. J. Heat Mass Transfer, **38**(11), pp. 2075–2088.
[4] Thorncroft, G. E., Klausner, J. F., and Mei, R., 1998, "An Experimental Investigation of Bubble Growth and Detachment in Vertical Upflow and Downflow Boiling," Int. J. Heat Mass Transfer, **41**, pp. 3857–3871.
[5] Maity, S., 2000, "Effect of Velocity and Gravity on Bubble Dynamics," M.S. thesis, University of California, Los Angeles.
[6] Al-Hayes, R. A. M., and Winterton, R. H. S., 1981, "Bubble Diameter on Detachment in Flowing Liquids," Int. J. Heat Mass Transfer, **24**, pp. 223–230.
[7] Marsh, J. A., Garoff, S., and Dussan, V. E., 1993, "Dynamic Contact Angle and Hydrodynamics Near a Moving Contact Line," Phys. Rev. Lett., **70**(18), pp. 2778–2781.
[8] Chibowski, E., and Gonzalez-Caballero, F., 1993, "Interpretation of Contact Angle Hysteresis," J. Adhes. Sci. Technol., **7**(11), pp. 1195–1209.
[9] Shoji, M., and Zhang, X. Y., 1994, "Study of Contact Angle Hysteresis. (In Relation to Boiling Surface Wettability)," JSME Int. J., Ser. B, **37**(3), pp. 560–567.
[10] Lin, S. Y., Chang, H. C., Lin, L. W., and Huang, P. Y., 1996, "Measurement of

Dynamic/Advancing/Receding Contact Angle by Video-Enhanced Sessile Drop Tensionmetry," Rev. Sci. Instrum., **67**(8), pp. 2852–2858.
[11] Ramanujapu, N., and Dhir, V. K., 1999, "Dynamics of Contact Angle During Growth and Departure of a Vapor Bubble at a Single Nucleation Site," Proceedings of 5th ASME/JSME Joint Thermal Engineering Conference, San Diego, CA, March 14-19.
[12] Klausner, J. F., Mei, R., Bernhard, D. M., and Zeng, L. Z., 1993, "Vapor Bubble Departure in Forced Convection Boiling," Int. J. Heat Mass Transfer, **36**(3), pp. 651–662.
[13] Klausner, J. F., Mei, R., and Zeng, L. Z., 1997, "Predicting Stochastic Features of Vapor Bubble Detachment in Flow Boiling," Int. J. Heat Mass Transfer, **40**(15), pp. 3547–3552.
[14] Bibeau, E. L., and Salcudean, M., 1994, "A Study of Bubble Ebullition in Forced-Convective Subcooled Nucleate Boiling at Low Pressure," Int. J. Heat Mass Transfer, **37**(15), pp. 2245–2259.
[15] Qiu, D., and Van der Geld, C. W. M., 1997, "Bubble Shapes and Forces at Detachment," Proceedings of International Engineering Foundation Conference on Convective Flow and Pool Boiling, Islee, Germany, May 18-23.
[16] Kandlikar, S. G., and Stumm, B. J., 1995, "A Control Volume Approach for Investigating Forces on a Departing Bubble Under Subcooled Flow Boiling," ASME J. Heat Transfer, **117**, pp. 990–997.
[17] Kirk, K. M., Merte, J. H., and Keller, R. B., 1995, "Low-Velocity Subcooled Nucleate Flow Boiling at Various Orientations," ASME J. Heat Transfer, **117**, pp. 380–386.
[18] Lee, H. S., and Herman Merte, J., 1996, "Hemispherical Vapor Bubble Growth in Microgravity: Experiments and Model," Int. J. Heat Mass Transfer, **39**(2), pp. 2449–2461.
[19] Qiu, D., and Dhir, V. K., 2000, "Single and Multiple Bubble Dynamics during Nucleate Boiling under Low Gravtiy Conditions," Proceedings of NHTC'00, 34th National Heat Transfer Conference.
[20] Straub, J., 2001, "Boiling Heat Transfer and Bubble Dynamics in Microgravity," Adv. Heat Transfer, **35**, pp. 57–172.
[21] Ma, Y., and Chung, J., 2001, "A Study of Bubble Dynamics in Reduced Gravity Forced Convection Boiling," Int. J. Heat Mass Transfer, **44**, pp. 399–415.
[22] Sussman, M., Smereka, P., and Osher, S., 1994, "A Level Set Approach for Computing Solutions to Incompressible Two-Phase Flow," J. Comput. Phys., **114**, pp. 146–159.
[23] Chang, Y. C., Hou, T. Y., Merriman, B., and Osher, S., 1996, "A Level Set Formulation of Eulerian Interface Capturing Methods for Incompressible Fluid Flows," J. Comput. Phys., **124**, pp. 449–464.
[24] Son, G., Dhir, V. K., and Ramanujapu, N., 1999, "Dynamics and Heat Transfer Associated with a Single Bubble During Nucleate Boiling on a Horizontal Surface," ASME J. Heat Transfer, **121**, pp. 623–631.
[25] Stephan, P., and Hammer, J., 1994, "A New Model for Nucleate Boiling Heat Transfer," Wärme-und Stoffübertragung, **30**, pp. 119–125.
[26] Son, G., 2001, "Numerical Study on a Sliding Bubble During Nucleate Boiling," KSME Int. J., **15**(7), pp. 931–940.
[27] Abarajith, H. S., and Dhir, V. K., 2002, "Effect of Contact Angle on the Dynamics of a Single Bubble During Pool Boiling Using Numerical Simulations," Proceedings of IMECE2002 ASME International Mechanical Engineering Congress & Exposition, New Orleans, LA, November 17-22.
[28] Abarajith, H. S., Dhir, V. K., and Son, G., 2004, "Numerical Simulation of the Dynamics of the Multiple Bubble Merger during Pool Boiling under Reduced Gravity Conditions," Japan-USA Seminar on Multiphase Flow, Grazie, Japan, December 12-16.
[29] Mukherjee, A., and Dhir, V. K., 2004, "Study of Lateral Merger of Vapor Bubbles during Nucleate Pool Boiling," ASME J. Heat Transfer, **126**, pp. 1023–1039.
[30] Takahira, H., and Banerjee, S., 2000, "Numerical Simulation of Three Dimensional Bubble Growth and Detachment in a Microgravity Shear Flow," *Microgravity Fluids Physics and Heat Transfer*, V Shie, ed. (Begell House, New York, 2000), pp. 80–87.
[31] Lay, J. H., and Dhir, V. K., 1995, "Shape of Vapor Stem During Nucleate Boiling of Saturated Liquids," ASME J. Heat Transfer, **117**, pp. 394–401.
[32] Kays, W. M., and Crawford, M. E., 1980, *Convective Heat and Mass Transfer*, McGraw-Hill, New York.

Numerical Study of a Single Bubble Sliding on a Downward Facing Heated Surface

Ding Li

Vijay K. Dhir[1]

Mechanical and Aerospace Engineering Department, Henry Samueli School of Engineering and Applied Science, University of California, Los Angeles, 420 Westwood Plaza, Los Angeles, CA 90095-1597
e-mail: vdhir@seas.ucla.edu

In this study, a complete three-dimensional numerical simulation of single bubble sliding on a downward facing heater surface is carried out. The continuity, momentum, and energy equations are solved using a finite-difference method. Level-set method is used to capture the liquid-vapor interface. The shape of the sliding bubble changes from a sphere, to an ellipsoid and finally to a bubble-cap. The wall heat flux downstream of the sliding bubble is much larger than that upstream of the bubble. This indicates that wall heat transfer is significantly enhanced by sliding motion of the bubble. The bubble shape and sliding distance predicted from numerical simulations is compared with data from experiments. [DOI: 10.1115/1.2717943]

Keywords: numerical simulation, bubble, boiling

Introduction

In boiling, the heat transfer rate is much higher than that for single phase convection. This increase in the heat transfer is not only because of phase change at the nucleation sites but also due to the contribution of the convective motion caused by bubble dynamics. In a number of heater geometries such as inclined surfaces, and cylinders and spheres bubbles slide along the heater surface prior to lift off from the surface. As such, understanding of the sliding bubble phenomenon is a prerequisite to modeling of nucleating boiling heat transfer on these geometries. Only a few experimental studies have been conducted on the dynamics of sliding bubbles and associated heat transfer. In this work, we use three-dimensional numerical simulation of a single bubble sliding on a downward facing heater surface to provide an improved understanding of the process. In the following, a brief review of studies available in the literature is provided.

Experimental Studies. Cornwell and Schüeller [1] experimentally studied the influence of sliding bubbles on boiling outside a tube bundle. The test fluid was R113. It was concluded that a very thin liquid film (a few microns thick) underneath the sliding bubbles accounted for the increase in heat transfer. Houston and Cornwell [2] compared the heat transfer rates with and without sliding bubbles. They concluded that the turbulence caused by the sliding bubbles is an important mechanism in enhancing the heat transfer from the surface. The evaporation under the bubble also played an important role, but it was not as large as that due to the convective motion due to sliding bubbles. They also concluded that the thickness of the liquid layer underneath the bubble should be of the order of a few microns.

Akiyama and Tachibana [3] proposed that the sliding bubble heat transfer augmentation could be modeled as a rough surface heat transfer problem with bubble diameter treated as the characteristic length. The heat transfer mechanism in fully developed nucleate boiling was assumed to be dominated by the ejection of the bubbles agitating the subcooled liquid and the thermal layer. Chung and Bankoff [4] reported that sliding bubble increases the microlayer evaporation significantly and calculated the total heat transfer to a bubble with a constant radius and step function lifetime.

The effect of vapor bubble sliding on heat transfer was further investigated by Thorncroft and Klausner [5]. They suggested that instead of superposing bulk turbulent heat transfer to that of phase change, the fact that these two are interrelated should be considered. They found that the influence of vapor bubble sliding on forced convection heat transfer could account for as much as 52% of the total energy transfer. They also argued that bubble dynamics in forced convection is strongly influenced by bulk flow behavior and bulk flow turbulent heat transport is influenced by bubble dynamics.

Qiu and Dhir [6] presented the flow pattern and heat transfer associated with a bubble sliding along a downward facing heater surface. The test fluid was PF5060. On a downward facing surface, a single bubble was created at an artificial cavity. The bubble shape changed from initially a sphere to elongated ellipsoids at the upper end of the surface. A thin liquid wedge was observed between the front of the bubble and the heater surface. Holographic interferometry was used to obtain the temperature field in the subcooled liquid. Flow pattern around and in the wake of the bubble was studied by using PIV. Vortices were observed to shed from the wake of the bubble, resulting in significant wall temperature drop. Manickam and Dhir [7] measured temperature gradient around the bubble interface and the heat transfer into or out of the bubble for saturated and low subcooling cases. They found that the bubble continues to grow as it slides along the heater surface. The condensation heat transfer around the bubble interface was small for $\theta < 30$ deg, where θ is the angle measured from the wall to the outward normal drawn from the center of bubble. Condensation heat transfer was found to increase until around $\theta = 80$ deg and then decreased in the wake region of the bubble.

Bayazit et al. [8] have also reported on the enhancement of heat transfer caused by a bubble sliding along an inclined surface. The experimental data were obtained on an electrically heated thin-foil surface that was exposed on its lower side to FC-87. A sequence of digital images was obtained from two cameras. The thermal imprint of the bubble was correlated to its motion and position. The bubble was generated using a bubble generator developed for these experiments. The heater surface was at 12 deg inclination from horizontal and the liquid subcooling was maintained at 5 °C for the experiments reported. Three regimes of bubble motion were observed: spherical, ellipsoidal, and bubble-cap. A model for

[1]Corresponding author.

Contributed by Heat Transfer Division of ASME for publication in the JOURNAL OF HEAT TRANSFER. Manuscript received May 17, 2006; final manuscript received December 1, 2006. Review conducted by Raj M. Manglik. Paper presented at the 2005 ASME Heat Transfer Summer Conference (HT2005), July 15, 2005–July 22, 2005, San Francisco, CA.

 Copyright © 2007 by ASME

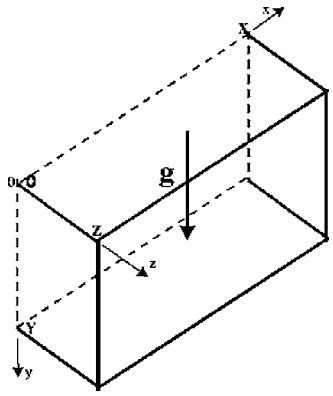

Fig. 1 Computational domain used in the numerical simulation

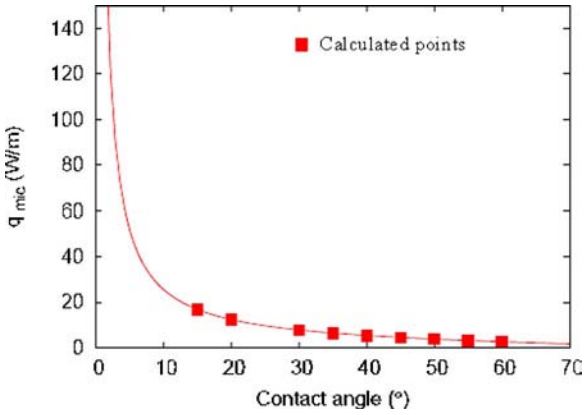

Fig. 2 Microlayer heat transfer per unit length in the circumferential direction as a function of contact angle (ΔT_w=0.5°C)

heat transfer within the microlayer underneath the bubble was used to infer the microlayer thickness. Preliminary results showed a microlayer thickness of 40–50 μm for these experiments.

Numerical Studies. Sussman et al. [9] presented a level-set approach for computing incompressible two-phase flow. By keeping the level set as a distance function, the interface was easily captured by the zero level-set. The calculations were carried out for air bubbles in water and falling water drops in air with satisfactory results. Though the level-set method is easy to use, the numerical discretization of the level-set formulation does not satisfy mass conservation, in general. Chang et al. [10] introduced a volume correction step to the level-set formulation in 1996. By solving an additional Hamilton-Jacobi equation to steady state, the mass was forced to be conserved.

Son et al. [11] developed a model for growth of an isolated bubble on an upward facing heated surface using complete numerical simulation. The model, based on Sussman's level-set method, captures the bubble interface and offers many improvements over previously published models. It yields the spatial and temporal distribution of the wall heat flux, the microlayer contribution, and the interface heat transfer. In the model a static contact angle was used both for the advancing and receding phases of the interface. The use of the static contact angle was justified on the basis that static angle represents the average value of the advancing and receding contact angles and the bubble is symmetrical in pool boiling case.

Also, the time over which the receding contact angles prevails is much shorter than that for the advancing contact angle. The numerical results agreed well with data from experiments. In 2001, Son [12] modified Chang et al.'s formulation and included the volume correction formulation into the boiling heat transfer model. More recently, Takahira et al. [13] have developed another mass correction algorithm to be used with the level set formulation by employing a multiplier of order one. The multiplier was evaluated from experience rather than a generalized algorithm. Majumder and Chakraborty [14] have proposed a level set formulation combined with the volume fraction function as an alternative to the step function. However, compared to the step function evaluated algebraically, the volume fraction formulation requires quite complicated geometric calculations between the volume fraction and a piecewise linear interface constructed from the level-set function. The above-mentioned numerical techniques for better mass conservation have not been extended to two-phase flows with phase change. Li and Dhir [15] extended Son's model [12] to flow boiling. By employing a dynamic contact angle and interface velocity relationship, the numerical results were found to agree well with data from experiments.

Numerical Model

This section presents the 3D computational model used in this study. The computational domain is divided into the microregion and the macroregion. The microregion is a thin film that lies underneath the bubble, whereas the macroregion consists of the bubble and the liquid surrounding the bubble. The governing equations for mass, momentum, and energy are numerically solved for each of these two domains. Combining the mass, momentum, and energy equations for the microlayer, the radial variation of the film thickness is obtained as [11]

$$\delta''' = f(\delta, \delta', \delta'', \delta''') \tag{1}$$

where the δ' denoted $\partial/\partial r$.

The boundary conditions for Eq. (1) are as follows:

(i) At $r=R_0$ (inner radius—outer radius of dry region)

$$\delta = \delta_0, \quad \delta' = \delta''' = 0 \tag{2}$$

where δ_0 is of the order of molecular size.

(ii) At $r=R_1$ (outer radius)

$$\delta = \frac{h}{2}, \quad \delta'' = 0 \tag{3}$$

where $h/2$ is the vertical distance to the first computational node for the level set function, from the wall. In implementing the above-presented boundary conditions the radius R_1 is determined from the solution of the macroregion. For a given dispersion constant, the microlayer formulation (Eq. (1)) and R_0 are solved with the five boundary conditions (Eqs. (2) and (3)). In this work an apparent contact angle is defined as

$$\tan\varphi = \frac{h/2}{(R_1 - R_0)} \tag{4}$$

For sliding bubbles, the apparent contact angle is different in the upstream and downstream directions as described later. The contact angles between the upstream and downstream sides are interpolated using

$$\varphi = \varphi_{dn} + \frac{(\varphi_{up} - \varphi_{dn})}{2}[1 + \tanh(\pi - 2\beta)] \tag{5}$$

where angle β varies from 0 (upstream side) to π (downstream side) and φ_{up} and φ_{dn} are the upstream and downstream contact angles, respectively. An expression for the rate at which vapor is produced from the microlayer is written as

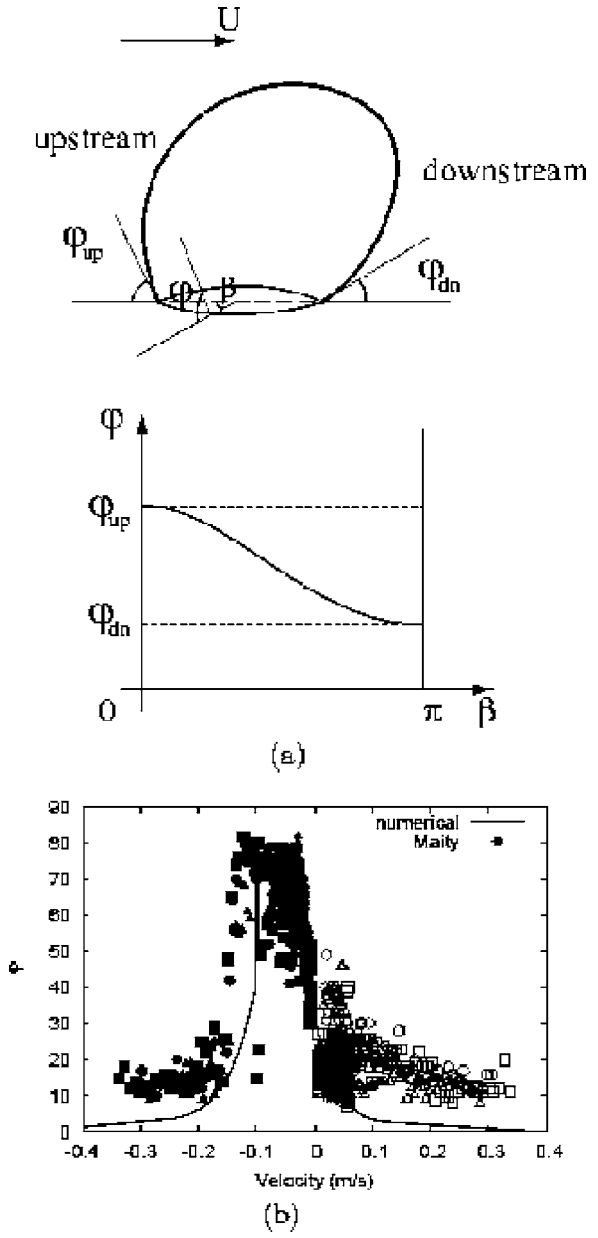

Fig. 3 (*a*) The definition of interface velocity and (*b*) dynamic contact angle as a function of interface velocity

$$\dot{V}_{\text{micro}} = \int_{R_0}^{R_1} \frac{k_l(T_w - T_{\text{int}})}{\rho_v h_{fg} \delta \Delta V_{\text{micro}}} \tag{6}$$

where ΔV_{micro} is a vapor side control volume near the microregion, which has been arbitrarily chosen to be $R_1 - 3h \leqslant r \leqslant R_1$ and $0 \leqslant y \leqslant h$. $\dot{V}_{\text{micro}}$ is included in the mass conservation equation used in the solution of the macroregion.

A staggered grid is used in the finite difference scheme. To accelerate computation, multigrid and block correction methods are used. The discretized equations are solved by a line-by-line TDMA (Tridiagonal Matrix Algorithm).

Figure 1 shows the computational domain used in the numerical simulation of the macroregion, $X=160$ mm, $Y=23$ mm, and $Z=11.5$ mm. Only half of the bubble is considered since the bubble is symmetric about the flow direction. Level-set formulation is used to track the interface. The level-set function, ϕ, is defined as the signed distance function from the interface. The negative sign is chosen for the vapor phase and the positive sign for the liquid phase. The distance function ϕ is zero at the interface separating the two phases. The shape of the growing bubble is tracked by noting the zero level-set. The governing equations of mass, momentum, and energy for the vapor-liquid region can be formulated as

Table 1 Thermophysical properties of PF-5060

Quantity	Unit	Liquid	Vapor
ρ	kg/m^3	1620.0	13.4
c_p	kJ/kg K	1.10	2.02
k	W/mK	0.0522	0.0248
μ	kg/ms	2.8×10^{-7}	2.57×10^{-7}
h_{fg}	J/kg	8.45×104	
β_T	K^{-1}	1.64×10^{-3}	
σ	N/m	8.27×10^{-3}	

$$\nabla \cdot \mathbf{u} = -\frac{1}{\rho}\left(\frac{\partial \rho}{\partial t} + \mathbf{u} \cdot \nabla \rho\right) + \dot{V}_{\text{micro}} \tag{7}$$

or after algebraic manipulation can be written as

$$\nabla \cdot \mathbf{u} = \frac{\mathbf{m}}{\rho^2} \cdot \nabla \rho + \dot{V}_{\text{micro}} \tag{8}$$

$$\rho(\mathbf{u}_t + \mathbf{u} \cdot \nabla \mathbf{u}) = -\nabla p + \rho \mathbf{g} - \rho \beta_T (T - T_{\text{sat}})\mathbf{g} - \sigma \kappa \nabla H + \nabla \cdot \mu \nabla \mathbf{u} + \nabla \cdot \mu \nabla \mathbf{u}^T \tag{9}$$

$$\rho c_{pl}(T_t + \mathbf{u} \cdot \nabla T) = \nabla \cdot k \nabla T \quad \text{for } H > 0$$

$$T = T_{\text{sat}} \quad \text{for } H = 0 \tag{10}$$

where

$$\mathbf{m} = \rho_l(\mathbf{u}_{\text{int}} - \mathbf{u}_l) = \rho_v(\mathbf{u}_{\text{int}} - \mathbf{u}_l)$$

$$\rho = \rho_v + (\rho_l - \rho_v)H$$

$$k^{-1} = k_l^{-1} H$$

$$\mu^{-1} = \mu_v^{-1} + (\mu_l^{-1} - \mu_v^{-1})H$$

$$\mathbf{u}_{\text{int}} = \mathbf{u} + \frac{\mathbf{m}}{\rho}$$

$$H = \begin{cases} 1, & \phi \geqslant +1.5h \\ 0, & \phi \geqslant -1.5h \\ \dfrac{0.5 + \frac{\phi}{3h} + \sin\left(\frac{2\pi\phi}{3h}\right)}{(2\pi)}, & \phi \leqslant +1.5h \end{cases}$$

The level-set function f is advanced at the rate of the interfacial velocity $\mathbf{u}_{\text{int}}$ and is reinitialized as

$$\phi_t + \mathbf{u}_{\text{int}} \cdot \nabla \phi = 0 \tag{11}$$

$$\phi_\tau = \frac{\phi_0}{\sqrt{\phi_0 + h^2}}(1 - |\nabla \phi|) \tag{12}$$

$$\phi_\tau = (V - V_0)|\nabla \phi| \tag{13}$$

where ϕ_0 is a solution of Eq. (11) and τ is an artificial time. To eliminate volume loss effects, Eq. (13) is added to the whole calculation procedure, where V is the bubble volume and V_0 is the bubble volume which should satisfy mass conservation. Generally, bubble volume, V, calculated from Eq. (12) is smaller than the volume of the bubble, V_0, because of the numerical discretization in the level set formulation. By solving Eq. (13) to attain steady state, the bubble volume V approaches V_0, which for con-

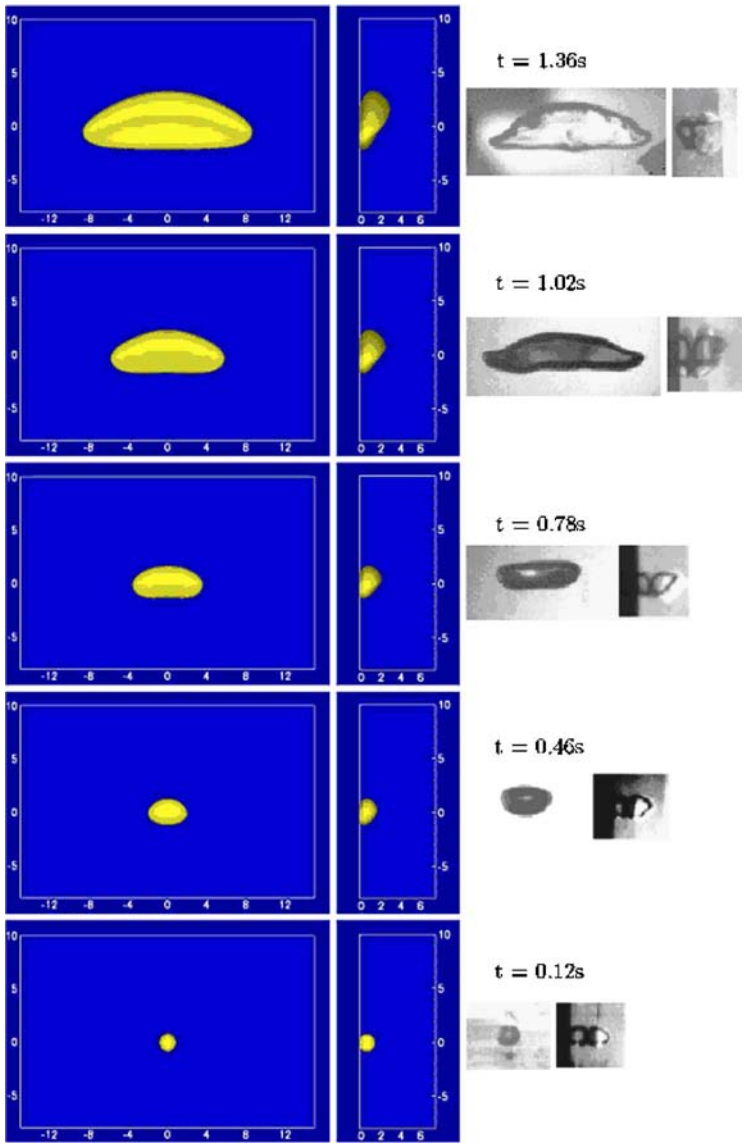

Fig. 4 Evolution of bubble shape for θ=75 deg, ΔT_w=0.5°C, ΔT_{sub}=0.6°C

stant liquid and vapor densities guarantees mass conservation at every time step.

The boundary conditions for the governing equations are as follows:

$$\begin{aligned}
&u=0, \quad v=0, \quad w=0, \quad T=T_{\text{sub}}, \quad \phi_x=0 \quad \text{at } x=0\\
&u=0, \quad v=0, \quad w=0, \quad T=T_w, \quad \phi_y=0 \quad \text{at } y=0\\
&u=0, \quad v=0, \quad w=0, \quad T_z=0, \quad \phi_z=0 \quad \text{at } z=0\\
&u_x=0, \quad v_x=0, \quad w_x=0, \quad T_x=0, \quad \phi_x=0 \quad \text{at } x=X\\
&u=0, \quad v=0, \quad w=0, \quad T_y=0, \quad \phi_y=0 \quad \text{at } y=Y\\
&u=0, \quad v=0, \quad w=0, \quad T_z=0, \quad \phi_z=0 \quad \text{at } z=Z
\end{aligned} \tag{14}$$

The vapor in the bubble was assumed to remain at the saturation temperature. As such, the energy equation in the vapor is not solved.

The simulations are carried out on a uniform grid with mesh points of $448\times64\times32$. All simulations consider only half of the bubble, exploiting the planar symmetry of the geometry. The initial temperature profiles are obtained according to similarity solution (Bejan, Ref. [16]) for laminar natural convection boundary layer as

$$\eta=\frac{x}{y}\text{Ra}_y^{1/4} \tag{15}$$

During the computations, chosen time steps are small enough to satisfy the Courant-Friedrichs-Levy (CFL) condition.

The volume expansion due to microlayer evaporation is added using the model by Son et al. [11]. Figure 2 shows q'_{mic} which is the microlayer heat transfer per unit length in the transverse direction as a function of contact angle. As can be seen from Fig. 2, the microlayer heat transfer increases significantly when the contact angle becomes small.

The dependence of contact angle on interface velocity is given in Fig. 3. In flow boiling, the contact angle which forms at the downstream side is defined as downstream contact angle and the corresponding interface velocity is taken as positive. The contact angle which forms at the upstream side is defined as upstream contact angle and the corresponding interface velocity as negative. Figure 3 shows the dynamic contact angle which was obtained

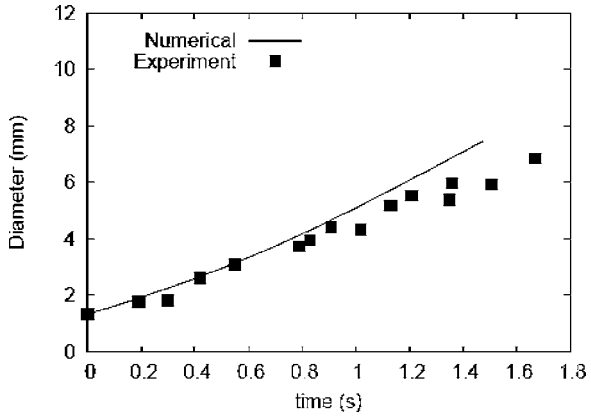

Fig. 5 The bubble diameter as a function of time for θ=75 deg, ΔT_w=0.5°C, ΔT_{sub}=0.6°C, experimental data obtained by Manickam and Dhir [7]

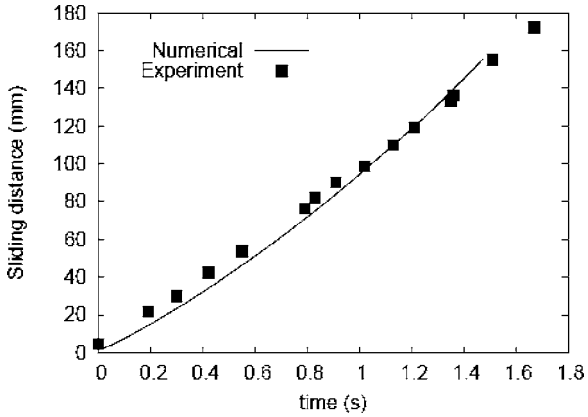

Fig. 6 The bubble sliding distance as a function of time for θ=75 deg, ΔT_w=0.5°C, ΔT_{sub}=0.6°C, experimental data obtained by Manickam and Dhir [7]

from the video pictures of Maity [17]. Note that Maity used water as the working fluid and the heating surface was part of a silicon wafer in his experiments. When the interface velocity is zero, the static contact angle is around 30–50 deg, as the interface velocity increases, the downstream contact angle decreases, which behaves like receding contact angle since the interface moves over wet surface. The upstream contact angle increases, which behaves like advancing contact angle since the interface moves over the dry region. However, at high velocities, both downstream and upstream contact angles decrease probably because of dragging of liquid underneath the rapidly moving interface. The solid line, which is the fit to the data, is used as the input to the numerical model.

Results

The thermophysical properties of PF-5060 used in calculation are listed in Table 1. The length scale and velocity scale are defined as $l_0=\sqrt{\sigma/g(\rho_l-\rho_v)}$ and $u_0=\sqrt{gl_0}$, respectively, in the numerical simulations. All the thermophysical properties are evaluated at one atmosphere pressure. Using these properties, the characteristic length scale for PF-5060 is 0.72 mm and characteristic velocity is 0.084 m/s. For the case discussed in this paper, the angle of inclination of the test surface was θ=75 deg with the vertical. The wall superheat and bulk fluid subcooling were taken to be 0.5°C and 0.6°C, respectively, so that the numerical results could be compared with the data available from experiments.

On the left-hand side of Fig. 4, both top view and side views obtained from numerical simulations as the bubble slides along the heater surface are shown. The bubble shape changes from almost a sphere initially to an ellipsoid and finally to a cap-shaped bubble at the downstream end of the inclined surface. The bubble shapes obtained from experiments are shown on the right-hand side and are found to compare reasonably well with the shapes previously obtained by Qiu and Dhir [6] and Manickam and Dhir [7]. However, the numerical model fails to predict sharp thinning of the bubble at the tips. This could be a result of the inaccuracy in the calculation of the liquid shear stress at the bubble tip and/or due to the size of the grid used in the simulations.

Figures 5 and 6 show the comparison of bubble growth and sliding distance between numerical simulation and experimental data, respectively. Since the bubble is not spherical in shape, the diameter of a bubble is the diameter of the sphere whose volume is equal to the bubble volume. It can be seen that the numerical simulation results agree well with experimental results.

The flow pattern around the sliding bubble predicted from numerical simulations is compared in Fig. 7 with the experimental data [6]. As the bubble slides, it pushes the liquid away from the wall in the front and there is obvious motion normal to the surface at the top of the bubble. A vortex can be clearly seen behind the sliding bubble though the size of the vortex in the numerical simulations is smaller than that found in the experiments. The bubble shape shown in Fig. 7 is the bubble shape in the midplane. The concave shape of the interface on the downstream side predicted from the numerical simulation is not consistent with experimental observations which shown flat or slightly convex interface. This discrepancy needs to be resolved through further work.

Figure 8 shows the temperature field around the bubble at the midplane before and after it passes location (~123 mm) upstream of the nucleation site. Before the bubble passed the location, the temperature field simply corresponds to a fully developed natural convection. The isotherms are parallel to the heater surface. After the bubble passes the location, the isotherms become much denser behind the bubble. This indicates that the heat flux increases significantly behind the bubble. In reality, the wall temperature may

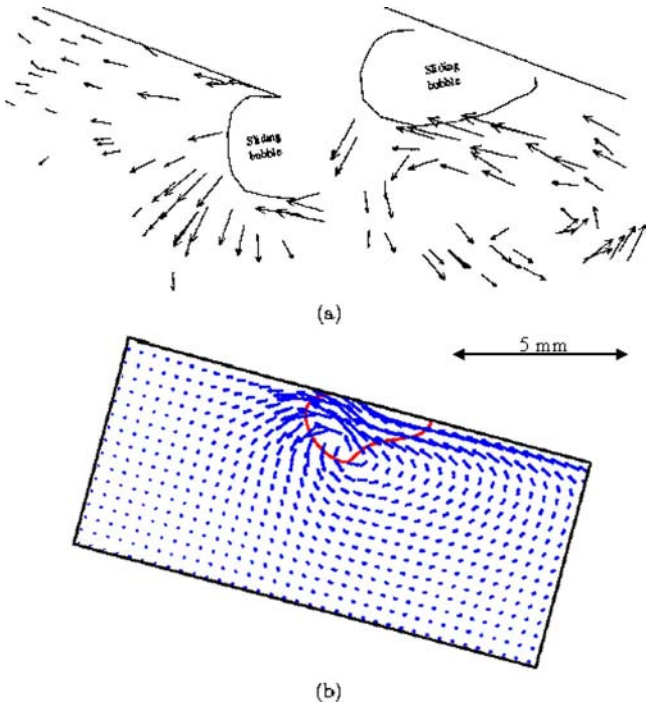

Fig. 7 Comparison of flow pattern (*a*) experimental results (Qiu and Dhir [6]) and (*b*) numerical simulation, for θ=75 deg, ΔT_w=0.5°C, ΔT_{sub}=0.6°C

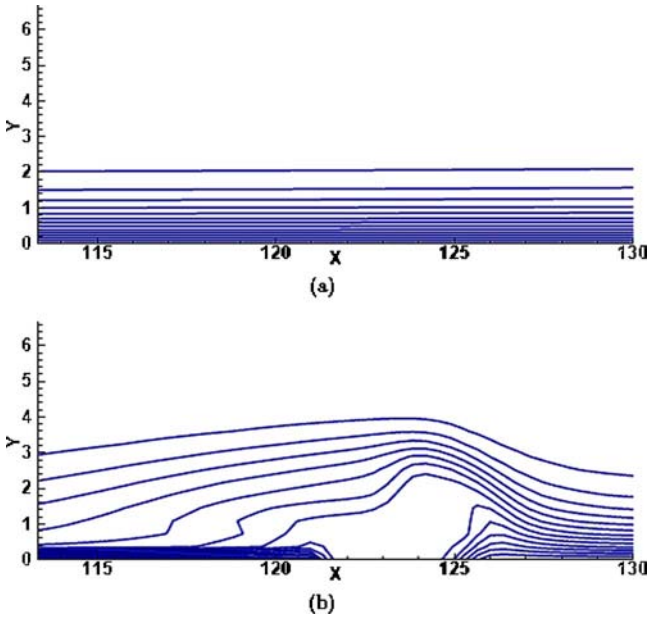

Fig. 8 Temperature field (*a*) before bubble passes and (*b*) after bubble has passed predicted from numerical simulation for θ =75 deg, ΔT_w=0.5°C, ΔT_{sub}=0.6°C. The temperature difference between each isotherm is 0.085°C.

decrease because of the high heat flux. In the numerical simulations, wall temperature was assumed to remain constant.

Figure 9 shows the temporal distribution of the components of the total interfacial heat transfer to the bubble. The microlayer heat transfer is dominant for this case. This is because the contact angle is very small as the bubble slides on the surface and the contact area increases significantly. The role of heat transfer associated with evaporation and condensation, respectively, is calculated by integrating the heat flux into or out of the bubble around the interface. The microlayer heat transfer rate is obtained by multiplying the heat transfer rate per unit length given in Fig. 2 by the circumference of the interface.

Figure 10 shows the temporal variation of Nusselt number based on the heater surface area averaged heat flux at the wall, Nu. Since these numerical simulations were carried out for the first bubble, for about 1.4 s, the magnitude of Nusselt number

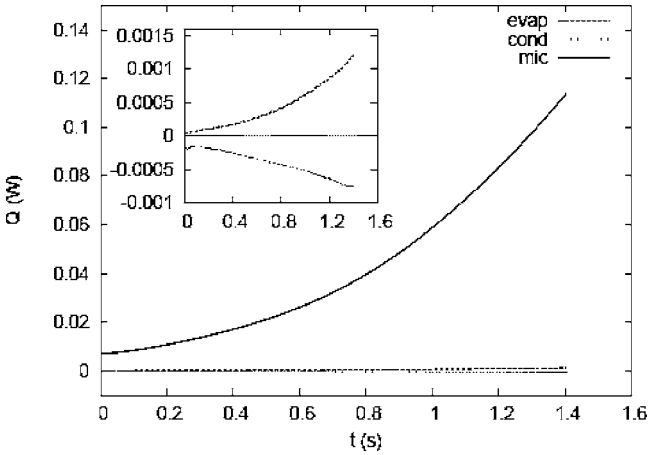

Fig. 9 Variation of the total heat transfer to the bubble for θ =75°, ΔT_w=0.5°C, ΔT_{sub}=0.6°C

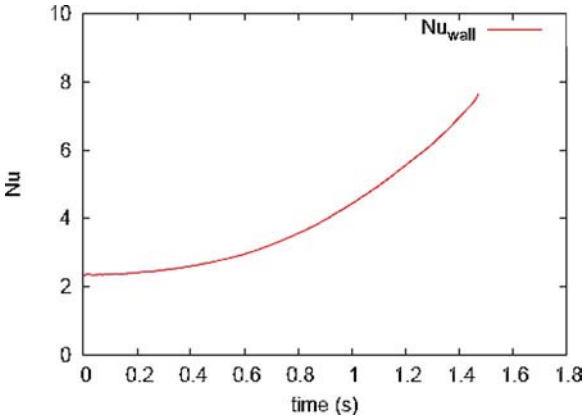

Fig. 10 Variation of Nusselt number with time for θ=75 deg, ΔT_w=0.5°C, and ΔT_{sub}=0.6°C

increases continuously as the bubble slides on the downward surface during this time period. The characteristic length scale is used in defining the Nusselt number.

Conclusions

(1) Numerical simulations of sliding bubble on a downward facing heater surface are carried out without any approximation concerning the bubble shape. The bubble shape is found to change from spheroids to ellipsoids and finally to a bubble-cap.
(2) The bubble growth is mainly due to the contribution from the liquid microlayer underneath the bubble.
(3) The temperature gradient on the wall behind the bubble is significantly increased by the sliding motion of the bubble leading to enhancement of heat transfer on the heater surface.

Acknowledgment

This work received support from NASA under the Microgravity Fluid Physics Program.

Nomenclature

c_p = specific heat
$\mathbf{g}$ = gravity vector
h = grid spacing
H = step function
k = thermal conductivity
$\mathbf{m}$ = mass flux vector
p = pressure
q'_{mic} = microlayer heat transfer rate per unit length
r = radius
Ra = Rayleigh number
u = velocity in the x direction
$\mathbf{u}$ = velocity vector
v = velocity in the y direction
$\dot{V}_{\text{micro}}$ = rate of vapor volume production from the microlayer
w = velocity in the z direction
X = length of computational domain in the x direction
Y = height of computational domain in the y direction
Z = depth of computational domain in the z direction

Greek

δ = microlayer thickness

ϕ = level set function
η = dimensionless similarity variable
φ = contact angle
κ = interfacial curvature
μ = dynamic viscosity
θ = inclination angle
ρ = density
σ = surface tension
τ = artificial time

Subscripts

dn = downstream
l = liquid
sat = saturation
t = $\partial/\partial t$
up = upstream
v = vapor
w = wall
x = $\partial/\partial x$
y = $\partial/\partial y$
z = $\partial/\partial t$
z = $\partial/\partial t$

Superscript

T = matrix transpose

References

[1] Cornwell, K., and Schüller, R. B., 1982, "A Study of Boiling Outside a Tube Bundle Using High Speed Photography," Int. J. Heat Mass Transfer, **25**, pp. 683–690.

[2] Houston, S. D., and Cornwell, K., 1996, "Heat Transfer to Sliding Bubble on a Tube Under Evaporation and Non-Evaporation Conditions," Int. J. Heat Mass Transfer, **39**, pp. 211–214.

[3] Akiyama, M., and Tachibana, F., 1974, "Motion of Vapor Bubbles in Sub-cooled Heated Channel," Bull. JSME, **17**, pp. 241–247.

[4] Chung, T., and Bankoff, S. G., 1990, "On the Mechanism of Forced Convection Sub-Cooled Nucleate Boiling," Int. J. Heat Mass Transfer, **112**, pp. 213–218.

[5] Thorncroft, G. E., and Klausner, J. F., 1999, "The Influence of Vapor Bubble Sliding on Forced Convection Boiling Heat Transfer," J. Heat Transfer, **121**, pp. 73–79.

[6] Qiu, D., and Dhir, V. K., 2002, "Experimental Study of Flow Pattern and Heat Transfer Associated With a Bubble Sliding on Downward Facing Inclined Surfaces," Exp. Therm. Fluid Sci., **26**, pp. 605–616.

[7] Manickam, S., and Dhir, V. K., 2003, "Holographic Interferometric Study of Heat Transfer Associated With A Single Vapor Bubble Sliding Along A Downward-Facing Heater Surface," ASME Summer Heat Transfer Conference, Las Vegas.

[8] Bayazit, B. B., Hollingsworth, D. K., and Witte, L. C., 2003, "Heat Transfer Enhancement Caused by Sliding Bubbles," J. Heat Transfer, **125**, pp. 503–509.

[9] Sussman, M., Smereka, P., and Osher, S., 1994, "A Level Set Approach for Computing Solutions to Incompressible Two-Phase Flow," J. Comput. Phys., **114**, pp. 146–159.

[10] Chang, Y. C., Hou, T. Y., Merriman, B., and Osher, S., 1996, "A Level Set Formulation of Eulerian Interface Capturing Methods for Incompressible Fluid Flows," J. Comput. Phys., **124**, pp. 449–464.

[11] Son, G., Dhir, V. K., and Ramanujapu, N., 1999, "Dynamics and Heat Transfer Associated With a Single Bubble During Nucleate Boiling on a Horizontal Surface," J. Heat Transfer, **121**, pp. 623–631.

[12] Son, G., 2001, "Numerical Study on a Sliding Bubble During Nucleate Boiling," KSME Int. J., **15**, pp. 931–940.

[13] Takahira, H., Horiuchi, T., and Banerjee, S., 2004, "An Improved Three-Dimensional Level Set Method for Gas-Liquid Two-Phase Flows," J. Fluids Eng., **126**, pp. 578–585.

[14] Majumder, S., and Chakraborty, S., 2004, "New Physically Based Approach of Mass Conservation Correction in Level Set Formulation for Incompressible Two-Phase Flows," J. Fluids Eng., **127**, pp. 554–563.

[15] Li, D., and Dhir, V. K., 2004, "A Numerical Study of Single Bubble Dynamics During Flow Boiling," ASME International Mechanical Engineering Congress & Exposition, Anaheim, CA.

[16] Bejan, A., 1984, *Convection Heat Transfer*, Wiley, New York.

[17] Maity, S., 2000, "Effect of Velocity and Gravity on Bubble Dynamics," MS thesis, University of California, Los Angeles, CA.

Simulation Algorithm for Multistream Plate Fin Heat Exchangers Including Axial Conduction, Heat Leakage, and Variable Fluid Property

I. Ghosh

S. K. Sarangi

Cryogenic Engineering Centre,
Indian Institute of Technology,
Kharagpur-721 302, India

P. K. Das[1]
Mechanical Engineering Department,
Indian Institute of Technology,
Kharagpur-721 302, India
e-mail: pkd@mech.iitkgp.ernet.in

The effect of axial conduction through heat exchanger matrix, heat exchange with the surroundings, and variable fluid properties are included in the simulation algorithm of multistream plate fin heat exchangers. The procedure involves partitioning of the exchanger in both axial and normal directions, writing conservation equations for each segment, and solving them using an iterative procedure. In the normal direction, the exchanger is divided into a stack of overlapping two-stream exchangers interacting through their common streams. In the axial direction, the exchanger is successively partitioned to 2^k segments, the final value of k being determined by the point where further partitioning has only marginal effect. The effects of axial conduction, heat leakage, and variable fluid properties are illustrated with the help of multistream heat exchanger examples solved by the above-mentioned technique. [DOI: 10.1115/1.2717938]

Keywords: heat exchangers, multistream, plate fin, axial conduction, heat leakage

1 Introduction

In addition to fluid film resistance, several other secondary effects play important roles in determining heat exchanger performance. Among them axial conduction through the matrix, dispersion through the fluid medium, heat transfer with the surroundings, and temperature dependent fluid properties [1,2] are important. Depending on the number of transfer units (NTU) and operating conditions of the exchanger, these physical phenomena can cause substantial deterioration of heat exchanger performance.

Most of the literature on the role of such secondary effects considers only two-stream heat exchangers. The effect of axial heat conduction in two-stream heat exchangers has been discussed by Barron [3] and by Shah [4]. Barron and Yeh [5] computed temperature distribution and heat exchanger effectiveness considering the effect of axial conduction along the separating walls. The temperature of the cold fluid stream was assumed to be constant and the deterioration in performance was found to depend on the axial conduction parameter. Kroeger [6] investigated the effect of axial heat conduction on the thermal performance of counterflow heat exchangers, while Chiou [7,8] examined its effect on the performance of cross flow heat exchangers. In heat exchangers with large axial temperature gradient, e.g., cryogenic heat exchangers, the effect of axial heat conduction on heat exchanger performance is significant, independent of the number of streams. Venkatarathnam and Pradeep Narayanan [9] have studied the deterioration of counterflow heat exchanger performance by axial heat conduction through cap sheets of the plate fin heat exchanger. The effects of longitudinal heat conduction on the performance of storage type heat exchangers have also been investigated by several workers [10,11].

Unless properly insulated, heat transfer from or to the surroundings can seriously degrade the performance of most heat exchangers. This effect has been analyzed by Chowdhury and Sarangi [12] and by Barron [13] for two-fluid heat exchangers. Chowdhury and Sarangi defined a heat leak parameter and correlated the terminal effectiveness of the heat exchanger to this parameter. Heat transfer from the surroundings to either one or both of the fluid streams in a binary heat exchanger is expressed in dimensionless form and a direct expression for the outlet temperature has been obtained by Barron [13]. More recently, the effect of heat transfer from the surrounding and longitudinal heat conduction in counterflow heat exchangers in the temperature range of 300 to 20 K has been studied by Gupta et al. [14].

Use of fluid properties at the inlet or outlet condition or at the mean fluid temperature often leads to errors, especially in situations where wide temperature differential exists between the entry and the exit. This is particularly true for cryogenic heat exchangers where the temperature range is large, fluid properties are temperature-dependent because of proximity to the critical state, and heat exchangers have high NTU. The effect of variable fluid properties on the performance of cryogenic heat exchangers has been examined by Chowdhury and Sarangi [15]. The local heat transfer coefficient (h) usually varies both as a function of temperature and flow velocity. Change in the fluid properties with temperature can alter the local heat transfer coefficient. The heat transfer coefficient also varies along the length due to boundary layer development. Shah [16] has made an extensive review on this subject and has outlined a method for incorporating the influence of these effects on two-stream heat exchanger performance. While most authors have ignored the secondary effects on multistream heat exchanger performance, Paffenbarger [17] has taken the effects of axial heat conduction and temperature dependent fluid properties into consideration. His method, however, is not only computationally intensive, but demands the use of specialized finite element software.

A simple and easier numerical technique of multistream plate fin heat exchanger simulation has been proposed elsewhere [18] involving partitioning of the heat exchanger in both axial and normal directions, writing conservation equations for each seg-

[1]Corresponding author.

Contributed by the Heat Transfer Division of ASME for publication in the JOURNAL OF HEAT TRANSFER. Manuscript received June 26, 2006; final manuscript received December 27, 2006. Review conducted by Satish G. Kandlikar.

 Copyright © 2007 by ASME

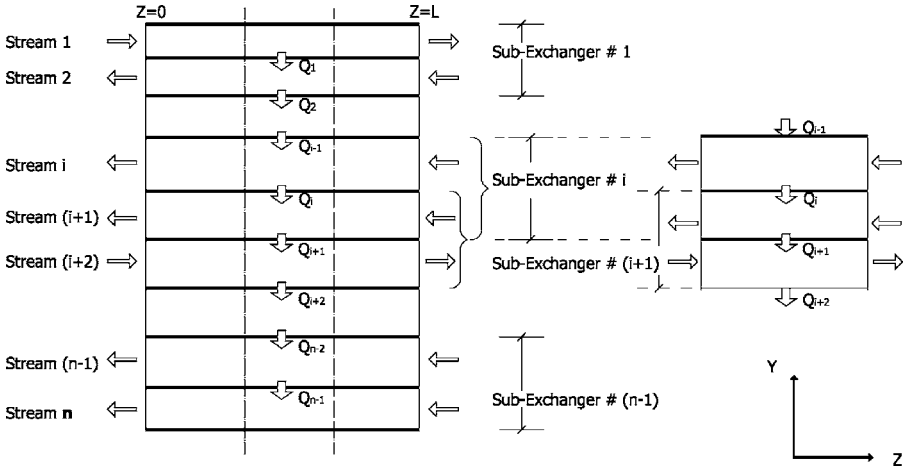

Fig. 1 A multistream plate fin heat exchanger seen as a stack of overlapping two-stream sub-exchangers

ment, and solving them using an iterative process. In the normal direction, the exchanger is divided into a stack of overlapping two-stream exchangers interacting through their common streams and boundaries. In the axial direction, the exchanger is successively partitioned to 2^k segments, the final value of k being determined by the point where further partitioning has only marginal effect. However, the basic algorithm does not take care of axial conduction, heat exchange with the surroundings, and variable fluid properties.

In the present work the algorithm given in [18] has been substantially modified to consider the effect of axial heat conduction in matrix, heat leak from the surroundings, and temperature dependent fluid properties. The algorithm basically uses "area splitting" and "successive partitioning" techniques to find out the temperature variation in different fluid streams in multistream plate fin heat exchangers.

2 Basic Design Approach (Without Secondary Effects)

A multistream heat exchanger having n fluid streams can be imagined as a combination of $(n-1)$ overlapping two stream units (sub-exchangers) stacked as a pile (Fig. 1). The division into two stream sub-exchangers can be understood by taking an example of a three-stream heat exchanger (Fig. 2), which is divided into two two-stream exchangers. Here, the central stream having mass flow rate $\dot{m}_2$ is common to both the sub-exchangers. However, the heat transfer area for the central channel is divided between the two sub-exchangers. For example, in the ith channel, $\alpha_i A_{f,i}$ is the part of secondary area in the thermal communication with the $(i-1)$th plate, while the remaining fraction $(1-\alpha_i)A_{f,i}$ communicates with the ith plate. The participating heat transfer area is assumed to be proportional to the heat flow rate:

$$\frac{A_{w,i-1}+\alpha_i \eta_{f,i} A_{f,i}}{A_{w,i}+(1-\alpha_i)\eta_{f,i} A_{f,i}} = -\left(\frac{Q_{i-1}}{Q_i}\right) \tag{1}$$

Assuming the sub-exchangers as stand-alone units, the outlet temperatures of the co-current or counter-current heat exchanger can be solved purely in terms of the inlet temperatures and transverse heat additions. Each sub-exchanger is modeled in a sequential manner, with an initial guess of Q_2 and the iterative process continues until the transverse heat flow rates and the exit temperatures converge within preset tolerance limits. This approach of apportioning the area of an intermediate stream between two sub-exchangers has been called the "*area splitting*" method [18].

The "area splitting" technique is based on the assumption that every separating plate is at a single uniform temperature. This assumption is valid only for an exchanger of infinitesimally small length. If a heat exchanger is partitioned into a large number of small segments, each individual segment will qualify to be designed by the *area splitting* method. Some of the existing design suggests dividing the exchanger into an arbitrary number of small segments at the beginning [19–21]. However, such partitioning may result in divergence of solution if the initial guess of the temperature profile is a poor one. Consideration of a large number of segments from the beginning may also be computationally expensive.

In our approach, the heat exchanger is not partitioned into a large number of segments in one operation. Instead, the exchanger is initially divided only into two segments. The governing heat transfer and energy conservation equations are solved for each of the two segments, yielding a new set of fluid outlet temperatures. The process of evaluating exit temperatures in each segment is repeated until all temperatures converge within predefined tolerance limits. Each segment of the exchanger is then further divided into two parts. Such division of the exchanger into successively smaller parts in multiples of 2 continues until fluid discharge temperatures over two consecutive levels of partitioning agree within an acceptable difference. We call this division procedure the "*successive partitioning*" method. This technique helps to avoid divergence of solution, which may occur in the conventional one-time

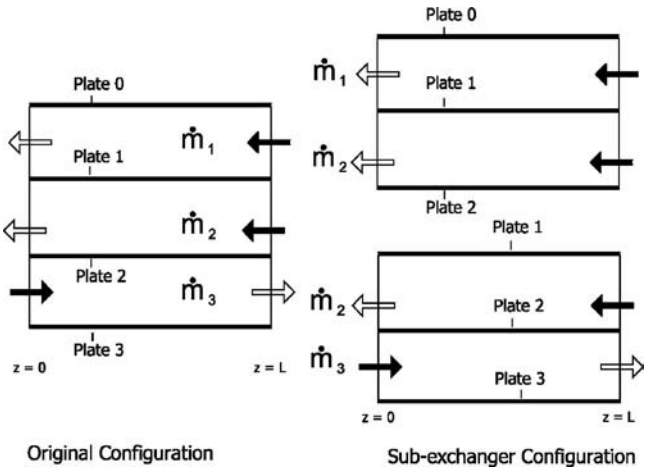

Fig. 2 Division of a three-stream exchanger into two-stream sub-exchangers

partitioning technique proposed by Prasad and co-workers [19–22].

3 Design Approach Considering Axial Conduction Through the Core

Axial heat conduction takes place along the separating plates as well as the fins that connect the two ends of the heat exchanger, which are at widely different temperatures. This auxiliary heat transfer can seriously affect the performance of a heat exchanger, particularly when the temperature gradient along the matrix is large.

In the numerical method adopted in Ref. [18], the exchanger is divided into several segments in the axial direction, and each segment of a plate (along with associated fins) is assumed to be at a single uniform temperature. Thus the axial temperature profile of a plate becomes a stepped function instead of a continuous one. As the plates are having different temperatures in a lengthwise span, it is quite likely that the flow of heat will take place along the plate length. Neglecting axial conduction is a mere simplification suggested in [18]. A methodology is proposed below to take care of this axial flow of heat within the framework of the basic model.

Let $T_{i,j}(k)$ be the temperature of the ith plate between locations k and $(k+1)$. The temperatures of the adjacent sections are then $T_{i,j}(k+1)$ and $T_{i,j}(k-1)$. The temperature differentials $\{T_{i,j}(k-1) - T_{i,j}(k)\}$ and $\{T_{i,j}(k) - T_{i,j}(k+1)\}$ are the driving potentials for conduction of heat along the flow direction. Let $Q_{ax,in}$ and $Q_{ax,out}$ be the heat flow rates into and out of the plate segment. One may consider two typical situations namely, co-and counter-flow of fluid streams adjacent to the plate of interest.

3.1 Analysis of Two-Stream Co-Current Heat Exchanger With Transverse Heat Addition and Axial Heat Conduction in the Matrix. When the area splitting approach discussed in an earlier section is extended to a multistream plate fin heat exchanger having **n** fluid streams, the multistream unit is considered to be a combination of $(\mathbf{n-1})$ overlapping two-stream sub-exchangers (Fig. 1). The general sub-exchanger #i consists of the ith and the $(i+1)$th fluid streams. Depending on the orientations of the streams in the original exchanger, the sub-exchangers so constructed can be of either co-current or counter-current arrangement. For example, the fluid streams in the ith sub-exchanger in Fig. 1 are in co-current arrangement, while those in the $(i+1)$th sub-exchanger are in counter-current configuration.

The fraction of area in thermal communication with the $(i-1)$th plate, i.e., α_i for the multistream unit, can be obtained from (1):

$$\alpha_i = \left(\frac{Q_{i-1}(A_w + \eta_{f,i}A_{f,i}) + Q_i A_w}{(Q_{i-1} - Q_i)A_f} \right) \tag{2}$$

The primary area A_w is considered equal for all the plates.

Figure 3 shows the schematic of a segment of a two-stream co-current heat exchanger bounded by sections k and $k+1$ (or k' and $k'+1$). The overall length of the segment is L. Q_i' is the rate of heat transfer from the matrix to the fluid per unit length within the segment. A small element dz along the length of the heat exchanger is considered within the segment. The heat input to the element from the adjacent layer above it is $(Q_{i-1}/L)dz$ and that to the adjacent layer below it is $(Q_{i+1}/L)dz$. If the incremental change in temperature of the ith fluid within the element dz is dt_i, then

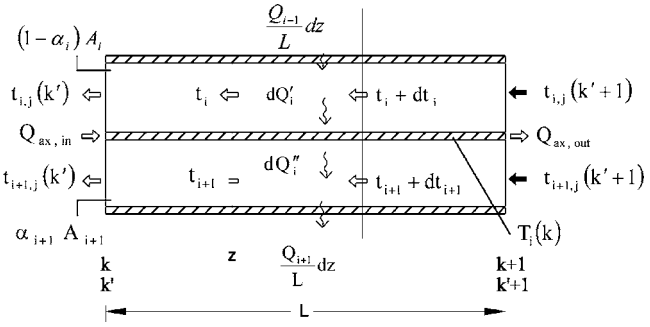

Fig. 3 Two-stream co-current heat exchanger with transverse heat addition and axial heat exchange with the neighboring segments

$$C_i dt_i = dQ_i' - Q_{i-1}\frac{dz}{L} \tag{3}$$

where

$$dQ_i' = h_i\{A_w + (1-\alpha_i)\eta_{f,i}A_{f,i}\}(t_i - T_i)\frac{dz}{L} \tag{4}$$

Similarly, for the $(i+1)$th fluid the incremental change in temperature within the element dz can be written as

$$C_{i+1}dt_{i+1} = Q_{i+1}\frac{dz}{L} - dQ_i'' \tag{5}$$

with

$$dQ_i'' = h_{i+1}\{A_w + \alpha_{i+1}\eta_{f,i+1}A_{f,i+1}\}(T_i - t_{i+1})\frac{dz}{L} \tag{6}$$

When axial heat conduction through the separating plate is not negligible, the heat transfer rates across the separating plate dQ_i' and dQ_i'' become different from each other. Applying energy balance over the ith separating wall, and considering heat flow due to axial conduction from the adjacent segments of the separating plate,

$$Q_i' + Q_{ax,in} - Q_i'' - Q_{ax,out} = 0 \tag{7}$$

Substituting expressions for Q_i' and Q_i'' from Eqs. (4) and (6) in Eq. (7) and solving the resulting equation, the separating plate temperature $T_i(k)$ comes out as:

$$T_i(k) = \frac{\{A_w + (1-\alpha_i)\eta_{f,i}A_{f,i}\}h_i t_i + \{A_w + \alpha_{i+1}\eta_{f,i+1}A_{f,i+1}\}h_{i+1}t_{i+1} + Q_{ax,i}}{\{A_w + (1-\alpha_i)\eta_{f,i}A_{f,i}\}h_i + \{A_w + \alpha_{i+1}\eta_{f,i+1}A_{f,i+1}\}h_{i+1}} \tag{8}$$

where

$$Q_{ax,i} = (Q_{ax,in} - Q_{ax,out}) \tag{9}$$

Using the expression in Eq. (8) for $T_i(k)$, Eqs. (3) and (5) can be rearranged to read:

$$d(\Delta T) = d(t_i - t_{i+1}) = dt_i - dt_{i+1}$$
$$= U\{A_w + (1-\alpha_i)\eta_{f,i}A_{f,i}\}\Delta T\left(\frac{1}{C_i} + \frac{1}{C_{i+1}}\right)\frac{dz}{L}$$
$$-\left(\frac{Q_{i-1} + K_{ax,1}}{C_i} + \frac{Q_{i+1} - K_{ax,2}}{C_{i+1}}\right)\frac{dz}{L} \quad (10)$$

the terms $K_{ax,1}$ and $K_{ax,2}$ being defined as

$$K_{ax,1} = \frac{Q_{ax,i}h_i\{A_w + (1-\alpha_i)\eta_{f,i}A_{f,i}\}}{h_i\{A_w + (1-\alpha_i)\eta_{f,i}A_{f,i}\} + h_{i+1}\{A_w + \alpha_{i+1}\eta_{f,i+1}A_{f,i+1}\}} \quad (11)$$

$$K_{ax,2} = \frac{Q_{ax,i}h_{i+1}\{A_w + \alpha_{i+1}\eta_{f,i+1}A_{f,i+1}\}}{h_i\{A_w + (1-\alpha_i)\eta_{f,i}A_{f,i}\} + h_{i+1}\{A_w + \alpha_{i+1}\eta_{f,i+1}A_{f,i+1}\}} \quad (12)$$

In Eq. (10), the product of the overall heat transfer coefficient (U) and the heat transfer area is given by the formula

$$\frac{1}{U\{A_w + (1-\alpha_i)\eta_{f,i}A_{f,i}\}} = \frac{1}{h_i\{A_w + (1-\alpha_i)\eta_{f,i}A_{f,i}\}} + \frac{1}{h_{i+1}\{A_w + \alpha_{i+1}\eta_{f,i+1}A_{f,i+1}\}} \quad (13)$$

Integrating Eq. (10) over the limit $z=0$ to $z=L$, we get

$$\left(\frac{t_{i,j}(k') - t_{i+1,j}(k') - \Phi_{PAx,i}}{t_{i,j}(k'+1) - t_{i+1,j}(k'+1) - \Phi_{PAx,i}}\right) = e^{-U(A_w + (1-\alpha_i)\eta_{f,i}A_{f,i})(1/C_i + 1/C_{i+1})} \quad (14)$$

where

$$\Phi_{PAx,i} = \frac{\left(\frac{Q_{i-1} + K_{ax,1}}{C_i} + \frac{Q_{i+1} - K_{ax,2}}{C_{i+1}}\right)}{U\{A_w + (1-\alpha_i)\eta_{f,i}A_{f,i}\}\left(\frac{1}{C_i} + \frac{1}{C_{i+1}}\right)} \quad (15)$$

Reduction of $K_{ax,1}$ and $K_{ax,2}$ to zero denotes a situation of negligible axial conduction, and results become identical to that derived in [18].

Applying energy balance to each of the fluid streams i and $(i+1)$ between locations k and $(k+1)$,

$$Q_i' = t_{i,j}(k'+1)C_i + Q_{i-1} - t_{i,j}(k')C_i \quad (16)$$

$$Q_i'' = t_{i+1,j}(k')C_{i+1} + Q_{i+1} - t_{i+1,j}(k'+1)C_{i+1} \quad (17)$$

Substituting Eqs. (16) and (17) in Eq. (7),

$$t_{i,j}(k'+1)C_i + Q_{i-1} - t_{i,j}(k')C_i - t_{i+1,j}(k')C_{i+1} - Q_{i+1} + t_{i+1,j}(k'+1)C_{i+1} + Q_{ax,i} = 0$$

On rearrangement,

$$t_{i+1,j}(k') = \frac{1}{C_{i+1}}[t_{i,j}(k'+1)C_i + t_{i+1,j}(k'+1)C_{i+1} + Q_{i-1} - Q_{i+1} + Q_{ax,i}] - \left(\frac{C_i}{C_{i+1}}\right)t_{i,j}(k') \quad (18)$$

Substituting the expression for $t_{i+1,j}(k')$ from Eq. (18) in Eq. (14) and rearranging, we get a closed form expression for the fluid temperature $t_{i,j}(k')$

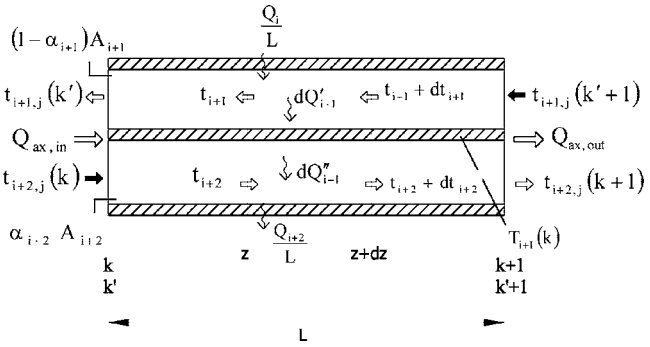

Fig. 4 Two-stream counter-current exchanger with transverse heat addition and axial heat exchange with the neighboring segments

$$t_{i,j}(k') = \frac{\Phi_{PAx,i} + \Psi_{P,i}\{t_{i,j}(k'+1) - t_{i+1,j}(k'+1) - \Phi_{PAx,i}\}}{\left(1 + \frac{C_i}{C_{i+1}}\right)} + \frac{t_{i+1,j}(k'+1)C_{i+1} + t_{i,j}(k'+1)C_i + Q_{i-1} - Q_{i+1}}{\left(1 + \frac{C_i}{C_{i+1}}\right)C_{i+1}} \quad (19)$$

with

$$\Psi_{P,i} = e^{-U(A_w + (1-\alpha_i)\eta_{f,i}A_{f,i})(1/C_i + 1/C_{i+1})} \quad (20)$$

The value of $t_{i,j}(k')$ computed from Eq. (19) may be used in Eq. (18) to yield $t_{i+1,j}(k')$.

3.2 Analysis of Two-Stream Counter-current Heat Exchanger With Transverse Heat Addition and Axial Heat Conduction in the Matrix. Heat transfer and energy conservation equations for a two-stream counter-current heat exchanger (Fig. 4) can be derived by following the same steps adopted for analysing a co-current exchanger. The governing equations are stated as:

$$\left(\frac{t_{i+1,j}(k') - t_{i+2,j}(k) - \Phi_{CAx,i}}{t_{i+1,j}(k'+1) - t_{i+2,j}(k+1) - \Phi_{CAx,i}}\right) = e^{-U(A_w + (1-\alpha_{i+1})\eta_{f,i+1}A_{f,i+1})(1/C_{i+1} - 1/C_{i+2})} \quad (21)$$

and

$$[t_{i+1,j}(k'+1) - t_{i+1,j}(k')]C_{i+1} + Q_i - Q_{i+2} + [t_{i+2,j}(k) - t_{i+2,j}(k+1)]C_{i+2} + Q_{ax,i+1} = 0$$

which may be recast to read:

$$t_{i+2,j}(k+1) = \frac{1}{C_{i+2}}[t_{i+1,j}(k'+1)C_{i+1} + t_{i+2,j}(k)C_{i+2} + Q_i - Q_{i+2} + Q_{ax,i+1}] - \left(\frac{C_{i+1}}{C_{i+2}}\right)t_{i+1,j}(k') \quad (22)$$

Equations (21) and (22) can be solved simultaneously to yield explicit relations for $t_{i+1,j}(k')$ and $t_{i+2,j}(k+1)$:

$$t_{i+1,j}(k') = \frac{\{t_{i+2,j}(k) + \Phi_{CAx,i} + \Psi_{C,i}(t_{i+1,j}(k'+1) - \Phi_{CAx,i})\}}{1 - \left(\frac{C_{i+1}}{C_{i+2}}\right)\Psi_{C,i}} - \frac{\Psi_{C,i}\{C_{i+1}t_{i+1,j}(k'+1) + C_{i+2}t_{i+2,j}(k) + Q_i - Q_{i+2} + Q_{ax,i+1}\}}{\left(1 - \frac{C_{i+1}}{C_{i+2}}\Psi_{C,i}\right)C_{i+2}} \quad (23)$$

with

$$\Phi_{CAx,i} = \frac{\left[\frac{(Q_i + K_{ax,1})}{C_{i+1}} - \frac{(Q_{i+2} - K_{ax,2})}{C_{i+2}}\right]}{U\{A_w + (1-\alpha_{i+1})\eta_{f,i+1}A_{f,i+1}\}\left(\frac{1}{C_{i+1}} - \frac{1}{C_{i+2}}\right)} \quad (24)$$

$$K_{ax,1} = \frac{Q_{ax,i+1}h_{i+1}\{A_w + (1-\alpha_{i+1})\eta_{f,i+1}A_{f,i+1}\}}{h_{i+1}\{A_w + (1-\alpha_{i+1})\eta_{f,i+1}A_{f,i+1}\} + h_{i+2}\{A_w + \alpha_{i+2}\eta_{f,i+2}A_{f,i+2}\}} \quad (25)$$

$$K_{ax,2} = \frac{Q_{ax,i+1}h_{i+2}\{A_w + \alpha_{i+2}\eta_{f,i+2}A_{f,i+2}\}}{h_{i+1}\{A_w + (1-\alpha_{i+1})\eta_{f,i+1}A_{f,i+1}\} + h_{i+2}\{A_w + \alpha_{i+2}\eta_{f,i+2}A_{f,i+2}\}} \quad (26)$$

$$\Psi_{C,i} = e^{-U(A_w + \alpha_{i+2}\eta_{f,i+2}A_{f,i+2})(1/C_{i+1} - 1/C_{i+2})} \quad (27)$$

Starting with a guess value for Q_2, each sub-exchanger is modeled in a sequential manner. Heat flow rates and fluid exit temperatures are computed using Eqs. (15)–(20) for co-current configurations and Eqs. (22)–(27) for counter-current configurations. The process is continued until all heat flow rates and exit temperatures converge within preset tolerance limits.

Adiabatic conditions have been assumed to exist at the entry and exit of the heat exchanger, i.e., at $k=0$ ($k'=2^j$) and $k=2^j$ ($k'=0$). For other segments, the rate of axial heat conduction $Q_{ax,in}$ and $Q_{ax,out}$ for any particular segment of the heat exchanger can be estimated only when the wall temperatures of the adjacent segments are known. At the beginning of the iteration process for each stage of *partitioning*, the plate temperatures are not known and the axial conduction terms are assumed to be absent. During the subsequent iteration steps, when some estimate of the plate temperatures is available, the rate of axial conduction in the ith plate can be calculated.

$$Q_{ax,in} = A_c k_c \lfloor T_{i,j}(k-1) - T_{i,j}(k) \rfloor$$

$$Q_{ax,out} = A_c k_c \lfloor T_{i,j}(k) - T_{i,j}(k+1) \rfloor \quad (28)$$

where A_c is the axial conduction area, given by the relation:

$$A_c = Wt_{sp} + WF\tfrac{1}{2}(h_{f,i}t_{f,i} + h_{f,i+1}t_{f,i+1}) \quad (29)$$

A computational algorithm, shown in Fig. 5, has been written to simulate multistream plate fin heat exchangers with axial conduction in the matrix.

To check the validity of the present iterative algorithm we wanted to compare its prediction with the available analytical solution of three-stream heat exchanger. Sekulic [23] derived an analytical solution for a parallel flow three-fluid heat exchanger in the absence of axial conduction, heat leakage to environment, and variable fluid properties, taking four different arrangements of the fluid streams, namely, co-current, counter-current, counter-current–co-current and co-current–counter-current. The analytical solution of a set of three coupled ordinary differential equations has been obtained through the Laplace transform technique. The present simulation exactly matches the analytical results of Sekulic [23] for all the four-fluid flow arrangements. Figures 6(*a*) and 6(*b*) show the comparison between these two procedures for counter-current–co-current and co-current–counter-current arrangements, respectively. The parameters for these two configurations have been taken as per the example of Sekulic [23].

It is difficult to define a dimensionless parameter like "effectiveness" for multistream heat exchangers. Therefore, the effects of axial conduction in the matrix, heat transfer with surroundings, and variable fluid properties on the heat exchanger performance are usually illustrated with the help of examples [17]. Using FEM analysis, Paffenbarger [17] simulated a multistream plate fin exchanger including axial conduction effects. To validate the analytical approach presented in this section, we have simulated the same exchanger. The results (Table 1 and Fig. 7) show good agreement with those reported by Paffenbarger [17].

Figure 8 presents the results of simulating a three-stream plate

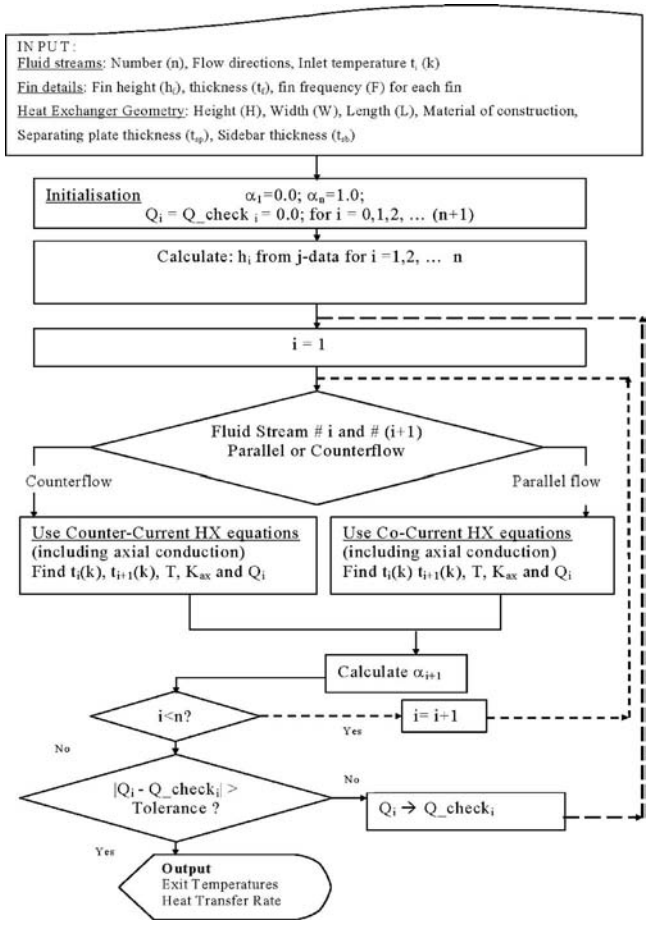

Fig. 5 Flow diagram describing the iterative scheme to calculate outlet temperatures in a given section with known inlet condition of the fluid streams

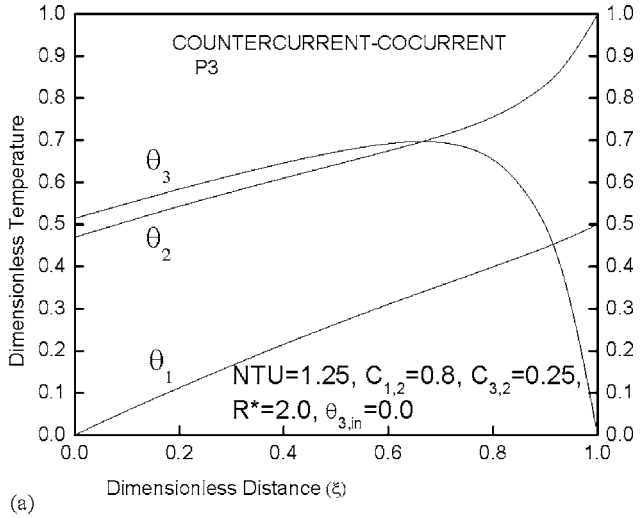

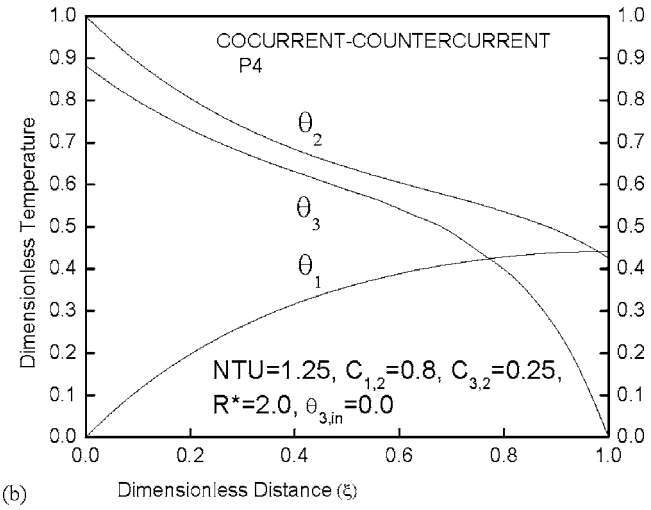

Fig. 6 Temperature distribution of three-stream heat exchanger in absence of secondary effects for (*a*) counter-current–co-current and (*b*) co-current–counter-current arrangement of the example in Ref. [23]

fin heat exchanger with specifications detailed in Table 2. The effect of the axial heat conduction on the heat exchanger performance is clearly discernible.

4 Heat Exchange With the Surroundings

Assuming negligible heat transfer through the headers at the entry and exit of a plate fin heat exchanger, heat transfer with the surroundings primarily occurs through the four walls of the exchanger. While the fluid flowing through the extreme layers of the exchanger exchange heat with the environment through cap sheets as well as through the side bars, fluid streams flowing through intermediate channels interact with the ambient through the side

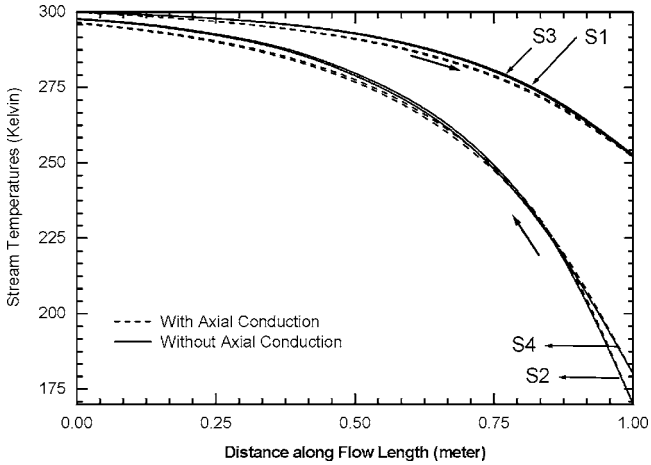

Fig. 7 Effect of axial conduction on a multistream plate fin heat exchanger performance (example II in Ref. [17]) simulated using the area splitting and successive partitioning method

bars only. The amount of heat exchange through the cap sheets and that through the side bars are estimated separately.

The quantity of heat, Q_0 and Q_n, leaking through the insulated top and bottommost plates (cap sheets) can be estimated as (Fig. 9):

$$Q_0 = \frac{(t_0 - \bar{t}_1)}{\left(\frac{1}{h_0 A_w} + \frac{t_{ins}}{k_{ins} A_w} + \frac{t_{plate}}{k_c A_w} + \frac{1}{h_1 (A_w + \alpha_1 \eta_{f,1} A_{f,1})}\right)} \tag{30}$$

$$Q_n = \frac{(\bar{t}_n - t_0)}{\left(\frac{1}{h_N A_w} + \frac{t_{ins}}{k_{ins} A_w} + \frac{t_{plate}}{k_c A_w} + \frac{1}{h_0 \{A_w + (1 - \alpha_n) \eta_{f,n} A_{f,n+1}\}}\right)} \tag{31}$$

where $\bar{t}_1$ and $\bar{t}_n$ are the average temperatures of the fluid streams in the two extreme channels. Heat input through the two terminal plates (cap sheets) changes the values of α_1 and α_n, which were taken as 0 and 1, respectively, in Ref. [18] in the absence of heat transfer from the ambient. Values of α_1 and α_N are now calculated from the relations:

$$\alpha_1 = \frac{Q_0 (A_w + A_{f,1}) + Q_1 A_w}{(Q_0 - Q_1) A_{f,1}} \quad \text{and} \quad \alpha_N = \frac{Q_{N-1} (A_w + A_{f,n}) + Q_n A_w}{(Q_{n-1} - Q_n) A_{f,n}} \tag{32}$$

Similarly, the amount of heat (Q_{leak}) being received by the intermediate streams through the sidebars (Fig. 10) can be computed from the formula:

Table 1 Comparison of simulated results predicted by FEM analysis [17] and the present solution method

	Fluid outlet temperatures (Kelvin) including axial conduction			
Solution method	Air (S1)	O_2 (S2)	Air (S3)	N_2 (S4)
FEM Analysis [17]	253.3	297.4	253.3	297.3
Area splitting and successive partitioning	251.4	296.3	250.8	296.0

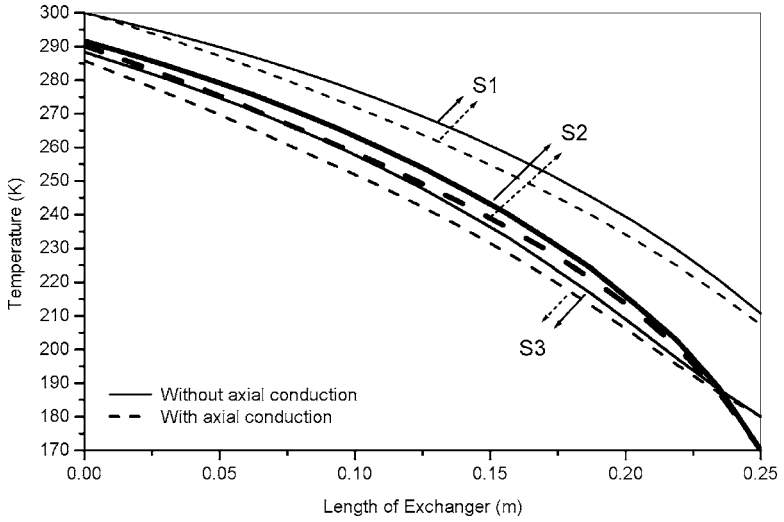

Fig. 8 Effect of axial conduction on a three-stream plate fin heat exchanger performance simulated using the area splitting and successive partitioning method. Specifications of the exchanger are given in Table 2.

$$Q_{leak,i} = \frac{(t_0 - \bar{t}_i)}{\frac{1}{A_{sb}}\left(\frac{1}{h_i} + \frac{t_{ins}}{k_{ins}} + \frac{t_{sb}}{k_c} + \frac{1}{h_0}\right)} \tag{33}$$

A_{sb} being the area of side bar in ith channel.

To account for the heat exchange through the side bars, an amount of heat-inflow ($Q_{leak,i}$) is added to the fluid stream in every layer and the governing equations are modified accordingly. A computational algorithm, similar to that described in Fig. 5, has been written to simulate multistream plate fin heat exchangers including effects of heat transfer with the ambient.

Results of simulation of two multistream plate fin heat exchanger examples (details given in Tables 3 and 4) including effects of heat exchange with the surroundings are shown graphically in Figs. 11 and 12. The performances of heat exchangers with exposure to the ambient have been compared with that of properly insulated units.

5 Variable Fluid Properties

In general, the assumption of constant thermophysical properties of process streams at their "mean" temperatures is a poor one. Usually the mean value corresponds to the arithmetic mean of entry and exit temperatures. An accurate and realistic analysis of a heat exchanger must take account the variation of fluid properties at appropriate temperature and pressure levels. To accommodate variations in fluid properties, the exchanger is divided into a large number of small segments over which the fluid properties can be assumed to remain constant.

The local heat transfer coefficient in an exchanger depends both on the fluid temperature (through temperature-dependent fluid properties) and flow length (the entrance length effect due to boundary layer development). While both the temperature effects as well as the thermal entry length effect are significant in laminar flow, the latter effect is generally not significant in turbulent flow [16]. The present analysis does not incorporate the variation of local heat transfer coefficient **h** with flow length, but considers the effect of temperature dependent fluid properties.

During "successive partitioning" of the exchanger into smaller segments, the thermophysical properties of fluid streams are evaluated at the mean temperatures in each small section. Assuming that the density, viscosity, and thermal conductivity of the fluid species are known at ambient conditions (300 K), those can be evaluated at any other temperatures using the appropriate idealized relations:

$$\mu_{t(K)} = \mu_{amb}\sqrt{\frac{t(K)}{300.0}} \tag{34}$$

Table 2 Three-stream plate fin heat exchanger specifications

Heat exchanger length (m)		0.25	
Width (m)		0.25	
Height (m)		0.22 (excluding thickness of end plates)	
Separating plate thickness (mm)		0.5	
Cap sheet thickness (mm)		3.0	
Fluid streams	Air (S1)	O_2 (S2)	N_2 (S3)
Inlet temperatures (K)	300	170	180
Mass flow rate (kg/s)	0.30	0.12	0.12
Fin surface specification [24]			
Fin type	Offset strip fin	Offset strip fin	Offset strip fin
Fin height (mm)	3.68	5.00	3.68
Fin spacing (no. of fins/in.)	30	28	30
Fin thickness (mm)	0.102	0.127	0.102
Flow orientation	Enters at $L=0$	Enters at $L=0.25$	Enters at $L=0.25$

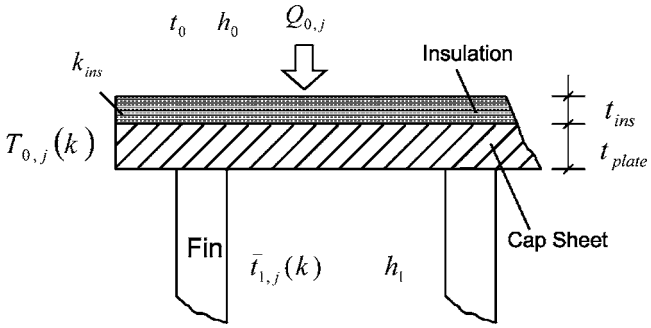

Fig. 9 Heat leak from the insulated top end plate

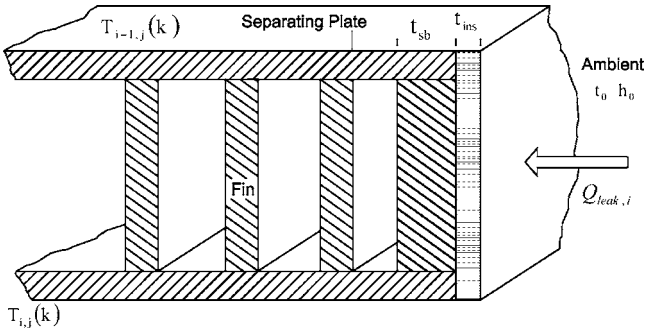

Fig. 10 Heat leak from the insulated side bar in the *i*th layer

$$k_{fluid,t(K)} = k_{fluid,amb}\sqrt{\frac{t(K)}{300}} \tag{35}$$

The specific heats of the fluids are assumed constant in the analysis. A provision has, however, been made in the program to consider variation of specific heat when necessary. Estimation of thermophysical properties at the mean temperatures is followed by the recalculation of the Reynolds number at every step. Depending on the type of fin used in different channels, correlations are provided for computing the dimensionless heat transfer coefficient **j** as a function of the Reynolds number. The local heat transfer coefficient is then estimated from the computed value of **j** for each channel in the segment under consideration.

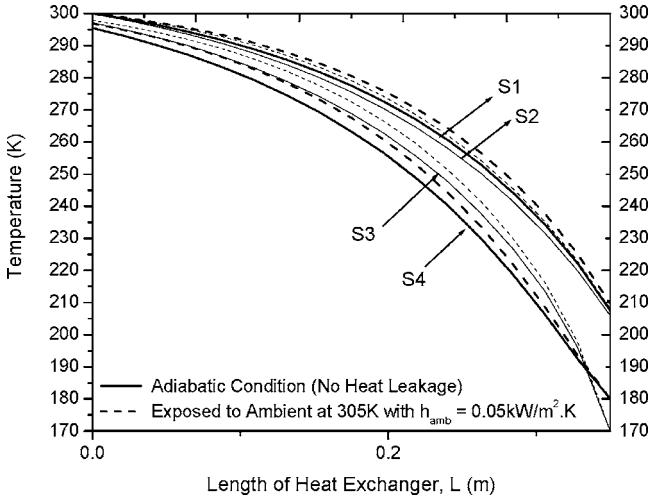

Fig. 11 Effect of external heat load on a four-stream plate fin exchanger performance (specifications given in Table 3)

Figure 13 shows the effect of including variation of fluid properties in the performance prediction of a four-stream plate fin heat exchanger. The specifications of the exchanger are the same as those given in Table 3.

Table 3 Four-stream plate fin heat exchanger specifications

Exchanger length (m)	0.35			
Width (m)	0.25			
Height (m)	0.12 (excluding thickness of end plates)			
Separating plate thickness (mm)	0.5			
Sidebar thickness (mm)	4.0			
Cap sheet thickness (mm)	4.0			
Fluid streams	Air (S1)	O_2 (S2)	Air (S1)	N_2 (S3)
Inlet temperatures (K)	300	170	300	180
Mass flow rate (kg/s)	0.08	0.06	0.08	0.06
Fin surface specification [24]				
Fin type	Offset	Offset strip	Offset strip	Offset strip fin
Fin height (mm)	3.68	5.00	3.68	3.68
Fin spacing (no. of fins/in.)	30	28	30	30
Fin thickness (mm)	0.102	0.127	0.102	0.102
Flow orientation (enters at)	L=0	L=0.35	L=0	L=0.35

Table 4 Three-stream plate fin heat exchanger specifications

Heat exchanger length (m)	0.5		
Width (m)	0.5		
Height (m)	0.18 (excluding thickness of end plates)		
Separating plate thickness (mm)	1.0		
Sidebar thickness (mm)	4.0		
Cap sheet thickness (mm)	4.0		
Fluid streams	Air (S1)	O_2 (S2)	N_2 (S3)
Inlet temperatures (K)	300	170	180
Mass flow rate (kg/s)	0.40	0.16	0.16
Fin surface specification [24]			
Fin type	Offset strip fin	Offset strip fin	Offset strip fin
Fin height (mm)	3.68	5.00	3.68
Fin spacing (no. of fins/in.)	30	28	30
Fin thickness (mm)	0.102	0.127	0.102
Flow orientation	Enters at L=0	Enters at L=0.5	Enters at L=0.5

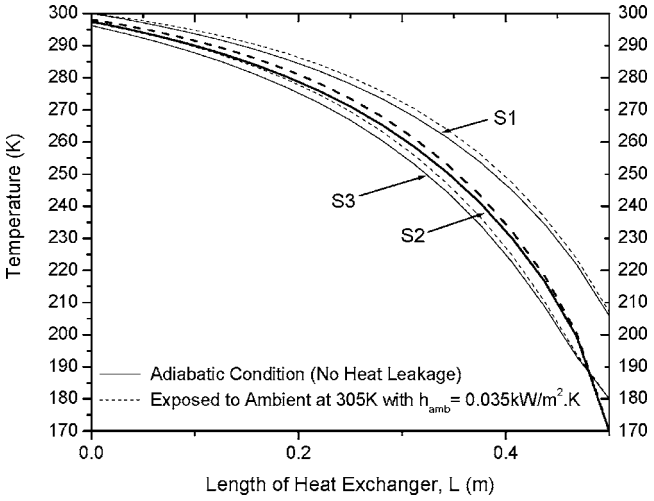

Fig. 12 Effect of external heat load on a three-stream plate fin exchanger performance (specifications given in Table 4)

6 Conclusion

In the present work, the basic algorithm [18] for the analysis of multistream plate fin heat exchangers through the successive partitioning and area splitting methods has been extended to include the effects of axial conduction in the heat exchanger core, heat transfer with the surroundings, and variable fluid properties. The present modifications increase the exactitude of the model and make it suitable for practical calculations. Simulation of the present algorithm has been verified with the analytical model [23] of a three-stream heat exchanger in the absence of axial conduction, heat leakage, and variable fluid properties. An excellent agreement between our iterative algorithm and the analytical model has been observed. Further validation of the algorithm including axial conduction in the heat exchanger matrix has been established by solving the multistream plate fin heat exchanger example reported by Paffenbarger [17], with a good agreement between the results. The proposed method of analyzing the multistream plate fin heat exchanger is simple and does not make use of any specialized software. As it is based on a self-correcting iterative procedure, the memory requirement and risk of divergence is minimized.

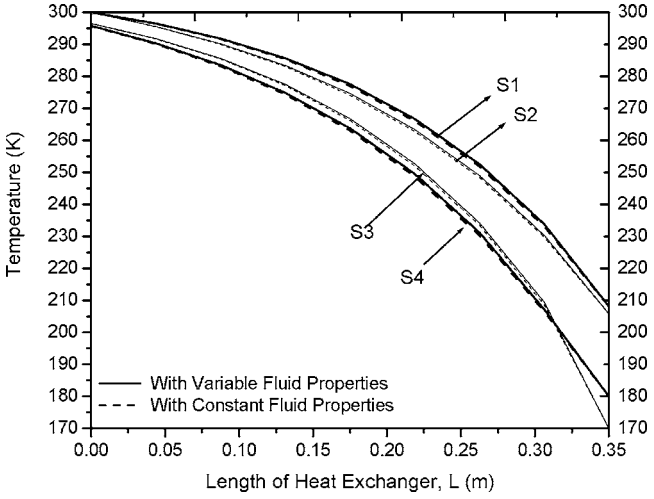

Fig. 13 Heat exchanger performance with and without variable fluid properties

The effect of heat leakage and fluid property variation has been shown with appropriately chosen heat exchanger examples. Though significant change in temperature profile due to fluid property variation is not seen for the chosen heat exchanger configuration, it can be relevant for heat exchangers with fluid streams having widely varying thermophysical properties.

Finally, though the present algorithm has been employed for plate fin heat exchangers, the basic design principle can be used for any multistream heat exchangers.

Nomenclature

A = heat transfer area
A_c = axial conduction area
A_w = primary (wall) heat transfer area
A_f = secondary (fin) surface area
C_i = heat capacity rate of fluid I
$C_{1,2}$ = heat capacity rate ratio as defined in Ref. [23]
$C_{3,2}$ = heat capacity rate ratio as defined in Ref. [23]
C_p = specific heat
F = fin frequency
h = local heat transfer coefficient
h_f = fin height
h_0 = heat transfer coefficient of surroundings
k,k' = discrete location
k_c = thermal conductivity of fin material
k_{ins} = thermal conductivity of insulation+
$K_{ax,1}$ = axial conduction parameters defined by (11) and (25)
$K_{ax,2}$ = axial conduction parameters defined by (12) and (26)
L = heat exchanger length
m = number of segments, i.e., 2^j
n = total number of fluid streams
NTU = number of transfer units
Q = amount of heat transfer
R^* = overall thermal resistance ratio as defined in Ref. [23]
S = fluid stream identifier
t = fluid temperature
T = separating wall temperature
t_0 = ambient temperature
t_{ins} = thickness of insulation
t_{plate} = thickness of heat exchanger cap sheets
t_{sb} = thickness of side bar
t_{sp} = thickness of separating plate
t_f = fin thickness
$\bar{t}$ = average fluid temperature
U = overall heat transfer coefficient
W = width of heat exchanger
x,y,z = length coordinates

Greek Symbols

α = fraction of area defined by (2)
Φ_{PAx} = parameter defined by (15)
Φ_{CAx} = parameter defined by (24)
η_f = fin temperature effectiveness
μ = viscosity of fluid
θ = nondimensional temperature as defined in Ref. [23]

Subscripts

ax = axial conduction
i = index of fluid streams
j = stage of partitioning
f = fin
amb = ambient

References

[1] Bejan, A., 1977, "The Concept of Irreversibility in Heat Exchanger Design: Counterflow Heat Exchangers for Gas-to-Gas Applications," ASME J. Heat Transfer, **99**(3), pp. 374–380.

[2] Chowdhury, K., and Sarangi, S., 1983, "A Second Law Analysis of the Concentric Tube Heat Exchanger: Optimisation of Wall Conductivity," Int. J. Heat Mass Transfer, **26**(5) pp. 783–786.

[3] Barron, R. F., 1999, *Cryogenic Heat Transfer*, Taylor & Francis, London, pp. 311–318.

[4] Shah, R. K., 1994, "A Review of Longitudinal Wall Heat Conduction in Recuperators," J. Energy, Heat Mass Transfer, **16**, pp. 15–25.

[5] Barron, R. L., and Yeh, S. L., 1976, "Longitudinal Conduction in a Three-Fluid Heat Exchanger," ASME Paper No. 76-WA, HT-9 2-7.

[6] Kroeger, P. G., 1967, "Performance Deterioration in High Effectiveness Heat Exchangers Due to Axial Heat Conduction Effects," Adv. Cryog. Eng., Vol. **12**, pp. 363–372.

[7] Chiou, J. P., 1978, "The Effect of Longitudinal Heat Conduction on Crossflow Heat Exchanger," ASME J. Heat Transfer, **100**, pp. 436–441.

[8] Chiou, J. P., 1980, "The Advancement of Compact Heat Exchanger Theory Considering the Effects of Longitudinal Heat Conduction and Flow Non-Uniformity," *Compact Heat Exchangers, History, Technological Advancement and Mechanical Design Problems*, R. K. Shah, C. F. McDonald, and C. P. Howard, eds., HTD Vol. 10, ASME, New York, pp. 101–121.

[9] Venkatarathnam, G., and Narayanan, S. P., 1999, "Performance of a Counter Flow Heat Exchanger With Longitudinal Heat Conduction Through the Wall Separating the Fluid Streams From the Environment," Cryogenics, **39**, pp. 811–819.

[10] Mondt, J. R., 1980, "Correlating the Effects Longitudinal Heat Conduction on Heat Exchanger Performance," *Compact Heat Exchangers, History, Technological Advancement and Mechanical Design Problems*, R. K. Shah, C. F. McDonald, and C. P. Howard, eds., HTD Vol. 10, ASME, New York, pp. 123–134.

[11] Shah, R. K., 1975, "A Correlation for Longitudinal Heat Conduction Effects in Periodic Flow Heat Exchangers," ASME J. Eng. Power, **97**, pp. 453–454.

[12] Chowdhury, K., and Sarangi, S., 1984, "Performance of Cryogenic Heat Exchangers With Heat Leak From the Surroundings," Adv. Cryog. Eng., **29**, pp. 273–280.

[13] Barron, R. F., 1984, "Effects of Heat Transfer From Ambient on Cryogenic Heat Exchanger Performance," Adv. Cryog. Eng., **29**, pp. 265–272.

[14] Gupta, P., and Atrey, M. D., 2000, "Performance Evaluation of Counter Flow Heat Exchangers Considering the Effect of Heat in Leak and Longitudinal Conduction for Low-Temperature Applications," Cryogenics, **40**(7) pp. 469–474.

[15] Chowdhury, K., and Sarangi, S., 1984, "The Effect of Variable Specific Heat of the Working Fluid on the Performance of Counterflow Heat Exchangers," Cryogenics, **24**, pp. 679–680.

[16] Shah, R. K., 1993, "NonUniform Heat Transfer Coefficients for Heat Exchanger Thermal Design," *Aerospace Heat Exchanger Technology*, R. K. Shah and A. Hashemi, eds., Elsevier, New York, pp. 417–445.

[17] Paffenbarger, J., 1990, "General Computer Analysis of Multistream Plate Fin Heat Exchangers," *Compact Heat Exchangers—A Festschrift for A. L. London*, R. K. Shah, A. D. Kraus, and D. Metzger, eds., Hemisphere, New York, pp. 727–746.

[18] Ghosh, I., Sarangi, S. K., and Das, P. K., 2006, "An Alternative Algorithm for the Analysis of Multisteam Plate Fin Heat Exchangers," Int. J. Heat Mass Transfer, **49**, pp. 2889–2902.

[19] Prasad, B. S. V., 1991, "The Performance Prediction of Multistream Plate Fin Heat Exchangers Based on Stacking Pattern," Heat Transfer Eng., **12**, pp. 58–70.

[20] Prasad, B. S. V., 1996, "Fin Efficiency and Mechanisms of Heat Exchange Through Fins in Multistream Plate Fin Heat Exchangers: Formulation," Int. J. Heat Mass Transfer, **39**, pp. 419–428.

[21] Prasad, B. S. V., 1997, "Fin Efficiency and Mechanisms of Heat Exchange Through Fins in Multistream Plate Fin Heat Exchangers: Development and Application of a Rating Algorithm," Int. J. Heat Mass Transfer, **40**, pp. 4279–4288.

[22] Prasad, B. S. V., and Gurukul, S. M. K. A., 1992, "Differential Methods for the Performance Prediction of Multistream Plate Fin Heat Exchangers," ASME J. Heat Transfer, **114**, pp. 41–49.

[23] Sekulic, D. P., 1994, "A Compact Solution of the Parallel Flow Three-Fluid Heat Exchanger Problem," Int. J. Heat Mass Transfer, **37**, pp. 2183–2187.

[24] Ghosh, I., 2004, "Experimental and Computational Studies on Plate Fin Heat Exchangers," Ph.D. thesis, Indian Institute of Technology, Kharagpur.

Journal of Heat Transfer

Technical Briefs

Technical Brief: Asymptotic Temperature Distribution in a Simulated Combustion Chamber

Anand B. Vyas
Visiting Assistant Professor
Department of Mathematical Sciences,
University of Delaware,
Newark, DE 19716

Joseph Majdalani[1]
Jack D. Whitfield Professor of High Speed Flows
Fellow ASME
Department of Mechanical, Aerospace, and
Biomedical Engineering,
University of Tennessee Space Institute,
Tullahoma, TN 37388
e-mail: drmajdalani@gmail.com

In an axisymmetric model of a solid rocket motor, a cylindrical combustion chamber with porous walls is considered. For a posited range of operating parameters, the energy equation is perturbed and linearized using the dimensionless Péclet number. The possibility of circumventing chemical reactions while retaining the essential physics of the problem is explored. This is accomplished by artificially introducing a distributed heat source above the propellant surface. The resulting energy equation is then solved to zeroth order. The analytical solution and corresponding temperature maps are verified qualitatively using comparisons with numerical simulations of the combustion chamber.
[DOI: 10.1115/1.2714591]

Keywords: asymptotic technique, thin sheet approximation, solid rocket motor, eigenfunction expansion

1 Introduction

Theoretical studies of aeroacoustic instability in solid rocket motors may be grouped under two categories: (1) those attempting to model unsteady combustion with limited emphasis on the internal flow details [1–6]; and (2) those attempting to describe the core flow details of a nonreactive mixture [7–11]. Over the years, both approaches have proven to be useful and complementary.

Exceptions to this classification exist and these can be illustrated in the resurging computational studies of Apte and Yang [12], Roh, Tseng and Yang [13], Roh and Culick [14], Venugopal et al. [15,16], and Vuillot and co-workers [17,18]. By focusing on numerical simulations, as opposed to analytical solutions of the internal flowfield, these studies have managed to combine the complex aeroacoustic interactions with the elements of combustion. Aside from these numerical studies, the intrinsic coupling between thermal and aeroacoustic modes has been often ignored in purely analytical studies.

In this work, we present a simple mathematical model that can couple the gas dynamics with the heat generated from propellant combustion. The model leads to a thermal solution of the flowfield that can mimic the effects of chemical reactions and entropy gradients that one normally associates with propellant combustion.

At first, the basic nature of the equations is examined. This enables us to identify small parameters that can be effectively used to simplify the model. The work is directed toward normalizing the energy equation by introducing a distributed heat source to replace the flame zone above the propellant surface. We ignore, at this stage, nonlinear heat radiation. Then, after providing estimates for various transport properties, we solve the ensuing equations using asymptotic expansions and compare our results to predictions made by other researchers.

2 Mathematical Model

As shown in Fig. 1, the coordinate system is so chosen that the longitudinal axis of the motor corresponds to the z axis. Due to symmetry, the domain of interest is reduced to $0 \leq r^* \leq R$, and $0 \leq z^* \leq L$. As usual, the internal radius of the cylindrical grain is denoted by R while the length of the grain is labeled L. A constant heat flux is imposed along the sidewall in a manner to account for the chemical reaction energy released during surface combustion.

The energy equation is written under the tacit assumptions that the flow is steady, incompressible, and axisymmetric with constant transport properties. Furthermore, we assume that the fluid enters the chamber at a uniform velocity V and that chemical reactions are confined to a thin sheet above the burning surface.

2.1 Governing Equation and Boundary Conditions. The energy equation under the stated assumptions can be expressed by

$$\rho c_p\left(u_r^*\frac{\partial T^*}{\partial r^*}+u_z^*\frac{\partial T^*}{\partial z^*}\right)-\left(u_r^*\frac{\partial p^*}{\partial r^*}+u_z^*\frac{\partial p^*}{\partial z^*}\right)$$
$$=\frac{k}{r^*}\frac{\partial}{\partial r^*}\left(r^*\frac{\partial T^*}{\partial r^*}\right)+k\frac{\partial^2 T^*}{\partial z^{*2}}+\dot{Q}^*$$
$$+2\mu\left[\frac{u_r^{*2}}{r^{*2}}+\left(\frac{\partial u_r^*}{\partial r^*}\right)^2+\left(\frac{\partial u_z^*}{\partial z^*}\right)^2+\frac{1}{2}\left(\frac{\partial u_z^*}{\partial r^*}\right)^2\right] \quad (1)$$

where the temperature boundary conditions correspond to

$$r^*=0,\quad \frac{\partial T^*}{\partial r^*}=0,\quad r^*=R,\quad T^*=T_w \quad (2)$$

[1]Corresponding author.

Contributed by the Heat Transfer Division of ASME for publication in the JOURNAL OF HEAT TRANSFER. Manuscript received February 5, 2006; final manuscript received July 17, 2006. Review conducted by Bengt Sunden.

 Copyright © 2007 by ASME

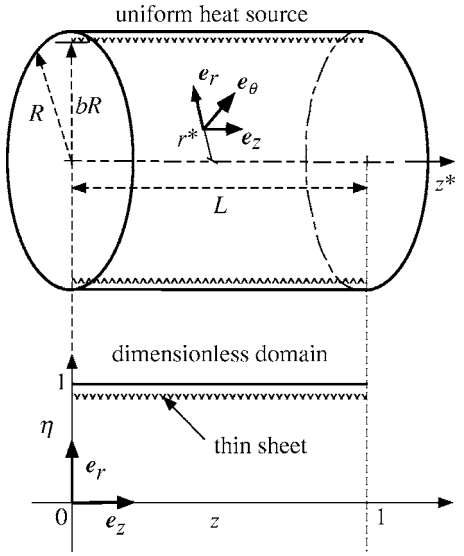

Fig. 1 Idealized motor chamber and system of coordinates illustrating the thin sheet approximation of the heat source

$$z^* = 0, \quad T^* = T_s, \quad z^* = L, \quad T^* = T_{ct} \tag{3}$$

Here T_w is the adiabatic flame temperature at the wall; T_s is the stagnation temperature at the head end; and T_{ct} refers to the throat condition at the downstream end. It is expedient to normalize Eqs. (1)–(3) using

$$r \equiv \frac{r^*}{R}; \quad z \equiv \frac{z^*}{L}; \quad u_r \equiv \frac{u_r^*}{V}; \quad u_z \equiv \frac{u_z^*}{V}; \quad p \equiv \frac{p^*}{\rho V^2}$$

$$\dot{Q} \equiv \frac{\dot{Q}^*}{\rho c_p (T_s - T_w)} \frac{R}{V} \tag{4}$$

and

$$T \equiv \frac{T^* - T_w}{T_s - T_w} \tag{5}$$

Following back substitution, the energy equation reduces to

$$u_r \frac{\partial T}{\partial r} + \phi u_z \frac{\partial T}{\partial z} - \mathrm{Ec}\left(u_r \frac{\partial p}{\partial r} + \phi u_z \frac{\partial p}{\partial z}\right) = \frac{1}{\mathrm{Pe}}\left[\frac{1}{r}\frac{\partial}{\partial r}\left(r\frac{\partial T}{\partial r}\right) + \phi^2 \frac{\partial^2 T}{\partial z^2}\right] + \dot{Q} + \frac{\mathrm{Ec}}{\mathrm{Re}}\left\{2\left[\frac{u_r^2}{r^2} + \left(\frac{\partial u_r}{\partial r}\right)^2 + \left(\frac{\partial u_z}{\partial z}\right)^2\right] + \left(\frac{\partial u_z}{\partial r}\right)^2\right\} \tag{6}$$

where $\phi = R/L$ is the motor's aspect ratio and Re, Pr, Pe, and Ec symbolize the Reynolds, Prandtl, Péclet, and Eckert numbers. These are given by

$$\mathrm{Re} = \frac{VR}{\nu}; \quad \mathrm{Pr} = \frac{\mu c_p}{k}; \quad \mathrm{Pe} = \mathrm{Re}\,\mathrm{Pr}; \quad \mathrm{Ec} = \frac{V^2}{c_p(T_s - T_w)} \tag{7}$$

The normalized boundary conditions become

$$T(1,z) = 0; \quad \frac{\partial T(0,z)}{\partial r} = 0; \quad T(r,0) = 1; \quad T(r,1) = \hat{T} \tag{8}$$

where

$$\hat{T} = \frac{T_{ct} - T_w}{T_s - T_w}; \quad T_s = \frac{1}{2} T_{ct}(\gamma + 1); \quad \gamma = 1.4 \tag{9}$$

The last relation is due to the fundamental dependence of the static temperature on the stagnation temperature for choked conditions at the downstream end. It can be developed from $T_s = T[1 + (1/2)(\gamma - 1)M^2]$ for $M = 1$.

2.2 Dynamic Similarity Parameters. Given a gas mixture at 1000–3500 K and 10–100 bar, the dynamic viscosity is calculated to be 10^{-5}–10^{-4} N s/m^2. Then using Chung's correlation [19], the thermal conductivity is found to be approximately 2.0 W/m K. For the stated range of temperatures and pressures, one obtains a Prandtl number of order 10^{-2}. The Péclet number can hence vary from a small to a very large value. As the injection Reynolds number is varied from 10 to 10^6, the Péclet number changes from 10^{-1} to 10^4. In this study, we consider the case corresponding to the lower end of the injection rate, namely, to that of a small Péclet number.

In addition to the reciprocal of the Reynolds number, the problem exhibits another small parameter that can be used in the asymptotic work. Using average values of $V \approx 5$ m/s, $T_s \approx 3500$ K, $T_w \approx 700$ K, and $c_p \approx 1500$ J/kg K, it can be seen that the Eckert number in Eq. (7) is of order 6×10^{-6}. Being the ratio of kinetic and thermal energies, a small Eckert number corresponds to a setting in which thermal energy dominates over mean kinetic energy. This result is generally true inside a solid rocket motor (SRM) except for a small region near the nozzle throat. The assumption of Ec being small enables us to decouple the energy equation from the momentum equation. As evidenced by Eq. (6), both velocity and pressure become weak functions of temperature. This realization justifies the decoupling of thermal effects in some SRM core flow models such as those used by Culick [20], Vuillot [21], Casalis et al. [22], Couton et al. [23–25], and others.

Finally, in the interest of algebraic clarity, the present analysis is carried out for $\phi^2 = 1$. This assumption typifies aspect ratios used in upper stage rocket motors. The same approach may be repeated for $\phi^2 \ll 1$.

3 Small Péclet Number Solution

While the Eckert number remains the smallest perturbation quantity in Eq. (6), the Péclet number can be used either as a small, or a large parameter depending on the size of Re. In rocket motors, the large Pe injection combination is the more likely scenario. In this section, however, the small Péclet, moderate injection case is considered. Our solution extends over the range Re $\sim$[10–100] that is of practical importance in some internal flow studies. In a recent core flow study carried out at the Center for Simulation of Advanced Rockets, an injection Reynolds number of 47.6 was used throughout the simulation [16].

3.1 Double Perturbation Expansions. Forthwith, one can multiply Eq. (6) by Pe and expand each variable in the two perturbation parameters, 1/Re and Pe. Next, terms of zeroth order in both perturbation parameters can be collected. One obtains the energy equation at zeroth order, namely

$$\frac{1}{r}\frac{\partial}{\partial r}\left(r\frac{\partial T^{(0,0)}}{\partial r}\right) + \frac{\partial^2 T^{(0,0)}}{\partial z^2} = -\dot{Q} \tag{10}$$

The first and second superscripts denote the order in 1/Re and Pe, respectively. Equation (10) is subject to the boundary conditions given by Eq. (8). Furthermore, it can be seen that the equation is linear and amenable to separation of variables. Using the method of superposition, a solution can be obtained and expressed in terms of eigenfunction expansions.

3.2 Eigenfunction Expansions. One may subdivide the temperature into three parts

$$T^{(0,0)} = T_1^{(0,0)} + T_2^{(0,0)} + T_3^{(0,0)} \tag{11}$$

This decomposition is deliberately pursued to facilitate the satisfaction of boundary conditions. Substitution into Eq. (10) gives rise to the following systems:

System 1

$$\frac{1}{r}\frac{\partial}{\partial r}\left(r\frac{\partial T_1^{(0,0)}}{\partial r}\right) + \frac{\partial^2 T_1^{(0,0)}}{\partial z^2} = 0$$

$$T_1^{(0,0)}(r,0)=1;\quad T_1^{(0,0)}(r,1)=0$$

$$T_1^{(0,0)}(1,z)=0;\quad \frac{\partial T_1^{(0,0)}(0,z)}{\partial r}=0 \tag{12}$$

System 2

$$\frac{1}{r}\frac{\partial}{\partial r}\left(r\frac{\partial T_2^{(0,0)}}{\partial r}\right)+\frac{\partial^2 T_2^{(0,0)}}{\partial z^2}=0$$

$$T_2^{(0,0)}(1,z)=0;\quad \frac{\partial T_2^{(0,0)}(0,z)}{\partial r}=0$$

$$T_2^{(0,0)}(r,0)=0;\quad T_2^{(0,0)}(r,1)=\hat{T} \tag{13}$$

and System 3

$$\frac{1}{r}\frac{\partial}{\partial r}\left(r\frac{\partial T_3^{(0,0)}}{\partial r}\right)+\frac{\partial^2 T_3^{(0,0)}}{\partial z^2}=-\dot{Q}$$

$$T_3^{(0,0)}(1,z)=0;\quad \frac{\partial T_3^{(0,0)}(0,z)}{\partial r}=0$$

$$T_3^{(0,0)}(r,0)=0;\quad T_3^{(0,0)}(r,1)=0 \tag{14}$$

Equations (12)–(14) consist of two Laplace equations with one nonhomogenous boundary condition, and one Poisson equation with homogenous boundary conditions. Their solution is described next.

3.3 Heat Source Addition. So far, we have only been concerned with the simplifications affecting the energy equation. The reaction energy released inside the combustion chamber is another ingredient that must be carefully evaluated. Since propellant physico-chemistry is not taken into consideration, the thermal energy release is distributed in the same manner that it is accounted for in basic two-dimensional models of premixed laminar flames (see Chu et al. [26], and Vyas et al. [27]). Here, we permit the heat to be delivered along a sheet above the propellant surface. This thin-sheet approximation is conveniently modeled using the Dirac delta function (see Fig. 1 for the tentative positioning of the heat source). Mathematically, this operation can be expressed by

$$\dot{Q}=\dot{q}(z)\,\delta(r-b) \tag{15}$$

where $\dot{q}(z)$ is the rate of heat generation that is allowed to vary along the chamber axis.

3.4 Leading Order Solution. Equations (12) and (13) can be solved using separation of variables and eigenfunction expansions. They can then be superimposed using Eq. (11) to construct the total solution at zeroth order in both perturbation variables. To start, we use

$$T_1^{(0,0)}(r,z)=\Phi(r)\Psi(z) \tag{16}$$

Substituting this product into Eq. (12), one gets

$$\frac{1}{\Phi}\frac{d^2\Phi}{dr^2}+\frac{1}{r}\frac{1}{\Phi}\frac{d\Phi}{dr}+\frac{1}{\Psi}\frac{d^2\Psi}{dz^2}=0 \tag{17}$$

with

$$\frac{d\Phi}{dr}(0)=0,\quad \Phi(1)=0,\quad \Psi(1)=0,\quad \Psi(0)=1 \tag{18}$$

At the outset, one obtains

$$T_1^{(0,0)}(r,z)=\sum_{n=1}^{\infty}K_n\sinh[\lambda_n(1-z)]J_0(\lambda_n r) \tag{19}$$

The nonhomogeneous boundary condition at $z=0$ can now be used to determine K_n. One finds

$$K_n=\frac{1}{\sinh(\lambda_n)}\frac{\int_0^1 rJ_0(\lambda_n r)dr}{\int_0^1 rJ_0^2(\lambda_n r)dr}=\frac{2}{\lambda_n J_1(\lambda_n r)\sinh(\lambda_n)} \tag{20}$$

Likewise, Eq. (13) can be solved to get

$$K_n=\frac{2\hat{T}}{\lambda_n J_1(\lambda_n r)\sinh(\lambda_n)} \tag{21}$$

Solutions of Eqs. (12) and (13) can be added to obtain

$$T_1^{(0,0)}+T_2^{(0,0)}=\sum_{n=1}^{\infty}\frac{2J_0(\lambda_n r)\{\sinh[\lambda_n(1-z)]+\hat{T}\sinh(\lambda_n z)\}}{\lambda_n\sinh(\lambda_n)J_1(\lambda_n r)} \tag{22}$$

Having reached a partial solution, one may solve the remaining system given by Eq. (14). One retrieves

$$T_3^{(0,0)}=\sum_{n=1}^{\infty}\sum_{m=1}^{\infty}B_{mn}\sin(m\pi z)J_0(\lambda_n r) \tag{23}$$

Expanding Eq. (15) and using the orthogonality of eigenfunctions, one determines the double eigenfunction expansion coefficients. These are

$$\dot{q}(z)\,\delta(r-b)=\sum_{n=1}^{\infty}\sum_{m=1}^{\infty}A_{mn}\sin(m\pi z)J_0(\lambda_n r) \tag{24}$$

and so

$$A_{mn}=\frac{\int_0^1\int_0^1\dot{q}(z)\,\delta(r-b)\sin(m\pi z)J_0(\lambda_n r)r\,dr\,dz}{\int_0^1\int_0^1\sin^2(m\pi z)J_0^2(\lambda_n r)r\,dr\,dz}$$

$$=\frac{4J_0(\lambda_n b)}{J_1^2(\lambda_n)}\int_0^1\int_0^1\dot{q}(z)\sin(m\pi z)dz \tag{25}$$

By substituting Eq. (23) into the left-handside of Eq. (14), it is possible to determine the A_{mn} coefficients by relating Eq. (23) to the double expansion coefficients of Eq. (25). One gets

$$B_{mn}=\frac{A_{mn}}{m^2\pi^2+\lambda_n^2} \tag{26}$$

This completes our leading-order solution in both perturbation parameters. We now have

$$T^{(0,0)}=\sum_{n=1}^{\infty}\frac{2J_0(\lambda_n r)\{\sinh[\lambda_n(1-z)]+\hat{T}\sinh(\lambda_n z)\}}{\lambda_n\sinh(\lambda_n)J_1(\lambda_n r)}$$

$$+\sum_{n=1}^{\infty}\sum_{m=1}^{\infty}B_{mn}\sin(m\pi z)J_0(\lambda_n r) \tag{27}$$

4 Results

To better understand the solution behavior, we have plotted the constant temperature contour maps derived from $T^{(0,0)}$. The heat source is distributed along a thin sheet located at a radial distance of $b=0.9$. We have chosen a spatially uniform heat generation in accordance with the standard thin sheet approximation. This may be justifiable insofar as averaging of unsteady flame variations over time yields a constant flame profile. We have considered three separate cases characterized by three orders of magnitude variations in the heat generation rate.

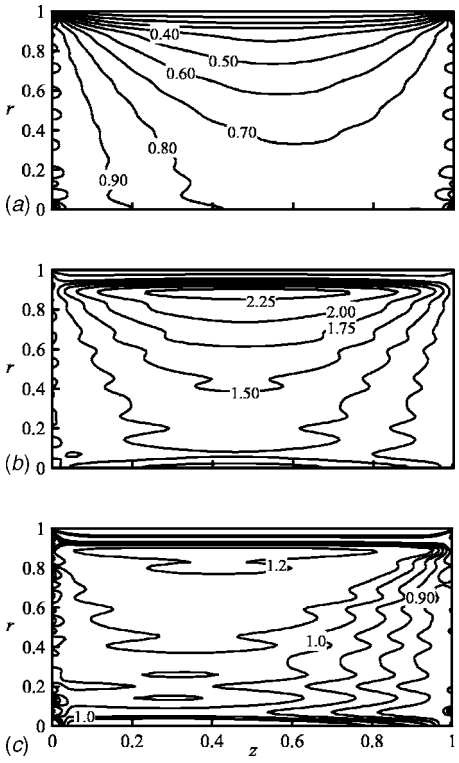

Fig. 2 Isotherms for $b=0.9$, $\hat{T}=0.8$, and (a) $\dot{q}=2.5$; (b) $\dot{q}=25$; and (c) $\dot{q}=12.5$

4.1 Case 1: $b=0.9$, $\hat{T}=0.8$, and $\dot{q}=2.5$. For a sufficiently low heat generation rate, we observe in Fig. 2(*a*) a linear temperature gradient that increases away from the wall. Since the maximum temperature occurs at the core, the solution with low heat input does not appear to be a suitable model of the flame zone. The reason can be attributed to the heat generation term being of the same order as the diffusive term. Note that the temperature variations along the boundaries are due to the asymmetric boundary conditions. The small fluctuations in the corresponding isotherms are due to the finite number of eigenvalues used in our code. Presently, we have used only 25 eigenvalues in the radial and axial directions. By carrying out a sensitivity analysis, we have found that further increases in the number of eigenvalues (e.g., to 30) do not affect the solution in the core. The small temperature variations along the boundaries, however, must be tolerated. It can be verified that the average values of these deviations over the radial and longitudinal lengths add up to the prescribed boundary values. The justification for $\hat{T}=0.8$ is based on Eq. (9). Since our analysis has indicated that the value of $\hat{T}$ varies between 0.77 and 0.8, the upper limit has been chosen. The skewed thermal contours in the downstream direction can be attributed to the relatively weak heat source. The slow variation in the temperature near the surface leads to a shallow temperature gradient that does not conform to temperature predictions in rocket motors. This rate of heat release is clearly not sufficient to reproduce the desired thermal field.

4.2 Case 2: $b=0.9$, $\hat{T}=0.8$, and $\dot{q}=25$. To better simulate rocket motor conditions, the heat source is first increased by one order of magnitude. As shown in Fig. 2(*b*), it can be seen that, for a large heat generation rate, a steeper gradient in temperature is obtained that can mimic the temperature gradient between the burning surface and the flame inside a solid rocket motor. The nearly symmetric temperature map is the outcome of a dominant heat source and a weak convective motion. Also, the intense heat generation near $r=0.9$ roughly approximates the mechanism of heat generation associated with a laminar premixed flame. However, by comparing the magnitude of the normalized temperature distribution to that obtained in a solid rocket motor, we realize that the observed distribution overestimates the maximum temperature in an actual motor. Since our normalized peak temperature of 2.2 corresponds to about 5000 K, it constitutes a modest exaggeration of practical values. In rockets, one expects this temperature to fall in the vicinity of 3500 K. Given that the imposed heat distribution rate is not derived from experimental data, it can be adjusted in a manner to produce more realistic temperature maps. We conclude that a more appropriate value for artificial heat generation should be used, namely, one that is closer to 12. When such a level is imposed, the thermal maps become a more adequate representation of the temperature field in a typical motor. This case is illustrated in Fig. 2(*c*). Therein, the weak temperature variation in the axial direction can be attributed to the weak injection-driven flow effect in relative proportion to the thermal heat dispersion effect. The rapid temperature variation near the wall is also consistent with the steep thermal gradients observed in rockets. Our analytical results appear to be in qualitative agreement with the numerical findings of Roh et al. [28] (cf. Fig. 2, p. 894).

5 Conclusions

An asymptotic investigation is carried out to estimate the transport properties and physical quantities arising in the energy equation applied to a simulated solid rocket motor chamber. The study reveals the presence of three contributing parameters. These are the Eckert number, the injection Reynolds number, and the Péclet number. The Eckert number is found to be so small that it leads to the decoupling of temperature effects on the mean flow motion. This confirms the routinely used assumptions made by previous investigators. In the present work, the small Péclet, moderate injection case is considered. Also, the use of the Dirac delta function to model the desired heat source displacement appears to be a viable artifact. The fair agreement with temperature maps in rocket motors provides the raison d'être for this basic formulation. In future work, the analysis may be extended to higher orders by fully incorporating the convective mean flow effects. Along similar lines, the heat source location may be adjusted by relating b to flame zone dynamics.

Acknowledgment

This project is sponsored, in part, by NSF grant No. CMS-0353518.

References

[1] Brewster, M. Q., 2000, *Solid Propellant Combustion Response: Quasi-Steady (QSHOD) Theory Development and Validation, Solid Propellant Chemistry, Combustion, and Motor Interior Ballistics*, V. Yang, T. B. Brill, and W.-Z. Ren, eds., AIAA Progress in Astronautics and Aeronautics, Washington, D.C., Vol. 185, pp. 607–637.

[2] T'ien, J. S., 1972, "Oscillatory Burning of Solid Propellants Including Gas Phase Time Lag," Combust. Sci. Technol., **5**, pp. 47–54.

[3] De Luca, L. T., 1992, *Theory of Nonsteady Burning and Combustion Stability of Solid Propellants by Flame Models, Nonsteady Burning and Combustion Stability of Solid Propellants*, L. T. De Luca, E. W. Price, and M. Summerfield, eds., AIAA Progress in Astronautics and Aeronautics, Washington, D.C., Vol. 143, pp. 519–600.

[4] Margolis, S. B., and Williams, F. A., 2000, *Structure and Stability of Deflagrations in Porous Energetic Materials, Solid Propellant Chemistry, Combustion, and Motor Interior Ballistics*, V. Yang, T. B. Brill, and W. Z. Ren, eds., AIAA Progress in Aeronautics and Astronautics, Washington, D.C., Vol. 185, pp. 549–590.

[5] Zemin, A. A., and Finjakov, S. V., 2000, *Burning Rate Response Functions of Composite-Modified Double-Base Propellants and HMX, Solid Propellant Chemistry, Combustion, and Motor Interior Ballistics*, V. Yang, T. B. Brill, and W. R. Ren, eds., AIAA Progress in Astronautics and Aeronautics, Washington, D.C., Vol. 185, pp. 639–662.

[6] Beddini, R. A., and Roberts, T. A., 1992, "Response of Propellant Combustion to a Turbulent Acoustic Boundary Layer," J. Propul. Power, **8**(2), pp. 290-296.

[7] Chedevergne, F., Casalis, G., and Feraille, T., 2006, "Biglobal Linear Stability Analysis of the Flow Induced by Wall Injection," Phys. Fluids, **18**(1), pp.

014103–014114.
[8] Griffond, J., and Casalis, G., 2001, "On the Nonparallel Stability of the Injection Induced Two-Dimensional Taylor Flow," Phys. Fluids, **13**(6), pp. 1635–1644.
[9] Apte, S., and Yang, V., 2001, "Unsteady Flow Evolution in a Porous Chamber With Surface Mass Injection. Part I: Free Oscillation," AIAA J., **39**(8), pp. 1577–1586.
[10] Majdalani, J., Barron, J., and Van Moorhem, W. K., 2001, "Experimental Classification of Turbulence in an Oscillatory Channel Flow With Transpiring Walls," *Proceedings ASME FEDSM 2001-1881*, New Orleans, LA, May 29–June 1, ASME, New York.
[11] Majdalani, J., Barron, J., and Van Moorhem, W. K., 2002, "Inception of Turbulence in the Stokes Boundary Layer over a Transpiring Wall," ASME J. Fluids Eng., **124**(9), pp. 1–7.
[12] Apte, S., and Yang, V., 2000, *Effect of Acoustic Oscillation on Flow Development in a Simulated Nozzleless Rocket Motor, Solid Propellant Chemistry, Combustion, and Motor Interior Ballistics*, V. Yang, T. B. Brill, and W.-Z. Ren, eds., AIAA Progress in Astronautics and Aeronautics, Washington, D.C., Vol. 185, pp. 791–822.
[13] Roh, T. S., Tseng, I. S., and Yang, V., 1995, "Effects of Acoustic Oscillations on Flame Dynamics of Homogeneous Propellants in Rocket Motors," J. Propul. Power, **11**(4), pp. 640–650.
[14] Roh, T. S., and Culick, F. E. C., 1995, "Transient Combustion Response of Homogeneous Propellants to Acoustic Oscillations in Axisymmetric Rocket Motors," *Proceedings AIAA 97-3325*, San Diego, CA, July 6–9.
[15] Venugopal, P., Najjar, F. M., and Moser, R. D., 2000, "DNS and LES Computations of Model Solid Rocket Motors," *Proceedings AIAA 2000-3571*, Huntsville, AL, July 16–19.
[16] Venugopal, P., Najjar, F. M., and Moser, R. D., 2001, "Numerical Simulations of Model Solid Rocket Motor Flows," *Proceedings AIAA 2001-3950*, Salt Lake City, UT, July 6–11.
[17] Vuillot, F., and Lupoglazoff, N., 1996, "Combustion and Turbulent Flow Effects in 2-D Unsteady Navier-Stokes Simulations of Oscillatory Rocket Motors," *Proceedings AIAA 96-0884*, Reno, NV, January 15–18.
[18] Vuillot, F., Dupays, J., Lupoglazoff, N., Basset, T., and Daniel, E., 1997, "2-D Navier-Stokes Stability Computations for Solid Rocket Motors: Rotational, Combustion and Two-Phase Flow Effects," *Proceedings AIAA 97-3326*, Seattle, WA, July 6–9.
[19] Reid, R. C., Prausnitz, J. M., and Poling, B. E., 1987, *The Properties of Gases and Liquids*, 4th ed., McGraw–Hill, New York.
[20] Culick, F. E. C., 1966, "Rotational Axisymmetric Mean Flow and Damping of Acoustic Waves in a Solid Propellant Rocket," AIAA J., **4**(8), pp. 1462–1464.
[21] Vuillot, F., 1995, "Vortex-Shedding Phenomena in Solid Rocket Motors," J. Propul. Power, **11**(4), pp. 626–639.
[22] Casalis, G., Avalon, G., and Pineau, J.-P., 1998, "Spatial Instability of Planar Channel Flow With Fluid Injection through Porous Walls," Phys. Fluids, **10**(10), pp. 2558–2568.
[23] Couton, D., Plourde, F., and Doan-Kim, S., 1999, "Analysis of Energy Transfers of a Sheared Flow Generated by Wall Injection," Exp. Fluids, **26**(3), pp. 222–232.
[24] Couton, D., Doan-Kim, S., and Vuillot, F., 1997, "Numerical Simulation of Vortex-Shedding Phenomenon in a Channel With Flow Induced through Porous Wall," Int. J. Heat Fluid Flow, **18**(3), pp. 283–296.
[25] Couton, D., Plourde, F., and Doan-Kim, S., 1996, "Cold Gas Simulation of a Solid Propellant Rocket Motor," AIAA J., **34**(12), pp. 2514–2522.
[26] Chu, W.-W., Yang, V., and Majdalani, J., 2003, "Premixed Flame Response to Acoustic Waves in a Porous-Walled Chamber With Surface Mass Injection," Combust. Flame, **133**(6129), pp. 359–370.
[27] Vyas, A. B., Majdalani, J., and Yang, V., 2003, "Estimation of the Laminar Premixed Flame Temperature and Velocity in Injection-Driven Combustion Chambers," Combust. Flame, **133**(6129), pp. 371–374.
[28] Roh, T. S., Apte, S., and Yang, V., 2000, *Combustion Dynamics of Homogeneous Solid Propellants in a Rocket Motor With Acoustic Excitations, Solid Propellant Chemistry, Combustion, and Motor Interior Ballistics*, V. Yang, T. B. Brill, and W.-Z. Ren, eds., AIAA Progress in Astronautics and Aeronautics, Washington, D.C., Vol. 185, pp. 885–906.

Heat Exchanger Design Methodology for Electronic Heat Sinks

Ralph L. Webb
Department of Mechanical and Nuclear Engineering,
Penn State University,
University Park, PA 16802
e-mail: ralph.webb@psu.edu

This paper discusses the "inlet temperature difference" (ITD) based heat-exchanger (and its variants) design methodology frequently used by designers of electronic heat sinks. This is at variance with the accepted methodology recommended in standard heat-exchanger textbooks—the "log-mean temperature difference," or the equivalent ε-NTU design method. The purpose of this paper is to evaluate and discuss the ITD based design methodology. The paper shows that the ITD based method is an approximation at best. Variants of the method can lead to either under- or overprediction of the heat transfer rate. Its shortcomings are evaluated and designers are directed to the well established and accepted design methodology.
[DOI: 10.1115/1.2717249]

Keywords: heat exchanger, heat exchanger design, electronic cooling, heat sinks

Introduction

Designers of electronic heat sinks frequently use the "inlet temperature difference" (ITD) for design of electronic heat sinks. This is at variance with typical design procedure for industrial, automotive, and air-conditioning heat exchangers, which use the "log-mean temperature difference" (LMTD), or the equivalent ε-NTU design method. This difference in methodology to define the driving temperature difference raises questions concerning the application and validity of the ITD driving temperature difference method. The purpose of this paper is to evaluate and discuss this question. The main thesis of this paper is to show that what is described herein as the ITD design method is not a valid design method.

The LMTD or ε-NTU Design Method

As shown in typical undergraduate heat transfer texts, one may calculate the heat transfer rate (q) using either the LMTD or ε-NTU design methods, which are equivalent methods.

For the LMTD method, one would write

$$q = F \cdot UA\Delta T_{\ln} \tag{1}$$

where $F=1$ for an electric heat input with a single coolant. For the ε-NTU design method, one would write

$$q = c_{\min}\varepsilon \mathrm{ITD} \tag{2}$$

where $\varepsilon = fcn$ (NTU, $C_{\min}/C_{\max}$) and depends on the flow geometry.

In the LMTD method, the term $1/UA$ is defined as the sum of the thermal resistances in series. For example, consider a water-cooled micro-channel heat sink, which has three thermal resistances in series: interface resistance (R_{int}), spreading resistance (R_{sp}), and convection resistance (R_{cv}). Thus

$$R_{\text{tot}} = R_{\text{int}} + R_{\text{sp}} + R_{\text{cv}} \tag{3}$$

The convection resistance is defined as $1/\eta hA$. The h value is given by published solutions or correlations for the Nusselt number. If the heat is transferred between an electric heat input source at temperature T_{hot} and the coolant, whose inlet and outlet temperatures are $T_{c,\text{in}}$ and $T_{c,\text{out}}$, respectively, then the LMTD is based on these temperatures. The LMTD is defined as

$$\mathrm{LMTD} = \frac{(T_{\text{hot}} - T_{c,\text{in}}) - (T_{\text{hot}} - T_{c,\text{out}})}{\ln[(T_{\text{hot}} - T_{c,\text{in}})/(T_{\text{hot}} - T_{c,\text{out}})]} \tag{4}$$

The ITD Design Method

It is common within the electronic cooling community to use a design method referred to here as the "ITD design method." This means that the driving temperature difference is based on $T_{\text{hot}} - T_{c,\text{in}}$ (=ITD), where T_{hot} is the hot source temperature and $T_{c,\text{in}}$ is the inlet coolant temperature and ITD is defined as the "inlet temperature difference." Consider the case of electric heat input (q) from a heat source at temperature (T_{hot}) of base area A_p, rejecting heat to a coolant flowing over the hot surface, as illustrated in Fig. 1. When using the ITD design method, it is common for electronic heat sink designers to use one of several definitions given below for the "overall thermal resistance"

$$R_{\text{tot,ITD}} = \frac{T_{\text{hot}} - T_{c,\text{in}}}{q} = \frac{\mathrm{ITD}}{q} \tag{5a}$$

They then assume that $R_{\text{tot,ITD}}$ is given by Eq. (3). The key deficiency and inaccuracy of this method is that the heat transfer rate (q) is insensitive to the fluid temperature rise (for constant $R_{\text{tot,ITD}}$). This results in overprediction of the heat transfer rate.

Simons [1] defines a thermal resistance to be added to Eq. (5*a*) to account for the effect of the coolant rise on the driving temperature difference. The modified definition for $R_{\text{tot,ITD}}$ is given by Eq. (5*b*)

$$R_{\text{tot,ITD}} = \frac{\mathrm{ITD}}{q} = R_{\text{tot}} + \frac{T_{c,\text{in}} - T_{c,\text{out}}}{2q} = R_{\text{tot}} + \frac{\Delta T_c/2}{q} \tag{5b}$$

where R_{tot} is given by Eq. (3). The second term in Eq. (5*b*) is defined as the "fluid thermal resistance" (R_{fluid}) and is equal to $1/(2\dot{m}c_p)$. By adding the R_{fluid} term, the calculated q is sensitive to the coolant rise. However, the result is not in exact agreement with that determined using the LMTD method.

A variant of Eq. (5*b*) is given in a recent textbook on electronic cooling as

$$R_{\text{tot,ITD}} = \frac{\mathrm{ITD}}{q} = R_{\text{tot}} + \frac{T_{c,\text{in}} - T_{c,\text{out}}}{q} = R_{\text{tot}} + \frac{\Delta T_c}{q} \tag{5c}$$

where R_{tot} is given by Eq. (3). The second term in Eq. (5*c*) is defined as R_{fluid} and is twice the value of R_{fluid} in Eq. (5*b*). It will be shown that the R_{fluid} defined as $\Delta T_c/q$ is incorrect and results in prediction of a q value less than that of the LMTD method.

The author has consciously chosen to not identify specific references that use one of the several $R_{\text{tot,ITD}}$ definitions given above. Identification of such references would be counterproductive of the intended goal of this paper. However, review of the electronic cooling literature will yield numerous references, which use Eqs. (5*a*), (5*b*), and (5*c*) to define $R_{\text{tot,ITD}}$.

Authors who use Eqs. (5*a*), (5*b*), and (5*c*) assume that the defined $R_{\text{tot,ITD}}$ is equal to the sum of the several series thermal resistances between the hot source (T_{hot}) and the entering coolant ($T_{c,\text{in}}$) as given by Eq. (3). Further, it is assumed that the convection resistance (R_{cv} in Eq. (3)) is equal to $1/(\eta hA)$.

A key purpose of this paper is to show that the R_{tot} defined by Eqs. (5*a*), (5*b*), and (5*c*) is not equal to the R_{tot} defined by Eq. (3). However, the definition of Eq. (5*b*) will provide the best approximation to Eq. (3). Equation (5*b*) defines the driving temperature as

Contributed by the Heat Transfer Division of ASME for publication in the JOURNAL OF HEAT TRANSFER. Manuscript received May 24, 2006; final manuscript received October 12, 2006. Review conducted by Bengt Sunden.

 Copyright © 2007 by ASME

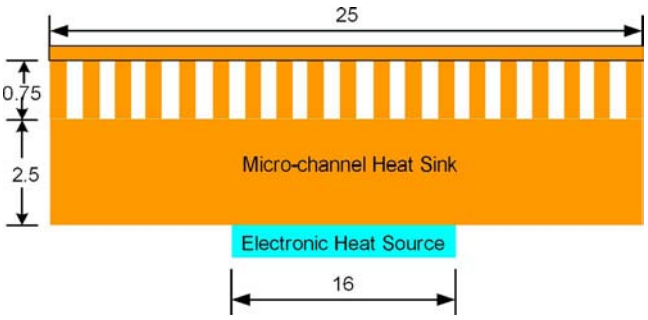

Fig. 1 Example of electronic micro-channel heat sink with water-cooled channels

the arithmetic temperature difference, rather than the log-mean temperature difference. Using Eqs. (5*a*), (5*b*), and (5*c*), one would predict q as

$$q = \frac{\text{ITD}}{R_{\text{tot,ITD}}} \tag{6}$$

This paper seeks to encourage adoption of the standard and accepted heat exchanger design methodology for the design of electronic cooling equipment.

Comparison of Design Methods

If Eqs. (1), (2), and (5*b*) are both valid, they must predict the same q for the same R_{tot} (as defined by Eq. (3)). Setting Eqs. (1) and (5*b*) equal, we obtain

$$R_{\text{tot,ITD}} = \frac{\text{ITD}}{\Delta T_{\ln}} \frac{1}{UA} \tag{7}$$

Because ITD > LMTD, $R_{\text{tot,ITD}} \geq 1/UA$. This means that it is not valid to define $R_{\text{tot,ITD}}$ as the sum of the component thermal resistances (Eq. (3)) for the ITD design method. The only condition, for which the ITD design method can give a q value equal to the LMTD method for single-phase flow is if ITD=LMTD. This can exist for only two cases: (1) if the coolant flow is infinite, which is an impractical situation, or (2) for a two-phase fluid, for which the fluid temperature is a constant (neglecting the effect of two-phase pressure drop on the vapor temperature). However, if the two-phase fluid is convection cooled by a gas or liquid loop, an additional single-phase resistance will be involved and the $R_{\text{tot,ITD}} \geq 1/UA$.

Example Problem

An example problem has been prepared to illustrate the difference in results obtained by the ITD and LMTD design methods. The example involves a water-cooled micro-channel heat sink similar to that shown in Fig. 1. The copper micro-channel heat sink in this example is 25 mm wide and 20 mm flow depth with two water passes. The fins are 0.752 mm high and 0.24 mm thick, placed on 0.427 mm pitch. There are 28 fins in each of the two passes. It has in integrated heat spreader 2.5 mm thick, with the same base area as the micro-channel plate. It receives heat from a 16 mm square electrically heated source that is soldered to the heat sink, and which does not involve a thermal interface resistance. Water enters at 35°C and the hot source temperature is constrained to 70°C. For simplicity the convection resistance is calculated using the Nusselt number for fully developed laminar flow with constant heat flux (Nu=5.3) in a 0.25 aspect ratio channel, as given by Eq. (349) in Shah and London [2]. The spreading resistance is calculated using the equation provided by Lee et al. [3]. For laminar flow, the convection heat transfer coefficient is constant (h=9972 W/m^2 K, and is independent of water flow rate. The $R_{\text{cv}}=1/\eta hA=0.0467$ K/W and $R_{\text{sp}}=0.031$ K/W, resulting in $R_{\text{tot}}=0.0777$ K/W ($R_{\text{cv}}+R_{\text{sp}}$). This example uses Eq. (1) to calculate the heat transfer rate (q) using the LMTD design method. The LMTD is based on T_{hot}, $T_{c,\text{in}}$, and $T_{c,\text{out}}$. An iterative calculation is necessary to calculate the LMTD, because the $T_{c,\text{out}}$ depends on q. Equations (5*a*), (5*b*), and (5*c*) have been used for the ITD design method. The same value of R_{tot} is used for both design methods. Table 1 shows the calculated heat transfer rate for different flow rates using the LMTD and various ITD design methods. The calculation is performed for water flow rates up to 20 g/s.

For the LMTD method, q increases with increasing water flow rate, because the LMTD increases with increasing water flow rate. Because the ITD is constant, the Eq. (5*a*) ITD method gives q =450 W for all water flow rates. The q defined by Eq. (5*b*) approximates the result of the LMTD method. Equation (5*c*) yields a q value lower than that of the LMTD method. Clearly, the Eq. (5*a*) ITD design method (and the Eqs. (5*b*) and (5*c*) variants) gives different results than those of the LMTD design method.

If a turbulent flow correlation were used for water flow rate >20 g/s, one would find that the LMTD would be further increased and higher values of q_{LMTD} would be predicted. At infinite water flow rate, the LMTD=ITD and both methods would give the same q.

Discussion

The example problem clearly shows that if one defines $R_{\text{tot,ITD}}=R_{\text{tot}}$ (Eq. (3)) the ITD method is insensitive to water flow rate and that the predicted results do not agree with those obtained by the LMTD method.

For completeness, the ε-NTU formulation is also presented and discussed. As given by Eq. (11.23) of Incropera and DeWitt [4], the ε-NTU design method gives

$$q = C_{\min}\varepsilon\text{ITD} \tag{8a}$$

Equation (8) may be rewritten as

$$\frac{\text{ITD}}{q} = \frac{1}{\varepsilon C_{\min}} \tag{8b}$$

Comparison of Eqs. (8*b*) and (5*a*) shows that the right-hand side of Eq. (8*b*) is not equal to R_{tot} as defined in Eq. (3). For an electric heat input with a single fluid, Eq. (11.36) of Incropera and DeWitt [4] shows that

Table 1 Results for example problem

Water flow (g/s)	Re_{Dh}	Rtot= $1/UA$ (K/W)	LMTD (K)	q_{LMTD} (W)	q_{ITD} Eq. (5*a*) (W)	q_{ITD} Eq. (5*b*) (W)	q_{ITD} Eq. (5*c*) (W)
5	634	0.0777	26.21	337	450	344	238
10	1152	0.0777	30.18	388	450	390	330
15	1671	0.0777	31.67	408	450	408	366
20	2190	0.0777	32.47	417	450	418	386

$$\varepsilon = 1 - \exp(\text{NTU}) \tag{9}$$

For this case, $C_{\min} = \dot{m}c_p$ and $\text{NTU} = hA/\dot{m}c_p$. For a heat flux input to a coolant, substitution of Eq. (9) in Eq. (8*b*) shows that the correct definition for ITD/q is given by

$$\frac{\text{ITD}}{q} = \frac{1}{\dot{m}c_p}\frac{1}{1 - e^{-\text{NTU}}} \tag{10}$$

Use of the ε-NTU is a more direct method of working the example problem, because it does not require an iterative solution to calculate the LMTD. However, it gives the same answer as the LMTD method.

Conclusions

1. Several conflicting "ITD design methods" appear in the electronic cooling literature. These methods are inconsistent with the well accepted LMTD or ε-NTU design methods.
2. The ITD design methods defined by Eqs. (5*a*), (5*b*), and (5*c*) are invalid for cooling systems that contain at least one single-phase coolant thermal resistance. The problem occurs because the methods do not correctly define the driving temperature difference.
3. The total thermal resistance ($R_{\text{tot,ITD}}$) defined by the ITD design method (Eq. (5*a*)) is greater than the R_{tot} (Eq. (3)) defined by the LMTD design method.
4. The Eq. (5*b*) definition, which includes "fluid thermal resistances," is approximately correct, but not exact.
5. Although it is possible to correct R_{ITD} to obtain the exact value of R_{tot} by adding appropriate "fluid thermal resistances" the process is unconventional and is cumbersome.
6. The well accepted LMTD or ε-NTU design methods are totally applicable to design of electronic heat sinks. Their use is strongly recommended.

Nomenclature

A = heat transfer surface area, A_p (area of flat heat source)
C = capacity rate ($=\dot{m}c_p$), $C_{\min}$ (minimum), $C_{\max}$ (maximum)
c_p = fluid specific heat
D_h = hydraulic diameter
h = heat transfer coefficient
ITD = inlet temperature difference ($T_{\text{hot}} - T_{c,\text{in}}$)
LMTD = log-mean temperature difference; also written as $\Delta T_{\ln}$.
$\dot{m}$ = mass flow rate
NTU = number of thermal units ($=UA/C_{\min}$)
q = heat transfer rate
T_c = coolant temperature, $T_{c,\text{in}}$ (inlet), $T_{c,\text{out}}$ (outlet)
T_{hot} = hot source temperature
R_{cv} = convection thermal resistance ($=1/\eta hA$)
R_{tot} = defined as $1/UA$, valid for LMTD or ε-NTU design methods
$R_{\text{tot,ITD}}$ = defined by Eq. (5*a*), (5*b*), and (5*c*) for ITD design method
R_{sp} = spreading thermal resistance
Re = Reynolds number, Re_{Dh} (based on hydraulic diameter)
U = overall heat transfer coefficient
ε = heat exchanger thermal effectiveness
η = surface efficiency for finned surface
ΔT_c = $T_{c,\text{out}} - T_{c,\text{in}}$

References

[1] Simons, R. E., 2006, "A Simple Thermal Resistance Model—Isoflux Versus Isothermal," *Electronics Cooling*, Vol. 12, No. 1, pp. 6–8.
[2] Shah, R. K., and London, A. L., 1978, *Laminar Flow Forced Convection in Ducts*, Academic, New York.
[3] Lee, S., Song, S., Au, V., and Moran, K. P., 1995, "Constriction/Spreading Resistance Model for Electronics Packaging," *Proceedings 4th ASME/JSME Thermal Engineering Joint Conference*, Vol. 4, ASME, New York, pp. 199–206.
[4] Incropera, F. P., and DeWitt, D. P., 1996, *Fundamentals of Heat and Mass Transfer*, 4th ed., Wiley, New York.

A Lumped Parameter Heat Transfer Analysis for Composting Processes With Aeration

Akira Nakayama[1]
Department of Mechanical Engineering,
Shizuoka University,
3-5-1 Johoku, Hamamatsu, 432-8561 Japan

Kiyohiko Nakasaki
Department of Chemical Engineering,
Shizuoka University,
3-5-1 Johoku, Hamamatsu, 432-8561 Japan

Fujio Kuwahara

Yoshihiko Sano

Department of Mechanical Engineering,
Shizuoka University,
3-5-1 Johoku, Hamamatsu, 432-8561 Japan

Keywords: composting process, aeration, mathematical model, porous media, lumped parameter

Introduction

Composting is the biological decomposition and stabilization of organic substrates. Heat is generated biologically to produce a final product that is stable, free of pathogens and weed seeds, which can be beneficially applied to land. As pointed out by Haug [1] and Li and Jenkins [2], composting is an ancient art, yet engineering that is still often conducted using a "handbook approach." However, such an approach lacks the knowledge to control various factors involved to achieve the desired end product and economics. A typical composting system with aeration is shown in Fig. 1, where the air is ventilated from the bottom to accelerate the biological processes. The air carries sensible and latent heat away as passing through the matrix, while it is essential to maintain organic decomposition leading to biological heat generation. Thus, the control of aeration requires heat transfer analysis if we are to maintain the optimum temperature for the composting system (which, according to Nakasaki et al. [3], coincides with the optimum reaction temperature of around 60°C). Mathematical modeling of composting processes in such a composting system is still in its infancy, although several attempts [3–8] have been made to simulate the composting reactions.

The authors [9] have recently introduced the volume-averaging theory previously established for the study of porous media with heat generation (e.g., Nakayama et al. [10]). We extended it to establish a complete set of the volume-averaged governing equations appropriate for the analysis of composting processes. As a first step towards our strategic efforts to establish a complete numerical prediction tool for composting operations, we propose a simple lumped parameter model, which can be obtained by integrating the foregoing governing equations.

[1]Corresponding author.

Contributed by the Heat Transfer Division of ASME for publication in the JOURNAL OF HEAT TRANSFER. Manuscript received June 6, 2006; final manuscript received January 14, 2007. Review conducted by Chang Oh.

Heat Balance Equation

The composting pile consists of solid, liquid, and gas. The solid phase includes biodegradable substrates, microbes, and humic substances converted from dead organisms and minerals, whereas the main contents of the gas phase are oxygen, nitrogen, carbon dioxide, and water vapor. Both substrates and microbes are of multi-components. However, we shall consider a composting system of one defined substrate and one defined microbe species. For simplicity and definiteness, let the gas phase (denoted by the super- or subscripts f) refer to the mixture of the gases and water vapor, and let the other, namely, the porous matrix (denoted by the super- and subscripts s), refer to the liquid water, biodegradable substrate, microbes, and uncompostable substances, all of which are assumed to be in thermal equilibrium within the matrix.

Heat is generated due to biological reactions, and transfers from the solid to fluid or vice versa. Under such a non-equilibrium condition, the two-energy equation model [9] may be used, in which two distinctive intrinsic average temperatures, namely, one for the gas $\langle T\rangle^f$ and the porous matrix $\langle T\rangle^s$, are introduced as follows

$$\rho_f c_{pf}\left(\varepsilon\frac{\partial\langle T\rangle^f}{\partial t}+\langle u_j\rangle\frac{\partial\langle T\rangle^f}{\partial x_j}\right)=\frac{\partial}{\partial x_j}\left(\varepsilon k_{fe}\frac{\partial\langle T\rangle^f}{\partial x_j}\right)+\frac{1}{V}\int_{A_{\text{int}}}k_f\frac{\partial T}{\partial x_j}n_j\,dA \tag{1}$$

$$\begin{aligned}(1-\varepsilon)(\langle W\rangle^s c_w+\langle S\rangle^s c_{\text{sub}}+\langle X\rangle^s c_x+\langle U\rangle^s c_u)\frac{\partial\langle T\rangle^s}{\partial t}\\ =\frac{\partial}{\partial x_j}\left((1-\varepsilon)k_{se}\frac{\partial\langle T\rangle^s}{\partial x_j}\right)-\frac{1}{V}\int_{A_{\text{int}}}k_f\frac{\partial T}{\partial x_j}n_j\,dA\\ +(1-\varepsilon)\left[H_w\frac{\partial\langle W\rangle^s}{\partial t}-H_{\text{sub}}\left(\frac{\partial\langle X\rangle^s}{\partial t}+\frac{\partial\langle S\rangle^s}{\partial t}\right)\right]\end{aligned} \tag{2}$$

The last term on the right-handside of (2) describes the net volumetric heat generation due to biological reactions. However, Nakayama et al. [10] analytically showed the difference in the two temperatures is quite small as long as the macroscopic characteristic length scale (i.e., the size of the static pile) is much greater than $\sqrt{k_f/h_v}$ where h_v is the volumetric heat transfer coefficient. Thus, we may combine the two energy equations, under the local thermal equilibrium (i.e., $T=\langle T\rangle^f=\langle T\rangle^s$), to obtain a single energy equation for the composting system

$$\begin{aligned}[(1-\varepsilon)(\langle W\rangle^s c_w+\langle S\rangle^s c_{\text{sub}}+\langle X\rangle^s c_x\\ +\langle U\rangle^s c_u)+\varepsilon\rho_f c_f]\frac{\partial T}{\partial t}+\rho_f c_f u_j\frac{\partial T}{\partial x_j}\\ =\frac{\partial}{\partial x_j}\left\{[(1-\varepsilon)k_{se}+\varepsilon k_{fe}]\frac{\partial T}{\partial x_j}\right\}+(1-\varepsilon)\left(H_w\frac{\partial\langle W\rangle^s}{\partial t}\right.\\ \left.-H_{\text{sub}}\frac{\partial(\langle S\rangle^s+\langle X\rangle^s)}{\partial t}\right)\end{aligned} \tag{3}$$

We integrate the foregoing heat balance equation over the entire composting matrix to obtain the following ordinary differential equation for a lumped parameter analysis

$$\begin{aligned}m_s c_s\frac{dT}{dt}=\rho_{\text{air}}c_{\text{air}}\dot{V}_{\text{air}}(T_a-T)+hA(T_a-T)+H_w\frac{dm_w}{dt}\\ -H_{\text{sub}}\frac{d(m_{\text{sub}}+m_x)}{dt}\end{aligned} \tag{4}$$

where T (°C) here is the temperature averaged over the entire composting matrix. Note

 Copyright © 2007 by ASME

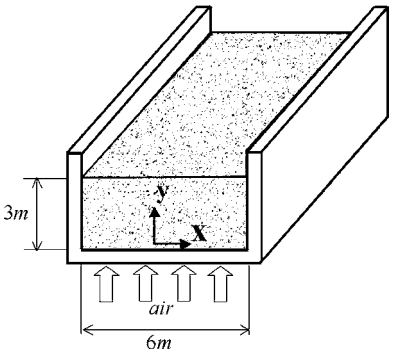

Fig. 1 Composting of static pile with aeration

$$m_s = m_w + m_{\text{sub}} + m_x + m_u \tag{5}$$

is the total mass of the composting matrix, while its specific heat capacity is given by

$$c_s = \frac{m_w c_w + m_{\text{sub}} c_{\text{sub}} + m_x c_x + m_u c_u}{m_s} = \frac{m_w c_w + (m_s - m_w) c_{\text{sub}}}{m_s} \tag{6}$$

where $c_{\text{sub}} = c_x = c_u$ is assumed. We may replace the properties of the gas phase by those of air. The first term on the right-hand side in Eq. (4) denotes the heat carried away by the air supplied at the volume flow rate of $\dot{V}_{\text{air}}$, while the second term represents the heat loss to the surroundings of the temperature T_a. Whether or not the lumped parameter can model the composting process to a quantifiable degree depends on the uniformity of the temperature and concentration distributions within the pile. Since the aeration makes the distributions uniform, the lumped parameter model of this kind is believed to give quantitative information for the average values in the aerated system.

Microbial Growth Rate Equation and Water Transport Equation

We may model the microbial growth rate according to Contois [11] as

$$\frac{dm_x}{dt} = -Y\frac{dm_{\text{sub}}}{dt} = \mu\left(\frac{m_w}{m_s}, T\right)\frac{m_{\text{sub}} m_x}{k_c m_x + m_{\text{sub}}} \tag{7}$$

where μ is the maximum specific growth rate, which is given by

$$\frac{\mu}{\mu_b} = \begin{cases} \dfrac{\dfrac{m_w}{m_s} - w_a}{K_a + \dfrac{m_w}{m_s}}\alpha(T) & : w_a \leqslant \dfrac{m_w}{m_s} \leqslant w_1 \\ \dfrac{w_1 - w_a}{K_a + w_1}\dfrac{w_2 - \dfrac{m_w}{m_s}}{w_2 - w_1}\alpha(T) & : w_1 \leqslant \dfrac{m_w}{m_s} \leqslant w_2 \\ 0 & : \text{otherwise} \end{cases} \tag{8}$$

and

$$\alpha(T) = \begin{cases} \exp\left[-\dfrac{E_A}{R_A}\left(\dfrac{1}{T+273} - \dfrac{1}{T_M+273}\right)\right] & : T \leqslant T_M \\ \dfrac{T_L - T}{T_L - T_M} & : T_M \leqslant T \leqslant T_L \\ 0 & : T_L \leqslant T \end{cases} \tag{9}$$

The coefficient α accounts for the empirical evidence found by Nakasaki et al. [3]. Thus, μ increases with the temperature following Arrhenius expression up to the optimum reaction temperature $T_M = 60\,^\circ\text{C}$, but decreases for any further temperature rise, as microbial activities are held back. Fujita [8] on the basis of the experiments using the mixtures consisting of dog foods, sludge, and sawdust, recommends the values as follows: $K_a = 0.04$, $w_a = 0.15$, $w_1 = 0.6$, $w_2 = 0.8$, $T_M = 60\,^\circ\text{C}$, $T_L = 80\,^\circ\text{C}$, $E_A = 29{,}000$ J/mol, $R_A = 8.314$ J/mol K.

The Contois constant k_c is related to the growth yield as $k_c Y = 4 \sim 20$. Here, we fix $k_c = 24$, $Y = 0.5$, and vary μ_b around a typical value 0.18/h (i.e., 5×10^{-5}/s), which depends on the degradability of the composting material.

In order to close the model, we introduce the water vaporization rate relationship proposed by Fujita [8], namely

$$\frac{dm_w}{dt} = -W_{\text{sat}}\dot{V}_{\text{air}}\frac{m_w}{m_s} \tag{10}$$

where the saturated vapor concentration is given by

$$W_{\text{sat}}(T) = 0.804\frac{\exp\left(11.96 - \dfrac{3994}{T+233.9}\right)}{1 - \exp\left(11.96 - \dfrac{3994}{T+233.9}\right)}\ [\text{kg/m}^3] \tag{11}$$

Normalization and Dimensionless Numbers

In order to normalize the water transport equation (10), microbial growth rate equation (7), and heat balance equation (4), we define dimensionless variables of the form

$$t^* \equiv \frac{\rho_{\text{air}} c_{\text{air}} \dot{V}_{\text{air}}}{m_{s0} c_{s0}} t \quad T^* \equiv \frac{T - T_a}{T_M - T_a}$$

$$m_w^* \equiv \frac{m_w}{m_{s0}} \quad m_{\text{sub}}^* \equiv \frac{m_{\text{sub}}}{m_{s0}} \quad m_x^* \equiv \frac{m_x}{m_{s0}} \tag{12}$$

and

$$m_s^* \equiv \frac{m_s}{m_{s0}} = 1 - (m_{w0}^* - m_w^*) - (m_{\text{sub}0}^* - m_{\text{sub}}^*)(1 - Y) \tag{13}$$

where the subscript "0" refers to as its initial value. The convection time scale $t_{\text{ref}} = m_{s0} c_{s0} / \rho_{\text{air}} c_{\text{air}} \dot{V}_{\text{air}}$ is used to normalize the time, while the difference between the optimum reaction temperature and ambient temperature is introduced to scale the system temperature. Using these dimensionless variables, the governing equations are normalized as follows

$$\frac{dm_w^*}{dt^*} = -F_w(T^*)\frac{m_w^*}{1 - (m_{w0}^* - m_w^*) - (m_{\text{sub}0}^* - m_{\text{sub}}^*)(1 - Y)} \tag{14}$$

$$\frac{dm_{\text{sub}}^*}{dt^*} = -DaF_{\text{sub}}(T^*, m_w^*)\frac{m_{\text{sub}}^*\left[m_{x0}^* + Y(m_{\text{sub}0}^* - m_{\text{sub}}^*)\right]}{m_{x0}^* + Y(m_{\text{sub}0}^* - m_{\text{sub}}^*) + (m_{\text{sub}}^*/k_c)} \tag{15}$$

$$\left(1-\frac{c_w}{c_{s0}}(m^*_{w0}-m^*_w)-\frac{c_{\rm sub}}{c_{s0}}(m^*_{\rm sub0}-m^*_{\rm sub})(1-Y)\right)\frac{dT^*}{dt^*}$$
$$=-(1+{\rm St})T^*-\left(\frac{H_w}{c_{s0}(T_M-T_a)}\right)F_w(T^*)\times\frac{m^*_w}{1-(m^*_{w0}-m^*_w)-(m^*_{\rm sub0}-m^*_{\rm sub})(1-Y)}+{\rm Da}\left(\frac{H_{\rm sub}}{c_{s0}(T_M-T_a)}\right)F_{\rm sub}(T^*,m^*_w)(1-Y)\times\frac{m^*_{\rm sub}[m^*_{x0}+Y(m^*_{\rm sub0}-m^*_{\rm sub})]}{m^*_{x0}+Y(m^*_{\rm sub0}-m^*_{\rm sub})+(m^*_{\rm sub}/k_c)} \quad (16)$$

where

$$F_w(T^*)\equiv\frac{c_{s0}W_{\rm sat}(T)}{\rho_{\rm air}c_{\rm air}} \quad (17a)$$

$$F_{\rm sub}(T^*,m^*_w)\equiv\left(\frac{\mu}{\mu_b}\right)\exp\left[\frac{E_A}{R_A}\left(\frac{1}{T_a+273}-\frac{1}{T_M+273}\right)\right] \quad (17b)$$

The foregoing normalization procedure reveals two important dimensionless parameters controlling the phenomena, namely, Stanton number St and Damkohler number Da, respectively, defined by

$${\rm St}\equiv\frac{hA}{\rho_{\rm air}c_{\rm air}\dot{V}_{\rm air}} \quad (18a)$$

$${\rm Da}\equiv\frac{c_{s0}m_{s0}}{\rho_{\rm air}c_{\rm air}\dot{V}_{\rm air}}\frac{\mu_b}{k_cY}\exp\left[-\frac{E_A}{R_A}\left(\frac{1}{T_a+273}-\frac{1}{T_M+273}\right)\right] \quad (18b)$$

The Stanton number accounts for the heat loss to the environment while the Damkohler number corresponding with the ratio of reaction rate to convection rate controls the biological heat generation within the matrix. Alternatively, the Damkohler number may be interpreted as the ratio of the convection time scale $t_{\rm ref}=m_{s0}c_{s0}/\rho_{\rm air}c_{\rm air}\dot{V}_{\rm air}$ to that of the microbial reaction. As we give St, Da, T_a (or $c_{s0}(T_M-T_a)/H_w$) and the initial values m^*_{w0}, $m^*_{\rm sub0}$, m^*_{x0}, and $T^*=0$, we may readily integrate the foregoing ordinary differential equations to determine $T^*(t^*)$, $m^*_w(t^*)$, and $m^*_{\rm sub}(t^*)$, and subsequently find $m^*_s(t^*)$ and $m^*_x(t^*)=m^*_{x0}+Y(m^*_{\rm sub0}-m^*_{\rm sub})$.

Results and Discussion

As a reference case, we consider a composting process within the same static pile as investigated by Fujita [8], in which the air continuously flows into the static pile from the bottom by forced ventilation and the exhaust gas escapes from the top exposed to the ambient air at the rate of $\dot{V}_{\rm air}=0.262$ m^3/s. The volume of the static pile is 235.5 m^3 and the initial total mass $m_{s0}=47{,}100$ kg such that the apparent density is 200 kg/m^3. Fujita [8] experimentally evaluated the heat transfer coefficients at the inner and outer walls in the range from 9 to 11 W/m^2 K. The overall thermal conductance through the concrete wall was estimated to be $hA=640$ W/K. The initial masses are given by $m_{w0}=28{,}260$ kg, $m_{\rm sub0}=14{,}130$ kg and $m_{x0}=471$ kg such that $m^*_{w0}=0.6$, $m^*_{\rm sub0}=0.3$, and $m^*_{x0}=0.01$. The physical properties used in computations are as follows: $\rho_{\rm air}=1.20$ kg/m^3, $c_{\rm air}=1400$ J/kg K, $c_w=4200$ J/kg K, $c_{\rm sub}=2100$ J/kg K, $H_w=2.44\times10^6$ J/kg, and $H_{\rm sub}=1.76\times10^7$ J/kg, such that $c_{s0}=m^*_{w0}c_w+(1-m^*_{w0})c_{\rm sub}=3360$ J/kg K, and $t_{\rm ref}=\rho_{\rm air}c_{\rm air}\dot{V}_{\rm air}/m_{s0}c_{s0}=100$ h (i.e., 3.6×10^5 s). For this reference case, we set $\mu_b=0.18$/h (i.e., 5×10^{-5}/s) and $T_a=20$°C, such that

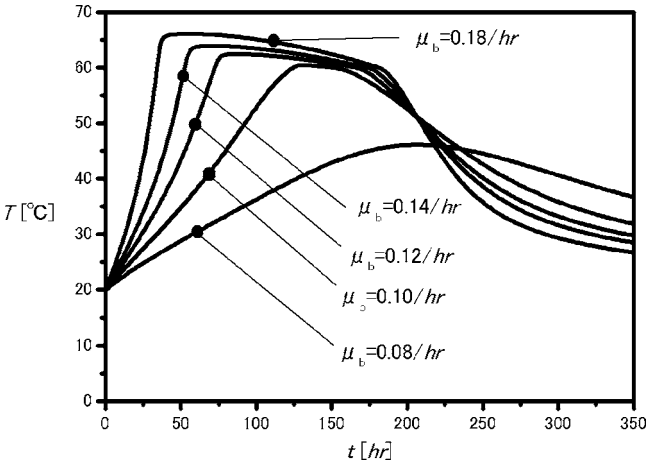

Fig. 2 Effects of μ_b on system temperature

$${\rm St}\equiv\frac{(hA/m_{s0})}{\rho_{\rm air}c_{\rm air}(\dot{V}_{\rm air}/m_{s0})}=1.48 \quad (19a)$$

and

$${\rm Da}\equiv\frac{c_{s0}}{\rho_{\rm air}c_{\rm air}(\dot{V}_{\rm air}/m_{s0})}\frac{\mu_B}{k_cY}\exp\left[-\frac{E_A}{R_A}\left(\frac{1}{T_a+273}-\frac{1}{T_M+273}\right)\right]=0.359 \quad (19b)$$

Effects of the Specific Growth Rate Coefficient μ_b and Ambient Temperature T_a (Da) on the Composting Process. Prior to a series of computations, the reference case described above was treated to check the present calculation procedure based on Runge-Kutta-Gill method (e.g., Nakayama [12]). The results obtained for the case of $\mu_b=0.18$/h are found in good accord with those reported by Fujita [8]. The difference in the system temperature between the two sets of the results remains within 3 °C. The specific growth rate coefficient μ_b may vary depending on the contents of the matrix. Fujita [8] carried out exhaustive measurements of μ_b using various mixtures consisting of dog foods, sludge, and sawdust, and found μ_b vary from 0.18/h to 0.08/h depending on the mixtures. The computational results obtained for various cases ranging from $\mu_b=0.18$/h to 0.08/h with the other values fixed are compared against the reference case in Figs. 2 and 3. As seen from Fig. 2, any decrease in μ_b results in lowering the

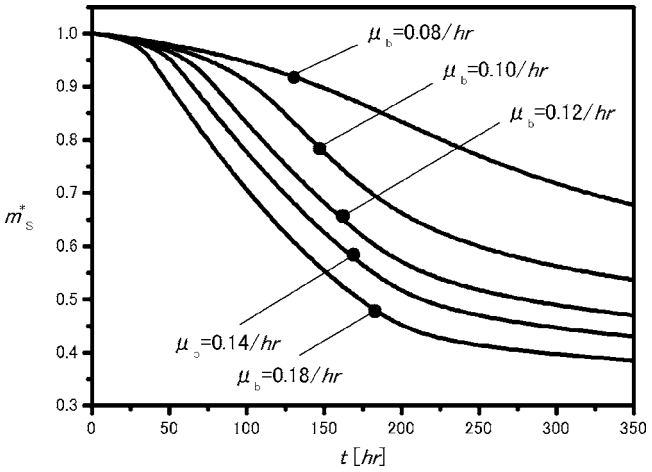

Fig. 3 Effects of μ_b on total mass

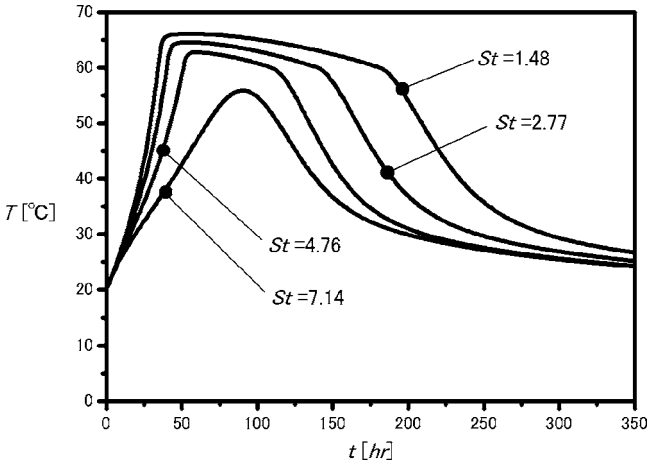

Fig. 4 Effects of heat loss per unit mass on system temperature

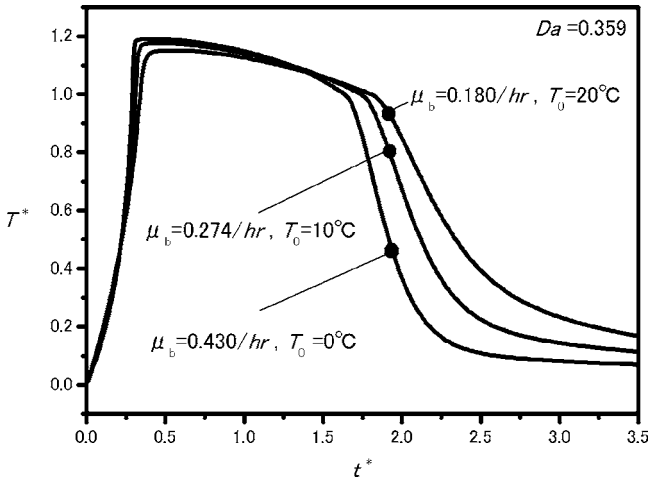

Fig. 6 Dimensionless presentation of system temperature

system temperature and a longer time to attain its peak temperature. Naturally, Fig. 3 shows that the total mass decreases more slowly for a smaller μ_b. Especially when μ_b as small as 0.08, the system temperature never exceeds the optimum reaction temperature of 60°C.

The effects of ambient temperature T_a on the system are similar to those of μ_b. We note from Eq. (19*b*) that any decrease in either μ_b or T_a results in lowering the value of Da. As will be shown later using the dimensionless presentation, it is the Damkohler number Da that virtually controls the time for the system to reach its peak temperature.

Effects of the Thermal Conductance (St) on the Composting Process. The size of the static pile directly reflects on the value of hA/m_{s0}, which naturally increases for a smaller size. Fujita [8] gives $hA/m_{s0}=0.0136$ W/kg K for $m_{s0}=47,100$ kg (i.e., the reference case) and $hA/m_{s0}=0.0445$ W/kg K for $m_{s0}=2.51$ kg. It is assumed that the air is supplied in such a fashion that the volume flow rate per unit mass of the matrix is held constant, say $\dot{V}_{\text{air}}/m_{s0}=5.56\times10^{-6}$ m^3/kg s (i.e., 0.02 m^3/kg h. This practice helps attain optimum microbial activities, without carrying much heat away from the system. Thus, for the same ambient conditions, a decrease in the size of the static pile results in an increase in St (see Eq. (19*a*)), while Da (see Eq. (19*b*)) stays constant. Computations were made for the cases ranging from $hA/m_{s0}=0.0136$ W/K kg to 0.0667 W/K kg (St=1.48 to 7.14) and the results are shown in Fig. 4. The figure clearly shows that heat loss shortens the plateau of high temperature period; and decelerates consumption of the mass in the system. It is essential to design the system such that St stays sufficiently small (say St<5) for the system temperature to exceed the optimum reaction temperature.

Dimensionless Presentation. In addition to the reference case, two distinctive cases; namely $(T_a,\mu_b)=(10°\text{C},0.247/\text{h})$ and $(0°C,0.43/\text{h})$, in which Da remains the same value Da=0.359 as the reference case $(T_a,\mu_b)=(20°\text{C},0.18/\text{h})$, are considered to investigate possible similarity in the results for fixed Da.

The temperature results for three cases are presented in dimensional and dimensionless forms in Figs. 5 and 6, respectively, while the temporal development of the total mass is plotted in Fig. 7 using a dimensionless form. Figure 6 clearly shows that all three normalized curves overlap one another in a considerably wide range, from the beginning of the temperature rise to the end of the temperature plateau. (After the plateau, the temperature drops faster for the lower ambient temperature.)

From both Figs. 6 and 7, we may conclude that, for a given Stanton number St, the Damkohler number Da virtually controls the system. Thus, it should be taken as one of the important parameters for designing the composting process with aeration.

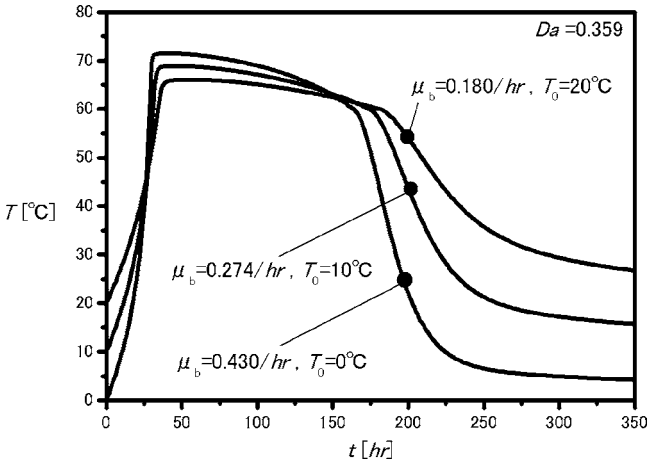

Fig. 5 Dimensional presentation of system temperature

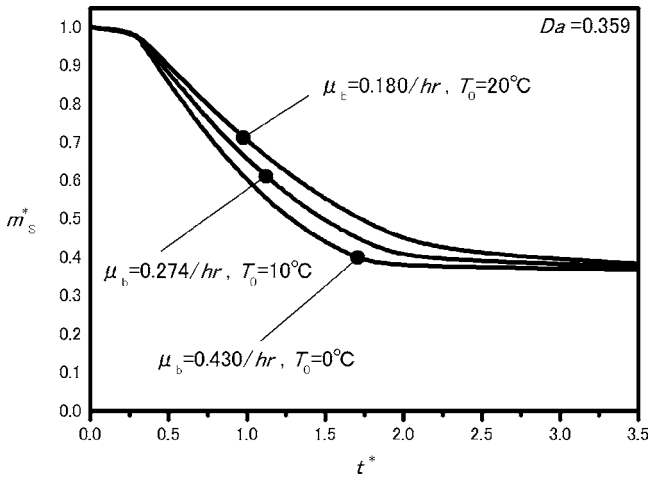

Fig. 7 Dimensionless presentation of total mass

Acknowledgment

The authors gratefully acknowledge the technical support provided by Mr. T. Nakashita, the president of Hoei Bussan Co., Japan.

Nomenclature

A = total surface area of the static pile (m^2)
c = heat capacity (J/kg k)
Da = Damkohler number
E_a = activation energy (J/mol)
h = overall heat transfer coefficient (W/m^2 K)
H_w = latent heat of water vaporization (J/kg)
H_{sub} = latent heat of metabolic reaction (J/kg)
k_c = Contios constant
k_{fe} = effective thermal conductivity of fluid (W/m K)
k_{se} = effective thermal conductivity of solid (W/m K)
m = mass (kg)
u = Darcian velocity (m/s)
R_A = universal gas constant (J/mol k)
$\langle S \rangle^s$ = volume average concentration of substrate (kg/m^3)
St = Stanton number
t = time (s)
T = system temperature (K)
T_a = ambient tempearture (K)
T_M = optimum reaction temperature (K)
$\langle U \rangle^s$ = volume average concentration of uncompostable (kg/m^3)
$\dot{V}_{air}$ = volume flow rate of air (m^3/s)
$\langle W \rangle^s$ = volume average concentration of water (kg/m^3)
$w_{a,1,2}$ = constants associated with the maximum specific growth rate
$\langle X \rangle^s$ = volume average concentration of microbes (kg/m^3)
Y = growth yield
α = function associated with the maximum specific growth rate
ε = volume fraction occupied by the gas phase
ρ = density (kg/m^3)
μ = maximum specific growth rate (s^{-1})
μ_B = coefficient associated with the maximum specific growth rate (s^{-1})

Subscripts and Superscripts

air = air
f = gas
s = matrix
sub = substrate
u = uncompostable
w = water
x = microbes
0 = initial

Special Symbol

$\langle \rangle^{f,s}$ = intrinsic average

References

[1] Haug, R. T., 1993, *The Practical Handbook of Compost Engineering*, Lewis Publishers, Boca Raton, FL.
[2] Li, C. H., and Jenkins, D. R., 2003, "Modeling and Numerical Simulation of Composting Process," CSIRO Mathematical and Information Sciences, Technical Report CMIS 03/26.
[3] Nakasaki, K., Kato, J., Akiyama, T., and Kubota, H., 1987, "A New Composting Model and Assessment of Optimum Operation for Effective Drying of Composting Material," J. Ferment. Technol., **65**(4), pp. 441–447.
[4] Nakasaki, K., Shoda, M., and Kubota, H., 1985, "Effect of Temperature on Composting of Sewage Sludge," Appl. Environ. Microbiol., pp. 1526–1530.
[5] Kaiser, J., 1996, "Modeling Composting as a Microbial Ecosystem: A Simulation Approach," Ecol. Modell., **91**, pp. 25–37.
[6] Das, K., and Keener, H. M., 1997, "Numerical Model for Dynamic Simulation of a Large Scale Composting System," Trans. ASAE, **40**(4), pp. 1179–1189.
[7] Li, C. H., and Glowinski, R., 1996, "Modeling and Numerical Simulation of Low-Mach-Number Compressible Flows," Int. J. Numer. Methods Fluids, **23**, pp. 77–103.
[8] Fujita, K., 1998, *Composting Technology*, Gihodo Publishers, Tokyo (in Japanese).
[9] Nakayama, A., Nakasaki, K., Kuwahara, F., and Fukazawa, T., 2006, "A Simulation Model Based on Porous Media for a Composting System," Proc. 43rd National Heat Transfer Conf., Vol. 3, pp. 741–742.
[10] Nakayama, A., Kuwahara, F., Sugiyama, M., and Xu, G., 2001, "A Two-Energy Equation Model for Conduction and Convection in Porous Media," Int. J. Heat Mass Transfer, **44**, pp. 4375–4379.
[11] Contois, D. E., 1959, "Kinetics of Bacterial Growth: Relationship Between Population Density and Specific Growth Rate of Continuous Culture," J. Gen. Microbiol., **21**, pp. 40–50.
[12] Nakayama, A., 1995, *PC-Aided Numerical Heat Transfer and Convective Flow*, CRC Press, Boca Raton, FL.

Decrease in Thermal Contact Conductance and the Contact Pressure of Finned-Tube Heat Exchangers Assembled With Different Size Bullets

Chakravarti Madhusudana

Wui-wai Cheng

School of Mechanical and Manufacturing Engineering,
The University of New South Wales,
NSW, 2052, Australia

The thermal contact conductance (TCC) at the mechanically bonded tube/fin interface of a heat exchanger may be controlled by varying the amount of initial expansion of the tube. However, in this case, the TCC also varies with the temperature because of the differential expansion between the tube and the fin. The objectives of the present study are to determine the improvement in TCC resulting from higher degrees of the tube expansion, to determine the variation in TCC with the maximum temperature, and to estimate the change in contact pressure with the temperature. This paper presents the results of heat transfer experiments on mechanically expanded finned-tube specimens. Experiments were conducted in an atmosphere of nitrogen. The results showed that the TCC is enhanced by increasing the degree of initial expansion. There is a practical limit, however, to the maximum expansion that can be attempted. For the direction of heat flow prevailing in the experiments, the TCC and the contact pressure of every specimen decreased with increasing temperature.
[DOI: 10.1115/1.2712859]

Keywords: thermal contact conductance, fin-tube heat exchanger, thermal contact resistance, bullet size, interstitial gas

Introduction

Compact heat exchangers are most commonly made with aluminum plate-fins and copper tubes. The interfaces between the tubes and fins are generally formed by mechanical expansion of the tubes into the fin collars. Due to the imperfect nature of the contact at the interface, an additional thermal resistance called thermal contact resistance (TCR) will exist [1]. The resistance manifests itself as an additional temperature drop at the interface (Fig. 1), so that the TCR may be defined as the ratio of the temperature drop (ΔT) to the heat flux (Q'') across the interface

$$R_c = \Delta T/Q'' \tag{1}$$

In Eq. (1), the resistance is defined on a unit area basis. Some authors, therefore, refer to it as *specific* thermal resistance.

The thermal contact conductance (TCC) is the reciprocal of TCR

$$h_c = Q''/\Delta T \tag{2}$$

Note that the heat transfer across the interface is partially through conduction at the solid-to-solid contact spots and partially through the gas gap. Because of the microscopic nature of the gas gaps, convection currents cannot exist in them. Furthermore, heat transfer by radiation is insignificant at temperatures below 300°C. Thus, the heat transfer across the gas gap is also by (molecular) conduction, so that we can write

$$h_c = h_s + h_g \tag{3}$$

in which h_s is the solid spot conductance and h_g is the gas gap conductance.

Because of the importance of TCR in many applications, a large number of theoretical and experimental studies in contact heat transfer have been carried out in the past five decades. Madhusudana [2] has described the details of recent research work in contact heat transfer. An overwhelming majority of previous work deals with flat contacts. The investigation into the contact heat transfer of fin-tube exchangers, however, would fall into the area of cylindrical joints. The following is a brief review of relevant work in this area.

Dart [3] identified the contact resistance between the fin and the tube to be an important parameter in the characterization of heat exchanger performance. In their detailed analytical and experimental study of interference-fitted finned tubes, Gardner and Carnavos [4] noted that, as the operating temperature increased, the fins expanded away from the tube wall due to their larger expansion coefficient. As the temperature was increased further, the contact pressure between the fin and tube wall would become zero and a gas gap would be introduced. Eckels [5] investigated the TCC of mechanically expanded plate finned-tube heat exchangers. He found the most significant sources of error to be the temperature and the mass flow rate measurements along with the assumed value of the fin resistance.

In their studies of TCR/TCC in heat exchangers, Sheffield et al. [6] reported that the TCR is typically up to 15% of the overall thermal resistance of heat exchanger. Nho and Yovanovich [7] found that the TCR, as a fraction of the overall resistance in a vacuum environment, ranged from 17.6% to 31.5%. These two findings indicate that the TCR is a significant factor in finned-tube heat exchangers. In other words, TCR could noticeably reduce the efficiency of the heat exchanger.

Recently, Critoph et al. [8] tested coils with collared aluminum fins and copper tubes, as well as aluminum tubes. Comparing brazed fins to mechanically bonded fins, they concluded that the contact resistance in mechanically bonded fins accounted for 12.5% of the resistance due to air-side convective heat transfer on the fin. They also examined the fin-tube interface under the microscope, and reported that a gap of 0.01 mm would increase the overall resistance by 10%. ElSherbini et al. [9] investigated the thermal contact resistance in plain fin-tube evaporators with collarless fins under dry and frost conditions. Two geometrically identical full aluminum fin-tube coils were examined. One of them had fins brazed to the tubes and the other one was made by pneumatic expansion of collapsed aluminum tubes in the fin stack. From the results obtained under dry conditions, they concluded that the contact resistance was very high, due to the small contact area caused by the absence of fin collars. The value of air-side resistance of brazed coil was 50% smaller than the unbrazed coil under dry conditions. In their tests under frost conditions, they noted that the thin layer of frost filled the gaps between the fins and tubes, and caused the high contact resistance to disappear. Kim et al. [10] investigated the thermal contact conductance of a set of fin-tube (aluminum fins and copper tubes) heat exchangers in vacuum. They concluded that the thermal contact conductance increases when the diameter of expansion ball increases, when the fin spacing decreases, and when the fin is of plate type rather than of slit type. Jeong et al. [11] also reported a similar result for the fin-tube heat exchangers. In both of the references, since the temperature of the hot stream and, consequently the heat input, were kept constant, the effect of temperature and the heat input on conductance could not be determined.

The above review of previous work on tube/fin heat exchangers thus indicates that:

Contributed by the Heat Transfer Division of ASME for publication in the JOURNAL OF HEAT TRANSFER. Manuscript received July 27, 2006; final manuscript received December 20, 2006. Review conducted by Yogesh Jaluria.

 Copyright © 2007 by ASME

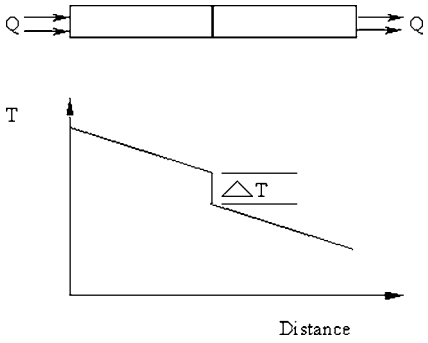

Fig. 1 Interfacial temperature drop due to thermal contact resistance

- TCR at the tube/fin interface is significant if they are mechanically bonded, in other words, the TCC is not infinite.
- All of the previous workers used an indirect method to estimate the TCR; that is, they estimated it by subtracting the sum of all other resistances (measured or estimated from correlations) from the overall resistance.
- Most investigators assumed the TCC to be constant. In particular, the change in contact resistance caused by temperature related differential expansion is often neglected.

These conclusions had also been previously noted by Madhusudana et al. [12].

The TCC may be increased either by increasing the contact pressure or by introducing soft conducting material into gaps in the interface. The first of these approaches will be investigated in this work. Increasing the apparent contact pressure will increase the actual contact area and consequently increase the TCC. The contact pressure at the time of assembly depends on the size of the expansion bullet used. During the operation of the heat exchanger, however, the heat input causes changes in temperature and temperature gradients, resulting in changes in the differential expansion between the tube and fin. This change in differential expansion also causes a change in the contact pressure and hence the TCC. The present study aims to investigate the effect of the size of the expansion bullet on the TCC of fin-tube heat exchangers. Another objective of the present study is to determine the variation of the conductance and contact pressure with temperature. The proposed experimental method allows direct measurement of TCC.

Analysis

If the total contact conductance h_c is known or measured, then from Eq. (3), the solid spot conductance can be determined as

$$h_s = h_c - h_g \tag{4}$$

In Eq. (4) gas gap conductance h_g could be estimated from the following equation [13]

$$h_g = \frac{k_g}{\delta_{\text{eff}}} \tag{5}$$

where

$$\delta_{\text{eff}} \approx 2.7\sigma \tag{6}$$

There are several theoretical expressions available for predicting the solid spot conductance (see, e.g., Mikic [14]). However, these are applicable to idealized isotropic, randomly rough surfaces whose asperties are undergoing perfectly plastic deformation.

The following equation, similar in form to that of Mikic, was empirically derived by Tien [15]

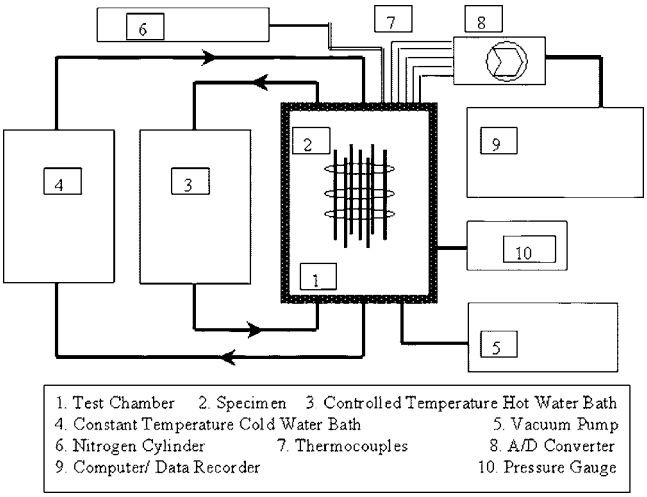

Fig. 2 Schematic diagram of the experimental apparatus

$$h_s = 0.55 \tan\theta \left(\frac{k_e}{\sigma}\right)\left(\frac{P}{H_v}\right)^{0.85} \tag{7}$$

Since Tien's correlation is based on experimental results of several investigators, and not based on idealized situations, Eq. (7) will be used in this paper to estimate the contact pressure.

Experimental Details

It is evident from Eqs. (5) and (7) that the factors affecting the TCC are the surface properties, microhardness of the materials, interface temperatures, heat flow across the interface, contact pressure, and the interstitial medium. The surface properties and the microhardness were directly measured in a Federal Surfanalyzer 5000 and a Carl-Zeiss Jena Vickers microhardness tester, respectively. Interface temperatures and heat flow across the interface are obtained simultaneously in the test apparatus for TCC measurement. The interstitial medium could be controlled by filling the enclosed chamber by a known gas.

In a cylindrical joint, it is difficult to measure contact pressure directly. As indicated in the previous section, it is estimated from the TCC measurements.

A test apparatus was specially made to determine the TCC for specimens with single fin and seven tubes. This apparatus uses the direct method in which TCC is calculated directly by measuring the temperature drop across the interface. As shown in Fig. 2, the experiment apparatus consists of test chamber, vacuum pump, pressure gauge, thermocouples, A/D converter, data recorder, a pair of water circulating reservoirs, and a specimen. The design details of the test apparatus were described in a previous paper [16].

Test Specimen

The geometry of the specimen is based on the heat exchanger model Heatcraft 3000 Series. The specimen consisted of a single fin and seven tubes, as shown in Fig. 4. The central tube provided the heating, whereas the six outer ones accomplished the cooling.

In this experimental investigation, three different specimens were examined. Each specimen is constructed with a corrugated aluminium fin of 0.12 mm thickness. The copper tubes are 100 mm long with a 9.52 mm outer diameter by 0.31 mm wall thickness. Three different size bullets have been used for expansion purposes. Their sizes are 9.42, 9.52, and 9.62 mm. Note that the 9.42 mm bullet is the one normally used in the industry for this tube size. Figure 3 also shows a typical bullet for mechanical expansion. The relevant material properties are given in Table 1.

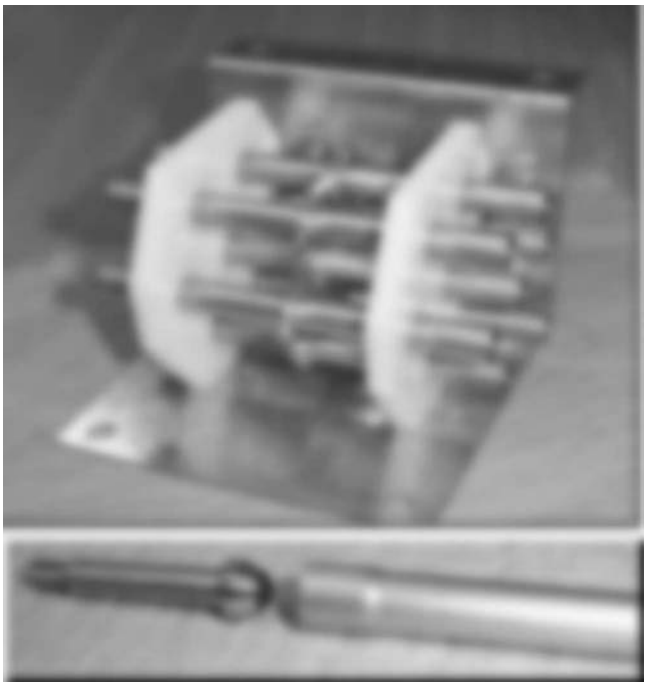

Fig. 3 Top: Specimen (single fin and seven tubes). Bottom: Mechanical expansion bullet and tube.

Thermocouple Locations and Calculations

Type-T thermocouples were used to measure the temperatures at particular positions on the test specimen. They were calibrated by comparing them with the standard reference instrument, namely, FLUKE – 2180A RTD Digital Thermometer from 5°C to 95°C with 5°C increments.

Figure 4 shows the location of the thermocouples. The outputs from thermocouples 1 and 2 were used for estimating the mean outer tube wall temperature at the contact interface of the fin collar and the center tube

$$T_H = \frac{T_1 + T_2}{2} \tag{8}$$

Thermocouples 13 and 14 were installed inside the hot water stream at the far ends of the inlet and outlet respectively. The thermocouples were immersed at the centre position of the hot tube to measure the inlet and outlet temperatures for estimating the total heat input ($\dot{Q}_{\text{in}}$) to the system.

$$\dot{Q}_{\text{in}} = \dot{m} C_p (T_{13} - T_{14}) \tag{9}$$

Thermocouples 3 and 4 were fixed at the outer surface of centre of the fin collar. The average value would be used to estimate the temperature of the outer surface of the center of the fin collar. Thermocouple numbers 5, 6, 7, 8, 15, and 16 perform similar functions on the cold tube/fin. Thermocouples 9 and 10 were fixed

Table 1 Relevant properties of tube and fin materials

Material	Copper (bare tube)	Aluminum (fin)
Surface roughness (rms), σ (μm)	0.338	0.275
Absolute slope of surface profile, tan θ	0.046	0.021
Microhardness, H_v (MPa)	571	287
Thermal conductivity ($W\,m^{-1}\,K^{-1}$)	401	237
Coefficient of linear expansion, $\alpha \times 10^{-6}$ (K^{-1})	16.5	23.1

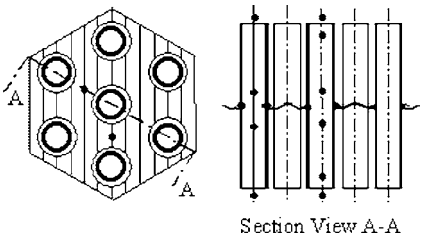

Fig. 4 Location of thermocouples on the specimen

midway from the center tube to the surrounding tube on the fin. The temperatures from these were used only to confirm that the distribution of heat transfer was uniform from the central to the outer tubes. They were not used in the calculations.

The thermal contact conductance was determined by the following equation

$$h_c = \frac{\dot{Q}_{\text{in}}}{A_c (T_H - T_{\text{collar}})} \tag{10}$$

Experimental Conditions and Uncertainties

Every specimen was tested in a nitrogen atmosphere. Nitrogen was used to represent a normal atmospheric condition while avoiding the effect of variable moisture content present in normal atmospheric air and any possible oxidation. Note that the thermal conductivity of nitrogen is similar to that of air. It varies from 0.0272 to 0.0305 W/(m K) over the range of the maximum temperature, 45°C to 85°C, obtained in the tests [17].

A water circulating cooler controls the water temperature of the cooling stream. Cold water flows through the six surrounding tubes in the specimen at a constant temperature of 5°C. The hot stream flows through the center tube in the specimen and the temperature range for the testing was from 45°C to 85°C.

All of the readings must satisfy the steady-state condition to be accepted as valid records. The assumption of the steady-state condition is defined and executed by a computation program. The program compares the difference between the present temperature reading (T_n) and the previous 900 temperature readings (T_{n-1}), with a maximum deviation of 0.2°C ($\Delta T_{\max}$). Since the sampling rate of every thermocouple is set at 1 second per sample, 900 sets of samples are processed in 15 min (900 s).

Uncertainties

The uncertainties in TCC measurement (Eq. (10)), are due to the uncertainties in the heat flux measurement and in the temperature drop. Allowance must also be made to any heat loss from the specimen to the surroundings.

The average uncertainty of the thermocouples was 0.1°C after calibration with the standard reference instrument. Since the heat flow is radial and the axial temperature difference is small, the heat loss by convection is likely to be small. It would still be desirable to perform an energy balance by looking at the heat delivered to the cold tubes. It was, however, not possible to measure the heat reaching the cold tubes separately because of the very small temperature differences obtaining in the cold tubes (the heat input from the single hot tube is divided into six cold tubes). It is, however, possible to calculate the heat loss due to convection between the hot and the cold tubes. Estimates of heat loss from the specimen to the surroundings in the nitrogen atmosphere indicated that the average value of the heat loss by convection for the whole range was 2.9% of the total heat flow.

An uncertainty analysis was performed applying the law of propagation of uncertainties [18], taking all of the above factors into account. The individual uncertainties as well as the overall uncertainty in the thermal contact conductance measurement are

Table 2 Average uncertainties in thermal contact conductance measurements

Size of expansion bullet (mm)	Uncertainty in ΔT	Uncertainty in Q	Uncertainty due to heat loss	Uncertainty in TCC
9.42	±0.62%	±6.16%	±2.90%	±6.84%
9.52	±1.14%	±9.17%	±2.90%	±9.68%
9.62	±1.03%	±4.32%	±2.90%	±5.30%

listed in Table 2 for each of the three specimens. It is clear that most of the uncertainty is in the heat flow measurement and not in the measurement of interface temperature drop or due to heat loss.

Results and Discussion

The solid spot conductance was determined by subtracting the gap conductance from the measured total conductance, as indicated in Eq. (4). It was observed that while the range of the total conductance, for all specimens, was from 228 to 619 kW/(m^2 K), the range for the gap conductance was from 23.2 to 25.9 kW/(m^2 K). In other words, the heat transferred across the gas gap is about 10% or less of the total heat flow across the interface. This is to be expected since both copper and aluminum are very good conductors of heat compared to nitrogen.

The variation of the solid spot conductance with temperature, for all of the specimens, is shown plotted in Fig. 5. It is at once noted that:

- The size of the expansion bullet has a significant influence on the TCC: the larger the expansion, the higher is the TCC.
- The TCC decreases as the temperature increases. This indicates that the expansion of the aluminum fin is larger than that of the copper tube and this differential expansion gradually relaxes the interface pressure obtained at the time of assembly by the mechanical expansion of the tube into the fin.

From the thermal conductance data as presented above, the corresponding variation in contact pressure may be computed using Eq. (7). The estimated contact pressures are plotted against temperature in Fig. 6. Also shown in this figure are the initial contact pressures obtained by extrapolation to 20°C. As the temperature was increased, the contact pressure decreased from 1.74 to 1.44 MPa, from 2.93 MPa to 2.45 MPa, and from 5.58 MPa to 5.05 MPa for the 9.42, 9.52, and 9.62 mm bullets, respectively.

There were some problems encountered in the manufacturing process using the 9.62 mm bullet. These include the difficulty in holding the tube during the expansion process and occurrence of

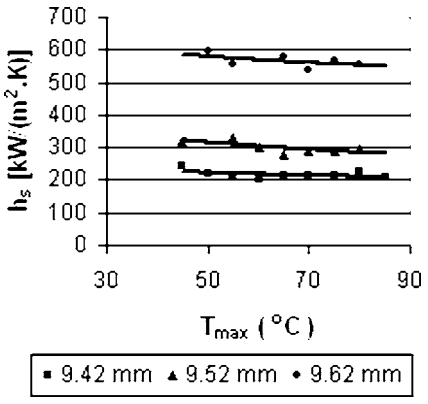

Fig. 5 Variation of solid spot conductance with maximum temperature

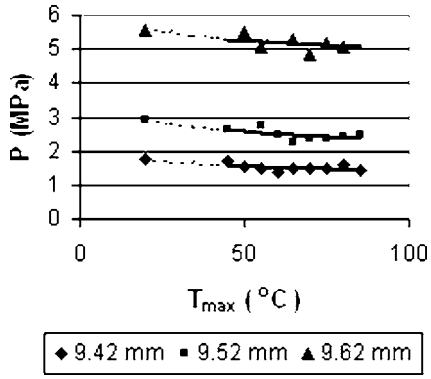

Fig. 6 Variation of contact pressure showing the estimated initial pressure

fractures on the tube wall surface. For this reason, this high degree of expansion is not recommended, although there is considerable enhancement in the contact conductance using this expansion.

Conclusions and Recommendations

The thermal contact conductance at the fin-collar tube-wall interface of a plate finned-tube heat exchanger, in a nitrogen environment, was experimentally investigated. Three specimens for the tests were made with the same materials (all copper tubes and aluminum fins) and geometry. The three specimens were characterized by bullets of different diameter (9.42, 9.52, and 9.62 mm) used for their expansion.

The results show that:

- The thermal contact conductance may be definitely enhanced by subjecting the copper tube to higher degrees of expansion; that is, by using expansion bullets of larger diameter. Difficulties in fabrication and material strength considerations, however, put a limit to the maximum expansion that can be achieved in practice.
- For the tube/fin combinations tested, the contact pressure is relaxed and the contact conductance decreased as the temperature is increased. The present test situation corresponds to what happens in the condenser of an air-conditioner. The heat flow direction is reversed in an evaporator and the contact pressure is likely to be reinforced in such a case.
- In the present series of tests, the gas gap conductance was about 10% of the total conductance.
- Further work should focus on extending the range of maximum temperature, and the generation of correlations incorporating recent data for thermal contact conductance.

Acknowledgment

This work was conducted under the Australian Research Council Linkage Grant No. LP0226446. The authors are grateful to Joe Chabo and Girmay Worres of Heatcraft Australia Pty Limited for their support and permission to publish this paper.

Nomenclature

A_c = the area of the apparent contact surface (m^2)
C_p = specific heat of pure water 4180 (J kg^{-1} K^{-1})
h = thermal conductance (kW m^{-2} K^{-1})
H_v = microhardness of the softer material (MPa)
k_e = harmonic mean of the solid thermal conductivities, $2k_1k_2/(k_1+k_2)$ (W m^{-1} K^{-1})
k = thermal conductivity (W m^{-1} K^{-1})
$\dot{m}$ = mass flow rate of the working fluid (kg s^{-1})
P = pressure (MPa)
$\dot{Q}_{in}$ = heat input to the system (W)

Q'' = heat flux (W/m^2)
R = thermal resistance ($m^2\,K\,W^{-1}$)
$\tan\theta$ = effective mean absolute slope of surface profile $\sqrt{(\tan^2\theta_{inner}+\tan^2\theta_{outer})}$
T = temperature (K)

Greek Symbols

δ_{eff} = effective distance across the interface (m)
σ = effective rms surface roughness $\sqrt{(\sigma_{inner}^2+\sigma_{outer}^2)}$ (m)

Subscripts

c = contact
H = hot fluid stream
g = air gap
max = maximum
s = solid spot

References

[1] Madhusudana, C. V., 1996, "Thermal Contact Conductance," *Mechanical Engineering Series*, Springer-Verlag, New York.
[2] Madhusudana, C. V., 2002, "Recent Research in Contact Heat Transfer, 16th National Heat and Mass Transfer Conference & 5th ISHMT / ASME Heat and Mass Transfer Conference, India.
[3] Dart, D. M., 1959, "Effect of Fin Bond on Heat Transfer," ASHRAE J., **1**, pp. 67–71.
[4] Gardner, K. A., and Carnavos, T. C., 1960, "Thermal Contact Resistance in Finned Tubing. Transactions of ASME," ASME Trans. J. Heat Transfer, **82**, pp. 279–293.
[5] Eckels, P. W., 1977, "Contact Conductance of Mechanically Expanded Plate Finned Tube Heat Exchangers," ASME Paper, August, pp. 15–17.
[6] Sheffield, J. W., Sauer, H. J., and Wood, R. A., 1987, "An Experimental Method for Measuring the Thermal Contact Resistance of Plate Finned Tube Heat Exchangers," ASHRAE J., **93**, pp. 776–785.
[7] Nho, K. M., and Yovanovich, M. M., 1989, "Measurement of Contact Resistance in Finned Tube Heat Exchangers," ASHRAE J. **95**(1), pp. 370–378.
[8] Critoph, R. E., Holland, M. K., and Turner, L., 1996, "Contact Resistance in Air-Cooled Plate Fin-Tube Air-conditioning Condensers," Int. J. Refrig., **9**, pp. 400–406.
[9] ElSherbini, A. I., Jacobi, A. M., and Hrnjak, P. S., 2003, "Experimental investigation of Thermal Contact Resistance in Plain-Fin and Tube Evaporators With Collarless Fins," Int. J. Refrig., **26**, pp. 527–536.
[10] Kim, C. N., Jeong, J., and Youn, B., 2003, "Evaluation of Thermal Contact Conductance Using a New Experimental-Numerical Method in Fin-Tube Heat Exchangers," Int. J. Refrig., **26**, pp. 900–908.
[11] Jeong, J., Kim, C. N., Youn, B., and Kim, Y. S., 2004, "A Study on the Correlation Between the Thermal Contact Conductance and Effective Factors in Fin-Tube Heat Exchangers With 9.52 mm Tube," Int. J. Heat Fluid Flow, **25**, pp. 1006–1014.
[12] Madhusudana, C. V., Fletcher, L. S., and Peterson, G. P., 1990, "Thermal Conductance of Cylindrical Joints—A Critical Review," J. Thermophys. Heat Transfer, **4**, pp. 204–211.
[13] Wahid, S. M. S., and Madhusudana, C. V., 2000, "Gap Conductance in Contact Heat Transfer," Int. J. Heat Mass Transfer, **43**, pp. 4483–4487.
[14] Mikic, B. B., 1974, "Thermal Contact Conductance: Theoretical Considerations," Int. J. Heat Mass Transfer, **17**, pp. 205–214.
[15] Tien, C. L., 1968, "A Correlation for Thermal Contact Conductance of Nominally Flat Surfaces in Vacuum," *Proceedings of the 7th Conference on Thermal Conductivity*, U.S. National Bureau of Standards, Gaithersburg, pp. 311–320.
[16] Cheng, W. W., and Madhusudana, C. V., 2004, "Design and Fabrication of a Test Apparatus for Measuring Thermal Contact Conductance in a Finned-Tube Heat Exchanger," *17th National Heat and Mass Transfer Conference & 6th ISHMT/ASME Heat and Mass Transfer Conference*, India.
[17] Cengel, Y. A., 1998, *Heat Transfer a Practical Approach*, WCB/McGraw-Hill, New York, p. 963.
[18] Holman, J. P., 1971, *Experimental Methods for Engineers*, 2nd ed., McGraw-Hill, New York, pp. 37–44.

Ablation and Aero-thermodynamic Studies on Thermal Protection Systems of Sharp-Nosed Re-entry Vehicles

S. Rameche Candane
Research Scholar

C. Balaji
Associate Professor

S. P. Venkateshan[1]
Professor
e-mail: spv@iitm.ac.in

Department of Mechanical Engineering,
Heat Transfer and Thermal Power Laboratory,
Indian Institute of Technology Madras,
Chennai 600036, India

A quasi-one-dimensional ablation analysis for a sharp-nosed, reusable, re-entry vehicle that could possibly be used in an unmanned space program, has been carried out by using an in-house code. The code is based on the boundary immobilization technique and the solution has been obtained using the tri-diagonal matrix algorithm (TDMA). The heat fluxes on the spherical nose cap that are used to determine the ablation rate of a thermal coating applied over the surface of the vehicle are obtained by performing a steady state aero-thermodynamic analysis. The aero-thermodynamic analysis for the viscous, compressible flow under consideration is carried out by using FLUENT 6.2. The computational fluid dynamics (CFD) simulations are performed at three locations on the trajectory that the vehicle follows, on re-entry. These simulations yield the temperature and heat flux distributions along the surface of the vehicle and the latter are given as input to the ablation code. The shell material of the vehicle is assumed to be zirconium boride (ZrB_2). *The code is validated with benchmark cases and the flow and heat transfer characteristics are also discussed. In brief, the present work presents a methodology for coupling an ablation code with CFD simulations from a commercial code, to study the effect of change of the nose region on the ablation process.*
[DOI: 10.1115/1.2717250]

Keywords: ablation, tri diagonal matrix algorithm (TDMA), ultra high temperature ceramics (UHTC), quasi-one dimensional model, boundary immobilization technique

1 Introduction

Since the advent of the modern computers, simulations have been extensively used in the prediction of aero-thermodynamic environments around re-entry vehicles and high-speed missile systems. The literature that is available on the aero-thermodynamic analysis of re-entry vehicles is vast. A brief review of the literature reveals that many studies on aero-thermodynamic analysis have been carried out with specially developed computational fluid dynamic (CFD) codes [1–9]. After the recent tragedy of Columbia, the thermal protection system of the vehicles is being given very important consideration as safety happens to be a prime factor of concern in manned orbital vehicles. The present study deals with an interfacing of the widely used CFD code FLUENT 6.2 with a quasi-one-dimensional ablation code developed using Fortran 90. The heat fluxes obtained from FLUENT for a steady-state analysis of the vehicle nose is given as an input for determining the thickness of the ablated material.

The surface of a vehicle is subjected to very high heat fluxes, consequent upon which the surface may melt. In order to prevent this, an expendable ablative surface/ shield is usually provided over the surface of the vehicle. This prevents the vehicle surface from taking high heat fluxes. The objective of the present work is to develop an ablation code that can effectively track the ablation front and can be coupled to the CFD results obtained from commercial software. The one-dimensional ablation problem is solved by using a Landau transformation [10] together with the finite volume approach of Blackwell and Hogan [11], to determine the thickness of the material ablated. The methodology explained can be effectively applied to the calculation of the recession rates at various locations of the re-entry vehicle, regardless of its shape (either flat or cylindrical or spherical), thereby facilitating a complete determination of the thermal protection system (TPS) for the vehicle.

2 Modeling

In order to make the analysis realistic and relevant, the geometry considered for the investigation is the nose cone of the unmanned space vehicle (USV), which is very similar to the one being developed by CIRA (Italian Aerospace Research Center). The schematic representation of the nose cone is shown in Fig. 1. From the reentry trajectory of Savino et al. [12], three points are selected for carrying out an aero-thermodynamic analysis using CFD. The operating conditions to be investigated are shown in Table 1. The free stream temperature and pressure are assumed to be invariant with altitude, as the assumption of steady state is made at all the three points on the trajectory.

The stagnation pressure and temperature are obtained using isentropic relations given by

$$\frac{T_{\text{stag}}}{T_\infty} = 1 + \frac{\gamma - 1}{2} M^2 \tag{1}$$

$$\frac{P_{\text{stag}}}{P_\infty} = \left(1 + \frac{\gamma - 1}{2} M^2\right)^{\gamma/\gamma - 1} \tag{2}$$

The numerical investigation has been carried out for ultra-high ceramic material (UHTC) zirconium boride (ZrB_2) and also by considering a layer of ablative material called Avcoat. The thermophysical properties of zirconium boride and Avcoat are taken from Ref. [13]

2.1 Computational Domain. The mesh is created using GAMBIT [14] and since the geometry is not complex, a structured mesh is used. The use of a structured mesh reduces the computational time considerably. The size of the mesh near the wall has to be fine enough to resolve the viscous sublayer and the successive ratio of the mesh had to be selected accordingly. The optimum number of cells required for performing the investigation is arrived at by performing a grid independence study with 75,000 cells and 140,000 cells. The dependent variables do not show any notable variation for these two cases. The number of cells generated here are 140,000, i.e., almost twice the number of cells considered in Ref. [12]. The very first cell near the wall is located at a distance of 10^{-08} m from the wall, which is sufficiently fine to capture the steep variations in the gradients near the wall even if the flow is turbulent. The wall y^+ value is less than 5 throughout the region near the surface.

[1]Corresponding author.

Contributed by the Heat Transfer Division of ASME for publication in the JOURNAL OF HEAT TRANSFER. Manuscript received April 21, 2006; final manuscript received December 17, 2006. Review conducted by Minking Chyu.

 Copyright © 2007 by ASME

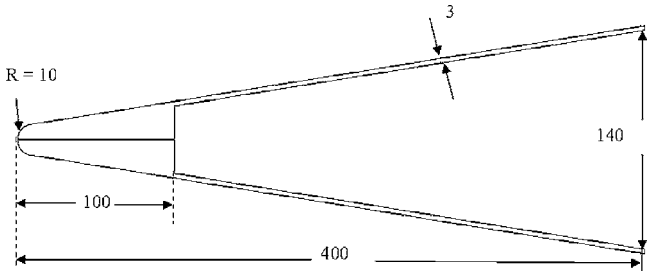

Fig. 1 Schematic of the internal structure of the USV nose cap, dimensions in millimeters

2.2 Numerical Modeling. The governing equations for continuity, momentum and energy solved by FLUENT [15] are given below

$$\frac{\partial \rho}{\partial t} + \frac{\partial}{\partial x_i}(\rho u_i) = 0 \tag{3}$$

$$\frac{\partial}{\partial t}(\rho u_i) + \frac{\partial}{\partial x_j}(\rho u_i u_j) = -\frac{\partial P}{\partial x_i} + \frac{\partial}{\partial x_j}\left[\mu\left(\frac{\partial u_i}{\partial x_j} + \frac{\partial u_j}{\partial x_i} - \frac{2}{3}\delta_{ij}\frac{\partial u_i}{\partial x_i}\right)\right] + \frac{\partial}{\partial x_j}(-X) \tag{4}$$

The energy equation is given by

$$\frac{\partial}{\partial t}(\rho E) + \nabla \cdot [u_i(\rho E + P)] = \nabla \cdot \left[\lambda \nabla T - \sum_j h_j J_j + (\bar{\tau} \cdot u_i)\right] + S \tag{5}$$

where sensible enthalpy h is defined for ideal gases as

$$h = \sum_{j'} m_{j'} h_{j'}$$

The solver is a coupled implicit solver with second-order unsteady formulation. The convergence criterion set for mass and momentum residuals is 10^{-3}, and for energy the residuals are 10^{-6}. The upwinding scheme is of second order.

2.3 Quasi-One-Dimensional Ablation. Following Blackwell and Hogan [11] the solution of one-dimensional ablation is obtained by solving the equations given below. The Landau transformation [10] for the present case is mathematically given as

$$\eta = \frac{L - z}{L - s}; \quad z = \eta s + (1 - \eta)L = L - \eta(L - s) \tag{6}$$

At $z=s$, $\eta=1$; at $z=L$, $\eta=0$. For axi-symmetric geometries, the z and r coordinate systems are related through

$$r = R_o - z; \quad z = R_o - r \tag{7}$$

The η and r coordinates are then related through

$$\eta = \frac{r - R_o + L}{L - s}; \quad r = R_o - L + \eta(L - s) \tag{8}$$

The one-dimensional governing equation for energy for an arbitrary geometry is

$$\rho C \frac{\partial T}{\partial t} = \frac{1}{r^m}\frac{\partial}{\partial r}\left(\lambda r^m \frac{\partial T}{\partial r}\right) \quad \begin{matrix} m = 0, \text{ planar} \\ m = 1, \text{ cylindrical} \\ m = 2, \text{ spherical} \end{matrix} \tag{9}$$

Using the chain rule and Eq. (8), the conduction equation can be transformed to

$$\rho C\left(\frac{\partial T}{\partial t} + \frac{\eta \dot{s}}{L - s}\frac{\partial T}{\partial \eta}\right) = \left\{\frac{1}{[R_o - L + \eta(L - s)]^m}\frac{1}{(L - s)^2}\frac{\partial}{\partial \eta} \times \{\lambda[R_o - L + \eta(L - s)]^m \frac{\partial T}{\partial \eta}\right\} \tag{10}$$

Equation (10) has a convection-like term that is not present in Eq. (9); this additional term is physically due to grid motion. The velocity of any line of η=constant is $\eta\dot{s}$, and it is the coefficient of the spatial derivative on the left side of Eq. (10). This can be seen by differentiating Eq. (8) with respect to time while holding η constant, resulting in the velocity V_b of any η=constant line

$$V_b(\eta, t) = \left(\frac{\partial z}{\partial t}\right)_\eta = \eta \dot{s}; \quad V_b(1,t) = \dot{s}; \quad V_b(0,t) = 0 \tag{11}$$

The outer surface of the ablator ($\eta=1$) moves with a velocity (surface recession rate) $\dot{s}$. The back surface of the ablator at ($\eta=0$) moves with a velocity of zero, and intermediate points have a velocity of $\eta\dot{s}$. The transformed partial differential equation is solved by using a finite difference technique. The solution of the finite difference form can be obtained by using the tridiagonal matrix algorithm (TDMA).

2.4 Coupling FLUENT Results With Ablation Code. The surface heat fluxes obtained through the FLUENT [15] code will not be accurate once the temperature of the surface exceeds the melting temperature of the material. In such cases the heat transfer coefficient determined from the FLUENT code is used for calculating the heat fluxes using expression (12)

$$Q = h_{\text{coeff}}(T_{\text{aw}} - T_w) \tag{12}$$

For a calorically perfect gas, the adiabatic wall temperature is given by

$$r = \frac{T_{\text{aw}} - T_\infty}{T_{\text{stag}} - T_\infty}$$

Hence

$$T_{\text{aw}} = r(T_{\text{stag}} - T_\infty) + T_\infty \tag{13}$$

where $r = \sqrt{\text{Pr}}$ for hypersonic laminar flows.

The heat fluxes thus obtained are given as an input to the ablation code for determining the ablated material thickness. In the present study, the ablation study on the material Avcoat is done using this procedure.

Table 1 Three points selected at the reentry trajectory

S. No	Time (s)	Altitude (km)	Velocity (m/s)	Temperature (K)	Pressure (Pa)	Mach number
1	328	45	2350	264.2	149.1	7.22
2	343	30	2400	226.5	1197.0	7.96
3[a]	352	20	2250	216.6	5529.3	7.63

[a]Peak heat flux condition.

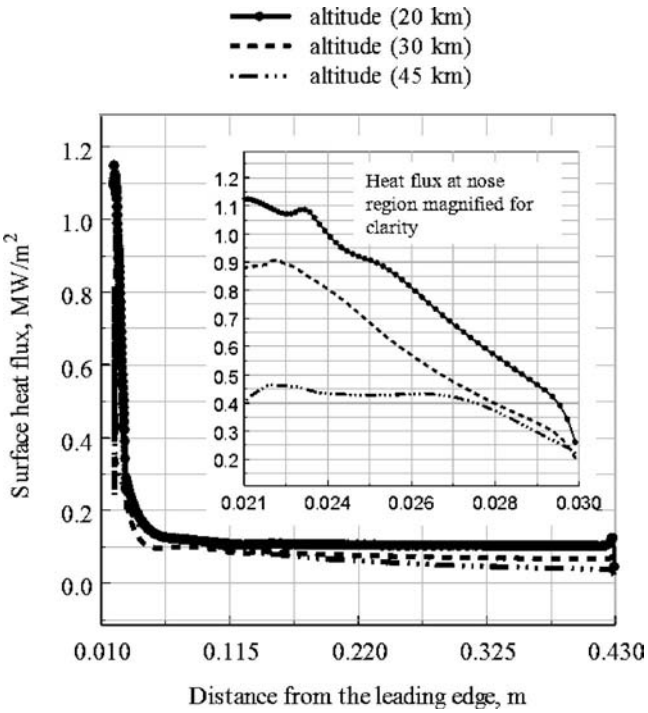

Fig. 2 Heat flux variation along the surface of the nose cap (for reentry conditions)

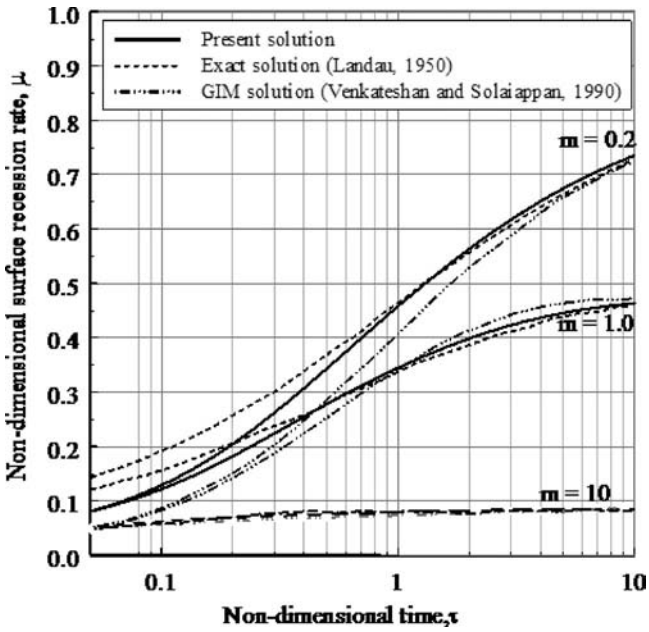

Fig. 3 Nondimensional surface recession rate history for planar ablation for different values of nondimensional latent heat of ablation

3 Results and Discussion

As a means of validating the FLUENT code, a benchmark case provided by Roy et al. [1] was considered and the comparison was found to be encouraging with the difference between the two predictions being within ±5%. For the nose cone of the USV considered for the present investigation, the simulations are carried out for three operating conditions (refer to Table 1). The Knudsen number for all three cases is much less than 0.001 and hence is in the continuum regime. Though the heat fluxes are obtained over the entire surface of the vehicle, the heat flux over the spherical nose cap is much higher than the other regions. Hence, the heat fluxes on the nose cap for the three re-entry conditions alone are shown in Fig. 2. It is seen that the peak heat flux takes a value of 1.1 MW/m^2 at an altitude of 20 km and this is used for performing the ablation analysis.

To validate the ablation code, the results of Landau [10] are considered. There are no analytical solutions for spherical geometries, hence, the code developed is validated for a planar geometry. A 5-mm-thick slab is considered with an adiabatic back boundary. The material considered for investigation on ablation has the following thermo-physical properties (values used by Landau [10]). It is assumed that an incident heat flux of 2 MW/m^2 is applied at $t=0$ and the re-radiation from the ablating surface is ignored. Figure 3 shows the variation of nondimensional surface recession rate μ with the nondimensional time τ for different values of nondimensional latent heat of ablation. It is found that the present code compares well with the works of Landau [10] and Venkateshan and Solaiappan [16]. From Fig. 4, it is seen that though the general integral method and present finite difference method agree well with the exact solution of Landau [10] at higher values of the nondimensional time, they are not able to reproduce the result at lower time levels. This is because of the steep variation in the nondimensional surface recession rate at very low values of nondimensional time. The rate of change is rather too large that even a very fine mesh is not able to capture the variation at very low time levels. This has been very rightly pointed out by Landau [10] himself. The numerical results obtained from the ablation code have also been compared with the experimental results of Tran et al. [17]. A comparison of the results is shown in Table. 2. The maximum error for the cases considered is within ±8%.

The heat fluxes obtained from FLUENT for the re-entry cases cannot as such be given as inputs for the ablation code, as the surface heat flux calculated by FLUENT is determined by assuming the material to be stable even after the material melting temperature is reached. This, however, is not practically true. Hence,

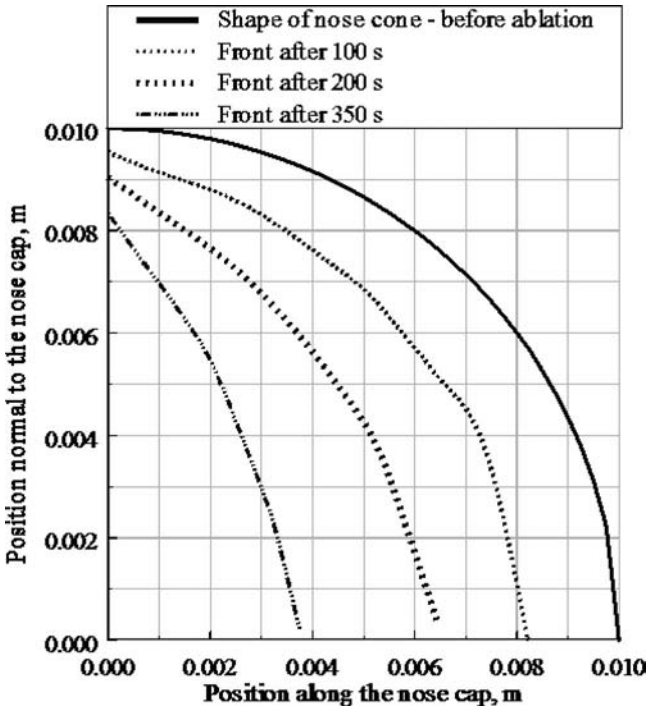

Fig. 4 Shape change predicted for nose cone

Table 2 Comparison of numerical results with experimental results of Tran et al.[a] (arc jet testing data)

Experimental models	Density (kg/m^3)	Heat flux (MW/m^2)	Test time (s)	Latent heat (MJ/kg)	Recession (mm)	Calculated recession (mm)
Avcoat	512.60	33.61	10	82.67	7.93	7.68
PICA-1	350.47	29.64	10	366.76	2.21	2.21
PICA-2	360.69	9.65	22	201.57	2.72	2.91
PICA-3	371.32	8.57	25	191.33	2.79	2.99

[a]See Ref. [17].

in the present investigation, the surface heat fluxes are calculated by making use of the heat transfer coefficient from FLUENT and these are again recalculated by assuming the surface temperature to be the same as the phase change temperature. The surface heat fluxes thus obtained are given as input to the code developed and the surface recession rate and time at which ablation starts are determined. The optimum number of nodes for the ablation code for the present case is found to be 96.

The effect of the shape change leads to a reduction in the heat flux predicted along the surface of the nose and hence, neglecting the effect of shape change is still advantageous from the point of safety but may lead to a relatively thicker thermal protection system. The shape change predicted for the spherical nose cap after 100 s, 200 s, and 350 s is shown in Fig. 4. The heat flux acting at the stagnation point is very high compared to the heat flux on the other nodes and hence the material removal at the stagnation region is more when compared to ablation in other regions, as expected. The shape change predicted for the nose cone including the effect of shape change on the predicted heat flux is shown in Fig. 5. As it is not possible to account for the shape change after every time step, the effect of shape change is accounted for at times of 100 s, 200 s, and 350 s. The shape change due to ablation leads to a notable change in the heat flux predicted along the surface of the nose. To account for this change in shape, the geometry is created again after time steps of 100 s, 200 s, and 350 s and analyzed using FLUENT. The surface heat transfer coefficient thus determined using FLUENT is made use of for calculating the actual heat flux that the nose cone may encounter. The profile of the nose after 350 s considering the effect of shape change in Fig. 5 shows that if the effect of shape change is considered the nose could last for a longer duration of flight. A design of the TPS could hence be improved upon by performing a similar analysis.

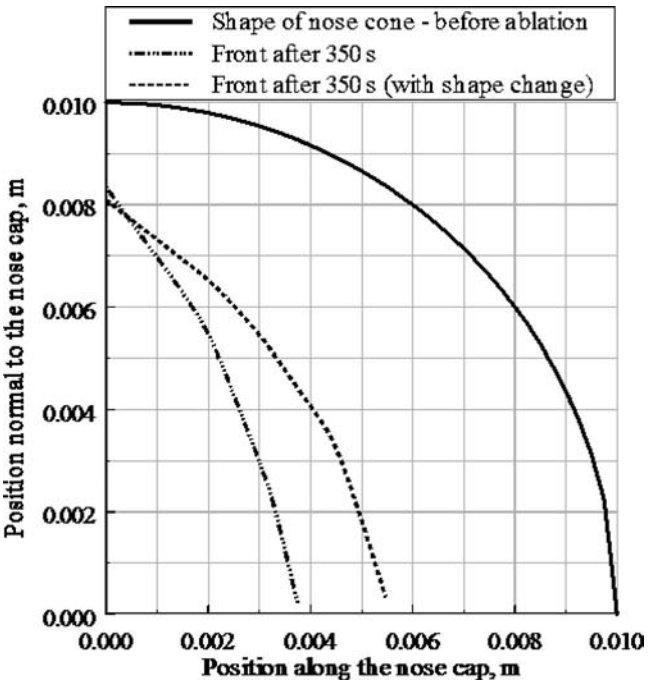

Fig. 5 Shape change predicted for nose cone including the effect of shape change on the predicted heat flux

4 Conclusions

The aero-dynamic performance of re-entry vehicles and ballistic missiles could be improved by providing sharp leading edges. The use of reusable re-entry vehicles in the days to come is mainly dependent on the thermal protection system that is provided on the surface of the vehicle. The ultra-high-temperature ceramic (Zirconium di boride) is capable of withstanding a maximum temperature of 3000 K and hence it could serve as an effective substitute for current thermal protection systems (based on the aerodynamic heating loads the vehicle is supposed to take). The present work has given a methodology to perform a complete aero-thermodynamic and ablation analysis for a sharp nosed reusable reentry vehicle. The computations are carried out using a SGI origin compute server and computational time taken for the simulations using FLUENT ranges from 12 h to 24 h. A coarse grid at the solid domain may yield results, which would be totally offset from actual values. The quasi-one-dimensional ablation code is seen to work well for the spherical nose cap and the coupling of the FLUENT results with the ablation code seems to yield good results. Hence, the prediction of aerodynamic heating and the recession rate of material could be effectively simulated using the methodology discussed in this study.

The present work is confined to ablation analysis considering the heat fluxes that are determined using FLUENT for the peak heat flux condition. It could be applied progressively to account for the shape change due to ablation along the complete trajectory. The shape change due to ablation will also change the surface heat flux. To account for this the heat flux has to be determined by changing the geometry based on the ablated material thickness and then performing the CFD investigation. The method could be computationally expensive if carried out for a mild change of shape, hence it is advisable to modify the geometry after a notable change in the shape and then perform the CFD analysis.

Nomenclature

a = ablation
alt = altitude, km
C = specific heat (J/kg K)
E = internal energy (J/kg)
h = enthalpy (J/kg)
h_{coeff} = heat transfer coefficient (W/m^2 K)
J = diffusion flux (kg/m^2 s)
L = thickness of slab (m)
Ma = Mach number
$m_{j'}$ = mass fraction
P = pressure (Pa)
Q = heat flux (W/m^2)
R = radius of cylinder/sphere (m)

r = radial coordinate (m)
s = surface recession (m)
$\dot{s}$ = surface recession rate ds/dt(m/s)
S = source term
T = temperature (K)
t = time (s)
u = x velocity component (m/s)
u_τ = frictional velocity $\sqrt{\tau_w/\rho}$(m/s)
v = y velocity component (m/s)
V_b = velocity (m/s) of recession (m/s)
y = distance from any wall (m)
y^+ = dimensional coordinate yu_τ/v
z = coordinate attached to original surface location (m)

Greek Symbols

α = thermal diffusivity (m^2/s)
δ_{ij} = Kronecker delta
γ = ratio of specific heats
$\eta = L - z/L$
$-s$; η = Landau coordinate
λ = thermal conductivity (W/m K)
μ = dynamic viscosity (kg/m s) or nondimensional recession rate $\rho L\dot{s}/Q$
ν = kinematic viscosity (m^2/s)
ρ = density (kg/m^3)
τ = nondimensional time $\tau = (t - t_a)/t_a$
$\ddot{\tau}$ = shear stress (N/m^2)
τ_w = wall shear stress (N/m^2)
Γ = effective diffusivity (m^2/s)

Subscripts

aw = adiabatic wall
b = boundary
coeff = coefficient
i = x component
i,j = component in plane x,y
j = y component
o = outer radius
stag = Stagnation condition
t = turbulent
w = wall
∞ = free stream condition

Acronyms

CFD = computational fluid dynamics
UHTC = ultrahigh-temperature ceramics

References

[1] Roy, C. J., Payne, M. A., and Oberkampf, W. L., 2003, "Verification and Validation for Laminar Hypersonic Flowfields, Part 1: Verification," AIAA J., **41**, pp. 1934–1943.
[2] Riley, C. J., Kleb, W. L., and Alter, S. J., 1999, "Aeroheating Predictions for X-34 using an Inviscid Boundary Layer Method," J. Spacecr. Rockets, **36**, pp. 206–215.
[3] Berry, S. A., Horvath, T. J., Difulvio, M., Glass, C., and Merski, N. R., 1999, "X-34 Experimental Aeroheating at Mach 6 and 10," J. Spacecr. Rockets, **36**, pp. 171–178.
[4] Henline, W. D., and Tauber, M. E., 1994, "Trajectory Based Heating Analysis for the European Space Agency / Rosetta Earth Return Vehicle," J. Spacecr. Rockets, **31**, pp. 421–428.
[5] Wurster, K. E., Riley, C. J., and Zoby, E. V., 1999, "Engineering Aerothermal Analysis for X-34 Thermal Protection System," J. Spacecr. Rockets, **36**, pp. 216–228.
[6] Joysula, E., 1999, "Computational Simulation Improvements of Supersonic High Angle of Attack Missile Flows," J. Spacecr. Rockets, **36**, pp. 59–66.
[7] Wurster, K. E., and Stone, H. W., 1993, "Aerodynamic Heating Environment Definition/Thermal Protection System Selection for the HL-20," J. Spacecr. Rockets, **30**, pp. 549–557.
[8] Murray, A. L., and Russell, G. W., 2002, "Coupled Aeroheating/Ablation Analysis for Missile Configurations," J. Spacecr. Rockets, **39**, pp. 501–508.
[9] Gong, L., and Richards, W. L., 1998, "Thermal Analysis of a Metallic Wing Glove for a Mach-8 Boundary Layer Experiment," *Proceedings at 7th AIAA/ASME Joint Thermophysics and Heat Transfer Conference*, AIAA-98-2580, Albuquerque, New Mexico, June 15–18.
[10] Landau, H. G., 1950, "Heat Conduction in a Melting Solid," Q. Appl. Math., **8**, pp. 81–94.
[11] Blackwell, B. F., and Hogan, R. E., 1994, "One Dimensional Ablation using Landau Transformation and Finite Control Volume Procedure," J. Thermophys. Heat Transfer, **8**, pp. 282–286.
[12] Savino, R., Fumo, M. D. S., Paterna, D., and Serpico, M., 2005, "Aerothermodynamic Study of UHTC Based Thermal Protection Systems," Aerosp. Sci. Technol., **9**, pp. 151–160.
[13] TPSX WEB V2, "Thermal Protection Systems Expert and Material Properties Database-Unrestricted," NASA Ames Research Center ⟨http://tpsx.arc.nasa.gov/cgi-bin/tpsx/unrestrict/V2/tpsx-frame.pl⟩
[14] *Gambit Users Guide*, 2005, Fluent Inc., Pune, India.
[15] *Fluent Users Guide*, 2005, Fluent Inc., Pune, India.
[16] Venkateshan, S. P., and Solaiappan, O., 1990, "A General Integral Method for One Dimensional Ablation," Waerme- Stoffuebertrag., **25**, pp. 141–144.
[17] Tran, H. K., Johnson, C., Rasky, D., Hui, F., Hsu, M.-T., Chen, T., Chen, Y. K., Paragas, D., and Kobayashi, L., 1997, "Phenolic Impregnated Carbon Ablators (PICA) as Thermal Protection System for Discovery Missions," NASA TM-110440, NASA, Washington, D.C.

Performance and Optimization of Flat Plate Fins of Different Geometry on a Round Tube: A Comparative Investigation

B. Kundu
Department of Mechanical Engineering,
Jadavpur University,
Kolkata 700 032, India
e-mail: bkundu123@rediffmail.com

Owing to a uniform thickness, the fin material of a flat plate fin near to the tip does not participate optimally in transferring heat. On account of this, two new fin geometries of flat plate fins are proposed for improving the heat transfer rate per unit volume. These projected fin geometries, namely flat plate fin circumscribing a circular tube by providing quarter circular cut at the corners of the tip (FQCT) and flat plate fin circumscribing a circular tube having circular arc to cut at the tip (FCAT) are suggested. The thermal performance of the said geometric fins has been determined by a semianalytical method. By using a rigorous semianalytical technique, optimization have been demonstrated in a generalized scheme either by maximizing the rate of heat duty for a given fin volume or by minimizing the fin volume for a given heat transfer duty. The optimization study has also been made with the additional length constraints imposed on one or both sides of the fluid carrying tube. Finally, it can be demonstrated from the optimization study that two proposed fins, namely FQCT and FCAT, can dissipate more rate of heat than the FCT with an identical fin volume and thermophysical parameters. It can also be highlighted that the optimum FQCT and FCAT can transfer heat at a higher rate in comparison with the annular disk fin when a space constraint exists. [DOI: 10.1115/1.2717255]

Keywords: annular disc fins, fin performance, flat plate fins, optimization, semianalytical method

1 Introduction

The rate of heat transfer between a gas and liquid stream is restricted because of the low heat transfer coefficient in the gas side. Owing to the thermophysical properties of the gases, the gas side resistance amount to 85% or more of the total thermal resistance. External fins are often attached to the primary surface to reduce this thermal resistance as a result size of heat exchanger reduces. However, the selection of any particular type of fins depends on the geometry of the primary surfaces. The radial or concentric annular disc fins are one of the most common choices for enhancing the rate of outside heat transfer from a circular tube. It is well known fact that the rate of heat conduction in the fin diminishes gradually along the length. This has given rise to a host of research activities for determination of an optimum fin shape.

Schmidt [1] was the first researcher to forward a systematic approach for the optimum design of fins. By a heuristic argument, he proposed that, for an optimum fin, temperature should be a linear function along the fin length. Proceeding from the linear temperature distribution along the fin length, Schmidt found that the profile of optimum straight fins is a concave parabolic shape. Duffin [2] forwarded a rigorous proof on the optimality criteria of Schmidt hypothesis [1] through the calculus of variation. However, both Schmidt [1] and Duffin [2] made a simplistic assumption to consider the negligible profile curvature while calculating a fin surface area. This assumption is known as length of arc idealization (LAI) in the literature of fins. Guceri and Maday [3] eliminated LAI and used calculus of variation to find out a profile of minimum volume circular fins for a given heat transfer duty. The optimum profile has been numerically determined through a Hamiltonian formulation. It is interesting to note that with the improvement suggested by Guceri and Maday [3], an optimum fin has neither a linear temperature profile nor possesses a concave parabolic shape. The resulting fin geometry needs a large surface area to dissipate a required amount of heat for a minimum volume. The optimum profile reported in Ref. [3] is reasonably close to Schmidt's concave parabolic profile [1] for a large initial fin length, but closer to the end contains some wavy irregularities. The volume of the fin found in Ref. [3] was only slight smaller than the volume of the Schmidt's fin with the same height. An important numerical finding in Ref. [3] is that with the lifted LAI assumption, the temperature distribution in the optimum fin is a linear in nature. Recently, Kundu and Das [4] have calculated the profile of different types of optimum thin fins, namely, longitudinal, annular, and spine subject to internal heat generation. They have described a technique for the optimization based on the variational principle. With the consideration of no heat generation, they have also found that the optimum fin profile for all the examined fins is a parabolic in nature.

All the above fin optimization problems [1–4] involve determining the shape (or profile) of a fin so that for a given rate of heat dissipation the volume of the material used is a minimum. The solution to this group of problem gives the fin shape with a curved surface. Such optimum shapes are relatively difficult to manufacture and are hence more expensive. Therefore, on the other hand, select was a suitable simple fin shape is a priory as well as, finding the dimensions that lead to the maximum heat transfer rate for a given fin volume. Equivalently, a given fin shape and a desired heat dissipation rate determine the dimensions so that the volume of the material used is a minimum. Again, it is a familiar that due to decrease in heat conduction with the fin length, a fin with varying cross section, such as circular, parabolic, triangular or trapezoidal, performs better than a rectangular fin as far as heat transfer rate per unit weight of the material is concerned. However, a fin with varying cross section is too complex to manufacture, and fragile at the sharp end. To avoid these difficulties, in most of the heat exchanger applications, an annular fin of constant thickness is extensively found.

The analysis of annular disk fins is available in a number of references [5–7]. The optimization of such fins has been conducted by Brown [8]. He indicated that for an optimum design condition of annular disk fins, an increase both in length and in thickness results in an increase in heat transfer duty. However, if there is a space constraint on one side of a tube or there is an angular variation of a tube temperature, annular disk fins cannot be used optimally to dissipate the maximum amount of heat for a given fin volume. If there is a space constraint on one or both sides of the tube, the fin volume increases with the fin thickness only for the annular disk fin. In this situation, it does not guarantee optional use of the fin material. Instead, a saving in fin material can be achieved if flat plate fins are employed.

El-Saden [9] presented an analysis of two-dimensional heat conduction in an eccentrically hollow, infinite long cylinder with internal heat generation. He had given a closed form solution for the estimation of temperature distribution in the fin with the help of the bipolar coordinate transformation. For dehumidification of air on the fin surface, Kazeminejad et al. [10] adopted a numerical

Contributed by the Heat Transfer Division of ASME for publication in the JOURNAL OF HEAT TRANSFER. Manuscript received February 15, 2006; final manuscript received January 13, 2007. Review conducted by Anthony M. Jacobi.

 Copyright © 2007 by ASME

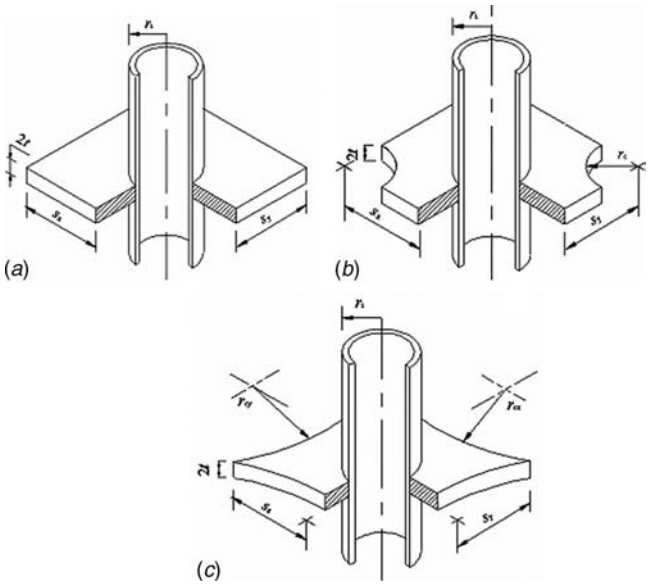

Fig. 1 Schematic diagrams of different flat fins: (*a*) FCT; (*b*) FQCT; and (*c*) FCAT

technique to determine the performance of eccentric annular fins. They have obtained the temperature profile in the fin using a finite difference scheme. For a variable base temperature, Kundu and Das [11] addressed a numerical technique for the performance analysis of an eccentric annular fin. Using a bipolar coordinate for the proper imposition of the boundary conditions, heat conduction equation in the fin has been solved by a finite difference method to evaluate the temperature profile. They have demonstrated that a saving in fin material may be achieved using an optimum eccentric annular fin instead of a concentric one if there exits a variable base temperature.

On the other hand, a flat fin on a round tube (Fig. 1) is the most popular fin pattern in heat exchanger applications owing to its simplicity, rigidity, and economical impact. The flat fins are generally made of a high conductive material. The profile of such fins is conventionally a rectangular shape. For slight thickness and high thermal conductivity, the temperature distribution in the thickness of the fin is negligibly small but the temperature variation along the fin length and the temperature in the peripheral direction of the tube cannot be neglected. Therefore, two-dimensional temperature field exists in every application of flat plate fins.

Sparrow and Lin [12] demonstrated a new technique to determine the thermal performance of plate fins in a fin-and-tube heat exchanger for both rectangular and equilateral triangular arrays of tubes. Their solution has satisfied the isothermal boundary condition at the tube surface. The adiabatic condition at the outer periphery of a symmetric sector of the fin has been satisfied approximately. The approximate method referred to as "The sector method" has been described by Shah [13] for predicting the efficiency of plate fins. The efficiency of various polygonal fins circumscribing tubes of different regular geometries has been numerically determined by Kuan et al. [14]. For the combined tubes and fin geometry, they also estimated the efficiency analytically replacing the actual fin by an equivalent annular fin of the same surface area.

It is a fact that the fin material of constant cross-sectional fins is not used economically near the fin tip. Actually, this unused material increases with the increase in length and it becomes maximum at the tip. In the case of an individual flat plate fin of rectangular or square shape circumscribing a circular tube, the distance of the corner at the tip from the tube center is a maximum. Therefore, for better performance of flat plate fins, fin material may be removed from the corners near the fin tip (Fig. 1(*b*)). Another new geometry of flat plate fin with circular arcs to cut near the tip has been proposed in the present work (Fig. 1(*c*)). These two modifications of flat plate fins are not only conducive to material saving but it can also be manufactured easily.

In the present work, the above two new geometric fins (Figs. 1(*b*) and 1(*c*)) have been proposed. The thermal performance and optimum design analysis of this type of fins and the conventional flat-plate fin have been investigated by a semianalytical technique. The temperature distribution in the fin is also determined. The fin efficiency and the fin effectiveness are estimated for a wide range of thermo-physical parameters. The optimum fin dimensions are calculated through a comprehensive semi-analytical method for different constraints and thermo-physical properties of a fin. A comparison has been made among the performance of the proposed flat plate fins with the conventional flat plate fin (FCT) and the annular disk fin (ADF). From the results, it can be shown that the proposed flat fins dissipate heat at a higher rate per unit fin volume than the conventional flat fins irrespective of its any design constraint applied. For the imposition of a length constraint on the optimization problem, a FCT may transfer more rate of heat than that of an ADF for an identical fin volume.

2 Theoretical Development

The geometry of a FCT described by thickness $2t$, length 2_{sx}, width 2_{sy}, and outer radius of a tube r_i is illustrated schematically in Fig. 1(*a*). A proposed new geometry of the flat plate fin of uniform thickness with quarter circular cut at the corners of the tip (FQCT) of radius r_c and flat fin of uniform thickness with circular arcs to cut near the tip (FCAT) of radii r_{cx} and r_{cy} are shown in Figs. 1(*b*) and 1(*c*), respectively. For the thermal analysis of all the above fin geometries, thermal conductivity of the fin material, convective heat transfer coefficient, temperature of the surrounding fluid, and temperature at the fin base are assumed to be constants. It is also assumed that the heat transfer from the fin to the surrounding are solely due to convection and there is no heat source in the fin.

2.1 Fin Performance. As the fin is symmetrical with respect to the planes *x-x* and *y-y*, one-fourth of the fin geometry can be taken for the thermal analysis. This smallest heat transfer module of a fin with the geometrical details is narrated in Figs. 2(*a*) and 2(*b*) for FQCT and FCAT fins, respectively. Selecting a cylindrical polar coordinate at the tube center and based on the aforementioned assumptions, the temperature distribution in all circumferential fins under steady-state condition is governed by the following differential equation expressed in nondimensional form as

$$\frac{\partial}{\partial R}\left(R\frac{\partial\theta}{\partial R}\right)+\frac{1}{R}\frac{\partial^2\theta}{\partial\phi^2}=Z_0^2R\theta \tag{1}$$

where

$$\mathrm{Bi}=hr_i/k,\quad T=t/r_i,\quad R=r/r_i,\quad \theta=(T_f-T_a)/(T_b-T_a),$$

$$\text{and } Z_0=\sqrt{\mathrm{Bi}/T} \tag{2}$$

For the thermal analysis, a recurring section *ABCDEFA* for the FQCT and *ABCDEA* for the FCAT are taken as shown in Figs. 2(*a*) and 2(*b*), respectively. The net heat conduction across the planes *x-x* and *y-y* in their transverse directions is zero because of the geometrical symmetry. At the fin tip surface, one may assume either negligible heat loss or heat transfer due to conduction in a direction normal to the tip surface equated with the convective heat loss from the tip. Thus the boundary conditions can be expressed mathematically as follows

$$\theta=1\quad \text{at } R=1\quad (0\leqslant\phi\leqslant\pi/2) \tag{3a}$$

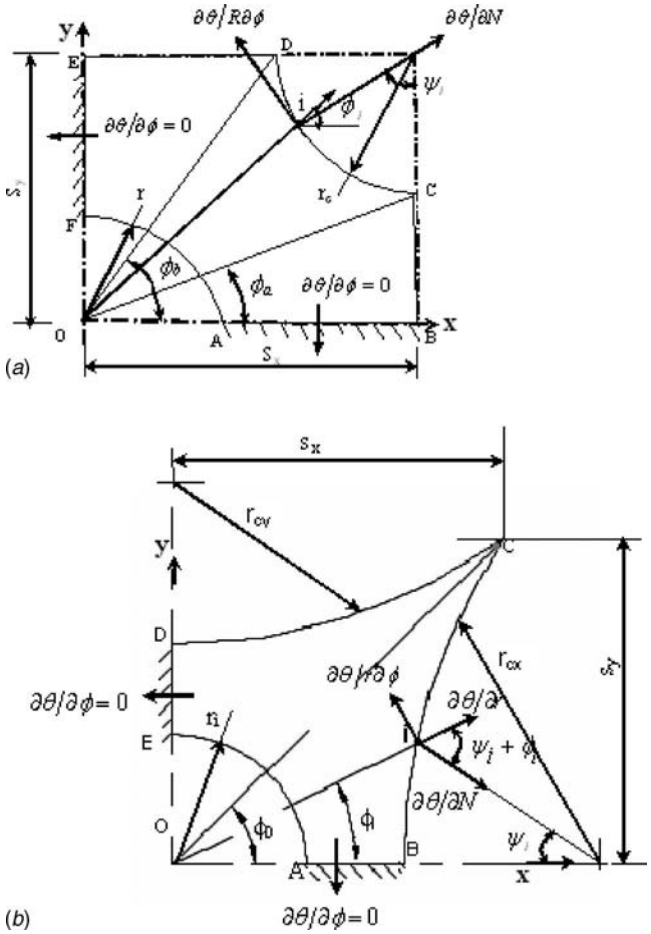

Fig. 2 Symmetric heat transfer module: (*a*) FQCT; and (*b*) FCAT

three conditions are matched exactly with their boundaries. But owing to the typical shape of the fin tip, the boundary condition (3*d*) cannot be exactly matched. For this reason, a large number of points on the boundary are chosen at which boundary condition (3*d*) is satisfied. Theoretically, for the analytical or closed form solution, an infinite number of points is to be selected along the boundary at the tip for obtaining the result. In actual practice, it is quite impossible to choose these huge points. Thus the points on the boundary have been selected in such a way that they yield the result with a desired accuracy. In other words, the number of points may be restricted due to the occurrence of numerical instability during the solution of the present problems. In this connection, it is of interest to note that the result estimated by using 20 points shows the same value (up to six decimal) in comparison with that calculated from the further increase in boundary points.

Equation (1) can be solved by the method of separating variables. Using boundary conditions (3*a*)–(3*c*), Eq. (1) can be expressed as follows

$$\theta(R,\phi) - \frac{I_0(Z_0R)}{I_0(Z_0)} = \sum_{j=1}^{\infty} \frac{C_j \cos(\lambda\phi)}{I_\lambda(Z_0)} \begin{vmatrix} I_\lambda(Z_0) & I_\lambda(Z_0R) \\ K_\lambda(Z_0) & K_\lambda(Z_0R) \end{vmatrix} \tag{5}$$

where C_j is the unknown constant. It depends on the thermophysical and geometric parameters of a fin. For different fin shapes, C_j is determined separately. To determine the constant C_j the boundary condition (3*d*) is applied. This has been achieved through a method of collocation as suggested originally by Sparrow and Lin [12]. The following mathematical steps may be needed to obtain the constant C_j for a FQCT and FCAT separately as

$$\partial\theta/\partial\phi = 0 \quad \text{at } \phi = 0 \quad (1 \leq R \leq R_t) \tag{3b}$$

$$\partial\theta/\partial\phi = 0 \quad \text{at } \phi = \pi/2 \quad (1 \leq R \leq R_t) \tag{3c}$$

$$\partial\theta/\partial N = -\beta Z_0^2\theta \quad \text{at } R = R_t \quad (0 \leq \phi \leq \pi/2) \tag{3d}$$

where

$$\beta = \begin{cases} \mathrm{Bi}^t T/\mathrm{Bi} & \text{convection from the tip} \\ 0 & \text{no heat loss from the tip} \end{cases} \tag{4}$$

and N is the direction normal to the tip.

From the above boundary conditions, it is clear that the first

$$\text{at } R = R_t = S_X/\cos\phi; \quad \cos(\phi)(\partial\theta/\partial R) - \sin(\phi)(\partial\theta/R\partial\phi) + \beta Z_0^2\theta = 0 \quad \text{for } (0 \leq \phi \leq \phi_a) \tag{6a}$$

$$\text{at } R = R_t = (S_X - R_C\sin\psi)/\cos\phi; \ \sin(\phi+\psi)(\partial\theta/\partial R) + \cos(\phi+\psi)\times(\partial\theta/R\partial\phi) + \beta Z_0^2\theta = 0 \quad \text{for } (\phi_a \leq \phi \leq \phi_b) \tag{6b}$$

$$\text{at } R = R_t = S_Y/\sin\phi; \quad \sin(\phi)(\partial\theta/\partial R) + \cos(\phi)(\partial\theta/R\partial\phi) + \beta Z_0^2\theta = 0 \quad \text{for } (\phi_b \leq \phi \leq \pi/2) \tag{6c}$$

where

$$\begin{bmatrix} \phi_a \\ \phi_b \\ \psi \end{bmatrix} = \begin{bmatrix} \tan^{-1}[(S_Y - R_C)/S_X] \\ \tan^{-1}[S_Y/(S_X - R_C)] \\ \sin^{-1}[(S_Y\cos\phi - S_X\sin\phi)/R_C] - \phi \end{bmatrix} \tag{7}$$

$$\text{at } R = R_t = R_{CX}\sin\psi/\sin\phi; \quad \cos(\phi+\psi)(\partial\theta/\partial R) - \sin(\phi+\psi)\times(\partial\theta/R\partial\phi) + \beta Z_0^2\theta = 0 \quad \text{for } (0 \leq \phi \leq \phi_0) \tag{8a}$$

$$\text{at } R = R_t = R_{CY}\sin\psi/\cos\phi; \quad \sin(\phi-\psi)(\partial\theta/\partial R) + \cos(\phi-\psi)\times(\partial\theta/R\partial\phi) + \beta Z_0^2\theta = 0 \quad \text{for } (\phi_0 \leq \phi \leq \pi/2) \tag{8b}$$

where

$$[\psi] = \begin{bmatrix} \sin^{-1}[\sin(\phi)(S_x + \sqrt{R_{CX}^2 - S_Y^2})/R_{CX}] - \phi & (0 \leq \phi \leq \phi_0) \\ \phi - \cos^{-1}[\cos(\phi)(S_Y + \sqrt{R_{CY}^2 - S_X^2})/R_{CY}] & (\phi_0 \leq \phi \leq \pi/2) \end{bmatrix} \tag{9}$$

Equations (6)–(9) can be expanded along the boundary at the tip by using Eq. (5) as follows

$$\sum_{j=1}^{n} C_j G_{ij} = P_i \quad \text{for } i = 1,2,\ldots\ldots,n \tag{10}$$

where, the expressions of C_j, G_{ij}, and P_i can be written for the FQCT and FCAT, respectively, as

$$[G_{ij}] = \frac{\cos(\lambda\phi_i)}{R_t I_\lambda(Z_0)} \begin{bmatrix} Z_0 R_t D_1 \cos\phi_i + E_1 D_2 & \text{for } (0 \leqslant \phi_i \leqslant \phi_a) \\ Z_0 R_t D_1 \sin(\phi_i + \psi_i) + E_2 D_2 & \text{for } (\phi_a \leqslant \phi_i \leqslant \phi_b) \\ Z_0 R_t D_1 \sin\phi_i + E_3 D_2 & \text{for } (\phi_b \leqslant \phi_i \leqslant \pi/2) \end{bmatrix} \tag{11}$$

$$\begin{bmatrix} D_1 \\ D_2 \end{bmatrix} = \begin{bmatrix} I_\lambda(Z_0) K_{\lambda+1}(Z_0 R_t) + I_{\lambda+1}(Z_0 R_t) K_\lambda(Z_0) \\ I_\lambda(Z_0 R_t) K_\lambda(Z_0) - I_\lambda(Z_0) K_\lambda(Z_0 R_t) \end{bmatrix} \tag{12}$$

$$\begin{bmatrix} E_1 \\ E_2 \\ E_3 \end{bmatrix} = \begin{bmatrix} \lambda\cos\phi_i + \lambda\sin(\phi_i)\tan(\lambda\phi_i) + \beta Z_0^2 R_t \\ \lambda\sin(\phi_i + \psi_i) - \lambda\cos(\phi_i + \psi_i)\tan(\lambda\phi_i) + \beta Z_0^2 R_t \\ \lambda\sin\phi_i - \lambda\cos(\phi_i)\tan(\lambda\phi_i) + \beta Z_0^2 R_t \end{bmatrix} \tag{13}$$

and

$$[P_i] = \frac{Z_0}{I_0(Z_0)} \begin{bmatrix} I_1(Z_0 R_t)\cos(\phi_i) + \beta Z_0 I_0(Z_0 R_t) & \text{for } (0 \leqslant \phi_i \leqslant \phi_a) \\ I_1(Z_0 R_t)\sin(\phi_i + \psi_i) + \beta Z_0 I_0(Z_0 R_t) & \text{for } (\phi_a \leqslant \phi_i \leqslant \phi_b) \\ I_1(Z_0 R_t)\sin(\phi_i) + \beta Z_0 I_0(Z_0 R_t) & \text{for } (\phi_b \leqslant \phi_i \leqslant \pi/2) \end{bmatrix} \tag{14}$$

$$[G_{ij}] = \begin{bmatrix} D_3 & \text{for } (0 \leqslant \phi_i \leqslant \phi_0) \\ D_4 & \text{for } (\phi_0 \leqslant \phi_i \leqslant \pi/2) \end{bmatrix} \tag{15}$$

where

$$D_3 = \frac{\cos(\lambda\phi_i)}{R_t I_\lambda(Z_0)} \begin{vmatrix} 0 & -Z_0 R_t \cos(\phi_i + \psi_i) & E_4 \\ I_\lambda(Z_0 R_t) & I_\lambda(Z_0) & -I_{\lambda+1}(Z_0 R_t) \\ K_\lambda(Z_0 R_t) & K_\lambda(Z_0) & K_{\lambda+1}(Z_0 R_t) \end{vmatrix} \tag{16}$$

$$D_4 = \frac{\cos(\lambda\phi_i)}{R_t I_\lambda(Z_0)} \begin{vmatrix} 0 & -Z_0 R_t \sin(\phi_i - \psi_i) & E_5 \\ I_\lambda(Z_0 R_t) & I_\lambda(Z_0) & -I_{\lambda+1}(Z_0 R_t) \\ K_\lambda(Z_0 R_t) & K_\lambda(Z_0) & K_{\lambda+1}(Z_0 R_t) \end{vmatrix} \tag{17}$$

$$\begin{bmatrix} E_4 \\ E_5 \end{bmatrix} = \begin{bmatrix} \lambda\cos(\phi_i + \psi_i) + \lambda\sin(\phi_i + \psi_i)\tan(\lambda\phi_i) + \beta Z_0^2 R_t & \text{for } (0 \leqslant \phi_i \leqslant \phi_0) \\ \lambda\sin(\phi_i - \psi_i) - \lambda\cos(\phi_i - \psi_i)\tan(\lambda\phi_i) + \beta Z_0^2 R_t & \text{for } (\phi_0 \leqslant \phi_i \leqslant \pi/2) \end{bmatrix} \tag{18}$$

and

$$[P_i] = \frac{Z_0}{I_0(Z_0)} \begin{bmatrix} \cos(\phi_i + \psi_i) I_1(Z_0 R_t) + \beta Z_0 I_0(Z_0 R_t) & \text{for } (0 \leqslant \phi_i \leqslant \phi_0) \\ \sin(\phi_i - \psi_i) I_1(Z_0 R_t) + \beta Z_0 I_0(Z_0 R_t) & \text{for } (\phi_0 \leqslant \phi_i \leqslant \pi/2) \end{bmatrix} \tag{19}$$

The above Eqs. (11)–(19) are functions of angle ϕ_i which can be selected as follows

$$\phi_i = \pi i/[2(1+n)] \tag{20}$$

Equation (10) provides a family of 'n' numbers of simultaneous equations. They are solved by the Gauss elimination method [15] to obtain 'n' numbers of unknown constants ($C_1 - C_n$). Temperature distribution in the fin can now be determined from Eq. (5) by substituting these unknown constants $C_1 - C_n$, when geometry of a fin, tip loss parameter β, and fin parameter Z_0 are known.

The rate of heat transfer through a flat plate fin can be calculated from the known temperature distribution in the fin by applying Fourier's law of heat conduction at the base as

$$[Q] = [q/4\pi k r_i (T_b - T_a)] = \left[-\frac{2T}{\pi} \int_0^{\pi/2} (\partial\theta/\partial R)_{R=1} d\phi \right]$$

$$= \left[\frac{Z_0 T}{I_0(Z_0)} \right] \{ C_1 W[K_0(Z_0), I_0(Z_0)] - I_1(Z_0) \} \tag{21}$$

where W is the Wronskian determinant given as

$$W[K_0(Z_0), I_0(Z_0)] = \begin{vmatrix} K_0(Z_0) & I_0(Z_0) \\ d[K_0(Z_0)]/dZ_0 & d[I_0(Z_0)]/dZ_0 \end{vmatrix} = 1/Z_0 \tag{22}$$

Combining Eqs. (21) and (22), it yields the dimensionless heat dissipation rate expressed as

$$[Q] = T[C_1 - Z_0 I_1(Z_0)]/I_0(Z_0) \tag{23}$$

The fin efficiency is defined as the ratio of actual heat transfer rate to the maximum or ideal heat transfer rate. The ideal heat transfer rate can be calculated if the entire fin surface is maintained at its base temperature. The ideal heat transfer rate for the aforementioned two geometric fins can be expressed in dimensionless form as

$$[Q_i] = \begin{bmatrix} q_i/4\pi k r_i(T_b - T_a) \\ \mathrm{Bi}[4S_XS_Y - \pi R_C^2 - \pi + 4\beta(S_X + S_Y - 2R_C + \pi R_C/2)]/2\pi \\ \mathrm{Bi}[4S_XS_Y - \pi - 2\psi_0 R_{CX}^2 - 2\psi_{00}R_{CY}^2 + D_5 + 4\beta(\psi_0 R_{CX} + \psi_{00}R_{CY})]/2\pi \end{bmatrix} \begin{matrix} \\ \text{for FQCT} \\ \text{for FCAT} \end{matrix} \tag{24}$$

where

$$\begin{bmatrix} D_5 \\ \psi_0 \\ \psi_{00} \end{bmatrix} = \begin{bmatrix} 2S_Y\sqrt{R_{CX}^2 - S_Y^2} + 2S_X\sqrt{R_{CY}^2 - S_X^2} \\ \sin^{-1}[\sin(\phi_0)(S_X + \sqrt{R_{CX}^2 - S_Y^2})/R_{CX}] - \phi_0 \\ \phi_0 - \cos^{-1}[\cos(\phi_0)(S_Y + \sqrt{R_{CY}^2 - S_X^2})/R_{CY}] \end{bmatrix} \tag{25}$$

Mathematically, the fin efficiency can be defined as

$$[\eta] = [Q/Q_i] \tag{26}$$

The fin effectiveness is defined as the ratio of the rate of actual heat transfer (Q) through a fin to that would be transferred (Q_e) through the same base surface area if the fin was not present

$$[Q_e] = \begin{bmatrix} q_e/4\pi k r_i(T_b - T_a) \\ \mathrm{Bi}\, T \end{bmatrix} \tag{27}$$

Thus the fin effectiveness can be defined as

$$[\varepsilon] = [Q/Q_e] \tag{28}$$

In this connection, it is worth noting that the performance analysis ofFCTs may be readily determined from the foregoing analysis of the FQCT with the only choice of zero value of R_C.

2.2 Optimization. An effort is made to carry out the optimum design analysis of the three types of flat fins followed by the previous analysis. The volume of the different fins can be expressed in nondimensional forms as follows

$$[U] = \begin{bmatrix} V/2r_i^3 \\ T(4S_XS_Y - \pi - \pi R_C^2) \\ T(4S_XS_Y - 2\psi_0 R_{CX}^2 - 2\psi_{00}R_C^2 + 2S_Y\sqrt{R_{CX}^2 - S_Y^2} + 2S_X\sqrt{R_{CY}^2 - S_X^2} - \pi) \end{bmatrix} \begin{matrix} \\ \text{for FQCT} \\ \text{for FCAT} \end{matrix} \tag{29}$$

In this section, it is noteworthy to mention that for the determination of the optimum dimensions, the tip heat transfer coefficient is assumed to be constant and it is equal to the lateral surface heat transfer coefficient. Thus the tip loss parameter β is a sole function of T for the present optimization analysis. For a given Bi, both the fin volume (U) and heat transfer rate (Q) are functions of T, S_X, S_Y, and radius of circular cut R_p (R_p=R_C for the FQCT, R_p=R_{CX}=R_{CY} for the FCAT). The optimum dimensions can be obtained either by maximizing the rate of heat transfer for a given fin volume or by minimizing the volume for a given heat transfer rate. The generalized conditions for optimality can be derived from the Euler–Lagrange equations [16]. If the Lagrange multiplier is eliminated from the Euler–Lagrange equations, the conditions for the optimality can be expressed as Jacobian determinants of Q and U with respect to T, S_x, S_y, and R_p separately. It yields

$$J\left(\frac{Q,U}{T,S_X}\right) = \frac{\partial(Q,U)}{\partial(T,S_X)} = \begin{vmatrix} \partial Q/\partial T & \partial Q/\partial S_X \\ \partial U/\partial T & \partial U/\partial S_X \end{vmatrix} = 0 \tag{30}$$

$$J\left(\frac{Q,U}{S_X,S_Y}\right) = \frac{\partial(Q,U)}{\partial(S_X,S_Y)} = \begin{vmatrix} \partial Q/\partial S_X & \partial Q/\partial S_Y \\ \partial U/\partial S_X & \partial U/\partial S_Y \end{vmatrix} = 0 \tag{31}$$

and

$$J\left(\frac{Q,U}{S_Y,R_p}\right) = \frac{\partial(Q,U)}{\partial(S_Y,R_p)} = \begin{vmatrix} \partial Q/\partial S_Y & \partial Q/\partial R_p \\ \partial U/\partial S_Y & \partial U/\partial R_p \end{vmatrix} = 0 \tag{32}$$

Equations (30)–(32) can be simplified by using Eqs. (23) and (29). It yields the following for the respective FQCT and FCAT as

FQCT

$$\begin{bmatrix} J(Q,U/T,S_X) \\ J(Q,U/S_X,S_Y) \\ J(Q,U/S_Y,R_p) \end{bmatrix} = \begin{bmatrix} 4S_Y\{I_0(Z_0)[C_1 + T\partial C_1/\partial T + Z_0^2 I_2(Z_0)] + 0.5Z_0 I_1(Z_0)[C_1 + Z_0 I_1(Z_0)]\} - \tau \\ S_X\partial C_1/\partial S_X - S_Y\partial C_1/\partial S_Y \\ R_C\pi\partial C_1/\partial S_Y + 2S_X\partial C_1/\partial S_Y \end{bmatrix} = \begin{bmatrix} 0 \\ 0 \\ 0 \end{bmatrix} \tag{33}$$

where

$$\tau = I_0(Z_0)(4S_XS_Y - \pi - \pi R_C^2)\partial C_1/\partial S_X = 0 \tag{34}$$

FCAT

$$\begin{bmatrix} J(Q,U/T,S_X) \\ J(Q,U/S_X,S_Y) \\ J(Q,U/S_Y,R_p) \end{bmatrix} = \begin{bmatrix} 2O_1O_2 - I_0(Z_0)O_3\partial C_1/\partial S_X \\ O_4\partial C_1/\partial S_X - O_2\partial C_1/\partial S_Y \\ O_5\partial C_1/\partial S_Y - O_4\partial C_1/\partial R_p \end{bmatrix} = \begin{bmatrix} 0 \\ 0 \\ 0 \end{bmatrix} \tag{35}$$

where

$$\begin{bmatrix} O_1 \\ O_2 \\ O_3 \\ O_4 \end{bmatrix} = \begin{bmatrix} I_0(Z_0)[C_1 + T\partial C_1/\partial T + Z_0^2 I_2(Z_0)] + 0.5 Z_0 I_1(Z_0)[C_1 + Z_0 I_1(Z_0)] \\ 2S_Y - R_p^2 \partial\psi_0/\partial S_X - R_p^2 \partial\psi_{00}/\partial S_X + \sqrt{R_p^2 - S_X^2} - S_X^2/\sqrt{R_p^2 - S_X^2} \\ 4S_X S_Y - 2\psi_0 R_p^2 - 2\psi_{00} R_p^2 + 2S_Y\sqrt{R_p^2 - S_Y^2} + 2S_X\sqrt{R_p^2 - S_X^2} - \pi \\ 2S_X - R_p^2 \partial\psi_0/\partial S_Y - R_p^2 \partial\psi_{00}/\partial S_Y + \sqrt{R_p^2 - S_X^2} - S_Y^2/\sqrt{R_p^2 - S_Y^2} \end{bmatrix} \tag{36}$$

and

$$O_5 = \begin{cases} -2\psi_0 R_p + S_Y R_p (R_p - S_Y)^{-1/2} & \text{for } 0 \leq \phi \leq \phi_0 \\ -2\psi_{00} R_p + S_X R_p (R_p - S_X)^{-1/2} & \text{for } \phi_0 \leq \phi \leq \pi/2 \end{cases} \tag{37}$$

For the estimation of the above derivatives like $\partial C_1/\partial T$, $\partial C_1/\partial S_X$, $\partial C_1/\partial S_Y$, and $\partial C_1/\partial R_p$, Eq. (10) is differentiated with respect to T, S_X, S_Y, and R_p separately. It yields

$$\begin{bmatrix} \sum_{j=1}^{n} (G_{ij}\partial C_j/\partial T + C_j \partial G_{ij}/\partial T) \\ \sum_{j=1}^{n} (G_{ij}\partial C_j/\partial S_X + C_j \partial G_{ij}/\partial S_X) \\ \sum_{j=1}^{n} (G_{ij}\partial C_j/\partial S_Y + C_j \partial G_{ij}/\partial S_Y) \\ \sum_{j=1}^{n} (G_{ij}\partial C_j/\partial R_p + C_j \partial G_{ij}/\partial R_p) \end{bmatrix} = \begin{bmatrix} \partial P_i/\partial T \\ \partial P_i/\partial S_X \\ \partial P_i/\partial S_Y \\ \partial P_i/\partial R_p \end{bmatrix}$$
$$\text{for } i = 1,2, \ldots \ldots ,n \tag{38}$$

A family of n number of equations containing the first-order partial derivatives, viz. $\partial C_j/\partial T$, $\partial C_j/\partial S_X$, $\partial C_j/\partial S_Y$, and $\partial C_j/\partial R_p$ are described in Eq. (38). To determine these derivatives, the first-order partial derivative $\partial G_{i,j}/\partial T$, $\partial G_{i,j}/\partial S_X$, $\partial G_{i,j}/\partial S_Y$, and $\partial G_{i,j}/\partial R_p$ are to be provided to proceed for solving Eq. (38). For this requirement, differentiating Eqs. (11)–(14), and Eqs. (15)–(19) is essential for the analysis of FQCT and FCAT, respectively.

The optimality criteria for flat-plate fins expressed in Eqs. (30)–(32) have been made based on the generalized approach of optimization. For determining the optimum design variables, we need to solve Eqs. (33) and (35) simultaneously with an equation of the constraint of either heat transfer duty or fin volume. The generalized Newton–Raphson technique [15] is adopted to solve these simultaneous equations. The convergence criteria and the root finding algorithm of this numerical scheme are found elsewhere [15]. Here it can be mentioned that to run any iteration, the second-order partial derivation of C_j with respect to T, S_X, S_Y, and R_p separately are provided and the second-order product derivation of C_j for the said variables are also necessary. The iteration of the said numerical method may be repeated until a desired accuracy (10^{-8} for the present problem) has been attained. Thus the final values of the dimensionless parameters like T_{opt}, $(S_X)_{\text{opt}}$, $(S_Y)_{\text{opt}}$, and $(R_P)_{\text{opt}}$ i.e., the optimum dimensionless thickness, the optimum dimensionless length, the optimum dimensionless width, and the optimum dimensionless radius of circular cut are estimated at the end of the iterations by satisfying this convergence criterion. Next, for the known values of the thermophysical and geometrical parameters, namely, the heat transfer coefficient h, the thermal conductivity of the fin material k, the outer radius of the tube r_i, the fin temperature at the root T_b and the ambient temperature T_a, one can easily calculate the optimum fin length (s_x), the optimum fin width (s_y), the optimum thickness (t), optimum radius (r_p), and either the maximum heat transferred duty or the minimum fin volume according to a design constraint adopted.

3 Results and Discussion

For the validation of the present theoretical model, no such existing result is available in the literature. However, in fin-and-tube heat exchangers, the heat from a particular tube dissipated by a square module of the plate circumscribing a circular tube [12] is equivalent to a system of transmitted heat through the square shape of a FCT with an insulated tip condition. Thus a direct evaluation of the fin efficiency of FCTs with insulated tip using the present analysis has been compared with that obtained by Sparrow and Lin [12]. For the analysis of a FCT, it is worth mentioning that the fin efficiency of a FCT can be determined from the performance analysis of both FQCT and FCAT if the geometrical parameter R_C or each R_{CX} and R_{CY} are considered to be zero or infinity respectively. For the computation, it is not practicable for choosing an infinite value of radius of circular cut. Thus, a very high value for R_{CX} or R_{CY} should be selected in such a way that with any changes from its value, the final result has not been affected. Figure 3 depicts the exact agreement between the present technique and the results obtained by Sparrow and Lin [12]. From the figures, it can also be established that the fin performance of FCTs calculated by the sector method [13] gives an

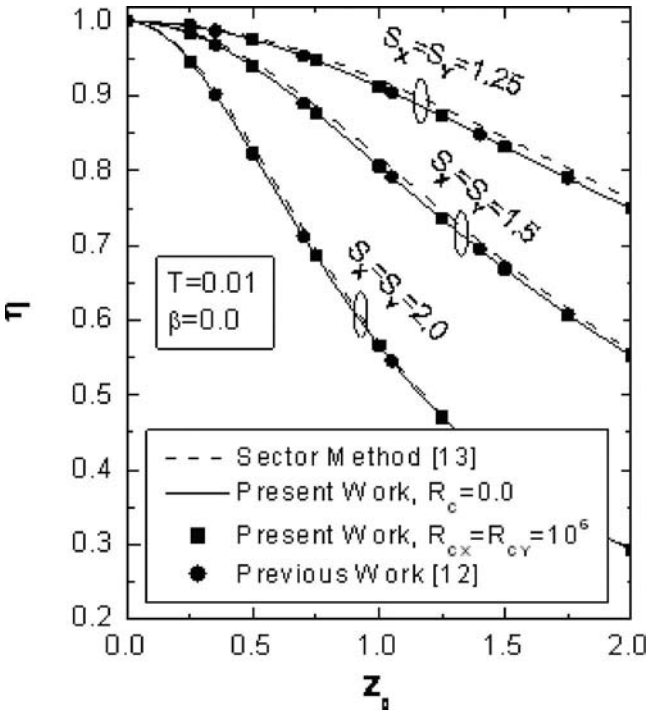

Fig. 3 Validation of the present result for FCTs with the existing results

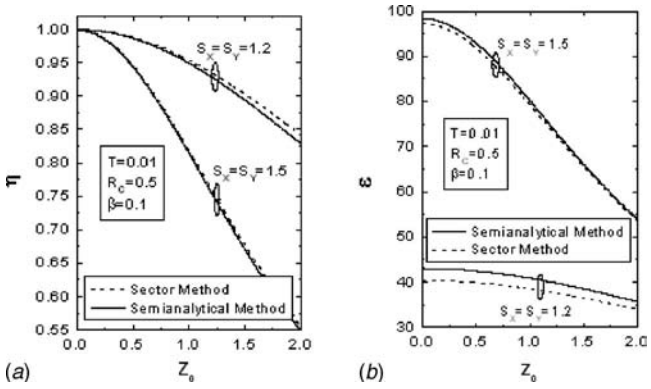

Fig. 4 Comparisons of semianalytical and sector methods on prediction of fin performances for FQCT: (*a*) fin efficiency; and (*b*) fin effectiveness

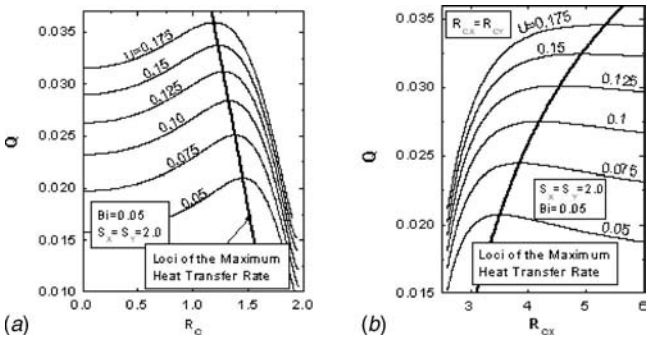

Fig. 6 Effects of radius of circular cut on the heat transfer rate for the constraints S_X, S_Y and U: (*a*) FQCT; and (*b*) FCAT

overprediction. But the fin efficiency of a FCT with insulated tip is strongly dependent on the fin parameter Z_0, half length S_X, and half width S_Y.

The fin performance of a FQCT and a FCAT computed by the present method of analysis can be compared with the corresponding value obtained by the sector method [13] which is depicted in Fig. 4. Both the fin efficiency and fin effectiveness predicted from the sector method are in closer assessment with that estimated from the semianalytical method. However, it was shown in previous investigations regarding accuracy of the prediction that the error occurring for the forecast of fin efficiency of circumferential fins on a round tube using the sector method gradually increases with the increase in two-dimensional temperature field. This observation has also been found in the present study.

From the present mathematical modeling, it can be mentioned that the temperature distribution in different flat fins is a function of the fin parameter Z_0, tip loss parameter β, dimensionless thickness T, and the shape of the fin. The isotherm lines drawn in the flat plate fin with different shapes are reproduced in Fig. 5 for $Z_0=1.3$, $S_X=S_Y=3.0$, and $\beta=0.0$. Due to the typical shape of a fin,

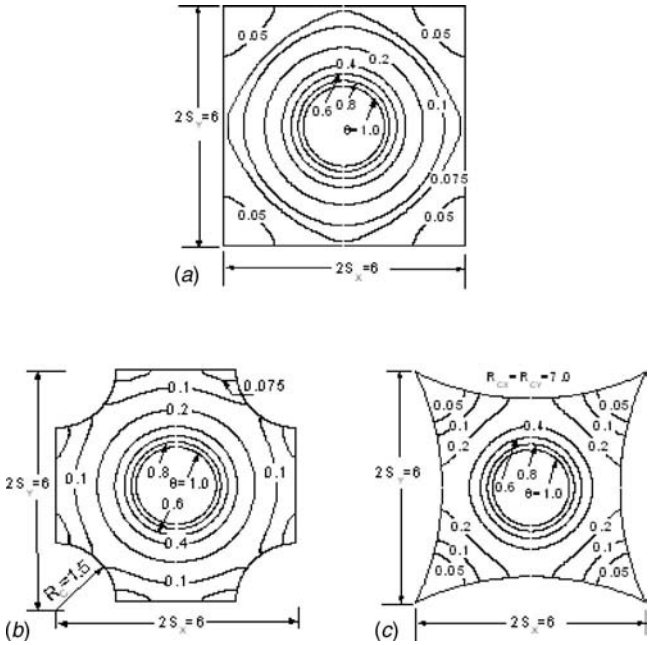

Fig. 5 Isotherms in the different flat fins for $Z_0=1.3$ and $\beta=0.0$: (*a*) FCT; (*b*) FQCT; and (*c*) FCAT

the heat conduction takes place in both the radial as well as in the peripheral direction. However, this two-dimensional effect is more prominent towards the fin tip. Also, the effect of radius of circular cut influences the increase in the two-dimensional temperature field.

In the present optimization problem of FCTs, both the constraint and optimality criteria are functions of S_X, S_Y, and T provided the coefficient of heat transfer at the tip and coefficient of heat transfer for the lateral surfaces are assumed to be the same. Again, Bi depends on h, r_i, and k which may be the known thermogeometric parameters for a desired fin design problem. Therefore, for a given Bi, the optimum design for a FQCT depends on S_X, S_Y, T, and R_C, whereas for a FCAT it depends on S_X, S_Y, T, R_{CX}, and R_{CY}. So, optimization of a FCT may be done through the optimization analysis of either FQCT or FCAT if the choice of R_C or both R_{CX} and R_{CY} is taken as zero or a very large value (say 10^{10}). The effects of the possible constraints on the optimization analysis have also been investigated in this assignment.

The effect of radius of circular cut near the tip for both the FQCT and FCAT on the heat transfer rate is shown in Fig. 6 while fin volume, Bi, and lengths S_X and S_Y have been taken as constant. With a constant fin volume in Fig. 6(*a*), the heat transfer rate increases initially with the increase in R_C, reaches a maximum value, and then declines with the further increase in R_C. All peaks on the constant volume curves represent the optimum design of a FQCT under a specified design condition. For a FCAT, a similar trend has also been noticed which is illustrated in Fig. 6(*b*). It can also be shown from these figures that loci of the optimum radius of the circular cut of the FQCT decreases with the increase in fin volume. But, in the case of FCATs, its value increases with the fin volume. From the figures, it may be concluded that the heat dissipation rate from the FQCT and FCAT for an optimum radius of circular cut is always higher than that from the FCT under the constraint of both length and volume. It may be further noted from Fig. 6(*a*) that with the increase in R_C from its optimum value, heat transfer rate Q decreases drastically with R_C, and heat dissipation rate from a FQCT with a larger radius of circular cut R_C may attain a smaller value than the corresponding FCT for an identical fin volume.

An optimization scheme for FQCT has been developed subject to maximizing heat transfer rate under the constraints of a space restriction parameter S_Y and fin volume U. The result is presented in Fig. 7 for the variation of the optimum parameters with U for different Biot numbers and a space constraint $S_Y=2.0$. Figure 7(*a*) illustrates the variation of the maximum heat transfer rate as a function of U. For comparison, heat transfer rate through an ADF under the same constraint is determined and this result is also plotted in the same figure. Under these design circumstances, it is noteworthy to mention that the heat dissipation rate from a FQCT is greater than that from the corresponding ADF. However, this incremental heat transfer rate is also a function of Bi. Figures

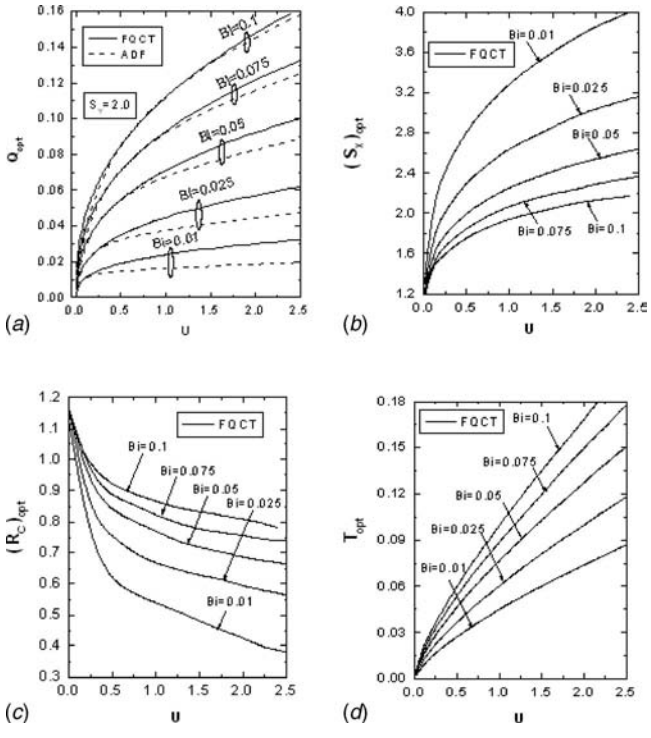

Fig. 7 Design variables of an optimum FQCT as a function of fin volume U for a space restriction S_Y: (*a*) Q_{opt}; (*b*) $(S_X)_{opt}$; and (*c*) $(R_C)_{opt}$; and (*d*) T_{opt}

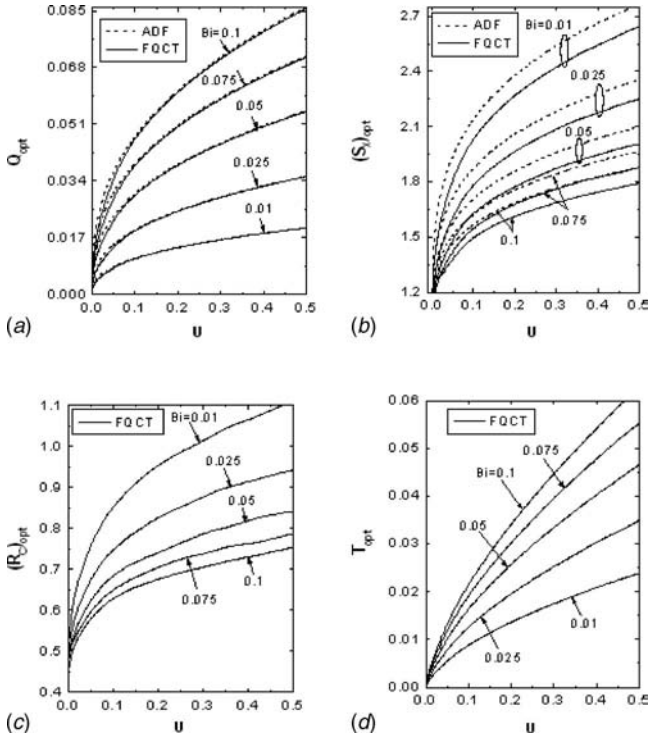

Fig. 8 Variation of the optimum design variables of FQCT with the dimensionless fin volume U: (*a*) Q_{opt}; (*b*) $(S_X)_{opt}$; (*c*) $(R_C)_{opt}$; and (*d*) T_{opt}

7(*b*)–7(*d*) represent the variation of the optimum length $(S_X)_{opt}$, optimum radius cut $(R_C)_{opt}$, and optimum half-thickness T_{opt} with the fin volume for a design condition. From these figures, it is clear that for a constant Bi, the optimum geometrical parameter $[(S_X)_{opt}$, $(R_C)_{opt}$, or $T_{opt}]$ increases or decreases monotonically with the fin volume. In the case of $(S_X)_{opt}$ and T_{opt}, they are related to the fin volume separately as an increasing function, whereas the optimum variable $(R_C)_{opt}$ decreases with an increase in fin volume. Finally, it can be demonstrated that for the fin design problem with length constraints, FQCT and FCAT are superior to ADF which would motivate the researcher to choose this type of fin geometry over ADF. Therefore, these design plots would be useful for estimating the optimum design variables of FQCT with a space restriction.

The optimization study has also been carried out by taking into consideration only fin volume as a constraint. From the optimization information, it can be pointed out that an optimum criterion is satisfied for the FCT and FQCT with the variation of all the design variables, whereas a FCAT has a tendency to convert an optimum FCT. It is also mentioned that the optimum dimensionless lengths S_X and S_Y are found to be of equal value $[(S_X)_{opt} = (S_Y)_{opt}]$ for all the flat-plate fins considered in the present analysis with the constraint of fin volume. This outcome is found probably due to a uniform base temperature and circular shape of the base considered in the analysis.

For the purposes of estimating the optimum design variables of FQCTs, plots have been generated for a wide range of thermogeometric parameters. The families of curves presented in Fig. 8 can be used as a guideline for the optimum design of FQCTs. Generally, for the design of a fin, Biot number must be determined from the flow condition of a required heat duty. For this, h should be estimated from the existing convective condition, and k and r_i should be known. Therefore, these known values of Q and Bi fix the design point on the plane of a design graph (Fig. 8(*a*)). From this design point, the required fin volume is determined directly from Fig. 8(*a*). Using these two pieces of information, the optimum length S_X, the optimum radius of circular cut R_C, and the optimum fin thickness can be calculated from Figs. 8(*b*)–8(*d*), respectively. In addition, an exercise has been devoted to compare the optimum variables for a FQCT and the corresponding ADF determined by using Brown's model [8] for the same fin volume and Biot number which is also shown in Figs. 8(*a*) and 8(*b*). From Fig. 8(*a*), it is clear that an optimum ADF transfers more rate of heat than that by the optimum FQCT. However, this superiority is insignificant. Furthermore from Fig. 8(*b*), it can be demonstrated that an optimum length S_X for FQCT is greater or smaller than the optimum outer radius (in the present notation S_X) for ADF depending solely upon the Biot number. For a lower value of Bi, this value for a FQCT is considerably lower than that for an ADF. Therefore from a design point of view, this knowledge may be essential for the selection of a fin geometry of either FQCT or ADF when the size of a heat exchanger would be given priority over the heat transfer rate.

4 Conclusions

Fins with varying thickness profiles like circular, parabolic, hyperbolic, triangular, etc. always perform better than the uniform thickness fin by means of heat transfer rate per unit volume of the fin material. Unfortunately, all these profiles have some serious disadvantages because they are too complex to manufacture, and too fragile at the sharp ends. Hence, they are more expensive for fabrication. In lieu of this uniform thickness fins are the simplest and most widely used. Modifications of the fin shape for the uniform thickness fin near the tip are still essential for the gradual decrease in heat conduction along the fin length.

In the present study, two new flat plate fin geometries, namely FQCT and FCAT, have been proposed for improving the heat transfer rate per unit volume with respect to a FCT without changing its profile shape. A semianalytical approach is adopted to compute the temperature distribution and fin performances of the

FQCT and FCAT. From the results, it is perceived that these two simple modified geometries used for the augmentation in heat transfer are shown to improve the fin efficiency for the same thermogeometric parameters. However, for the fin effectiveness, a reversed trend has been found.

Optimization of these two modified fins has been done in a generalized scheme. From the optimization results, it can be demonstrated that, for both the volume and length constraints, there exists an optimum radius of circular cut for both the fins. In the absence of the length constraint, it may not be possible to reach an optimum point for a FCAT. However, for the FQCT, heat transfer rate is maximized at a particular radius of circular cut under the same design condition. From a comparative study, it may be demonstrated that the heat transfer rate through an optimum ADF is marginally greater than that through an optimum FQCT for a given fin volume and Bi. However, a smaller envelope shape of a FQCT may be obtained in comparison with the corresponding ADF at the optimum point. This comparative result may be justified for the lower value of Bi. But under an additional length constraint, FQCT may transfer more rate of heat than an ADF. Nevertheless, for any circumstances, the proposed flat plate fin (FQCT or FCAT) dissipates more rate of heat compared to a conventional flat plate fin (FCT) for identical volume and thermophysical parameters. Therefore, the proposed flat fins may be adopted by a designer for better utilization of fin material and consequently they provide a better fin efficiency. For the imposition of length constraints according to the requirement of a design, an alternative ADF using a proposed flat plate fin has been reasonably established.

Finally, it can be mentioned that any other modification of the geometrical shape of the plate fin is possible, for example, considering a straight cut or a reversed circular arc cut at the corner of the tip. The analysis of this typical geometry can be done by using the present analysis with a slight modification. This optimized geometry may be able to provide a higher heat dissipation rate than a conventional plate fin under the same constraints.

Acknowledgment

This research is financially supported by the Jadavpur University (Research Project Grant No. P-1/1057/05 under Seed Support of Potential for Excellence Scheme) whose assistant is hereby gratefully acknowledged.

Nomenclature

ADF = annular disk fin

Bi = Biot number based on the lateral surface heat transfer coefficient, hr_i/k

Bi^t = Biot number based on the tip surface heat transfer coefficient, $h^t r_i/k$

C_j = unknown constants determined from the tip boundary condition

FCAT = flat plate fin of uniform thickness with circular arc to cut at the tip

FCT = flat plate fin of uniform thickness circumscribing a circular tube

FQCT = flat plate fin of uniform thickness with quarter circular cut at the corner of the tip

G_{ij} = variable used in Eq. (11)

h = convective heat transfer coefficient on the lateral surface ($\mathrm{W/m^2\,K}$)

h^t = convective heat transfer coefficient on the tip surface ($\mathrm{W/m^2\,K}$)

i = ith point on the tip

J = Jacobian determinant defined in Eqs. (30)–(32)

$I_m(Z)$ = modified Bessel function of first kind of order m and argument Z

k = thermal conductivity of the fin material (W/m K)

$K_m(Z)$ = modified Bessel function of second kind of order m and argument Z

n = total number of points on the tip at which the tip boundary condition is considered

P_i = variable used in Eqs. (14) and (19) for the FQCT and FCAT, respectively

q = actual rate of heat dissipation (W)

Q = dimensionless actual heat dissipation rate $[q/4\pi k r_i(T_b-T_a)]$

q_e = heat dissipation rate from the base surface with considering no fin condition (W)

Q_e = dimensionless heat dissipation rate $[q_e/4\pi k r_i(T_b-T_a)]$

q_i = ideal heat dissipation rate (W)

Q_i = dimensionless ideal heat dissipation rate $[q_i/4\pi k r_i(T_b-T_a)]$

r = radial distance of any point in the fin measured from the tube center (m)

R = dimensionless radial distance, r/r_i

r_c = radius of circular cut at the corner of the tip (m)

R_C = dimensionless radius of circular cut, r_c/r_i

r_{cx} = radius of circular arc cut at the tip as shown in Fig. 2 (m)

R_{CX} = dimensionless radius arc cut at the tip, r_{cx}/r_i

r_{cy} = radius of circular arc cut at the tip as shown in Fig. 2 (m)

R_{CY} = dimensionless radius arc cut at the tip, r_{cy}/r_i

r_i = outer radius of the tube (m)

r_t = radial tip distance from the tube center (m)

R_t = dimensionless radial tip distance, r_t/r_i

s_x = half fin length (m)

S_X = dimensionless fin length, s_x/r_i

s_y = half fin width (m)

S_Y = dimensionless fin width, s_y/r_i

t = half fin thickness (m)

T = dimensionless fin thickness, t/r_i

T_a = temperature of the surrounding fluid (K)

T_b = fin base temperature (K)

T_f = local fin temperature (K)

U = dimensionless fin volume, $V/2r_i^3$

V = fin volume ($\mathrm{m^3}$)

W = Wronskian determinant, see Eq. (22)

x,y = Cartesian coordinate shown in Fig. 2 (m)

Z_0 = fin parameter, $(\mathrm{Bi}/T)^{1/2}$

Greek Letters

β = tip loss parameter, $\mathrm{Bi}^t T/\mathrm{Bi}$

ε = fin effectiveness defined in Eq. (28)

η = fin efficiency defined in Eq. (26)

λ = eigenvalue, $2(j-1)$

θ = dimensionless temperature $(T_f-T_a)/(T_b-T_a)$

ϕ = angular position of any point in the fin (rad)

ϕ_0 = angle, see Fig. 2(b) (rad)

ϕ_a = $\tan^{-1}[(S_y-R_C)/S_x]$, see Fig. 2(a) (rad)

ϕ_b = $\tan^{-1}[S_y/(S_x-R_C)]$, see Fig. 2(a) (rad)

ϕ_i = angular position of ith point on the tip boundary of a fin (rad)

ψ = angle defined in Eqs. (7) and (9) for FQCT and FCAT, respectively (rad)

ψ_0, ψ_{00} = angle defined in Eq. (25) (rad)

ψ_i = angle, see Fig. 2 (rad)

τ = defined in Eq. (35)

Subscripts

i = ith point

opt = optimum

References

[1] Schmidt, E., 1926, "Die Warmeubertragung durch Rippen," Z. Ver. Dtsch. Inc., **70**, pp. 885–889.

[2] Duffin, R., 1959, "A Variational Problem Relating to Cooling Fins," J. Math. Mech., **8**, pp. 47–56.

[3] Guceri, S., and Maday, C. J., 1975, "A Least Weight Circular Cooling Fins," ASME J. Eng. Ind., **97**, pp. 1190–1193.

[4] Kundu, B., and Das, P. K., 2005, "Optimum Profile of Thin Fins with Volumetric Heat Generation—a Unified Approach," ASME Trans. J. Heat Transfer, **127**, pp. 945–948.

[5] Kern, Q. D., and Kraus, D. A., 1972, *Extended Surface Heat Transfer*, McGraw–Hill, New York.

[6] Kraus, A. D., 1988, "Sixty-Five Years of Extended Surface Technology (1922–1987)," Appl. Mech. Rev., **41**, pp. 321–364.

[7] Aziz, A., 1992, "Optimum Dimensions of Extended Surfaces Operating in a Convective Environment," Appl. Mech. Rev., **45**, pp. 155–173.

[8] Razelos, P., and Imre, K., 1980, "The Optimum Dimensions of Circular Fins with Variable Thermal Parameters," ASME J. Heat Transfer, **102**, pp. 420–425.

[9] Brown, A., 1965, "Optimum Dimensions of Uniform Annular Fins," Int. J. Heat Mass Transfer, **8**, pp. 655–662.

[10] Kazeminejad, H., Yaghoubi, M. A., and Sepehri, M., 1993, "Effects of Dehumidification of Air on the Performance of Eccentric Circular Fins," Int. J. Heat Mass Transfer, **207**, pp. 141–146.

[11] Kundu, B., and Das, P. K., 1999, "Performance Analysis of Eccentric Annular Fins with a Variable Base Temperature," Numer. Heat Transfer, Part A, **36**, pp. 751–766.

[12] Sparrow, E. M., and Lin, S. H., 1964, "Heat Transfer Characteristics of Polygonal and Plate Fins," Int. J. Heat Mass Transfer, **7**, pp. 951–953.

[13] Shah, R. K., 1985, "Compact Heat Exchanger," *Handbook Heat Transfer Applications*, 2nd ed., W. M. Rohsenow, J. P. Hartnett, and E. N. Ganic, eds., McGraw–Hill, New York.

[14] Kuan, D. Y., Aris, R., Davis, H. T., 1984, "Estimation of Fin Efficiencies of Regular Tubes Arrayed in Circumferential Fins," Int. J. Heat Mass Transfer, **27**, pp. 148–151.

[15] Scarborough, J. B., 1966, *Numerical Mathematical Analysis*, Oxford & IBH, New Delhi, India.

[16] Stoecker, W. F., 1989, *Design of Thermal System*, 3rd ed., McGraw–Hill, New York.

Journal of Heat Transfer

Discussion

Discussion: "An Integral Equation for the Dual-Lag Model of Heat Transfer" (Kulish, V. V., and Novozhilov, V. B., 2004, ASME J. Heat Transfer, 126, pp. 805–808)

D. Milov
RRA,
56 Burlington Street,
Lexington, MA 02420

In this paper, the authors claim in the abstract and the conclusion that the "solution with dual phase lag depends only on the difference between the two lags." Then, they proceed to derive an integral solution for the temperature history.

I show first that this conclusion is erroneous and second that the Laplace transform method they use is incorrect.

The authors claim that the system of the dual lag Eqs. (1) and (3) in their paper is equivalent to the new system of Eqs. (6) and (7) in their paper. This is quite incorrect for the following reasons:

1. To obtain Eq. (6) from Eq. (1), the authors perform the shift in time $t_{\text{old}}+\tau_q \Rightarrow t_{\text{new}}$, where t_{old} corresponds to the time in Eq. (1) and t_{new} is the time in Eq. (6).

   With this shift Eq. (3) becomes using the new time

$$\frac{\partial T}{\partial \mathrm{t}}(x,t-\tau_q) = -\frac{1}{\rho c_p}\frac{\partial q''(x,t-\tau_q)}{\partial x}$$

   whereas the authors assume that Eq. (3) does not change with the transformation of time applied to obtain Eq. (6) from Eq. (1).
2. It follows that the derivation of Eq. (7) is wrong. Equation (7) is correct only if $\tau_q=0$.

Thus, their conclusion that the "solution with dual phase lag depends only on the difference between the two lags" is wrong.

The solution that follows Eq. (7) can be applicable only when $\tau_q=0$ as pointed out in the previous discussion. In this case, Eq. (8) is fine but its Laplace transform Eq. (10) is not.

To find the Laplace of Eq. (8), we multiply both sides by $e^{-\mathrm{st}}$ and then integrate over time from $\Delta\tau$ to infinity following the notation in the subject paper.

The result is not Eq. (10) as the authors claim but the following equation

$$\frac{d^2\Theta}{dx^2} = se^{s\Delta\tau}\int_{\Delta\tau}^{\infty}\theta(x,t)e^{-\mathrm{st}}\,dt - \theta(x,\Delta\tau).$$

Here the Laplace transform of the temperature rise is defined as

$$\Theta(x,s) = \int_0^{\infty}\theta(x,t)e^{-\mathrm{st}}\,dt$$

I suggest that the subject paper be retracted.

Contributed by the Heat Transfer Division of ASME for publication in the JOURNAL OF HEAT TRANSFER. Manuscript received May 26, 2005; final manuscript received January 30, 2006. Review conducted by Yogesh Jaluria.

 Copyright © 2007 by ASME

Closure to "Discussion of 'An Integral Equation for the Dual-Lag Model of Heat Transfer' (Milov, D., 2007, ASME J. Heat Transfer, 129, p. 927)"

Vladimir Kulish
e-mail: mvvkulish@ntu.edu.sg

Vasily Novozhilov

Nanyang Technological University,
50 Nanyang Avenue,
Singapore, 639798

Both comments from our opponent are incorrect.

Comment 1.

For the purpose of mathematical model derivation, relations (1) and (3) are identities which hold for any $-\infty < t < +\infty$. They are invariant with respect to any shift of independent variable and those shifts can be made completely independently in those relations without compromising their correctness for any $-\infty < t < +\infty$.

Contributed by the Heat Transfer Division of ASME for publication in the JOURNAL OF HEAT TRANSFER. Manuscript received June 2, 2005; final manuscript received June 6, 2005. Review conducted by Vijay Dhir.

For example, one can write this pair of relations in the form

$$q''(x,t+\tau_q) = -k\frac{\partial T}{\partial x}(x,t+\tau_T) \qquad (*)$$

$$\frac{\partial T}{\partial t}(x,t+\tau_q) = -\frac{1}{\rho c_p}\cdot\frac{\partial q''(x,t+\tau_q)}{\partial x} \qquad (**)$$

both are true for any $-\infty < t < +\infty$.

Now one can substitute (*) into (**), make transformation of variable $t+\tau_q=\tilde{t}$ and get (6). This is just another way to derive Eq. (6). Of course, the original derivation in the paper is absolutely correct.

Comment 2.

Laplace transform of Eq. (8) is its integration from 0 to ∞ (as it should be), and not from $\Delta\tau$ to ∞. The way we make it is clear from the initial condition (9) which is set at $t=0$. This initial condition leads to transform equation in the form (10).

Note that for real materials $\Delta\tau < 0$ (see comments on p. 807 of the paper).

The way we specify domain in (8), i.e., $t \in [\Delta\tau, \infty[$ is just to emphasize that Eq. (6) also holds true for $t \in [\Delta\tau, 0]$. In fact, for the boundary conditions that we are considering the both sides of (8) are identically zero at this interval.

In order to see this, analyse the final integral equation (18). (We have requested to remove (*) from the formulas (17–19) at the proof stage, but it is still there. These equations should contain t only, not t^*.) Considering $t \in [\Delta\tau, \infty[$ one would see that for imposed fluxes that are identically zero for $t < 0$ (we are considering only such fluxes) the integral term turns into zero in the interval $t \in [\Delta\tau, 0[$.

 Copyright © 2007 by ASME